Satellite and model analysis of long-term changes in tropospheric composition, with a focus on European ozone

Matilda Alice Pimlott

Submitted in accordance with the requirements for the degree of
Doctor of Philosophy

The University of Leeds

School of Earth and Environment

August 2023

Intellectual Property and Publication Statements

The candidate confirms that the work submitted is her own, except where work which has formed part of jointly authored publications has been included. The contribution of the candidate and the other authors to this work has been explicitly indicated below. The candidate confirms that appropriate credit has been given within the thesis where reference has been made to the work of others.

The work in Chapter 4 of the thesis has appeared in publication as follows:

Pimlott, M.A., Pope, R.J., Kerridge, B.J., Latter, B.G., Knappett, D.S., Heard, D.E., Ventress, L.J., Siddans, R., Feng, W., Chipperfield, M.P. 2022. Investigating the global OH radical distribution using steady-state approximations and satellite data. *Atmospheric Chemistry and Physics*. 22(16), pp.10467–10488.

I led the work with the support of the co-authors. Martyn Chipperfield, Richard Pope, Brian Kerridge and I conceptualised and planned the research study. I performed the TOMCAT model simulations and the processing and analysis of the model, satellite and aircraft data (OH calculation etc.). I wrote all sections of the main manuscript with comments and feedback from Richard Pope, Martyn Chipperfield, Wuhu Feng, Dwayne Heard and Brian Kerridge. Section S3 in the supplementary material was written by Richard Pope. I wrote all other sections in the supplementary material. I created all the plots in the main manuscript. Figure S5 in the supplementary material was created by Richard Pope. I created all others in the supplementary material. The level 2 satellite data was provided by Brian Kerridge, Barry Latter, Richard Siddans and Lucy Ventress.

Acknowledgements

Firstly, I am extremely grateful to my supervisor team at Leeds, Martyn Chipperfield and Richard Pope. You have given me so much help, support and guidance in these last 4 years and I cannot thank you enough! Thank you for your patience and for all the skills and knowledge you've helped me to develop.

Thank you to all members of Team TOMCAT that I have had the pleasure of meeting and working with through my years at Leeds - Emily, Carlo, Sandip, Wuhu, Xin, Yang, Ailish, Zihao, Chris W, Chris K, Mike, Linchang, Andreas and Antonio. Thank you for listening to all my presentations, helping me with my numerous computing issues and providing support, guidance and friendship along the way.

A big thank you to Brian Kerridge and his team at the Rutherford Appleton Laboratory, especially Richard and Barry. Thank you for all your help with the satellite data and I especially enjoyed my visit to Harwell, thank you all for being so welcoming. Thank you Brian for all your feedback, advice and support, it was really appreciated.

Another big thank you to Dwayne Heard for his support and advice on the OH work. Thank you to several other staff members across ICAS for your help along the way – Steve Turnock, Kirsty Pringle, Graham Mann, Steve Arnold and Richard Rigby.

Last, but definitely not least, I'd like to thank my family and friends, especially Tommy, Zeller, Richard, William and Rosie. I couldn't have done it without your overwhelming support and belief in me during these last 4 years.

This project was funded by the Panorama Natural Environment Research Council (NERC) Doctoral Training Partnership (DTP), under grant NE/S007458/1.

Abstract

Air pollution is a major issue which causes ~7 million deaths annually worldwide. Within Europe, despite reductions in emissions, recommended thresholds for pollutants such as ozone (O_3) are regularly exceeded. This thesis uses satellite tropospheric composition data and an atmospheric model to quantify long-term changes in European O_3 and the global hydroxyl radical (OH), both central to tropospheric chemistry.

Novel application of a simplified steady-state approximation to IASI satellite data is used to quantify the spatio-temporal distribution of mid-tropospheric OH. This satellite-derived OH compares well with modelled OH and aircraft observations. Between 2008 – 2017, annual global OH varied by -3.1 and +4.7%, driven by O_3 and carbon monoxide (CO) inter-annual variability. The method could be further improved with the inclusion of terms involving nitrogen oxides (NO_x).

Three long-term (1996 – 2017) lower tropospheric (0 – 6 km) O_3 satellite records (GOME, SCIAMACHY and OMI), show small European-wide trends (0.0 to -0.2 DU year^{-1}), with relatively large uncertainties. The model and ozonesonde records are broadly consistent, supporting a negligible trend. Overall, this indicates that lower Europe-wide tropospheric O_3 has remained stable in the satellite era. Small local negative O_3 trends occurred over central Europe in the model, which model experiments show were predominantly driven by emissions over meteorological factors.

Activity restrictions during the COVID-19 pandemic caused reductions in O_3 precursor emissions, with initial studies showing O_3 reductions in the 2020 Northern Hemisphere free troposphere. Here, a study of the European satellite record reveals peak O_3 reductions in April and May 2020 (~2 DU), repeating in spring 2021. Reducing the precursor emissions yields large negative model anomalies peaking in May 2020. The reduction in emissions is the larger influence, compared to meteorology, explaining ~60% of the decrease. The meteorological reduction was driven by a large anomaly in the flux of stratosphere-troposphere O_3 exchange (-64%).

Table of Contents

List of Figures

List of Tables

Abbreviations

AK	**A**veraging **K**ernel
ATC	**A**cross-**T**rack **C**orrection
ATom	**A**tmospheric **T**omography Mission
BC	**B**lack **C**arbon
BCF	**B**ias **C**orrection **F**actors
BDC	**B**rewer-**D**obson **C**irculation
BL	**B**oundary **L**ayer
CTM	**C**hemistry **T**ransport **M**odel
DJF	**D**ecember, **J**anuary, **F**ebruary
DOFS	**D**egrees **O**f **F**reedom for **S**ignal
DU	**D**obson **U**nit
ECMWF	**E**uropean **C**entre for **M**edium-**R**ange **W**eather **F**orecasts
EEA	**E**uropean **E**nvironment **A**gency
EMEP	**E**uropean **M**onitoring and **E**valuation **P**rogramme
ESA	**E**uropean **S**pace **A**gency
EU	**E**uropean **U**nion
GHG	**G**reen**H**ouse **G**as
GOME	**G**lobal **O**zone **M**onitoring **E**xperiment
IASI	**I**nfrared **A**tmospheric **S**ounding **I**nterferometer
IR	**I**nfra**R**ed
JJA	**J**une, **J**uly, **A**ugust
LST	**L**ocal **S**olar **T**ime
MAM	**M**arch, **A**pril, **M**ay
MB	**M**ean **B**ias
MDA8	**M**aximum **D**aily **8**-h running **A**verage
NH	**N**orthern **H**emisphere
NMB	**N**ormalised **M**ean **B**ias
OC	**O**rganic **C**arbon
ODS	**O**zone-**D**epleting **S**ubstances
OHR	Hydroxyl radical **R**eactivity

OMI	**O**zone **M**onitoring **I**nstrument
OE	**O**ptimal **E**stimation
SCIAMACHY	**SC**anning **I**maging **A**bsorption Spectro**M**eter for **A**tmospheric **CH**artograph**Y**
SH	**S**outhern **H**emisphere
SHADOZ	**S**outhern **H**emisphere **AD**ditional **OZ**onesondes
SON	**S**eptember, **O**ctober, **N**ovember
STE	**S**tratosphere-**T**roposphere **E**xchange
SZA	**S**olar **Z**enith **A**ngle
RAL	**R**utherford **A**ppleton **L**aboratory
RF	**R**adiative **F**orcing
UTLS	**U**pper **T**roposphere-**L**ower **S**tratosphere
UV	**U**ltra**V**iolet
Vis	**Vis**ible
VOC	**V**olatile **O**rganic **C**ompound
WOUDC	**W**orld **O**zone and **U**ltraviolet Radiation **D**ata **C**entre

Chapter 1 Introduction

1.1 Motivation

Globally, air quality is a substantial environment issue. It is estimated that in 2019 alone, ambient air pollution caused 4.2 million premature deaths (World Health Organization, 2022). In the same year, 99% of the global population were living in areas where the air did not meet the World Health Organisation (WHO) guidelines on safe air to breathe. Air pollution has been shown to cause strokes, heart disease, lung cancer and chronic and acute respiratory diseases such as asthma (World Health Organisation, 2018). There is an increasing wealth of tropospheric composition data products, e.g. surface, satellite, balloon and aircraft observations with which to study air quality. However, there are still gaps in knowledge and uncertainties within this research area, especially relating to the long-term changes in tropospheric species. Satellite-derived observations are now available for the past few decades, which provide enhanced spatio-temporal information compared to other observations. These satellite records have the potential for the evaluation of long-term changes, either directly or indirectly, and therefore provide the opportunity to address this gap in knowledge.

The overarching aim of this thesis is to explore the use of satellite tropospheric composition records to understand long-term changes in two important species in the troposphere, ozone (O_3) and the hydroxyl radical (OH). Tropospheric O_3 is an atmospheric pollutant, as acute and chronic exposure is harmful to both humans and plants. It is also a greenhouse gas (GHG) and is a large contributor to the total global radiative forcing (RF). OH is a highly reactive radical and a strong oxidant. It is therefore known as the ‘detergent’ of the atmosphere due to its control on the lifetime of many other important species e.g. methane (CH_4), ozone-depleting substances (ODS) and air pollutants. Therefore, enhancing our understanding of the interannual to decadal changes in both species is important. These two species (OH and O_3) are closely linked in the troposphere, as O_3 is the key primary source of OH, and OH is the major sink of many species important to O_3 e.g. CO, CH_4, and it is also key in the production of O_3 by oxidising volatile organic compounds (VOCs) to form peroxy radicals. Investigating both species in this thesis aims to provide important information about these links. As there are currently no available satellite retrievals of OH, this work focuses on developing a novel method of deriving OH from other satellite species, and the subsequent application of this method to studying long-term changes in OH. For O_3, this work focuses on studying the satellite retrieval products already available, to better understand what information can be provided about long-term changes in tropospheric composition.

Direct in-situ measurements of OH are scarce due to its short lifetime (~1 second in the daytime) and very low abundance (Stone et al., 2012). Current indirect methods of inferring global OH provide little spatial information, and reductions in the viability of methods involving the commonly used tracer, 1,1,1-trichloroethane (methyl chloroform, MCF), highlights the importance of developing other methods to infer OH. Currently, there are no tropospheric satellite retrievals of OH. However, satellite retrievals of other species could be used to constrain some of the key source and sink terms of OH, deriving OH using a steady-state approximation. Utilising satellite data would provide a much higher level of spatial and temporal information about OH than currently available from direct observations. This thesis aims to explore the potential of using satellite retrievals of key OH source and sink species to derive global OH, using a simplified steady-state approximation, and what this satellite-derived OH record can provide about the long-term changes in OH.

Despite declining regional precursor gas emissions, the secondary pollutant tropospheric O_3 is a persistent issue in Europe, with 16,800 premature deaths attributed to acute O_3 exposure in 2019 (European Environment Agency, 2021). An estimated 34% of the European urban population were exposed to O_3 concentrations above the European Union (EU) standards (maximum daily 8-hour running average (MDA8) < 120 µg/m^3) and 99% above WHO guidelines (MDA8 < 100 µg/m^3) in 2019 (European Environment Agency, 2021). Satellite retrievals of tropospheric O_3 present a relatively new approach to studying this important pollutant, providing a comprehensive spatio-temporal record since the mid-1990s. As part of the Tropospheric Ozone Assessment Report (TOAR-I), Gaudel et al. (2018) presented variation in the magnitude and sign of tropospheric O_3 trends across Europe from several satellite records, highlighting inconsistencies between the records. This thesis aims to further explore long-term trends in lower tropospheric O_3 and the variation between instruments across several satellite records produced by the Rutherford Appleton Laboratory (RAL).

The global COVID-19 pandemic resulted in ‘lockdowns’ across many European countries in 2020 and 2021. The reduction in many activities produced a large decrease in the emissions of many primary pollutants in the observational record, including the O_3 precursor gases, NO_x (nitrogen dioxide (NO_2) & nitric oxide (NO)) and VOCs. This coincided with a large reduction (~7%) in tropospheric O_3 observed by ozonesondes across the northern hemisphere (NH) free troposphere in the spring and summer of 2020 (Steinbrecht et al., 2021). A combination of NASA satellite records (ending in August 2021) showed that this reduction in the NH repeated in the spring/summer 2021 (Ziemke et al., 2022). The factors controlling this reduction, e.g. the relative effect of reduced emissions and meteorology, are currently poorly understood. This thesis aims to investigate what information several satellite records of the troposphere and model simulations above Europe can provide about 2020/2021 for O_3 in relation to previous years, and to extend the analysis of the O_3 record to the end of 2021. The change in anthropogenic surface emissions and secondary pollutants (e.g. O_3) due to activity restrictions during the global pandemic also provides an opportunity to study the impact to OH during this period, which is currently poor constrained by observations.

1.2 Aim and research questions

The overall aim of this thesis is to improve our understanding of long-term changes and variation in tropospheric composition, with a particular focus on European tropospheric O_3 and global OH, which are two closely linked species that are very important to tropospheric chemistry, human health impacts and the global radiative effective. There are three specific research gaps which this thesis will explore:

1. Information about OH abundance, distribution and long-term variation.
2. More robust quantification of long-term European O_3 trends.
3. Characterisation and quantification of European O_3 and global OH variation, compared to previous years, in spring/summer 2020 and 2021, in the context of the global COVID-19 pandemic.

The first research gap will be addressed in Chapter 4 by developing a new indirect method to derive OH distribution and temporal variation, using satellite retrievals of tropospheric composition (e.g. tropospheric O_3, a key source of OH) and a simplified steady-state approximation. The following research questions will be addressed:

1.1: In what regions of the atmosphere are different steady-state approximations for [OH] valid?

1.2: Can satellite data be applied to a simplified steady-state approximation and how does it compare to modelled [OH]?

1.3: How does the satellite-derived [OH] distribution compare to direct measurements of [OH] in the free troposphere?

1.4: What is the uncertainty associated with the satellite-derived OH?

1.5: What can this method tell us about long-term variations in [OH] and it’s source and sink terms (e.g. O_3)?

Following on from the investigation of long-term OH variation, the second research gap will be addressed in Chapter 5 by studying long-term trends in European tropospheric O_3 in the RAL satellite record. The following research questions will be addressed:

2.1: What are the trends in satellite-observed lower tropospheric O_3 over Europe since 1996?

2.2: How do these trends vary spatially and seasonally?

2.3: How do these trends vary between instruments? What could be causing the differences?

2.4: Are these trends captured by a model and other observations of the troposphere (e.g. ozonesondes)?

2.5: How do variations in O_3 precursor gas emissions and meteorology impact these trends?

The third research gap will be addressed in Chapter 6 by studying variation in European tropospheric O_3 records during the spring/summer of 2020 and 2021, and the corresponding temporal evolution in approximated OH. The following research questions will be addressed:

3.1: What happened to satellite-observed lower tropospheric O_3 in the spring/summer of 2020 and 2021? How does this compare to previous years?

3.2: How does the satellite record compare to the ozonesonde and surface data records in the spring/summer of 2020 & 2021?

3.3: What information can atmospheric chemistry transport model simulations provide about the causes of the spring/summer 2020 reduction of lower tropospheric O_3? Can a quantification of the relative contribution of emissions and meteorology be calculated?

3.4: What happened to global satellite-derived OH in 2020?

These three research gaps and their associated research questions will help to address the overall aim of the thesis, to better understand long-term changes in tropospheric O_3 and OH.

1.3 Thesis layout

This thesis consists of 7 chapters, including this one. Chapter 2 describes the background to the relevant concepts in the thesis, including tropospheric O_3 and OH radical chemistry, previous literature on European tropospheric O_3 trends, O_3 observations methods in the free troposphere and methods of inferring OH concentrations. Chapter 3 describes the datasets used e.g. satellite, ozonesondes, and also the TOMCAT 3-D model. Chapters 4 – 6 present the results of the thesis, with each chapter starting with a review of the most relevant literature. Chapter 4 presents an investigation into deriving the OH radical from satellite data and steady-state approximations. Chapter 5 presents an evaluation of long-term tropospheric O_3 trends in the satellite record. Chapter 6 presents a study of more recent tropospheric O_3, and approximated OH, focusing on the spring/summer of 2020 and 2021 in the satellite record. Lastly, Chapter 7 presents a synthesis and summary of the key scientific findings of the thesis, answers to the research questions and outlook for further work.

Chapter 2 Tropospheric ozone and the hydroxyl radical

This chapter describes the background to the concepts relevant to understanding the thesis aims and results. Further specific literature relevant to each results chapter is discussed at the start of those chapters. Section 2.1 summarises the current state of European air quality, with a focus on tropospheric O_3. Section 2.2 describes O_3 in the atmosphere, the tropospheric budget, controlling factors and summarises the current literature on long-term trends across observations and models. Section 2.3 describes OH in the atmosphere and summarises the methods used to infer OH. Section 2.4 summarises methods of observing O_3 in the free troposphere, with a focus on satellite retrievals. Lastly, Section 2.5 describes recent campaigns of observing OH in the free troposphere.

2.1 European air quality

Despite improvements, air pollution is still the largest environmental health risk in Europe (European Environment Agency, 2022). Emissions of all major primary pollutants (including O_3 precursor gases) have declined since 2005 across 27 European countries (EU-27), as shown in Figure 2.1 (European Environment Agency, 2021). These pollutants include sulphur dioxide (SO_2), NO_2, ammonia (NH_3), PM_{10} (particulate matter smaller than 10 µm in diameter), $PM_{2.5}$ (particulate matter smaller than 2.5 µm in diameter), non-methane VOCs, carbon monoxide (CO), CH_4 and black carbon (BC). Between 2005 – 2019, emissions of SO_2 decreased the most (76%) and those of NH_3 the least (8%). However, despite improving air quality over Europe, currently some air pollutants still exceed EU/WHO standards and air pollution is still the largest environmental health risk in Europe (European Environment Agency, 2022). In 2019, across 27 EU member states, 307,000 premature deaths were attributed to long-term $PM_{2.5}$ exposure, 40,400 to long-term NO_2 exposure and 16,800 to acute O_3 exposure (European Environment Agency, 2021).

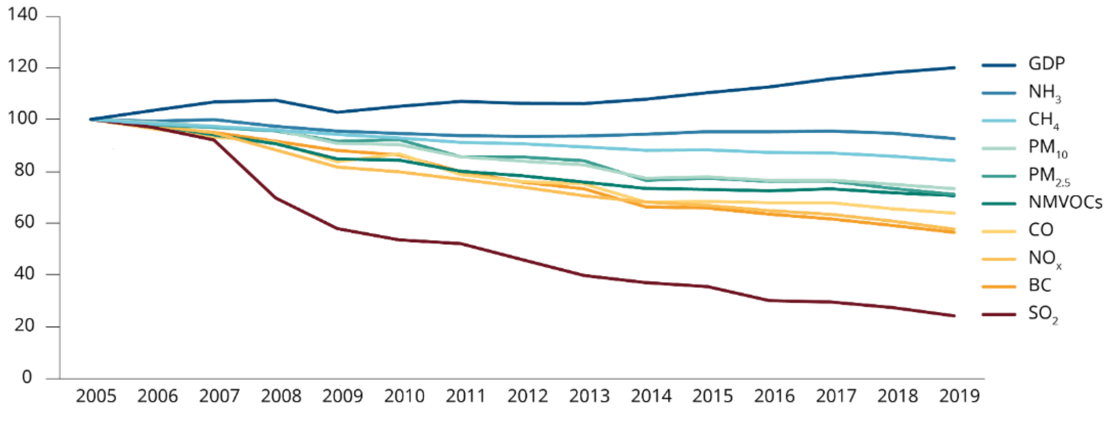

Figure 2.1: Changes in primary pollutant emissions for EU-27 countries. From 2005 to 2019 as a % of 2005 levels. EU-27 gross domestic product (GDP), as a % of 2005 GDP, is also shown. Taken from European Environment Agency (2021).

There is a still-present problem with tropospheric O_3 in Europe, with O_3 concentrations have not decreased as fast as some primary pollutants, with most stations missing the EU targets. In 2019, across the European Environment Agency's (EEA) 2170 air quality monitoring stations (European Environment Agency, 2021):

- 99% of the EU urban population was exposed to O_3 levels which exceeded the 2021 WHO guidelines and 34% were exposed to O_3 levels exceeding the EU standards. This EU exceedance level was higher than for other pollutants e.g. NO_2 (4%), $PM_{2.5}$ (4%) and PM_{10} (15%).
- Long-term EU O_3 objectives of MDA8 (<120 µg/m^3, maximum of 25 days of exceedances a year) were only met at 12% of stations, with all countries reporting stations which exceeded the objective (Figure 2.2).
- WHO guideline of O_3 <100 µg m^{-3} (MDA8) was only met at 3% of stations.

Average O_3 values for 2019 are shown on a country basis in Figure 2.2, and the distribution of the 93.2 percentile of O_3 MDA8 (represents the 26th highest value in the series, to account for the 25 days of exceedances allowed in the target value) at the monitoring sites in 2019 is shown in Figure 2.3. These figures show that O_3 values are highest in southern and central Europe, specifically Bosnia & Herzegovina, Switzerland, Italy, Cyprus, Greece and Austria. However, the network of monitoring stations is very sparse across some parts of Europe, which leads to uncertainty in these estimates for the regions not densely covered by monitoring stations (Figure 2.3).

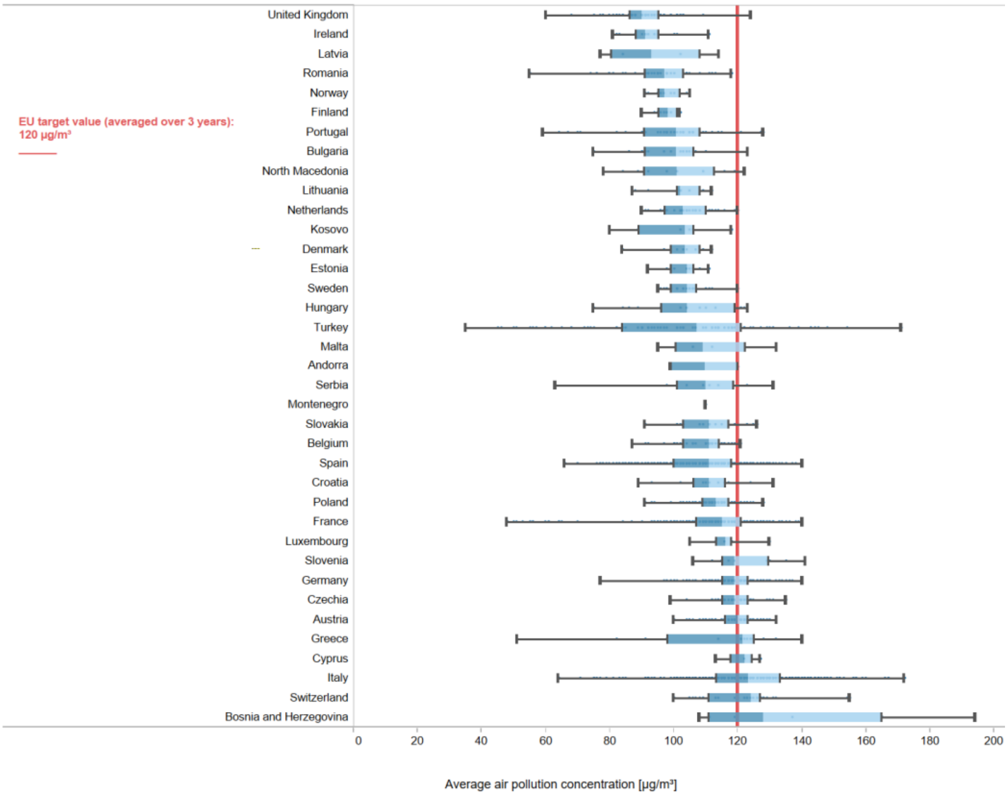

Figure 2.2: Average O_3 concentrations for each European country in 2019 (not averaged across 3 years as in EU target value of <120 µg m^{-3}). Average, maximum, minimum and 25th/75th percentiles are shown. The red line represents the EU target threshold (<120 µg m^{-3}). Taken from European Environment Agency (2021).

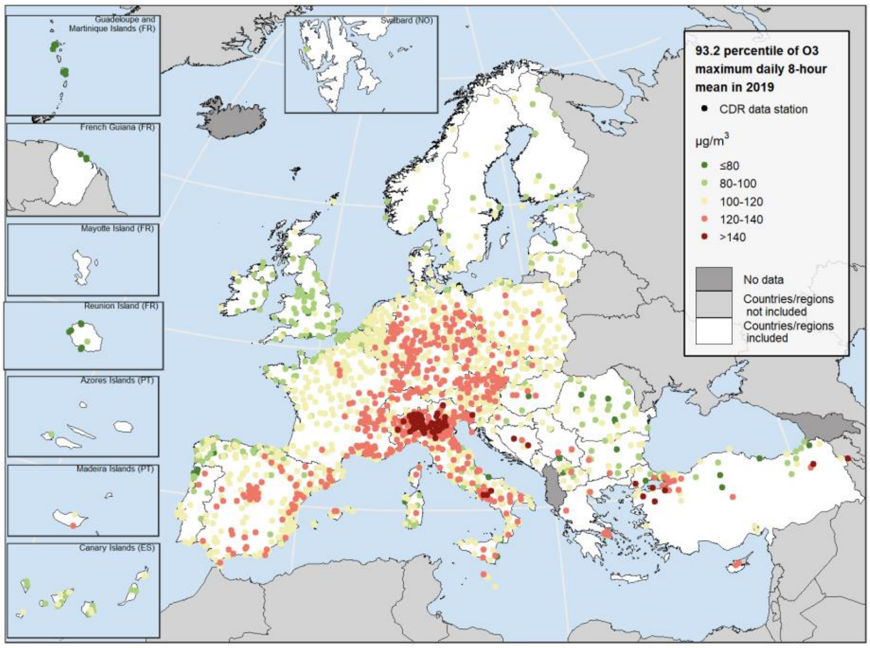

Figure 2.3: O_3 concentrations at surface sites across Europe in 2019. The figure shows the 93.2 percentile of the O_3 MDA8. This percentile corresponds to the 26th highest daily maximum of the running 8-hour mean. The orange/red dots (above 120 µg m^{-3}) represent an exceedance of the 120 µg m^{-3} target threshold value for this metric. Taken from Jaume et al. (2021).

2.2 Tropospheric ozone

2.2.1 Ozone in the troposphere & stratosphere

O_3 is a trace gas in the atmosphere, which is both naturally present and produced by anthropogenic processes. The majority of O_3 (~90%) is in the stratosphere, a region of the atmosphere which extends from ~8 – 18 km to ~50 km altitude. The region in the stratosphere with the highest O_3 concentrations is known as the ‘ozone layer’, as shown in Figure 2.4 (Fahey and Hegglin, 2011). O_3 in this region is often known as ‘good ozone’ as it absorbs incoming solar ultraviolet (UV) B radiation which would otherwise be harmful to humans and plants. Additional UV radiation reaching the surface could cause an increase in incidences of skin cancer, eye cataracts and suppressed immune systems in humans, and also adversely impact crops, plants and ocean plankton (Fahey & Hegglin, 2011). The abundance of O_3 in the O_3 layer is up to ~ 10 ppm.

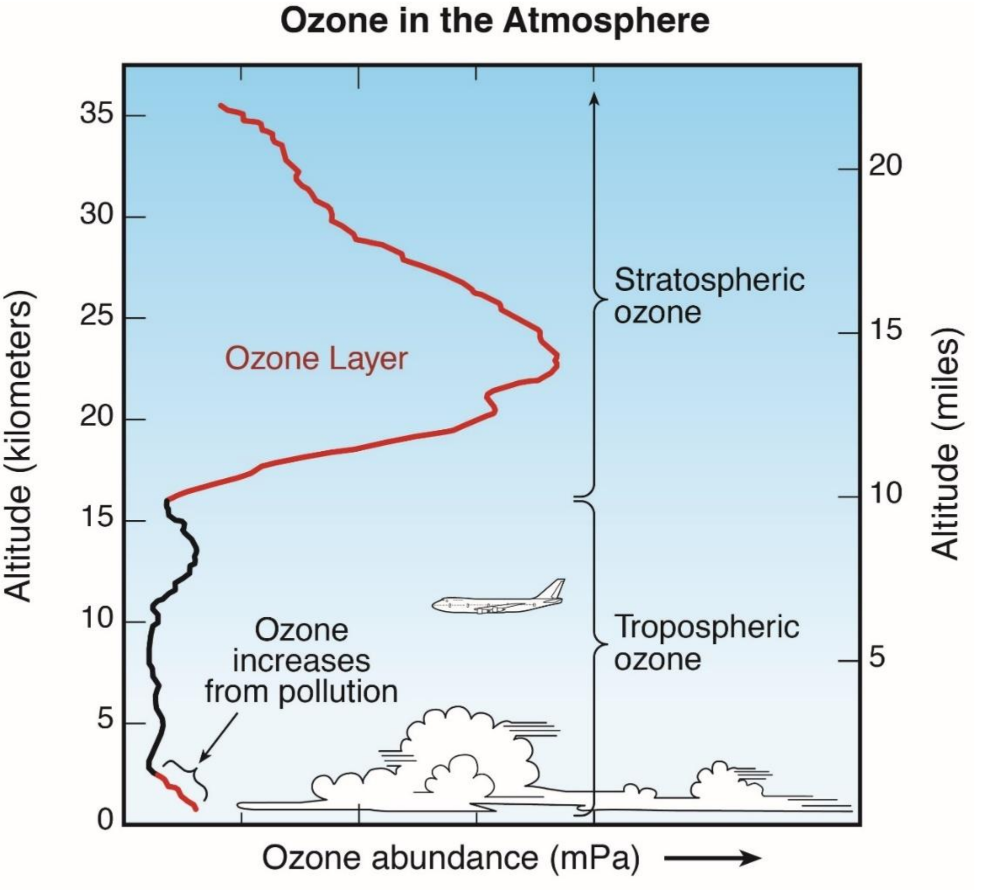

Figure 2.4: Schematic diagram of O_3 in the troposphere and stratosphere. Taken from Fahey & Hegglin (2011).

The remaining 10% of atmospheric O_3 is located in the troposphere. The troposphere is the region of the atmosphere between the surface and the tropopause. The tropopause was defined by the World Meteorological Organisation (WMO) in 1957 as the lowest level at which the temperature lapse rate decreases to 2 K km^{-1} or less, and the average lapse rate between this level and all higher levels within the next 2 km does not exceed 2 K km^{-1} (World Meterological Organization, 1957; Stohl et al., 2003). There has been subsequent studies, defining the tropopause based on other thermal, chemical and dynamical characteristics (e.g. Reed and Danielsen (1958), Holton et al. (1995), Bethan et al. (1996)). In the tropics, the tropopause is around 16 – 18 km altitude, decreasing with decreasing temperature towards the poles, where it can be as low as 6 – 8 km altitude (Stohl et al., 2003). The abundance of O_3 in the troposphere is ~ 20 – 100 ppb.

Tropospheric O_3 is known as ‘bad ozone’ because of the harmful impact on human and plant health. In humans, O_3 is a lung irritant, with acute exposure causing reductions in lung function and capacity, increased respiratory symptoms (e.g. coughing), increased reactivity, permeability and inflammation of the airways, exacerbation of diseases such as asthma, emphysema and chronic bronchitis, and increased mortality from respiratory and cardiovascular diseases (Lippmann, 1991; Fahey and Hegglin, 2011; Zhang et al., 2019). The evidence is less conclusive on the long-term exposure health impacts of O_3, however, there is evidence to suggest that chronic exposure is associated with increased mortality from respiratory and cardiovascular diseases, new-onset asthma in children and asthma exacerbation (Nuvolone et al., 2018). The health impacts are caused by O_3 being a strong oxidant, which induces oxidative damage to the lining fluid and cells of the lungs, causing immune-inflammatory responses within the lungs and body (Zhang et al., 2019). For vegetation, O_3 can cause damage in several ways, including causing visible injury (e.g. discolouration), and also reducing crop yields and forest growth through reducing rates of photosynthesis and speeding up leaf senescence (final stage of leaf development) (Ashmore, 2005). The major damage occurs due to uptake of O_3 by the plant stomata, where it reacts with plant surfaces to form other reactive oxygen species, which can damage cell structures and membranes, impacting photosynthesis and plant growth (Wilkinson et al., 2012; Hayes et al., 2020). Globally the impact of O_3 on crop losses was estimated to cause an economic loss of between US$14 – 26 billion in 2000 (Van Dingenen et al., 2009). Across Europe, studies have shown wide-spread vegetation damage from O_3 exposure, with evidence across 17 European countries (Mills et al., 2011).

O_3 is also an important GHG, with an estimated effective RF for O_3 in both the troposphere and stratosphere of 0.47 W m^{-2} (uncertainty range of 0.24 – 0.71 W m^{-2}) between 1750 – 2019, relative to a total effective RF of 2.72 W m^{-2} from this time period (Skeie et al., 2020; IPCC, 2021). O_3 has been estimated to have caused ~0.23°C of warming from 1750 - 2019, relative to a total of 1.27°C (IPCC, 2021). O_3 in both the troposphere and stratosphere is the 3rd largest contributor to the total change in effective RF between 1750 – 2019, after CO_2 (2.16 W m^{-2}) and a combination of other well-mixed GHGs (CH_4, N_2O, halogens, causing 0.54, 0.21, 0.41 W m^{-2}, respectively) (Skeie et al., 2020; IPCC, 2021). This RF is more heavily influenced by tropospheric O_3 compared to stratospheric O_3 (IPCC, 2021). It will also be important in the future as well, Iglesias-Suarez et al. (2018) estimated that under the RCP8.5 scenario, there would be a net O_3 RF of 435 ± 108 mWm^{-2} in 2100, relative to 2000.

2.2.2 Budget

The tropospheric O_3 burden was estimated at ~ 335 ± 10 Tg by Wild (2007), derived from ozonesonde measurements of the 1980s/1990s. Model intercomparison studies have shown similar values (Wild et al., 2020), e.g. ACCENT showed a mean burden of 344 ± 39 Tg (Stevenson et al., 2006), HTAP showed a mean burden of 328 ± 41 Tg (Fiore et al., 2009) and ACCMIP showed a mean burden of 337 ± 23 Tg (Young et al., 2013). The tropospheric O_3 budget is controlled by photochemical (production and destruction) and physical (transport and removal at the Earth's surface) processes (Monks et al., 2015). Chemical production is the main source of global tropospheric O_3, producing ~ 5000 Tg yr^{-1} (Monks et al., 2015). Stratosphere-troposphere exchange (STE) provides a net source of ~ 550 ± 140 Tg yr^{-1} (Olsen et al., 2001; Hsu et al., 2005; Monks et al., 2015). For removal, dry deposition occurs at the Earth's surface on vegetation and other surfaces. Models suggest a net removal of ~ 1000 ± 200 Tg yr^{-1} (Monks et al., 2015). Table 2.1 shows the range of values in the source and sink fluxes across 2 model intercomparison studies and a comparison of 17 published chemistry transport model (CTM) studies. As Table 2.1 shows, there is a large uncertainty on all of these O_3 budget terms, with different model studies showing large differences (Wild, 2007). Aside from differences in the surface precursor emission values, these differences are caused by representation of key processes in the models such as STE, wet and dry deposition, humidity and lightning (Wild, 2007). The definition of the tropopause can also affect the tropospheric O_3 burden calculated. Wild (2007) found that ~ ±15% of the variability in the burden from 3 O_3 climatologies was due to tropopause choice.

		ACCENT (Stevenson et al., 2006)	**CTM studies 2000 – 2004 (Wild, 2007)**	**ACCMIP (Young et al., 2013)**
Number of models		21	17	15
Source ($Tg\ yr^{-1}$)	Chemical Production (Source)	5110 ± 606	4465 ± 514	4877 ± 853
	STE (Source)	552 ± 168	529 ± 105	477 ± 96
Sink ($Tg\ yr^{-1}$)	Chemical Loss (Sink)	4668 ± 727	4114 ± 409	4260 ± 645
	Dry Deposition (Sink)	1003 ± 200	949 ± 222	1094 ± 264
Tropospheric Burden (Tg)		344 ± 39	314 ± 33	337 ± 23

Table 2.1: Summary of the sources, sinks and burden of tropospheric O_3 in the model intercomparison studies of ACCENT, ACCMIP and across published CTM studies between 2000 – 2004.

The relative dominance of the budget terms varies geographically, with net chemical production occurring over the continent in the boundary layer (BL), due to high precursor emissions, and in the upper troposphere, where there is slow destruction (Monks et al., 2015). For net chemical destruction, this occurs in the marine BL and mid-troposphere, due to low concentrations of precursor gases, and also in urban areas, due to the high NO_x concentrations (titration, see Section 2.2.2.1) and in polar areas due to localised halogen-catalysed O_3 destruction (Monks et al., 2015). Any variation in these processes, e.g. precursor gas emissions (natural or anthropogenic, geographical distribution), air-mass transport and STE, can influence tropospheric O_3 trends. The following sub-sections discuss the budget source and sink terms in more detail.

2.2.2.1 Photochemical production and destruction

Tropospheric O_3 is a secondary pollutant as it is not directly emitted. O_3 can be present in the troposphere due to transport from the stratosphere (Jacob, 1999), with the remaining O_3 produced photochemically in the troposphere. It can have a lifetime of hours in polluted urban environments to weeks in the free troposphere, with an average of ~ 22 days (Young et al., 2013; Monks et al., 2015). The longer lifetime in the free troposphere allows it to be transported across the hemisphere to different continents (Monks et al., 2015).

Production involves the presence of the precursor gases, NO_x and a range of VOCs. VOCs in the atmosphere include CO and hydrocarbons such as CH_4, ethane (C_2H_6), propane (C_3H_8) and isoprene (C_5H_8). The primary reaction that forms O_3 is the photolysis of NO_2, producing oxygen atoms $O(^3P)$, which then combine with O_2 in the atmosphere, as shown in Equations 2.1 and 2.2 (Jacob, 1999; Monks et al., 2015):

$$\mathrm{NO_2} + h\nu\ (\lambda < 430\ \mathrm{nm}) \rightarrow \mathrm{NO} + \mathrm{O(^3P)}$$ **Equation 2.1**

$$\mathrm{O_2} + \mathrm{O(^3P)} + \mathrm{M} \rightarrow \mathrm{O_3} + \mathrm{M}$$ **Equation 2.2**

where M represents any inert third body molecule in the atmosphere (commonly N_2 and O_2). Collision with M is required to stabilise the excited product by removing the excess energy, which is dissipated eventually as heat (Jacob, 1999).

O_3 production by NO_2 photolysis is summarised in Figure 2.5(a), with NO_x chemistry a key control on O_3. In a relatively unpolluted environment, with an absence of hydrocarbons, a null cycle is established within NO_x and O_3 chemistry as the main source of NO_2 is the destruction of O_3, as given in Equation 2.3.

$$\mathrm{NO} + \mathrm{O_3} \rightarrow \mathrm{NO_2} + \mathrm{O_2}$$ **Equation 2.3**

For net production of O_3, the reaction of NO to form NO_2 must not involve O_3, which would lead to a null cycle. VOCs (including CO and CH_4) are oxidised by the OH radical in the atmosphere to produce peroxy radicals (e.g. hydroperoxyl, HO_2, methyl peroxy, CH_3O_2). The peroxy radicals produced can react with NO to form NO_2 (Figure 2.5(b)), resulting in net O_3 production. O_3 photoloysis is the major primary production reaction for OH in the troposphere, however, VOC and NO_x presence allows OH to be regenerated.

The oxidation of CO and CH_4 by OH to form peroxy radicals is shown in Equations 2.4 and 2.5, respectively.

$$\mathrm{OH} + \mathrm{CO}\ (+\mathrm{O_2}) \rightarrow \mathrm{CO_2} + \mathrm{HO_2}$$ **Equation 2.4**

$$\mathrm{OH} + \mathrm{CH_4}\ (+\mathrm{O_2}) \rightarrow \mathrm{CH_3O_2} + \mathrm{H_2O}$$ **Equation 2.5**

If NO_x is present, the peroxy radiacals (HO_2 & CH_3O_2) generated will react with NO, as shown in Equations 2.6 and 2.7, respectively (Wayne, 1991).

$$\mathrm{HO_2} + \mathrm{NO} \rightarrow \mathrm{OH} + \mathrm{NO_2}$$ **Equation 2.6**

$$\mathrm{CH_3O_2} + \mathrm{NO} \rightarrow \mathrm{CH_3O} + \mathrm{NO_2}$$ **Equation 2.7**

The methoxy radical (CH_3O) generated in Equation 2.7 can react to form formaldeyde which can be photolysed to form HO_2.

Other VOCs are also oxidised by OH, following a similar reaction to CH_4, which produces peroxy radicals which can react with NO to form NO_2. This is shown in generic reaction of a hydrocarbon (R-H) in Equations 2.8 to 2.11.

$$\mathrm{OH + RH\,(+O_2) \rightarrow RO_2 + H_2O}$$ **Equation 2.8**

$$\mathrm{RO_2 + NO \rightarrow NO_2 + RO}$$ **Equation 2.9**

$$\mathrm{RO + O_2 \rightarrow HO_2 + R'CHO}$$ **Equation 2.10**

$$\mathrm{HO_2 + NO \rightarrow OH + NO_2}$$ **Equation 2.11**

R' represents daughter alkyl radicals or groups. Equations 2.8 to 2.11 show the propagation reactions of the oxidation of a generic VOC. NO is converted into NO_2 ready for O_3 production and the OH radical is regenerated which can then go on to oxidise further VOCs.

The loss or termination reactions for the chain reactions described here, are shown in Equations 2.12 and 2.13. Hydrogen peroxide (H_2O_2) and nitric acid (HNO_3) can be dissolved in cloud droplets and therefore removed from the system (wet deposition) (Wayne, 1991).

$$\mathrm{OH + NO_2 + M \rightarrow HNO_3 + M}$$ **Equation 2.12**

$$\mathrm{HO_2 + HO_2 \rightarrow H_2O_2 + O_2}$$ **Equation 2.13**

Another loss pathway for HO_2, is its uptake onto aerosol surfaces, a process which is currently poorly understood (Dyson et al., 2023). A recent study by Dyson et al. (2023) found that modelled aerosol HO_2 uptake was important in HO_2 loss (~29%) during low NO concentrations in Beijing, China.

This production of O_3 is most efficient at medium NO_x concentrations. At high NO_x concentrations, NO_x is removed from the cycle by reaction of OH with NO_2 forming HNO_3 which is then washed out of the atmosphere in wet deposition. This reduces the amount of free radicals and NO_x available to form O_3. O_3 is also destroyed through the reaction with NO (Equation 2.3), known as 'NO_x titration'. Therefore, through a combination of these two processes, in urban areas with very high NO_x concentrations, there can be be surpressed O_3 concentrations. At high NO_x concentrations, additional VOCs increases the amount of free radicals, and therefore leads to greater O_3 production.

Tropospheric O_3 production is dependent on the balance of NO_x and VOCs in the atmosphere and therefore can vary locally based on emissions of these species (Jacob, 1999). Figure 2.6 shows the relationship between NO_x and VOC emissions. The area in the bottom right (labelled 'C') is known as the NO_x-limited regime, a region of VOC saturation where varying the NO_x emissions has the dominant impact on the O_3 concentration. The area in the top left (labelled 'A') is the VOC-limited region, a region of NO_x saturation where varying the VOC emissions has the largest impact on the O_3 concentration. In Figure 2.6, moving from 'A' to 'B' along a line of constant NO_x emissions, but increasing VOC emissions will increase O_3 production. The same is true of moving from 'C' to 'B' along a line of constant VOC emissions but increasing NO_x emissions. For areas with high O_3 levels, different action plans would be required to reduce the O_3 concentration depending on which regime was present, as varying the NO_x in a VOC-limited region (or vice versa) would have little or a negative effect on trying to decrease O_3 concentrations.

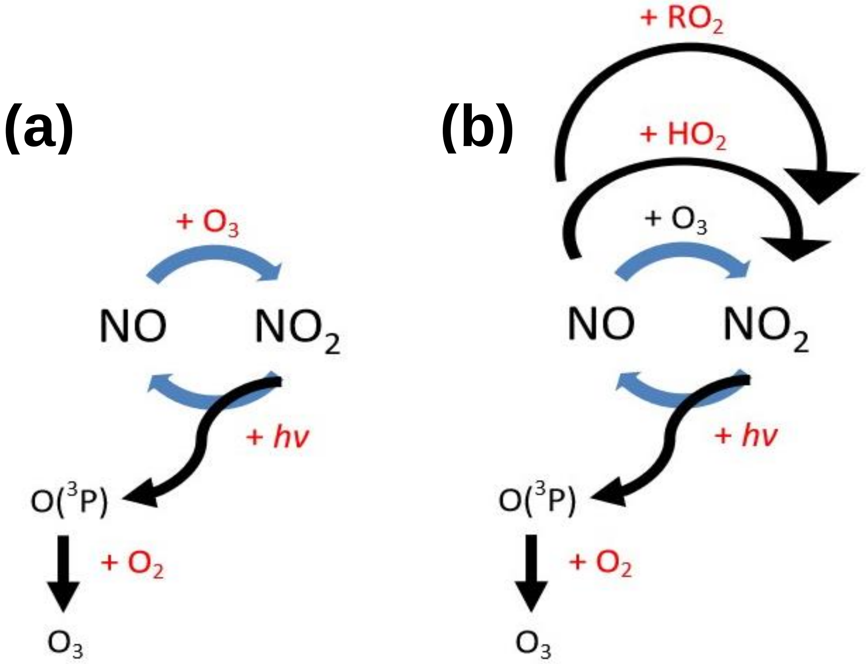

Figure 2.5: (a) Cycling of NO_x to produce and destroy O_3, a null cycle in the absence of hydrocarbons. b) Cycling of NO_x to produce O_3 in the presence of hydrocarbons. RO_2 representes the peroxy radical generated by the generic reaction of a non-methane hydrocarbon (R-H) and OH.

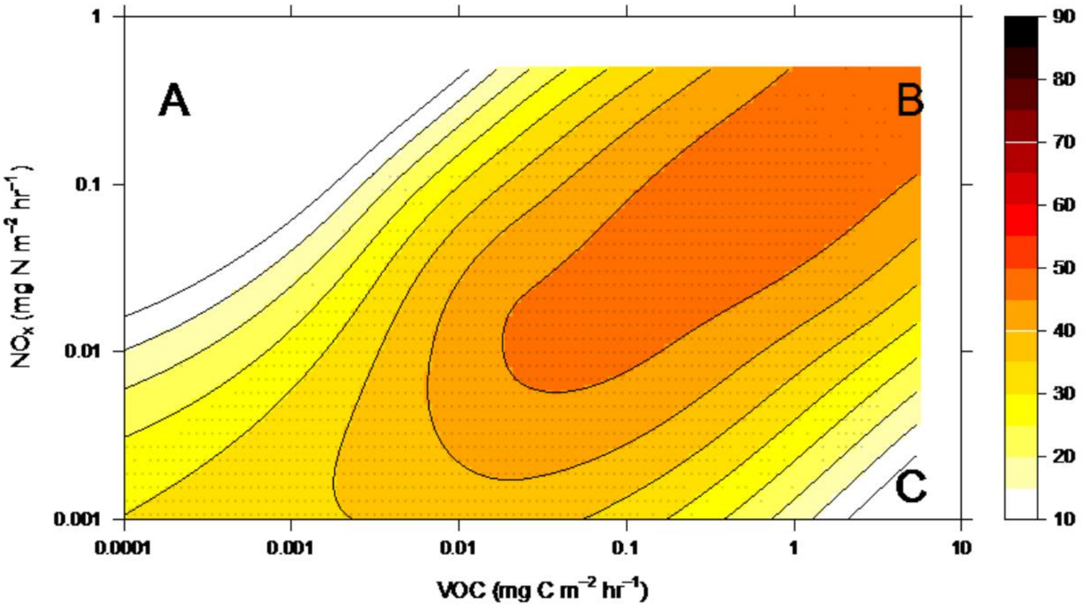

Figure 2.6: O_3 mixing ratios (ppb) varying with NO_x and VOC emissions as simulated by UKCA global chemistry-climate model (UMUKCA). 'A' indicates the NO_x-saturated region (VOC-limited), 'C' indicates the VOC-saturated region (NO_x-limited). Taken from Monks et al. (2015).

2.2.2.2 Surface dry deposition

Surface deposition is an important sink of O_3. Dry deposition can take place on the surface of vegetation or O_3 can undergo uptake by the stomata of vegetation, with the latter the process which can cause harm to the vegetation (Fowler et al., 2009; Monks et al., 2015). Vegetation physiological activity and associated gas exchange, solar radiation, air temperature, air humidity and soil moisture are the key controls on stomatal uptake of O_3 (Fowler et al., 2009). Stomatal uptake has been shown to account for ~ 40% – 60% of total deposition over a plant canopy (Fowler et al., 2009). Deposition can also occur on any other surface, including the soil, snow and water (Fowler et al., 2009). Non-stomatal deposition is controlled by solar radiation, surface temperature, wind speed and surface wetness (Fowler et al., 2009). Other notable controls of O_3 in the canopy, are where soil emissions of NO are very large as this suppress the O_3 concentration (see Equation 2.3), and large emissions of VOCs from vegetation can also rapidly reduce O_3 concentrations (Monks et al., 2015).

2.2.2.3 Stratosphere-troposphere exchange

STE is an important source of tropospheric O_3, providing a net O_3 source of ~ 550 ± 140 Tg yr^{-1} (Olsen et al., 2001; Hsu et al., 2005; Monks et al., 2015), with a broader estimate of around 400 – 600 Tg yr^{-1} (Hsu et al., 2005). STE describes the transport of gases in both directions, known as stratosphere-to-troposphere transport (STT) and troposphere-to-stratosphere transport (TST) (Boothe and Homeyer, 2017). STT transports O_3-rich air into the troposphere and TST transports air rich in water vapour and tropospheric pollutants into the stratosphere. In this thesis, the term STE will be predominantly used to refer to STT, in the context of influencing the amount of O_3 in the troposphere.

On a global scale, STE is dominated by TST in the tropics and STT outside the tropics (extratropics) (Boothe and Homeyer, 2017). This is due to upwelling from the tropics in the troposphere, transport to the stratospheric extratropics and a downward mass flux in the middle and high latitudes (Stohl et al., 2003; Boothe and Homeyer, 2017). This stratospheric overturning process is driven by Brewer-Dobson circulation (BDC) (Brewer, 1949; Dobson, 1956). BDC is the circulation of air from the tropical tropopause, ascending diabatically into the tropical stratosphere, where it is moved dynamically towards the poles and downward to the extratropical lower stratosphere by Rossby and gravity waves breaking in the extratropical middle atmosphere (Stohl et al., 2003; Boothe and Homeyer, 2017). A schematic diagram of BDC is shown in Figure 2.7.

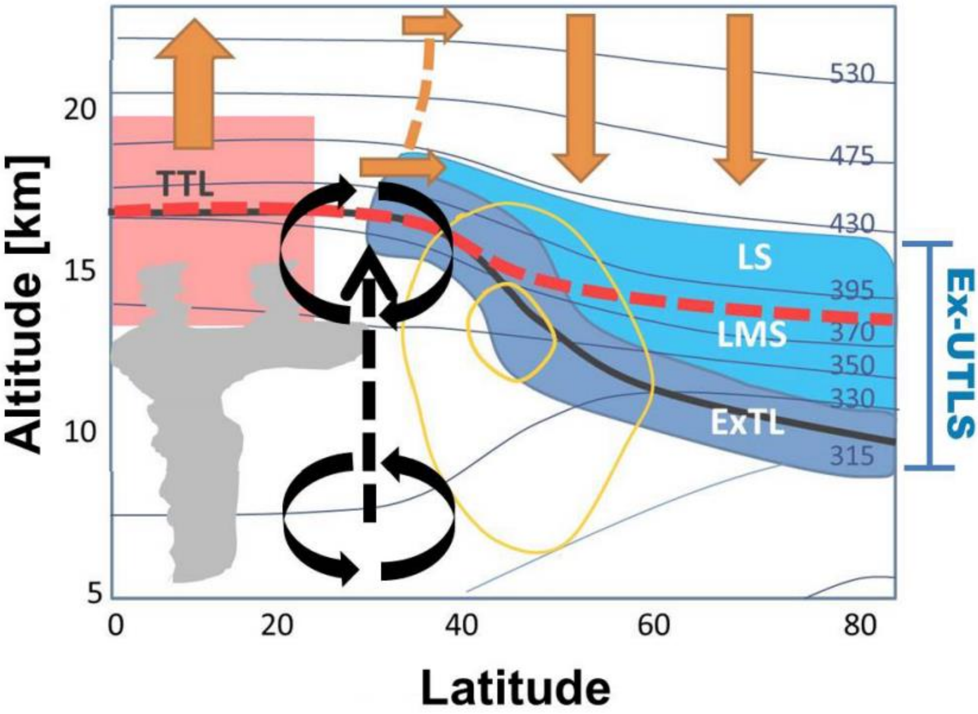

Figure 2.7: Schematic of the dynamical structure of the upper troposphere/lower stratosphere for the NH summer. The thick solid black line shows the thermal tropopause. The thin solid lines represent isentropes and the thick red dashed line represents the 380 K isentrope. The red region is the tropical tropopause layer. The blue regions labelled LS, LMS and ExTL represent the lower stratosphere, lowermost stratosphere and extratropical tropopause layer, respectively. The thin yellow lines represent the jet stream. The thick orange arrows show the movement of air masses within the stratosphere (BDC). The upper horizontal arrow represents deep circulation and the lower horizonal arrow represents shallow circulation. Taken from Müller et al. (2016).

STE occurs near the tropopause and is driven by dynamical processes, across different spatial and temporal scales (Boothe and Homeyer, 2017). STE in the extratropics has been shown to occur near extratropical cyclones. This exchange is mostly STT and is caused by clear-air turbulence along edges of stratospheric intrusions (or tropospheric folds) in the upper troposphere (Boothe and Homeyer, 2017). Reutter et al. (2015) found that 50 – 60% of STE across the North Atlantic occurred in the vicinity of cyclones. Stratospheric intrusion events have been found to reach the surface, however, more typically they reach the middle or upper troposphere (Hocking et al., 2007; Tarasick, Carey-Smith, et al., 2019). Aside from extratropical cyclones, stratospheric intrusions can also develop along the cyclonic side of upper tropospheric jet streams, however, these exchange less air (Boothe and Homeyer, 2017).

STE has been shown to impact tropospheric O_3 variation, with studies showing O_3 variation in the upper and lower troposphere to be well correlated with lower stratospheric O_3 variation. Tarasick et al. (2005) found a strong correlation between tropospheric and stratospheric O_3 in ozonesondes above Canada from 1980 – 2001. Ordóñez et al. (2007) found that changes in lowermost stratospheric O_3 were a dominant influence on variability and trend of background tropospheric O_3 from 1992 – 2004. More quantitatively, Tarasick, Carey-Smith, et al. (2019) found that across several ozonesonde campaigns in Canada between 2005 – 2007, STT was responsible for 3.1% of O_3 in the BL (0 – 1 km), 13% in the lower troposphere (1 – 3 km) and 34% in the middle and upper troposphere (3 – 8 km). Neu et al. (2014) found that variation in stratospheric circulation (~40%) lead to approximately half of the variation seen in the NH mid-latitudes tropospheric O_3. Griffiths et al. (2020) found that a decrease in stratospheric O_3 (from ODS) in a model between 1979 – 1994 reduced STT, however, this was offset but an increase in tropospheric O_3 due to increased precursor emissions.

Due to the 1987 Montreal Protocol, and its later amendments, stratospheric O_3 is recovering from the depletion of the stratospheric O_3 layer, with a likely return date to global 1960 levels by ~ 2070 (varying with region) (Pyle et al., 2022). This increase in stratospheric O_3 has been predicted to increase STE into the troposphere (Banerjee et al., 2016) and to reduce the photolysis rates in the troposphere, due to the change in radiation reaching the surface below the O_3 layer (Zhang et al., 2014). Zhang et al. (2014) finds a larger impact to simulated O_3 destruction rates than the production rates from stratospheric O_3 recovery, reducing OH concentrations and increasing tropospheric O_3 lifetime. In addition to the recovery of stratospheric O_3 due to a reduction in ODS, climate models have predicted an increase in BDC (Butchart, 2014), increasing O_3 in the mid-latitude lower stratosphere (Butchart et al., 2006). Hegglin and Shepherd (2009) predict a STE flux increase of 23% between 1965 – 2095 for a moderate emissions scenario.

2.2.3 Precursor gases

The key tropospheric O_3 precursor gases are NO_x and VOCs (including CO and CH_4). These gases are key to O_3 production, and therefore are important to the study of O_3 distribution and long-term changes. Here, a summary of the key sources of these precursor gases is provided and an outline of how emissions and concentrations of these gases have changed over the last few decades.

The key tropospheric sources of NO_x are combustion of fossil fuels (estimated global source of ~ 21 Tg N year^{-1} (Jacob, 1999)). A large proportion of these emissions are from road transport, e.g. in 2020 road transport was responsible for the majority (37%) of European NO_x emissions (European Environment Agency, 2022). The other main sources of NO_x are biomass burning (from tropical agriculture and deforestation, ~ 12 Tg N year^{-1}) and emissions from denitrifying bacteria in soil (~ 6 Tg N year^{-1}) and electrical storms (lightning, ~ 3 Tg N year^{-1}) (Wayne, 1991; Jacob, 1999). During combustion of fossil fuels, some NO_x will be produced due to oxidation of organic nitrogen present in the fuel. Additionally, in combustion engines, at very high temperatures (~ 2000 K) there is thermal decomposition of the air producing NO, as shown in Equations 2.15 - 2.17 (Jacob, 1999):

$$\mathrm{O_2 \rightarrow O + O} \qquad \textbf{Equation 2.14}$$

$$\mathrm{O + N_2 \rightarrow NO + N} \qquad \textbf{Equation 2.15}$$

$$\mathrm{N + O_2 \rightarrow NO + O} \qquad \textbf{Equation 2.16}$$

The oxidation of CO, CH_4 and VOCs leads to O_3 production, and therefore it is important to understand their sources and sinks. The large CO sources are anthropogenic, predominantly from fossil fuel combustion (global estimated source of ~ 700 Tg year^{-1}) and biomass burning (associated with tropical agriculture, ~ 500 Tg year^{-1}) (Zheng et al., 2019). There are also smaller natural sources e.g. emissions from vegetation (~ 200 Tg year^{-1}) and the oceans (~ 20 Tg year^{-1}). Oxidation of CH_4 (~ 900 Tg year^{-1}) and other hydrocarbons (~300 Tg year^{-1}) is also another major source of CO (Zheng et al., 2019). The major sources of CH_4 are a combination of anthropogenic (global estimated source of ~ 330 Tg year^{-1}) and natural emissions (~ 370 Tg year^{-1}) (Saunois et al., 2020). The key anthropogenic emissions are from agriculture and waste, e.g. enteric fermentation in animals (wild/domesticated, ~ 100 Tg year^{-1}), landfills (~ 60 Tg year^{-1}) and rice cultivation (~ 30 Tg year^{-1}). Additional anthropogenic sources are from fossil fuels (~ 110 Tg year^{-1}) and biomass burning (~ 30 Tg year^{-1}). The major natural emissions are from wetlands (~ 150 Tg year^{-1}), freshwater (~ 160 Tg year^{-1}), onshore geological sources (~ 40 Tg year^{-1}) and termites (~ 10 Tg year^{-1}) (Saunois et al., 2020). For other VOCs there are many different natural and anthropogenic sources, e.g. emissions from vegetation, soils, the ocean, fires, solvents and vehicle exhausts (Wayne, 1991; Sindelarova et al., 2014). Biogenic VOCs (BVOCs) are the largest source of atmospheric VOCs, with an estimated annual total emission of ~ 760 Tg (Carbon, C) year^{-1}, consisting mostly of isoprene (C_5H_8, ~ 70%) and monoterpenes (~ 10%) (Sindelarova et al., 2014). Smaller sources of VOCs include anthropogenic (~ 80 Tg (C) year^{-1}), biomass burning (~ 30 Tg (C) year^{-1}) and oceans (~ 52 Tg (C) year^{-1}) (Safieddine et al., 2017).

Overall, many studies have shown a decrease in emissions and concentrations of European O_3 precursor gases in the last few decades. Emissions of O_3 precursor gases across Europe have shown large reductions between 2005 and 2019 (Figure 2.1), by ~ 30% for NMVOCs and ~ 45% for NO_x (European Environment Agency, 2021). There are many observational studies across Europe of reductions in surface NO_x and VOCs concentrations e.g. European Alpine sites show small decreases of NO_x and CO between 1995 – 2007, with the large decreases in winter and smallest decreases in summer (Gilge et al., 2010). The NO_x and CO reductions were ~ 0 – 2% year^{-1} during 1997 – 2007, which is smaller than the negative emission trend estimates over central Europe (~ 3 – 5 % year^{-1} for NO_x, ~ 6% year^{-1} for CO) (European Environment Agency, 2009; Gilge et al., 2010). Two European surface site networks have shown a reduction in NO_x concentrations, of ~ 1.9% year^{-1} (EU-AIRBASE network - urban) and 1.7% year^{-1} (EU-EMEP network - rural), between 1990 – 2010 across the European domain (Xing et al., 2015). Concentrations of VOCs are also decreasing in the urban environment, as at an urban site, von Schneidemesser et al. (2010) showed decreases between 1998 – 2008 of up to 26% year^{-1} for 18 individual VOCs and 12% year^{-1} for CO. In the free troposphere, using satellite data, Pope et al. (2018) found significant reductions of tropospheric column NO_2 across pollution hotspots in the UK from 2005 – 2015 e.g. -0.23 ± 0.05 $\times 10^{15}$ molecules cm^{-2} year^{-1} above London.

2.2.4 Seasonal cycle

On a global scale, the seasonal variation of O_3 is largest in the NH mid-latitudes, showing the lowest values in Autumn (Oct/Nov) and ~ 30% larger values in early Summer (June) (Monks et al., 2015). This large seasonality could be explained by the STE flux which is lowest in November and highest in May. Tropospheric O_3 annual variation is shown in Figure 2.8 (Boleti et al., 2020), which highlights the variation across clusters of European surface sites. For continental Europe (‘Central North’, ‘Central South’, ‘West’ and ‘Po Valley’ in Figure 2.8), the peak O_3 is around summer (June – July) due to high photochemical production from enhanced solar radiation. These sites show lower O_3 concentrations in winter due to the high NO_x concentrations suppressing O_3 (Wilson et al., 2012). For more remote continental and marine sites (‘North’ in Figure 2.8) the peak O_3 is earlier in the year (March – April), possibly due to enhanced stratospheric input and hemispheric-wide photochemical production and transport, although there is no overarching consensus (Monks, 2000; Parrish et al., 2013). For these remotes sites, where there is less NO_x, there are also lower O_3 concentrations in summer due to enhanced photochemical destruction (Parrish et al., 2013). The tropospheric O_3 seasonal cycle has been shown to vary over time; Parrish et al. (2013) showed that the seasonal cycles at several NH mid-latitude sites have shifted, at a rate of 3 – 6 days per decade since the 1970s, so that peak concentrations are earlier in the year.

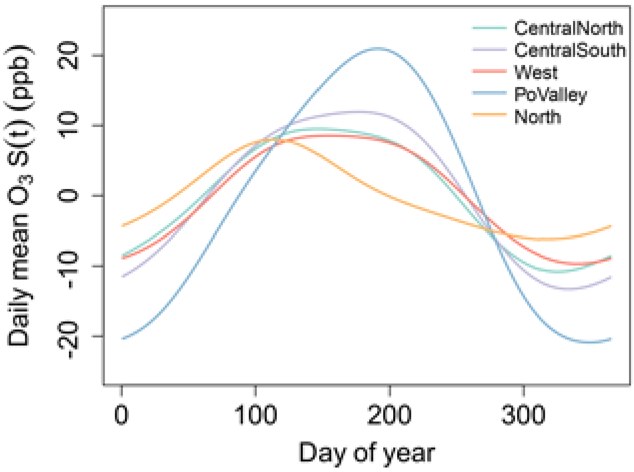

Figure 2.8: Annual cycle of surface tropospheric O_3 across 5 clusters of European surface sites (see Boleti et al. (2020)). S(t) represents the seasonal variation. Taken from Boleti et al. (2020).

2.2.5 Diurnal variation

Free tropospheric O_3 shows a diurnal cycle, an example of which is shown in Figure 2.9 using aircraft measurements from the MOZAIC-IAGOS programme (‘Measurement of Ozone and water vapour by Airbus in-service airCraft’ (MOZAIC) and ‘In-service Aircraft for a Global Observing System (IAGOS)) (Petetin et al., 2016). The largest diurnal variation is found nearest the surface (1000 & 950 hPa in Figure 2.9) and also during the spring and summer (March, April, May (MAM)/June, July, August (JJA)). This large variation is likely due to more active O_3 production and loss processes at the surface, especially high values of photochemical production found during summer. Lower values of O_3 are found overnight due to dry deposition and NO titration. No discernible diurnal cycle could be seen above 750 hPa, therefore there is a large variation in diurnal cycle across the pressure regions within the troposphere.

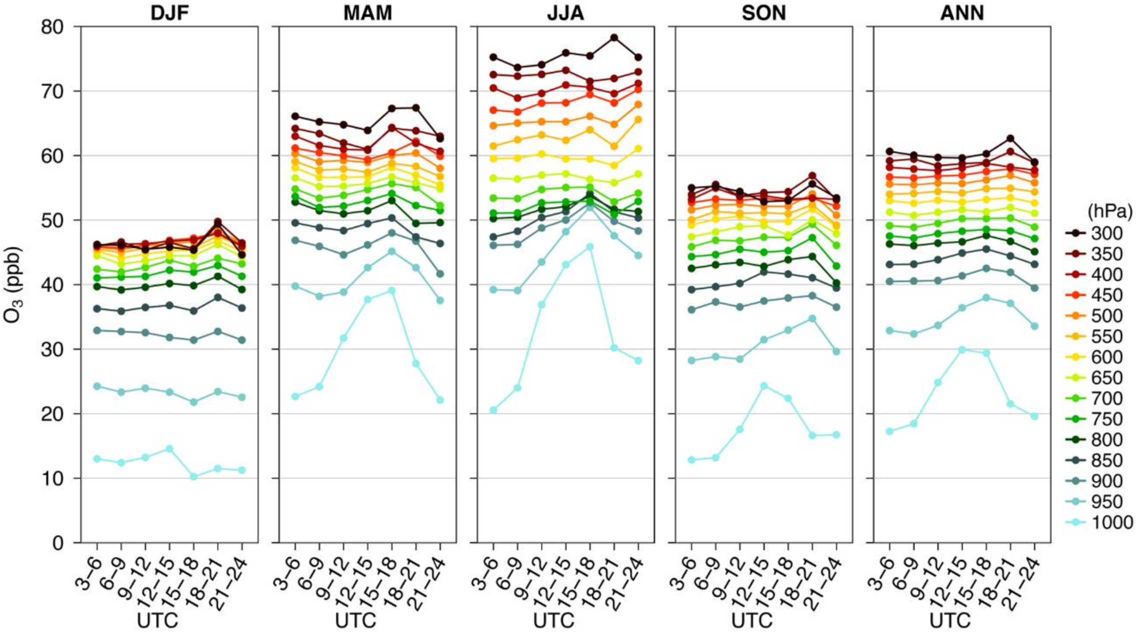

Figure 2.9: Seasonal diurnal variation in the average O_3 mixing ratios above Frankfurt, Germany, for 1994 – 2012. ANN represents the annual averages. 15 pressure levels are shown. Taken from Petetin et al. (2016).

2.2.6 Other influences on tropospheric ozone

Aside from the previously discussed photochemical production, STE and diurnal influences, there are additional processes which can control tropospheric O_3 and its long-term variation. Long-distance transport can control O_3 as, due to the relatively long lifetime of O_3 in the free troposphere, it can be transported at the hemispheric scale (Monks et al., 2015). The transport direction is mostly from west to east in the mid-latitudes, so pollution plumes can be transported from North America to Europe (Lewis et al., 2007; Derwent et al., 2018). Derwent et al. (2018) found baseline O_3 from transport across the Atlantic increased from the 1980s, but has begun to decline since around 2010. Transport patterns are also seasonally affected, due to variations in wind patterns and the transition between summer and winter monsoons (Monks et al., 2015).

Another influence is short-term climate variability (e.g. on the scale of a few years), which can impact transport, and can also impact photochemistry on a regional scale (Monks et al., 2015). Examples of climatic fluctuations include the El Niño–Southern Oscillation (ENSO), the Pacific North American pattern (PNA) and the North Atlantic Oscillation (NAO). Changes in emissions associated with ENSO, e.g. increases in biomass burning emissions, can impact the tropospheric O_3 burden. Rowlinson et al. (2019) found that during the El Niño event of 1997 – 1998, the simulated tropospheric O_3 burden was decreased by changes in transport and lower humidity but was increased by enhanced NO_x and CO production from fire emissions. Longer scale climatic variability (on the decadal scale) can also impact long-term O_3 variation; for example, Lin et al. (2014) showed that decadal cooling of the eastern equatorial Pacific Ocean lead to a weakening of the spring transport of O_3 from Eurasia to the Mauna Loa Observatory in the 2000s.

2.2.7 Global distribution

The global distribution of tropospheric O_3 from surface sites is shown in Figure 2.10 from Gaudel et al. (2018). Figure 2.10 highlights the sparse nature of measurements of surface O_3 outside of Europe, North America and East Asia (specifically South Korea and Japan). In the NH winter, the higher O_3 values (>40 ppb) are found at high elevations e.g. western USA, mountainous regions of Europe (Alps, Apennines and Pyrenees), central Japan and the Himalayas (Gaudel et al., 2018). In the NH summer, the higher O_3 values (>50 ppb) are found mostly in the northern mid-latitudes, e.g. western USA, southern Europe and East Asia (China, South Korea, Japan).

The global O_3 distribution from aircraft and ozonesondes at different levels in the free troposphere is shown in Figure 2.11 (Gaudel et al., 2018). In the aircraft observations for the upper troposphere (9 – 12 km), the highest values are found in the NH poleward of 20°N in the summer, at the time of maximum photochemical activity. Overall, there is very little information about the southern hemisphere (SH) from the aircraft observations, but there are some high values around the equator in spring (September, October, November (SON)) likely due to biomass burning. Broadly the ozonesondes (Trajectory-mapped Ozonesonde dataset for the Stratosphere and Troposphere - TOST) show higher O_3 values in the NH, especially poleward of 20°N in the spring and summer. The SH shows lower O_3 for most seasons, aside from some high O_3 values in the middle and upper troposphere in the SH winter and spring, which coincide with the peak biomass burning period during spring (SON) in these regions. Near the surface (2 – 3 km), the highest values are found in the NH, in the spring and summer.

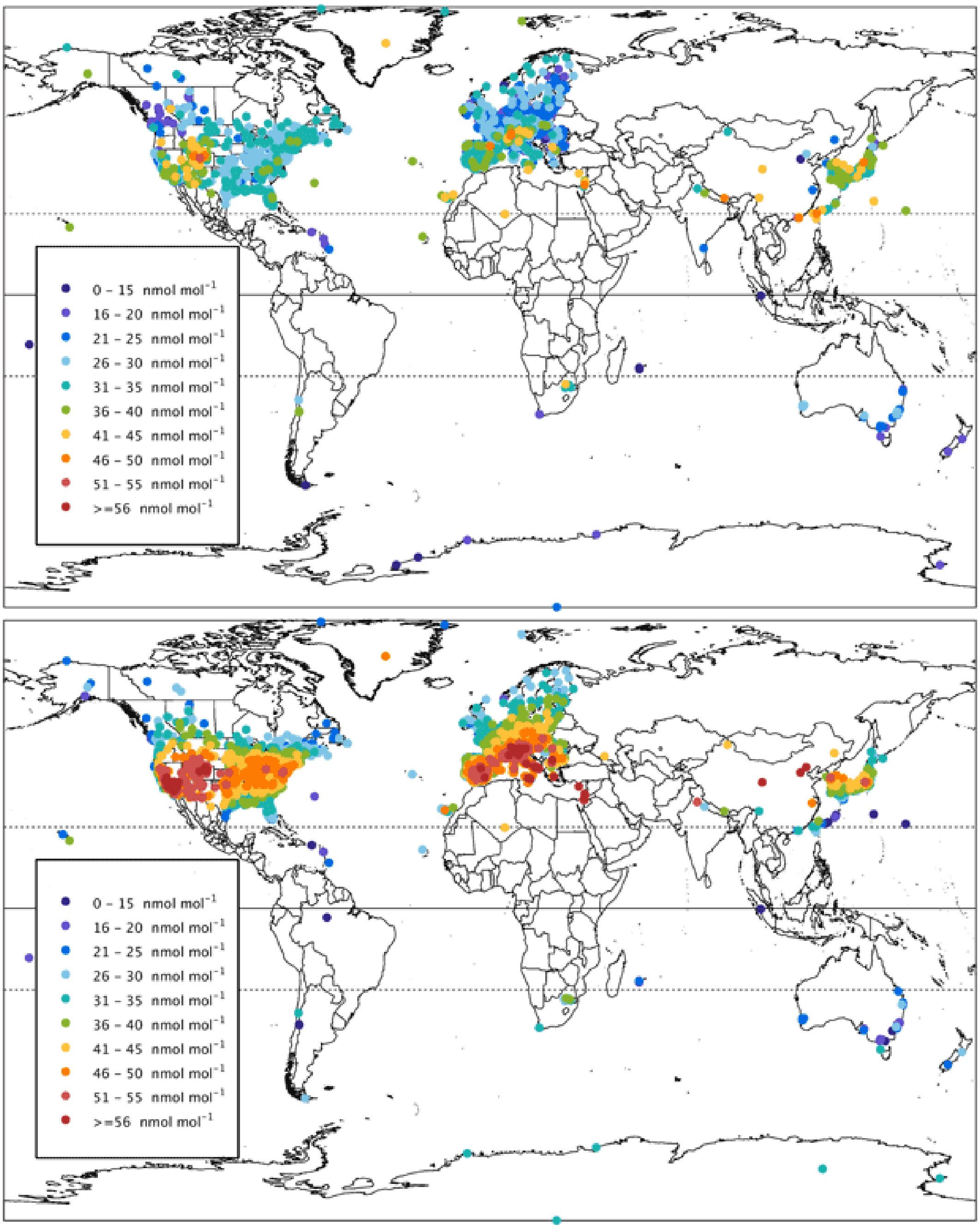

Figure 2.10: Global average daytime O_3 (ppb) from 2010 – 2014 at 2702 non-urban surface sites. Top panel shows December, January, February (DJF) and bottom panel shows JJA. Taken from Gaudel et al. (2018).

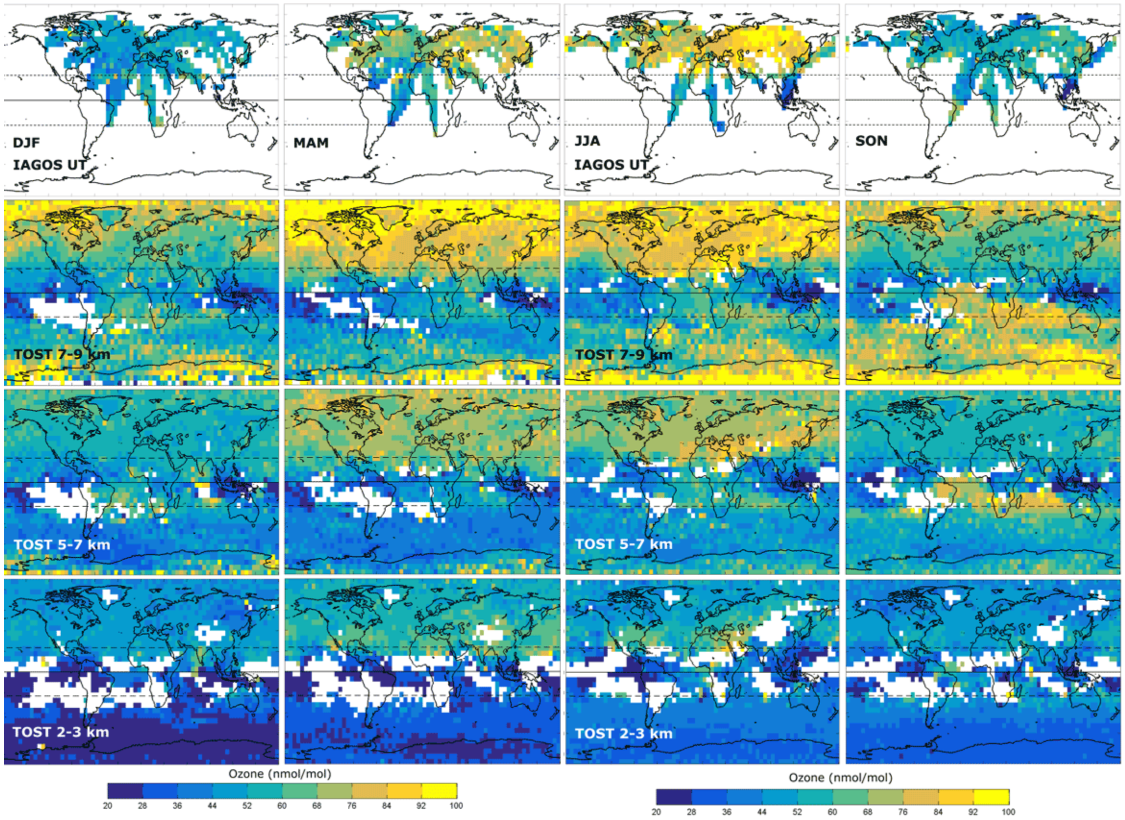

Figure 2.11: Global free tropospheric O_3 distribution in DJF (left) and MAM (left middle), JJA (right middle) and SON (right) from IAGOS (top panels: aircraft, 9 – 12 km, 2009 – 2013) and TOST (lower 3 panels: ozonesondes, 2008 – 2012). Adapted from Gaudel et al. (2018).

2.2.8 Trends in European tropospheric ozone

European tropospheric O_3 is controlled by a range of processes including emission of surface precursor gases, atmospheric chemistry, meteorology (e.g. long-range transport, local temperature) and STE. These processes control the concentration of O_3 throughout the troposphere and different measurement techniques can provide important information on its spatial distribution and temporal evolution (e.g. surface sites can provide information on the impact of O_3 on air quality while ozonesondes can provide information in the upper troposphere on O_3-climate interactions). Therefore, the following sub-section discusses the spatiotemporal evolution of surface O_3 characteristics (e.g. historical baseline, peak values, regional patterns) and FT O_3 trends using a range of observational methods.

2.2.8.1 Surface – historical

Broadly, studies have shown a large increase in tropospheric O_3 over the last century, however, there are issues with using and comparing historical datasets (before ~ 1970s) because of problems with their accuracy and therefore these estimates have a large uncertainty. Also, archived air cannot be used to retrospectively study O_3 due to its instability, so other methods must be considered (Parrish et al., 2021). Due to the issues with studying historical O_3 datasets, the estimates of long-term changes in the literature are wide ranging. One estimate of the historical increase of European tropospheric O_3 found a large increase of ~ 12 – 16 ppb O_3 between historic (pre-1975) and modern measurements (1990s onwards) (Figure 2.12) (Tarasick, Galbally, et al., 2019). Based on all historical measurements, they concluded that northern temperate and high latitude O_3 has increased between 32% – 53% (12-hour daytime average) and 43% – 71% (MDA8) since 1975. Another approach including using a few long-term datasets of baseline O_3 (e.g. alpine sites) suggesting an increase of northern mid-latitude baseline tropospheric O_3 between 1950 – 2000 by a factor of 2.1 ± 0.2 (110% increase), based on a synthesis of results from the Hemispheric Transport of Air Pollution (HTAP) project and TOAR-1 (Parrish et al., 2012; Parrish et al., 2014; Parrish et al., 2021).

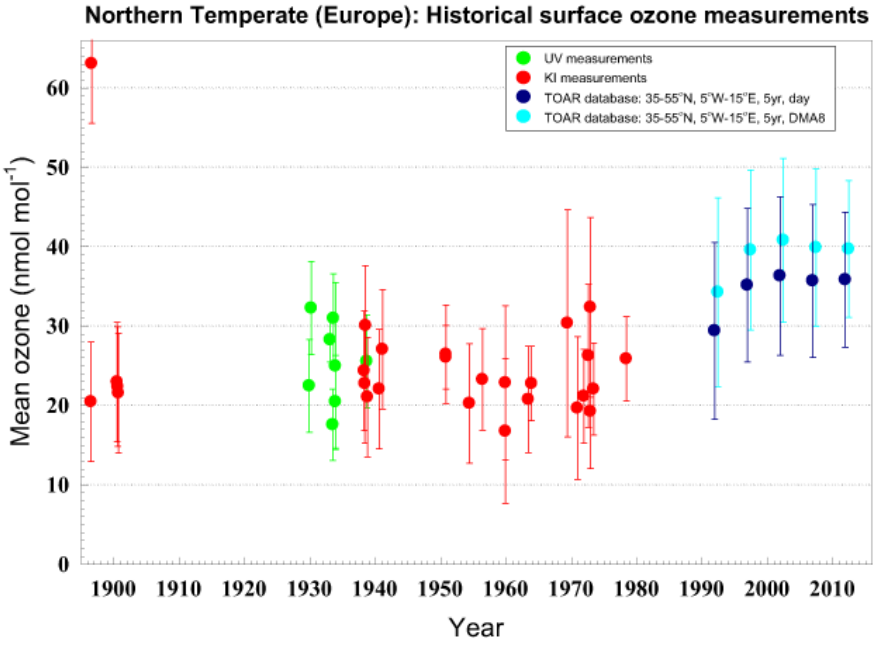

Figure 2.12: Northern temperate region historical and modern measurements of surface O_3 (30°N-60°S) from mostly European surface sites. The modern measurements (1995 onward) are 5 yearly averages at “rural” sites below 2000 m altitude. Light blue shows daily 8-hour maxima data and the dark blue shows daytime averages. Taken from Tarasick et al. (2019).

2.2.8.2 Surface – baseline/background

There is evidence that the background O_3 levels of Europe have increased since around the 1980s. Background (or baseline) O_3 usually refers to O_3 at a particular site that is not influenced by strong local effects (Wilson et al., 2012). It is often represented by the lower percentiles (e.g. 5th, 10th) in O_3 concentration distributions or at remote surface sites. Increasing background O_3 is problematic as during high episodes of local/regional O_3 production, the total O_3 will be exacerbated by enhanced background concentrations.

A key long-term monitoring site of tropospheric O_3 is at the Mace Head Atmospheric Research Station on the west coast of Ireland (western edge of Europe) (Derwent et al., 2013; Derwent et al., 2018). This site monitors the air masses that move over the North Atlantic and into Europe, which at the point of Mace Head represent air masses unaffected by any local European emissions, and so are representative of baseline concentrations. Derwent et al. (2018) presents 30 years of measurements from Mace Head (1987 – 2017), filtering for NH mid-latitude baseline air masses. The increase in baseline O_3 was largest in the 1980s and 1990s, especially in winter and spring, stabilising in the 2000s, and beginning to decline in the 2010s. A linear fit of this record shows a positive trend of +0.27 ±0.09 ppb year^{-1}. A non-linear fit shows a slope of 0.34 ±0.07 ppb year^{-1} with a deceleration term of 0.0225 ± 0.008 ppb year^{-1}, which suggests a declining annual growth rate from 1987 – 2017. Earlier Mace Head studies do show larger linear trends e.g. +0.37 pbb yr^{-1} for 1987-1992 (Derwent et al., 1994) and +0.49 pbb yr^{-1} for 1987-2003 (Simmonds et al., 2004). It has been suggested that with baseline O_3 beginning to stabilise and decline from the 2000s onwards, reductions in local European surface precursor emissions may become more evident in the future in reducing tropospheric O_3, as previously these reductions were balanced by a long-term increase in baseline O_3 (Derwent et al., 2018).

Some of the longest continuous records of modern era O_3 are from alpine surface sites. Alpine surface sites are partly representative of background O_3 due to their altitude, although sometimes can be affected by BL O_3 (Logan et al., 2012). There is evidence to suggest these sites show a positive tropospheric O_3 trend in the 1980s and 1990s which becomes less positive and possibly negative over the 2000s and 2010s. Logan et al. (2012) found that alpine surface data shows summer O_3 increased by 6.5 – 10 ppb from 1978 – 1989 and 2.5 – 4.5 ppb from 1990 – 1999 and decreased by 4 ppb from 2000 – 2009. Similarly, Oltmans et al. (2013) showed that for an alpine site in Germany (Zugspitze) O_3 increased by around 15 ppb between 1981 and 2000, with no real change between 2000 and 2010.

Several studies of background O_3 from a range of surface sites have shown increasing O_3. These studies range from a limited number of sites, to a large monitoring network, but overall mostly show a positive trend. For example, Jenkin (2008) found a significant positive trend of 0.3 – 0.5 µg m^{-3} yr^{-1} from 1990 – 2006 at a remote Scottish site. Alternatively, Wilson et al. (2012) found a positive trend of 0.13 ± 0.02 ppbv yr^{-1} for the 5th percentile of 158 European rural sites from 1996 – 2005 and Yan et al. (2019) found that from 1995 – 2012 there have been positive trends in the lower percentiles of O_3 (~ 5th – 30th percentiles) at all site types across 685 sites in the European Airbase network. Seasonally, Yan et al. (2019) found that spring and summer have their greatest positive trends at the lower percentiles. Across these studies there is no clear consensus on the cause of this positive trend. In contrast to the increase in the background O_3 found by the above studies, Derwent and Parrish (2022) found a decrease in the annual maximum 8-hourly mean O_3 across 32 low elevation rural surface sites (EMEP (European Monitoring and Evaluation Programme) network) in continental NW Europe, with a linear trend of -0.45 ppb year^{-1} between 1989 – 2018. This reduction was attributed to a decline in O_3 from enhanced regional photochemical production, from a reduction in surface precursor emissions.

There are confounding factors in studying long-term tropospheric O_3 trends, e.g. Wilson et al. (2012) found that extreme events in particular years e.g. European heatwave of 2003 generated a large interannual variability which masked long-term trends. Other trend masking factors included meteorological variability and shifts in emission source patterns (Wilson et al., 2012). Jenkin (2008) found that tropospheric O_3 is influenced by a combination of global, hemispheric, regional and local scale effects, which impacts trends varying with space and time. Across the UK, Jenkin (2008) found the 3 important influences to be increasing hemispheric background O_3 (impacting the O_3 transported to the UK from North America), short term high O_3 during summertime from regional European scale photoproduction and the reduction of local removal of O_3 by NO, due to NO_x emission reductions.

Increases and variation in background O_3 have been attributed to global effects in the NH. Ordóñez et al. (2007) used ozonesondes and high-altitude surface O_3 measurements to study if the changes in the lower stratospheric O_3 lead to the positive trend of lower troposphere background O_3 from 1992 to 2004 across Europe. They suggest that an enhanced contribution from stratospheric O_3, especially in the winter and spring, could be the process responsible for the increasing background O_3 seen over Europe. Koumoutsaris et al. (2008) used model simulations to suggest that the positive tropospheric O_3 anomalies at northern mid-latitudes in spring 1998 were due to the El Niño event of the previous year. Their results showed that the El Niño in 1997 caused increased STE and the increased export and transport of Asian and North American pollution towards Europe in the following spring. Between 1987 – 2005, positive O_3 anomalies in spring were found in years after an El Niño year.

2.2.8.3 Surface – peak

Peak O_3 concentrations, especially in the summer, have been shown to be decreasing across Europe. Peak O_3 events are often represented by the higher percentiles (e.g. 95th) or maximum O_3 in concentration distributions. Jenkin (2008) and Munir et al. (2013) found negative trends of maximum O_3 at both rural and urban sites in the UK during 1990 – 2006 and 1993 – 2011, respectively. Yan et al. (2019) found for the 95th percentile in summer daytime O_3 concentrations across the European Airbase network from 1995 – 2012, the 685 rural, urban and suburban sites all showed large statistically significant negative trends (-1.19, -0.96 and -1.09 $\mu g\ m^{-3}\ y^{-1}$, respectively). The annual trends were also negative for all the site types at the 95th percentile, although smaller (-0.85,-0.51 and -0.78 $\mu g\ m^{-3}\ y^{-1}$, respectively) due to less negative or positive trends in the spring, autumn and winter seasons. Yan et al. (2019) attributes these negative trends in peak summertime O_3 to the decrease in precursor gas emissions over Europe due to European legislation, as peak concentrations are more sensitive to changes in local emissions compared to long-distant transport. Model sensitivity experiments by Yan et al. (2019) suggest that the decreases in the 95th percentile O_3 are due to the decline in precursor gases, especially NO_x. Jenkin (2008) also attributed elevated summer O_3 events in the UK to regional-scale photochemistry of emitted NO_x and VOCs over NW

Europe. Under anti-cyclonic (stable) conditions air masses move slowly over NW Europe, thereby enhancing levels of precursor gases (NO_2 and VOCs). The increased photochemistry rates in summer leads to greater O_3 production and when the air mass eventually moves across the UK, greater O_3 concentrations are experienced. The negative trends in peak summertime O_3 are therefore attributed by Jenkin (2008) to the decrease in precursor emission over Europe due to European legislation.

2.2.8.4 Surface – rural & urban

Surface O_3 measurements are often impacted by spatial variation, usually divided between rural and urban (and also sometimes remote and suburban). Urban sites generally have less O_3 than rural sites as the high levels of NO_x in urban areas causes a reduction in O_3 from reaction by NO (Jenkin, 2008). Jenkin (2008) found that the rural sites had more negative trends of summertime peak O_3 than urban and remote sites. The effect of transported precursor gases is regional, with precursor gas transport the primary source of O_3 to rural sites, as these regions do not produce large quantities of emissions. Therefore, Jenkin (2008) attributes the greater negative trends of rural sites to decreasing levels of regional precursor gases from European legislation. In urban areas, reducing the precursor gases also decreases the O_3-supressing effect caused by high NO_x concentrations, therefore reducing the negative trend. Yan et al. (2019) found that urban sites had a greater positive trend in mean annual O_3 (0.22 – 0.83 $\mu g\ m^{-3}\ yr^{-1}$) compared to suburban sites (0.09 – 0.42 $\mu g\ m^{-3}\ yr^{-1}$). In comparison, they found no significant trends in annual mean O_3 at rural sites due to the balance between increasing O_3 in winter and decreasing O_3 in summer. This suggests that urban O_3 could comparatively become an increasing problem in Europe in the future.

2.2.8.5 Free troposphere – ozonesondes & aircraft

Aside from satellite data, key measurements of O_3 in the free troposphere are from commercial aircraft and ozonesondes, which show high vertical sensitivity, however the spatial coverage of these observations can be quite limited (Cooper et al., 2014). Oltmans et al. (2013) found an increase in O_3 from a European ozonesonde launch site between 500 – 700 hPa from the beginning of the 1970s to the end of the 1980s, and a slow decline to 2010. A trend of between ~ 3 – 5 % $decade^{-1}$ was seen across pressures of the surface – 300 hPa for 1970 – 2010, but near-zero trends are shown across these pressures when only 1980 – 2010 is considered. This ozonesonde record differs in comparison with an alpine site (Zugspitze, Germany), where the increase in O_3 seen continues into the 1990s, stabilising in the 2000s (Oltmans et al., 2013). Logan et al. (2012) show that aircraft data agrees better with the alpine sites, with increasing O_3 during the 1990s, and show that the ozonesondes, alpine sites and aircraft agree coherently on decreasing O_3 since 1998. Between 1994 – 2013 ozonesonde observations showed very little change above southern France (Gaudel et al., 2018). The IAGOS commercial aircraft monitoring network found O_3 increases in winter (11% increase) and autumn (5% increase) above Frankfurt, Germany (300 – 1000 hPa), in a comparison of 1994 – 1999 and 2009 – 2013, but very little change in spring and summer (Gaudel et al., 2018).

Two recently wider studies across Europe show broadly positive trends in free tropospheric O_3. Gaudel et al. (2020) showed trends in the median O_3 values from IAGOS over Europe of +1.3 ± 0.2 ppbv decade^{-1} (2.5%) for a tropospheric column (950 – 250 hPa) and +1.3 ± 0.2 ppbv decade^{-1} (2.4%) for a ‘free troposphere’ column (700 – 300 hPa) between 1994 – 2016 (Figure 2.13). Compared to other global regions, the European aircraft O_3 trends show little variation in these trends across the different pressure levels of the troposphere (950 – 250 hPa) for the 1st, 5th, 50th and 95th percentiles, apart from a zero trend between 950 – 750 hPa in the 95th percentile (see Figure 2.13). Christiansen et al. (2022) found a mix of trends across 7 European ozonesonde records in the free troposphere between 1990 – 2017 (Figure 2.14). The trends across all levels range from ~ -1 – +4 ppb decade^{-1}, with an average of 1.9 ± 1.1 ppb decade^{-1} (3.4 ± 2.0% decade^{-1}) and half of the sites showing a positive trend. The mix of trends highlights the potential of spatial differences across the European region, particularly the variation in positive and negative trends, which demonstrates the large local variation in tropospheric O_3 and it’s controls.

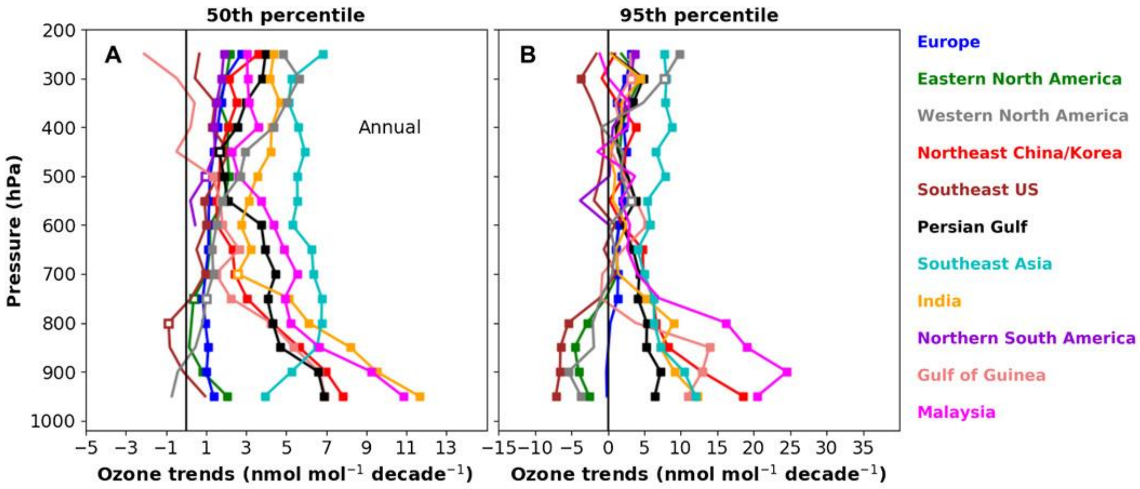

Figure 2.13: Trends in 50th and 95th percentiles of O_3 (ppbv decade^{-1}) for 50hPa pressure intervals above different global regions. Trends are calculated from 1994 – 2016 for Europe, western North America, eastern North America, southeast United States, Northeast China/Korea, Southeast Asia, India, northern South America and the Gulf of Guinea. Trends are calculated for 1995 – 2016 for Malaysia and 1998 – 2016 for the Persian Gulf. Adapted from Gaudel et al. (2020).

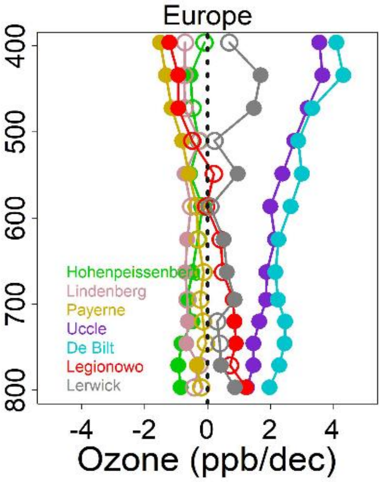

Figure 2.14: Median ozonesonde trends (ppb decade^{-1}) across 3 regions at 400 – 800 hPa for 1990 – 2017. Solid circles represent statistically significant trends, open circles represent insignificant trends. Adapted from Christiansen et al. (2022).

2.2.8.6 Free troposphere – satellite

Satellite instruments can provide high levels of temporal and spatial information about tropospheric O_3 in comparison to ozonesondes and aircraft, however, the vertical sensitivity is limited and column observations can be influenced by the methods used to determine O_3 in the troposphere (e.g. removing the stratospheric contribution). Currently, there are few studies of European long-term trends of tropospheric O_3 from satellite retrievals, using observations from a range of different satellite instruments and across limited spatial regions of Europe. Ebojie et al. (2016) found a non-significant negative trend of -0.9 ± 0.5 % yr^{-1} for southern Europe from 2003 - 2011 using tropospheric column data from the SCanning Imaging Absorption SpectroMeter for Atmospheric CHartographY (SCIAMACHY). Pope et al. (2018) found no significant sub-column O_3 trends across England and Wales from 2005 – 2015 using retrievals from the Ozone Monitoring Instrument (OMI). However, there was a significant positive O_3 trend in Scotland (representing background O_3), of 0.172 Dobson units (DU) year^{-1}.

The most significant comparison of tropospheric O_3 products is Gaudel et al. (2018), presenting trends for several satellite tropospheric column product, which are discussed further in Chapter 5 (Section 5.1). However, the trends are presented mostly by latitude bands, not a European region. In the most relevant latitude band to Europe (30°N – 60°N) the satellite products show a wide range of trends, varying in sign and magnitude. Two OMI products showed positive trends, with +0.16 DU year^{-1} (OMI/Microwave Limb Sounder (MLS)) and +0.13 DU year^{-1} (GOME (Global Ozone Monitoring Experiment) & OMI), with another OMI product showing a near-zero trend of +0.03 DU year^{-1} (OMI-RAL). In contrast, two products from the Infrared Atmospheric Sounding Interferometer (IASI) show a negative trend of -0.50 DU year^{-1} (IASI-FORLI) and a near-zero trend of -0.03 DU year^{-1} (IASI-SOFRID).

2.3 Hydroxyl radical

A key species in atmospheric chemistry is the hydroxyl radical (OH) due to its very important role in the oxidation of many different species. Notably for this thesis, OH is important for the oxidation of VOCs, CO and CH_4 which leads to the net formation of O_3, as seen in Section 2.2.2.1 (Jacob, 1999). OH is often referred to as the ‘detergent’ of the atmosphere due to its highly oxidising nature from its unpaired electron, meaning that it is responsible for much of the oxidation of anthropogenic pollutants in the troposphere. Therefore, OH largely determines the oxidation capacity of the troposphere and controls the lifetimes of many important species. Some of the key species controlled by OH include important GHGs (e.g. CH_4), ODS (e.g. hydro-chlorofluorocarbons), as well as other short-lived anthropogenic and natural pollutants (e.g. VOCs, NO_x and CO) (Lelieveld et al., 2016). OH has a very short lifetime in the troposphere, ~1 second in the daytime, and a very low abundance, with global tropospheric mean OH concentration of $\sim 1 \times 10^6$ molecule cm^{-3}.

The importance of OH to tropospheric oxidation capacity was recognised in the early 1970s (Levy, 1971). There have been many scientific investigations into OH since, especially in relation to the lifetime of CH_4, e.g. McNorton et al. (2016), Rigby et al. (2017) and Turner et al. (2019). A better understanding of the spatial and temporal distribution of the primary sink of CH_4, the OH radical, could help the interpretation of recent trends in CH_4, such as the 2000–2007 concentration stabilisation period (Turner et al., 2019).

2.3.1 Chemical production

One of the most important primary sources of OH in the troposphere is the photolysis of O_3 by UV radiation (< 340 nm wavelength). This forms $O(^1D)$ which then reacts with water vapour (H_2O) to form OH (Stone et al., 2012; Lelieveld et al., 2016), as shown in Equations 2.17 and 2.18:

$$\mathrm{O_3} + h\nu\ (\lambda < 340\ \mathrm{nm}) \rightarrow \mathrm{O_2} + \mathrm{O(^1D)}$$ **Equation 2.17**

$$\mathrm{O(^1D)} + \mathrm{H_2O} \rightarrow 2\mathrm{OH}$$ **Equation 2.18**

The OH radical formed is very reactive due to the unpaired electron on the oxygen atom. The formal notation of the radical is ‘HO·’, with the dot representing the unpaired electron, however, within the literature the dot is omitted and the radical is presented as ‘OH’ (Lelieveld et al., 2016). After the OH radical is formed, it can attack reduced and partly oxidised gases (e.g. CH_4, CO, VOCs), removing them from the atmosphere and forming peroxy radicals (e.g. HO_2). A key example of this, the reaction of CO and OH to form HO_2, is shown earlier in Equation 2.4 (Section 2.2.2.1). OH and HO_2 are closely coupled and collectively known as HO_x. The peroxy radicals can then form peroxides and participate in many other atmospheric reactions (e.g. O_3 formation) and can also reform OH (Stone et al., 2012; Lelieveld et al., 2016).

There are also secondary reactions that form OH, known as OH recycling, which involve the peroxy radicals formed by OH as described above. In polluted air, the important secondary production reaction is the reaction of NO and HO_2 (see Equation 2.11). In less polluted air, two important recycling reactions are the reaction of O_3 and HO_2 (Equation 2.19) and photolysis of hydrogen peroxide (H_2O_2) (Equation 2.20).

$$O_3 + HO_2 \rightarrow 2O_2 + OH$$ **Equation 2.19**

$$H_2O_2 + h\nu\ (\lambda < 550\ \text{nm}) \rightarrow OH + OH$$ **Equation 2.20**

2.3.2 Distribution

The modelled average annual OH distribution in the troposphere is shown in Figure 2.15 (Lelieveld et al., 2016). For this distribution, the highest OH values are found in the tropics, with decreasing OH values with increasing latitude. The average column values range from 1×10^5 to 22×10^5 molecule cm^{-3}. The annual zonal mean OH distribution (Figure 2.15 – right panel) shows that the high OH values in the tropics can extend up to the tropical tropopause. The main region of high OH tropical maximum values extends up to ~ 300 – 400 hPa, and there is and additional region of maximum values in the tropics at ~ 150 – 200 hPa. The high FT OH in the tropics is due to emissions from vegetation and lightning NO_x emissions from deep thunderstorm clouds, especially above central Africa where there is intense deep convection and lightning (Lelieveld et al., 2016). In the NH extratropics, the OH distribution is similar over both the continental and marine boundary layers, which is due to the transport and mixing of species (oxidants – O_3, and precursor gases NO_x and VOCs) from polluted continental regions across the oceans (Atlantic/Pacific), whereas, weaker sources and transport of pollutants in the SH means that OH is higher over the continental boundary layer (Lelieveld et al., 2016).

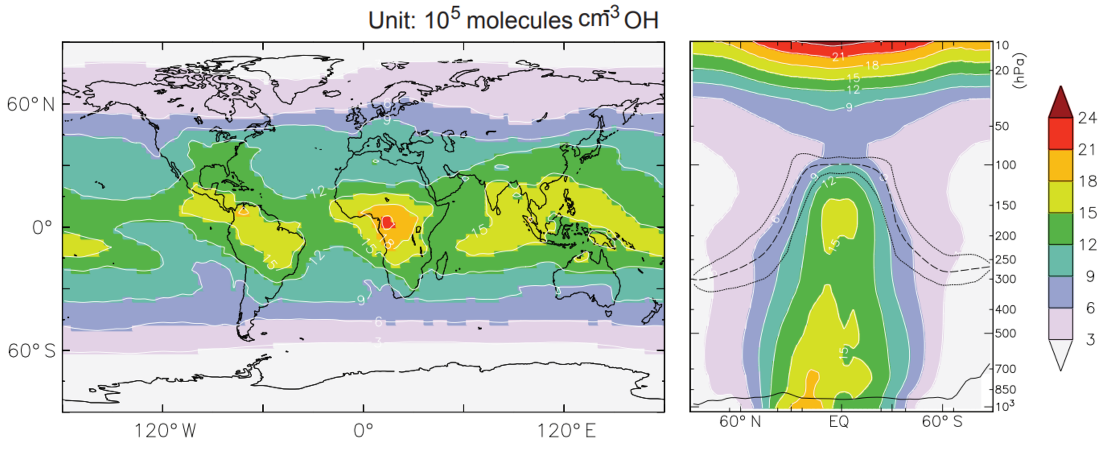

Figure 2.15: Global distribution of OH (units of ×10^5 molecule cm^{-3}). Modelled tropospheric annual mean (left panel) and zonal annual mean (1000 – 10 hPa, right panel). Dashed line shows the mean tropopause (with solid surrounding lines showing annual maximum and minimum tropopause pressures). Solid line near the surface is the average BL pressure. Taken from Lelieveld et al. (2016).

2.3.3 Inferring and modelling the hydroxyl radical

Considering its importance, there is limited information available on the OH radical distribution and temporal variation. This is due to limited direct in-situ measurements because of the short lifetime (~ 1 second in the daytime) and low abundance (Stone et al., 2012). Direct measurements of OH include surface field campaigns and aircraft campaigns across different global locations, however, this provides limited spatio-temporal information. Also due to the lack of homogeneity in the processes which control the formation and loss of OH globally, it is difficult to use these sparse field measurements to infer a global mean OH (Montzka et al., 2011; Liang et al., 2017).

A common method of inferring global mean OH indirectly is to use observations of trace gases which are oxidised by OH as a tracer, e.g. 1,1,1-trichloroethane (known as methyl chloroform, CH_3CCl_3, MCF) (Lovelock, 1977; Singh, 1977; Montzka et al., 2011; Patra et al., 2021). MCF can be used as a tracer as its major sink is OH and the sources are well known (Liang et al., 2017). Although this method can provide a global mean, it still provides relatively limited spatial distribution otherwise e.g. only at the hemispheric scale (Patra et al., 2014). It also relies on very accurate estimates of the emissions and use of a CTM (Monks et al., 2017). MCF is an ODS, so it is regulated under the legislation initiated by the 1987 Montreal Protocol. Its production has been phased out by countries since the late 1990s and has experienced a sharp decline in atmospheric abundance (Reimann et al., 2005). This reduces the viability of using this method in the long-term, due to the MCF concentrations decreasing to within the uncertainty estimates of the method (Liang et al., 2017). Therefore, there is a demand for another method of calculating the global OH abundance. Other methods include using observations of a different tracer or tracers e.g. using ^{14}CO measurements (Krol et al., 2008), using a single or combination of hydrofluorocarbons and hydrochlorofluorocarbons oxidised by OH (Huang and Prinn, 2002; Liang et al., 2017). Wolfe et al. (2019) used satellite observations of formaldehyde (HCHO) as a proxy for OH based on HCHO production and loss rates.

The MCF method can be used to study long-term interannual variability of OH (Prinn et al., 2005; Montzka et al., 2011; Rigby et al., 2017; Patra et al., 2021), which is discussed further in Chapter 4. Studying the interannual variability of OH provides information on the stability of the oxidation capacity of the troposphere (Montzka et al., 2011) and is of interest in the context of the recent varying CH_4 growth rate (Turner et al., 2017). The accuracy of this method depends on accurate estimates of MCF emissions, which has shown to be challenging (Reimann et al., 2005; Rigby et al., 2017).

CTMs and chemistry-climate models can be used to simulate the OH distribution, abundance and its long-term variability e.g. Dalsøren et al. (2016), Stevenson et al. (2020) and Zhao et al. (2020). Wild et al. (2020) found that chemistry-climate models show large variation in the drivers of global OH (e.g. surface NO_x emissions, biogenic isoprene emissions, deposition rates, atmospheric humidity, cloud depth, turbulence in the BL) which may contribute towards the variation in modelled CH_4 lifetimes in the troposphere.

2.3.4 Hydroxyl radical reactivity

The inverse of OH lifetime, OH reactivity (OHR), is also measured in the field and can provide additional information on the tropospheric oxidation capacity and OH radical abundance. If OHR and other relevant OH sink trace gas measurements can be made together e.g. during aircraft campaigns such as NASA's Atmospheric Tomography Mission (ATom) (Wofsy et al., 2018), then OHR can be calculated and compared with the direct measurements. OHR is calculated by summing individual sink terms, which consist of measured trace gas concentrations (of sources/sinks) multiplied by their respective reaction rate coefficients with OH (Yang et al., 2016). However, multiple field campaigns have shown that there is often a large difference between the measured and calculated OHR, known as the "missing" reactivity (Ferracci et al., 2018). This substantial missing reactivity can account for 20% – 80% (20% is usually outside of the OHR uncertainty range) of the measured OHR (Yang et al., 2016). An example of missing reactivity is shown in Figure 2.16 from Thames et al. (2020) using ATom aircraft observations in the marine BL. They found missing reactivity of up to ~ 2.5 s^{-1}. There are several proposed reasons for the "missing" reactivity found in the literature, including: short-lived VOCs that were not measured (Kovacs et al., 2003); unidentified biogenic emissions and photo-oxidation products in the rainforest (Edwards et al., 2013; Nölscher et al., 2016); the presence of unidentified VOC with an ocean source (Thames et al., 2020); and uncertainty in tropospheric reaction rates in the literature (Kim et al., 2022).

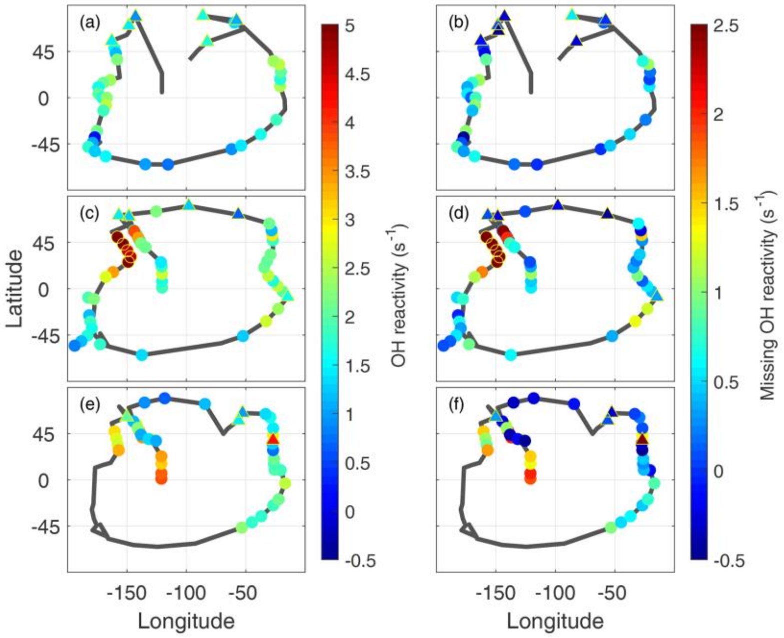

Figure 2.16: Global measurements of OHR (left) and calculated missing reactivity (right). Top panels are ATom-1, middle are ATom-2 and bottom are ATom-3. Triangles indicate that measurements were taken over land, circles indicate measurements over the ocean. Taken from Thames et al. (2020).

2.4 Observation methods for ozone in the free troposphere

This thesis uses several datasets of observations of the free troposphere, from satellite instruments and ozonesondes. The following sub-section provides an overview of these observation techniques, with a key focus on satellite retrievals, explaining the technique and scientific basis in further detail and the key limitations associated with this method.

2.4.1 Satellites

Instruments on board satellites are used to monitor atmospheric composition using remote sensing techniques. The observations of trace gases used in this thesis are from instruments on satellites with polar orbits. Polar orbits are a low earth orbit, at ~ 750 – 800 km altitude, taking ~ 100 minutes per orbit and completing ~ 14 orbits in a day (Martin, 2008). The path that the satellite follows is almost perpendicular to the equator and crosses above (or near to) the north and south poles, as shown in Figure 2.17. Satellites following this near-polar orbit have a fixed orbit plane with reference to the sun. This produces a sun-synchronous orbit which passes over most points at the same local solar time (LST) each day. These orbits provide large spatial coverage but temporal information is limited to two local times at any location (am & pm). Alternatively, satellites with geostationary orbits (altitude of ~ 36,000 km) which continuously cover the same location centred on the equator, are beginning to cover regions of the globe and monitor atmospheric composition e.g. the Geostationary Environment Monitoring Spectrometer (GEMS) above East Asia, launched in 2020 (Kim et al., 2020). These satellites provide high levels of temporal information and are likely to provide new insights in the future.

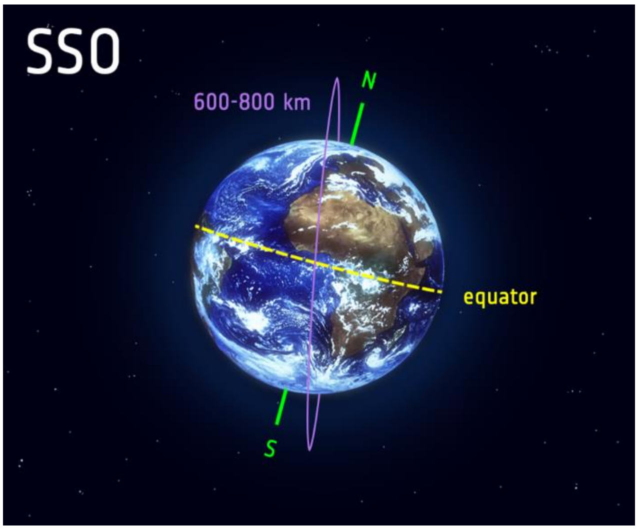

Figure 2.17: Diagram of a polar and a sun-synchronous orbit of Earth. Taken from European Space Agency (2023).

Satellite instruments monitor trace gases by two main passive methods, solar backscatter and thermal IR emission (Martin, 2008). The solar backscatter method compares the radiation that reaches the satellite, having passed through the atmosphere (Earth radiance), and the solar irradiance (Gottwald et al., 2006). The intensity of the radiation (UV, Visible (Vis), Near Infrared (NIR) and Short Wave Infrared (SWIR)) will have been attenuated by different processes in the atmosphere, such as scattering by air molecules (Rayleigh and Raman scattering), scattering and absorption by aerosol and cloud particles (Mie scattering), absorption and emission by trace gases and surface reflection (Gottwald et al., 2006), as shown in Figure 2.18. An example of a comparison between the Earth radiance and the solar irradiance, measured by OMI at the top of the atmosphere, is shown in Figure 2.19 (Levelt et al., 2006). Trace gases exhibit characteristic absorption patterns in different wavelength bands, due to rotational transformations (IR/microwave), vibrational-rotational transitions (IR) and electronic transitions (UV/Vis), which allows their identification (Gottwald et al., 2006). For the thermal IR emission method, the spectra measured by the instrument at the top of the atmosphere is a composed of the initial long-wave IR emission (Earth's black body emissions) which has passed through the atmosphere, interacting with IR absorbing molecules (Martin, 2008; Clerbaux et al., 2009; Clerbaux et al., 2010).

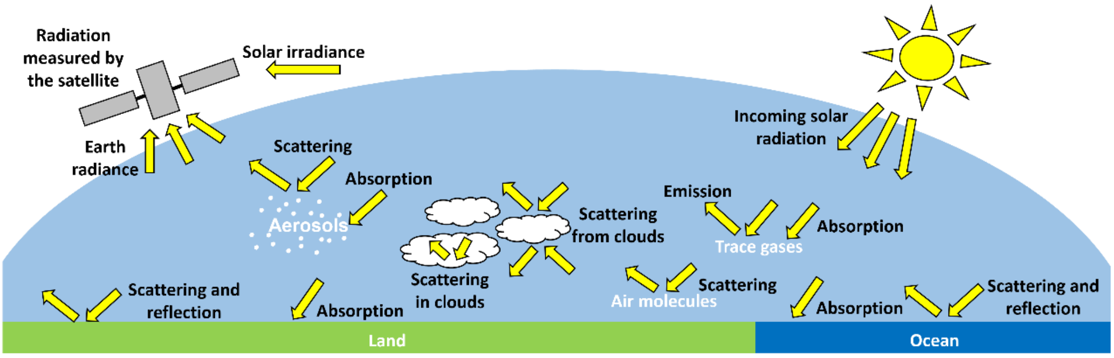

Figure 2.18: Schematic diagram of the processes which impact the pathways of solar radiation (UV-Vis-NIR and SWIR) through the atmosphere and interactions with the surface (Gottwald et al., 2006).

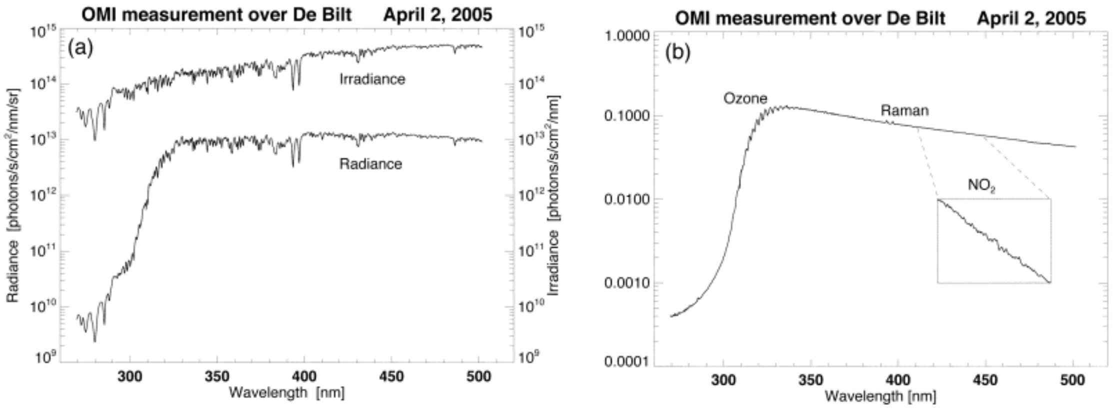

Figure 2.19: (a) Example of OMI solar irradiance and measured Earth radiance above the Netherlands in 2005. (b) Ratio of radiance to irradiance for the spectra in panel (a). Taken from Levelt et al. (2006) (© 2006 IEEE).

Satellites have been used to observe aerosols and trace gases in the atmosphere since the mid-1970s (Gottwald et al., 2006; Martin, 2008). The era of monitoring trace gases in the troposphere began in the mid-1990s with the launch of GOME on the satellite ERS-2 (Martin, 2008; Streets et al., 2013). Over time the spatial resolution of the instruments has increased, from the coarse resolution of 40 km × 320 km for GOME (launched in 1995) to the recent instrument TROPOMI which has a resolution of 7 km × 3.5 km (launched in 2017) (Burrows et al., 1999; Veefkind et al., 2012). This has greatly improved the spatial information available from satellite data, allowing analysis to be done on smaller spatial scales and giving improved information on the individual sources and transport methods of atmospheric pollutants. The 5 instruments which are used in this thesis are described in greater detail in Section 0.

In the case of O_3, total column O_3 has been measured since the Backscatter Ultraviolet (BUV) experiment (1970s), a UV nadir viewing sensor, aboard the NASA satellite Nimbus 4 (Gottwald et al., 2006). Observations of tropospheric O_3 are more recent. Initially tropospheric O_3 was derived by subtracting an estimate of the stratospheric column O_3 from the total column O_3, starting with studies by Fishman and Larsen (1987) and Fishman et al. (1990). This was done by using information about the O_3 profile from the Stratospheric Aerosol and Gas Experiment (SAGE) and total column O_3 from the Total Ozone Mapping Spectrometer (TOMS). A more recent example of a similar methodology is from Ziemke et al. (2006), subtracting MLS retrievals of stratospheric column O_3 from total column O_3 retrievals from OMI, both aboard the AURA satellite. Direct retrievals of tropospheric information, from the temperature dependence in the Huggins band (see Section 2.4.1.3) was first proposed by Chance et al. (1997) and utilised by Munro et al. (1998) from RAL on data from GOME. This technique has subsequently been used in other retrieval schemes e.g. Van Der A et al. (2002), Liu et al. (2010) and Cai et al. (2012). Increases in spectral resolution of the instruments over time, in the relevant bands to O_3, has also allowed for retrievals of O_3 with height information (van der A et al., 2002).

2.4.1.1 Retrieval methods

Retrieval methods (or inverse methods) are required to estimate the variable of interest e.g. O_3 concentration, from the indirect observation (Maahn et al., 2020). Optimal estimation (OE) is a retrieval technique which is widely used for deriving information from satellite measurements (Rodgers, 1976; Miles et al., 2015). Measurements, prior information and the corresponding uncertainties are combined in OE algorithms to provide an estimate of the state vector (Maahn et al., 2020). The principle of this method is that if a measurement, e.g. radiation spectra, has sensitivity to the atmospheric variable of interest e.g. O_3 concentration, a model could be used to compute what measurement the instrument would make for a particular atmospheric state. Then the model (known as a forward model) could be inverted to provide information about the atmospheric variable of interest from the measurement (Maahn et al., 2020). OE is an example of a physical retrieval method, which uses and inverts a forward model through an iterative process, converging on a solution (Maahn et al., 2020). This method of retrieval is based on the observations and forward models having an inherent uncertainty and can be represented by probability distributions, this means that the solution includes an uncertainty estimate (Maahn et al., 2020).

Due to the large number of unknowns, and the lack of unique solutions, the retrieval/inversion problem is often ill-posed (Maahn et al., 2020). Prior information is required with the forward model to constrain the problem, for example, an O_3 climatology profile (Maahn et al., 2020). The accuracy of the prior information used has a large impact on the accuracy of the retrieval.

A forward model contains all the relevant physics to the measurement (Rodgers, 2000). It is used to predict what would be measured, given a particular state vector (Siddans, 2019). Inverting the forward model will provide state vectors which map onto the remote observations (Maahn et al., 2020). Prior information (e.g. an O_3 profile climatology) is used to constrain the ill-posed problem, so that the most likely state is selected from the possible solutions (Maahn et al., 2020). In the case of atmospheric trace gas retrievals, the forward model will be a radiative transfer model. A radiative transfer model simulates how electromagnetic radiation is transferred along the viewing path through the atmosphere, as it is emitted and absorbed by trace gases (Met Office, 2023).

As an example, the OE technique used by RAL for UV-Vis instruments is described below. It is based on the standard OE algebra for the non-linear problem in Rodgers (2000). The technique is based around minimising the cost function (χ^2) as shown in Equation 2.21 (Miles et al., 2015):

$$\chi^2 = \left(\boldsymbol{y} - F(\boldsymbol{x})\right)^T \boldsymbol{S}_y^{-1}\left(\boldsymbol{y} - F(\boldsymbol{x})\right) + (\boldsymbol{x}_a - \boldsymbol{x})^T \boldsymbol{S}_a^{-1}(\boldsymbol{x}_a - \boldsymbol{x})$$

Equation 2.21

where $\boldsymbol{y}$ is the measurement vector, $\boldsymbol{x}$ is the state vector, $\boldsymbol{x}_a$ is the a priori vector, F is the forward model, $\boldsymbol{S}_y$ is the measurement error covariance matrix and $\boldsymbol{S}_a$ is the a priori error covariance matrix. The iterative updating of the state vector is shown in Equation 2.22:

$$\begin{aligned}\boldsymbol{x}_{i+1} = \ & \boldsymbol{x}_i + \left(\boldsymbol{K}_i^T \boldsymbol{S}_y^{-1} \boldsymbol{K}_i + \boldsymbol{S}_a^{-1} + \gamma \boldsymbol{I}\right)^{-1} \boldsymbol{K}_i^T \boldsymbol{S}_y^{-1} \\ & (\boldsymbol{y} - F(\boldsymbol{x}_i) + \boldsymbol{K}_i(\boldsymbol{x_i} - \boldsymbol{x}_a))\end{aligned}$$

Equation 2.22

where γ is the step size and $\boldsymbol{K}$ is the weighting function (at iteration i) as defined in Equation 2.23:

$$K_i = \frac{\delta F(\boldsymbol{x}_i)}{\delta x_i}$$

Equation 2.23

The error of the solution (S_x) are defined by the covariance matrix in Equation 2.24:

$$\boldsymbol{S_x} = \left(\boldsymbol{S_a^{-1}} + \boldsymbol{K^T S_y^{-1} K}\right)^{-1}$$

Equation 2.24

This error is a measure of the random error of the retrieval and is presented for the satellite records used in Chapter 5 (see Section 5.3.1.3) and Chapter 6 (see Section 6.3.1.3). It includes both errors from measurement noise and smoothing error from the prior constraint (Miles et al., 2015).

A measure of how much information a satellite retrieval provides is the degrees of freedom for signal (DOFS). It describes the number of independent pieces of information, given the prior state, which can be obtained from a measurement.

2.4.1.2 Retrieval process limitations and uncertainties

The associated uncertainties and limitations with the OE retrieval method are summarised as follows:

- There is no unique solution to the problem. There could be several different state vectors that map to an observation (Maahn et al., 2020). Different retrieval methods will provide different solutions.
- There are uncertainties in the forwards model e.g. how well the model represents the relevant physics (Maahn et al., 2020). These models contain many approximations and assumptions, which may be due to limitations in understanding of physical processes or to enhance computational efficiency.
- There are uncertainties associated with the measurements, i.e. noisy observations going into the retrieval process due to instrument imperfections (Maahn et al., 2020). If the instrument uses multiple channels or multiple instruments are used in the retrieval then there are random uncorrelated errors for each element, as well as correlated errors between the different elements (Maahn et al., 2020).
- Inaccurate prior information will lead to an inaccurate solution. Therefore, it is important how closely the prior information represents the current case. For example, during extreme events the retrieval will have a lower accuracy (Maahn et al., 2020).

2.4.1.3 Tropospheric ozone

Remote sensing of O_3 from satellite is based on understanding how O_3 absorbs radiation in the atmosphere. The key bands of O_3 absorption in the UV/Vis wavelengths are the Hartley, Huggins (both UV) and Chappuis bands (Vis). The Hartley band is wavelengths of 200–310 nm, the Huggins band is wavelengths of 320–360 nm and the Chappuis bands are between wavelengths of 450–850 nm. Information about O_3 in the troposphere comes from the Huggins band, due to the temperature-dependent spectral structures (Chance et al., 1997; Munro et al., 1998). Absorption peaks in the Hartley and Huggins bands can be seen in the example from OMI in Figure 2.19, with a lower ratio of Earth radiance and solar irradiance in the wavelength band of 270 – 330 nm.

Column (or sub-column) O_3 is usually presented in DU. One DU represents the number of O_3 molecules that would create a pure O_3 gas layer 0.01 mm thick at standard temperature and pressure (273 K and 1013.25 hPa, respectively) (BIRA-IASB, 2023). It was defined with reference to total column O_3, where the average value is ~ 300 DU, which would equal 3 mm of pure O_3 gas layer at standard temperature and pressure. A column of air of 1 DU would contain 2.69×10^{20} O_3 molecules for each m^2 at the base of the column.

2.4.1.4 Other trace gases

Satellite retrievals of CH_4, CO and H_2O are used in this thesis, from IASI. Retrievals of CH_4 are based on the SWIR and thermal IR spectral bands, with a spectral range of 1232 – 1288 cm^{-1} (7764 – 8117 nm) used in the RAL CH_4 retrieval scheme (Siddans et al., 2017). The RAL retrieval scheme used for H_2O, O_3 and CO is based on 139 channels between 662.5 – 1900 cm^{-1} (15094 – 5263 nm) (Siddans, 2019; Trent et al., 2023).

2.4.2 Ozonesondes

Ozonesondes are small O_3 monitoring instruments launched aboard balloons from stations around the world. The technique was pioneered in the 1930s, with the first measurements of O_3 from a balloon sonde made in 1934 near Stuttgart in Germany (Tarasick, Galbally, et al., 2019). Ozonesondes provide high vertical resolution O_3 profiles (typically 100 – 200 m) of the free troposphere, and are often used to validate satellite observations. However, they provide limited horizonal and temporal resolution, with routine launches at only ~ 100 sites globally (see Figure 3.10), typically launching around once per week (Tarasick, Galbally, et al., 2019). Regular use of ozonesondes in Europe, North America, Australia and Antarctica began towards the end of the 1960s. Modern ozonesonde instrument techniques include Electrochemical Concentration Cell (ECC), Brewer-Mast, Brewer-GDR, Indian KC and Japanese KC (Tarasick, Galbally, et al., 2019). These techniques are all based on the reaction of O_3 with potassium iodide. There are associated limitations with this monitoring technique, such as poor preparation of the sonde, issues with monitoring sharp O_3 gradients, interference from other gases in polluted areas, pump rate and temperature errors, radiosonde pressure biases and background currents (Tarasick, Galbally, et al., 2019). Ozonesondes have the benefit of being able to be launched in cloudy conditions so are not biased towards clear-sky conditions, such as other instruments e.g. satellite instruments (Gaudel et al., 2018).

2.4.3 Other ozone observation methods

There are also several other methods for observing O_3 in the free troposphere, aircraft, lidar and ground-based solar viewing Fourier Transform Infra-Red (FTIR), which are briefly summarised here. Regular monitoring of O_3 from commercial aircraft started in 1975, with a collaboration of NASA and US airlines called the Global Atmospheric Sampling Program (GASP) (Tarasick, Galbally, et al., 2019). O_3 has also been measured on research aircraft, often with a focus on observing a specific atmospheric event, providing temporal and spatial bias to sampling (Tarasick, Galbally, et al., 2019). Two large programmes of monitoring O_3 using UV absorption monitors on Airbus commercial aircraft are MOZAIC and the successor programme IAGOS, which have provided monitoring since 1994. The IAGOS database contains measurements from over 60,000 commercial flights (Gaudel et al., 2020). MOZAIC and IAGOS aircraft measurements have been shown to be around 5% higher than ozonesonde measurements in the lower troposphere and 8% higher in the upper troposphere (between 1994 – 2012) (Tarasick, Galbally, et al., 2019). Spatial sampling is biased in these measurements according to airport location and popular flight routes. Lidar is an active remote sensing technique used to monitor tropospheric O_3, through a technique called UV Differential Absorption Lidar (DIAL) (Tarasick, Galbally, et al., 2019). It is used at ground-based sites and on aircraft and can measure O_3 from around 100 m to the tropopause. The vertical and temporal resolution can be high, for example, up to 50 – 100 m in the lower troposphere and measurements every minute (Tarasick, Galbally, et al., 2019). However, the sensing period is limited by the requirement of human operators, and so is usually around 2 - 4 times per week (Gaudel et al., 2018). Ground-based solar viewing Fourier Transform Infra-Red (FTIR) instruments are a remote sensing technique used to observe tropospheric O_3 since 1980 (Tarasick, Galbally, et al., 2019). Observations from a global network of FTIR are provided by the Infrared Working Group of the Network for Detection of Atmospheric Composition Change (NDACC). The instruments have a very high spectral resolution (at least 0.005 cm^{-1}) and usually several observations are taken each day, with an uncertainty of ~ 14% (Gaudel et al., 2018; Tarasick, Galbally, et al., 2019).

2.5 Observation methods for the hydroxyl radical in the free troposphere

In this thesis, aircraft measurements of [OH] are used from the ATom campaign (Wofsy et al., 2018; Brune et al., 2019) (see Section 3.4 for further details), which was a large campaign that sampled the Atlantic and Pacific oceans in all seasons across 3 years. Previous aircraft campaigns have provided enhanced information about OH on a smaller regional scale. Notable regional scale campaigns measuring OH include (Stone et al., 2012): SUCCESS (Subsonic aircraft: Contrails and Cloud Effect Special Study) in 1996 above the USA (Brune et al., 1998); PEM (Pacific Exploratory Missions) in 1996 and 1999 above the south Pacific (Mauldin et al., 2001); SONEX (Subsonic assessment, Ozone and Nitrogen oxide Experiment) in 1997 above the northern Atlantic (Brune et al., 1999); TRACE-P (TRansport and Chemical Evolution over the Pacific) in 2001 above the western Pacific (Eisele et al., 2003); and INTEX (INtercontinental Chemical Transport EXperiment) in 2004 and 2006 over North America, the western Atlantic and the Pacific (Ren et al., 2008).

2.6 Summary

Overall, this chapter summarises the concepts and literature relevant to the results presented later in this thesis (Chapters 4, 5 and 6). O_3 and the OH radical are two important species in the troposphere that require continued study, including using new methods, to better determine their long-term variations. There are many studies of European surface O_3 showing long-term changes in baseline, median and peak values. However, there are only limited studies of the free troposphere, which could be further explored using the increasing breath of satellite-derived tropospheric O_3 products available. For OH, there has so far been limited methods of deriving OH concentrations from atmospheric observations which can provide spatial and temporal information. Satellite-derived products could be a solution, proving a method to study long-term changes in OH. The following chapter (Chapter 3) will summarise the satellite data products used here in greater detail and provide a background to the model used, the other key source of data in this work.

Chapter 3 Datasets and model

This chapter presents an overview of the key datasets used in this thesis, from satellite, ozonesonde and aircraft. The model used in this work, TOMCAT, is also described and information provided about its setup.

3.1 Satellite datasets

This thesis uses and investigates several records of satellite-derived tropospheric composition from RAL. IASI data is used in chapter 4; GOME, SCIAMACHY and OMI in chapter 5; and IASI and GOME-2 in chapter 6. This section presents an overview to the instruments, corresponding satellites and the retrieval schemes used. Further detailed description on how these satellite datasets are used is documented in the result chapters (Sections 4.3.4, 5.3.1 and 6.3.1).

3.1.1.1 IASI

The Infrared Atmospheric Sounding Interferometer (IASI) is aboard EUMETSAT's MetOp series of 3 satellites (A, B and C) and was designed by the Centre National d'Etudes Spatiales (CNES) based on a Fourier Transform Spectrometer (Clerbaux et al., 2009). MetOp-A was launched in October 2006, ceasing operation in November 2021 and MetOp-B was launched in September 2012 and is still in operation at present (EUMETSAT, n.d.; Clerbaux et al., 2009). The MetOp series of satellites have a sun-synchronous, near polar orbit (98.7° inclination), at a mean altitude of 817 km, with a equator crossing time of 9:30 LST. The swath has a width of 2200 km, and in the nadir viewing mode, there are four circular fields of view across-track with a diameter of 12 km, covering a square 50 × 50 km^2, shown in Figure 3.1. The IASI instrument measures in the IR wavelength range (645 – 2760 cm^{-1}) with a spectral resolution of 0.3 - 0.5 cm^{-1} (Clerbaux et al., 2009).

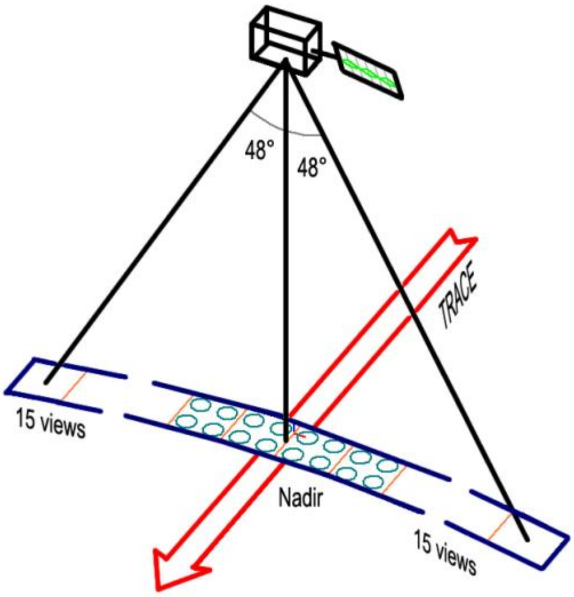

Figure 3.1: Diagram of IASI observing mode. Taken from Clerbaux et al. (2009).

Chapters 4 and 6 use RAL's Infrared and Microwave Sounding (IMS-Extended) scheme for retrievals of O_3, H_2O and CO. The IMS-extended scheme is described in the supplement of Pope et al. (2021) and a comparison of IASI-IMS-Extended O_3 with ozonesonde observations is presented in the supplement of Pimlott et al. (2022) (Section S3). Briefly, the IMS scheme was initially developed to retrieve H_2O, temperature and stratospheric O_3 profiles from IASI, the Microwave Humidity Sounder (MHS) and the Advanced Microwave Sounding Unit (ASMU). A description of the IMS scheme can be found in Siddans (2019). The scheme uses the OE technique (described in Section 2.4.1.1). The scheme has been extended to also retrieve tropospheric O_3, CO profiles and column amounts of other trace gases (known as IASI-IMS-Extended) (Pope et al., 2021). The extension of the scheme builds on new capabilities of the radiative transfer model used (Radiative Transfer for TOVS 12 (RTTOV12), Saunders et al. (2017)) in the modelling of atmospheric scattering. In this thesis, the IASI record from 2008 – 2017 is from IASI aboard MetOp-A and the record from 2018 – 2021 is from IASI aboard MetOp-B.

Chapters 4 and 6 also use CH_4 from the improved version (v2.0) of RAL's CH_4 retrieval scheme (Siddans et al., 2020; Knappett et al., 2022) (v1.0 is described in Siddans et al. (2017)). Another tropospheric O_3 product from a different retrieval scheme, provided by the Université de Toulouse and the Centre National de la Recherche Scientifique (CNRS) (IASI-SOFRID, SOftware for a Fast Retrieval of IASI Data Version 3.5), is used in Chapter 6. The IASI-SOFRID product is first described in Barret et al. (2011). The scheme uses the RTTOV radiative transfer model (Saunders et al., 1999) and the optimal estimation method and an O_3 a priori based on an ensemble of ozonesondes from the World Ozone and Ultraviolet Radiation Data Centre (WOUDC), Southern Hemisphere Additional Ozonesondes (SHADOZ) and the aircraft campaign MOZAIC (Rodgers, 2000; Barret et al., 2011; Barret et al., 2020). In their validation of IASI-SOFRID, Barret et al. (2020) found a difference of less than 2.5% in comparison with ozonesondes for tropospheric column O_3 in the NH, and up to 9.5% in the SH.

3.1.2 RAL UV-Vis retrieval scheme

The UV-Vis retrieval scheme used by RAL for GOME, SCIAMACHY, GOME-2 and OMI is initially described in Munro et al. (1998), with updates described in Miles et al. (2015). To summarise here, the RAL retrieval of vertical O_3 profiles is based on optimal estimation, as discussed in Section 2.4.1.1 (Rodgers, 2000; Miles et al., 2015). It is a sequential three-step approach:

- Step 1 – A fit is performed to the sun-normalised radiance spectrum in the long-wave tail of the Hartley band (wavelengths between 266–307 nm). This provides mostly information about the mid-upper stratosphere, retrieving an O_3 profile that is used in step 3. The O_3 absorption in this region is strongly wavelength dependent, giving information about the altitude from where the radiation was backscattered, but not from below peak O_3 (e.g. not from below the stratosphere)

(Munro et al., 1998). The fit is a direct fit of the sun-normalised radiance (r) as defined in Equation 3.1 (Miles et al., 2015):

$$r = \frac{I}{I_0}\pi \qquad \textbf{Equation 3.1}$$

where I is the measured Earthshine radiance and I_0 is the direct-sun irradiance measurement.

- Step 2 – Retrieving an effective surface albedo from the sun-normalised radiance spectrum at wavelengths of 336 nm for each ground pixel.
- Step 3 – The retrieved O_3 profile and error covariance matrix from the fit in step 1 and the retrieved effective albedo contribute to prior information for a final fit in step 3. The temperature dependence on the spectral structure in O_3 absorption in the Huggins Band (323–335 nm) is utilised to provide information about the lower stratosphere and troposphere, extending the retrieval down, closer to the surface.

The a priori O_3 profiles are from the McPeters-Labow-Logan climatology, which is derived from ozonesondes (McPeters et al., 2007; Keppens et al., 2018). European Centre for Medium-Range Weather Forecasts (ECMWF) ERA-interim meteorological fields (pressure and temperature profiles) are used in the retrieval. The retrieved O_3 profile is on a fixed pressure grid of: surface pressure, 450, 170, 100, 50, 30, 20, 10, 5, 3, 2, 1, 0.5, 0.3, 0.17, 0.1, 0.05, 0.03, 0.017, 0.01 hPa, which is approximately equivalent to altitudes of: 0, 6, 12, 18 km, then every 4 km up to 80 km. For the combined band retrieval, DOFS is typically 5 – 6 (Miles et al., 2015). The radiative transfer model used is based on GOMETRAN++ (Rozanov et al., 1997) updated with several improvements to processing speed (Miles et al., 2015).

The accuracy of radiometric calibration is important for the first step, the fit of the sun-normalised radiance. The calibration is performed in the laboratory before launch. However, during the instrument's operation the diffuser, which scatters the incoming radiation, can become contaminated, leading to bias in the observation (known as 'UV degradation'). GOME (also SCHIAMACHY and GOME-2) has experienced degradation of the UV photometric throughput, due to this damage of the instrument's optical elements (Liu et al., 2007; Miles et al., 2015). The degradation has varied over time, which adds uncertainty when considering long-term trends, with larger uncertainty for shorter wavelengths. For example, GOME measurements of Earth radiance and solar irradiance have degraded in different ways over the operation period, starting in around 1998 (van der A et al., 2002; Cai et al., 2012). This degradation can have a large impact on the data, causing biases of up to ~30% for tropospheric column O_3 (Liu et al., 2007).The retrieval schemes used for GOME and SCIAMACHY here, have a correction applied to account for this UV degradation (Miles et al., 2015). The correction is based on the ratio between climatological modelled UV sun-normalised radiance and the observed sun-normalise radiance spectrum for the record. In contract, the OMI instrument has a different instrument design, and is considered to have experienced negligible UV degradation, with OMI radiances varying by only 1 – 2% (Schenkeveld et al., 2017; Levelt et al., 2018).

3.1.3 GOME

The Global Ozone Monitoring Experiment (GOME) instrument was aboard the European Space Agency's (ESA) second European Remote Sensing Satellite (ERS-2) launched in April 1995 and which ceased operation in 2011 (European Space Agency, n.d.; Burrows et al., 1999). The orbit of ERS-2 was sun-synchronous and near-polar (98.5° inclination), with an average altitude of 795 km and an equator crossing time of 10:30 LST. The satellite had a nadir viewing mode, a swath with an across-track width of 960 km, a ground-pixel resolution of 40 × 320 km^2 and achieved global coverage in 3 days (43 orbits). GOME measured in the UV-Vis wavelength range (240-790 nm) at a spectral resolution of 0.2 – 0.4 nm (Burrows et al., 1999). Tropospheric sub-column O_3 retrievals from GOME (RAL UV-Vis retrieval scheme) are used in Chapter 5.

The failure of the tape recorder aboard ERS-2 caused a reduction in geographical sampling from around 2003 onwards (Van Roozendael et al., 2012). This caused the GOME instrument to lose global coverage towards the end of its operation. As shown in total column retrievals of O_3 in Koukouli et al. (2012), the reduction in sampling was predominantly in the SH, but does reach up to around latitudes of 30°N. The European domain studied here (30°N – 70°N) is not within the affected latitude, however, this is still a limitation to consider.

3.1.4 SCIAMACHY

The Scanning Imaging Absorption Spectrometer for Atmospheric Chartography (SCIAMACHY) instrument was aboard ESA's Envisat launched in March 2002 and which ceased operation in April 2012 (Bovensmann et al., 1999; Ebojie et al., 2016). The orbit of Envisat was sun-synchronous and near-polar (98.55° inclination), with an average altitude of 800 km and an equator crossing time of 10:00 LST. The satellite had 3 viewing modes, limb, nadir and solar/lunar occultation, a swath with an across-track width of 960 km and a ground-pixel resolution of 30 × 60-240 km^2. SCIAMACHY measured in the UV, Vis and NIR wavelength range (240-2380 nm) at a spectral resolution of 0.2-1.5 nm (Bovensmann et al., 1999). Tropospheric O_3 retrievals from SCIAMACHY (RAL UV-Vis retrieval scheme) are used in Chapter 5.

3.1.5 OMI

The Ozone Monitoring Instrument (OMI) is aboard NASA's AURA satellite, launched in July 2004 and is still in operation at present (Levelt et al., 2006). The AURA satellite has a sun-synchronous and near polar (98.2° inclination) orbit at an average of 705 km altitude. The satellite crosses the equator at 13:45 LST (ascending node) and flies as part of a formation called the 'A-train'. OMI uses a nadir viewing mode with a swath width of 2600 km and a ground resolution of 13 × 24 km^2, providing nearly global coverage every day (Figure 3.2). OMI measures in the UV-Vis wavelength range (270 – 500 nm) with a spectral resolution of 0.45 – 1.0 nm (Levelt et al., 2006). Tropospheric O_3 retrievals from OMI (RAL UV-Vis retrieval scheme) are used in Chapter 5.

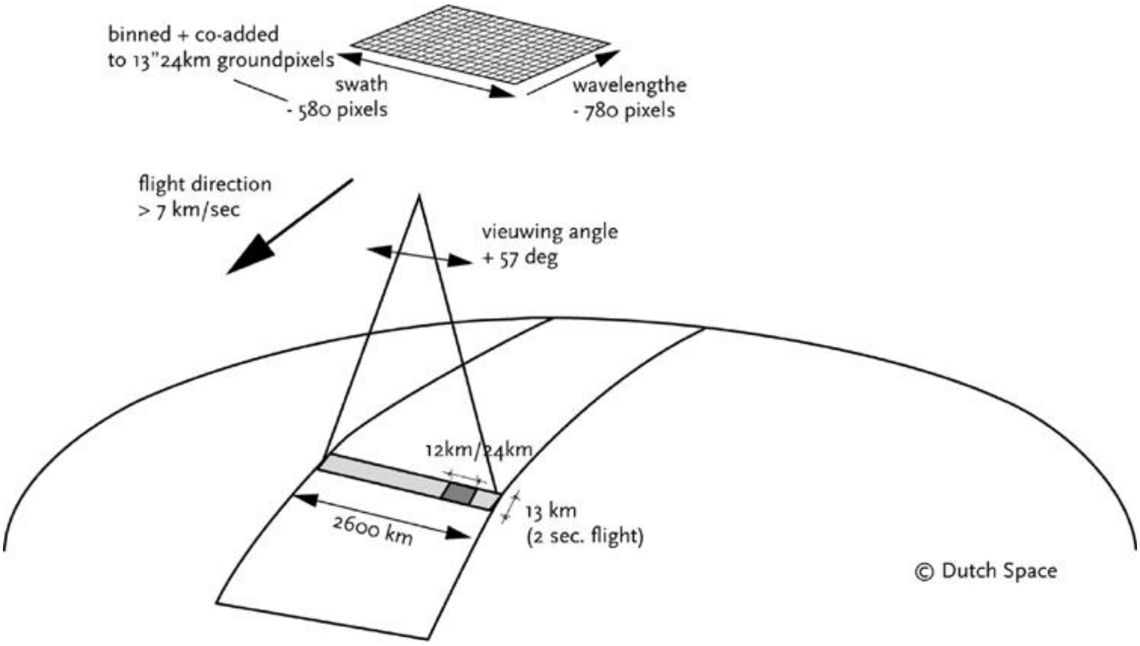

Figure 3.2: Diagram of the OMI measurement principles. Taken from Levelt et al. (2006) (© 2006 IEEE).

3.1.6 OMI row anomaly

The instrument OMI uses 2-D detectors, where one dimension obtains the spectral information, and the other detects the spatial information (Levelt et al., 2006). It has 60 across-track viewing angles or ‘rows’. In the RAL product used in this thesis, the 60 rows are ‘co-added’, creating a product with only 30 rows. The OMI instrument has been impacted by the OMI row anomaly since around 2007, with large changes occurring in 2009 and early 2011, however, since then it has been relatively stable (Schenkeveld et al., 2017; Levelt et al., 2018). The row anomaly impacts the quality of all wavelengths of radiance data from a specific viewing direction, corresponding to a row in the 2-D detectors of OMI. It was caused by damage to the insolation blankets that cover OMI, which has blocked part of the field of view (Levelt et al., 2018). The impact depends on channel (UV/Vis), latitude and season. Since 2014 the percentage of affected rows ranges from 30% (Vis) - 37% (UV1) (Schenkeveld et al., 2017). The impact of the row anomaly on the results, and the method used to analyse the data, is discussed in Section 5.3.1.1.

3.1.7 GOME-2

The Global Ozone Monitoring Experiment-2 (GOME-2) is aboard EUMETSAT’s MetOp series of satellites (as described in Section 3.1.1.1) (Callies et al., 2000; Munro et al., 2016). GOME-2 measures in the UV-Vis wavelength range (240 – 790 nm) with a spectral resolution of 0.26 - 0.51 nm. The instrument has a swath width of 1920 km and a ground resolution of 80 × 40 km^2 (Munro et al., 2016). Tropospheric O_3 retrievals from GOME-2 from MetOp-B (GOME-2B) (RAL UV-Vis retrieval scheme) are used in Chapter 6.

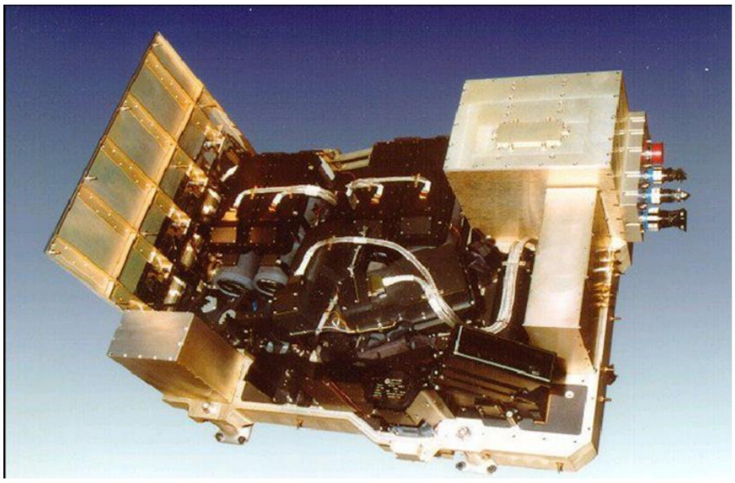

Figure 3.3: Photograph of the GOME-2 instrument. Taken from Munro et al. (2016).

Miles et al. (2015) assessed the performance of the RAL retrieval scheme for GOME-2A, by validating against 2 years of ozonesondes (2007 – 2008). After application of averaging kernels (AKs) to the sonde profiles there was an average retrieval bias of 6% (1.5 DU) in the lower troposphere, with a positive bias (satellite overestimation) in the NH of 10% (2 DU). For cloud-free pixels, they found a small bias of 0.7 DU with TOMCAT in August 2008s, and a correlation between pixels of 0.66.

3.1.8 Uncertainty and limitations

Satellite data has associated uncertainty and limitation in use. Malfunctions of the instrument, e.g. the OMI row anomaly, GOME tape recorder failure and UV degradation to GOME and SCIAMACHY , can reduce the volume and quality of data provided. As with the OMI row anomaly and UV degradation, this reduction in data volume and quality, can vary through the record (Miles et al., 2015).

Different retrieval algorithm schemes will produce different results, which leads to uncertainty in the observations. Implementation of the scheme, such as choice of a priori, which spectroscopic data and other forward model parameters to use, can also impact the result (Gaudel et al., 2018). For example, Liu et al. (2013) highlighted the variation caused by using different O_3 cross-sections on OMI O_3 profile retrievals, showing that using two different cross sections caused biases of 5 – 20 DU for tropospheric O_3. The accuracy of the retrieval scheme also replies on the assumptions in the forward model.

Another key considerations for satellite observations is the presence of clouds and aerosols. Clouds scatter radiation, which reduces the instrument’s sensitivity to trace gases below the cloud (Martin, 2008), and cloudy observations are generally filtered out during the processing, e.g. Gaudel et al. (2018) presents 8 satellite products with cloud fraction filtering ranging from < 13 – 30 %. Aerosols can also decrease the instrument’s sensitivity depending on their single scattering albedo and vertical distribution (Martin, 2008).

3.1.9 Averaging kernels

AKs provide information about the vertical sensitivity of the satellite retrievals. AKs provide a quantification of the relative sensitivity of the retrieval to the ‘true state’ of the retrieved layers (Rodgers, 2000; Gaudel et al., 2018). The AKs will vary with the different properties of each sounding e.g. land or ocean retrieval, day or night retrieval, spectral range, spectral resolution, choice of a priori and measurement noise (Gaudel et al., 2018).

Following on from the optimal estimation equations earlier in Section 2.4.1.1, the AKs are calculated using the weighting function ($\mathbf{K}$) as shown in Equation 3.2

$$\mathbf{A} = \mathbf{GK} \qquad \textbf{Equation 3.2}$$

where $\mathbf{G}$ is the gain matrix, which defines the sensitivity of the retrieval to measurement perturbations (Rodgers, 2000; Miles et al., 2015). $\mathbf{G}$ is calculated as shown in Equation 3.3:

$$\mathbf{G} = \left(\mathbf{K}^{\mathrm{T}}\mathbf{S}_{\mathbf{y}}^{-1}\mathbf{K} + \mathbf{S}_{\mathbf{a}}^{-1}\right)^{-1}\mathbf{K}^{\mathrm{T}}\mathbf{S}_{\mathbf{y}}^{-1} \qquad \textbf{Equation 3.3}$$

where, as before, $\mathbf{S}_{\mathbf{y}}$ is the measurement error covariance matrix and $\mathbf{S}_{\mathbf{a}}$ is the prior error covariance matrix.

In comparing satellite observations with model data it is important to apply the AKs to the model profiles to make the comparison more robust, due to the enhanced information about vertical sensitivity. Applying the AKs to the model maps the sensitivity of the retrieval onto the model profile. For each satellite retrieval, a model profile is co-located from the nearest grid box and AKs applied, which is then used to form the monthly average. The AKs are applied as shown in Equation 3.4:

$$\boldsymbol{Y_{SC}} = (\mathbf{I} - \mathbf{A})\, \boldsymbol{apr} + \boldsymbol{A}.\boldsymbol{X_{SC}} \qquad \textbf{Equation 3.4}$$

where $\boldsymbol{Y_{SC}}$ is the model sub-column with AKs applied, $\boldsymbol{I}$ is the identify matrix, $\boldsymbol{apr}$ is the a priori of the satellite sub-column, $\boldsymbol{A}$ is the AK matrix of the sub-column and $\boldsymbol{X_{SC}}$ is the model profile without AKs applied.

Example profiles of AKs, satellite O_3 and model O_3 are shown in Figure 3.4 for GOME and Figure 3.5 for SCIAMACHY (used in Chapter 5). Figures 3.4 and 3.5 show that for the lowest sub-column (1000 – 450 hPa, lowest point on profile), applying the AKs, reduces the model O_3 for GOME and SCIAMACHY in their respective years for January, however, has little impact for July. All the AK profiles in Figures 3.4 and 3.5 show sensitivity in the troposphere, with high AK values from the lowest two sub-columns between around 1000 – 170 hPa. This demonstrates that these satellite records are appropriate to use in the study of tropospheric O_3.

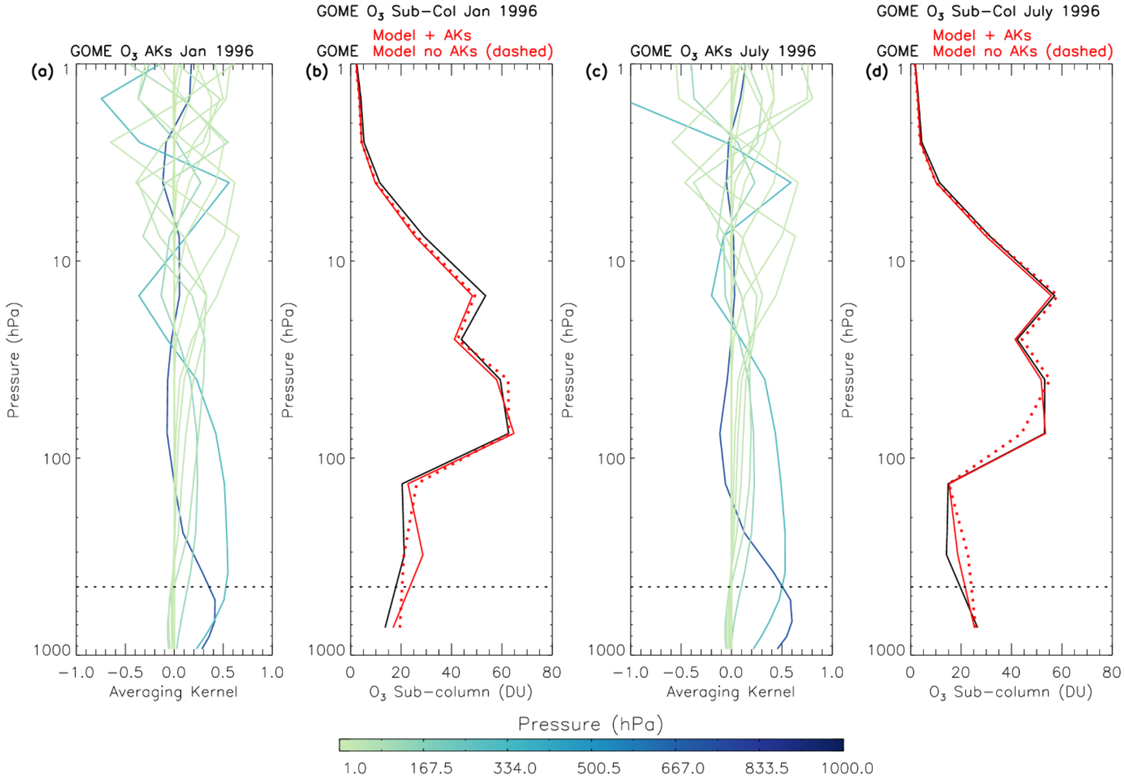

Figure 3.4: (a) GOME O_3 AK profile averaged for January 1996. (b) O_3 profiles averaged in January 1996 for GOME, TOMCAT with AKs and TOMCAT without AKs (both model profiles are co-located with the GOME retrievals). (c) As (a) for July 1996. (d) As (b) for July 1996. A dotted line highlights 450 hPa. Sub-column values are plotted on the pressure axis as mid-points for their sub-column.

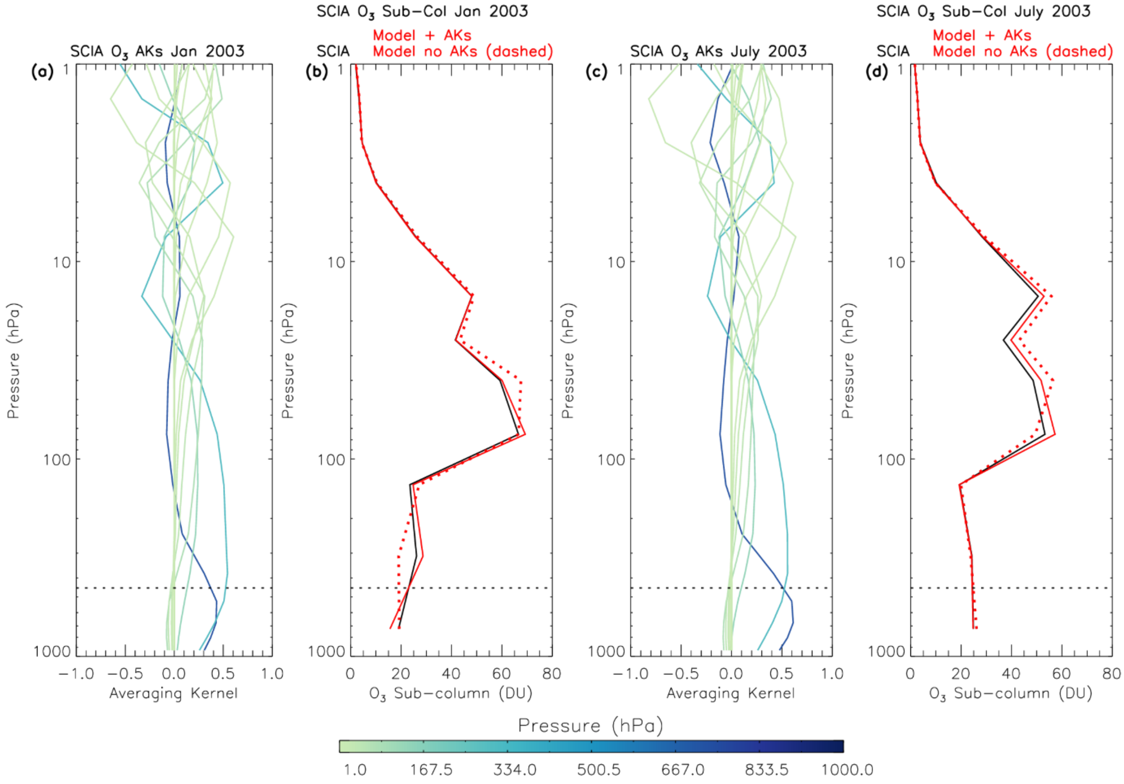

Figure 3.5: As Figure 3.4 for SCIAMACHY in January and July 2003.

3.2 Chemistry transport model

In this thesis, the TOMCAT CTM is used to simulate tropospheric O_3. CTMs are numerical models which are widely used to simulate chemistry and transport in the atmosphere. An 'off-line' CTM, such as TOMCAT, uses meteorological fields (e.g. winds, temperatures) from reanalyses or another model, as they do not calculate their own meteorology (Chipperfield, 2006). In comparison to models that do simulate their own meteorology (e.g. general circulation models (GCM)), off-line CTMs benefit from being computationally cheaper and, as they are constrained by 'real' meteorological analysis, they allow for a better comparison with observations. In contrast, models that simulate their own meteorology are needed for future predictions and to study chemical-radiative-dynamical feedbacks (Chipperfield, 2006).

3.2.1 TOMCAT model description

TOMCAT/SLIMCAT is a global off-line Eulerian 3-D CTM (Chipperfield, 2006). It has been used for an extensive range of studies of the chemistry of the troposphere and stratosphere, e.g. Rowlinson et al. (2019) used TOMCAT to study the impact of ENSO on tropospheric O_3 and CH_4, and Dhomse et al., (2021) used TOMCAT, machine learning and satellite data to create a long-term stratospheric O_3 profile record. The version of TOMCAT used in this thesis has a horizontal resolution of 2.8° × 2.8° and 31 vertical levels between the surface and 10 hPa (shown in Figure 3.6), with ~ 5 – 7 levels in the BL and ~10 in the mid-troposphere, depending on latitude. The model uses a hybrid vertical co-ordinate system (σ - p), with the near-surface levels following the terrain (σ) and higher levels (<100 hPa) using pressure levels (p).

The model is driven by 6-hourly ERA-Interim (Chapters 4 and 5) or ERA-5 (Chapter 6) meteorological reanalyses, of wind, temperature and humidity, from ECMWF. The ERA-Interim product was released in 2006, covering the time period from 1979 – August 2019 (Dee et al., 2011; Hersbach et al., 2020). ERA-5 is a new reanalysis product from ECMWF, to replace ERA-interim, which covers 1950 – present (Hersbach et al., 2020). The spatial resolution for ERA-5 is higher, with a 31 km grid, compared to a 80 km grid for ERA-interim and benefits from improvements in model physics, core dynamics and data assimilation (Hersbach et al., 2020). Large-scale advection of tracers in TOMCAT is based on the Prather (1986) scheme in the meridional, zonal and vertical directions (Chipperfield, 2006; Monks et al., 2017). Transport on a sub-grid scale (e.g. BL mixing and convective transport) is based on Tiedtke (1989) and Holtslag and Boville (1993).

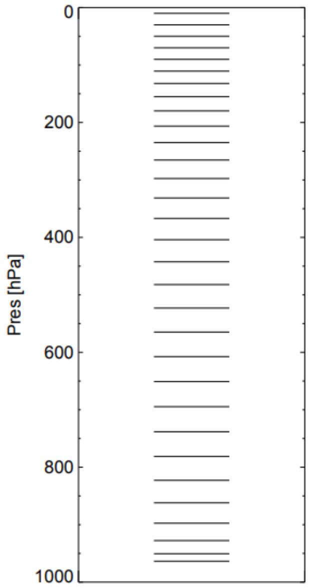

Figure 3.6: Representation of average global pressure levels for the TOMCAT model setup used in this thesis. Taken from Monks et al. (2017).

TOMCAT is coupled with the Global Model of Aerosol Processes (GLOMAP), which calculates aerosol chemistry and microphysics (Spracklen et al., 2005; Mann et al., 2010). GLOMAP includes size-resolved primary emissions, formation of new particles, condensation, coagulation, cloud processing, dry deposition, sedimentation, nucleation and impact scavenging (Mann et al., 2010). There are four aerosol size distributions (nucleation, Aitken, accumulation and coarse) and four aerosol components (sulphate, BC, organic carbon (OC) and sea-salt).

For the simulations in this thesis, the full chemistry mode of TOMCAT is used. A description of the tropospheric chemistry scheme can be found in Monks et al. (2017) (updated from Arnold et al. (2005)). The full chemistry scheme includes 79 species, including 16 species that are emitted, and ~200 chemical reactions. Isoprene oxidation is based on the Mainz Isoprene Mechanism (Pöschl et al., 2000), the emission and destruction of ethene, propene, toluene and butane is based on the Extended Tropospheric Chemistry scheme (ExtTC) (see supplement of Monks et al. (2017)) and that of monoterpenes is based on the MOZART-3 chemical mechanism (Kinnison et al., 2007). The kinetic reaction rates used are from the 2005 recommendations of the International Union of Pure and Applied Chemistry (IUPAC, Atkinson et al. (2006)) and the Leeds Master Chemical Mechanism (MCM) from 2004. Some of the surface emissions used in this thesis have been updated compared to those described in Monks et al. (2017). The surface emissions used in each results chapter are described in Sections 4.3.5, 5.3.3.1 and 6.3.4. The surface monthly mean emissions are read into the model on a 1° × 1° grid and re-gridded online to the model spatial resolution and linearly interpolated temporally to the model timestep (Monks et al., 2017). NO_x emissions from lightning are coupled to model convection, which is derived from the meteorological reanalyses. Therefore, lightning NO_x emissions vary due to the seasonality and spatial pattern of convective activity (Stockwell et al., 1999). The simulations were run on the Leeds high performance computing facility, ARC3. The model output of 3D tracer fields and meteorological variables was sub-sampled daily at 9.30 and 13.30 LST to match that of the satellite overpass used in this thesis.

The simulations have also been setup with an update to the climatological cloud fields (from the International Satellite Cloud Climatology Project (ISCCP) (Rossow and Schiffer, 1999)) using reanalyses of cloud fraction from ECMWF, which is described in Rowlinson et al. (2019). This update provides cloud fields which vary by year, improving the representation of interannual variability and photolysis rates in the model.

3.2.1.1 STE representation in TOMCAT

In Chapters 5 and 6 a tracer for STE is used from the TOMCAT simulations to understand the impact of O_3 transport from the stratosphere. This tracer represents tagged stratospheric O_3. In the stratosphere, the tracer equals the stratospheric O_3 as calculated by the model. When the tracer enters the troposphere, there are no additional sources of the tracer, but the sink processes for O_3 in the troposphere all apply, e.g. photolysis, reaction with species such as HO_x/NO_x and surface deposition (Monks et al., 2017). The lifetime of the tracer depends on the model sink reactions and surface deposition, as with untagged tropospheric O_3.

3.2.1.2 Surface dry deposition representation in TOMCAT

Surface deposition is an important sink for tropospheric O_3. TOMCAT uses the dry deposition scheme described by Giannakopoulos et al. (1999). Dry deposition velocities are based on fixed land cover fields and sea-ice fields that vary seasonally from the NCAR community land model (CLM). These fields were reclassified from 16 types to the five TOMCAT land types (water, forest, grass/crop/shrub, desert/bare ground and snow/ice) (Hollaway, 2012; Monks et al., 2017). The deposition velocity is then based on the local time of day and season and weighted based on the proportion of each grid-box covered by each land type (Hollaway, 2012; Monks et al., 2017).

3.2.2 Model performance

3.2.2.1 OH radical

Two recent studies have evaluated TOMCAT OH: Monks et al. (2017) and Rowlinson et al. (2019). The TOMCAT version and model set up used in Chapter 4 is most similar to that in Rowlinson et al. (2019), due to the updated cloud fields from ECMWF reanalyses, which will impact the photolysis in the model, which is relevant to OH production. Rowlinson et al. (2019) found an average global tropospheric concentration of 1.04×10^6 molecule cm^{-3} and an average CH_4 lifetime of 8.0 years. This is similar to several other studies, such as: A global mean concentration of 1.08×10^6 molecule cm^{-3} from the Monks et al. (2017) TOMCAT version (CH_4 lifetime of 7.9 years); $0.94 \pm 0.1 \times 10^6$ molecule cm^{-3} by Prinn et al. (2001) from inferred OH observations from MCF (CH_4 lifetime of 9.3 years); $1.08 \pm 0.6 \times 10^6$ molecule cm^{-3} from the POLARCAT Model Intercomparison Project (POLMIP) (Emmons et al., 2015); and the multi-model mean of

1.11 ± 0.2 $\times 10^6$ molecule cm^{-3} from the Atmospheric Chemistry and Climate Model Intercomparison Project (ACCMIP) (CH_4 lifetime of 9.7 years) (Naik et al., 2013). The comparison found by Rowlinson et al. (2019) (Figure 3.7), using the evaluation methodology of 12 sub-domains by Lawrence et al. (2001). Figure 3.7 shows that in the vertical distribution, the two TOMCAT studies (Monks et al. (2017) & Rowlinson et al. (2019)) show the largest TOMCAT [OH] to be between the surface and 750 hPa near the equator. Comparatively, Spivakovsky et al. (2000), using the MCF method, and the ACCMIP multi-model mean [OH] (Naik et al., 2013) have the largest OH values higher up in the troposphere. All [OH] records show a similar latitudinal distribution, with higher values in the tropics and lower values in the SH. (Emmons et al., 2015). Differences between the model OH datasets could be due to modelled clouds and their impact on photolysis in the model (Emmons et al., 2015), as shown here (Figure 3.7), with the primary difference between Rowlinson et al. (2019) TOMCAT and Monks et al. (2017) TOMCAT being an update to cloud fields. Nicely et al. (2017) found that across 8 CTMs, differences in OH were caused by variations in chemical mechanisms, photolysis frequency and local O_3, CO and NO_x concentrations.

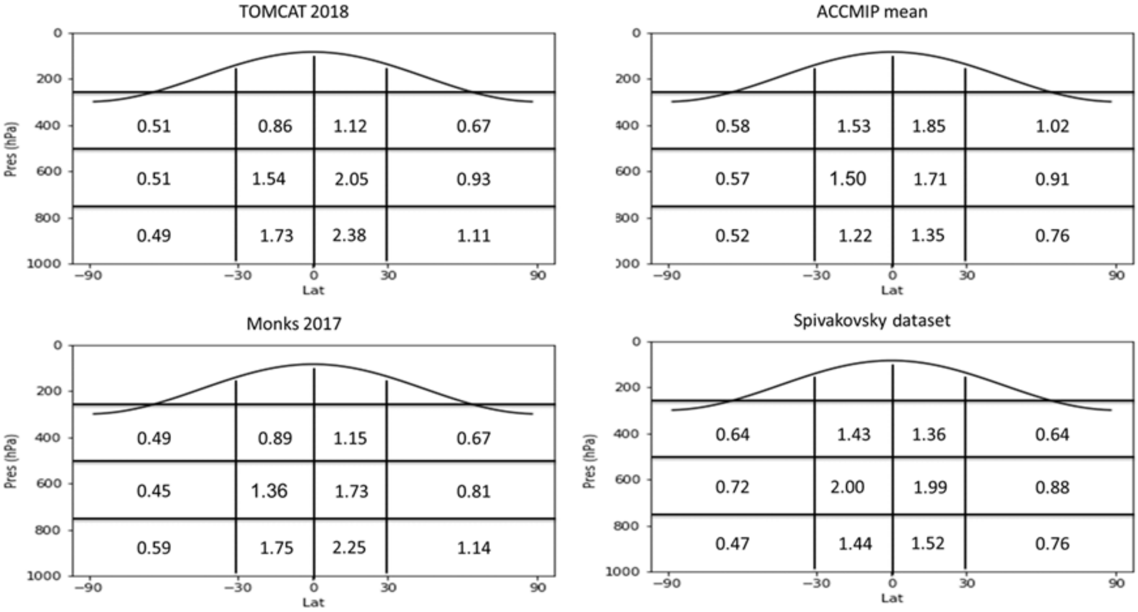

Figure 3.7: Annual zonal mean [OH] from 2000, in units of 10^6 molecule cm^{-3}, divided into 12 regions. [OH] from Rowlinson et al. (2019) is labelled as 'TOMCAT 2018', [OH] from Monks et al. (2017) is labelled as 'Monks 2017'. The 'Spivakovsky dataset' is from Spivakovsky et al. (2000) based on MCF observations and 'ACCMIP mean' is based on a multi-model mean from ACCMIP (Naik et al., 2013). Taken from Rowlinson et al. (2019).

3.2.2.2 Tropospheric ozone

Rowlinson et al. (2019) has evaluated TOMCAT model tropospheric O_3 profiles using ozonesondes (Figure 3.8) for 1995 - 2011. Generally, TOMCAT agrees well with the ozonesonde profiles, capturing the seasonal variation and absolute values closely. A low normalised mean bias (NMB) of 1.1% was found for 700 – 1000 hPa and 2.1% for 300–700 hPa. Rowlinson et al. (2019) also found a global tropospheric burden of 342 Tg for

TOMCAT in 2000, which is similar to other values found in the literature e.g. 337 ± 23 Tg from the ACCMIP multi-model mean (based on an ensemble of 15 global models) (Young et al., 2013). Monks et al. (2017) also compares TOMCAT O_3 with ozonesondes, highlighting the latitudinal differences. In two tropospheric pressure regions studied (750 – 1000 hPa and 450 – 750 hPa), TOMCAT mostly underestimates O_3 compared to the observations. The biases are not contained within uncertainty of the observations in the high latitudes of both the SH and NH. Here the model shows underestimates of O_3 in the winter months, which suggests the model has issues with representing O_3 photochemistry in the winter in cold, remote and dark regions or deposits too much O_3 onto surfaces with ice/snow. This negative wintertime bias in the SH is also seen in the ACCMIP multi-model mean (Young et al., 2013). There is an overestimate of summertime O_3 near the surface in the TOMCAT NH, which is likely due to issues with the surface deposition scheme in the model (Monks et al., 2017). Broadly, model inputs (e.g. emissions), chemistry scheme, temporal and spatial resolution, physical processes (e.g. deposition, transport and meteorology) and any missing processes are potential causes of differences between models and observations of tropospheric O_3 (Young et al., 2018). Wild (2007) found that the modelled tropospheric O_3 budget between different models was sensitive to the size and location of lightning NO_x emissions, humidity and dry deposition, and model resolution strongly impacted the estimation of STE and dry deposition.

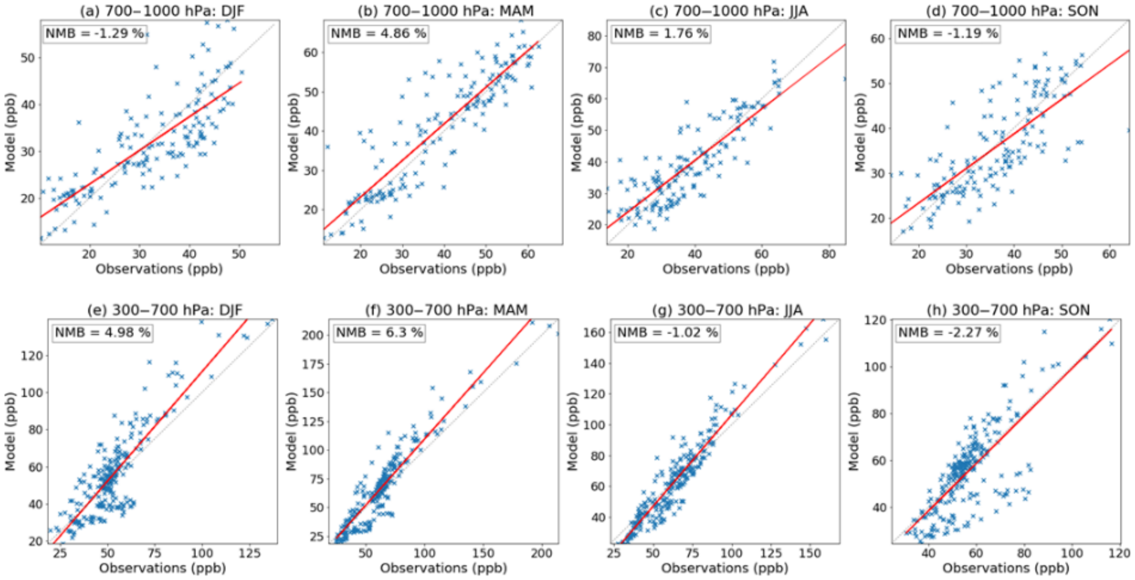

Figure 3.8: Seasonal comparison of TOMCAT model O_3 and ozonesonde O_3 observations during 1995 – 2011 (ppbv, left to right – DJF, MAM, JJA and SON). Panels (a) – (d) show mean O_3 concentrations for 700 – 1000 hPa and panels (e) – (h) show mean O_3 concentrations for 300 – 700 hPa. Taken from Rowlinson et al. (2019).

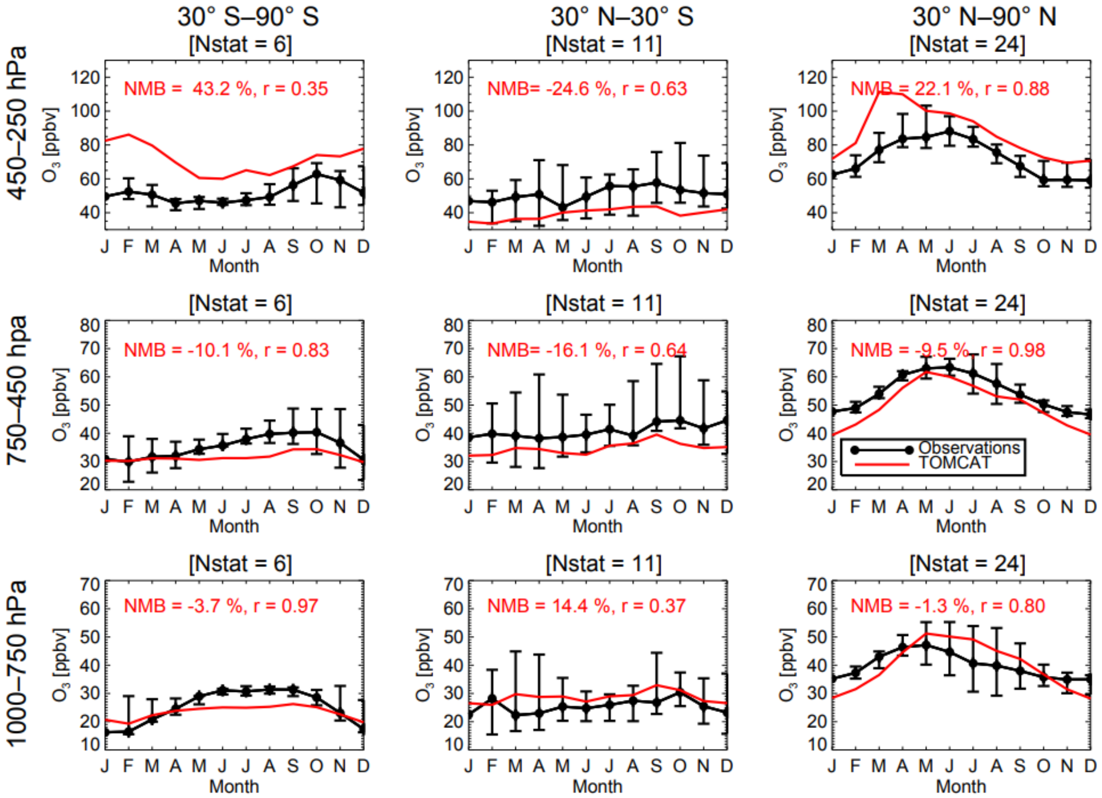

Figure 3.9: Monthly comparison of median O$_3$ (ppbv), compared to an ozonesonde O$_3$ climatology for 3 latitude bands (90°S – 30°S, 30°S – 30°N and 30°N – 90°N) and 3 pressure ranges (750 – 1000 hPa, 450 – 750 hPa and 250 – 450 hPa). The error bars on the observations show the 25th and 75th percentiles of the observed concentrations. Taken from Monks et al. (2017).

3.3 Ozonesondes

In this thesis, Ozonesonde data from the World Ozone and Ultraviolet Radiation Data Centre (WOUDC) is used (WOUDC, 2021). The WOUDC is one of the six World Data Centres which are part of the World Meteorological Organisation's Global Atmospheric Watch programme. It contains O$_3$ data for 500 stations globally, providing ozonesonde data from 1951 to the present. The launch sites of ozonesondes for 4 years (1996, 2003, 2010 and 2017) during the study period in chapter 5 (1996 – 2018) are shown in Figure 3.10. Globally, the launch sites in this datasets are predominantly in the NH, with most locations in Europe, North America and East Asia. The number of ozonesonde launch sites decreases during the Chapter 5 study time period, as highlighted by the reduction in sites in 2017, which only had 17 launch sites globally (Figure 3.10), compared to 58 in 2003. In chapter 5, ozonesonde data from European ozonesonde launches from 1996 – 2018 (Figure 3.10) is used, and in chapter 6, ozonesonde data from 13 stations across Europe from 2000 – 2021 is used.

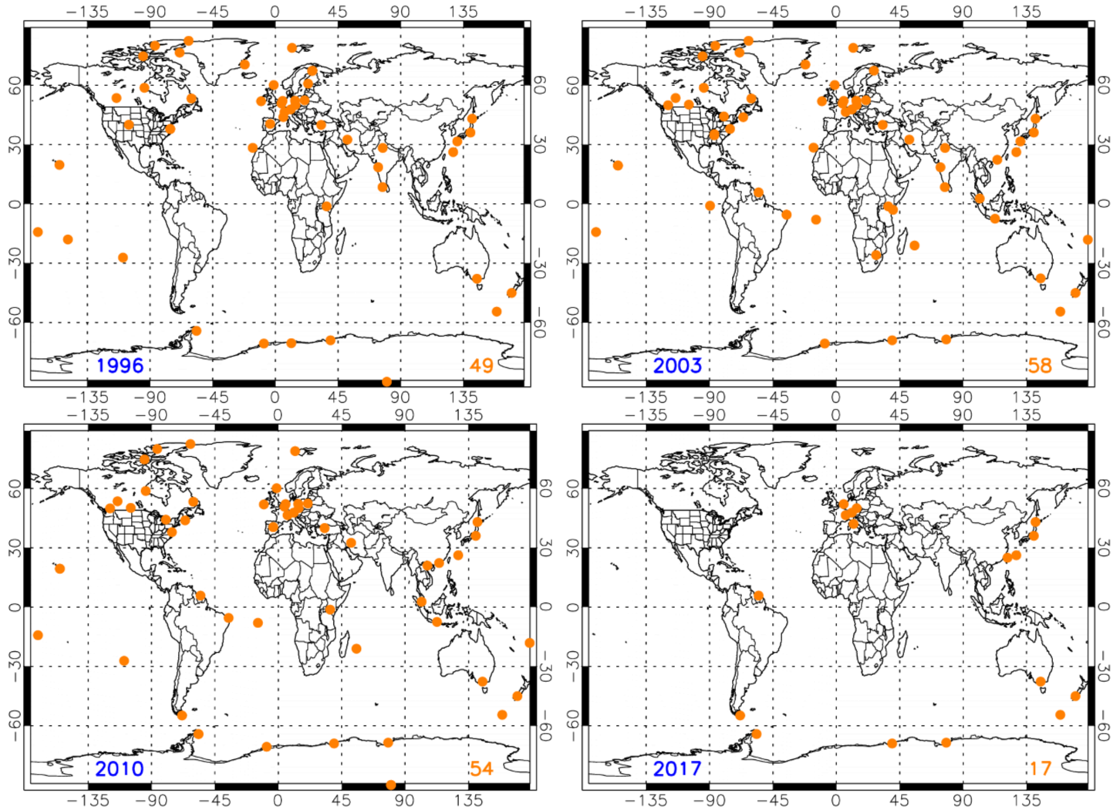

Figure 3.10: Locations of ozonesonde launch sites for 1996, 2003, 2010 and 2017 (WOUDC, 2021). The number of launch sites in each year is given in the lower right corner of each panel.

Comparisons of different types of ozonesonde (WOUDC predominantly contains ECC and Brewer-Mast ozonesondes) show that they agree within ~ 5% (Stübi et al., 2008). In a comparison between WOUDC ozonesondes and MOZAIC aircraft measurements, Logan et al., (2012) found a mean bias of 0.9 ± 2.8 ppb in the lower troposphere.

3.4 Aircraft observations

NASA’s Atmospheric Tomography mission (ATom) observed many different atmospheric variables from a suite of instruments aboard an aircraft, including OH and OHR, as used in this thesis (Wofsy et al., 2018). There were four campaigns, following a very similar flight route, as shown in Figure 3.11, using NASA’s DC-8 aircraft. The campaigns ran between 2016 – 2018: 28th July to 22nd August 2016 (ATom-1); 26th January to 22nd February 2017 (ATom-2); 28th September to 26th October 2017 (ATom-3); 24th April to 21st May 2018 (ATom-4). The atmosphere was sampled across both hemispheres over the Pacific and Atlantic Oceans and covered all seasons. Vertically, the aircraft ascended and descended between 0.15 km and 10 – 13 km altitude around 6 – 9 times per flight (Brune et al., 2019).

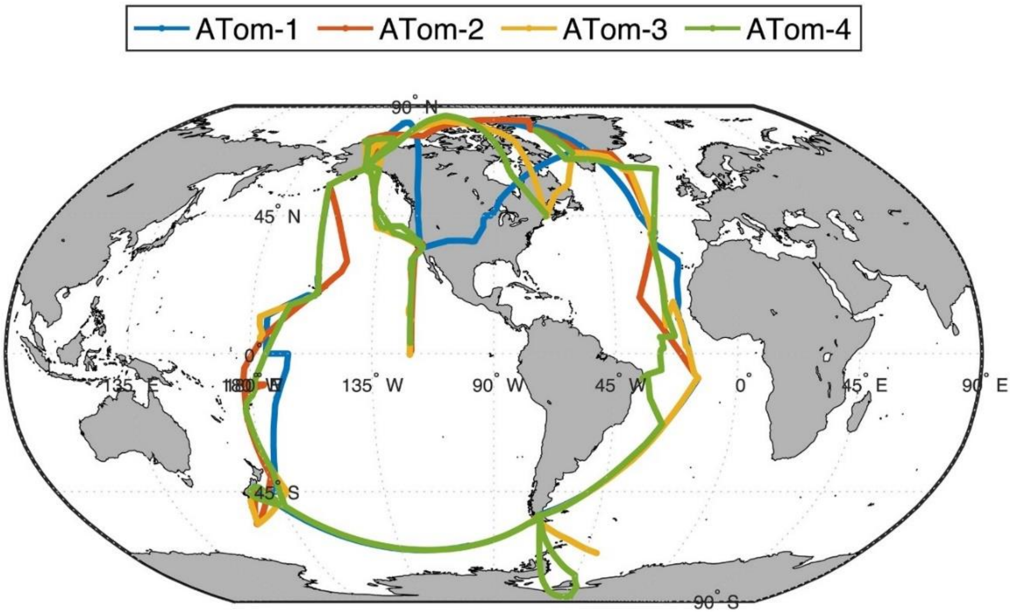

Figure 3.11: Map of ATom flight paths. Taken from Brune et al. (2020).

The Penn State Airborne Tropospheric Hydrogen Oxides Sensor (ATHOS) instrument, aboard the ATom mission, provided measurements of OH and OHR (Faloona et al., 2004; Brune et al., 2019). The technique used by ATHOS is fluorescent assay by gas expansion (FAGE), which was developed by Hard et al. (1984) and Stevens et al. (1994). Air is drawn into the instrument, where it crosses perpendicular to a 308-nm laser beam. The laser beam is absorbed by OH in the air causing fluorescence. This fluorescence signal is then measured by detectors. The estimated 2σ uncertainty on the OH and OHR measurements is ~ 35% and 0.8 s^{-1} respectively. The estimated limit of detection for OH is 0.018 pptv. In their comparison of modelled [OH] and ATom [OH] measurements, Travis et al. (2020) found a good agreement between the two records for ATom-1 and ATom-2 (Figure 3.12). The largest area of non-agreement was the NH summer (ATom-1) below ~ 2 km, likely due to excessive OH production or an underestimation of the ocean VOC sink in the model (Travis et al., 2020).

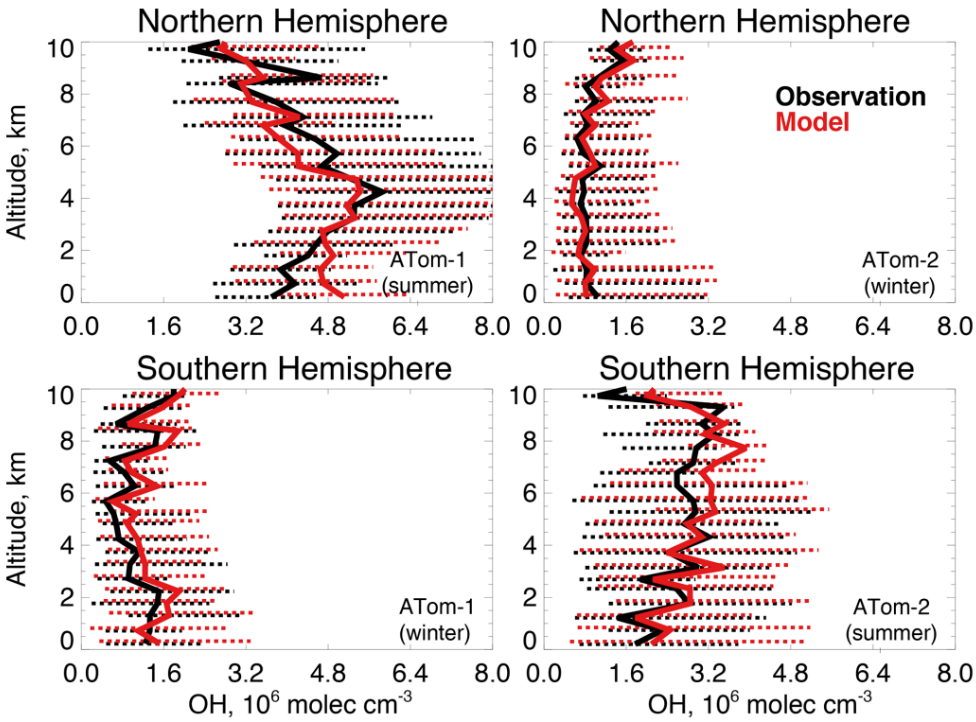

Figure 3.12: Comparison of median [OH] observations from ATom-1 (2016) and ATom-2 (2017) with modelled [OH] from GEOS-Chem. Presented for the SH and NH. Taken from Travis et al. (2020).

3.5 Summary

This chapter has summarised the key datasets used in this thesis, the satellite, ozonesonde and aircraft records and also described the TOMCAT model and the setup used. Data products from 5 satellite instruments are used in this thesis, which vary in terms of sampling patterns, overpass time, instrument technique (UV-Vis vs. IR), and instrument-unique caveats (e.g. the OMI row anomaly). These products are used in conjunction with TOMCAT simulations and independent measurements of the free troposphere (ozonesondes and aircraft data) to provide insight into long-term changes in tropospheric composition.

Chapter 4 Global hydroxyl radical distribution and long-term variation derived from satellite data

4.1 Introduction

There is a scarcity of direct in situ measurements of OH that provide comprehensive spatial and temporal information about this important species. Measuring OH is challenging, due to its short lifetime and low abundance, and there are few instruments available (Stone et al., 2012; Lelieveld et al., 2016). Field campaigns (Stone et al., 2012) and aircraft missions (Wofsy et al., 2018; Brune et al., 2019) are the current sources of in situ measurements available, which both have limited spatial and/or temporal scope. Therefore, indirect methods to infer OH are currently in demand.

The most established indirect method of inferring global OH is to use MCF concentrations to derive a global mean OH concentration, as discussed in Section 2.3.3. However, the regulation of MCF under the legislation initiated by the 1987 Montreal Protocol, has led to a large decline in its abundance in some regions since the mid-1990s. This reduces the viability of this method, and highlights the importance of developing new methods (Huang and Prinn, 2002; Rigby et al., 2017; Liang et al., 2017). The MCF method is also unable to provide much spatial information about OH, which would be very valuable to understanding the distribution of the many important atmospheric species that OH reacts with.

Since around the 1990s there has been an increasing wealth of tropospheric satellite data, which can provide spatial and temporal information about many different atmospheric species, however, this does not extend to OH. These satellite datasets are global and some span over a decade, so have the potential to provide enhanced information indirectly about OH. Currently, there are limited initial studies of the use of satellite data to infer information about global OH. Wolfe et al. (2019) used satellite formaldehyde observations and budget to calculate remote tropospheric column OH. The method was developed using aircraft data from ATom to establish formaldehyde production/loss and OH concentrations. Anderson et al. (2023) used satellite retrievals of O_3, H_2O, CO, NO_2 and HCHO in a machine learning model to predict tropospheric column OH in the tropics, finding a median normalised error of 28.3% in comparison with ATom aircraft measurements.

The methodology developed in this chapter to exploit satellite data uses a steady-state approximation, which is appropriate to use for OH due to its very short daytime lifetime. Using steady-state approximations to calculated OH is an established method, and has been used at many field studies, e.g. Cantrell (1996) and Eisele (1996) at Mauna Loa Observatory, Savage et al. (2001) and Smith et al. (2006) at the Mace Head Atmospheric Research Centre, Ireland, Creasey et al. (2003) at Cape Grim in the Southern Ocean, Bloss et al. (2007) in coastal Antarctica and Slater et al. (2020) in central Beijing.

However, currently this method has not been used with satellite data as the input terms, as investigated in this chapter.

Steady-state approximations have had varied success in deriving OH. For example, Eisele (1996) showed that the comparison between observed and calculated OH depended on which type of air mass was present. They found that free tropospheric air masses showed better agreement than air masses from the BL. Cantrell et al. (1996) found a mixture of good agreement and overestimated OH from a combined steady-state calculation of OH, HO_2 and CH_3O_2 over 33 days at the Mauna Loa Observatory. Savage et al. (2001) found that measured and calculated OH were well correlated, but the calculated OH produced an overestimate of ~ 30%. This chapter utilises a simplified approximation, using only the key source and sink terms of OH. Models using only simplified chemistry have been shown to capture the chemistry of some unpolluted regions, e.g. in Cape Grim in the SH, Sommariva et al. (2004) used a ‘detailed’ and ‘simple’ box-model to study OH in unpolluted marine air. The ‘simple’ box-model, based only on CO, CH_4 and inorganic reactions, agreed within ~ 5% – 10% of the ‘detailed’ box-model (also contained NMVOCs). The modelled OH was an over-estimate (by 10% – 20%) compared to measured OH.

Enhanced information about OH temporal variation is important to understanding key aspects of atmospheric chemistry, e.g. variation in the important GHG CH_4, on the interannual and decadal scales (Turner et al., 2019; Zhao et al., 2020). Several studies using MCF observations, in combination with box-model analyses, show similar annual OH anomalies between 1995 and 2010 (Montzka et al., 2011; Rigby et al., 2017; Turner et al., 2017; Patra et al., 2021). They show similar OH anomalies from 1995 – 2010, as mostly negative (~ -6% – 0%) from 1995 – 1999, mostly positive (~ 0% – 6%) from 1999 – 2007 and mostly negative again (~ -5% – 0%) from 2007 – 2010. From 2010 onwards, the results differ, with Rigby et al. (2017) and Turner et al. (2019) showing consistently negative anomalies (~ -4% – 0%) from 2010 – 2018, and with Naus et al. (2019) and Patra et al. (2021) showing some positive anomalies in this period, e.g. ~ 0% – 4% from 2010 – 2015. Modelling studies showed different results, for example, He et al., (2020) found negative anomalies (~ -5% – 0%) from 1995 – 2005 and then positive anomalies (~ 0% – 4%) from 2005 – 2017. Zhao et al., (2020) found a multi-model mean increase of 0.7×10^5 molecule cm^{-3} from 1980 – 2010 (equivalent to ~ 0.1 – 0.5% yr^{-1}), as shown in Figure 4.1. The greatest rate of increase was in the final decade (2000–2010), and was predominantly due to an increase in the primary production term ($O(^1D) + H_2O$), though also to a decrease in the CO sink term (OH + CO). Some model studies have also shown that OH interannual variability is influenced by the El Niño-Southern Oscillation (ENSO). Low OH concentrations were associated with El Niño years, due to enhanced biomass burning, and therefore increased CO emissions (OH sink) and high OH concentrations with La Niña years (Figure 4.1), as shown in Zhao et al. (2020) and Anderson et al. (2021).

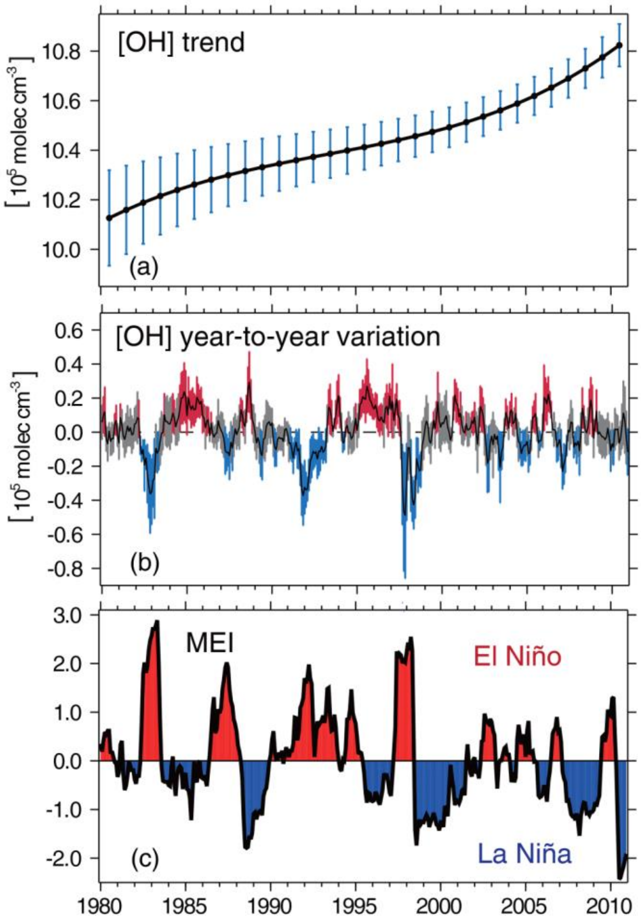

Figure 4.1: Global tropospheric OH variation. (a) Annual tropospheric mean OH (CH_4-weighted) from the CCMI models with year-to-year variation removed. (b) Anomaly of detrended and de-seasonalised monthly mean OH (CH_4-weighted). (c) Bimonthly multivariate ENSO index. Taken from Zhao et al. (2020).

4.2 Research questions

The aim of this chapter is to investigate the potential use of satellite data and a simplified steady-state approximation to provide information about OH. The chapter will address the following research questions:

1. In what regions of the atmosphere are different steady-state approximations for [OH] valid?
2. Can satellite data be applied to a simplified steady-state approximation and how does it compare to modelled [OH]?
3. How does the satellite-derived [OH] distribution compare to direct measurements of [OH] in the free troposphere?
4. What is the uncertainty associated with the satellite-derived OH?
5. What can this method tell us about long-term variations in [OH] and it's source and sink terms (e.g. O_3)?

The work from this chapter was published in the journal *Atmospheric Chemistry and Physics* (Pimlott et al., 2022).

4.3 Methods & data

4.3.1 Hydroxyl radical steady-state approximations

In the troposphere, the OH radical has a very short lifetime, so a steady-state approximation can be used to estimate its concentration. A generalized version of this approximation is shown in Equation 4.1:

$$[\mathrm{OH}]_{\mathrm{steady-state}} = \frac{k_{A+B}[\mathrm{A}][\mathrm{B}] + \ldots + j_C[\mathrm{C}] + \ldots}{\sum k_D[\mathrm{D}] + \ldots} \qquad \textbf{Equation 4.1}$$

where the numerator represents a sum of the source terms and the denominator represents a sum of the sink terms, which can both vary in number, impacting the ‘complexity’ of the expression. k_{A+B} is the reaction rate constant of A and B to form OH and j_C is the photolysis coefficient of C to form OH. k_D is the reaction rate constant of D and OH, where D represents an individual sink species. The accuracy of the approximation depends partly on the number of source and sink terms which can be included. In this study, the number of source and sink terms depends on the availability of observations (e.g. satellite, model, aircraft) to provide a constraint for each.

In this chapter, three different steady-state approximations are proposed with varying complexity, to investigate how accurate they are in different regions of the atmosphere. The simplest is based on only 1 source term (based on a steady-state approximation for $O(^1D)$, see Equations 2.17 and 2.18) and 3 sink terms (based on the reaction of OH with CH_4, CO and O_3), and is shown in Equation 4.2:

$$[\mathrm{OH}]_{\mathrm{steady-state}} = \frac{\left(\frac{2j_1k_1[\mathrm{O_3}][\mathrm{H_2O}]}{k_2[\mathrm{N_2}] + k_3[\mathrm{O_2}] + k_1[\mathrm{H_2O}]}\right)}{(k_4[\mathrm{CH_4}] + k_5[\mathrm{CO}] + k_6[\mathrm{O_3}])} \qquad \textbf{Equation 4.2}$$

where j_1 is the photolysis coefficient for $O_3 \rightarrow O(^1D) + O_2$, k_1 is the reaction rate constant for $O(^1D) + H_2O$, k_2 and k_3 are the reaction rate constants of $O(^1D)$ with respect to N_2 and O_2, k_4, k_5 and k_6 are the rate constants for reaction of OH with CH_4, CO and O_3, respectively. The relevant reactions here are presented in full in Appendix A (Table A.1) and Section 4.3.2 (Table 4.2). The proposed simplified steady-state approximation (S-SSA) contains some of the key source/sinks of OH in the troposphere, and contains species which have satellite observations available for them.

The other two steady-state approximations are more complex. The full chemistry steady-state approximation (FC-SSA) contains all reactions involving OH in the TOMCAT model full chemistry scheme, as described in Monks et al. (2017). It contains 26 source terms and 51 sink terms and captures the most comprehensive tropospheric chemistry of the three approximations. The final approximation is based on a steady-state approximation proposed in Savage et al. (2001) (Sav-SSA) (based on Grenfell et al. (1999)) and contains 5 source and 12 sink terms. It is therefore simplified with respect to FC-SSA, but more complex than S-SSA, providing a suitable intermediate approximation for the analysis. All three steady-state approximations are summarised in full in Appendix A (Table A.1).

4.3.2 Application of the steady-state approximation

In this chapter, datasets from satellite instruments, TOMCAT and an aircraft campaign (ATom) are used as the input species of the different steady-state approximations. The specific methods of application and j_1 used in each case are summarised in Table 4.1. For all cases, the nitrogen and oxygen are assumed to have a fixed volume mixing ratio of 0.78 and 0.21 respectively. The rate constants (k_1- k_6) used in the S-SSA are summarised in Table 4.2. The rate constants used in the additional reactions in the more complex steady-state approximations (e.g. FC-SSA and Sav-SSA) are the same as those used in TOMCAT, which can be found in Monks et al. (2017).

Dataset		**Relevant Figures**	**Description**	**j_1 used**
Model	Not in comparison with the satellite data	Figure 4.5	Data averaged into monthly means, which were applied to the approximation.	Model (2010/2017)
	In comparison with the satellite data	Figure 4.13	Data co-located with the satellite retrievals, and then applied on a retrieval-by-retrieval basis.	Model (2010/2017)
Satellite	2010/2017	Figure 4.12	Applied on a retrieval-by-retrieval basis.	Model (2010/2017)
	2008 – 2017	Figures 4.24 - 4.27	Applied on a retrieval-by-retrieval basis.	Model (2010)
Aircraft		Figures 4.15 - 4.21	Applied on a measurement-by-measurement basis.	Measured (see Table 4.4)

Table 4.1: Summary of how the steady-state approximations were applied to the model, satellite and aircraft data. The relevant figures to each cases are provided.

Reaction	Rate coefficient		Reference
$\mathbf{O(^1D) + H_2O \rightarrow 2OH}$	k_1	$1.63 \times 10^{-10}\exp\left(\frac{60}{T}\right)$	(Burkholder et al., 2019)
$\mathbf{O(^1D) + N_2 + (O_2) \rightarrow O_3 + N_2}$	k_2	$2.10 \times 10^{-11}\exp\left(\frac{115}{T}\right)$	(Monks et al., 2017)
$\mathbf{O(^1D) + O_2 + (O_2) \rightarrow O_3 + O_2}$	k_3	$3.20 \times 10^{-11}\exp\left(\frac{67}{T}\right)$	(Atkinson et al., 2006; Monks et al., 2017)
$\mathbf{OH + CH_4\ (+O_2) \rightarrow H_2O + CH_3OO}$	k_4	$1.85 \times 10^{-12}\exp\left(\frac{-1690}{T}\right)$	(Atkinson et al., 2006; Monks et al., 2017)
$\mathbf{OH + CO\ (+O_2) \rightarrow HO_2 + CO_2}$	k_5	$1.44 \times 10^{-13}\exp\left(\frac{1+[N_2]}{4.2\ \times 10^{-19}}\right)$	(Atkinson et al., 2006)
$\mathbf{OH + O_3 \rightarrow HO_2 + O_2}$	k_6	$1.70 \times 10^{-12}\exp\left(\frac{-940}{T}\right)$	(Burkholder et al., 2019)

Table 4.2: Summary of the rate coefficients used in the S-SSA. The rate coefficients have units of cm^3 molecule^{-1} s^{-1}. T refers to temperature in K.

4.3.3 Hydroxyl radical reactivity

The denominator of Equation 4.2 is known as the OH reactivity (OHR). It can be measured and also derived by the summation of sink terms, using a model and/or observed species. As with the steady-state expression of OH, the accuracy of an OHR calculation is dependent on the number of sink terms which are included. Therefore, it is also dependent on the availability of observations for the sink species. Comparison of OHR measurements (e.g. from the aircraft mission ATom) can be used to evaluate the denominator of a steady-state approximation, e.g. Equation 4.2. The denominator of Equation 4.2 is used as a simplified expression for OHR, as shown in Equation 4.3:

$$\mathrm{OHR} = (k_4[\mathrm{CH_4}] + k_5[\mathrm{CO}] + k_6[\mathrm{O_3}]) \qquad \textbf{Equation 4.3}$$

4.3.4 Satellite data

In this chapter, level 2 satellite profile retrievals derived by RAL of CH_4, CO, O_3 and H_2O from IASI, aboard the MetOp-A satellite, are used (Section 3.1.1.1). From the satellite profiles, an average is taken across the 600 – 700 hPa pressure layer, as this is the focus of the study. The data used for 2010 and 2017 is fully processed (spatially and temporally). The longer record (2008 – 2017) used here to study OH temporal variation is sub-sampled temporally (1-in-10 days) and spatially (1-in-4 pixels), due to these years not being available as a fully processed record. There is a close comparison between the partially and fully sampled records for latitude-averaged S-SSA OH (averaged across the 600 – 700 hPa pressure layer, Figure 4.2). 2010 shows an average monthly correlation coefficient of 0.89, and 2017 shows an average of 0.85 (Figure B.1).

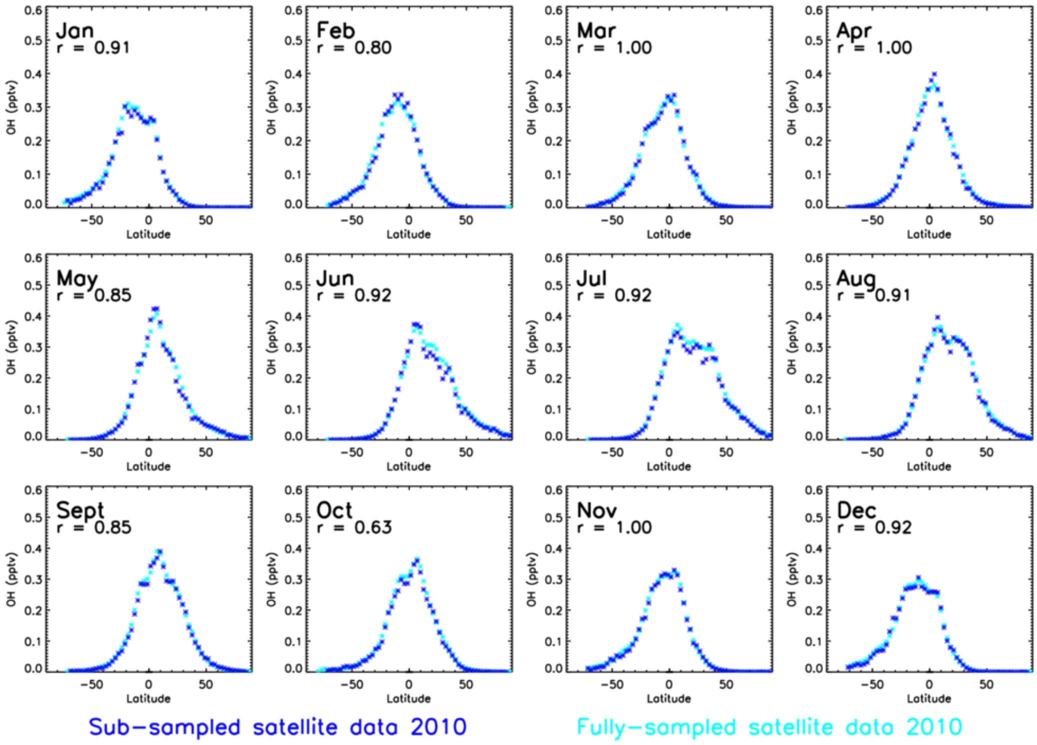

Figure 4.2: Zonal mean comparison of S-SSA OH (latitude-averaged) between sub-sampled and fully sampled satellite data for all months in 2010 (averaged across 600 – 700 hPa pressure layer). The Pearson correlation coefficient (r) is displayed for each month. See Appendix B (Figure B.1) for 2017.

4.3.4.1 Biases of satellite retrievals

The four satellite products (H_2O, CO, O_3 and CH_4) have been compared to observations to calculate the bias. Trent et al. (2023) evaluated H_2O (and temperature) IMS-Extended profiles from Metop-A as part of ESA's Climate Change Initiative project. In a comparison with radiosondes, they found a bias of ~10% for H_2O (and 0.5K for temperature) globally across 9.5 years of data. IMS-Extended CO retrievals were evaluated by Pope et al. (2021) (see supplement). IMS-Extended CO column averages from 2007 – 2020 were compared with analyses from the Copernicus Atmospheric Monitoring Service (CAMS), finding the uncertainty in the IMS-Extended CO to be ~ 10%. IMS-Extended O_3 profiles were evaluated in Pimlott et al. (2022) by R. Pope (see supplement - Section S3). The retrieved O_3 profiles were compared with ozonesondes from WOUDC and SHADOZ, finding a bias of ~ 10% to 20% in the pressure layer of interest to this work (600 – 700 hPa) depending on latitude and season. IASI CH_4 is evaluated by Siddans et al., (2017) for 2007 to 2015. Regionally, systematic differences of ~ 10 ppbv were found. Using an average of 1800 ppbv, this equates to an uncertainty of ~ 0.55%.

4.3.4.2 Vertical sensitivity of satellite retrievals

The retrievals from the IMS-Extended scheme (H_2O, CO and O_3) are represented on 101 levels within the scheme. However, the amount of information that can be resolved in the lower atmosphere varies between the species. Global monthly averaged AKs are shown, as an example, in Figure 4.3 for January 2010 and in Appendix C (Figure C.1) for June 2010. For H_2O, a large number of independent layers can be resolved between the surface and ~200 hPa. There is a relatively large number of DOFS, at ~10. For CO, the peak of the AKs is spread out, providing little vertical sensitivity. There is only enough information to retrieve one independent layer, which is centred on the mid troposphere (~600 hPa). For O_3, the AKs peak at several different levels in the troposphere and stratosphere. The number of DOFS is ~ 3 to 4. The AK peaks closest to the surface is around ~600 hPa. The CH_4 measurements are from a different RAL retrieval scheme to the IASI-IMS-Extended, the IASI v2.0 CH_4 retrieval scheme (Siddans et al., 2017), which retrieves CH_4 on a set of coarsely spaced levels. The output files contain layer-averaged mixing ratios and their corresponding AKs. The DOFS is larger than 2 in the tropics but drops to below 2 at higher polar latitudes. Overall, the surface to 450 hPa layer (lowest layer) average is well resolved from layers above, peaking around 700 hPa.

The analysis presented in this chapter focuses on a mid-tropospheric pressure region, of 600 – 700 hPa. For the 4 satellite input species discussed, the AKs have peaks around this region, with sensitivity within the free troposphere. Therefore, this data is appropriate to use in this study due to this confidence in the sensitivity of the satellites to this region. The AKs show a relatively suitable vertical sensitivity in the mid-troposphere, so there will be small smoothing errors. Therefore it is reasonable for the satellite-derived OH and TOMCAT OH to be directly compared. Additionally, there are no AKs for OH available to use when comparing with a model, as in this study OH has been derived from a combination of several satellite records, not a direct retrieval.

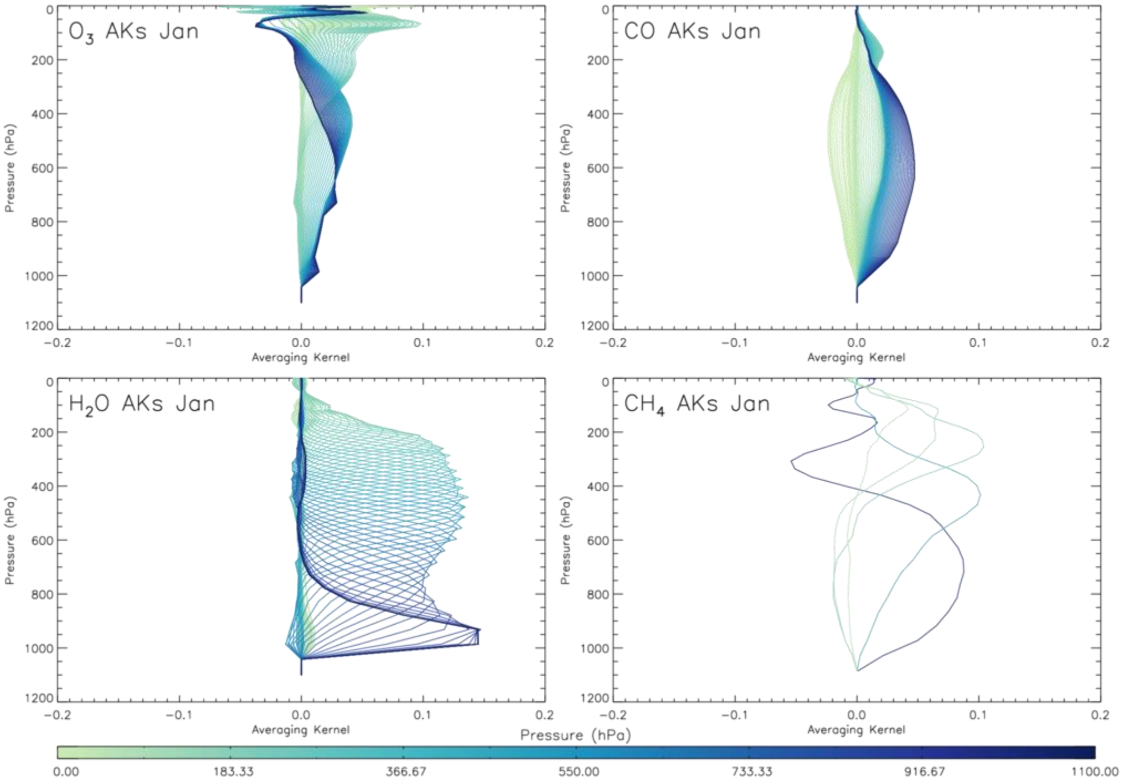

Figure 4.3: Globally averaged vertical AKs for January 2010 for O_3 (top left panel), CO (top right panel) and H_2O (bottom left panel) retrievals from the IASI IMS-Extended scheme and CH_4 retrievals (bottom right panel) from the IASI scheme. See Appendix C for June 2010.

4.3.4.3 Impact of cloud filtering

The co-located retrievals of H_2O, O_3 and CO data and CH_4 are filtered for a geometric cloud fraction of 20% or less (i.e. 0.2 fractional coverage or less). Therefore, satellite soundings which include opaque clouds filling most of the field of view are discarded. TOMCAT has no cloud filtering, therefore this could produce a clear sky bias. However, the model is driven by ECMWF meteorological fields. These same fields are also used in the satellite retrieval, so overall, the model and satellite should be reasonably consistent.

4.3.4.4 Satellite-derived hydroxyl radical uncertainty

Systematic errors of the four satellite-retrieved species (CO, O_3, CH_4 and H_2O) are used to estimate the uncertainty on satellite-derived S-SSA, based on Equation 4.2. The estimation and equations used are shown in Appendix D. The estimated uncertainty is ~ 0.5 – 0.7 ×10^6 molecule cm^{-3} or ~ 23 – 24%. This estimation did not include uncertainty on the rate constants (j_1, $k_{1\text{-}6}$) which are a potential additional source of uncertainty. TOMCAT j_1 and ATom j_1 measurements are compared in Appendix D showing a reasonable agreement.

4.3.4.5 Daily number of retrievals

The average daily number of retrievals of the S-SSA satellite input species (CO, O_3, H_2O, CH_4) per grid-box varies between 0 and 24, with an average of ~6 (Figure 4.4). This suggests that there are sufficient retrievals of the input species in the S-SSA to calculate values of OH for most grid-boxes every day.

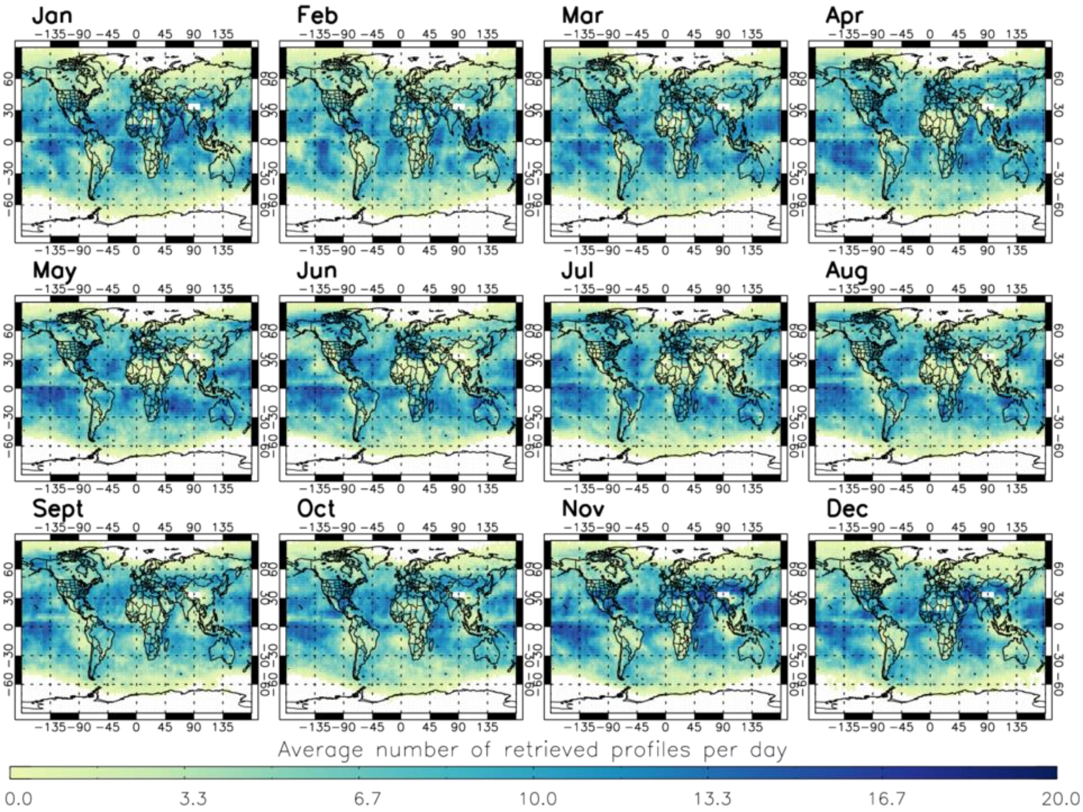

Figure 4.4: Average number of daily retrievals for each grid-box for each month in 2010 from the 4 input species used in the S-SSA calculation.

4.3.5 TOMCAT model setup

The emissions used in the TOMCAT simulations in this chapter are summarised in Table 4.3. The emission datasets used are from the most up-to-date emission inventories e.g. the Coupled Model Intercomparison Project Phase 6 (CMIP6) (Feng et al., 2020), and long-term, widely-used, robust estimates e.g. GFED version 4. (van der Werf et al., 2017). The model simulation was run for 2010 and 2017, with a spin up period of 6 months for each years. To match the MetOp-A daytime overpass time, the simulation was setup to be sampled daily at 9:30 am LST globally.

Type	Description		Reference
Anthropogenic	*NO_x, CO & VOCs*	The Coupled Model Intercomparison Project Phase 6 (CMIP6).	(Feng et al., 2020).
	Butane (C_4H_{10})	The Streets v1.2 inventory.	(Monks et al., 2017)
	CH_4	Emission Database for Global Atmospheric Research (EDGAR) v4.2 inventory.	(Olivier et al., 2012)
Natural (soils/ oceans)	*NO_x, CO & VOCs*	The project ‘Precursors of Ozone and their Effect on the Troposphere’ (POET).	(Olivier et al., 2003; Granier et al., 2005)
	CH_4	Soil sink flux comes from the Soil Methanotrophy Model (MeMo). Wetland emissions from the Joint UK Land Environment Simulator (JULES).	(Murguia-Flores et al., 2018) (Clark et al., 2011)
	C_4H_{10}	MACCity	(Monks et al., 2017)
Biogenic	*CO & VOCs*	The Chemistry-Climate Model Initiative (CCMI). These emissions are fixed annually.	(Morgenstern et al., 2017)
Aircraft	*NO_x*	Based on estimated aircraft movements in 2002 produced for the European QUANTIFY project.	(Lamarque et al., 2010) (http://www.pa.op.dlr.de/quantify/)
Biomass burning	*NO_x, CO & VOCs*	The Global Fire Emissions Database (GFED) version 4.	(van der Werf et al., 2017)
CH_4 scaling	Volume mixing ratio scaled to a best estimate based on the globally averaged surface CH_4 volume mixing ratio from NOAA for each year.		(Dlugokencky, 2020)
Aerosols	*SO_2, BC & OC*	MACCity	(Granier et al., 2011)

Table 4.3: Summary of the surface emissions used in the TOMCAT simulation in this chapter.

4.3.6 ATom aircraft data

In this chapter, ATom measurements of OH, OHR, O_3, CO, CH_4, H_2O and j_1 are used from all four campaigns, filtered for 08:00–11:00 LST, to compare with the 09:30 MetOp-A overpass time. A pressure range of 600–700 hPa is also selected, where the S-SSA agrees best with the full chemistry model. As in Travis et al. (2020), the measurements are filtered to remove those strongly influenced by extreme events e.g. stratospheric air (O_3/CO > 1.25) or biomass burning (acetonitrile concentration > 200 ppt). Therefore the measurements used here are more representative of the average tropospheric compositive, not extreme events. The measurements used here were merged into two-minute sampling intervals by Wofsy et al. (2018). The instruments used to measure the noted species in ATom and the uncertainties of these measurements are shown in Table 4.4.

Species	Instrument	Uncertainty
OH	ATHOS (Faloona et al., 2004; Brune et al., 2020)	± 35% (2σ confidence level), limit of detection - 0.018 pptv
OHR	ATHOS (Faloona et al., 2004; Brune et al., 2020)	± 0.8 s^{-1} (2σ confidence level)
CH_4	NOAA Picarro (Karion et al., 2013)	± 0.7 ppbv
CO	NOAA Picarro (Karion et al., 2013)	± 8.9 ppbv
H_2O	Diode laser hygrometer (DLH) (Podolske et al., 2003)	± 5%
O_3	NOAA-NO_y O_3 (Ryerson et al., 2000)	± 2.0 ppb
j_1	CCD Actinic Flux Spectroradiometers (CAFS) (Shetter and Müller, 1999)	± 20%

Table 4.4: Table of instruments and associated uncertainties of the relevant ATom measurements (Wofsy et al., 2018).

4.3.7 Comparison metrics

For the comparison of OH datasets e.g. satellite-derived, modelled, aircraft, mean bias (MB) and NMB are calculated using Equations 4.4 and 4.5:

$$\mathrm{MB} = \frac{1}{N}\sum(x - y) \qquad \textbf{Equation 4.4}$$

$$\mathrm{NMB} = \frac{\sum(x - y)}{\sum y} \times 100 \qquad \textbf{Equation 4.5}$$

where x is one dataset (usually the observations), y is the other dataset (usually the model) and N is the number of data points.

4.4 Results & discussion

4.4.1 Application of the simplified steady-state approximation to model data

Initially, TOMCAT model data of O_3, CO, CH_4 and H_2O was applied to the S-SSA to assess how well S-SSA OH represents the model OH in different regions of the atmosphere. A zonal mean comparison between the TOMCAT OH and the TOMCAT S-SSA OH is shown in Figure 4.5. Broadly, the agreement is best between 400 – 800 hPa, with an overestimation in the TOMAT S-SSA OH at the surface, and an underestimation higher up in the atmosphere. Average differences across these regions for January and June are shown in Table 4.5. At pressures <400 hPa, the average differences are very large (~85%), with a large underestimation from TOMCAT S-SSA OH. Nearer the surface, at pressures > 800 hPa the average across the region is much smaller (~2%/6% for Jan/Jun), however, in a latitude-longitude plot (Appendix E/Figure E.1) there are large differences which aren't represented in the zonal mean plot (Figure 4.4) and the averaged [OH] for the pressure region. Also, in the BL there is complex OH chemistry, with more source and sink terms dominating, which is unlikely to be well represented by the simplified approximation used here. Therefore, the investigation has been focused above the BL.

The average difference between TOMCAT OH and TOMCAT S-SSA OH is ~34%/31% (Jan/Jun) for a mid-tropospheric region of 400 – 800 hPa. The peak grid-box values correspond well in this region, with peak values of 5.4×10^6 molecule cm^{-3} (Jan) and 7.3×10^6 molecule cm^{-3} (Jun) for TOMCAT S-SSA OH, and peak values of 5.6×10^6 molecule cm^{-3} (Jan) and 8.3×10^6 molecule cm^{-3} (Jun) for TOMCAT OH. Within this 400 – 800 hPa pressure region, the 600–700 hPa layer is further investigated, as it shows better agreement in the global mean and zonal mean structure than the wider pressure region (Table 4.5). There is smaller difference of ~ 31%/26% (Jan/Jun) for a pressure layer of 600 – 700 hPa. This analysis was repeated with a TOMCAT simulation for another year, 2017. Results from 2017, for the analysis here and also following sections, are shown in Appendix F. In 2017, a similar result to 2010 was found, with an agreement of ~ 31%/27% (Jan/Jun) for the 600 – 700 hPa pressure layer (Figure F.1).

Therefore, for the following analysis, the pressure region 600–700 hPa was selected for investigation due to the good agreement between TOMCAT S-SSA OH and TOMCAT OH. In the 600 – 700 hPa region, OH contributes to ~15% of the tropospheric OH burden. From diagnosis of the model output, influence of OH in this region to CH_4 oxidation is slightly higher, contributing to ~19% of CH_4-loss-weighted OH. Across the broader pressure region of 400 – 800 hPa, OH contributes to ~ 51% of the tropospheric OH burden and ~ 60% of the CH_4-loss-weighted burden.

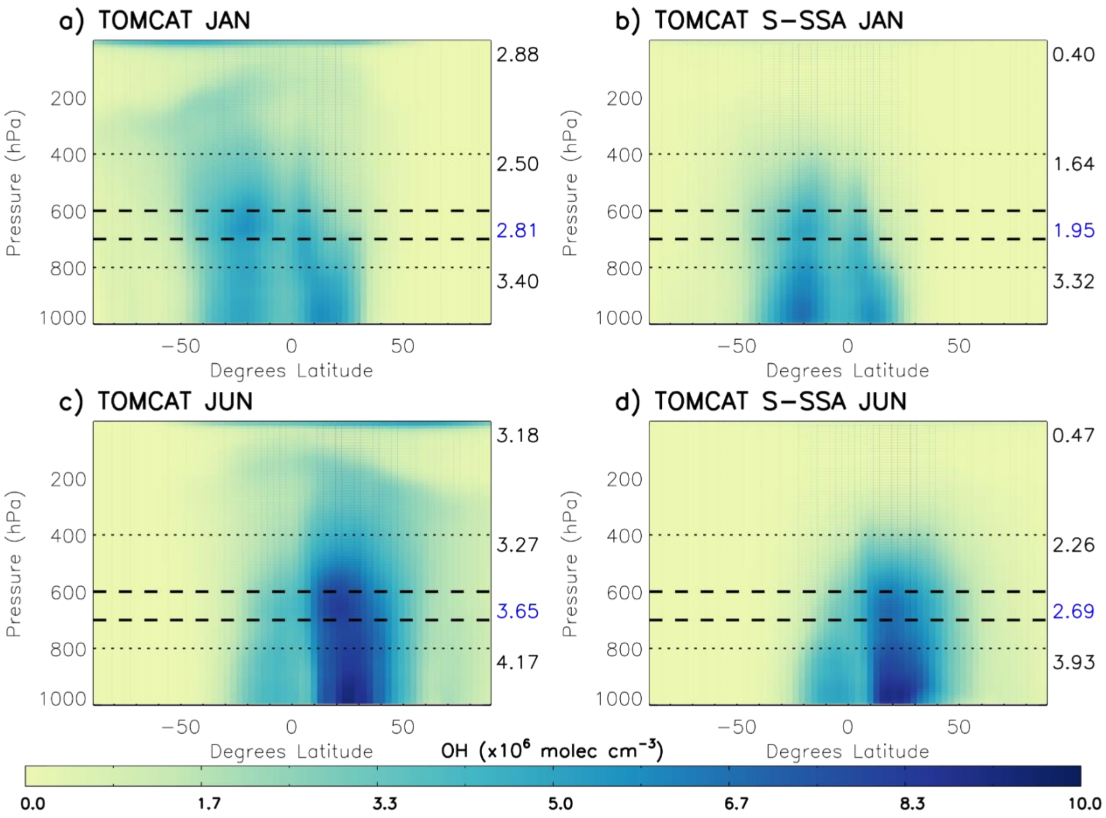

Figure 4.5: (a) TOMCAT OH in January 2010, (b) TOMCAT S-SSA OH in January 2010, (c) TOMCAT OH in June 2010, (d) TOMCAT S-SSA OH in June 2010. The dashed lines represent the proposed area of best agreement (600–700 hPa). The numbers on the right edge of each plot represent the mass-weighted mean OH of the pressure region shown by the dotted lines (from top to bottom): < 400 hPa, 400 – 800 hPa, 600 – 700 hPa (blue) and 800 hPa – surface. All units are in ×10^6 molecule cm^{-3}. See Appendix F for 2017.

	S-SSA OH average – TOMCAT OH average (×10^6 molecule cm^{-3})	
Pressure range	**January**	**June**
< 400 hPa	-2.48 (-86%)	-2.71 (-85%)
400 – 800 hPa	-0.86 (-34%)	-1.01 (-31%)
> 800 hPa	-0.08 (-6%)	-0.24 (-2%)
600 – 700 hPa	-0.86 (-31%)	-0.96 (-26%)

Table 4.5: Comparison of mass-weighted global mean TOMCAT OH and TOMCAT S-SSA OH for different pressure ranges. Percentage difference relative to the TOMCAT OH mean given in brackets.

For the selected mid-tropospheric layer of best agreement (600 – 700 hPa), Figure 4.6 highlights the spatial differences between TOMCAT OH and TOMCAT S-SSA OH. For January, the TOMCAT S-SSA underestimates OH by up to ~2 ×10^6 molecule cm^{-3} across the NH and areas of the oceans in the SH, predominantly between the equator and 30°S, e.g. over the Atlantic and the edges of the Pacific. The TOMCAT S-SSA overestimates OH by up to ~2 ×10^6 molecule cm^{-3} across areas of the SH continents, e.g. South America, and by up to ~1 ×10^6 molecule cm^{-3} across the Indian Ocean and centre of the Pacific Ocean. The peak values seen across the SE Indian Ocean and southern African continent agree well. For June, TOMCAT S-SSA underestimates OH across areas of the NH continent, e.g. by up to ~4 ×10^6 across the northern African continent and China. There is a small overestimate of ~1 ×10^6 across the landmasses near the equator. There is a good agreement around the NH oceans, between the equator and 30°N. Overall, the best spatial agreement between TOMCAT S-SSA OH and TOMCAT OH is around the equator, although this varies on the season. For peak values, these are found mostly in the same locations, however, the TOMCAT S-SSA produces a peak value underestimate compared to TOMCAT.

As the S-SSA is very simple, a poor agreement between the S-SSA and TOMCAT full-chemistry OH is likely due to omission of source or sink species in that region. This is especially true here, when comparing TOMCAT input species in the S-SSA with TOMCAT modelled OH, as the input species fields are consistent with the model (i.e. same meteorology/temperature). The relative impact of different source and sink terms to the agreement are discussed in the following section.

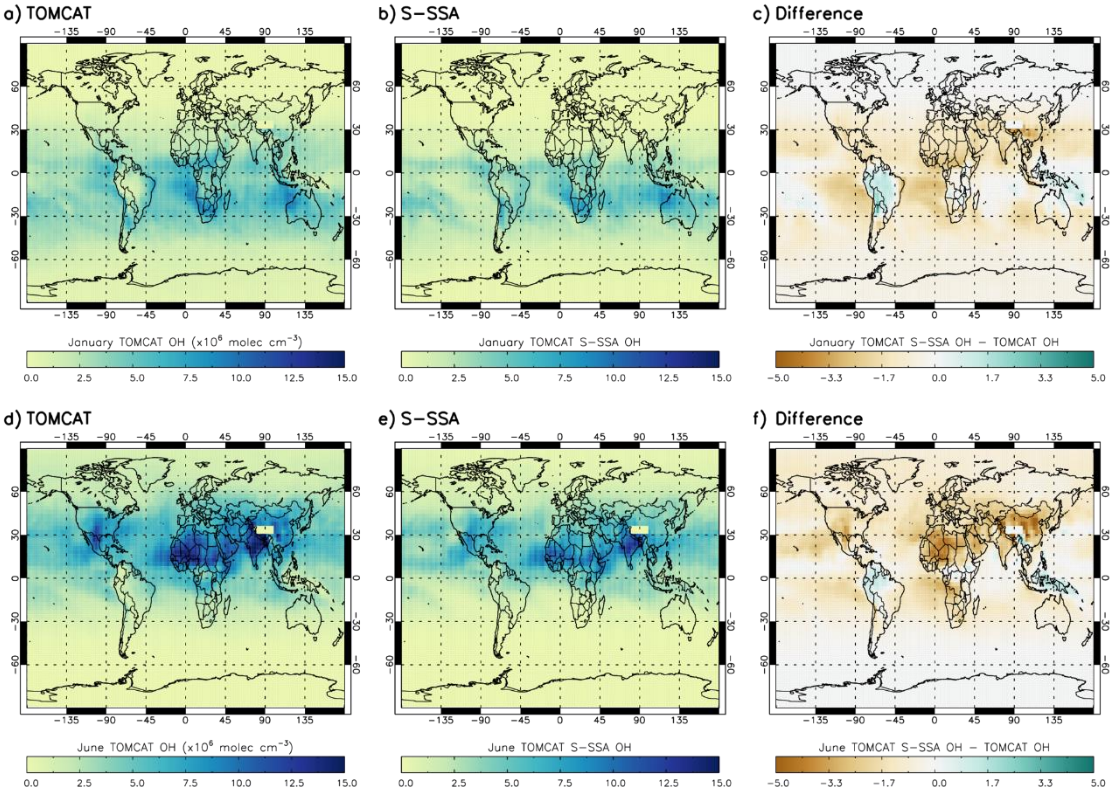

Figure 4.6: [OH] averaged over the 600-700 hPa range for (a) TOMCAT, (b) TOMCAT S-SSA and (c) the difference (TOMCAT S-SSA subtract TOMCAT) for January 2010. Panels (d)-(f) represent comparisons for June 2010. All values are in units of ×10^6 molecule cm^{-3}.

4.4.2 Reactions omitted from the simplified steady-state approximation

This chapter aims to derive information about [OH] from satellite data. Therefore, several source and sink reactions that could be important to OH chemistry, which don't have satellite retrievals available, have been omitted from the S-SSA. To analyse how important the other source and sink terms are in different pressure regions, TOMCAT data of the relevant species has been applied to a more complex steady-state approximation, Sav-SSA (Appendix A/Table A.1), which showed a good agreement to the full model OH in most regions of the atmosphere. Latitude-averaged total source term and percentage contribution to the total source term are shown in Figure 4.7 for January 2010 (Appendix G, Figure G.1, for June 2010). Higher up in the atmosphere, at pressures < 400 hPa, the reaction of NO and HO_2 (Equation 4.6), dominates the total source term, so is an important missing source reaction here.

$$\mathrm{HO_2 + NO \rightarrow OH + NO_2}$$ **Equation 4.6**

Although OH and HO_2 are very closely linked in chemical cycles, this is not represented in the S-SSA. Not including this source term in the S-SSA is causing the poor agreement seen at pressures < 400 hPa (Figure 4.5).

In the pressure layer of interest here (600 – 700 hPa), the NO + HO_2 source term is approximately the second most dominant source term, after O_3 photolysis (Figure 4.7). In regions where NO + HO_2 shows a large percentage contribution to the total source term, it is likely that the S-SSA is not sufficiently capturing the important OH chemistry. The regional impact of this important source term in the 600 – 700 hPa pressure layer to the total production term of the Sav-SSA is shown in Figure 4.8. In January, the NO + HO_2 source term shows a very large percentage contribution between 30°N and 60°N (of up to 100%). However, it should be noted that the [OH] is very low there and therefore this is relatively unimportant. For latitudes below 30°N, the spatial pattern of NO + HO_2 contribution is similar to the spatial pattern of negative differences between S-SSA [OH] and TOMCAT [OH] (Figure 4.6(c)), e.g. across the NH and in the SH Atlantic and Pacific Ocean next to South America. This indicates that an improvement in agreement could be achieved in these regions by adding this additional source term. In June, across the SH (~ 60°S to the equator) the NO + HO_2 source term show a large percentage contribution. As with January, this is where [OH] is low, so is relatively unimportant. In the NH, the NO + HO_2 source term makes a larger contribution over land, compared to the oceans. Over the oceans around the equator, there is a very low contribution, which corresponds to the good agreement of TOMCAT S-SSA [OH] and TOMCAT [OH] (Figure 4.6(f)).

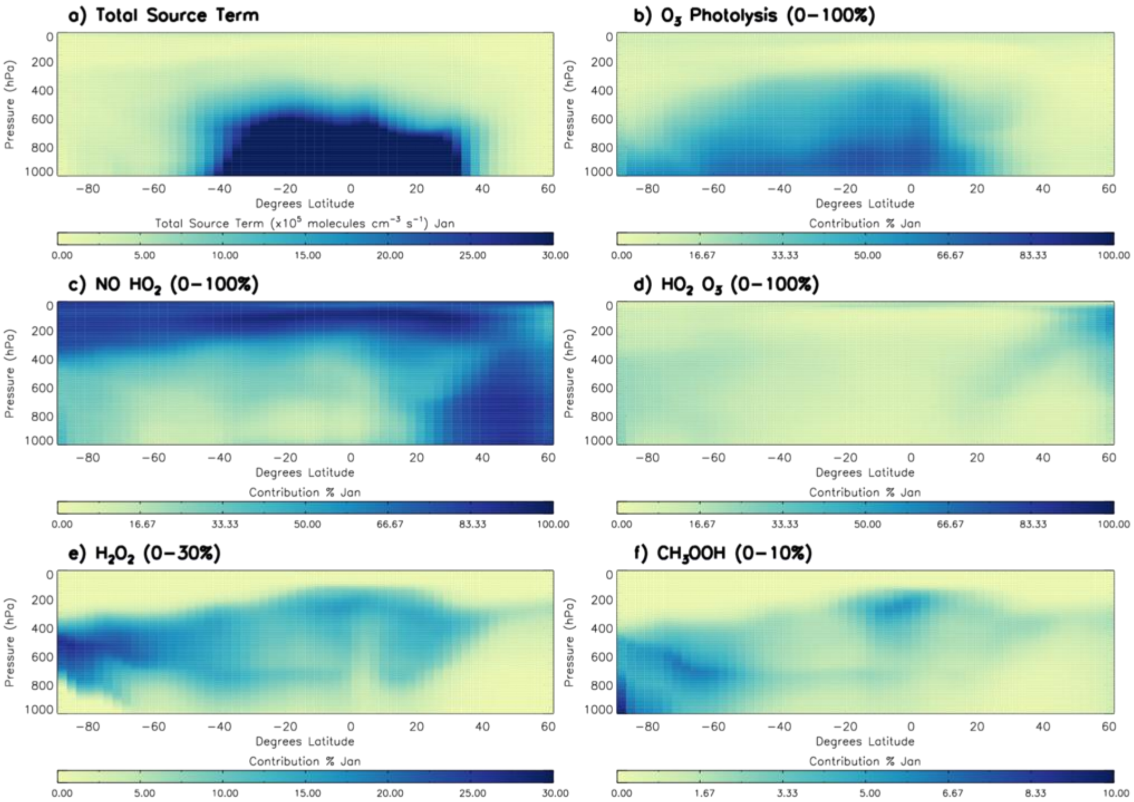

Figure 4.7: January 2010 latitude averaged (a) total Sav-SSA source term and (b) – (f) the different source terms as a percentage contribution of the total source term. The individual source terms are: (b) photolysis of O_3 to form $O(^1D)$ which reacts with H_2O for form OH, (c) reaction of NO + HO_2, (d) reaction of HO_2 + O_3, (e) photolysis of H_2O_2 and (f) photolysis of CH_3OOH. The data is presented from 90°S–60°N due to polar night at latitudes >60°N during January. Note the differing scales on the panels. See Figure G.1 (Appendix G) for June 2010.

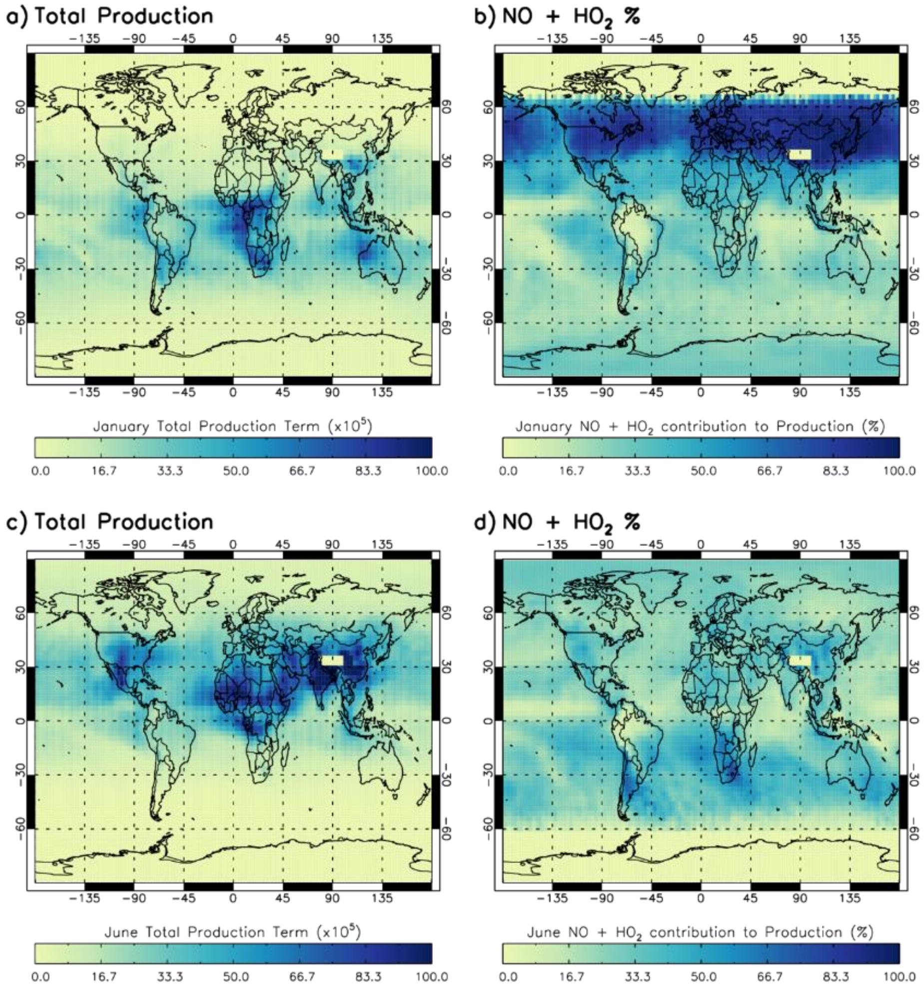

Figure 4.8: (a) Total production term for Sav-SSA in January 2010 with units of ×10^5 molecule cm^{-3} s^{-1}, (b) percentage contribution of the NO + HO_2 source reaction to the total production term of Sav-SSA in January 2010. Panels (c) and (d) are repeated for June 2010. All panels show the average across the 600-700 hPa pressure region.

Additional NO_x terms (1 source and 2 sinks) were added into the S-SSA approximation using TOMCAT data for January 2010 (Figure 4.9, Appendix G/Figure G.2 for June 2010). The additional terms are shown in Equations 4.6 - 4.8:

$$\mathrm{NO_2 + OH + M \rightarrow HONO_2 + M}$$ **Equation 4.7**

$$\mathrm{NO + OH + M \rightarrow HONO + M}$$ **Equation 4.8**

Therefore the S-SSA with NOx (S-SSA-NO_x) is as shown in Equation 4.9:

$$[\mathrm{OH}]_{\mathrm{steady-state}} = \frac{\left(\frac{2j_1 k_1[\mathrm{O_3}][\mathrm{H_2O}]}{k_2[\mathrm{N_2}]+k_3[\mathrm{O_2}]+k_1[\mathrm{H_2O}]}\right)+k_7[\mathrm{NO}][\mathrm{HO_2}]}{k_4[\mathrm{CH_4}]+k_5[\mathrm{CO}]+k_6[\mathrm{O_3}]+k_8[\mathrm{NO_2}]+k_9[\mathrm{NO}]}$$ **Equation 4.9**

where k_7, k_8 and k_9 are the reaction rate constants for Equations 4.6, 4.7 and 4.8 respectively (Monks et al., 2017).

In January, S-SSA-NOx produces an overestimate of ~0 – 5 ×10^6 molecule cm^{-3} in some regions in comparison to TOMCAT (Figure 4.9). There is a similar overestimate for June 2010, with values in the range of ~0 – 8 ×10^6 molecule cm^{-3} (Figure G.2). There are also some regions where adding the NO_x terms improves the comparison to TOMCAT, for example, it reduces the underestimate found in S-SSA in the NH in January and in the SH in June. For example, the maximum grid-box underestimate in January is reduced from 4.4 ×10^6 molecule cm^{-3} to 0.4 ×10^6 molecule cm^{-3}. This is likely due to the large % contribution of this source term in NH in January and in SH in June (Figure 4.8).

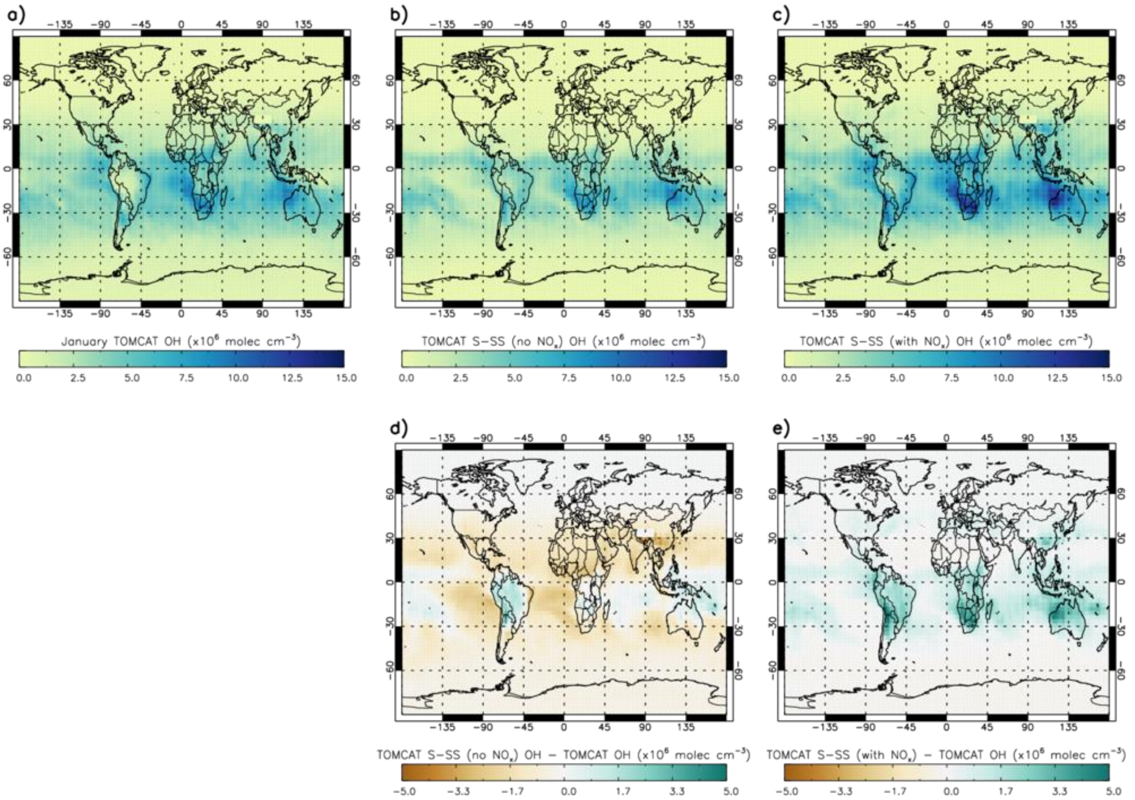

Figure 4.9: Comparison of [OH] for January 2010. (a) TOMCAT [OH], (b) S-SSA [OH], (c) S-SSA with NO_x sources/sinks ($NO + HO_2$, $NO + OH + M$, $NO_2 + OH + M$), (d) difference between S-SSA [OH] and TOMCAT [OH] and (e) difference between S-SSA [OH] with NO_x sources/sinks and TOMCAT [OH]. All values are averaged for the 600-700 hPa pressure region. See Figure G.2 (Appendix G) for June 2010.

As demonstrated, the NO_x reactions are important for OH chemistry in some regions, with $NO + HO_2$ a key source reaction (Figures 4.8 and 4.9). However, with an aim to derive [OH] from satellite, we cannot include these species currently, as there are no satellite observations of NO or HO_2 that would be appropriate to use in the method e.g. in the relevant pressure range, although this could potentially be derived from column data. This is a potential area of further study as co-located tropospheric NO_2 satellite data from another instrument on MetOp-A, GOME-2 (Munro et al., 2016), exists. However, this would require an additional method e.g. using a steady-state approximation to derive NO, and a method to derive HO_2.

For sink terms, the total sink term of the Sav-SSA and the relative contribution of the individual sink terms to this total is shown in Figure 4.10. In the region of interest, the combination of CO, CH_4 and O_3 dominates the total sink term for the mid troposphere layer of interest and above (Figure 4.10(a)). However, at pressures > 800 hPa, there are some other sink terms, which combined are causing up to ~ 70% of the total sink term.

These sink species include NO_2, dimethyl sulphide (DMS), hydrogen (H_2), hydrogen peroxide (H_2O_2), NO, SO_2, HCHO and a combination of hydrocarbons (e.g. alkanes and alkenes). These missing sink terms could explain the overestimate seen at pressures > 800 hPa in January (Figure 4.5).

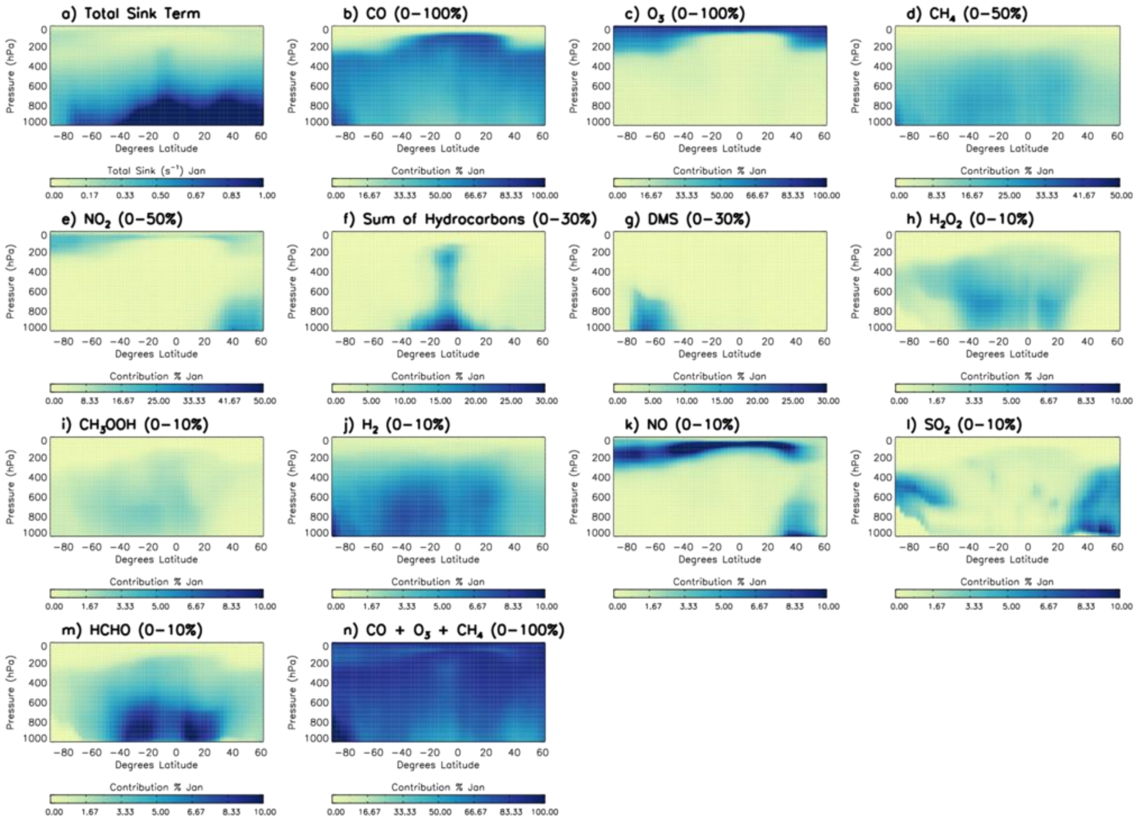

Figure 4.10: January 2010 latitude averaged (a) total Sav-SSA sink term and (b) – (n) the different sink terms as a % of the total sink term. The individual sink terms are: b) CO, (c) O_3, (d) CH_4, (e) NO_2, (f) sum of hydrocarbons (C_2H_4, C_2H_6, C_3H_6, C_3H_8, C_5H_8, C_4H_{10}), (g) dimethyl sulfide (DMS), (h) H_2O_2, (i) CH_3OOH, (j) H_2, (k) NO, (l) SO_2, (m) HCHO and (n) sum of CO, O_3 and CH_4 (total sink term for S-SSA/Equation 4.2).The data is presented from 90°S–60°N due to polar night at latitudes >60°N during January. Note the differing scales on the panels. See Figure G.3 (Appendix G) for June 2010.

The regional relative contribution of two of the larger sink species, the sum of hydrocarbons and formaldehyde (HCHO), across 600 – 700 hPa, are investigated further (Figure 4.11). Within the sum of the hydrocarbons, the dominant sink term is from the reaction of OH with isoprene (C_5H_8). Figure 4.11 shows that isoprene has a large contribution to the total sink term across South America and Indonesia in both January and June. There are regions where the S-SSA overestimates TOMCAT OH (Figure 4.6), which corresponds closely to these regions with a large sink contribution from isoprene. This indicates that the lack of the isoprene sink term in the S-SSA is causing the overestimation seen in this region. Therefore, in these regions, the S-SSA cannot capture the OH chemistry sufficiently. The HCHO contribution is more diffuse, representing ~10% of the total sink term in both January and June.

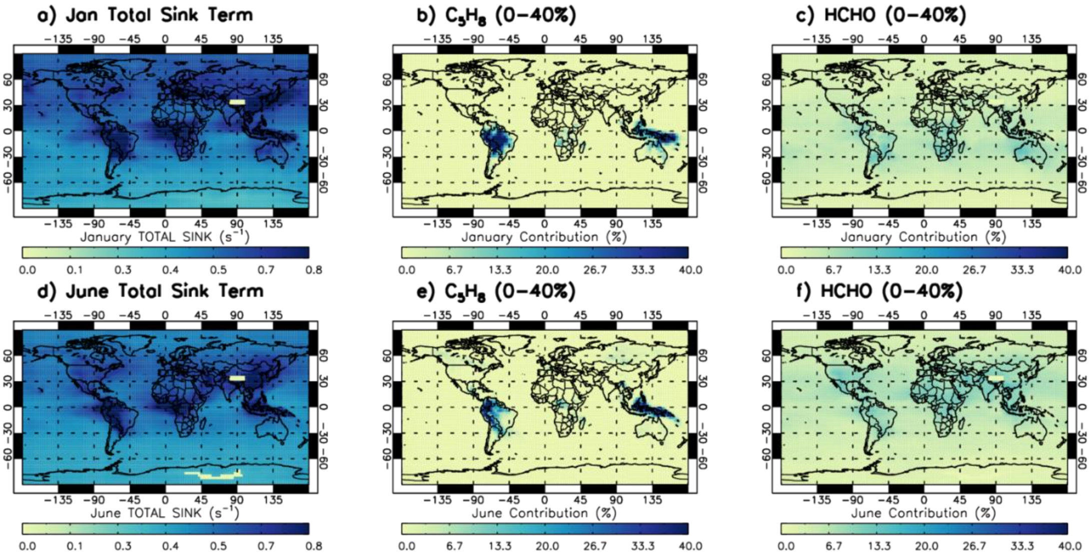

Figure 4.11: (a) Total sink term for Sav-SSA in January 2010 with units of s^{-1}, (b) percentage contribution of the OH + C_5H_8 term to the total sink term in Sav-SSA for January 2010, (c) percentage contribution of the OH + HCHO term to the total sink term in Sav-SSA for January 2010. Panels (d) to (e) are repeated for June 2010. The percentage range for the panel colour bar is labelled (e.g. 0-40%).

As with the missing source terms, adding these additional sink terms could improve the accuracy of the S-SSA in relation to modelled OH e.g. TOMCAT. Again, there are issues with available satellite retrievals for these species that would be appropriate to use in the method. GOME-2 (aboard MetOp-A with IASI) can provide tropospheric columns of NO_2 and other species e.g. HCHO, SO_2, which could potentially be used. For most of the other species, satellite data is not available, either in the relevant pressure region or on a similar/co-located instrument. Using data from different instruments also introduces problems, such as how to combine observations with different vertical resolutions or overpass times.

Overall, these missing source and sink terms should be considered when interpreting the results from the S-SSA. As shown here, the relative contribution of different source and sink terms varies both spatially and seasonally.

4.4.3 Application of the simplified steady-state approximation to satellite data

Satellite-retrieved O_3, CO, CH_4 and H_2O and model j_1 are applied to the S-SSA (Equation 4.2) as described in Section 4.3.2. The global satellite-derived mass-weighted monthly average [OH] in 2010 (600 – 700 hPa) ranges from 2.1 ×10^6 molecule cm^{-3} in January to 2.9 ×10^6 molecule cm^{-3} in July (Figure 4.12). Similar values are found for 2017, ranging from 2.0 ×10^6 molecule cm^{-3} in December to 2.8 ×10^6 molecule cm^{-3} in July (Appendix F/Figure F.2). There is seasonal OH variation, with the higher [OH] values (> 5.0 ×10^6 molecule cm^{-3}) predominantly in the SH in ~ December – February (SH summers), with a maximum grid-box value of 10.6 ×10^6 molecule cm^{-3} (Figure 4.12). These larger [OH] move to the tropics (30°S – 30°N) between ~ March – May, with a maximum grid-box value of 10.9 ×10^6 molecule cm^{-3}. The higher [OH] are present in the NH in ~ June – August (NH summer) with a maximum grid-box value of 28.1 ×10^6 molecule cm^{-3}. Lastly, the larger [OH] are present around the tropics again in ~ September – November, with a maximum grid-box value of 11.4 ×10^6 molecule cm^{-3}.

Monthly averages of TOMCAT, TOMCAT FC-SSA, TOMCAT S-SSA and satellite S-SSA [OH] for the 600 – 700 hPa pressure layer in January and June are compared (Figure 4.13). Overall the spatial pattern is very similar between the 4 estimates of OH distribution. TOMCAT FC-SSA shows a very good agreement with TOMCAT for [OH] global averages, with an underestimate of < 6%. This highlights that using a steady-state approximation to calculate OH matches well with the numerical integration scheme inside the model. Therefore, when a comprehensive number of source and sink terms are included, the resulting [OH] is accurate compared to modelled OH.

Between TOMCAT OH and satellite S-SSA OH, there is reasonable agreement in both January and June 2010 (Figure 4.13). In January both estimates have comparable locations of peak values, e.g. over north-western Australia and southern Africa. TOMCAT has a maximum grid-box value of 9.7 ×10^6 molecule cm^{-3} and the satellite S-SSA has a maximum grid-box value of 10.3 ×10^6 molecule cm^{-3}. The global average values are 2.85 ×10^6 and 2.21 ×10^6 molecule cm^{-3} for TOMCAT and the satellite S-SSA respectively, showing a difference of ~22%. In June, there are comparable peak value locations in both estimates over southern Asia and northern Africa. The global average values are 3.80 ×10^6 and 2.73 ×10^6 molecule cm^{-3} for TOMCAT and the satellite S-SSA respectively, showing a difference of ~28%. Despite broadly good agreement, one area of poor agreement in June are the peak values seen over North America in TOMCAT, which are not seen in the satellite S-SSA. Across all the months of 2010 (Jan – Dec), the difference in global weighted mean varies between 20% – 30%, with the largest difference in April and the lowest in July. Between all grid-boxes of TOMCAT and the satellite S-SSA [OH] in January and June 2010, there is a Pearson's correlation coefficient value of 0.85 and 0.83 for January and June, respectively, and a NMB of 24% and 32%, respectively (Figure 4.14). The difference between TOMCAT S-SSA and satellite S-SSA global average OH is ~ 10% in January and ~ 3% in June, suggesting that the input species in the S-SSA show a good agreement between TOMCAT and the satellite.

Overall, applying satellite data to the S-SSA can successfully produce a reasonable agreement with TOMCAT OH, showing a good spatial comparison and a global average underestimate of around 20% – 30% (Figure 4.13). 2017 shows similar results (Appendix F/Figure F.3), with a global underestimate for the satellite S-SSA of 21% in January and 28% in June.

To place these results in the context of previous studies, the airmass-weighted average has been calculated (Lawrence et al., 2001), to compare with other datasets (e.g. some of those in Figure 3.7 from Rowlinson et al. (2019)). The best pressure region for which to compare the satellite S-SSA OH is the 500 – 750 hPa layer, as this is closest to the

600 – 700 hPa layer used here (Table 4.6). However, there are several differences between the datasets which are likely to cause large variations, e.g. Spivakovsky et al. (2000) and Rowlinson et al. (2019) represent averages across both daytime and nighttime, whereas the [OH] in this work are for 9:30, which impacts the key OH source from O_3 photolysis. Also, Spivakovsky et al. (2000) represents a climatology and Rowlinson et al. (2019) represents the year 2000, whereas the [OH] in this work is for 2010. Aside from the NH latitudes above 30°N, the [OH] in this work (both S-SSA and TOMCAT full model) are higher than the other estimates, which is consistent with these estimates being for mid-morning, so will have more average O_3 photolysis than the times in the other studies e.g. overnight. In the NH, at latitudes between 30°N – 90°N, the average [OH] in the S-SSA is much lower than the other methods. This may be explained by 9:30 LST being during the nighttime in the NH high latitudes during winter, which would reduce O_3 photolysis, compared to a daily average.

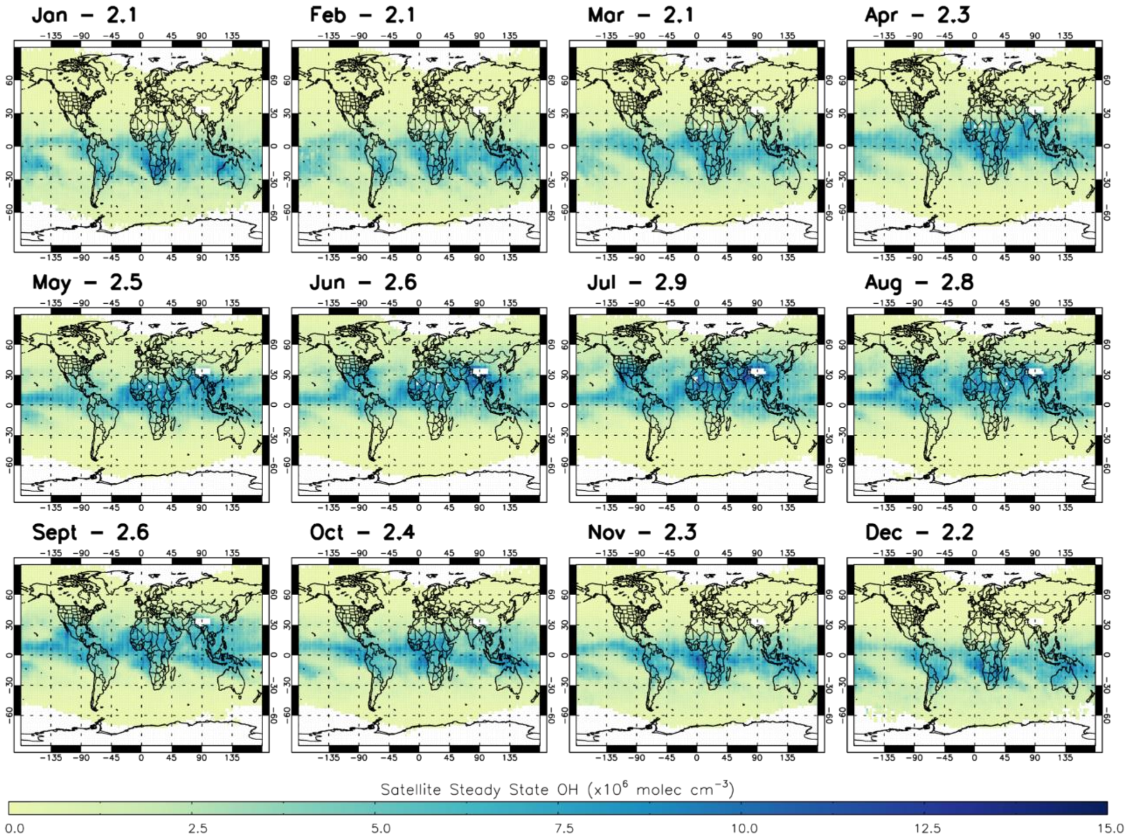

Figure 4.12: Global satellite-derived OH (S-SSA) in units of ×10^6 molecule cm^{-3} for each month of 2010. Mass-weighted global monthly means are presented above each panel. See Figure F.2 (Appendix F) for 2017.

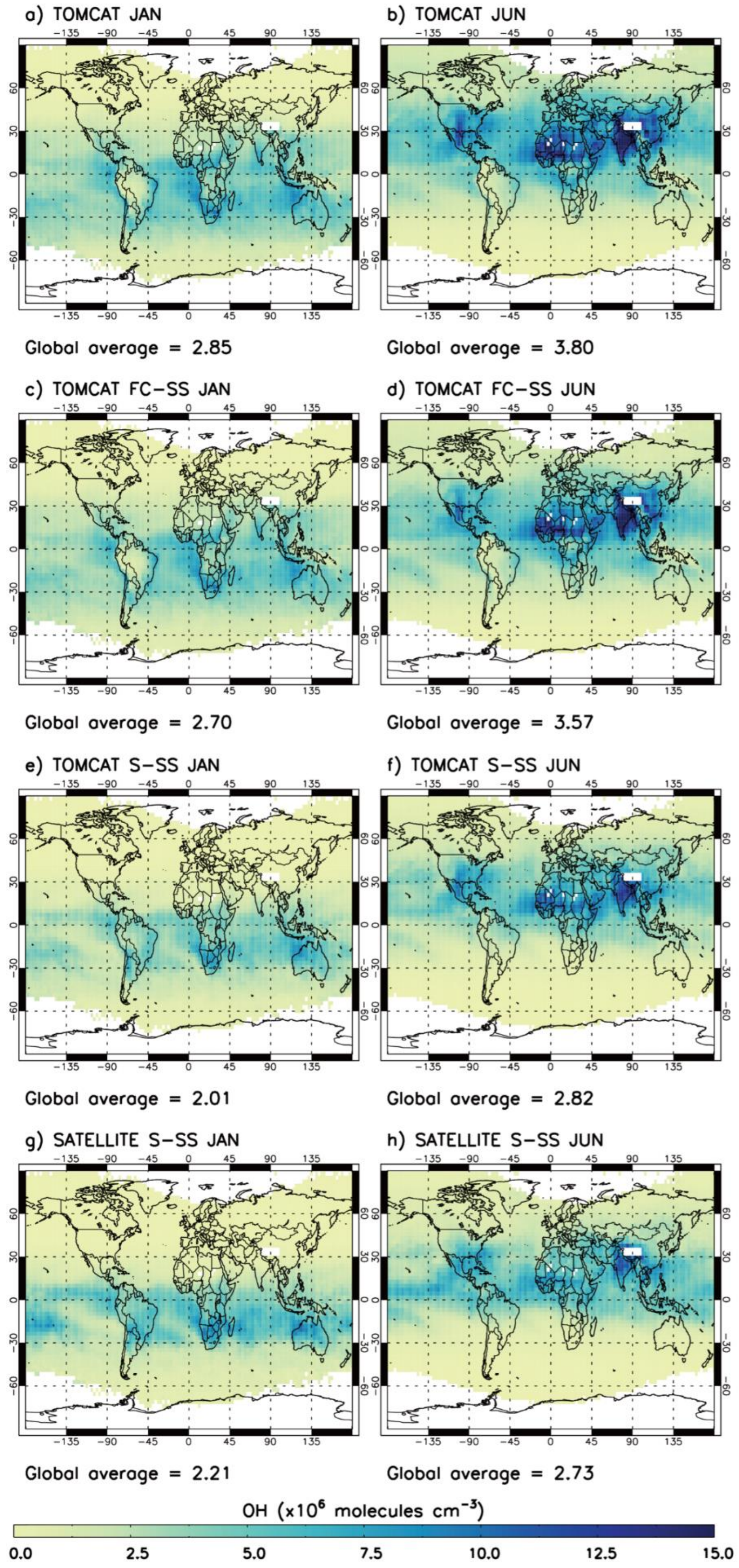

Figure 4.13: (a) TOMCAT OH in January 2010, (b) repeated for June 2010, (c) TOMCAT FC-SSA OH in January 2010, (d) repeated for June 2010, (e) TOMCAT S-SSA OH in January 2010, (f) repeated for June 2010, (g) satellite S-SSA in January 2010, (h) repeated for June 2010. All averaged across the 600 – 700 hPa pressure layer. Global average OH values for the selected pressure layer are given below each panel in units of ×10^6 molecule cm^{-3}. See Figure F.3 (Appendix F) for 2017.

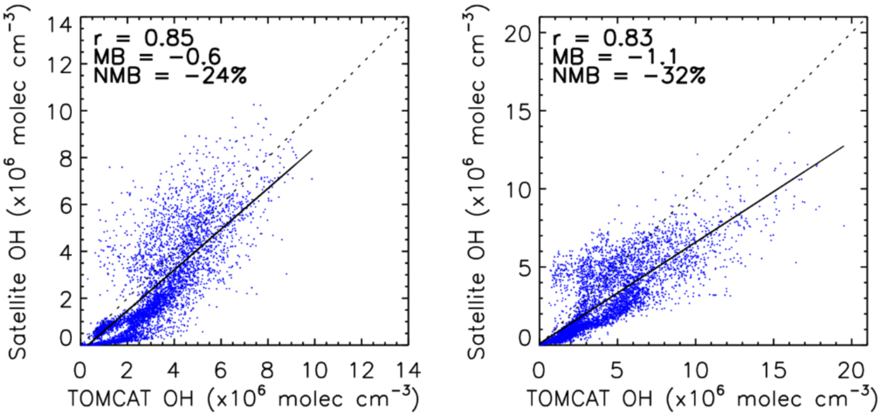

Figure 4.14: Scatterplot of the [OH] for all grid-boxes from the satellite S-SSA in comparison with TOMCAT full model for January (left panel) and June (right panel) 2010. Units of ×10^6 molecule cm^{-3}. MB represents the mean bias (satellite – TOMCAT) and NMB represents the normalised mean bias (normalised relative to TOMCAT).

Dataset	**90°S – 30°S**	**30°S – Eq**	**Eq – 30°N**	**30°N – 90°N**
Satellite S-SSA [OH] **(~9:30)**	1.23	4.01	2.05	0.05
TOMCAT S-SSA [OH] **(~9:30)**	1.49	3.40	1.96	0.08
TOMCAT [OH] **(~9:30)**	2.54	4.49	3.26	0.52
Spivakovsky et al. (2000)	0.72	2.00	1.99	0.88
Rowlinson et al. (2019) TOMCAT	0.51	1.54	2.05	0.93

Table 4.6: Annual zonal airmass-weighted averages for the 500 – 750 hPa pressure layer from this study (satellite S-SSA, TOMCAT S-SSA and TOMCAT full model [OH]) and the Spivakovsky et al. (2000) climatology based on MCF observations and TOMCAT [OH] from another study, Rowlinson et al. (2019) (Figure 3.7). The Rowlinson et al. (2019) TOMCAT is based on 6-hourly output (rather than sampling based on a 9:30 satellite overpass time). All in units of ×10^6 molecule cm^{-3}.

4.4.4 Application of the simplified steady-state approximation to aircraft data

There are limited direct measurements of OH in the free troposphere for which to assess the method developed in this chapter against, however, one example is the ATom aircraft mission which measured a wide spatial area and across difference seasons. ATom measurements of CH_4, CO, O_3, H_2O and j_1 across the 4 campaigns are applied to the S-SSA, calculating OH (OH-calc) and compared to measurements of OH by the ATHOS instrument (OH-obvs) (Figure 4.15). After filtering, 174 sets of measurements were used in the [OH] calculations (35/34/38/67 for A1/2/3/4 respectively) for 600 – 700 hPa. Combining all 4 campaigns, shows that the S-SSA underestimates the measured OH by ~ 0.82 ×10^6 molecule cm^{-3} or ~25.8 %. The NMB varies between 21.1% - 25.2% (0.55 – 1.28 ×10^6 molecule cm^{-3}) for ATom-1,3 and 4, with a much higher NMB of 48.8% (0.86 ×10^6 molecule cm^{-3}) for ATom-2. This NMB is smaller than the uncertainty of the OH measurements, which is ~35 % (Brune et al., 2019). Although ATom-2 shows a higher percentage difference, the absolute average difference value is more similar to the other campaigns (0.86 ×10^6 molecule cm^{-3}). OH-calc and OH-obvs are well correlated, with a correlation coefficient of 0.78 for the combined record (ranging from 0.56 to 0.86).

As stated above, the average difference between OH-obvs and OH-calc is ~26%, which is in a similar order of magnitude to the large uncertainty of 35% for the OH measurements from the ATHOS instrument. Despite the large scale of the ATom campaign, it provides only a limited spatial and temporal comparison for which to assess the S-SSA methodology, which is a limitation that must be considered. As the difference between OH-obvs and OH-calc is within the large measurement error and considering the limited spatiotemporal comparison, the datasets are sufficiently correlated to justify further study and use of the S-SSA in the 600 – 700 hPa pressure layer.

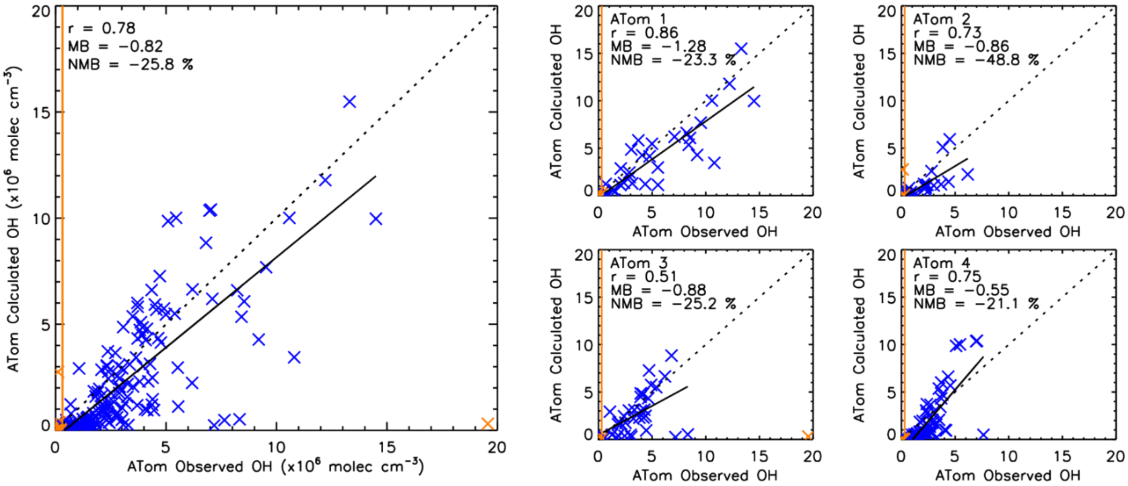

Figure 4.15: Left panel – Combination of the 4 ATom campaigns. Right 4 panels – individual ATom campaigns (labelled). Comparison of OH-calc and OH-obvs, both from ATom. ATom observations are filtered for 600 – 700 hPa and 08:00 – 11:00 LT. Orange data points are excluded as either below the limit of detection (0.018 pptv / 0.31 ×10^6 molecule cm^{-3}) or as an outlier (> mean + 3.0 standard deviations). Displayed at the top of each panel is: the Pearson's correlation coefficient (r); the MB (OH-calc subtract OH-obvs); and the NMB (% with respect to OH-obvs)

In consideration of the impact of the spatial region on the comparison, higher [OH] is found near the equator, aside from some exceptions, e.g. around 45°N in ATom-1 or around 30°S in ATom-2 (Figure 4.16). For most latitudes OH-obvs is larger than OH-calc, aside from some exceptions in ATom-2 and ATom-4, with the differences ranging from -9.7 ×10^6 molecule cm^{-3} to 4.1 ×10^6 molecule cm^{-3}. Broadly, the differences are smallest in the SH (90°S – 30°S) and around the equator (30°S – 30°N). The small differences in the SH are mostly due to the lower values here, suggesting that the small differences around the equator indicate good agreement here despite larger [OH]. The largest differences are found in the NH, where several outlier [OH] are found.

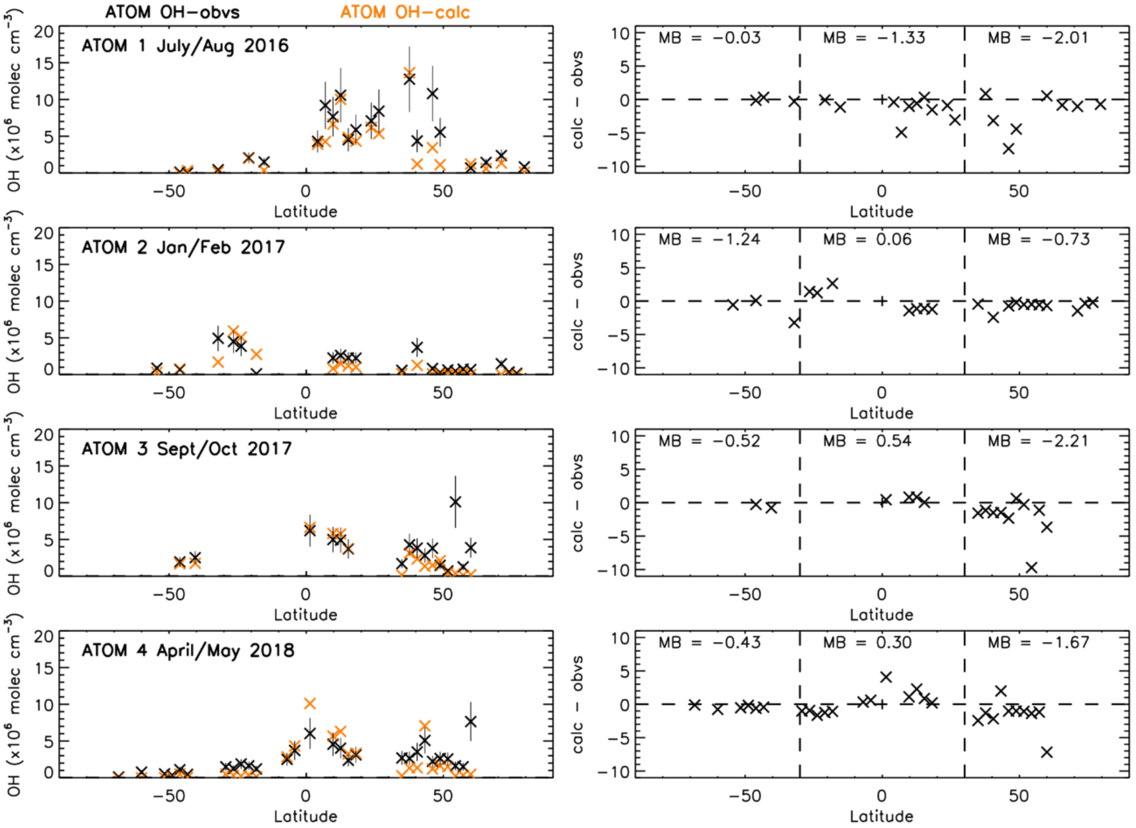

Figure 4.16: Left panels – latitude-averaged ATom OH (pptv) for the 4 ATom campaigns (labelled). Includes error bars of 35%. Right panels – latitude-averaged OH difference between OH-calc and OH-obvs for the 4 ATom campaigns. The mean difference is labelled for 3 different regions of latitude. The regions are 90°S – 30°S, 30°S – 30°N and 30°N – 90°N. Units are ×10^6 molecule cm^{-3}.

To compare satellite S-SSA (OH-sat) and ATom OH-obvs, OH-obvs has been overlayed onto a base map of the satellite-derived OH (Figure 4.17), which has been averaged across the days for each ATom campaign in 2017 (~ 1 month per campaign), as it is more representative of the actual time period of ATom (2016 – 2018) than 2010. Overall, the comparison is challenging due to the sparsity of ATom measurement points compared to the satellite [OH] field, and also the difference in years for ATom-1 (2016) and ATom-4 (2018). The agreement between OH-sat and OH-obvs is mixed, with some areas of good agreement. Examples of good agreement include: peak [OH] regions e.g. in ATom-1 off the western coast of Mexico (equator - 30°N); and good agreement in low [OH] regions, e.g. over the North Atlantic ocean in ATom-2. There are also areas of poor agreement, e.g. high OH-obvs near Alaska and low values in the OH-sat in ATom-3 and 4. OH-sat is an underestimate for OH-obvs, with a NMB (for nearest satellite grid-box) ranging from -35.1% to -60.1. The Pearson's correlation coefficient varies from 0.15 to 0.75. Overall, as stated above, the resolution and temporal differences between the two records may contribute to the poor agreement.

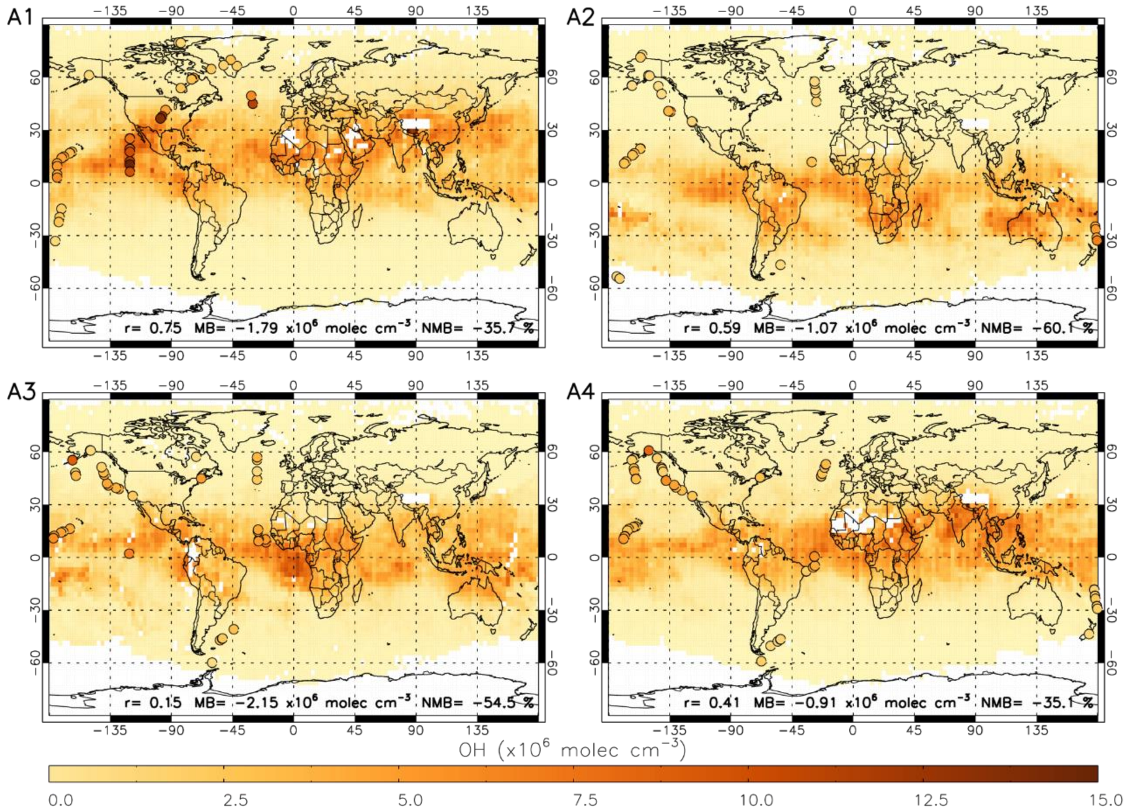

Figure 4.17: Satellite S-SSA OH for 4 time periods averaged for the days of the 4 ATom campaigns (ATom: 2016 – 2018, satellite: 2017), for the 600 – 700 hPa layer (A1 represents ATom-1 etc.). The ATom OH measurements (OH-obvs) are overlayed onto the top of the satellite map as coloured circles (both using the same colour bar). Displayed at the bottom of each panel is: the Pearson's correlation coefficient (r), MB (nearest satellite grid cell subtract OH-obvs) and the NMB (% wrt OH-obvs).

To further assess the impact of latitude on the OH-sat and ATom OH-obvs, the comparison of OH-sat and OH-obvs is differentiated by latitude, highlighting that the differences are larger at the higher NH latitudes (e.g. 30°N – 90°N) (Figure 4.18). Therefore, the statistics for all latitudes, 30°N – 90°N and 90°S – 30°N are presented. Across all 3 latitude ranges the correlation coefficient is similar (0.55, 0.67, 0.61 respectively). However, the average difference is much higher at the higher NH latitudes, with a 74% underestimate (of OH-sat wrt OH-obvs), compared to only a 12% underestimate for the 90°S-30°N latitude range. As shown in Section 4.4.2, the OH source reaction of HO_2 + NO represents a larger contribution to the total production in the NH high latitudes in winter (~ ATom-2,3,4). This could be the cause of the poor agreement at NH high latitudes, as the S-SSA may not be able to provide enough information about the chemistry of OH to provide an accurate representation.

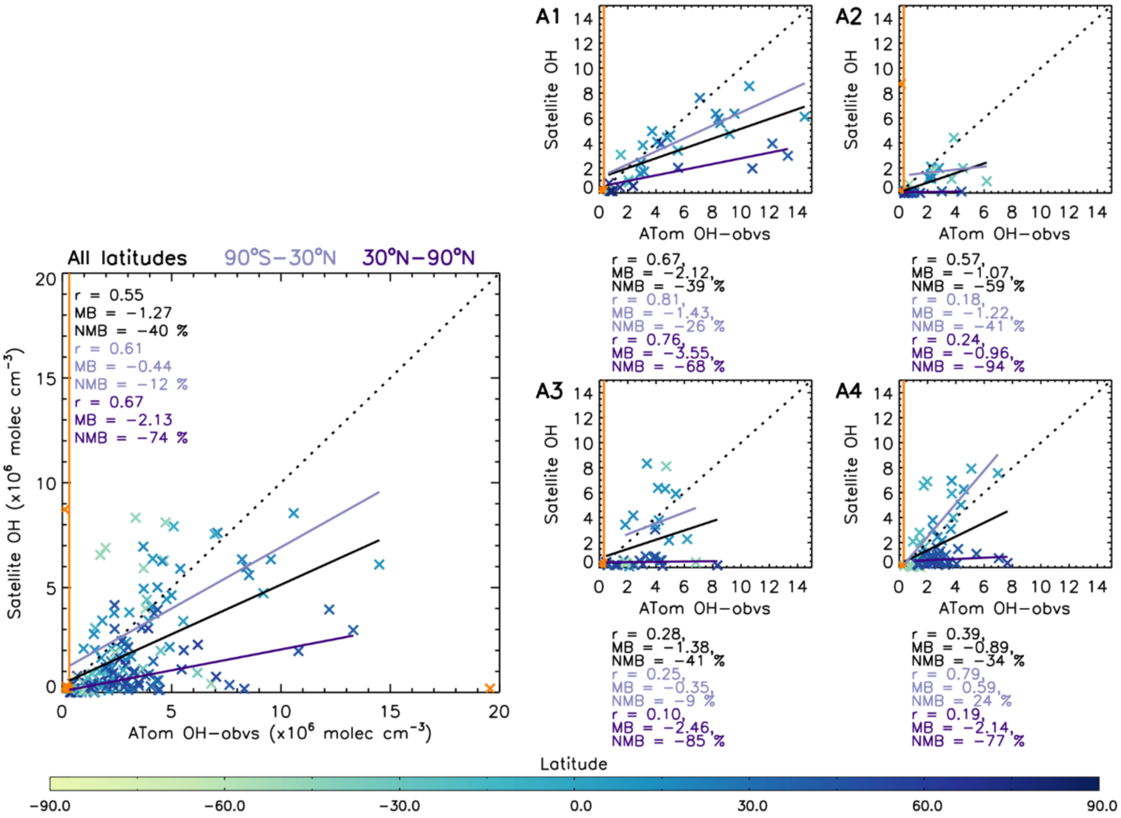

Figure 4.18: Left panel – Combination of the 4 ATom campaigns. Right 4 panels – individual ATom campaigns (A1 represents ATom-1 etc.). Comparison of OH-obvs and satellite S-SSA (using the nearest satellite [OH] to ATom measurement - from the averaged 2017 satellite OH grid (OH-sat)). ATom observations are filtered for 600–700 hPa and 08:00–11:00 LST. The datapoints are coloured by latitude, as shown on the colour bar. Orange data points are excluded as either below the limit of detection (0.018 pptv / 0.31 ×10^{6} molecule cm^{-3}) or as an outlier (> mean + 3.0 standard deviations). Displayed below each panel is: the Pearson's correlation coefficient (r); the MB (calculated from OH-sat – OH-obvs); and the NMB (% with respect to OH-obvs). These values (for all latitudes) are repeated for 2 additional latitude ranges: 90°S–30°N and 30°N–90°N.

4.4.5 Impact of omitted source terms using aircraft data

NO_x has been shown to be an important source of OH across some global regions. Here, the impact of adding in NO_x reactions to the S-SSA when applied to the ATom data is compared (Figure 4.19). The comparison is between OH-calc, and OH-calc using the S-SSA including 3 NO_x reactions (Equations 4.6 - 4.8) as shown in Equation 4.9 (OH-calc-NO_x). Adding the additional 3 NO_x terms does improve the overall agreement, by reducing the bias (relative to OH-obvs) from -20.6% to +13.2%. The change from a negative to positive difference is consistent with the comparison of S-SSA with and without NO_x reactions using model data (Figure 4.9 and Appendix G/Figure G.2). However, the correlation remains very similar for both S-SSAs (r = 0.76/0.78). Overall, these results agree with those found in Section 4.4.2 that the NO + HO_2 source term, not represented in the S-SSA, can make a large contribution to the total source term.

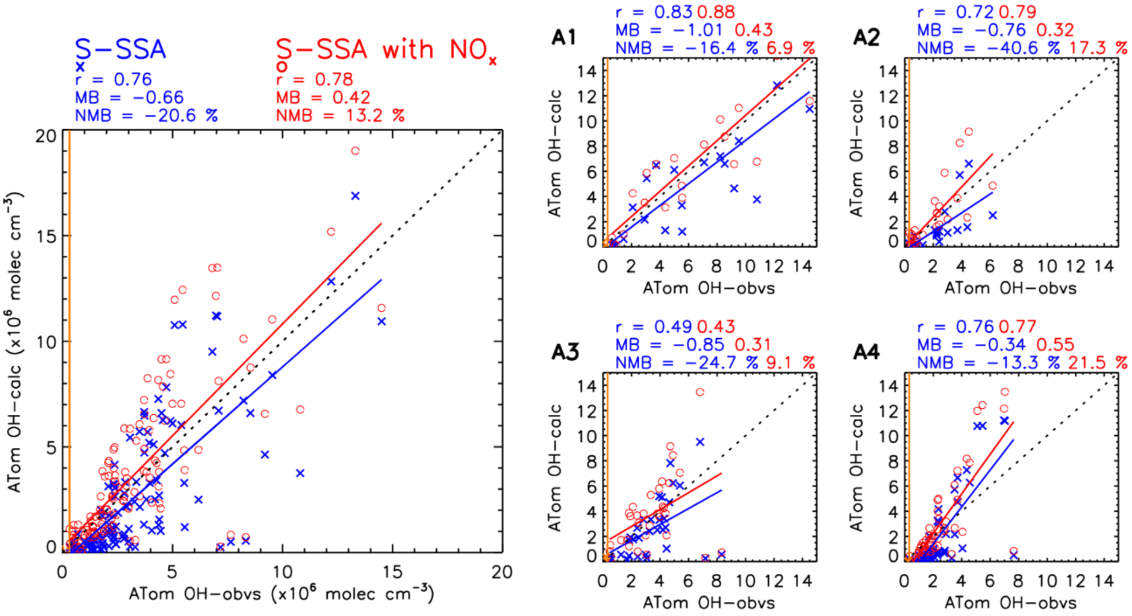

Figure 4.19: As Figure 4.15 but with the addition of OH-calc including 3 NO$_x$ reactions (NO + HO$_2$, NO + OH + M, NO$_2$ + OH + M) (OH-calc-NO$_x$, red/circle). OH-calc without the additional NOx reactions is shown in blue and as crosses. Statistics for OH-calc (left) and OH-calc-NOx (right) are displayed above each panel. The statistics for OH-calc differ compared to Figure 4.15 due to using only measurements which had NO$_x$ measurements available.

4.4.6 Hydroxyl radical reactivity

OHR measurements have the potential to be compared with the denominator of the S-SSA expression (Equation 4.3). ATom OHR measurements (OHR-obvs) and OHR calculated using ATom measurements in Equation 4.3 (OHR-calc) are compared (Figure 4.20), however, there are only a few available observations of OHR in the time period and pressure layer of interest (08:00–11:00 LST and 600–700 hPa), ranging from 11–17 in total per campaign. Overall, across the 4 campaigns OHR-calc is an underestimate of -36.7%. This bias ranges between -57.6% and +20.1% for the individual campaigns. An overestimate is found for ATom-4, compared to an underestimate the other campaigns. OHR-obvs and OHR-calc are not well correlated (r = -0.02 for the combined record, ranges between -0.23 and +0.20 for the individual campaigns). However, the uncertainty of the OHR measurements is large (0.8 s^{-1}) and 80% of calculated OHR values fell within the range of measurement uncertainty from OHR-obvs (dashed lines in Figure 4.20). Across the 4 campaigns, ~75 % of latitude-averaged OHR-calc values are within the large uncertainty of the latitude-averaged OHR-obvs (Figure 4.21). Broadly, the ~25 % exceptions occur in the NH. The largest difference is -1.6 s^{-1} in ATom-1, as well as one uncertainty exceedance in the SH with a difference of -2.9 s^{-1}.

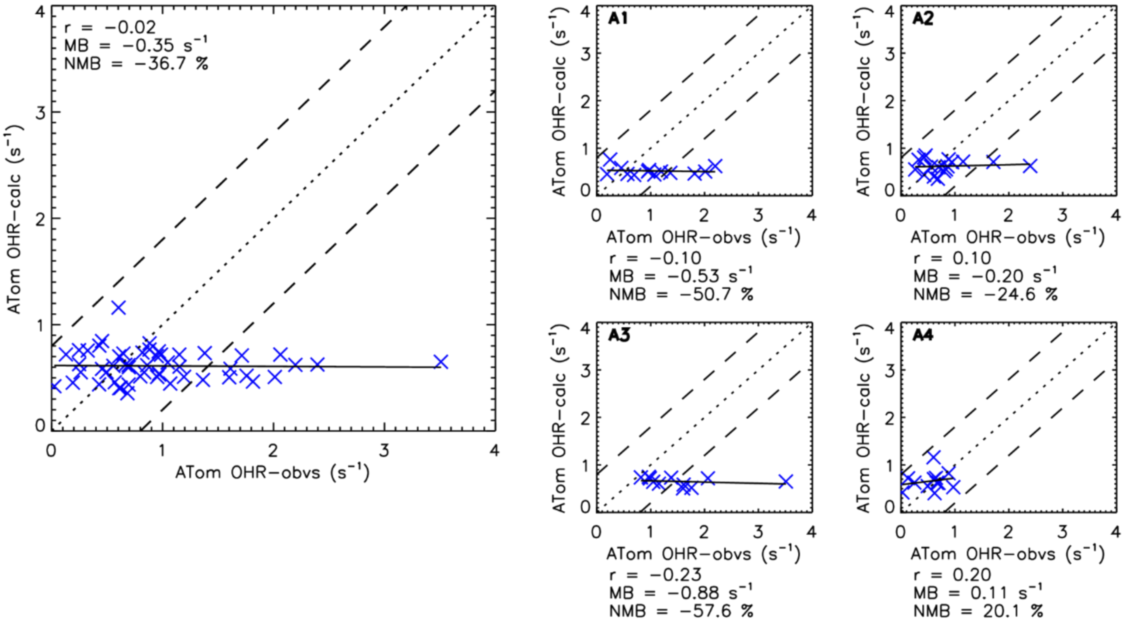

Figure 4.20: Left panel – Combination of the 4 ATom campaigns. Right 4 panels – individual ATom campaigns (A1 represents ATom-1 etc.). Comparison of OHR-obvs and OHR-calc. The dashed lines represent the ± OHR uncertainty (corresponding to the ± 0.8 s^{-1} measurement uncertainty) and the dotted lines show the 1:1 line. ATom OHR measurements are filtered for 600–700 hPa and 08:00–11:00 LST.

Travis et al. (2020), studying ATom-1 and ATom-2, also found large differences between calculated OHR (from ATom measurements of other sink species) and OHR measurements. The difference was found in both the NH and SH, and ranged in altitude from ~4 km to surface for ATom-1, and ~3 km to the surface for ATom-2. The selected pressure range used in this chapter (600 – 700 hPa) equates to approximately 3 to 4 km altitude. Therefore, the finding of a better agreement in ATom-2 at this pressure/altitude region (NMB = -24% for ATom-2, NMB = -51% for ATom-1), is consistent with Travis et al. (2020). Generally, an underestimate of OHR measurements by calculated OHR is well-documented, and commonly known as “OH missing reactivity”. Here, we find an average “missing reactivity” of 0.34 s^{-1}, with a peak value of 2.9 s^{-1}. Thames et al. (2020) found similar “missing reactivity” values in the marine BL for ATom-1,2 and 3 which varied from 0 to 2.5 s^{-1}, with an average of 0.5 s^{-1}.

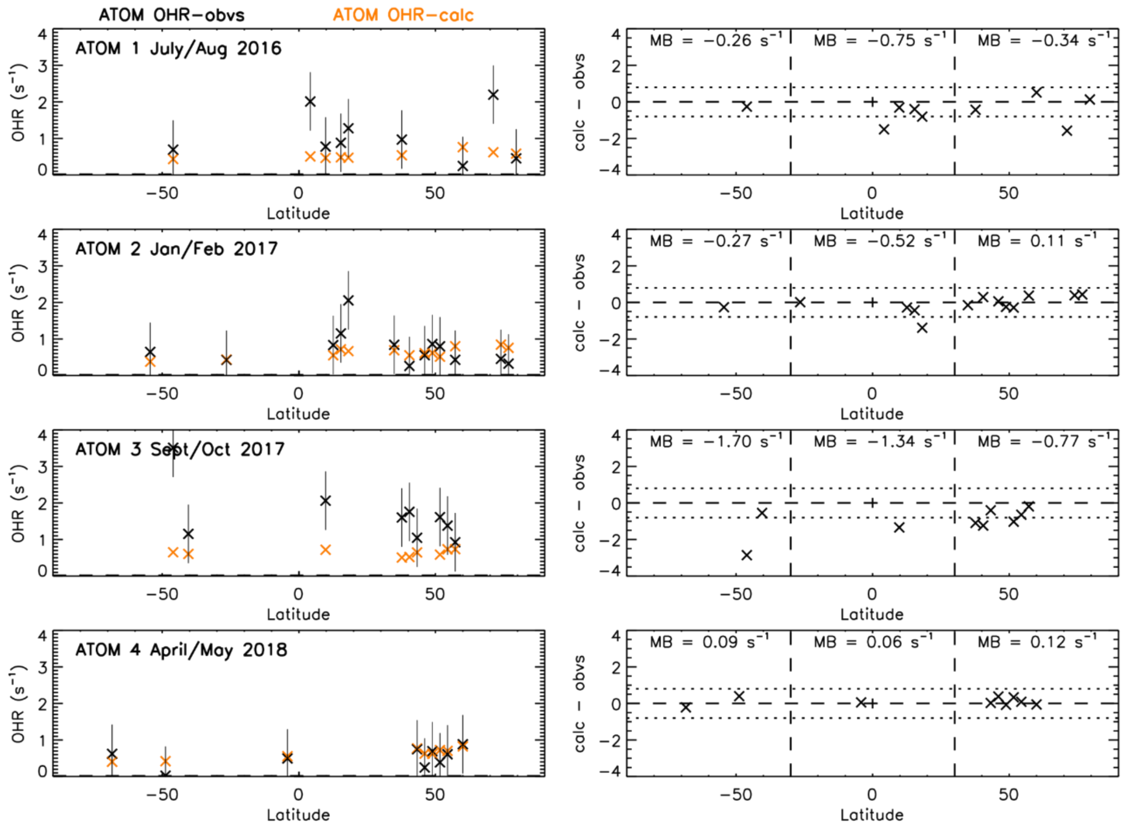

Figure 4.21: Left panels – latitude-averaged ATom OHR (s^{-1}) for the 4 ATom campaigns (labelled). Includes error bars of ± 0.8 s^{-1}. Right panels – latitude-averaged OH difference between OH-calc and OH-obvs for the 4 ATom campaigns. The mean difference is labelled for 3 different regions of latitude. The regions are 90°S–30°S, 30°S–30°N and 30°N–90°N. Units are ×10^{6} molecule cm^{-3}.

4.4.7 Temporal variation in satellite-derived hydroxyl radical

Satellite data for 2008 – 2017 is applied to the S-SSA to study the long-term change in [OH] that can be derived from this satellite-derived record. The IASI record differs from that used in this chapter so far for 2010/2017, as it is sub-sampled (temporally and spatially), however, the agreement between the sub-sampled and fully sampled data is very good, and therefore appropriate to use here (Figure 4.2). Across the 2008 – 2017 satellite S-SSA record, a fixed year of model j_1 (2010 - monthly varying) has been used. As this value is fixed, any potential influence due to variation in j_1 e.g. from variation in stratospheric O_3 overhead, which impacts the radiation reaching the troposphere as some UV radiation is absorbed by stratospheric O_3, is removed. This should be considered when interpreting these results.

The satellite S-SSA [OH] annual average has been calculated for 4 latitude regions (Figure 4.22). The 4 latitude regions are global (all latitudes), NH (equator – 90°N), SH (90°S – equator) and tropics (15°S – 15°N). As shown in the model and aircraft data, a region closer to the equator shows better agreement with measurements of OH in some cases. Therefore, a tropical region has been included in the analysis of OH temporal variation. Between 2008 – 2017, the global average varied between 2.1 – 2.3 ×10^{6} molecule cm^{-3}, with an average of 2.2 ×10^{6} molecule cm^{-3} for the time period, and the tropical region varied between 4.1 – 4.8 ×10^6 molecule cm^{-3}, with an average of 4.4 ×10^6 molecule cm^{-3}. The global [OH] anomaly across the time period ranges between -3.0% to +4.7% and the tropics anomaly ranges from around -6.9% to +7.7%, as shown in Figure 4.22.

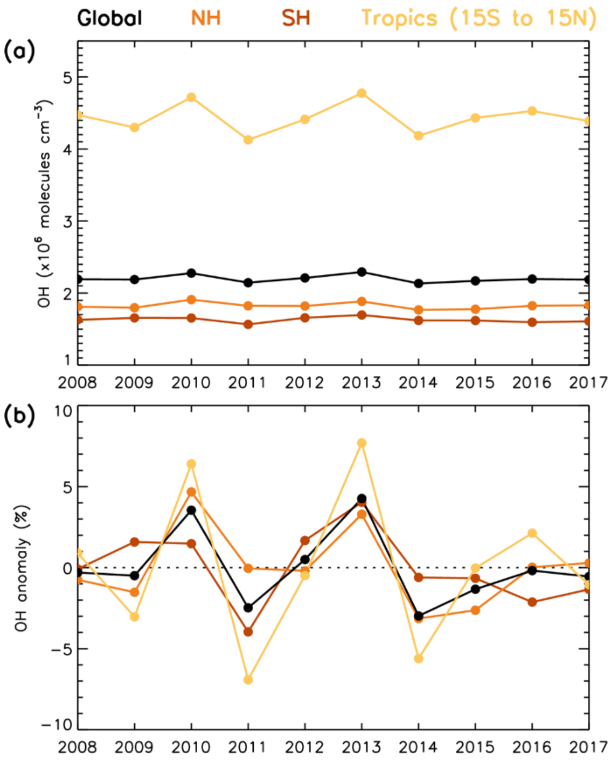

Figure 4.22: (a) Annual satellite-derived OH for 2008–2017 (pressure layer 600 – 700 hPa) in units of ×10^6 molecule cm^{-3}. (b) Annual percentage satellite OH anomaly relative to an annual average baseline (2008–2017). Annual timeseries are presented for all latitudes (global), equator – 90°N (NH), 90°S – equator (SH) and 15°S – 15°N (tropics).

Monthly average satellite S-SSA [OH] is higher in the tropics, decreasing towards the poles (Figures 4.23). The hemispheres show a seasonal cycle, with the highest values in their respective summers and lowest values in their respective winters. The monthly satellite OH anomaly varies between: -0.10 and +0.15 ×10^6 molecule cm^{-3} for the global average; -0.15 and +0.11×10^6 molecule cm^{-3} for the NH average; -0.21 and +0.21 ×10^6 molecule cm^{-3} for the SH average; and -0.37 and +0.54 ×10^6 molecule cm^{-3} for the tropical average (Figure 4.24). Mostly, all 4 latitude bands follow a similar pattern. Notable positive anomalies (given here for the tropical band) occur in mid-2010 (+0.30 ×10^6 molecule cm^{-3}), the end of 2012 and beginning of 2013 (+0.54 ×10^6 molecule cm^{-3}), mid-2015 (+0.15 ×10^6 molecule cm^{-3}) and mid-2016 (+0.14 ×10^6 molecule cm^{-3}). Notable negative anomalies occur in mid-2009 (-0.27 ×10^6 molecule cm^{-3}), 2011 to mid-2012 (-0.37 ×10^6 molecule cm^{-3}), end of 2015 and beginning of 2016 (-0.21 ×10^6 molecule cm^{-3}) and the end of 2017 (-0.22 ×10^6 molecule cm^{-3}). Monthly anomaly plots for temperature and the other satellite input species are shown in Appendix H (Figures H.1 – H.5).

In comparison with other studies of [OH] temporal variability, e.g. using MCF observations and CTMs, these values are similar. For example, Patra et al., 2021 found a range of ~ -6% to +6% in their global [OH] anomaly during the same time period (however, using a longer baseline). However, as this study is for a specific mid-tropospheric pressure region, this cannot be a direct comparison.

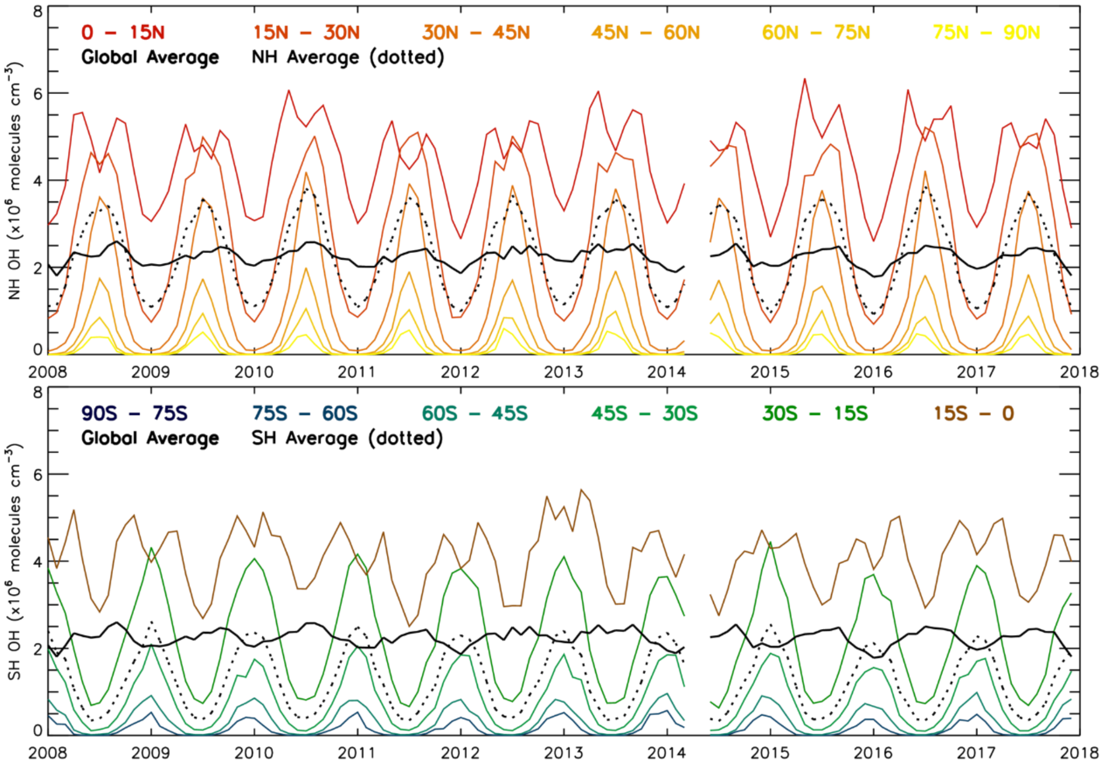

Figure 4.23: Monthly mean satellite OH for 2008–2017 (pressure layer 600 – 700 hPa) for 15° latitude bands across the NH (top panel) and SH (bottom panel). The latitude bands are labelled at the top of both panels. Displayed on each panel are the global (solid black line) and hemispheric averages (dotted black line). Units of ×10^6 molecule cm^{-3}.

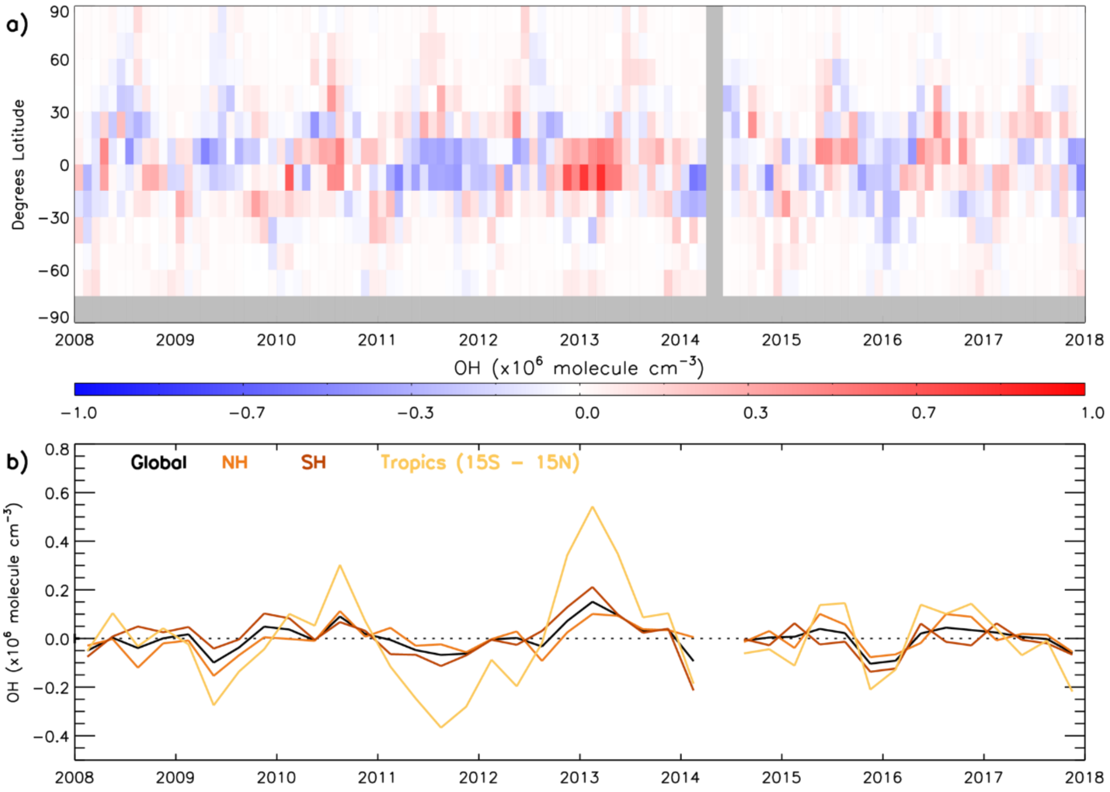

Figure 4.24: Monthly mean satellite OH anomaly for 2008–2017 (pressure layer 600 – 700 hPa): (a) 15° latitude bins and (b) 3-month average for global (all latitudes), NH (equator – 90°N), SH (90°S – equator) and tropics (15°S – 15°N). Anomaly is relative to a monthly average baseline (2008–2017).

To diagnose the relative variation of the components of the S-SSA from 2008 – 2017, the monthly variation of the 3 individual sink terms and the combined source term for the 600 – 700 hPa pressure layer is derived (Figure 4.25). CO is the largest (and therefore dominant) sink term. Across the NH and SH averages, CO ranges between 0.20–0.45 s^{-1}. The next largest sink term is CH_4, which varies between 0.10–0.15 s^{-1}. The smallest sink term is O_3, with is consistently around 0.04 s^{-1}. As the CO sink term is much larger than the others, this indicates that any variation in CO will likely dominate the resulting variation in the total sink term. Across the record, the CO sink term is predominantly larger in the NH, compared to the SH, with differences of up to ~ 0.2 s^{-1}, largest in the first half of the year. The NH/SH difference in the other two sink terms is negligible, therefore the CO sink term will contribute less to the total sink term in the SH, especially in the first half of the year. This is consistent with aircraft measurements below 3 km in Travis et al. (2020) and from free troposphere model data in Lelieveld et al. (2016). Despite a positive trend in satellite CH_4 of 4.5 ppb yr^{-1} across this pressure range from 2008 – 2017, when the rate constant is applied, the CH_4 sink term doesn't show any comparable variation on the scale of the CO sink, with no large positive trend that would impact the CH_4 sink term (Figure 4.25). The source term varies from ~ 5 – 15 $\times 10^5$ molecule cm^{-3} s^{-1} for the global, NH and SH averages and from ~ 15 – 28 $\times 10^5$ molecule cm^{-3} s^{-1} for the tropical band.

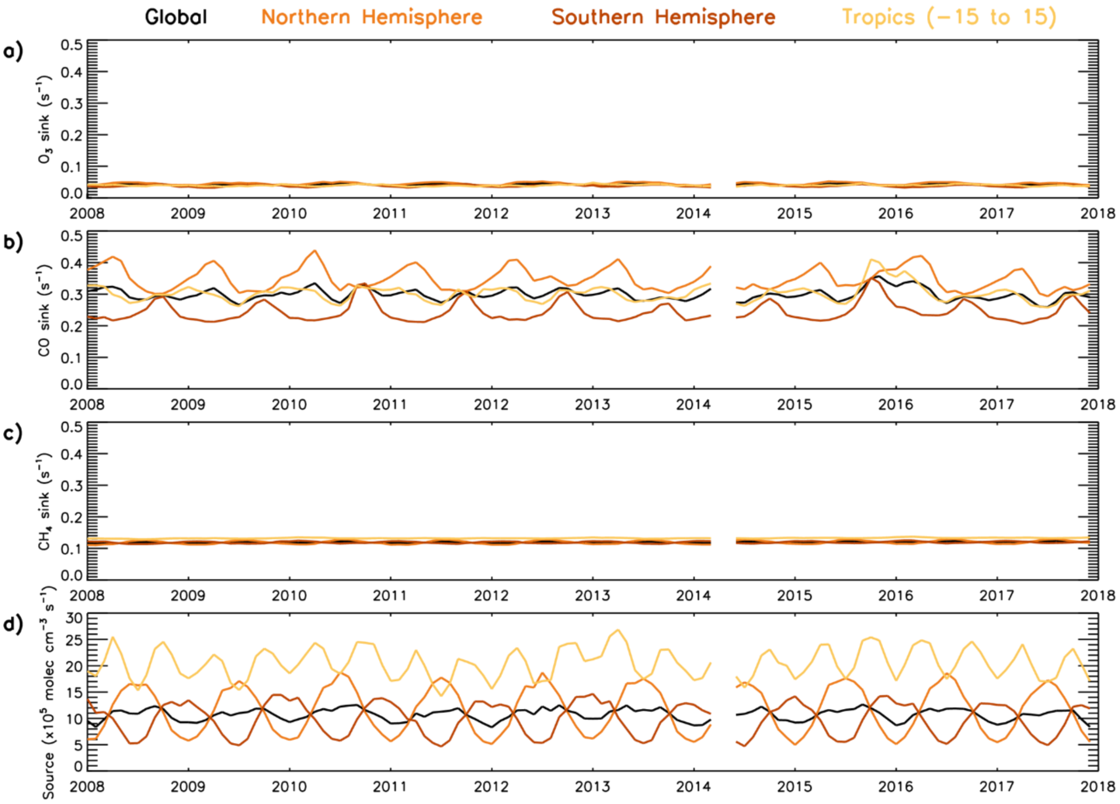

Figure 4.25: Monthly variation in the S-SSA components for 2008 – 2017. Global, NH, SH and tropical average time series for: (a) $k_6[O_3]$, (b) $k_5[CO]$, (c) $k_4[CH_4]$ and (d) $2j_1k_1[O_3][H_2O]/(k_2[N_2]+k_3[O_2]+k_1[H_2O])$.

Between 2008 – 2017, there are several notable positive [OH] anomalies: mid-2010; end of 2012/beginning of 2013; mid-2015 and mid-2016; which all coincide with positive source term anomalies, and small/near-zero anomalies in the sink terms (Figure 4.26.). The following notable negative [OH] anomalies: mid-2009; 2011 to mid-2012 and end of 2017; all coincide with negative source term anomalies, and a small/near-zero anomaly in the sink term. For the negative anomalies at the end of 2015/beginning of 2016, they coincide with a very large positive sink term anomaly. This produces a negative anomaly, even though there is a large positive anomaly in the source term at the same time. The large sink term anomaly coincides with a very large positive anomaly in CO at most latitudes (Figure H.3), which is +12% averaged across all latitudes and +20% in the tropical region. In 2015 – 2016, there was an El Niño event, as shown by the positive values in the Multivariate ENSO Index (MEI.v2) (Figure 4.26(d)). This CO anomaly is likely caused by this El Niño event, due to a large increase in global fire emissions (Huijnen et al., 2016). The event started at the end of 2014, peaking towards the end of 2015 and continuing to around half way through 2016 with a maximum MEI.v2 value of +2.2 (Figure 4.26(d)). In good agreement, Voulgarakis et al. (2015) also found that biomass burning was the key driver of CO and OH variability. Stevenson et al. (2020) found that a key driver of OH change since the 1980s were changes in anthropogenic emissions of CO, which agrees with the work here, but also of NO_x, which is not represented here. If NO_x could be added to the S-SSA, the approximation could be used to comment on the relative importance of NO_x variation to OH variation. Another variable not represented here is variation in j_1, which could vary due to incoming solar radiation changes (clouds/stratospheric O_3), which could likely have an impact on OH interannual variability. Nicely et al. (2018) found that several other factors were influencing [OH] temporal variation in opposing directions, as a positive trend in OH due to varying stratospheric O_3, tropospheric H_2O, NO_x and Hadley cell expansion was equal to the negative trend in OH from increase CH_4 concentrations between 1980 –2015, with little impact from varying temperature. Opposing factors could be influencing the [OH] here, which would require further investigation to diagnose.

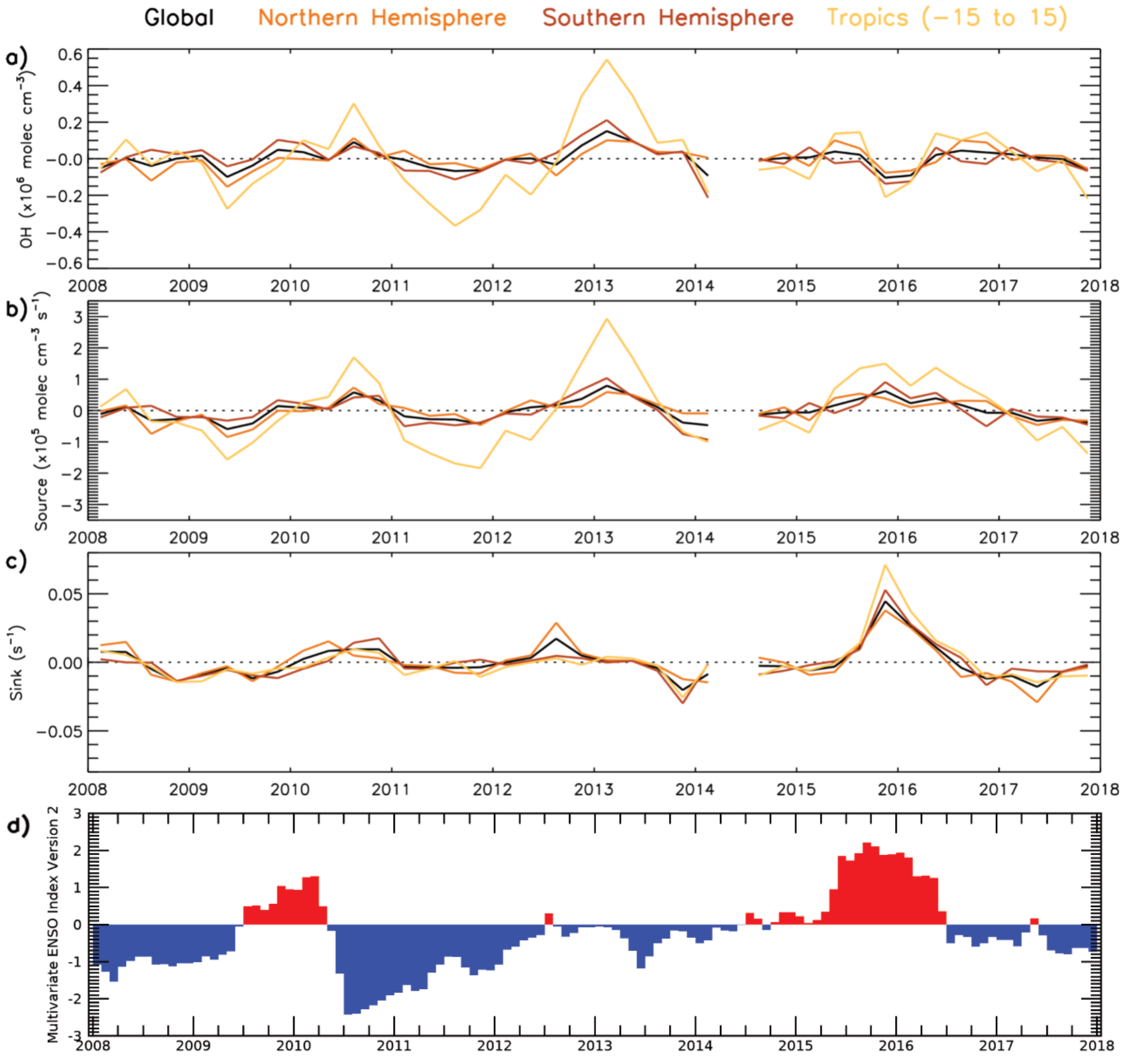

Figure 4.26: Monthly anomalies for 2008 – 2017. Global, NH, SH and tropical average time series for: (a) OH, (b) $2j_1k_1[O_3][H_2O]/(k_2[N_2]+k_3[O_2]+k_1[H_2O])$ (total source term), (c) $k_4[CH_4] + k_5[CO] + k_6[O_3]$ (total sink term) and (d) Bimonthly Multivariate ENSO index (NOAA, 2021). Anomalies are relative to a monthly average baseline (2008–2017).

As discussed, the source term is a key driver of [OH] variation in the S-SSA approximation. The source term has two satellite input species, O_3 and H_2O. To determine the relative importance of O_3 and H_2O to the source term, the source term calculation has been repeated with two scenarios, using either a fixed monthly value of O_3 or H_2O. The fixed values were calculated by averaging all years (2008 – 2017) for each month. Figure 4.27(b) shows the fixed O_3 (varying H_2O) and Figure 4.27(c) shows the fixed H_2O (varying O_3). Depending on which scenario reproduces the original anomaly time series (Figure 4.27(a)) the best, it would indicate that the species varying in that scenario is more dominant in varying the S-SSA source term. The fixed H_2O scenario reproduces the original source term better, explaining 66% of the variability (R^2=0.66) globally and 60% in the tropics (R^2=0.60). For the fixed O_3 scenario, the R^2 value is lower (R^2=0.16), explaining only 16% of the variability globally and 7% in the tropics (R^2=0.07). Therefore, fixing the H_2O has a much smaller impact than fixing the O_3, in relation to the original source term. This highlights that variations in O_3 are driving the source term. Broadly, interannual differences in tropospheric O_3 are from variation in anthropogenic and natural surface emissions of precursor gases (NO_x and VOCs), transport patterns of O_3 within the troposphere, surface deposition, transport of O_3 from the stratosphere and other meteorological factors e.g. temperature. Therefore, these are likely factors affecting long-term changes in the S-SSA [OH].

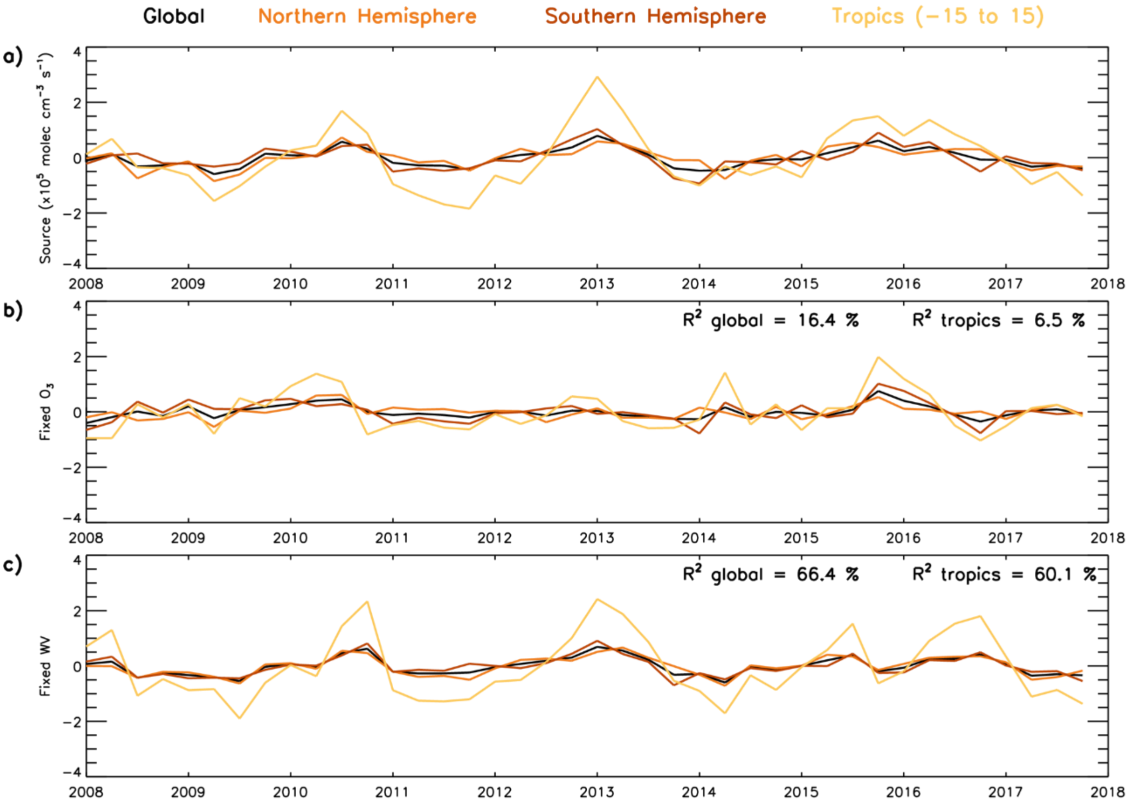

Figure 4.27: Monthly anomalies for 2008 – 2017. Global, NH, SH and tropical average time series for: (a) OH S-SSA source, (b) OH S-SSA source calculated with fixed monthly O_3 concentrations (source fixed-O_3) and (c) OH S-SSA source calculated with fixed monthly water vapour concentrations (source fixed-wv). Fixed O_3/water vapour calculated as monthly average from 2008 – 2017. R^2 value presented at the top of panels (b) and (c) for both the global and tropical latitude regions. All data is in units of ×10^5 molecule cm^{-3} s^{-1}.

4.5 Summary

In this chapter, a novel method has been developed and evaluated, using satellite observations and a simple steady-state approximation, to estimate mid-tropospheric

[OH]. The method and results can complement existing methods to measure [OH] or infer [OH] indirectly, as current methods have limitations, such as the limited network of surface sites, infrequent flight campaigns and the MCF-type approach to estimate global mean [OH]. As demonstrated, the use of satellite data can provide enhanced spatio-temporal information about the OH radical.

Steady-state approximations can be used to estimate [OH], with accuracy varying with the complexity of the approximations, i.e. the number of source and sink terms included. Limiting the number of terms in the approximation also impacts the regions of the atmosphere where the expression is valid. The method was developed using TOMCAT simulation data. A simplified steady-state approximation (S-SSA) was applied to simulated O_3, CO, H_2O, CH_4 and O_3 photolysis rates from TOMCAT in 2010 and 2017. The best agreement between modelled and S-SSA derived [OH] was found in a mid-tropospheric region broadly around 400 – 800 hPa (with the further focus on 600 – 700 hPa). In the 600 – 700 hPa pressure region, the modelled [OH] was underestimated by the S-SSA by ~ 26% – 31% (mass-weighted global mean [OH]). There was a reduced agreement near the surface (pressures > 800 hPa) and higher up in the atmosphere (pressures < 400 hPa). Using more complex steady-state approximations showed that additional terms were important in these regions, for example the HCHO and isoprene were important sink terms near the surface, and the source term reaction of NO + HO_2 was important higher up in the atmosphere. NO + HO_2 was also found to be regionally important in the mid-tropospheric pressure region of best agreement (600 – 700 hPa), showing a large contribution to the total source term in some regions e.g. 30°N – 60°N in January 2010. The S-SSA is not likely to sufficiently capture the important OH chemistry in these regions.

Satellite retrievals of O_3, CO, H_2O and CH_4 were successfully applied to the S-SSA in the 600 – 700 hPa pressure region, producing global [OH] distributions for all months of 2010 and 2017. The satellite-derived OH showed a global average underestimation of 22% in January 2010 and 28% in June 2010 compared to the modelled [OH], with similar results in 2017. To assess the method with respect to direct measurements of the free troposphere, measurements from the aircraft mission ATom were applied to the S-SSA in the 600 – 700 hPa pressure region, comparing the derived [OH] to direct [OH] measurements from the same mission. The aircraft-derived [OH] underestimated measured [OH] by an average of ~ 26%, however, the [OH] measurements have a large uncertainty of ~ 35%. Measurements of OH reactivity (OHR) from ATom in the 600–700 hPa layer were used to compare with the denominator of the S-SSA expression. There were few values to compare, showing a bias of ~ -37%. However, ~80% of these comparisons did fall within the uncertainty of the OHR measurement instrument.

Lastly, the S-SSA method was used to investigate the interannual variability of mid-tropospheric [OH], utilising 10 years of satellite observations. Between 2008 – 2017, the global annual mean [OH] anomaly varied from -3.0% to +4.7%. The influence of important terms in the OH budget were presented, highlighting the balance between the source and sink terms over time. Variation in the S-SSA [OH] was found to be determined primarily by the combined source term, driven by O_3, and by the CO sink term. In the tropics, OH variation reflected that of O_3 (peaks in 2008, 2010 and the largest in 2013) and CO (negative anomaly at the end of 2015/beginning of 2016). The positive CO anomaly coincided with a strong El Niño event in 2015/16.

Chapter 5 Trends in European tropospheric ozone derived from satellite data

5.1 Introduction

Trends in satellite tropospheric O_3 derived from different instruments have shown contrasting trends for some regions around the world, e.g. Europe. Gaudel et al. (2018) presented long-term trends for several satellite tropospheric column O_3 products for different latitude bands (Figure 5.1). The products were OMI/MLS from NASA Goddard Space Flight Centre (GSFC), GOME & OMI from the Smithsonian Astrophysical Observatory (SAO - GOME_OMI), OMI from RAL (OMI-RAL), IASI from the Université Libre de Bruxelles and LATMOS/IPSL (IASI-FORLI) and IASI from CNRS (IASI-SOFRID). In the most relevant band to Europe, 30°N – 60°N, the OMI product showed positive trends, with +0.16 DU year^{-1} (OMI/MLS, 2005 – 2016) and +0.13 DU year^{-1} (GOME & OMI, 1996 – 2015). In contrast, the IASI-FORLI product showed a negative trend of -0.50 DU year^{-1} (2008 – 2016). The OMI-RAL product (2005 – 2015) and IASI-SOFRID (2008 – 2015) product showed small near-zero trends of +0.03 DU year^{-1} and -0.03 DU year^{-1}, respectively. This chapter aims to explore 3 RAL UV-Vis satellite records in further detail, highlighting the potential causes of differences between the records.

Spatially Gaudel et al. (2018) show that the trends within Europe vary (Figure 5.2), with OMI/MLS showing positive trends across all the grid-boxes (5° × 5°), IASI-FORLI showing negative trends across all grid-boxes, and the other products showing a variation across the region. Overall, this disagreement shows that these trends need to be studied in greater detail, to explore what information the satellite record can provide about long-term tropospheric O_3 trends. In this thesis, additional RAL satellite products are used, such as GOME, SCIAMACHY and a higher resolution version of OMI, to try and improve our understanding of these trends. In this context, to extend the work in Gaudel et al. (2018), comparisons with a 3-D chemical transport model, such as TOMCAT, can provide a common framework for comparing the impact of different sampling and vertical sensitivity between the instruments.

The limited number of other studies of long-term variation in European free tropospheric O_3 are highlighted in Chapter 2 (Section 2.2.8.5). Two key recent European-wide studies showed a mixture of trends across Europe. Gaudel et al. (2020) found small trends in median O_3 from aircraft observations of ~1.3 ppb decade^{-1} for 700 – 300 hPa between 1994 – 2016. Christiansen et al. (2022) found trends of median O_3 of between ~ -1 to 4 ppb decade^{-1} across 7 European ozonesonde sites.

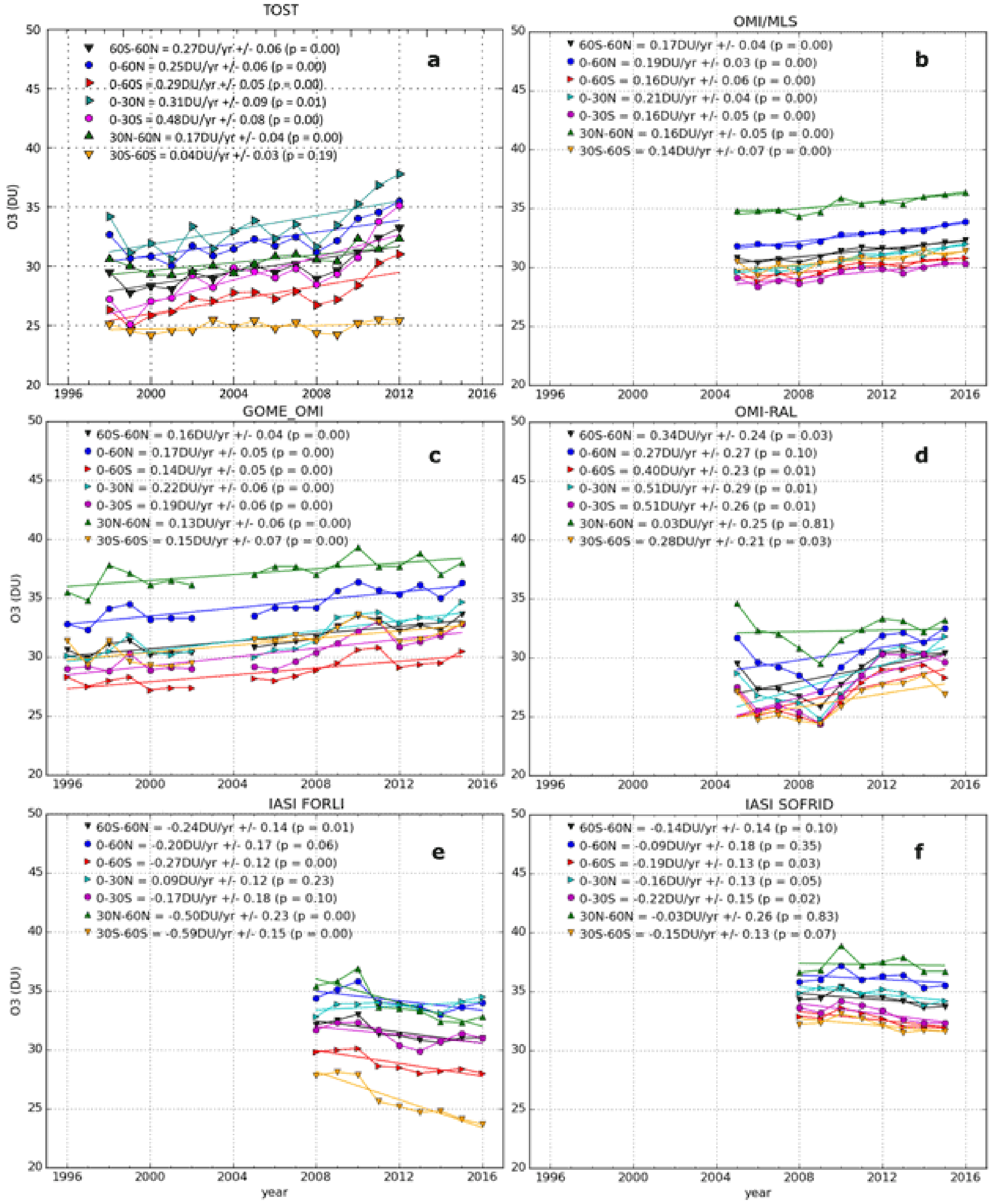

Figure 5.1: Timeseries and trends in tropospheric column O_3 for latitude bands observed by (a) ozonesondes, (b) OMI/MLS, (c) GOME & OMI, (d) OMI-RAL, (e) IASI-FORLI and (f) IASI-SOFRID. Trends are in DU year^{-1}. Taken from Gaudel et al. (2018).

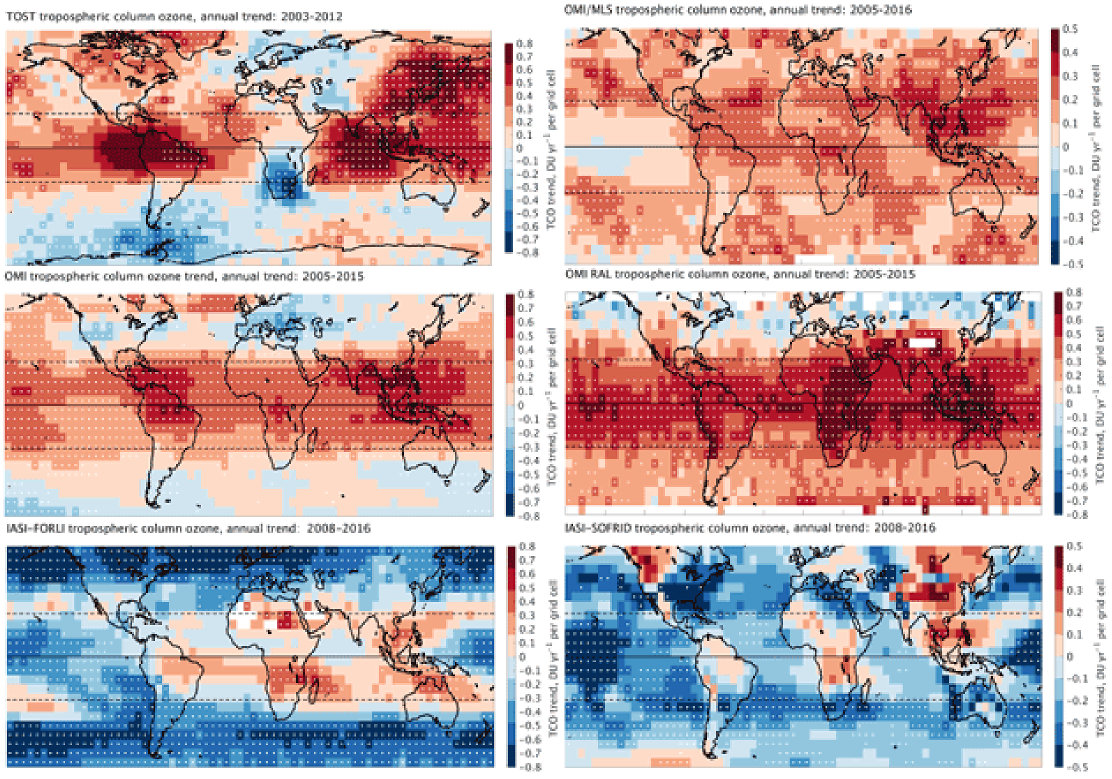

Figure 5.2: Trends in tropospheric column O_3 for each 5° × 5° grid-box observed by (top left) ozonesondes (2003 – 2012), (top right) OMI/MLS (2005 – 2016), (middle left) OMI (2005 – 2015), (middle right) OMI-RAL (2005 – 2015), (bottom left) IASI-FORLI (2008 – 2016) and (bottom right) IASI-SOFRID (2008 – 2016). Trends are in DU year^{-1}. Note the variation in colour scale. Taken from Gaudel et al. (2018).

5.2 Research questions

To evaluate the satellite tropospheric O_3 record over Europe in greater detail, this chapter will address the following research questions:

1. What are the trends in satellite-observed lower tropospheric O_3 over Europe since 1996?
2. How do these trends vary spatially and seasonally?
3. How do these trends vary between instruments? What could be causing the differences?
4. Are these trends captured by a model and other observations of the troposphere (e.g. ozonesondes)?
5. How do variations in O_3 precursor gas emissions and meteorology impact these trends?

5.3 Data & methods

5.3.1 RAL tropospheric ozone products

In this chapter, three tropospheric O_3 data records produced by RAL (GOME, SCIAMACHY and OMI) are used. For this analysis level 2 tropospheric sub-columns are used, which represent a pressure region of the surface to 450 hPa (~ 6km altitude). The data is filtered using factors such as cloud fraction (< 0.2) and solar zenith angle (SZA, < 80°), and then gridded to the TOMCAT model resolution (2.8° × 2.8°). Bias correction factor (BCF) are applied to the three records, as shown by the example for GOME in Figure 5.3. The BCFs are produced by RAL, based on comparisons with ozonesondes. The corrections vary by month and latitude, comprising of 6 latitude bands (90°S - 60°S, 60°S - 30°S, 30°S - equator, equator - 30°N, 30°N - 60°N, 60°N - 90°N). The BCF is applied by interpolating the BCF from the 6 latitude bands to the TOMCAT model grid (to avoid large step changes) and then subtracting it from the grid of monthly O_3 for each month. Applying the BCFs should reduce the systematic uncertainties with respect to the ozonesondes and make the satellite records more comparable to each other. To study Europe, the record is filtered to within a domain of 30°W – 45°E and 30°N – 70°N (Figure 5.4).

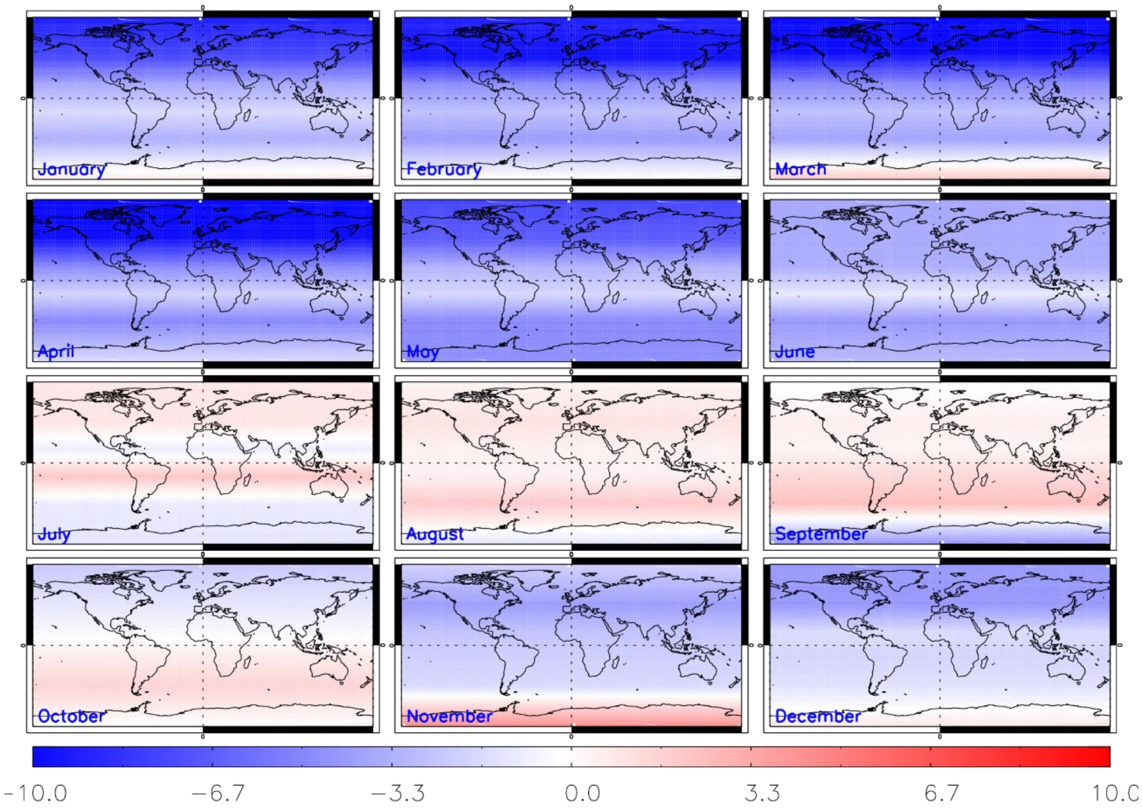

Figure 5.3: Monthly BCF applied to the GOME record for all years (DU).

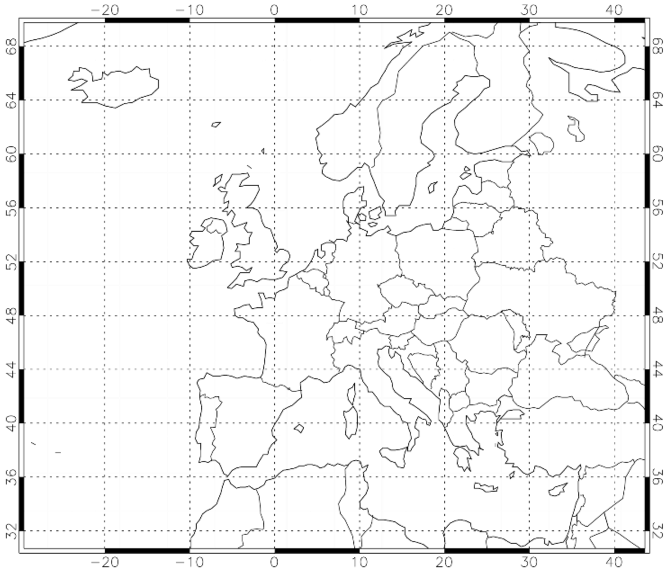

Figure 5.4: Map of European domain selected for analysis (30°W – 45°E and 30°N – 70°N).

The number of satellite data sub-column retrievals used in each monthly mean value after filtering is shown in Figure 5.5. This shows that GOME and SCIAMACHY have not degraded (in terms of data produced which pass the quality control step) by a large amount over the course of the study period, as GOME only shows a small decrease in the average yearly number of good retrievals. Although SCIAMACHY has a large volume of retrievals which pass quality control in 2011, the data shows anomalously low O_3 values, potentially due to instrument degradation towards the end of its lifetime. Therefore, 2011 has been excluded from the analysis. August/September 2009 in SCIAMACHY; October – December 1997, July 2003 and January 2009 in GOME; and June 2016 in OMI; all show a very low number of data points that pass the quality control (less than 75% of average value for each month). Therefore, these months are also excluded from the analysis. OMI shows a large decrease in the volume of data from 2009 onwards. This degradation in OMI is likely due to the documented ‘row anomaly’ (Section 3.1.6) (Schenkeveld et al., 2017; Levelt et al., 2018).

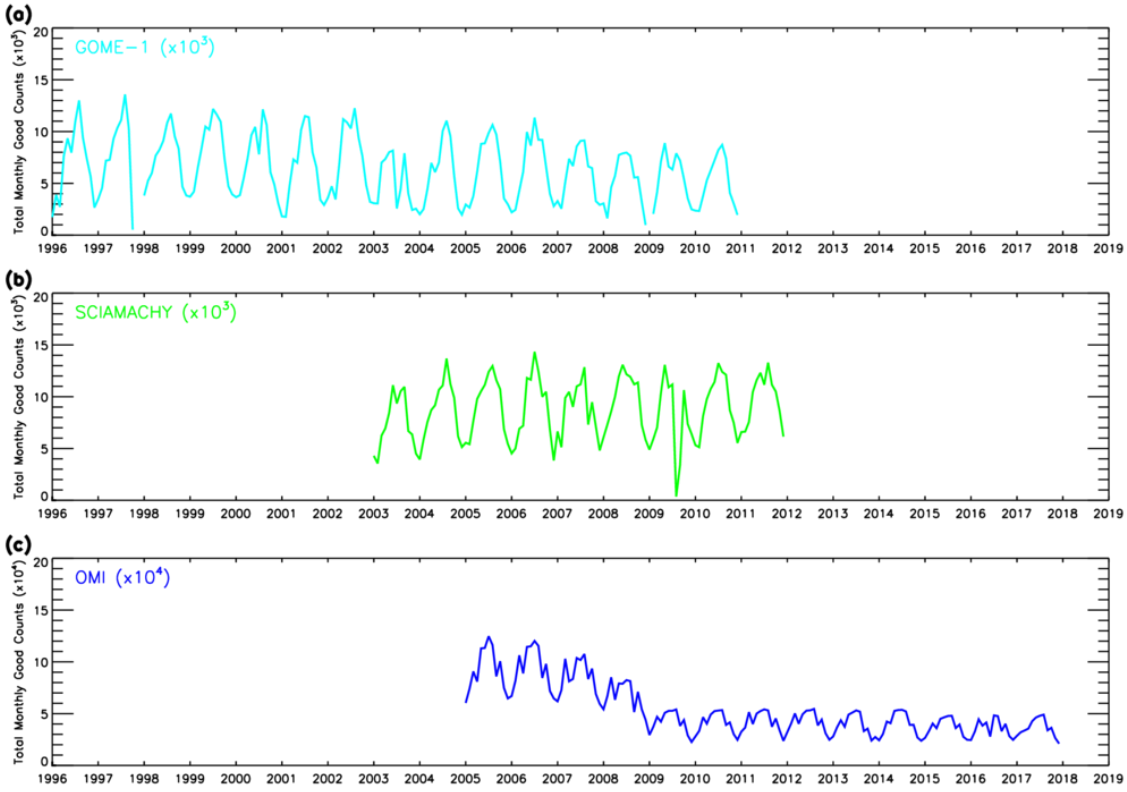

Figure 5.5: Timeseries of number of satellite sub-column values used the domain monthly mean for each month of the: (a) GOME (×10^3); (b) SCIAMACHY (×10^3); and (c) OMI (×10^4) satellite records. Note the differing scale in panel (c).

5.3.1.1 OMI row selection

Due to the row anomaly, the OMI O_3 profile product suffers from a reduction in the availability of data which passes the quality assurance flags (e.g. low cloud cover). Here, multiple rows from across-track positions in the swath provide limited or negligible useable data. It is therefore important to investigate which rows will provide a suitable record to study long-term trends in satellite tropospheric O_3. The availability of data passing the quality assurance across the 30 rows (produced from the 60 OMI rows during the retrieval processes) is shown in Figure 5.6, highlighting the missing data in the middle rows from 2008/2009 onwards. The rows to select were assessed based on the O_3 seasonal cycle, position relative to the swath edge and if a complete record was available. A timeseries of each row is presented in Appendix I (Figure I.1). To create a ‘best estimate’ (BE) I selected only rows with a consistent seasonal cycle (e.g. amplitude, shape) across the timeseries, showing minimal change over time, especially in comparison with the first 3 years of the mission before the OMI row anomaly occurred. A consistent seasonal amplitude over this time period is a reasonable approach given the seasonality present in ozonesonde records (Figure 5.28). Rows with an inconsistent seasonal cycle, or large periods of missing data, were removed (Figure 5.7, Appendix I). The rows selected during the time period to be in the calculation of the OMI mean O_3 sub-column (BE selection) are shown in Figure 5.6; this selection is used in the following OMI analysis and results.

Rows near the edge of the swath, e.g. rows 1, 3, 57 and 59 have a greater 'stratospheric influence'. This is due to the larger viewing angle of these rows, meaning they have a longer viewing path, which is also true at high latitudes (large SZA). In a longer viewing path there are more O_3 molecules which absorb more photons, preventing photons from the surface and troposphere from reaching the satellite. This could potentially lead to total absorption in the absorption bands relevant to the O_3 retrievals, providing less information about the troposphere below the O_3 layer in the stratosphere. Therefore, these positions are sometimes disregarded when studying tropospheric O_3. However, in this case, they are present for the whole record (see Appendix I) unlike many others due to the OMI row anomaly, so can provide important information on long-term trends, which is the aim of this chapter. These outer edge rows are consistent at lower pressure ranges, not showing any anomalous points. Therefore, they have been retained in the BE selection here and subsequent data analysis.

There are many positions which have only a partial record available (rows 23 – 55) (Figure 5.6). In the BE selection, these partial records were included, using years which show a complete record (e.g. row 21 has been used to the end of 2013, not afterwards as the record become incomplete). This approach utilises all the information available, however it does introduce a sample bias between the start and end of the record with information from a different number of rows.

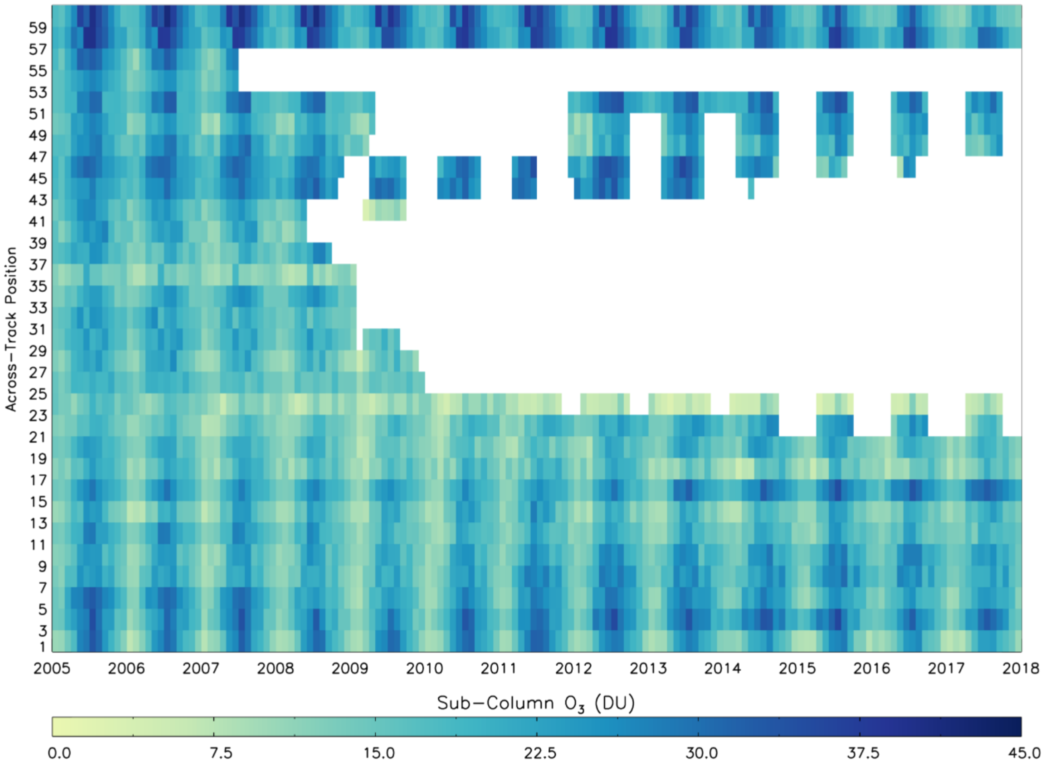

Figure 5.6: Timeseries of OMI sub-column O_3 for each across-track position/row (DU). The data is shown for each month from 2005 – 2017 and for 30 rows (numbered 1 – 59). The blank space indicates no useable data available.

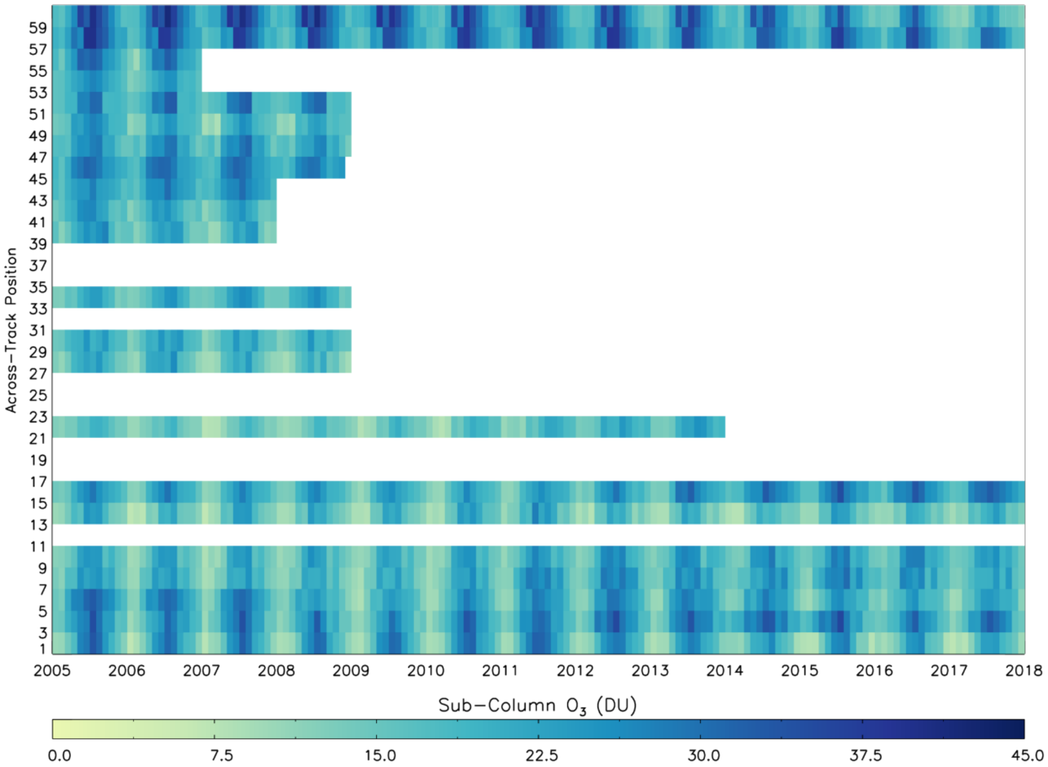

Figure 5.7: Same as Figure 5.6, but the additional white spaces indicate the (partial/complete) rows which were excluded for analysis ("best estimate" selection) due to an inconsistent seasonal cycle or lack of useable data for the whole year.

To investigate the uncertainty that retaining or discarding different rows produces, the OMI record has been processed (with corresponding across-track corrections (ATC) calculated – see Section 5.3.1.2) using 4 selections of rows (Figure 5.8). The selections are: the BE as described above and shown in Figure 5.7 (1); the BE without using the outside 4 positions (2 at both edges of the swath – 1, 3, 57 and 59) (2); the BE without using the partially complete records (3); and using all the data that passed the quality control (as shown in Figure 5.6) (4). The largest difference from the BE is from the "all positions" selection, with an average difference of 2.0 DU (8.5%) across the record (Figure 5.8). The difference in the trend is also the greatest, showing a large significant negative trend of -0.17 DU year^{-1} from all positions, compared to the near-zero trend from the BE. The other 2 selections show smaller differences, with excluding the outside positions showing on average a difference of 1.4 DU (5.8%) and a small insignificant positive trend of 0.09 ± 0.05 DU year^{-1}, and excluding partial records showing a very small average difference of 0.1 DU (0.3%) and a near-zero trend of -0.03 ± 0.04 DU year^{-1}. The selection also impacts the seasonal cycle amplitude (difference between minimum and maximum values in a year), ranging from 9.9 – 13.4 DU across the 4 selections. These results indicate the sensitivity of the OMI results to the selection of viewing rows and quantifies the uncertainty in the OMI timeseries and calculated trends presented in this chapter depending on the OMI rows used.

Another indication of the uncertainty is shown in comparing the trends between the 9 rows which were used for the full record (Appendix I/Figure I.1). The trends range from -

0.79 to +0.50 DU year^{-1}, with approximately half of the rows showing a negative anomaly and the other half showing a positive anomaly. The average trend across the selected OMI rows (whole and partial) with ATC applied is near-zero, which reflects the spread of trends for the individual rows.

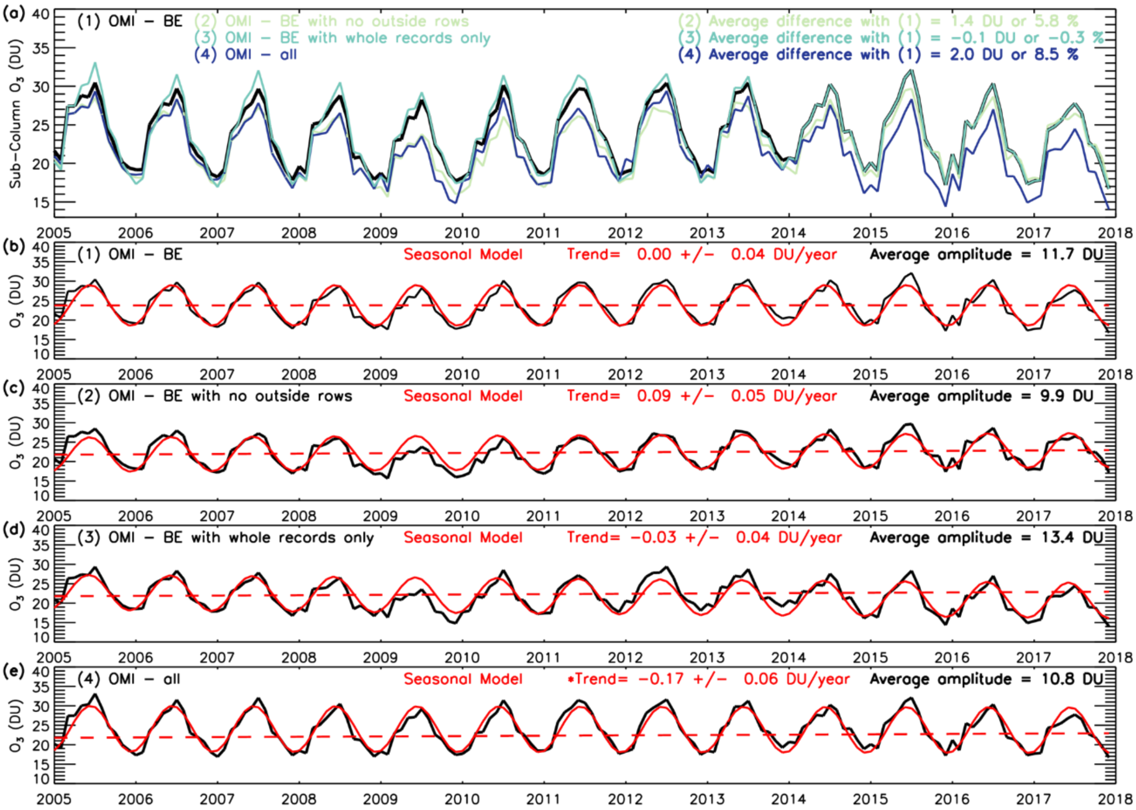

Figure 5.8: (a) European monthly average sub-column O_3 (surface – 450 hPa, DU) for OMI using 4 selections of OMI viewing positions (labelled 1 – 4). The selections are as follows: (1) The best estimate (BE) (Section 5.3.1.1); (2) BE but with no outside viewing positions included; (3) BE but only including the positions which have a complete record for the time period; and (4) using all available data (which passes quality control). Panels (b) – (e) show the individual timeseries for all selections (1 – 4), with a seasonal model based on the record. The calculated linear trend from this seasonal model (DU year^{-1}) is displayed on each panel. An * before the word "Trend" indicates that the trend is significant at the 95% confidence level.

5.3.1.2 OMI across-track corrections

ATCs are applied to reduce the higher O_3 values from the stratospheric influence towards the edge of the swath, which can result in around-orbit stripes (Figure 5.9(a)). The result of applying the ATCs is highlighted in an example for February 2005 (Figure 5.9(b)), where the striping pattern is smoothed. The stripes are most prominent across the Pacific Ocean, which is of lesser importance to the European domain. ATCs are calculated here by taking the yearly median value of the O_3 sub-column for all selected rows, and compare this to the median yearly value for each row, with the difference providing the ATC. Another consideration in calculating the ATC is the impact of using varying numbers of OMI rows over time. As the number of rows in the O_3 mean calculation changes over the time record, the ATC have been re-calculated for each year depending on the selected records (Figure 5.10).

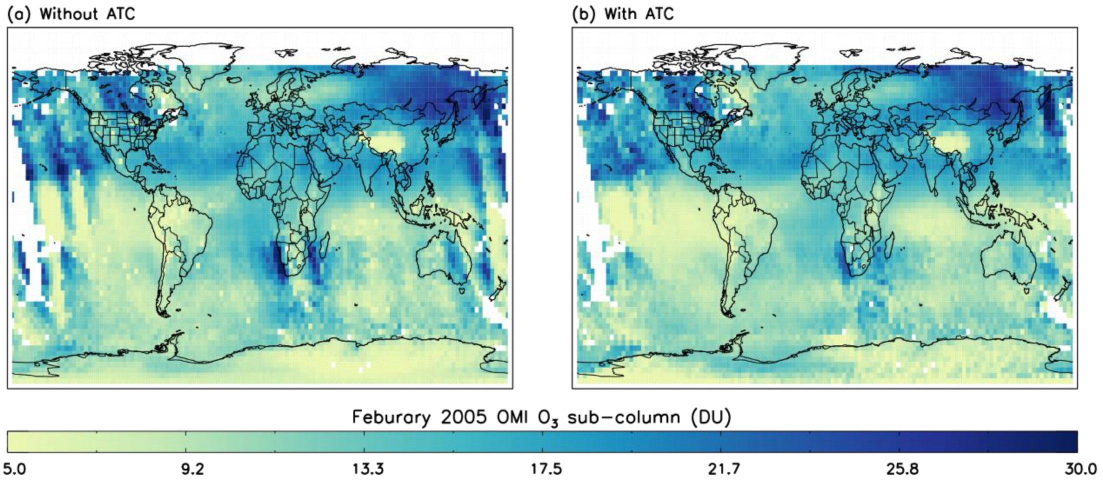

Figure 5.9: OMI sub-column O_3 for February 2005 (a) before and (b) after ATC application.

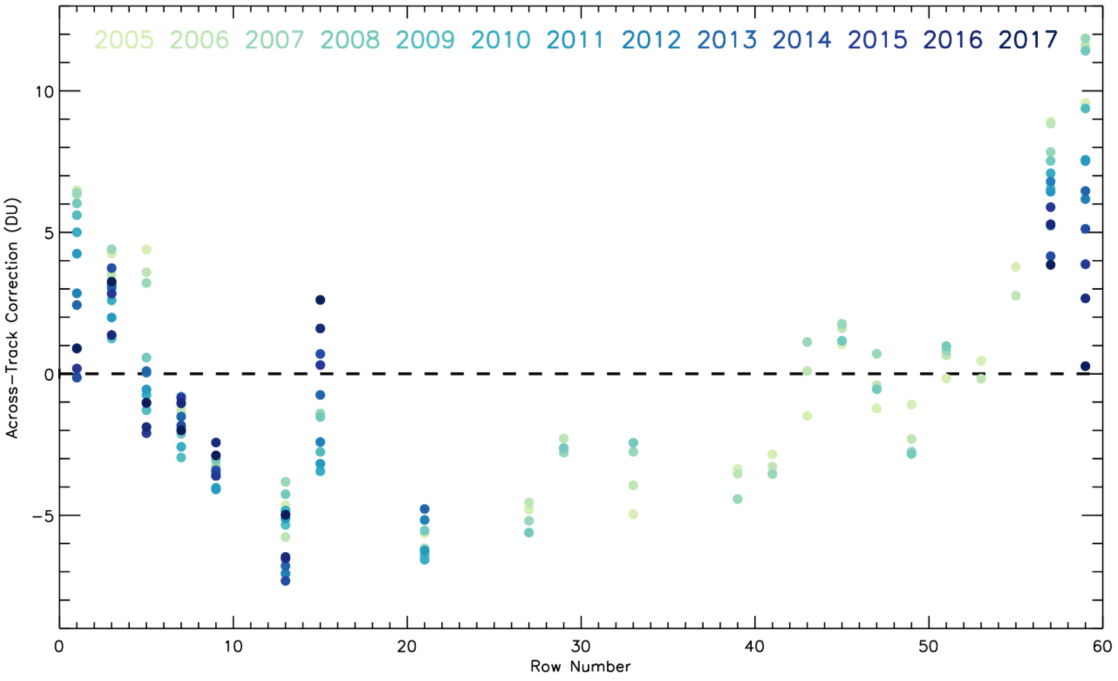

Figure 5.10: ATC (DU) for each row from 2005 – 2017. The points are colour-coded by year as indicated in the legend at the top of the panel. There are 30 rows, indicated on the x-axis by the odd numbers between 1 – 60 (e.g. 1, 3, 5, … 57, 59).

5.3.1.3 Satellite uncertainties

There are several known instrument issues, such as the OMI row anomaly, the GOME tape recorder failure and UV degradation for GOME and SCIAMACHY. Another source of error is calculated by RAL in the retrieval process ($\boldsymbol{S_x}$ - solution error covariance matrix), which represents the random error of the retrieval. As in Pope et al. (2015), when multiple retrievals are averaged together to form a monthly mean value, the random errors will partially cancel, which will reduce the random error by a factor of $\frac{1}{\sqrt{N}}$ (where N is sample size). Once the daily level-2 swath data has been mapped onto a regular grid (e.g. array dimensions of 128 × 64 × number of days in each month), the monthly average per grid-box can be determined using this daily gridded data. Therefore, the monthly mean retrieved random error, per grid-box, can be scaled by $\frac{1}{\sqrt{N}}$ where N is the number of days within the month a grid-box has usable data (i.e. one or more retrievals which pass the quality assurance criteria used to derive a daily grid-box value). Table 5.1 presents the average random error of each grid-box value and also the scaled random error based on averaging the daily sub-columns across the month of retrievals. The random errors for each month vary across the timeseries (Figure 5.11). The random errors for the monthly values (~ 6%) need to be considered when interpreting the long-term trend results.

Instrument	Average random error for each grid-box	Range in monthly averages	Scaled random error for monthly averages	Range in monthly averages
GOME	6.2 DU (31.6%)	21.4% – 47.7%	1.1 DU (5.7%)	3.8% – 10.7%
SCIA	6.1 DU (31.1%)	23.1% – 44.9%	1.1 DU (5.6%)	4.1% – 8.5%
OMI	7.5 DU (31.5%)	21.9% – 49.3%	1.4 DU (5.7%)	3.9% – 9.3%

Table 5.1: Summary of average random errors from the 3 satellite instruments – GOME, SCIAMACHY and OMI.

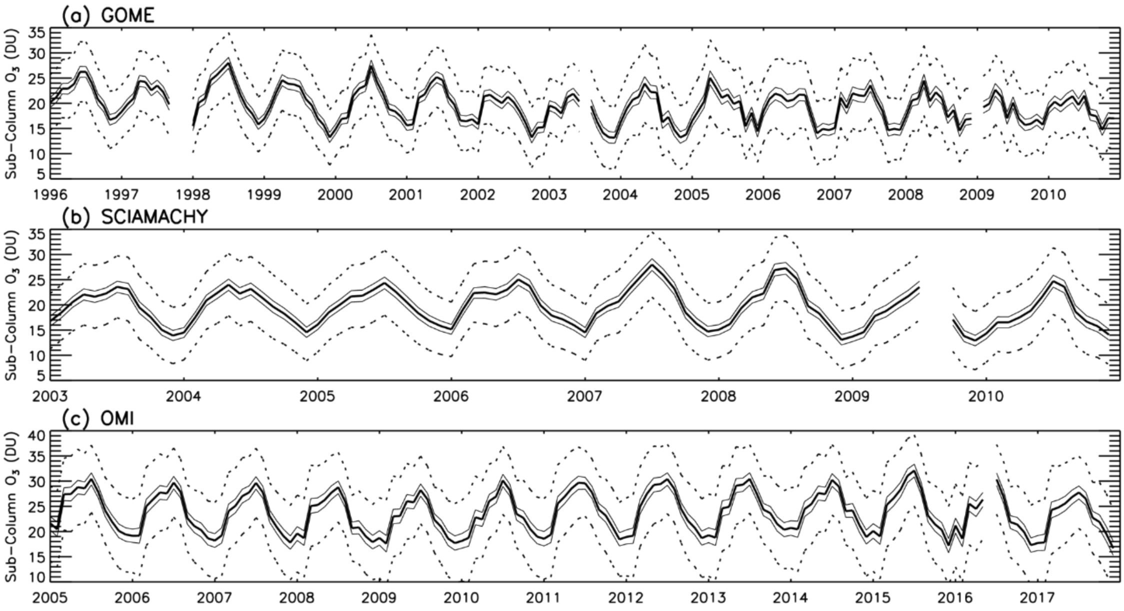

Figure 5.11: Sub-column (surface – 450 hPa) satellite O_3 records (DU) for (a) GOME (1996 – 2010), (b) SCIAMACHY (2003 – 2010) and (c) OMI (2005 – 2017). The monthly averaged scaled random error is shown as ± the record (thin lines) and the average error for each grid-box is shown as ± the record (dotted lines).

5.3.2 Trend model

To quantify the trends in tropospheric O_3, a trend model with a seasonal component is used, as shown in Equation 5.1:

$$Y_t = C + BX_t + A\sin(\omega X_t + \phi) + N_t \qquad \textbf{Equation 5.1}$$

where Y_t is the monthly sub-column O_3 for month t, C is the sub-column O_3 for the first month of the record, X_t is the number of months after the first month of the record, $A\sin(\omega X_t + \phi)$ is the seasonal component (A is the amplitude, ω is the frequency (the period is set to 1 year, $\omega = \frac{\pi}{6}$) and ϕ is the phase shift). N_t represents the model errors/residuals unexplained by the fit function, including interannual variability. C, B, A and ϕ represent the fit parameters which are based on a non-linear least squares fit. This trend model is based on a function in Weatherhead et al. (1998) and used in several studies looking at long-term trends in tropospheric species e.g. van der A et al. (2006), van der A. et al., (2008) and Pope et al. (2018).

In Weatherhead et al. (1998), a derivation for the precision of the trend is given, as a function of the autocorrelation, the length of the timeseries (in months) and the variance in the remainder. The trend precision, σ_B, is calculated as shown in Equation 5.2:

$$\sigma_B \approx \left[\frac{\sigma_N}{n^{\frac{3}{2}}}\sqrt{\frac{(1+\alpha)}{(1-\alpha)}}\right] \qquad \textbf{Equation 5.2}$$

where n is the number of years in the record, α is the autocorrelation in the residuals and σ_N is the standard deviation in the residuals. The autocorrelation is calculated using a lag of one timestep (one month), as in Pope et al. (2018). A common decision rule for trend detection is that the linear trend, B (from Equation 5.1), is real at the 95th confidence level if Equation 5.3 is true (Weatherhead et al., 1998; van der A et al., 2006):

$$\left|\frac{B}{\sigma_B}\right| > 2. \qquad \textbf{Equation 5.3}$$

Trends are presented in this chapter in DU year^{-1} with ± the precision (σ_B).

5.3.3 TOMCAT model

5.3.3.1 Model setup

The emissions used in the TOMCAT simulations in this chapter are summarised in Table 5.2. Although some emission sources are the same as Chapter 4, they are repeated here for clarity. A timeseries of the average total and anthropogenic surface emissions NOx, CO and a combination of VOCs is shown in Figure 5.12, which is shown in more detail for all VOCs individually and across four regions of Europe in Appendix J. NOx, CO and VOCs all show a decrease over the 23-year period. The model was run from 1996 – 2018, with one year of spin up. To compare the model with satellite records with two different equator crossing overpass times, ~ 10:00 for Envisat (SCIAMACHY) and ERS-2 (GOME) and ~ 13:30 for Aura (OMI), the model runs here have been setup to sample 3-D fields of the model daily at these two local solar times.

Type	Description		Reference
Anthropogenic	NO_x, *CO & VOCs*	CMIP6 - Combination of historical emissions (1996 – 2014) and SSP245 future emissions projections (2015 – 2018).	(Riahi et al., 2017; Gidden et al., 2019; Feng et al., 2020).
	CH_4	EDGAR v4.2 inventory.	(Olivier et al., 2012)
Natural (soils/ oceans)	NO_x, *CO & VOCs*	POET	(Olivier et al., 2003; Granier et al., 2005)
	CH_4	Soil sink flux from MeMo. Wetland emissions from JULES.	(Murguia-Flores et al., 2018) (Clark et al., 2011)
Biogenic	*CO & VOCs*	CCMI - These emissions are fixed annually.	(Morgenstern et al., 2017)
	Isoprene & monoterpenes	JULES and the UK Earth System Model (UKESM) (calculated online). These emissions are annually varying.	(Clark et al., 2011; Sellar et al., 2019)
Aircraft	NO_x	CAMS global aviation emissions (CAMS-GLOB-AIR). Used due to issues in the CMIP6 NO_x aircraft emissions between the historic emissions and the future scenario projections.	(Granier et al., 2019)
Biomass burning	NO_x, *CO & VOCs*	GFED version 4.	(van der Werf et al., 2017)
CH_4 scaling	Scaled to a best estimate based on the globally averaged surface CH_4 value from NOAA for each year.		(Dlugokencky, 2020)
Aerosols	SO_2, *BC & OC*	MACCity	(Granier et al., 2011)

Table 5.2: Summary of the surface emissions used in the TOMCAT simulation in this chapter.

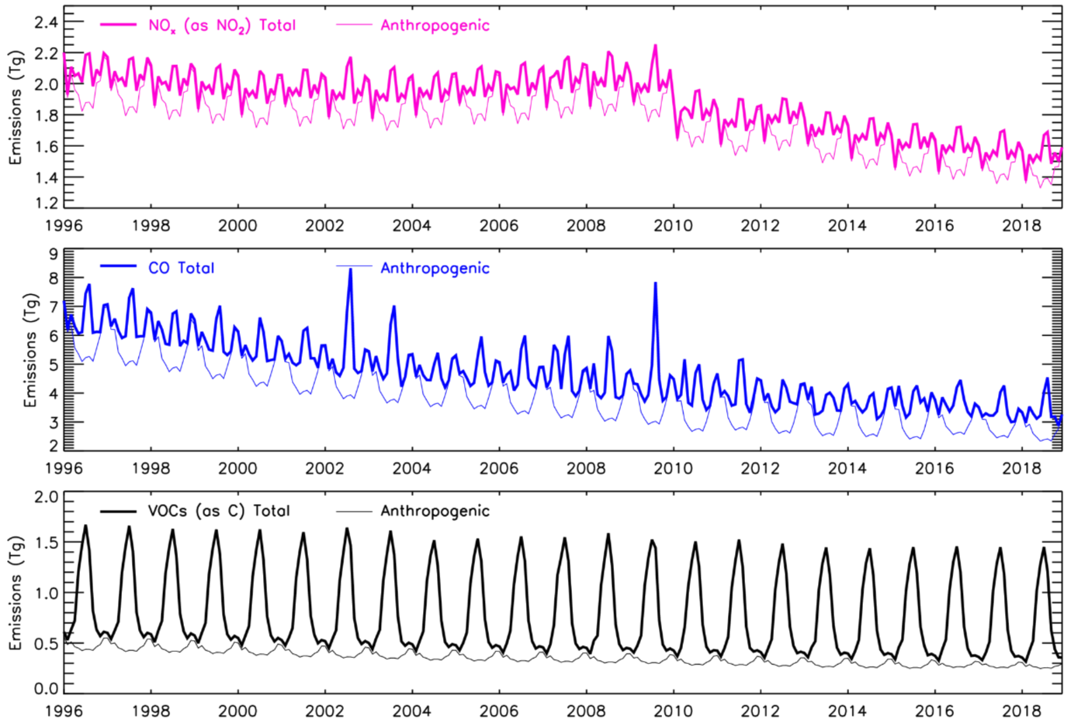

Figure 5.12: European total (thick) and anthropogenic (thin) surface emissions (Tg) for NO$_x$ (as NO$_2$), CO and a combination of VOCs (as Carbon) between 1996 – 2018.

5.3.3.2 Deriving tropospheric sub-columns

To derive the TOMCAT tropospheric sub-column, the sub-column thickness (mass of air per column surface area, kg m^{-2}) is calculated using the hydrostatic approximation between barrier pressure levels, as shown in Equation 5.4:

$$\rho \times dz = -\frac{dp}{g}$$ **Equation 5.4**

where dp is the pressure difference between the barrier pressure levels, dz is the difference in height, g is the gravitational constant and ρ is the density of air. For each vertical grid-box, the sub-column thickness is multiplied by the mass mixing ratio (mmr) of O_3 to derive the sub-column O_3 value (O_3 SC), which is converted into units of molecules cm^{-2}, as shown in Equation 5.5:

$$O_3\ SC = mmr \times layer\ thickness \times \frac{10^7 \times Avogadro's\ Const.}{O_3\ molecular\ mass}$$ **Equation 5.5**

This is then converted into DU by dividing the sub-column value by 2.69 ×10^{16} and then the sub-columns are totalled across the chosen pressure boundaries, here the surface and 450 hPa. To apply the AKs to the model profiles, a realistic simulation of O_3 throughout the atmosphere is required. Since TOMCAT simulates O_3 up to 10 hPa, a more robust representation of upper troposphere-lower stratosphere (UTLS) O_3, where AKs have peak sensitivity, was achieved by merging TOMCAT tropospheric O_3 with upper atmosphere O_3 profiles from the SLIMCAT model at the tropopause. The SLIMCAT profiles were provided by W. Feng (National Centre for Atmospheric Science

& University of Leeds), and are from a separate simulation, with targeted stratospheric chemistry. However, both TOMCAT and SLIMCAT are forced by the same meteorological reanalyses and provide the best estimate of O_3 in their respective regions. The tropopause was defined chemically as where the O_3 volume mixing ratio (vmr) reached 100 ppbv (at pressures <500 hPa), giving an estimated tropopause pressure at which to merge the datasets. The model sub-columns were then totalled between the surface and 450 hPa to generate a sub-column value from this pressure region. For each satellite retrieval, a model profile is co-located from the nearest grid-box and AKs applied, which is then used to form the monthly average. Example AK and model profiles are shown for the GOME and SCIAMACHY in Section 3.1.9. The example profiles show that for the model surface to 450 hPa sub-column (represented by the lowest point on the profiles) the O_3 value is reduced by applying the AKs in January 1996 for GOME and January 2003 for SCIAMACHY.

5.3.4 Ozonesondes

The ozonesonde data for 1996 - 2018 is from WOUDC (WOUDC, 2021), filtered to select only records within 3 hours of the satellite overpass times/model output times (10:00 and 13:30) and within the European domain. For each ozonesonde profiles, tropospheric sub-columns (surface – 450 hPa) were calculated for comparison to the satellite and model records in a methodology similar to the model data (Section 5.3.3.2), however the data is not co-located with any satellite retrievals. The sub-columns are averaged for each month. For ozonesonde-model comparison, a model record has been produced that is co-located with the locations of the ozonesonde measurements, from the nearest model grid-box.

5.3.5 Model sensitivity experiments

To study the relative impact of emissions and meteorology on the long-term tropospheric O_3 trends, two model sensitivity experiments were performed. The model was run with fixed emissions and fixed meteorological fields. The fixed emissions simulation used fixed annual surface emissions (and a fixed value for the scaled CH_4 mixing ratio) from the year 2008, as this is around the mid-point of the timeseries. The fixed meteorology run used repeating meteorological fields from the year 2008. Sub-columns (surface – 450 hPa) were calculated, but these sub-columns were not co-located with any satellite retrievals, as the model sensitivity experiments are compared to model control simulation only.

5.4 Results & discussion

5.4.1 Comparison of satellite records

Monthly European average O_3 records for OMI, GOME and SCIAMACHY are compared between 1996 – 2017 (Figure 5.13). All three records show a O_3 seasonal cycle of higher values in summer and lower values in the winter, with an average seasonal ‘amplitude’ (difference between maximum and minimum monthly value for each year) of 9.6, 10.8 and 11.7 DU for GOME, SCIAMACHY and OMI, respectively. SCIAMACHY and GOME show a large variation in seasonal cycle (1 standard deviation of ~2.2 and 1.8 DU, respectively), with notable large examples e.g. GOME in 2000, and smaller examples, e.g. GOME in 2010. OMI shows a smaller variation in seasonal cycle (1 standard deviation of ~1.1 DU). Variation in the amplitude of the seasonal cycle could potentially mask overall long-term changes, therefore, this effect could potentially be larger in the GOME and SCIAMACHY records. Broadly the GOME timeseries indicates a decrease from 1996 – 2002/2003 and then a stabilisation. The SCIAMACHY timeseries is fairly consistent, but shows two large peaks in the summer of 2007 and 2008. The OMI record also shows a distinctive pattern over the record, with decreasing values towards 2009, increasing towards ~ 2015 after which the timeseries begins to decrease again.

There are six overlapping years between the records, 2005 – 2010 (Figure 5.13(b)), which allows for a direct comparison. Within these overlapping years, GOME and SCIAMACHY show similar absolute values, apart from higher SCIAMACHY values in the summers of 2007 and 2008. OMI shows much larger values than the other two records, on average 4.5 DU larger than GOME and 3.9 DU higher than SCIAMACHY. Despite a large absolute difference, OMI and SCIAMACHY show the best correlation (r = 0.91), compared to GOME and SCIAMACHY (r =0.62) and GOME and OMI (r = 0.64). GOME has the smallest average seasonal cycle ‘amplitude’ at 8.5 DU and SCIAMACHY and OMI show similar ‘amplitudes’ of 11.2 DU. There are several sampling related factors which could contribute to the differences between the instruments, such as spatial resolution (GOME has the coarsest resolution), vertical sensitivity and overpass time (~10:00 for GOME and SCIAMACHY and ~13:30 for OMI) due to diurnal variation in the thickness of the BL and O_3 mixing ratios (although the variation in this does decrease with altitude), and also spatial resolution and vertical sensitivity. Other instrument specific caveats e.g. the OMI row anomaly, UV degradation in GOME/SCIAMACHY could also be contributing to the differences. Large disagreements between instruments has been demonstrated before e.g. in Gaudel et al. (2018), however, if these differences cannot be explained, this reduces confidence in using these satellite products to study long-term changes in tropospheric composition.

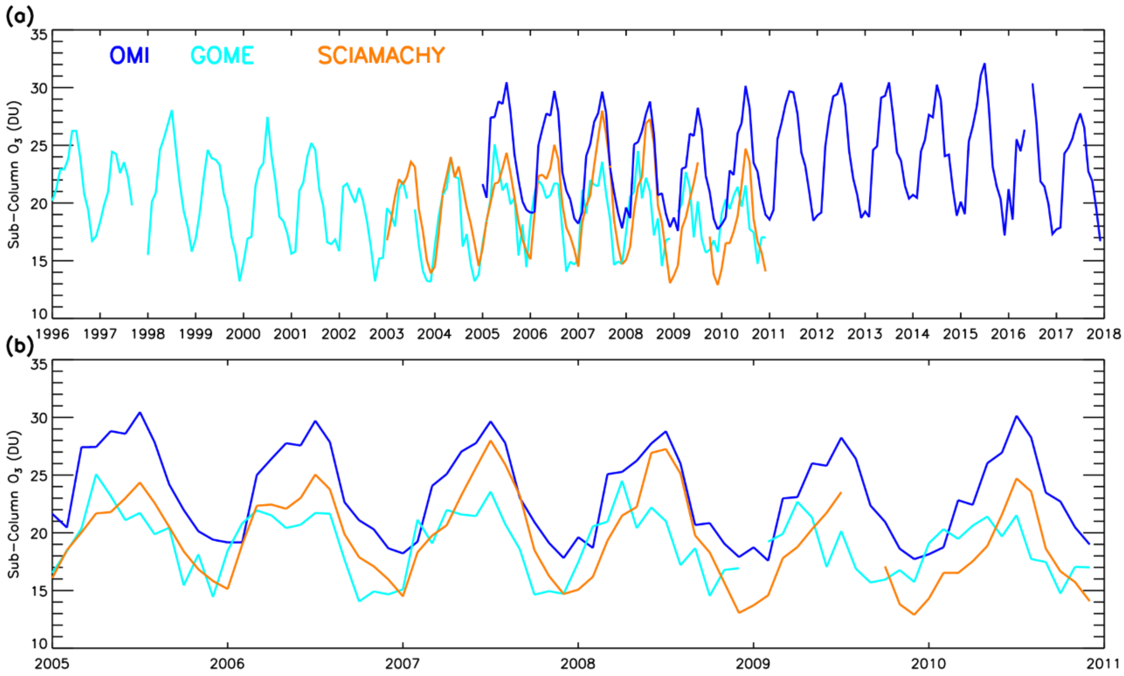

For 2005–2010:	Correlation co–efficient	Average difference	Average "amplitude"
	GOME & SCI = 0.62	GOME − SCI = −0.5	GOME = 8.5
	GOME & OMI = 0.64	GOME − OMI = −4.5	SCI = 11.2
	SCI & OMI = 0.91	SCI − OMI = −3.9	OMI = 11.2

Figure 5.13: European monthly average sub-column (surface – 450 hPa) satellite O_3 records (DU) between (a) 1996 – 2017 and (b) 2005 – 2010. Below the panels are statistics for the 2005 – 2010 overlap years: the correlation coefficient between the records, the mean difference between the records (DU) and the average difference between the minimum and maximum O_3 values for each year ("amplitude") (DU).

5.4.2 Comparison of satellite and model records

The model (co-located and with AKs applied – 'TOMCAT with AKs') shows a reasonable agreement with the satellite records for GOME and SCIAMACHY, with mean differences of 1.4 DU for both and correlations of 0.74 and 0.92, respectively (Figure 5.14). In contrast, for OMI, the model shows a large underestimate, with a mean difference of 4.0 DU. Applying the AKs to the model output causes a large impact to the monthly average record (Figure 5.14), and therefore is considered to be very important in comparing and contrasting the model and satellite records. The application of the AKs improves the agreement between the satellite and model for GOME and SCIAMACHY, broadly by decreasing the absolute sub-column value to be more in alignment with the satellite, by ~ 2.6 DU in both cases, and improving the correlation from 0.72 to 0.74 for GOME and from 0.83 to 0.92 for SCIAMACHY. For OMI, the application of the AKs also decreases the sub-column value, however this increases the underestimate by the model of the satellite record, from 1.0 DU to 4.0 DU. In contrast to SCIAMACHY and GOME, applying the AKs to the TOMCAT record co-located with OMI reduces the correlation from 0.82 to 0.75. The reduction in agreement between OMI and the model when the AKs are applied is currently unexplained.

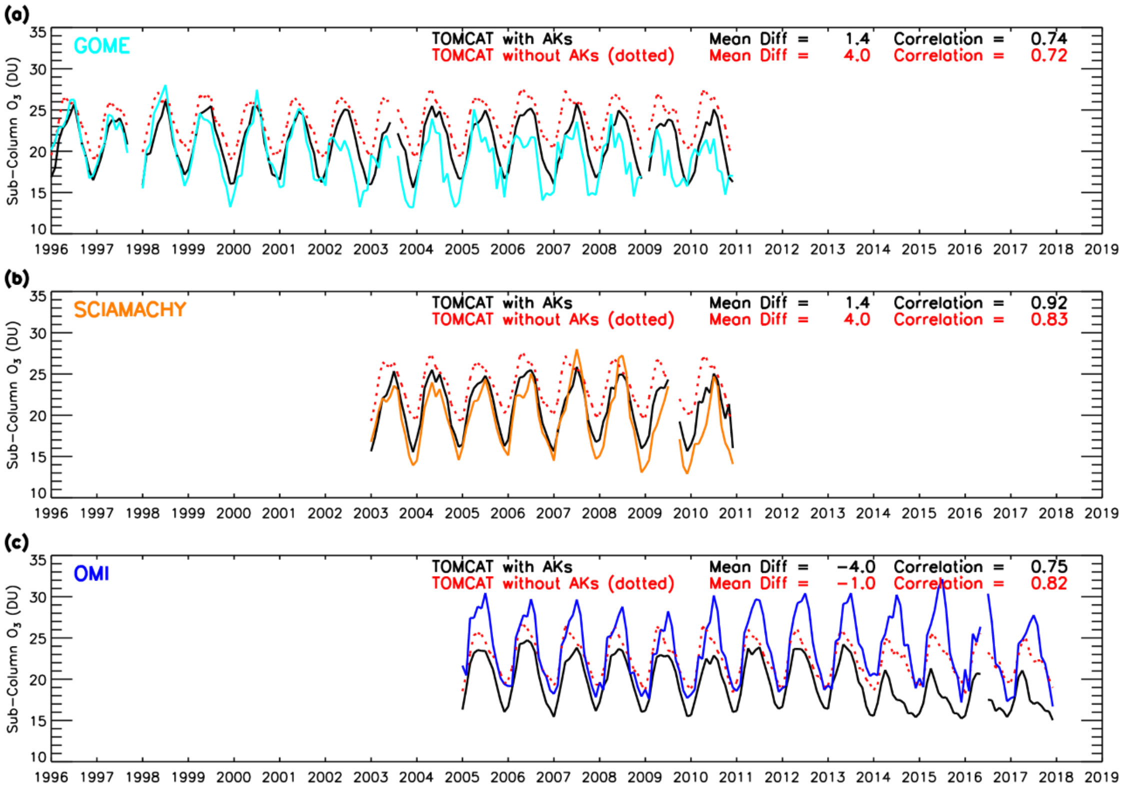

Figure 5.14: European monthly average sub-column (surface – 450 hPa) satellite and model O_3 records (DU) between 1996 – 2017 for (a) GOME, (b) SCIAMACHY and (c) OMI. The model records are co-located with the satellite data for each record; for GOME and SCIAMACHY the model simulation with an overpass time of 10:00 is used, and for OMI the model simulation with an overpass time of 13:30 is used. The model records are shown both with (TOMCAT with AKs) and without (TOMCAT without AKs) AKs applied. The correlation and mean difference between the model and satellite record (mean difference is the TOMCAT record (with or without AKs) subtract the satellite record) (DU) is shown at the top of each panel with AKs (black) and without AKs (red).

5.4.2.1 Trends

The GOME record shows a small, significant negative trend of -0.21 DU year^{-1} across the 15-year record (Figure 5.15). The term significant used here reflects if the linear trend satisfies Equation 5.3, which is a common decision rule for a trend being real at the 95% confidence level. It does not reflect the relatively large satellite uncertainty (~ 1.1 DU), which reduces the confidence in these results. This negative trend is not captured in the model record, as TOMCAT with AKs applied shows a zero trend, TOMCAT without AKs applied (but still co-located with the satellite data) shows a very small but significant positive trend of +0.06 DU year^{-1}. For SCIAMACHY, there is a small insignificant negative trend (to the 95% confidence level) of -0.20 DU year^{-1} across the 8-year record (Figure 5.16). This trend is also not captured in the model record, as TOMCAT with and without AKs applied show near-zero trends. OMI shows a zero trend across the 13-year record, although there is large inter-annual variability within this period (Figure 5.17). This near-zero trend is not captured by the model, as TOMCAT with AKs applied shows a significantly negative trend of -0.26 DU year^{-1} due to low values in 2014 – 2017 which are occur after the AKs applied, indicating an impact of the vertical sensitivity of the instrument or another currently unexplained reason. Overall, across all 3 records, there is relatively limited change in European tropospheric O_3, despite reductions in precursor gas emissions across Europe during this time period. However, this small change should be considered in relation to the large interannual variation (see in Figure 5.13) and large uncertainties which have the potential to mask any possible changes across the records.

For all three records, the model doesn't capture the trend, despite being co-located to the satellite retrievals and vertical sensitivity accounted for. This indicates that something in the model is not being represented well e.g. O_3 STE, surface precursors, O_3 transport, O_3 surface deposition, etc. Several studies have found that trends in the free troposphere from observations are not captured by models e.g. Parrish et al. (2014), Young et al. (2018) and Christiansen et al. (2022). Christiansen et al. (2022) found that one model represented 75% of the observed trend across 25 ozonesonde sites globally between 1990 - 2017, and another model represented < 20% of the trend. Model trend underestimates may be due to uncertainties in the natural and anthropogenic precursor gas emissions and model representation of STE. Christiansen et al. (2022) found that dynamics (e.g. STE) to be more important for capturing the trends in the model in the middle to upper troposphere, and emissions to be more important at the surface. The disagreement between observational and model trends could also be due to the large uncertainties involved in observations e.g. the uncertainties associated with the satellite data products used in this study. Overall, this reduces confidence that the model has represented the troposphere well in comparison to observations.

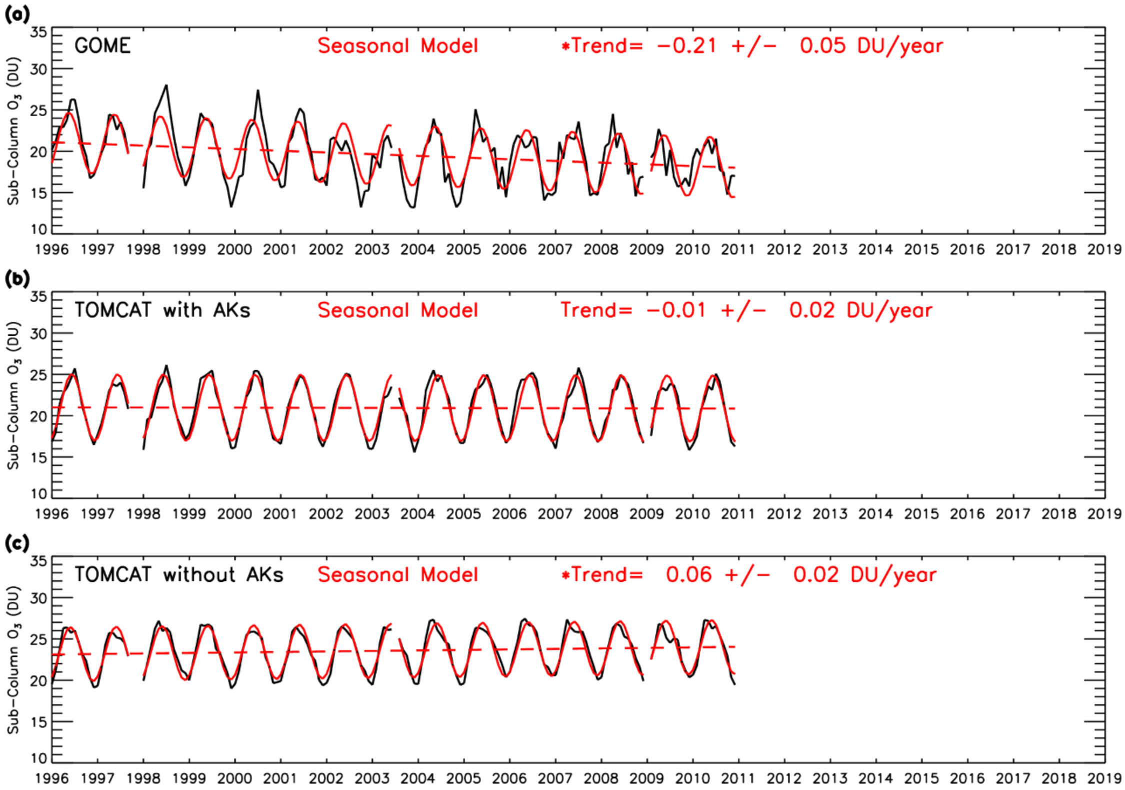

Figure 5.15: **European monthly average sub-column O_3 (surface – 450 hPa, DU) for (a) GOME, (b) co-located TOMCAT with GOME AKs applied and (c) co-located TOMCAT without AKs applied. A seasonal model based on the record is shown on each panel. The calculated linear trend from this seasonal model (DU year^{-1}) is displayed on each panel. An * before the word “Trend” indicates that the trend is significant at the 95% confidence level.**

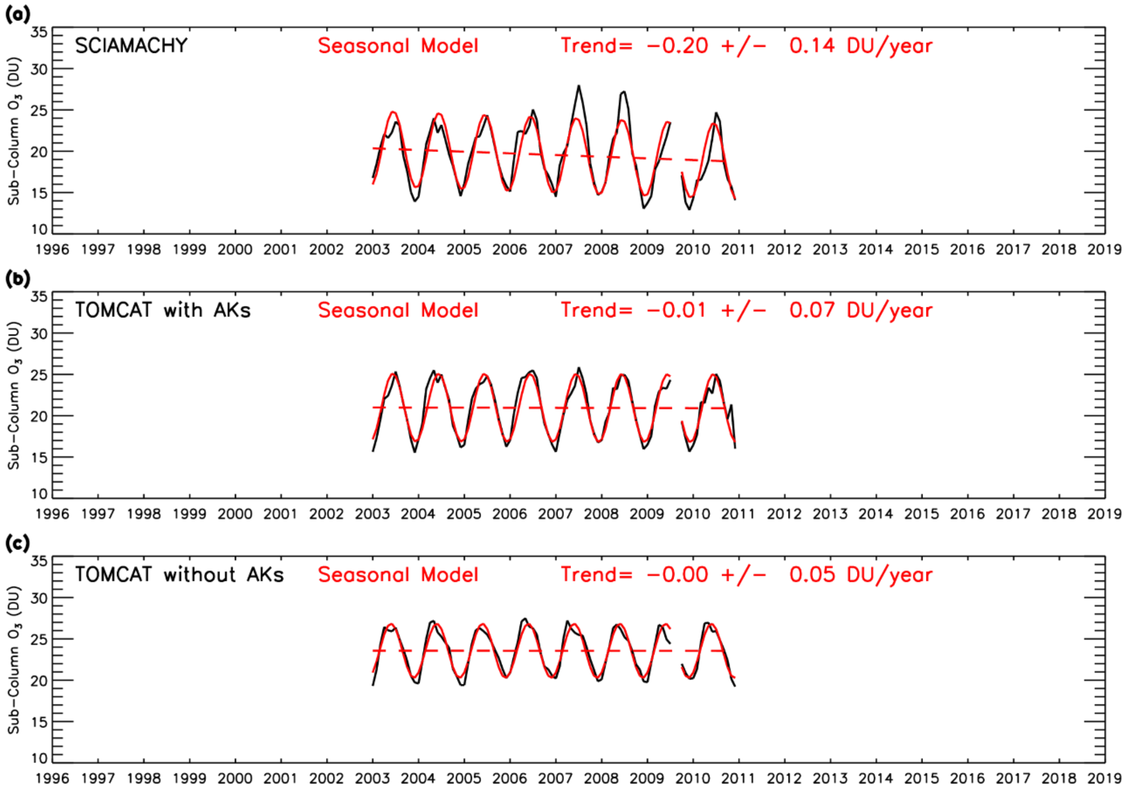

Figure 5.16: European monthly average sub-column O_3 (surface – 450 hPa, DU) for (a) SCIAMACHY, (b) co-located TOMCAT with SCIAMACHY AKs applied and (c) co-located TOMCAT without AKs applied. A seasonal model based on the record is shown on each panel. The calculated linear trend from this seasonal model (DU year^{-1}) is displayed on each panel. An * before the word "Trend" indicates that the trend is significant at the 95% confidence level.

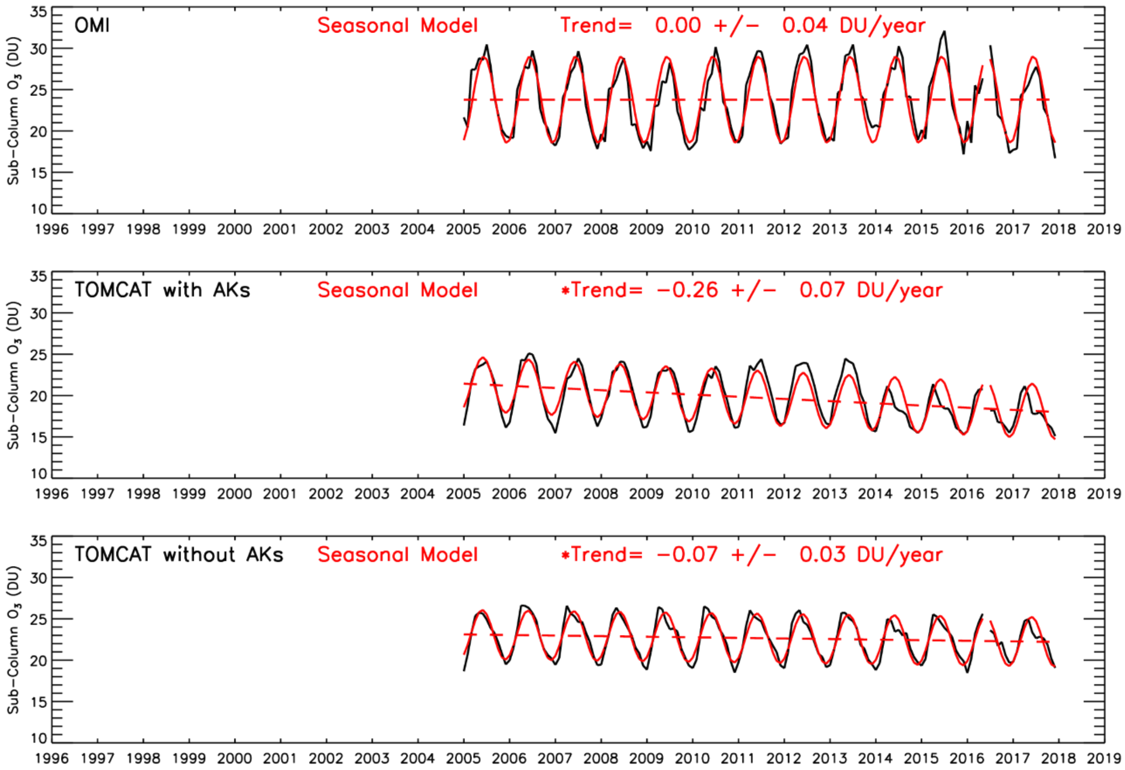

Figure 5.17: European monthly average sub-column O_3 (surface – 450 hPa, DU) for (a) OMI, (b) co-located TOMCAT with OMI AKs applied and (c) co-located TOMCAT without AKs applied. A seasonal model based on the record is shown on each panel. The calculated linear trend from this seasonal model (DU year^{-1}) is displayed on each panel. An * before the word "Trend" indicates that the trend is significant at the 95% confidence level.

5.4.2.2 Seasonal trends

The satellite trends show mostly little variation across the seasons (Table 5.3). For GOME, there are significant negative trends for each season except winter (DJF) which shows a near-zero trend, with -0.16, -0.43 and -0.26 DU year^{-1} for MAM, JJA and SON, respectively. For SCIAMACHY, there are significant negative trends for DJF (-0.31 DU year^{-1}) and MAM (-0.54 DU year^{-1}), a small positive trend for JJA (+0.19 DU year^{-1}) and a small negative trend for SON (-0.20 DU year^{-1}). The summer positive trend from SCIAMACHY is due to the high summer values in 2007 and 2008, which are towards the end of the time period. For OMI, there are no significant trends across any of the seasons and are all near-zero. There are very small negative trends for DJF (-0.05 DU year^{-1}) and MAM (-0.05 DU year^{-1}) and very small positive trends in JJA (+0.04 DU year^{-1}) and SON (+0.06 DU year^{-1}). As with the monthly record, the co-located model records with AKs applied are not capturing the satellite seasonal trends. The seasonal trends for the co-located model records are predominantly near-zero for TOMCAT-SCIAMACHY and TOMCAT-GOME, apart from MAM (-0.11 DU year^{-1}) and SON (+0.08 DU year^{-1}) for TOMCAT-SCIAMACHY (Table 5.3). For TOMCAT-OMI, there are significant negative trends for all seasons, albeit varying in magnitude, with -0.07, -0.20, -0.57 and -0.28 DU year^{-1} for DJF, MAM, JJA and SON respectively.

Overall, for GOME and SCIAMACHY, smaller and/or positive trends (DJF for GOME, JJA for SCIAMACHY, respectively) are reducing the magnitude of the all month timeseries negative trends averaged for all seasons. Therefore, the other seasons are showing larger negative trends, of up to -0.43 DU year^{-1} for GOME and -0.54 DU year^{-1} for SCIAMACHY, suggesting larger O_3 change than when considering the monthly record only. However, there is some variation between the two records, as GOME shows smallest trend in DJF, and a larger negative trend in JJA, whereas SCIAMACHY shows a larger negative trend in DJF and a positive trend in JJA. This could be explained by the different time periods they cover, however, the conflict does reduce the overall confidence in the results. In the case of OMI, the very small trend across the monthly timeseries does not appear to be due to a cancellation of different seasonal trends, as the trends are very small across all seasons.

Record	**Time period**	**Trend (DU year^{-1})**			
		DJF	**MAM**	**JJA**	**SON**
GOME	1996 - 2010	-0.01	-0.16	-0.43	-0.26
TOMCAT-GOME (with AKs)		-0.04	-0.01	-0.02	-0.02
SCIAMACHY	2003 – 2010	-0.31	-0.54	0.19	-0.20
TOMCAT-SCIAMACHY (with AKs)		-0.03	-0.11	-0.04	0.08
OMI	2005 - 2017	-0.05	-0.05	0.04	0.06
TOMCAT-OMI (with AKs)		-0.07	-0.20	-0.57	-0.28

Table 5.3: Summary of the seasonal trends for the satellite records and co-located TOMCAT model records (with AKs applied) of tropospheric sub-column O_3, for their individual time periods (DU year^{-1}).

5.4.2.3 Spatial distribution

The spatial distribution of sub-column O_3 for GOME, SCIAMACHY, OMI and TOMCAT (with no co-location or AKs applied) is shown in Figures 5.18, 5.19, 5.20 and 5.21, respectively. GOME shows a noisy signal, especially towards the northern latitudes. The northern Atlantic shows a decrease over the record, as does the Mediterranean and central Europe. SCIAMACHY shows a more spatially coherent signal over Europe. There are moderate O_3 values in the Mediterranean from 2003 – 2005, increasing to show high O_3 values in 2006 – 2008 and then much lower values in 2009 – 2010. The Atlantic and central Europe show a similar pattern. For OMI, the signal is more spatially coherent. The lower values in OMI in 2009 are predominantly from the Atlantic and central/northern Europe, with the Mediterranean/southern Europe showing mostly consistent values through 2006 – 2009. TOMCAT shows a consistent O_3 distribution throughout the 23-year record, apart from a notable increase in the O_3 across the domain from around 2005 – 2008. Overall, there does appear to be some regional variation in the satellite tendencies across the European domain, which is further explored using regional trends.

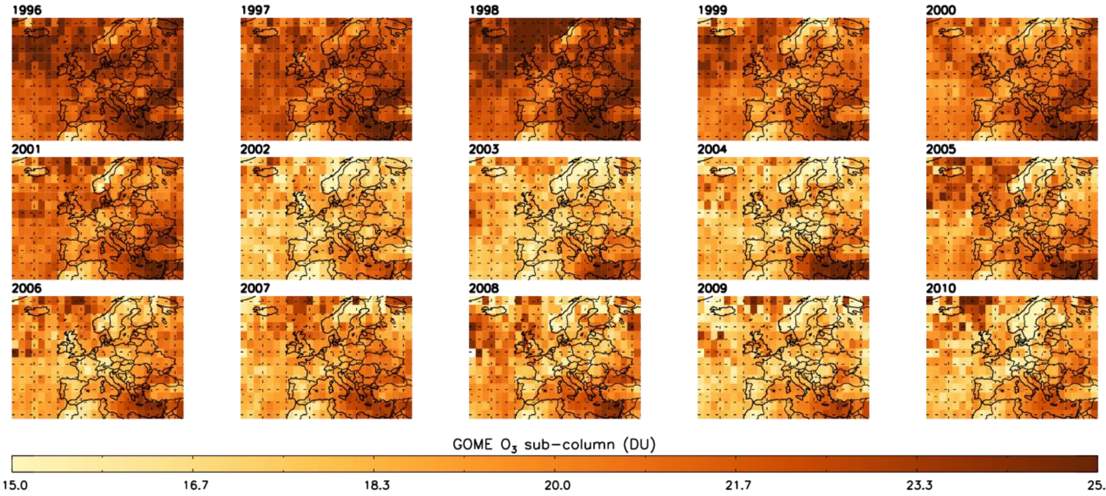

Figure 5.18: Annual average European sub-column O_3 (surface – 450 hPa, DU) from GOME for all years between 1996 – 2010.

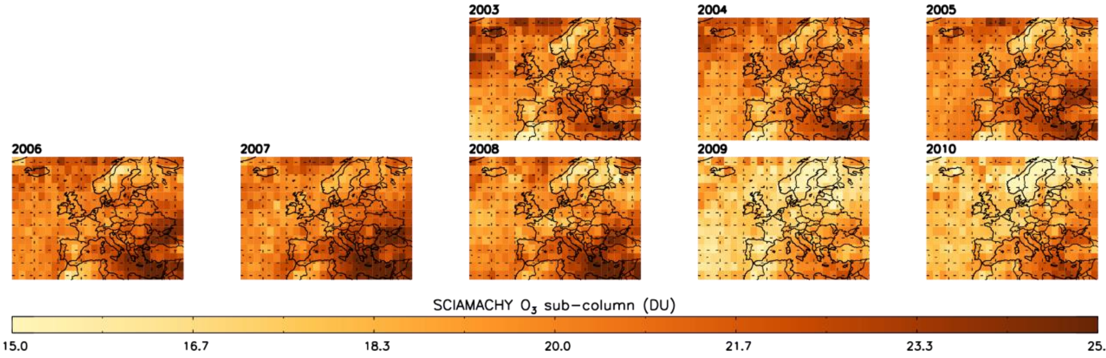

Figure 5.19: Annual average European sub-column O_3 (surface – 450 hPa, DU) from SCIAMACHY for all years between 2003 – 2010.

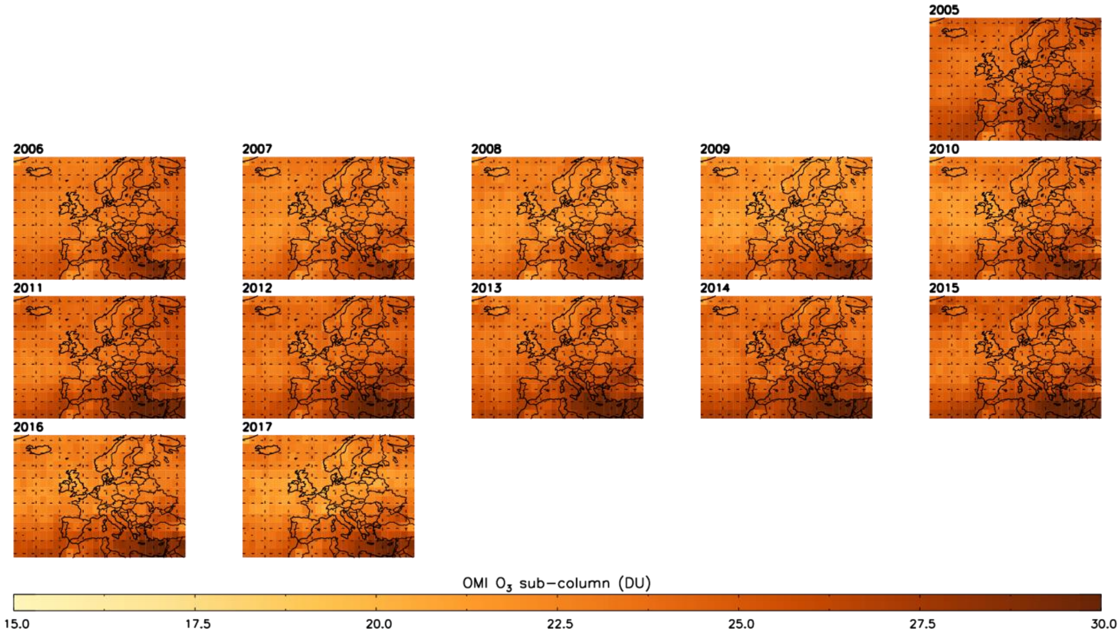

Figure 5.20: Annual average European sub-column O_3 (surface – 450 hPa, DU) from OMI for all years between 2005 – 2017. Note different scale to Figure 5.18, 5.19 and 5.21.

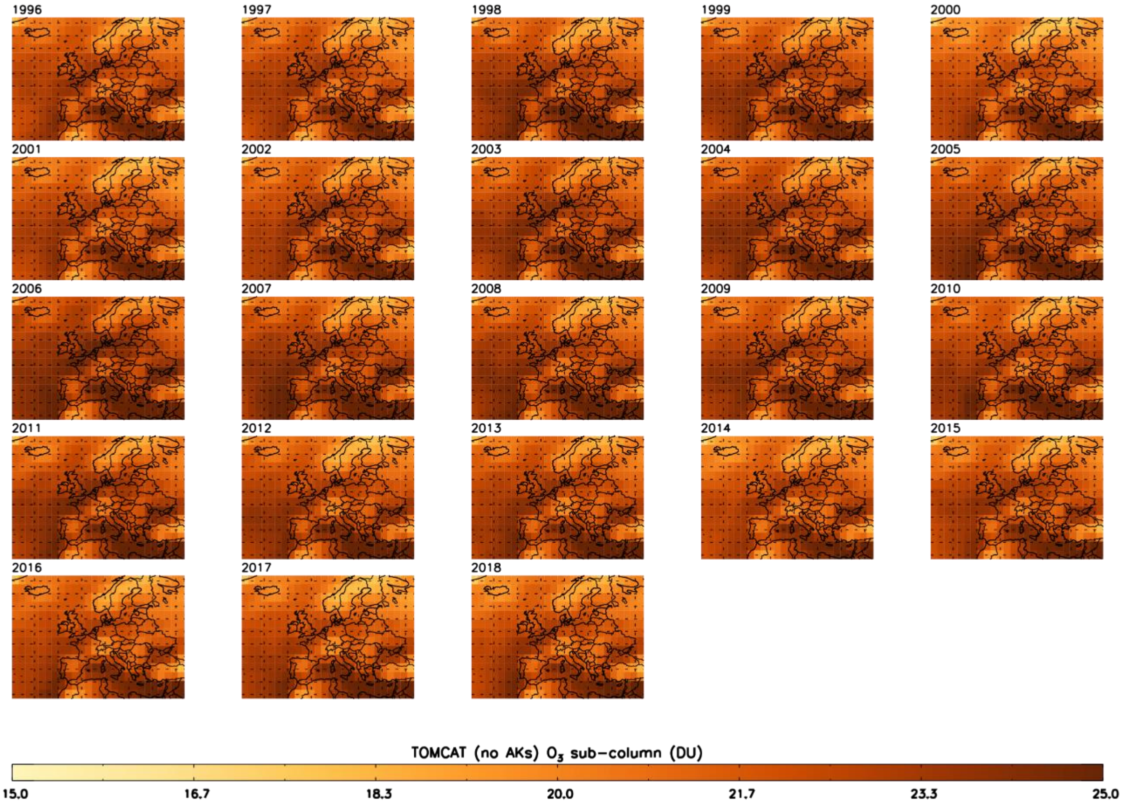

Figure 5.21: Annual average European sub-column O_3 (surface – 450 hPa, DU) from TOMCAT (no co-location or AKs applied) for all years between 1996 – 2018.

5.4.2.4 Regional trends

Based on the annual spatial distributions, four regions were selected to calculate of sub-domain trends (Figure 5.22). The regions are the Atlantic (30°W – 10°W, 30°N – 70°N,

Figure 5.23), Mediterranean (10°E – 40°E, 30°N – 45°N, Figure 5.24), Eastern Europe (15°E – 40°E, 35°N – 60°N, Figure 5.25) and Western Europe (10°W – 15°E, 35°N – 60°N, Figure 5.26).

For GOME, the regional trends are consistent across the four regions, all trends are significant at the 95% confidence level and range between -0.18 to -0.23 DU year^{-1}. This is very similar to the whole European domain GOME trend of -0.21 DU year^{-1}. The uncertainty in the seasonal model application is low, with all regional trends having an uncertainty of ± ~0.06 DU year^{-1}. For SCIAMACHY, the variation between regions is larger, although all show negative trends. The largest negative trend is in Eastern Europe, of -0.33 DU year^{-1} and is significant. The Atlantic and Western Europe show significant negative trends of -0.28 and -0.26 DU year^{-1}, respectively. The Mediterranean shows a smaller, insignificant negative trend of -0.13 DU year^{-1}. As they cover different time periods, this could indicate a temporal change for the Mediterranean region, of negative to positive trends. For OMI the regional trends are all insignificant and near-zero. The largest is the trend for the Mediterranean, with a small positive trend of +0.10 DU year^{-1}.

In comparison with the model (TOMCAT co-located with the satellite and AKs applied) over the Atlantic region, the model doesn't capture the negative trends seen in GOME and SCIAMACHY and shows a large negative trend for the OMI record, in contrast to the near-zero trend in the satellite. A similar pattern is found for the Eastern and Western Europe regions. For the Mediterranean, again, the negative trend for the GOME and SCIAMACHY records are not represented in the model, which shows near-zero trends. Here, OMI shows a very small positive trend of +0.10 DU year^{-1}, whereas TOMCAT shows a negative trend of approximately a similar magnitude (-0.13 DU year^{-1}). Broadly this pattern is similar for the total domain, suggesting a fairly spatially consistent difference between the satellite and model. Again, this poor agreement between model and satellite reduced confidence in how well the model is representing the troposphere. Differences could be caused by poor representation of key processes in the model, or the large uncertainties associated with the satellite observations.

For GOME, there is a consistent negative trend across most grid-boxes in the whole European domain (Figure 5.27), which is consistent with the similar negative trends across the four regions and suggests that there is no spatial cancellation of trends for the domain average. For SCIAMACHY, the stronger negative trends are towards the northern area of the Atlantic region and towards the north east area of the Eastern Europe region. The Mediterranean region to contain a mixture of positive and negative trends for SCIAMACHY, which is consistent with this region having the smallest negative trend for SCIAMACHY (Figure 5.24). For OMI, the trends are much smaller across all grid-boxes compared to the other satellite records, apart for some larger values in the south of the domain (~ +0.25 DU year^{-1}). Broadly there are positive trends from 30°N – 40°N, near-zero trends from 40°N – 48°N, negative trends from 48°N – 60°N and a mixture of positive (in the west) and negative trends (in the east) in the 60°N – 70°N band. This highlights that for OMI there is some degree of spatial cancellation leading to a very small trend across the whole domain. The co-located model records (Appendix K/Figure K.1) show much smaller trends across the domain and GOME and SCIAMCHY, and much larger ones for OMI. The most convincingly captured record is SCIAMACHY, with the model showing negative anomalies across most of the domain, with positive anomalies in the Mediterranean. This suggests that the model is reasonably capturing the SCIAMACHY record, after accounting for sampling pattern and vertical sensitivity. In contrast, the agreement is very poor for the model record co-located with OMI, highlighting a potential issue with this record.

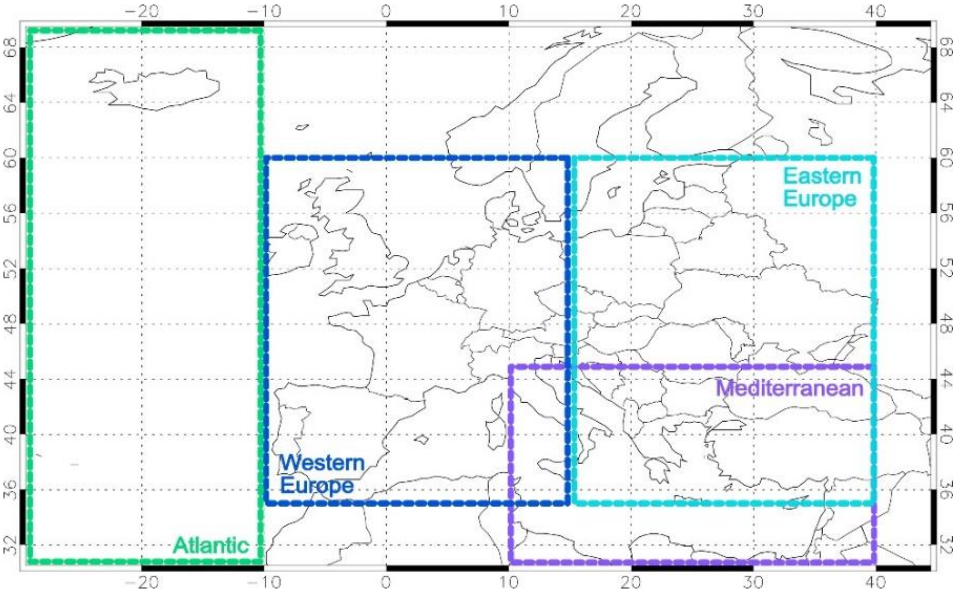

Figure 5.22: Locations of European regions used in the analysis: Atlantic (30°W – 10°W, 30°N – 70°N), Mediterranean (10°E – 40°E, 30°N – 45°N), Western Europe (10°W – 15°E, 35°N – 60°N) and Eastern Europe (15°E – 40°E, 35°N – 60°N).

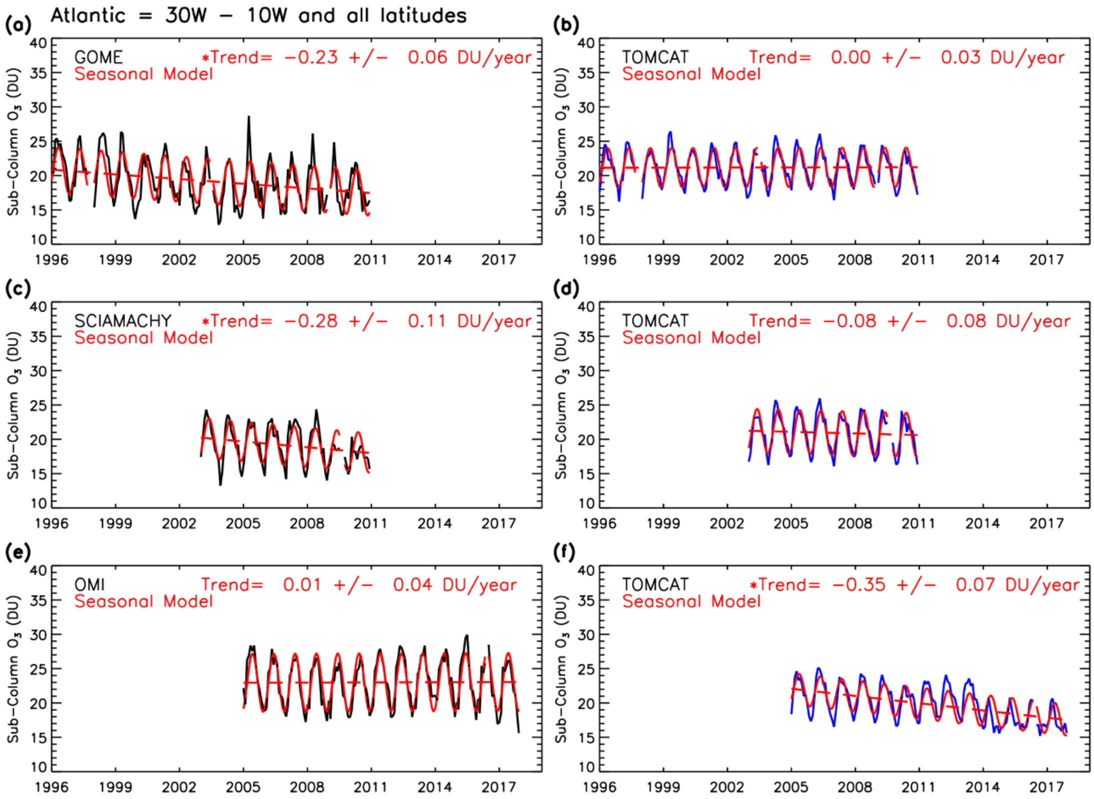

Figure 5.23: Timeseries of Atlantic (30°W – 10°W, 30°N – 70°N) regional monthly average sub-column satellite O_3 records (surface – 450 hPa, DU) between 1996 – 2017 for (a) GOME, (b) co-located TOMCAT with GOME AKs applied, (c) SCIAMACHY, (d) co-located TOMCAT with SCIAMACHY AKs applied, (e) OMI and (f) co-located TOMCAT with OMI AKs applied.

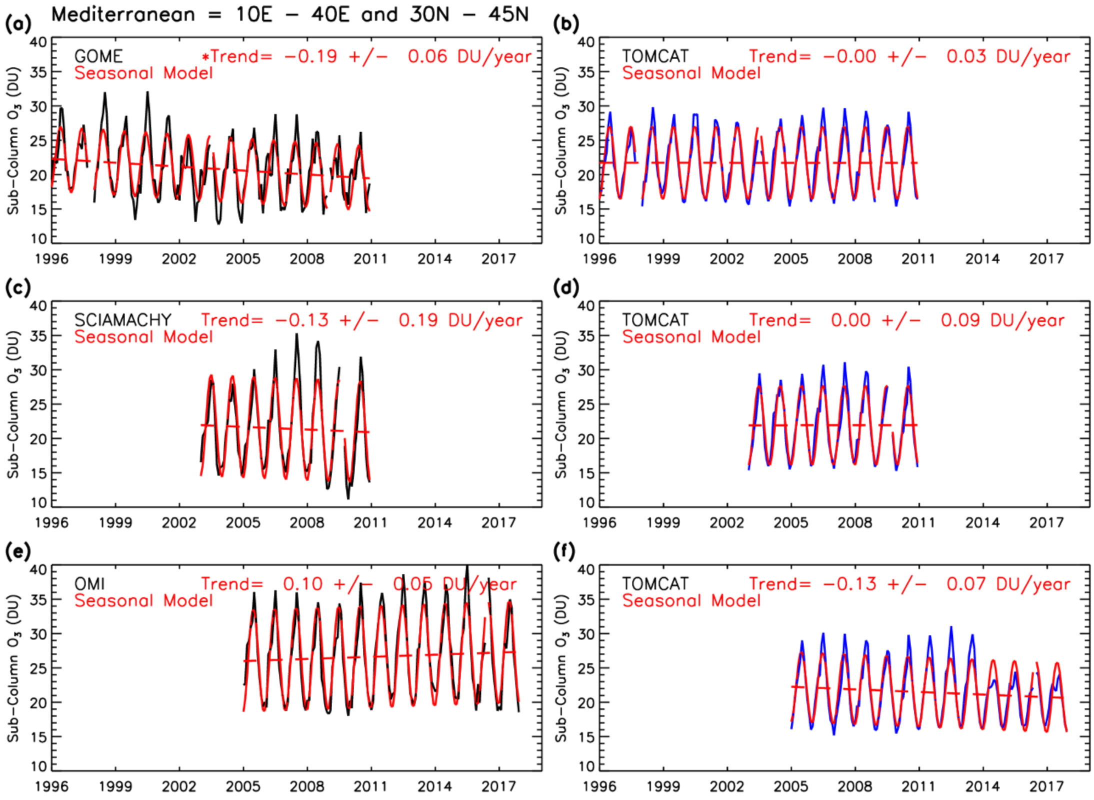

Figure 5.24: Same as Figure 5.23 but for the Mediterranean (10°E – 40°E, 30°N – 45°N).

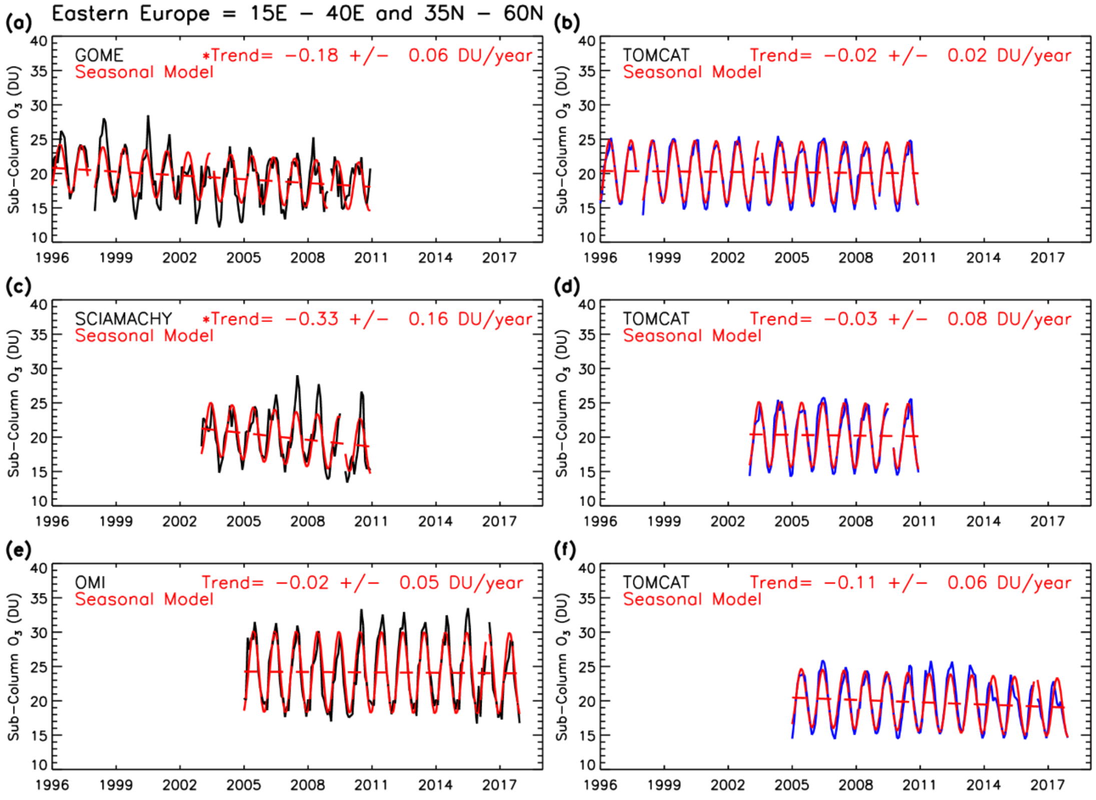

Figure 5.25: Same as Figure 5.23 but for Eastern Europe (10°E – 40°E, 30°N – 45°N).

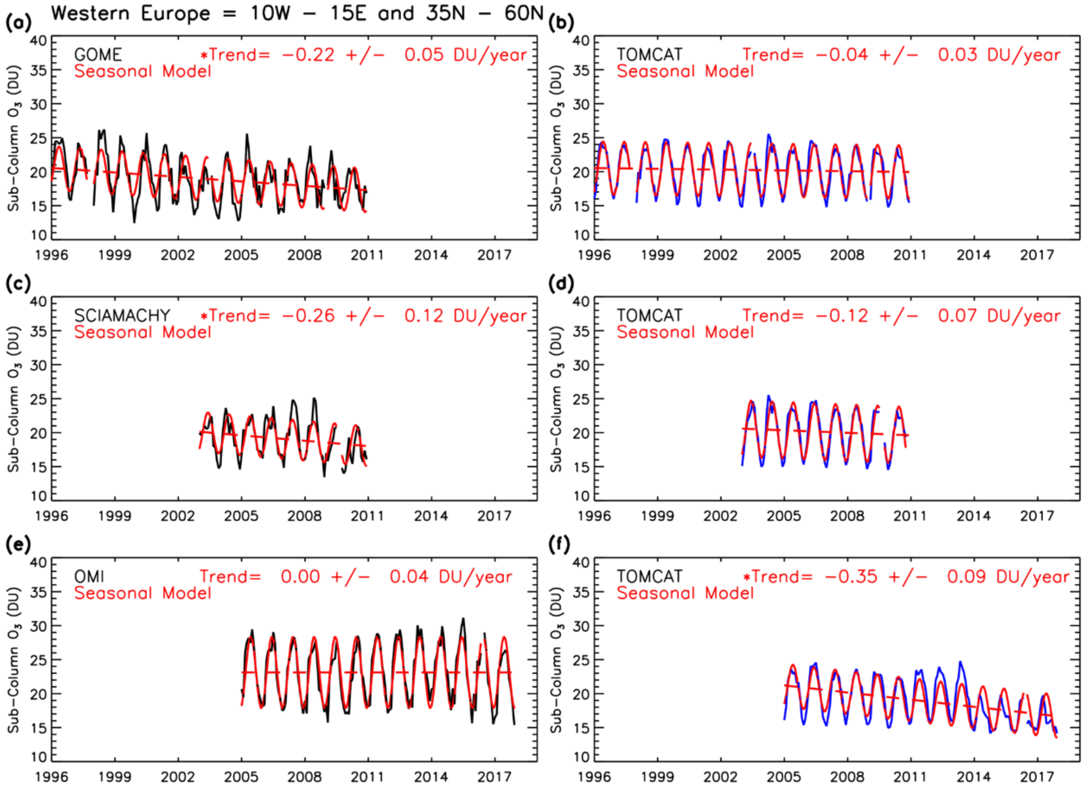

Figure 5.26: Same as Figure 5.23 but for Western Europe (10°E – 40°E, 30°N – 45°N).

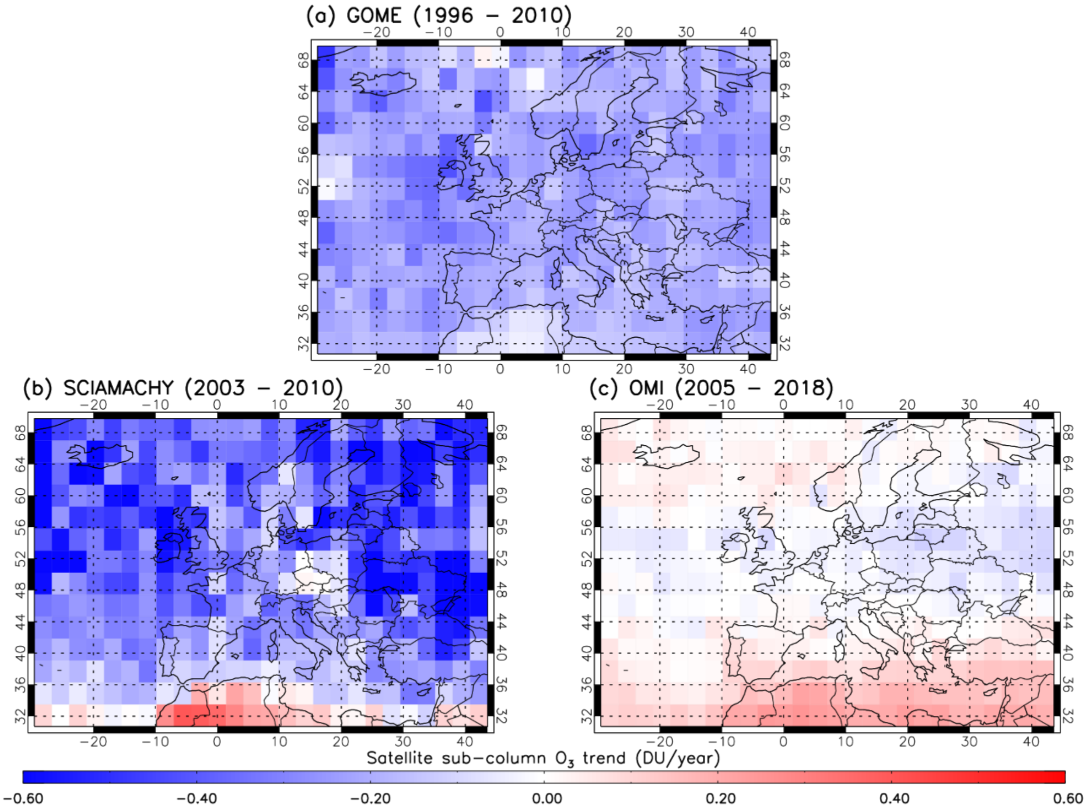

Figure 5.27: Linear component of the linear-seasonal trend model applied to a timeseries of satellite sub-column O_3 (surface – 450 hPa) for each grid-box across the European domain (DU year^{-1}) for (a) GOME, (b) SCIAMACHY and (c) OMI. The respective time periods are labelled.

5.4.3 Ozonesonde record

Ozonesondes provide an independent observational record of the free troposphere, with which to compare to the satellite records. There is a fairly close agreement between the co-located model and the ozonesonde records for both overpass times (10:00 and 13:00, ozonesonde selected at ± 3 hours), with a Pearson's correlation of 0.90 for both, however, there is an offset of around 2.44/2.16 DU, with larger values in the model record (Figure 5.28). When the trend model is applied, all four records show a consistent near-zero trend. The 10:00 (± 3 hours) ozonesonde record shows a trend of 0.01 ± 0.01 DU year^{-1} and the co-located TOMCAT record shows a trend of 0.01 ± 0.02 DU year^{-1}. For the 13:30 (± 3 hours) ozonesonde record, there is a trend of 0.02 ± 0.01 DU year^{-1}, and a trend of 0.01 ± 0.02 DU year^{-1} for the co-located TOMCAT record. These near-zero trends are smaller than the ozonesonde trends presented in Christiansen et al. (2022) (~ +3% decade^{-1}) for the European region. However, as well as a different selection of sondes used, they showed trends in the ozonesonde record starting in 1990, a time period of which several studies found to show positive trends in the free troposphere, e.g. Logan et al. (2012), before the stabilisation after ~ 2000 found in those studies. Overall, the ozonesonde record indicates very little change in tropospheric O_3 across the whole time period.

From 2012 onwards there is a significant drop in the number of available ozonesonde measurements to include in the averaged timeseries (Figure 5.28(c)). Despite this, the standard error of the ozonesonde record after 2012 only increases slightly in the summer months (Figure 5.28(d)). On an annual scale, between 1996 – 2014 there is an average annual standard error of 0.4 DU with a relatively small increase to 0.6 DU between 2015 – 2018. This suggests that although there is a lower number of ozonesondes after 2012, the spread of the data is broadly consistent with pre-2012 levels.

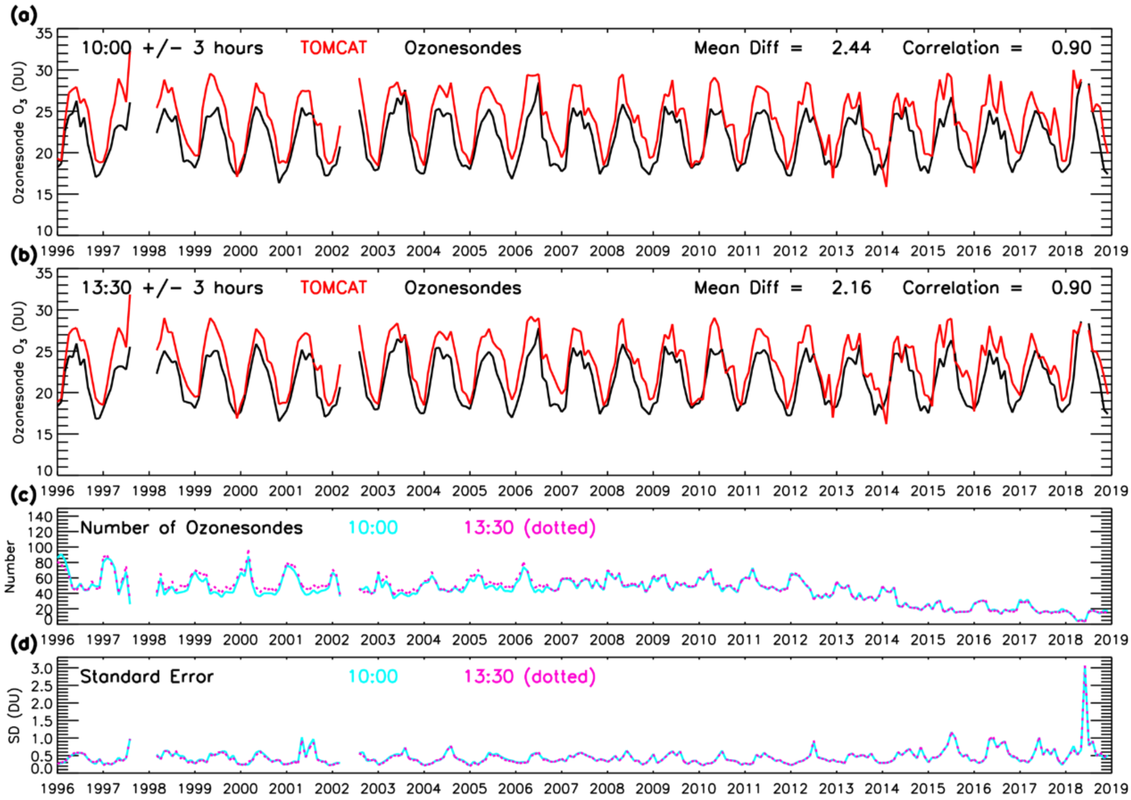

Figure 5.28: European monthly averaged sub-column O_3 from ozonesondes and co-located TOMCAT model data (DU) filtered for (a) 10:00 ± 3 hours and (b) 13:30 ± 3 hours. The mean difference (model subtract ozonesonde) (DU) and correlation between the two records is labelled at the top of panels (a) and (b). (c) The number of ozonesondes that contributes to each average per month for each time selection. (d) The standard error of the ozonesondes for each month (DU).

5.4.4 Six-year satellite record overlap period (2005-2010)

There are six years across the whole time record (1996-2018) where all three satellite records are available, 2005-2010. In this overlap period, all three satellite records can be compared to better understand the differences between the records.

5.4.4.1 Satellite

During the overlap years, all three records show consistent significant negative trends, with GOME showing the smallest (-0.17 DU year^{-1}), SCIAMACHY showing the largest (-0.47 DU year^{-1}) and OMI showing a value in between (-0.36 DU year^{-1}) (Table 5.4). Across the monthly anomalies of the three satellite records (Figure 5.29(b)) there are several periods of consistency between them. The spring of 2005 shows consistent positive anomalies between the three records, reaching around +2.3, +1.3 and +3.0 DU for GOME, SCIAMACHY and OMI, respectively. A similar positive anomaly is found across all three records in the spring of 2006. A positive anomaly of up to around +2.0 – 2.5 DU is found across the late spring/summer/early autumn of 2007 for GOME and SCIAMACHY, but it is not present in OMI. SCIAMACHY and OMI show a consistent negative anomaly during most of 2009, of up to around -2.6 DU in SCIAMACHY and -2.1 DU in OMI, with GOME showing a negative anomaly of up to -2.4 DU over the summer months of 2009. All three records show a negative anomaly of -2.1, -2.9 and -2.6 DU for GOME, SCIAMACHY and OMI, respectively, in the spring of 2010. For the absolute records, there is a moderate Pearson correlation coefficient of 0.61 between GOME and SCIAMACHY and 0.64 between GOME and OMI, and a higher coefficient of 0.91 between SCIAMACHY and OMI. Overall, this highlights that although there are some considerable differences between the records during this overlap period, especially the much higher values of the OMI record, the records are showing some consistency in their temporal variation. This consistency increase the confidence in the overall results, as the satellites do show relatively similar stories when compared across the same time period, however, there are still some considerable differences. Spatially, SCIAMACHY and OMI show the largest trends due to nearly all grid-boxes showing negative trends, compared to GOME, which shows a mixture of positive and negative trends (Figure 5.30). Any differences could be explained by differences in the vertical sensitivities of the instruments, sampling patterns, overpass times and any instrument specific caveats e.g. OMI row anomaly.

	Satellite trend (DU year^{-1})	**TOMCAT with AKs trend (DU year^{-1})**	**TOMCAT without AKs trend (DU year^{-1})**
GOME	-0.17 ± 0.05	-0.15 ± 0.02	-0.01 ± 0.02
SCIAMACHY	-0.47 ± 0.14	-0.10 ± 0.07	-0.05 ± 0.05
OMI	-0.36 ± 0.04	-0.19 ± 0.07	-0.07 ± 0.03

Table 5.4: Summary of trends for the satellite and co-located model (with/without AKs applied) European monthly average sub-column (surface – 450 hPa, DU) O_3 records between 2005 – 2010. TOMCAT records are co-located with their respective satellite records.

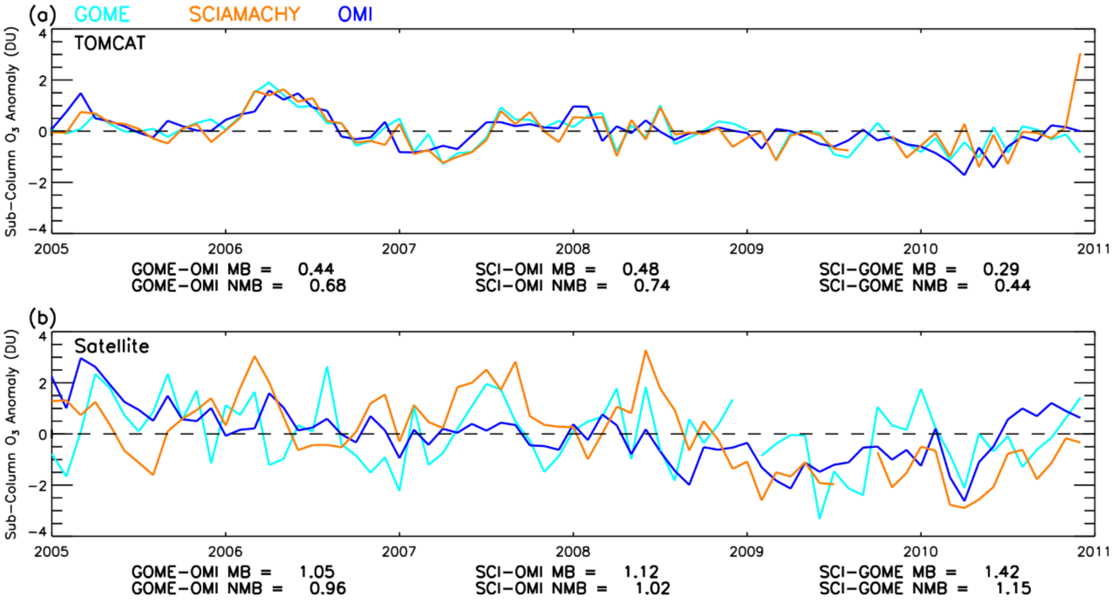

Figure 5.29: European monthly average sub-column (surface – 450 hPa) anomalies (DU) of: (a) mod-GOME, mod-SCIAMACHY and mod-OMI and (b) GOME, SCHIAMACHY and OMI. The values given below each plot refer to the MB and NMB between the co-located TOMCAT records or satellite records labelled.

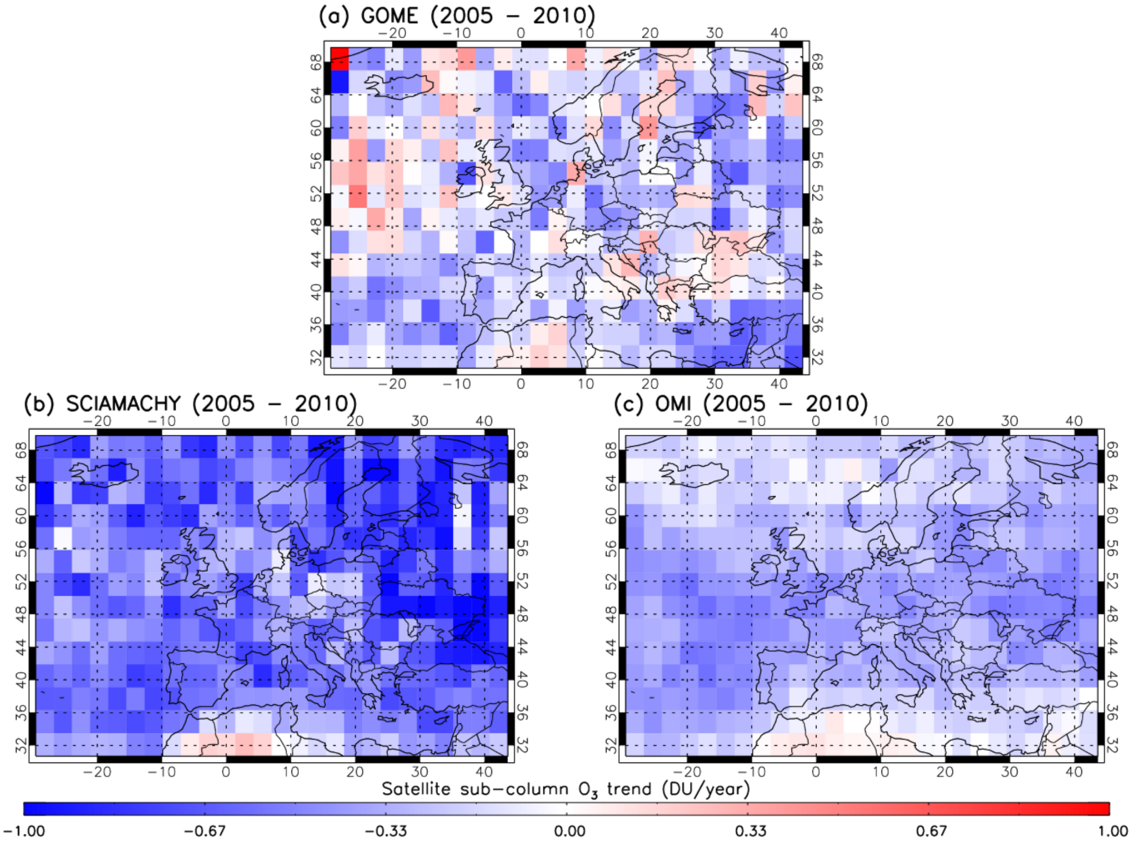

Figure 5.30: Same as Figure 5.27 but for the 6-year satellite record overlap period (2005-2010).

5.4.4.2 Model

For the model records with AKs applied (mod-GOME, mod-SCIAMACHY and mod-OMI), the satellite trend is captured by the model for GOME only, both having a significant negative trend of -0.17/-0.16 DU year^{-1} (Table 5.4). For SCIAMACHY, the model shows a smaller trend of -0.10 DU year^{-1}, unlike the larger negative trend of -0.47 DU year^{-1} seen in the satellite. For OMI, the model shows a significant negative trend (-0.19 DU year^{-1}), around half the magnitude of the satellite trend (-0.36 DU year^{-1}). Therefore, in this six-year overlap period, the model does capture the trends in the satellite more convincingly than across the whole record. The model records with AKs applied are also consistent between the three records, with Pearson's correlation coefficients of 0.80 between the mod-SCIAMACHY and mod-OMI, 0.97 between mod-SCIAMACHY and mod-GOME and 0.81 between mod-OMI and mod-GOME. Applying the AKs to the model also impacts the trend, making the trend more negative, and so more like the satellite, in all 3 cases (Table 5.4). This shows that the trend is sensitive to the vertical sensitivity of the satellite instruments, and therefore it is important to consider the satellite vertical sensitivity when studying the trends.

For the model records with AKs applied, the monthly anomalies for all three records are fairly consistent, showing a similar pattern across the timeseries (Figure 5.29(a)). There are notable anomalies such as up to +1.4 DU in spring 2005, +1.5 – +2.0 DU in spring/summer 2006, -0.7 – -1.2 DU in spring 2007, +0.5 – +1.0 DU in winter 2007/2008 and -1.1 – -1.6 DU around spring 2010. In comparison with the satellite anomalies, across the 6 years, the broad pattern of positive anomalies before 2009 and more negative ones after 2009 is similar between the satellite and co-located model records.

The consistency of the anomalies between mod-GOME, mod-SCIAMACHY and mod-OMI (all based on the model simulation) is compared with the 3 independent satellite records, GOME, SCIAMACHY and OMI (Figure 5.29). To quantify this comparison, the NMB between the 3 records are presented for both the satellite and co-located model records. Here, the NMB refers to the MB normalised according to the standard deviation of one of the records in each pairing, to account for the larger anomalies seen in the satellite record. Mod-GOME, mod-SCIAMACHY and mod-OMI show smaller normalised differences (~ 0.4 – 0.7 DU), compared to the 3 satellite records (~ 1.1 – 1.4 DU), suggesting broadly a greater consistency. This larger consistency between the model co-located records provides some evidence to indicate that the differences between the satellite records are not entirely due to factors related to sampling variation (e.g. overpass time and resolution) and vertical sensitivity. This is because these factors have been taken into consideration in the model records by co-locating the model to the satellite profile locations/times and then applying the AKs to the model profiles. Therefore, as the satellite records show larger differences than the co-located model records, these additional differences must be due to other factors, not just the sampling and vertical sensitivity as commonly stated.

5.4.5 Model experiments

To distinguish the influences of emissions and meteorology variation on long-term tropospheric sub-column O_3 trends, two additional TOMCAT simulations were performed, one with a repeating fixed year of emissions and the other with a repeating fixed year of meteorology (fixed year of 2008 for both). The timeseries of the TOMCAT control simulation (TOMCAT-control), the simulation with fixed emissions (TOMCAT-fixed-emiss) and the simulation with fixed meteorology (TOMCAT-fixed-met) is shown in Figure 5.31. Both experiment simulations show a close agreement with the control run, with a Pearson's correlation coefficient of 0.99 for TOMCAT-fixed-emiss & TOMCAT-control and 0.98 for TOMCAT-fixed-met & TOMCAT-control. Over the timeseries, TOMCAT-fixed-emiss is on average 0.41 DU larger than TOMCAT-control and TOMCAT-fixed-met is 0.16 DU smaller than TOMCAT-control. Figure 5.31(d) and (e) show that 2008 was a year of emissions which caused higher O_3 concentrations than typically. Using a fixed year of 2008 emissions in the simulation for the other years of the record generates a positive difference relative to the control, with higher O_3 in TOMCAT-fixed-emiss across most other years. For the fixed meteorology simulation, the meteorology of 2008 is shown to be more consistent with an average across the time period, with both positive and negative differences. The pattern of monthly anomalies for TOMCAT-fixed-emiss is very similar to TOMCAT-control (r = 0.88), highlighting the importance of varying meteorology in explaining short-term monthly tropospheric O_3 variation. The TOMCAT-fixed-met simulation is less well correlated with TOMCAT-control (r = 0.57) but does still show an influence e.g. there are notable periods in 1998 and 2015 where TOMCAT-control is more consistent with TOMCAT-fixed-met compared to TOMCAT-fixed-emiss.

For the three simulations, all have near-zero trends (-0.01/0.00/-0.01 DU year^{-1} for the control/fixed-met/fixed-emiss), highlighting the limited impact that fixing either the emissions or meteorology has on the overall trend across the 23-year period. Due to the large impact of emissions in 2008, sub-temporal trends were created for before and after 2008 (1996 – 2008 and 2008 – 2018, Figure 5.32). All three model runs show a similar pattern, with a very small positive trend for 1996 – 2008 of +0.07 DU year^{-1}, +0.03 DU year^{-1} and +0.04 DU year^{-1} for TOMCAT-control, TOMCAT-fixed-emiss and TOMCAT-fixed-met respectively, and a small negative trend for 2008 – 2018 of -0.07 DU year^{-1}, -0.03 DU year^{-1} and -0.03 DU year^{-1}, respectively. Overall, this experiment indicates that neither fixing emissions nor meteorology has a large impact on the average long-term trends of tropospheric O_3 across the European domain. Therefore, the near-zero trend in the control is not due to a possible cancellation of trends from a large impact of emissions and meteorology, despite the reduction in key O_3 surface precursor gases, e.g. NO_x and VOCs, used in the simulation (Figure 5.12). As discussed earlier, in the model different processes are more important to tropospheric O_3 variation at the surface (e.g. local surface emissions) and higher up in the troposphere (meteorology, transport, STE). Therefore, the near-zero trend across the time period could be influenced by a balance of these different processes within the surface – 450 hPa sub-column, which could be further studied by investigating the TOMCAT trends across the pressure levels within the surface – 450 hPa pressure region.

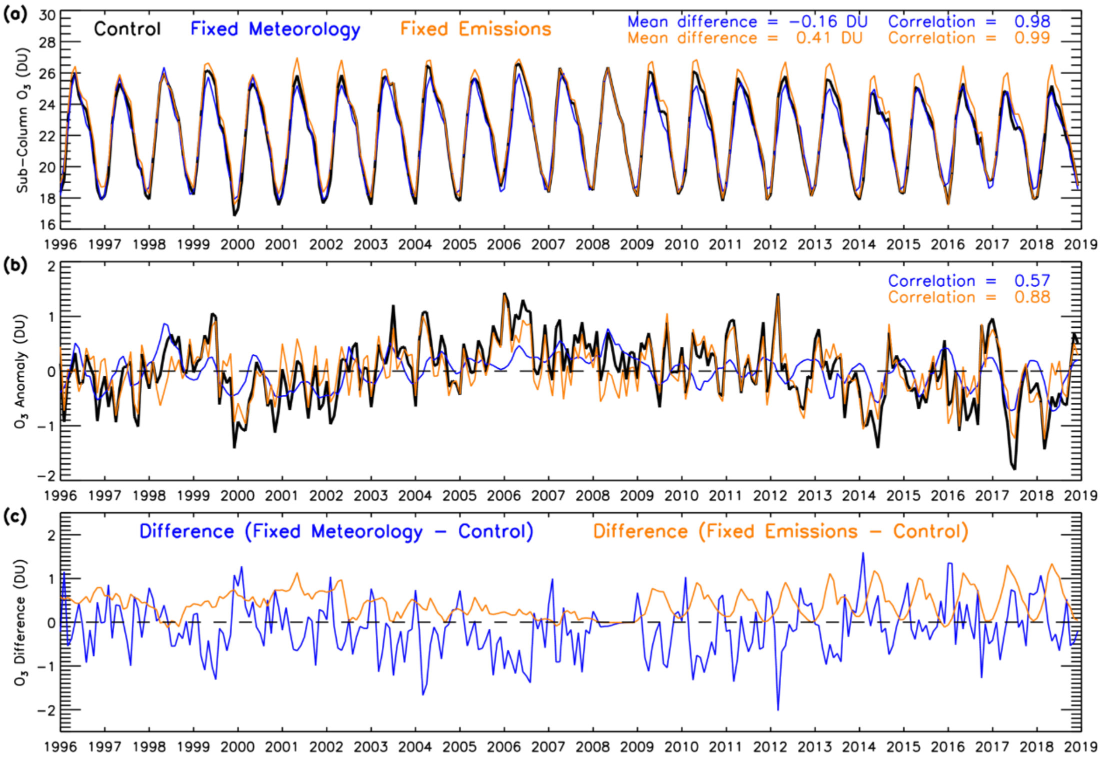

Figure 5.31: (a) Timeseries from 1996 – 2018 of European average monthly sub-column O_3 (surface – 450 hPa, DU) for TOMCAT-control, TOMCAT-fixed-emiss and TOMCAT-fixed-met. (b) Monthly mean anomalies (relative to a monthly average baseline (1996 – 2018)) for the 3 simulations (DU). (c) Difference between TOMCAT-control the two fixed simulations (DU).

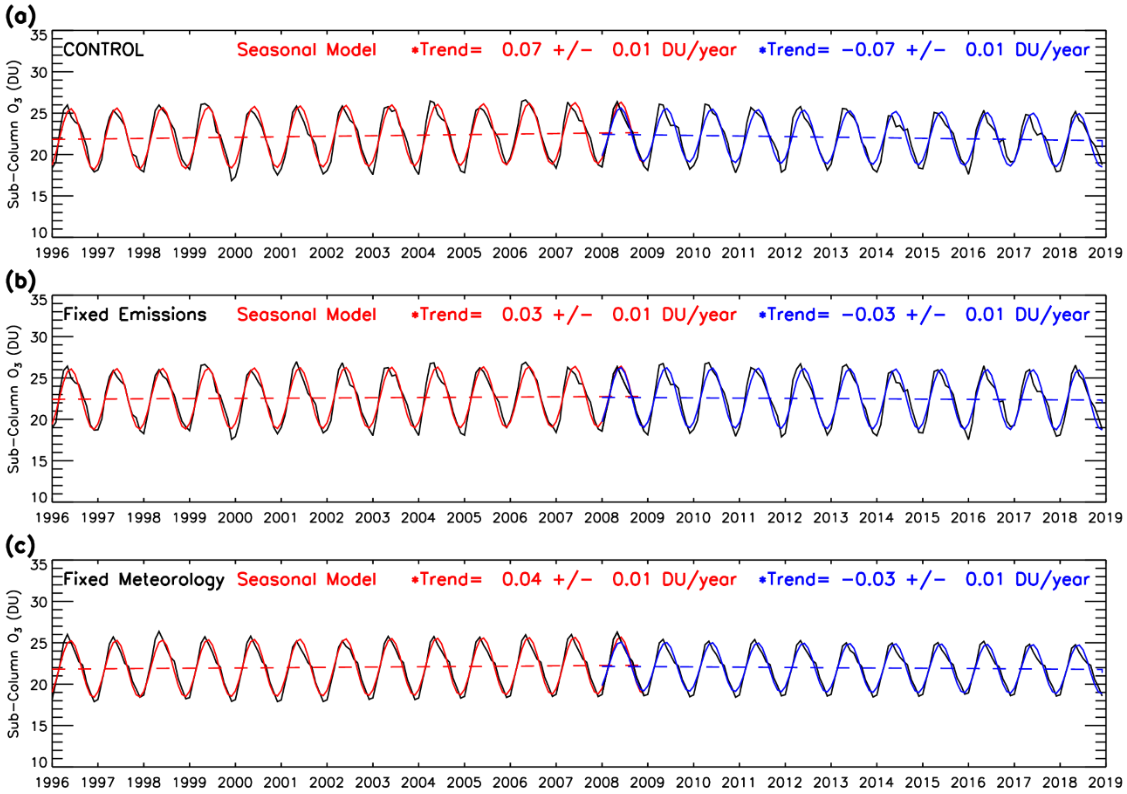

Figure 5.32: Timeseries of European monthly average sub-column O_3 (surface – 450 hPa, DU) for (a) TOMCAT-control, (b) TOMCAT-fixed-emiss and (c) TOMCAT-fixed-met. A seasonal model based on the record from 1996 – 2008 is shown in red, and 2008 – 2018 is shown in blue. The calculated linear trend from each seasonal model (DU year^{-1}) is displayed on each panel. An * before the word "Trend" indicates that the trend is significant at the 95% confidence level.

For each grid-box across the European domain, the trends for all three simulations are very small, ranging from -0.04 to 0.05 DU year^{-1} (Figure 5.33). TOMCAT-control shows negative trends across central continental Europe, with the largest negative values around Italy and the Balkans, and also across the North Atlantic. There are positive trends across the southern North Atlantic, the Southern Mediterranean counties in Northern Africa and NE Europe. Figure 5.33 also highlights which regions in TOMCAT-control reflect the trends in either TOMCAT-fixed-emiss or TOMCAT-fixed-met, and thus show a greater impact from meteorology or emissions. The region of negative trends in TOMCAT-control over central continental Europe and positive trends in the southern North Atlantic and North Africa are present in the TOMCAT-fixed-met (varying emissions) run and are regions where the trend is likely to be dominated by changes in surface emissions from the land. As central continental Europe produces large quantities of O_3 precursor surface emissions, this confirms the expectation that the tropospheric O_3 trend across central Europe has been more dominated by emissions than meteorology. The negative trends in the Northern Atlantic and the North Sea and positive trends across the NE of Europe are present in the TOMCAT-fixed-emiss run (varying meteorology) and are regions where the trend is likely to be dominated by changes in meteorology. Although the anomalies in the model simulations are much smaller than those of the satellite records (Figure 5.27), there is some evidence of a similar spatial pattern. For example, the positive anomalies in southern Europe around the Mediterranean in TOMCAT-fixed-met are seen in the SCIAMACHY and OMI records and the negative anomalies across central and eastern Europe in TOMCAT-fixed-met are seen in all three satellite records. This similarity in spatial distribution of anomalies indicates that the satellite records might be showing evidence of impact dominated by surface precursor emissions, as seen in TOMCAT-fixed-met simulation.

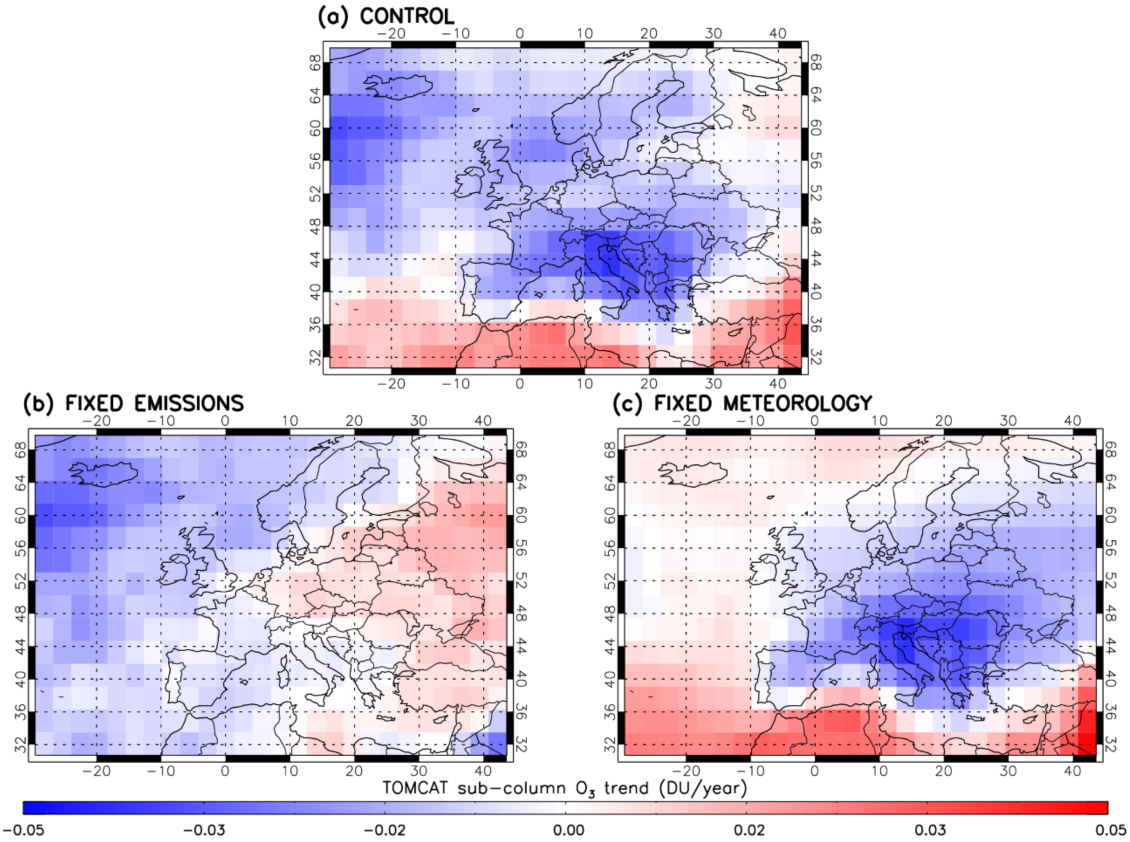

Figure 5.33: Linear trend for seasonal model applied to a timeseries of model sub-column O_3 (surface – 450 hPa) for each grid-box across the European domain (DU year^{-1}) for (a) TOMCAT-control, (b) TOMCAT-fixed-emissions and (c) TOMCAT-fixed-met.

STE can impact tropospheric O_3 variation and trends (Tarasick et al., 2005; Ordóñez et al., 2007; Neu et al., 2014). The simulations use a fixed climatological value of stratospheric O_3, but the flux of STE will vary between the years. STE shows variation between 1996 – 2018, with monthly anomalies varying between -0.9 and +0.7 DU and between -42% and 21% (Figure 5.34). There is a zero linear trend across the time period. This suggests that although STE can have an impact of year-to-year O_3 variability, there is no strong trend in the simulated STE flux, that has influenced tropospheric O_3.

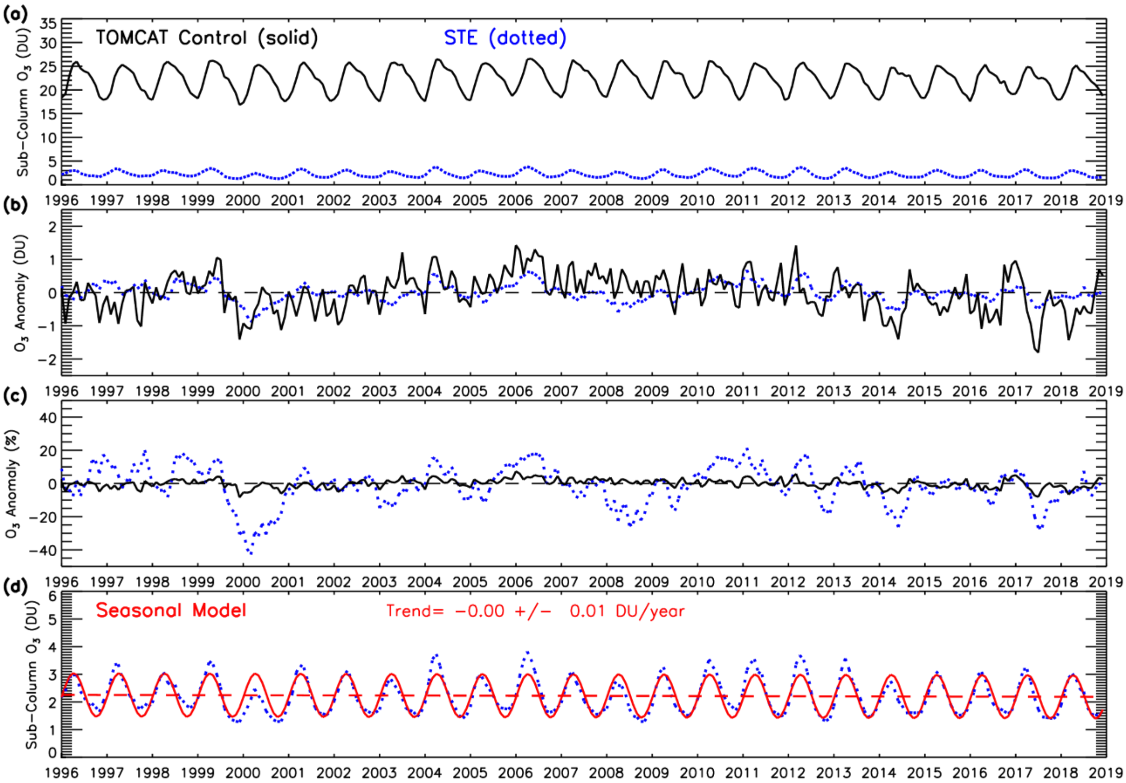

Figure 5.34: (a) European monthly average sub-column O_3 and a monthly sub-column O_3 based on the % of tropospheric O_3 from STE from 1996 – 2018 (DU) (labelled as STE). (b) Absolute anomalies for both records (DU) (relative to a monthly average baseline (1996–2018)). (c) as (b) as a %. (d) Seasonal model, linear trendline and calculated trend (DU year^{-1}) for the STE sub-column record. An * before the word "Trend" indicates that the trend is significant at the 95% confidence level.

5.5 Summary

In this chapter, records of three satellite-derived tropospheric O_3 records instruments were examined, in combination with the ozonesonde record and TOMCAT simulated O_3 between 1996 – 2018. The aim was to better understand what information these datasets can provide about long-term trends in European lower tropospheric O_3.

Three RAL UV-Vis lower tropospheric O_3 records (from GOME, SCIAMACHY and OMI) showed small changes between 1996 - 2017. GOME shows a negative trend of -0.2 DU year^{-1} from 1996 – 2010; SCIAMACHY shows a negative trend of -0.2 DU year^{-1} from 2003 – 2010; and OMI showed a near-zero trend from 2005 – 2017. Overall, despite a reduction in the key O_3 precursor gas emissions during this time period, the satellite observations indicate only a small negative to near-zero trend, suggesting further measures will be needed to tackle the tropospheric O_3 issue in Europe. However, European tropospheric O_3 has a large inter-annual variability and these satellite datasets have a large uncertainty, which makes distinguishing long-term trends difficult. European tropospheric O_3 is also influenced by many factors e.g. surface emissions, transport, meteorology and STE, which vary in importance across a tropospheric column, making it difficult to distinguish the drivers of the trends, especially as the co-located model records with the satellite instrument showed a poor agreement, generally not capturing the satellite trends.

A key consideration of the results in this chapter is the large uncertainty in satellite retrievals when considering small long-term trends. The average random error for each grid-box for the 3 instruments was ~ 6 – 7 DU (~ 31%), which was scaled to 1.1 – 1.4 DU (~ 6%) across the monthly average. This is relatively large compared to the small trends found, e.g. -0.21 DU year^{-1} for GOME, which reduces the robustness of the conclusions that can be made. Other sources of uncertainty have been presented and discussed, such as the OMI row selection which showed variations in the monthly average and trend depending on which rows were selected. In the future, as the instruments and the retrieval schemes advance and retrieval errors and uncertainties are reduced, small trends such as those found here can be concluded with more robustness.

During the 6-year overlap period (2005 – 2010) all three records show similar negative trends and temporal variation. GOME and SCIAMACHY show consistent absolute sub-column O_3 values, with the OMI record showing a larger offset, with a mean difference of ~4 DU larger than the other two records. Despite the offset in the overlap years, there is consistency between the three satellite products, showing similar negative trends (-0.2 to -0.5 DU year^{-1}) and similar anomalies across the time period. The higher consistency between the co-located model records during this overlap period suggests that sampling and vertical sensitivity differences between the satellite instruments are not entirely responsible for the differences seen in the satellite record anomalies, with the remaining differences currently unexplained. These differences require further investigation to explain what is causing them.

European ozonesondes show little variation from 1996 – 2018, which corresponds well with the near-zero trend in the sonde co-located TOMCAT record. Model experiments of fixing either the meteorology or emissions in the TOMCAT simulations, showed little impact compared to the control simulation, all showing a negligible trend throughout the period averaged across the domain. This indicates that there is no clear cancellation of trends from opposing larger influences of emissions and meteorology, despite consistent surface precursor emission reductions during this period. However, there could be some spatial cancellation, as the small model trends of some regions are shown to be driven more by either emissions or meteorology. Emissions had a larger influence on the regional trends across mainland Europe and the Mediterranean, likely due to emission reductions over the period, and meteorology was the more dominant influence on the trends across the Atlantic.

Chapter 6 Investigating the response of European tropospheric ozone to the COVID-19 lockdowns in 2020 & 2021

6.1 Introduction

Following on from Chapter 5, which investigates long-term tropospheric O_3 trends between 1996 – 2018, this chapter presents results on the more recent years of tropospheric O_3. The focus is on free tropospheric O_3 across Europe in 2020 and 2021, in response to the low spring/summer free tropospheric O_3 across the NH, initially described by Steinbrecht et al. (2021). As the result of a global pandemic caused by COVID-19 (disease from SARS-CoV-2, severe acute respiratory syndrome coronavirus-2), several countries worldwide implemented a 'lockdown' of many daily life activities to prevent the spread of the disease (Forster et al., 2020; WHO, 2020; Zhou et al., 2020). This resulted in a widespread reduction in surface emissions including O_3 precursor gases (NO_x and VOCs) (Forster et al., 2020). The first national European lockdowns started around the beginning of March, with Italy the first country in Europe to announce a national lockdown (European Commission, 2023).

Using changes in activity data, Forster et al. (2020) estimated a global reduction of ~ -30% for NOx and ~ -20% for VOCs in April 2020 and Guevara et al. (2021) estimated average reductions across Europe of ~ -33% for NO_x and -8% for VOCs in March/April 2020. Furthermore Guevara et al. (2021) found that the countries with the severest lockdowns, e.g. France, Italy and Spain, had even higher average reductions, of ~ -50% for NO_x and -14% for VOCs. Across Europe, many of these lockdowns started around spring/summer, which coincides with the low values of free tropospheric O_3 described by Steinbrecht et al. (2021) across the NH. Another notable event for tropospheric O_3 during winter/spring 2019/2020 was the very large stratospheric Arctic O_3 depletion caused by a very cold, strong and long-lasting polar vortex (Wohltmann et al., 2020; Weber et al., 2021; Feng et al., 2021).

Steinbrecht et al. (2021) found that during the spring and summer of 2020, measurements of the NH free troposphere (mostly from ozonesonde stations) showed lower than usual values of O_3. This negative anomaly in April – August 2020 was around an average of 7% lower (at 1 - 8 km altitude) than a climatological mean for 2000 – 2020 (Figure 6.1). The occurrence of these low O_3 values, at a large number of stations, is very unusual, and had not been seen in the record since at least 2000. Steinbrecht et al. (2021) also presented results from CAMS and NASA's GMI model suggesting that the low springtime Arctic stratospheric O_3 values contributed to less than 25% of this free tropospheric O_3 negative anomaly, and attribute most of the O_3 reduction to the simulated emission reductions.

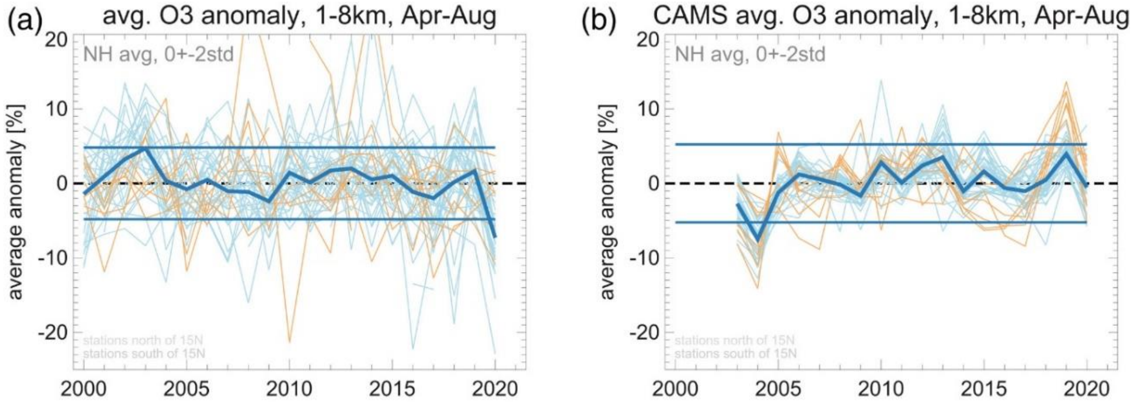

Figure 6.1: Annual mean O_3 anomalies (%, relative to a 2000 – 2020 average) between 1 – 8 km from April to August from a) ozonesonde measurements and b) CAMS atmospheric composition reanalyses. The light blue lines represent stations north of 15°N, the orange lines represent stations south of 15°N and the thick blue line represents an average of the stations north of 15°N. Taken from Steinbrecht et al. (2021).

Chang et al. (2022) investigated further the negative anomaly in European ozonesondes, comparing the 2020 free troposphere profiles (700 – 300 hPa) to a long-term (1994 – 2019) trend and the IAGOS aircraft tropospheric O_3 record. They show that including 2020 in a fused ozonesonde-aircraft record (1994 – 2019), the trend decreases from 0.65 ppbv decade^{-1} (without 2020) to 0.36 ppbv decade^{-1} (with 2020), and 2020 has a mean anomaly of -3.6 ppbv. This highlights the size of the negative anomaly with respect to the previous years. Clark et al. (2021) also studied the IAGOS record, showing a negative anomaly of 10% for spring 2020, compared to an average of spring 2016-2019 in the free troposphere above Frankfurt.

From the satellite record, Ziemke et al. (2022) showed that the low spring/summer free tropospheric O_3 was also present in the NASA satellite record. They show that a merged record of tropospheric O_3 from 3 instruments (EPIC aboard Deep Space Climate ObserVatoRy (DSCOVR), OMI aboard Aura and OMPS aboard the Suomi National Polar Partnership (SNPP)) found a comparatively uniform negative anomaly in tropospheric column O_3 between 20°N - 60°N. This negative anomaly of around 7 - 8% (3 DU), compared to a baseline of 2016 – 2019, was repeated again in the next year, 2021 (Figure 6.2). They also presented satellite results of NH NO_2, showing a reduction of around ~10 – 20% in spring/summer 2020 and 2021, attributing this as the likely cause to the negative O_3 anomalies (Figure 6.2). They suggested that high values of wildfire emissions (many are tropospheric O_3 precursor gases) in August – September 2020 and 2021, could have reduced the negative anomalies in tropospheric O_3 towards the end of the year.

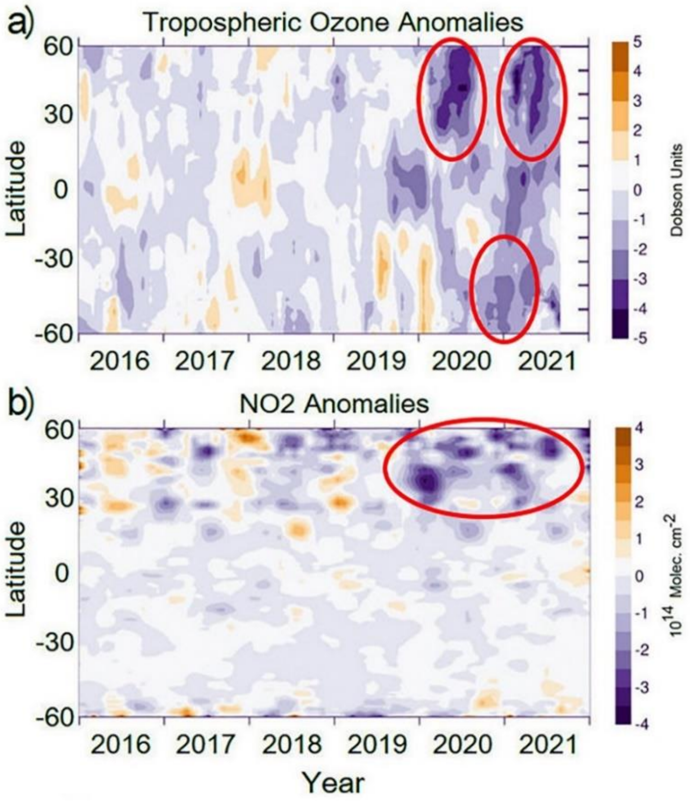

Figure 6.2: Monthly mean zonal tropospheric column anomalies between 60°S and 60°N for 2016 - 2021, for a) O_3 (DU) and b) NO_2 from OMI (10^{14} molecules cm^{-2}). Red ovals show areas of large negative anomalies. Taken from Ziemke et al. (2022).

Also from the satellite record, Cuesta et al. (2022) used a combination of IASI and GOME-2 in a multispectral synergism to investigate near-surface (lowermost tropospheric (LMT), below 3 km altitude) tropospheric O_3 in the spring (1st – 15th April) of 2020. They found an enhancement of LMT O_3 in central Europe and northern Italy (typically VOC-limited regions) compared to the previous year (2019) and a reduction elsewhere in Europe (typically NO_x-limited regions) (Figure 6.3). Figure 6.4 shows the change in LMT O_3 after the observations have been adjusted to account for meteorological impacts using a model showing more consistent negative anomalies across the domain in the satellite, highlighting the importance of considering the meteorological impact to 2020.

There are several modelling studies that have investigated the impact of emission reduction on free troposphere O_3. The studies use different methods to estimate the size of these emission reductions. Bouarar et al. (2021) modelled scenarios of reductions in primary pollutant emissions during the pandemic, based on emission reductions by Doumbia et al. (2021), finding zonally averaged NH free tropospheric O_3 to be around 5 – 15% lower than a baseline of 2001 – 2019. One third of this reduction is attributed to reductions in air traffic, one third is attributed to a reduction in surface emissions and the final third is attributed to meteorology, which includes the very low 2020 springtime Arctic stratospheric O_3. Miyazaki et al. (2021) found a reduction in the global tropospheric O_3 burden of around 2% in May and June 2020. Nussbaumer et al. (2022) used a mixture of model and aircraft results to investigate the chemical processes affecting tropospheric O_3 over Europe, focusing on the upper troposphere. They found a -55% reduction in NO_x mixing ratios from a 2020 aircraft campaign compared to a ‘no-lockdown’ model scenario in the upper troposphere, due to a reduction in air traffic. They found a significant deceleration in the O_3 cycling, but found that there was little effect on net O_3 production rates.

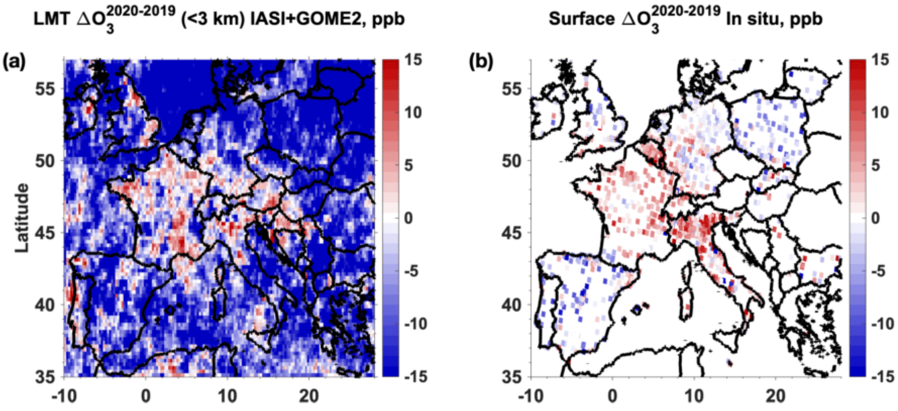

Figure 6.3: Spatial distribution of difference in O_3 between the 1st – 15th April in 2020 and in 2019 from a) combination of IASI and GOME-2 in the LMT and b) surface stations in the EEA network. Adapted from Cuesta et al. (2022).

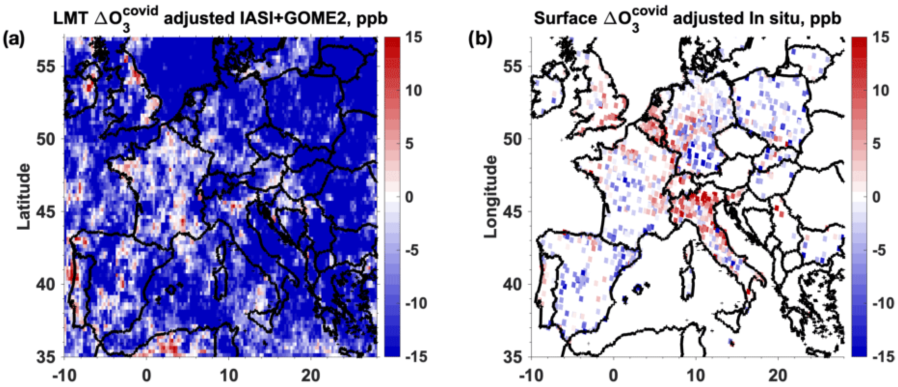

Figure 6.4: Same as Figure 6.3 but observations have been adjusted to remove the influence of meteorological conditions. Adapted from Cuesta et al. (2022).

This chapter focuses on the free troposphere O_3 anomalies across Europe in the spring/summer of 2020 and 2021, which are predominantly found to be negative in the literature. In contrast, as highlighted by Cuesta et al., (2022) and discussed above, at the surface both positive and negative anomalies were found in 2020. For example, Ordóñez et al. (2020) found that daily maximum NO_2 decreased consistently across Europe at background stations by 5 – 55 % in 2020 compared to 2015 – 2019, whereas, MDA8 O_3 decreased over Iberia but increased everywhere else in Europe. They attributed the O_3 changes to be dominated by meteorology, rather than emissions reductions, as in the case of NO_2. Grange et al. (2021) found an increase of O_3 by 30% for roadside monitoring sites and 21% for urban background sites across Europe in during the peak activity restrictions. Souri et al. (2021) used a model constrained with satellite observations of NO_x and VOCs from TROPOMI showing that surface MDA8 O_3 increased by ~4% across Europe, and used a fixed emission scenario to suggest that meteorology contributed 42% of the surface MDA8 O_3 increase, with remaining 58% from changes in anthropogenic emissions.

Aside from the study Ziemke et al. (2022) described above, there are few other studies of tropospheric O_3 in 2021 compared to 2020. One study of 2021 is from Pey and Cerro (2022) of surface site tropospheric O_3, showing that the background O_3 reductions of 2020 across SW Europe (over ~15% at most sites) are repeated in March and April of 2021, but to a lesser extent.

Parrish et al. (2022) presents an extrapolation of surface tropospheric O_3 data, at NH mid-latitude baseline sites, from a longer timeseries than that considered in Chapters 5 and 6. As described in Chapter 2, surface NH baseline tropospheric O_3 has been shown to have increased from around the 1980s to around 2000, when the growth rate plateaued, with fairly low variation since then. Parrish et al. (2022) found lower baseline O_3 around 2016 – 2018, which suggests the start of a negative trend through the 2010/2020s, which is fit with a quadratic trendline from 1980 – 2018 (Figure 6.5). Extrapolating this trendline to 2020, produces a much lower tropospheric O_3 value than the previous ~10 years, suggesting that low tropospheric O_3 values in 2020 could, in part, be due to this decreasing trend in baseline O_3.

In addition to O_3, the change in emissions in the spring/summer 2020 is likely to have had an impact on OH. In the literature, there are currently few observation-constrained estimates of OH anomalies in 2020. Miyazaki et al. (2021) used top-down estimates of NO_x emission reductions (using multi-constituent satellite data assimilation) to model the impact of tropospheric O_3 and OH, finding a global average tropospheric mean negative OH anomaly of -4.0% in May 2020, varying up to 20% – 30% locally (compared to a 2010 – 2019 baseline). The methodology developed in Chapter 4 presents an opportunity to derive OH concentrations in the spring/summer of 2020.

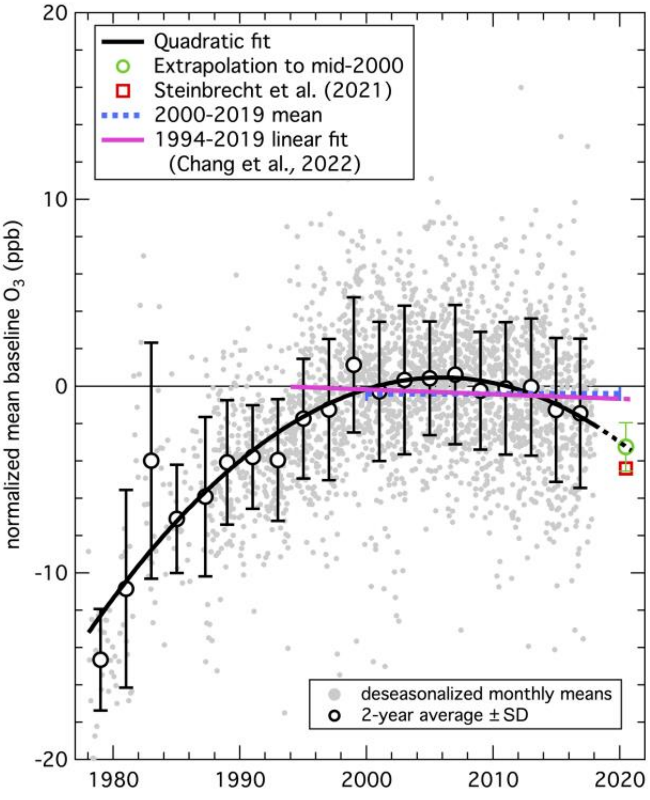

Figure 6.5: NH mid-latitude baseline O_3 from 1978 – 2018. The grey dots are the O_3 measurements from North America and western Europe. The open circles represent 2-year averages from the grey points with the error bars representing ± SD. A quadratic fit to the grey points is shown as a solid black line (with extension to mid-2020 shown in green). The 2020 annual mean from Steinbrecht et al. (2021) is shown as a red square. The results of (Chang et al., 2022) are shown in purple. . Taken from Parrish et al. (2022).

6.2 Research questions

This chapter will address the following research questions:

1. What happened to satellite-observed lower tropospheric O_3 in the spring/summer of 2020 and 2021? How does this compare to previous years?
2. How does the satellite record compare to the ozonesonde and surface data records in the spring/summer of 2020 & 2021?
3. What information can atmospheric chemistry transport model simulations provide about the causes of the spring/summer 2020 reduction of lower tropospheric O_3? Can a quantification of the relative contribution of emissions and meteorology be calculated?
4. What happened to global satellite-derived OH in 2020?

6.3 Data & methods

6.3.1 Satellite tropospheric ozone products

In this chapter, two tropospheric O_3 data records produced by RAL (GOME-2B and IASI-IMS-Extended) and one record produced by the Université de Toulouse and CNRS (IASI-SOFRID) are presented. The two retrieval schemes are described in more detail in Chapter 3. The GOME-2B record has been processed with a similar methodology to Chapter 5, using level 2 tropospheric sub-columns for Europe with a pressure range of the surface – 450 hPa. Tropospheric sub-columns (surface – 450 hPa) were derived for the IASI-IMS-Extended record using the same method as described in Chapter 5 (Section 5.3.3.2). The number of retrievals/sub-column values which passed the filtering process and are used in the monthly means are shown in Figure 6.6. Neither record shows a large change in retrievals passing the filtering process across the time period, which suggests it is appropriate to use these records for the analysis. Due to the reduction in anthropogenic emissions predominantly coming from the land across Europe, a land mask is used in the analysis. The land mask was produced as part of the Hemispheric Transport of Air Pollution (HTAP) Phase 2 programme (Koffi et al., 2016) and has been interpolated onto the TOMCAT grid (Figure 6.7).

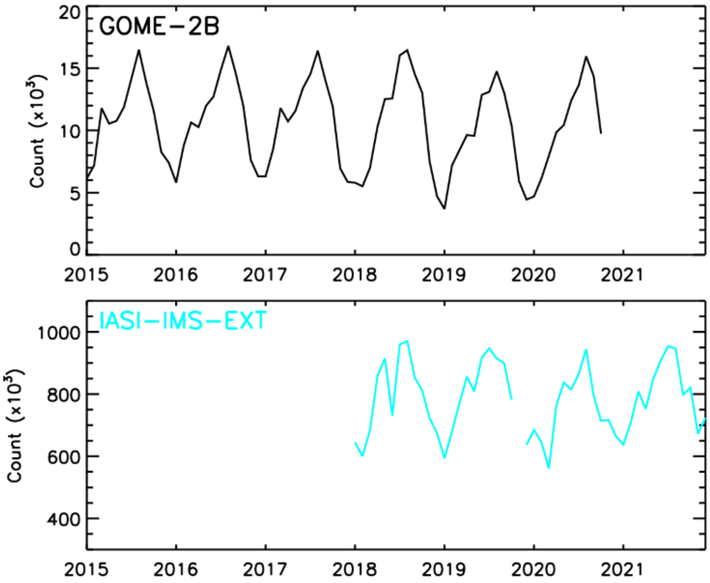

Figure 6.6: Timeseries of number of satellite sub-column values used in a monthly mean of (a) GOME-2B (×10^3) and (b) IASI-IMS-Extended (×10^3).

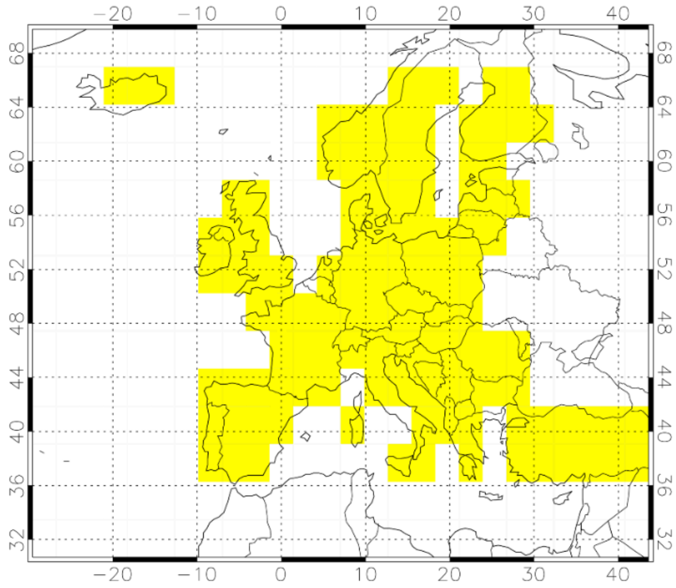

Figure 6.7: Land mask used in analysis. Yellow represents the grid-boxes selected as over land.

The IASI-IMS-Extended record is compared to another record from a different IASI retrieval scheme (IASI-SOFRID). For a longer timeseries, the IASI-IMS-Extended record, as described above, is also compared to a temporally partially processed record (1-in-10 days) for 2008 – 2017, as used in Chapter 4. To identify the impact of using a partially processed record, the partially processed (level 2) record has been compared with a level 3 product of IASI-IMS-Extended which was processed for significantly more days (1-in-2 days). The two records are well correlated, with a Pearson's correlation coefficient of 0.94, and a small average difference of 0.5 DU (Figure 6.8). This good comparison suggests it would be suitable to use the partially processed record in comparison with the MetOp-B fully processed record from 2018 – 2021.

Due to differences in the retrieval process between IASI-IMS-Extended and IASI-SOFRID, the products will have different vertical sensitivities. IASI-IMS-Extended shows better sensitivity for the lower troposphere (Figure 6.9), where this study is focused. For the surface to 450 hPa sub-column, IASI-IMS-Extended has an average DOFS of 0.5 in

January and 0.7 in July, and IASI-SOFRID has smaller average DOFS of 0.2 in both January and July.

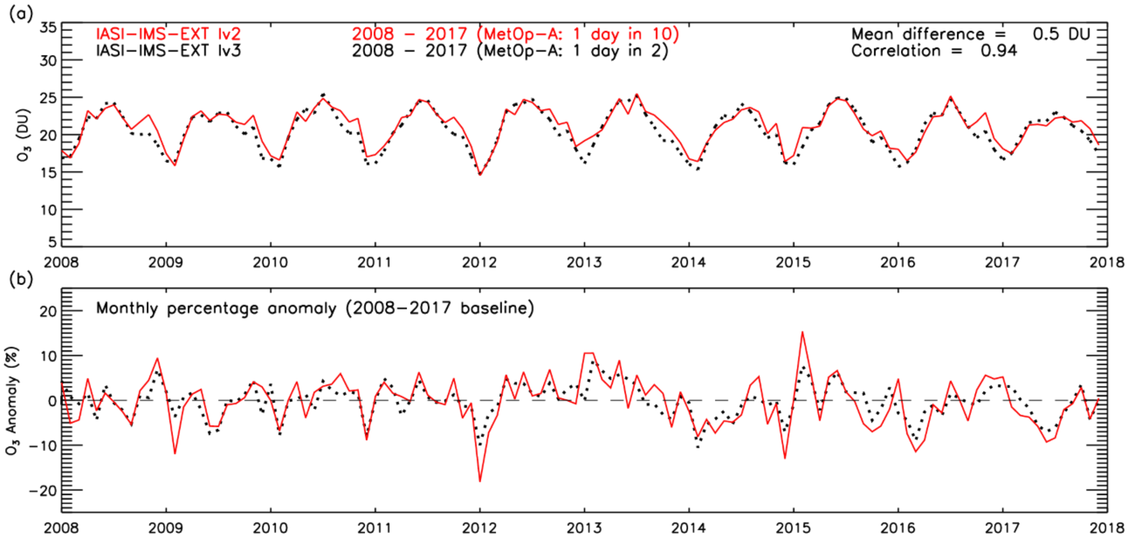

Figure 6.8: Comparison of temporally partially processed IASI-IMS-Extended record (from MetOp-A), between 1 in every 10 days and 1 in every 2 days, for 2008 - 2017. (a) Monthly mean European sub-column O_3 (surface – 450 hPa) for the 1 in every 10 days record (red solid line) and 1 in every 2 days record (black dotted line). (b) Monthly mean percentage anomalies for the two records, relative to a monthly average baseline (2008–2017).

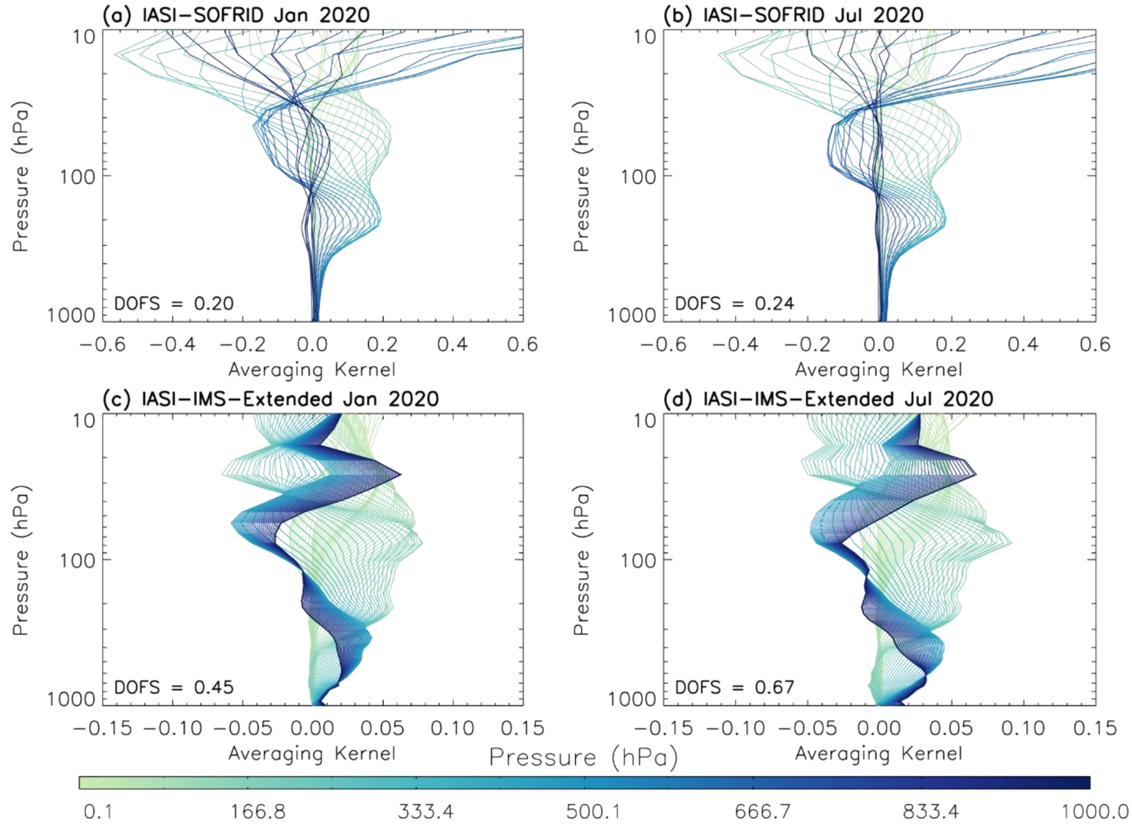

Figure 6.9: Average AKs above Europe for IASI-SOFRID in (a) January 2020 and (b) July 2020. Average AKs above Europe for IASI-IMS-Extended in (c) January 2020 and (d) July 2020. AKs are shown from 10 – 1000 hPa. Note the differing range on the AK axis between the two products.

6.3.1.1 GOME-2B trend

In the GOME-2B record, there is a large negative trend between 2015 and 2020 of -1.8 DU year^{-1} (Figure 6.10). This large negative trend is not consistent with other observations, such as ozonesondes (Section 5.4.3), and is most likely due to UV degradation of the instrument. With the aim to establish the relative impact of 2020 tropospheric O_3 to the previous years, detrending the record is appropriate, to account for the strong negative trend. Using a linear model to detrend the data creates a pattern within the record (Figures 6.10(a) and 6.10(b)), of very low values in 2017, increasing to 2020. This suggests that the trend from 2015 to 2020 is not linear, with a larger negative trend between 2015 and 2017, and a smaller negative trend between 2017 and 2020. Therefore, a non-linear model (2nd order polynomial) has been used to detrend the data (Figures 6.10(c) and 6.10(d)). This produces a record without the pattern of dipping in 2017 and increasing to 2020. The R^2 value is also slightly better for the polynomial trend line, with 0.58, compared to 0.55 for the linear trendline. The detrended record shown in Figure 6.10(d) is added to the average O_3 across the original record (17.6 DU), with the detrended record used in the analysis shown as the black line in Figure 6.10(e).

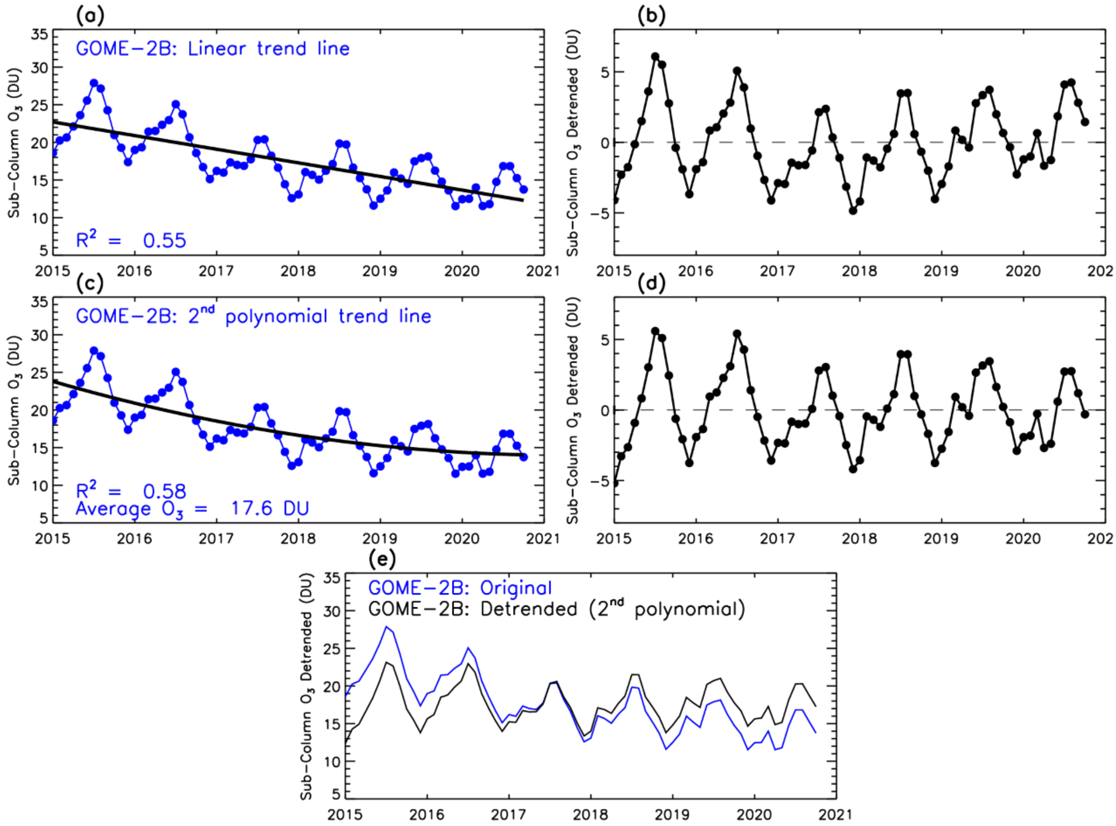

Figure 6.10: Timeseries of European monthly average sub-column (surface – 450 hPa) O_3 record (DU) derived from GOME-2B between January 2015 and October 2020. (a) Original GOME-2B record for 2015 – 2020 with a linear trend line. (b) GOME-2B detrended using the linear trend model. (c) Original GOME-2B record with a 2nd-order polynomial trend line. (d) GOME-2B detrended using the 2nd-order polynomial trend model. (e) Original GOME-2B record and detrended GOME-2B record, using the 2nd-order polynomial trend model.

6.3.1.2 OH calculation

IASI composition data from MetOp-B is used to extend the methodology from Chapter 4, to investigate what information the satellite observations can provide about OH in 2020. The IASI-IMS-Extended record of O_3, H_2O and CO and RAL's IASI CH_4 retrieval scheme record of CH_4 from 2018 – 2020 is used in the method developed in Chapter 4, calculated over the broader 400 – 800 hPa pressure layer. The photolysis rate constant for O_3 (j_1) used are daily averages (at 9.30 LST) from a TOMCAT simulation of 2010, which is repeated annually in the calculation.

6.3.1.3 Satellite uncertainties

The retrieval error calculated by RAL ($\boldsymbol{S_x}$ (solution error covariance matrix) in Section 3.4.1.1), represents the random error of the retrieval (Table 6.1 and Figure 6.11). For GOME-2B the average random error across the record is 8.2 DU (46.7%). As in Chapter 5 (Section 5.3.1.3) and Pope et al. (2015) the random errors will partially cancel out due to averaging across multiple grid-box values. The errors have been scaled (by $\frac{1}{\sqrt{N}}$) using N as the number of days in the month with retrievals. GOME-2B has an average random error of 1.5 DU (8.4%). For the IASI-IMS-Extended record, to represent the uncertainty in the presented monthly means, the standard deviation for the retrievals for each grid-box (2.8° × 2.8°) across Europe has been calculated for each day. This provides a representation of the range in values from the satellite retrievals in every grid-box each day. This standard deviation has been averaged across the grid-boxes and over each month. The average uncertainty across 2018 – 2021 is 4.7 DU (23.1%). This uncertainty estimate has been scaled as above, to highlight the impact of multiple measurements on the uncertainty. The averaged scaled uncertainty is 0.85 DU (4.2%). As in Chapter 5, these random errors are large and should be considered when interpreting the results.

Instrument	**Average random error/ uncertainty for each grid-box**	**Range in monthly averages**	**Scaled random error/uncertainty for monthly averages**	**Range in scaled monthly averages**
GOME-2B	8.2 DU (46.7%)	34.7% – 67.9%	1.5 DU (8.4%)	3.8% – 10.7%
IASI-IMS	4.7 DU (23.1%)	18.5% – 29.7%	0.85 DU (4.2%)	3.3% – 5.6%

Table 6.1: Summary of average random errors for GOME-2B and uncertainty for IASI-IMS-Extended.

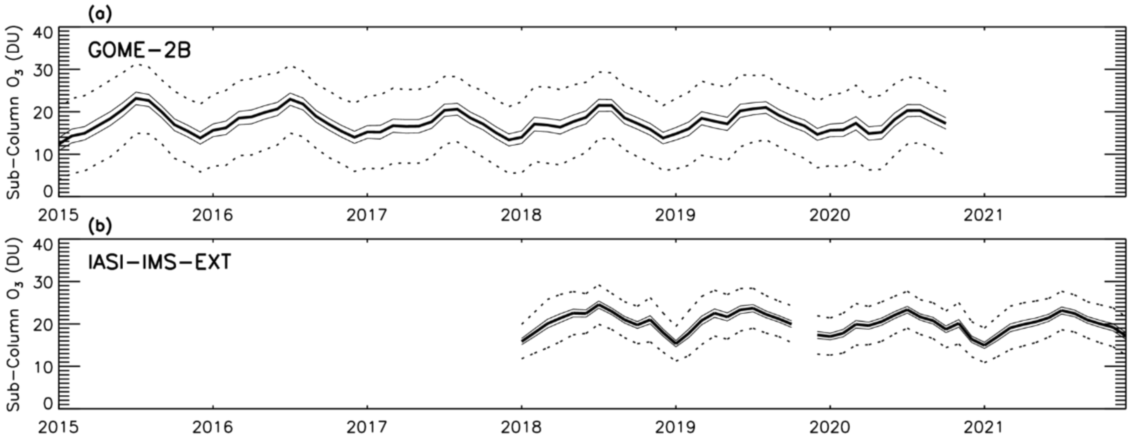

Figure 6.11: Sub-column O_3 (surface – 450 hPa) record of (a) GOME-2B (detrended) and (b) IASI-IMS-Extended between 2015 – 2021. For (a) the monthly averaged random error is shown as ± the record (dotted lines) and the scaled random error is shown as ± the record (solid thin lines). For (b) the uncertainty is shown as ± the record (dotted lines) and the scaled uncertainty is shown as ± the record (solid thin lines).

6.3.2 Ozonesondes

The ozonesonde data is processed by the same methodology as in Chapter 5, deriving tropospheric sub-columns (surface – 450 hPa). The ozonesonde record was averaged for each month from 2000 – 2020 and across all profiles which sit within the European domain. The locations of these launch sites during the time period 2000 – 2020 are shown in Figure 6.12. Only 7 sites, all in central Europe, provided profiles (after filtering) in 2020. This highlights the reduced spatial coverage and sampling of the ozonesonde record, especially in comparison with that of the satellite records.

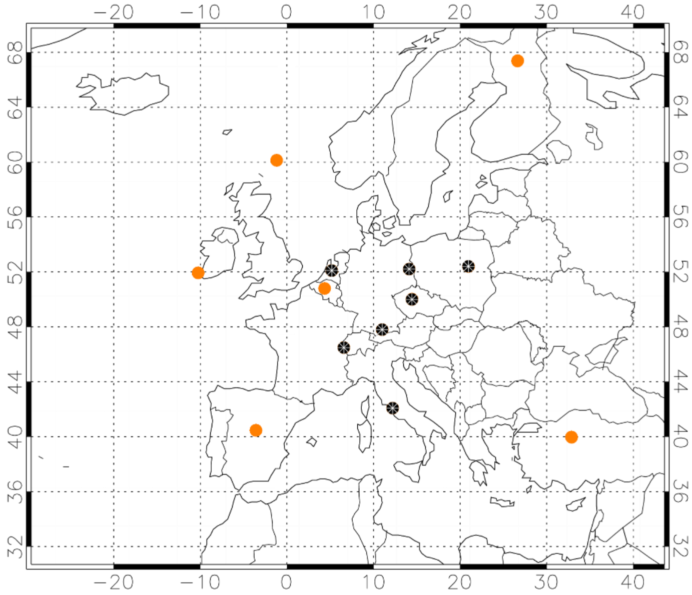

Figure 6.12: Locations of ozonesonde launch sites for ozonesonde record between 2000 and 2020. Sites with launches in 2020 are shown in black with a white asterisk. Sites with launches in 2000 – 2019 (but not in 2020) are shown in orange.

6.3.3 Surface data

The surface measurements used here are from the European Monitoring and Evaluation Programme (EMEP), a network of monitoring sites, providing measurements of many atmospheric species from the 1970s to the present. The EMEP surface monitoring data is provided in the database EBAS (EBAS, 2022), which is operated by the Norwegian Institute for Air Research (NILU) (Tørseth et al., 2012). Here, EMEP data from surface sites between 2010 – 2020 is used. There are 165 sites across Europe providing data during this time period, with 115 sites that provide above 90% of a complete monthly timeseries (Figure 6.13). The EMEP data has a timestep of around 1 hour, which is averaged for each site, to create a daily and then monthly average timeseries. To create a monthly mean anomaly timeseries, the sites were only included if for each month, 10 out of the potential 11 years (2000 – 2020) were available. The instrument used to measure O_3 has a precision of ~ ± 2% - 3% (Monteiro et al., 2012; Wilson et al., 2012).

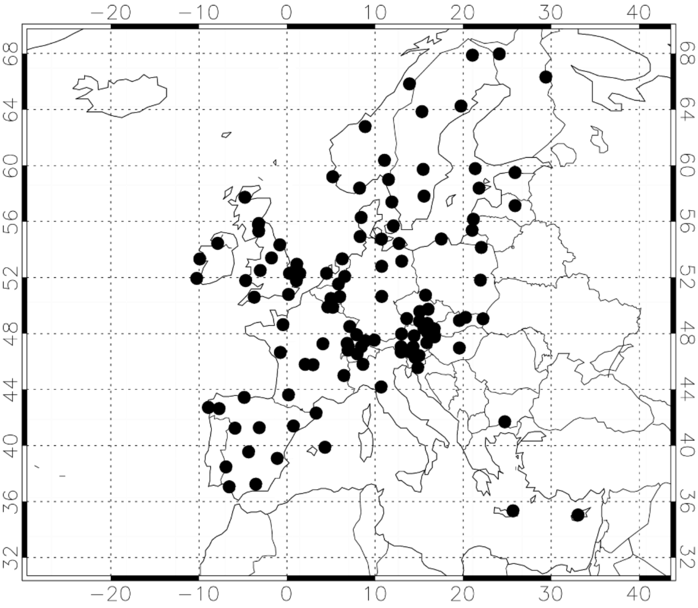

Figure 6.13: Locations of 115 EMEP sites used in this analysis (90% monthly data available from the 2010 – 2020 timeseries).

6.3.4 TOMCAT model

The model was run for 2017 – 2020, with one year of spin-up. The sources of the surface emissions fields are the same as in Chapter 5 (Table 5.2). The major difference between the model as described in Chapter 5 and here, is the use of ERA-5 meteorological fields to force the model, compared to the ERA-Interim fields used in Chapter 5 (ERA-5 spatial resolution is higher and has improvements in model physics, core dynamics and data assimilation (Hersbach et al., 2020)). The switch from ERA-Interim to ERA-5 was required as the ERA-Interim reanalysis product only covers 1979 – 2019, .

The model was run with these surface emission files as a 'business as usual' (BAU) case from the years 2017 – 2021. The model was also run using scaled emissions, based on either 2020 or 2021. To determine the impact of meteorology, the model was run for the years of 2017 – 2019 using the fixed scaled emissions of 2020. However, this was not a continuous run between 2017 – 2019, instead, the years were run individually, using initial conditions from the BAU scenario at the start of each year. This was implemented to determine the impact of the scaled emissions in each individual year, rather than a cumulative effect from the previous years.

For 2020 and 2021, the anthropogenic surface emission fields are scaled based on changes in activity data presented in Forster et al. (2020). The scaling factors were calculated by R. Pope (University of Leeds, National Centre for Earth Observation), varying monthly and spatially across the TOMCAT 2.8° × 2.8° grid. The scaling factors also varied by species, covering NO_x, CO, SO_2, BC, OC and VOCs, with one scaling factor for all VOC species. The scaling factors were applied to the anthropogenic emissions only. An example of the scaling factors applied to the NO_x emissions is shown in Figures 6.14 and 6.15. In this example for NO_x, in January and February there is a limited global reduction, with only reductions seen over China. From March to December there are reductions in the majority of regions of the globe, with some of the highest percentage reductions shown in April. The scaled anthropogenic emissions are also shown in Figure 6.16, in comparison with the unscaled BAU emissions. In 2021, the scaling factors present a continuation of the reduction in emissions across the species impact most by the scaling, with a relatively consistent reduction compared to the BAU emissions across all months of 2021 (Figure 6.16).

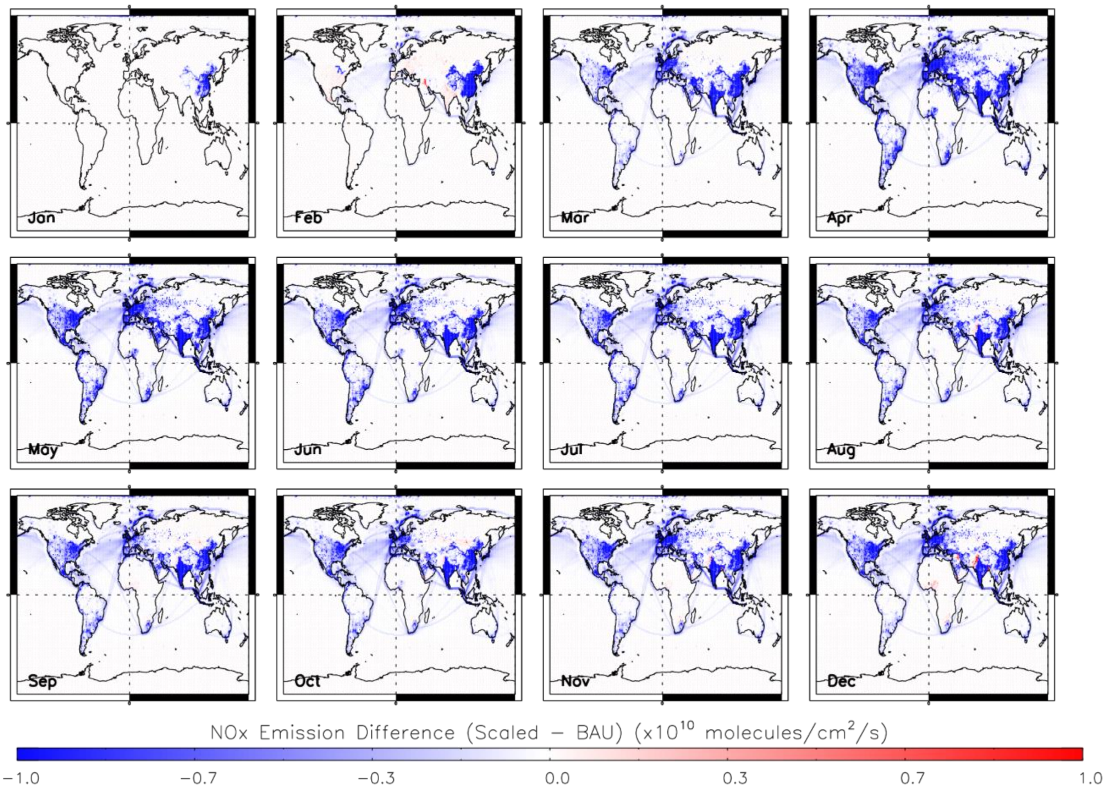

Figure 6.14: The absolute difference in NO_x emissions from applying scaling factors for all months of 2020 ($\times 10^{10}$ molecules cm^{-2} s^{-1}).

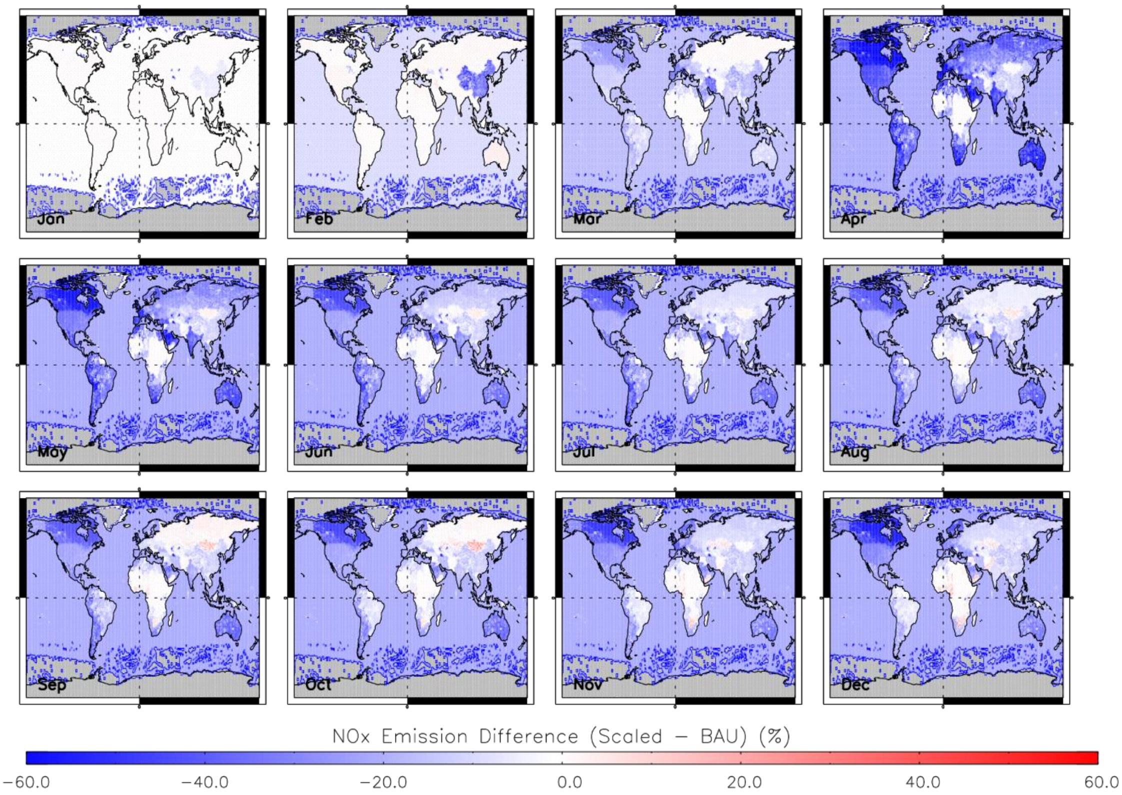

Figure 6.15: Same as Figure 6.14, but the difference is shown as a percentage.

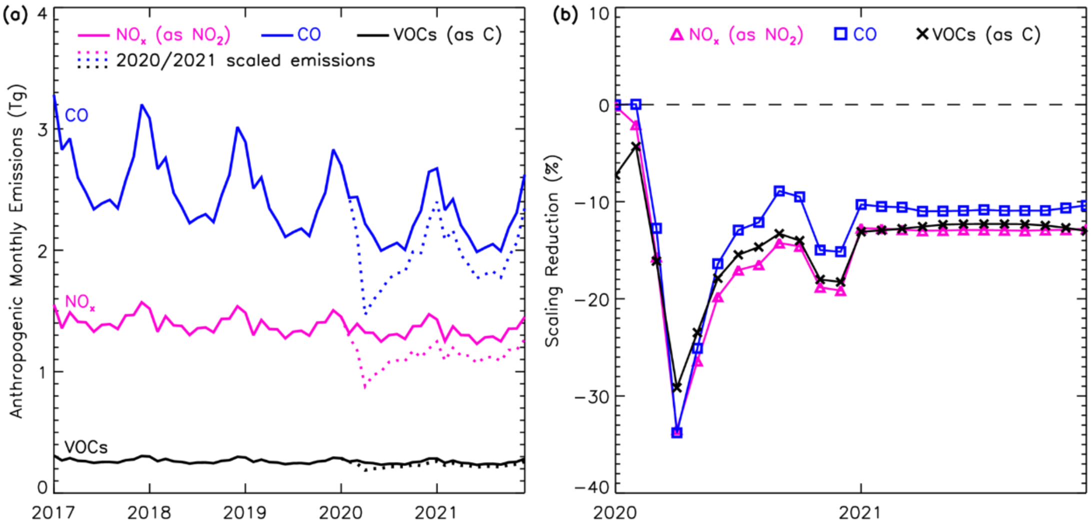

Figure 6.16: (a) European anthropogenic surface emissions (Tg) for NO$_x$ (as NO$_2$), CO and a combination of VOCs (as Carbon) between 2017 – 2021. The solid line represents the emissions used in the BAU scenario and the dotted represents the emissions used for the scaled emission scenario in 2020 and 2021. (b) Percentage reduction of the scaled emissions of NO$_x$, CO and a combination of VOCs during 2020 and 2021, compared to the BAU emissions.

6.4 Results & discussion

6.4.1 Satellite records

6.4.1.1 GOME 2B

The GOME-2B sub-column tropospheric O_3 record from January 2015 to October 2020 shows a strong negative trend (linear trend of -1.8 DU year^{-1}) during this time period (Figure 6.17). In order to study 2020 relative to the other years, without the influence of a strong negative trend, the record has been detrended using a 2nd order polynomial trend (Figures 6.10 and 6.17). The detrended monthly anomaly timeseries (Figure 6.17) shows a negative anomaly of -2.4 DU (-15.8%) in April and -2.8 DU (-18.2%) in May 2020. Two standard deviations (2σ) across the entire monthly record is 2.0 DU (12.1%), which signifies that ~ 95% of the data lies within this value from the average. Therefore, the two months of April and May 2020 are larger than 2σ from the average, which shows the relative size of these anomalies compared to the record. The following months of June, July and August also show large (but within 2σ from the mean) negative anomalies, of -1.4 DU (7.7%), -1.5 DU (7.2%) and -1.2 DU (6.0%), respectively. These results provide further evidence, building on the literature (Steinbrecht et al., 2021; Ziemke et al., 2022), that there was a large tropospheric O_3 reduction in spring/summer of 2020, and also that the reduction occurred specifically in Europe.

Spatially, in March there is a mixture of positive and negative anomalies, including some large positive anomalies in NE Europe. National lockdowns across some parts of Europe did start around mid-March (e.g. Italy), however this was not universal across Europe. An enhancement of O_3 in this region could be due to reductions in surface emissions of NO_x, which would reduce the O_3 titration effect by NO, leading to increased O_3. Increased O_3 in this region could also be due to enhanced O_3 production (from increased precursor gas emissions, or a meteorological effect e.g. high temperatures), reduced O_3 destruction in this region or variation in transport of O_3. Consistent negative anomalies across the European domain begin in April and May 2020, apart from some positive anomalies over NE Europe (Russia and the Baltic states) in April (Figure 6.18). In May, the negative anomalies are larger over the continent, compared to the Atlantic, which could indicate a greater impact from emissions as they are predominantly emitted above the land. The consistency of negative anomalies across most of the domain in May indicates how wide-spread this tropospheric O_3 reduction was, pointing to a significant event e.g. consistent lockdowns across Europe. Conversely, in June, the negative anomalies are largest over the Atlantic, with smaller negative anomalies over land, which could suggest the reduction is from O_3 transported across the Atlantic. In July, southern Europe, particularly over the Mediterranean, shows small positive anomalies, with large negative anomalies across the domain in a band above 40°N and below 60°N. In August, the negative anomalies are smaller and less consistent than in previous months, and are predominantly across the central European continent, with small positive anomalies in the North.

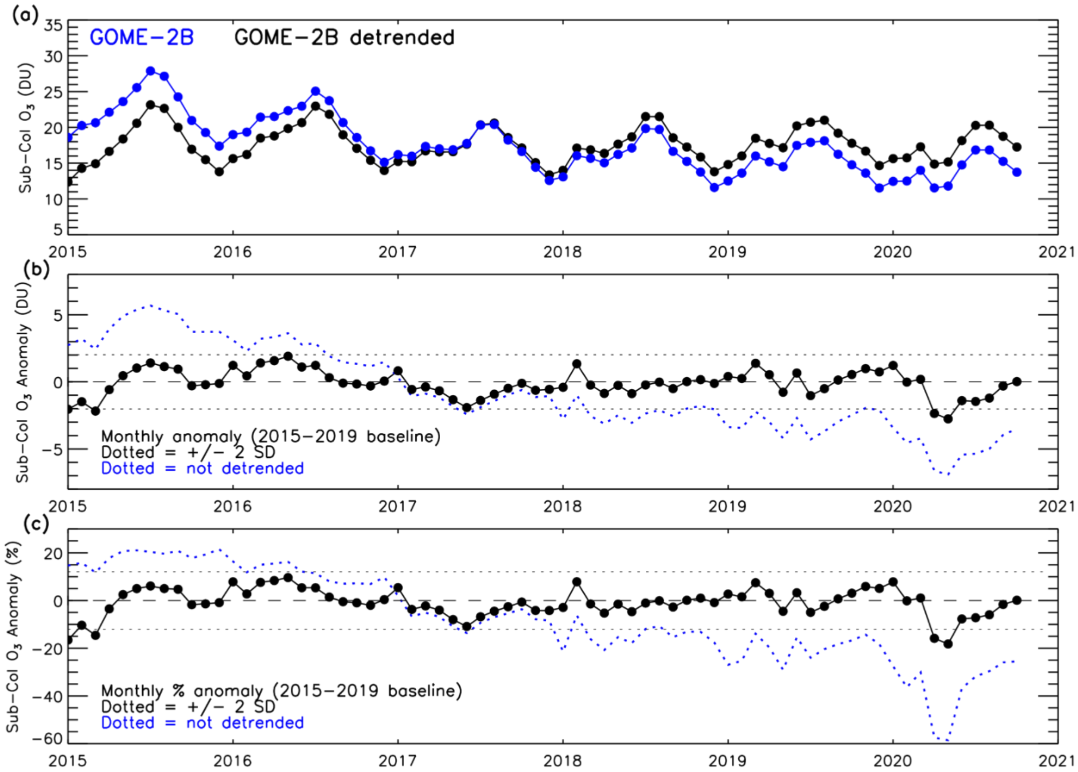

Figure 6.17: (a) European monthly average sub-column (surface – 450 hPa) O_3 record (DU) derived from GOME-2B between January 2015 and October 2020. (b) Monthly mean absolute anomalies for the records (2015 – 2019 monthly average baseline). (c) Monthly mean percentage anomalies (2015 – 2019 monthly average baseline). The blue dots/lines indicate the original record prior to detrending (dashed in panels (b) and (c), the black dots/lines represent the detrended record. Black dotted lines indicate ± 2σ from the average of the record.

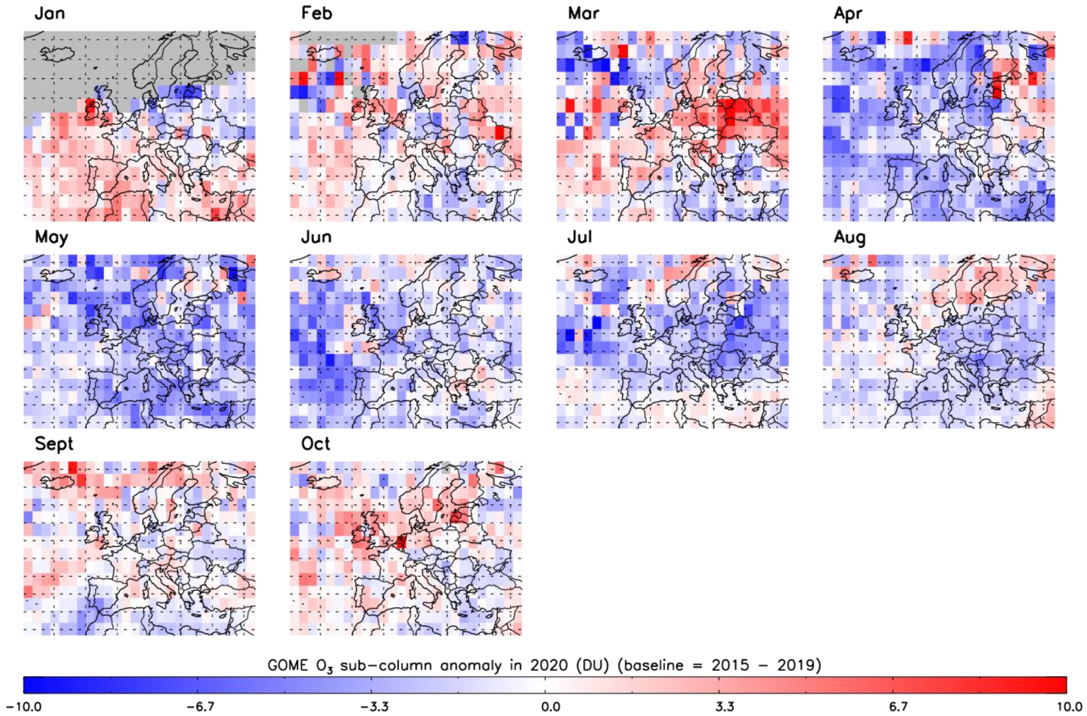

Figure 6.18: GOME-2B sub-column (surface – 450 hPa) O_3 anomaly for January – October 2020 (DU) relative to a monthly average baseline (2015–2019).

6.4.1.2 IASI-IMS-extended

In 2020, across the European domain, the months of April and May show large negative anomalies in the IASI-IMS-extended O_3 record, of -2.4 DU (-12%) and -1.6 DU (-7.6%), respectively (Figure 6.19). The anomalies calculated here, are compared to a relatively short monthly average baseline (2018 – 2019). Both of these values are lower or very close to -2σ from the mean, which is 1.5 DU (7.6%) (calculated across the entire monthly record). The results are similar in April for over just land, with a negative anomaly of -2.3 DU (-12.5%), and larger for May, at -2.6 DU (-13.1%). Both months are lower than -2σ (1.7 DU or 9.1%). There are also relatively large negative anomalies for the rest of 2020, especially in June (-0.9 DU/-3.9%), August (-1.0 DU/-4.6%) and October (-1.1 DU/-6.0%). The anomaly values over land are similar for most months, but do show a larger negative anomaly in July (difference of 4.8%). Again, as with GOME-2B, these results indicate that there was a large tropospheric O_3 reduction in the spring/summer of 2020, and it did occur across Europe in particular.

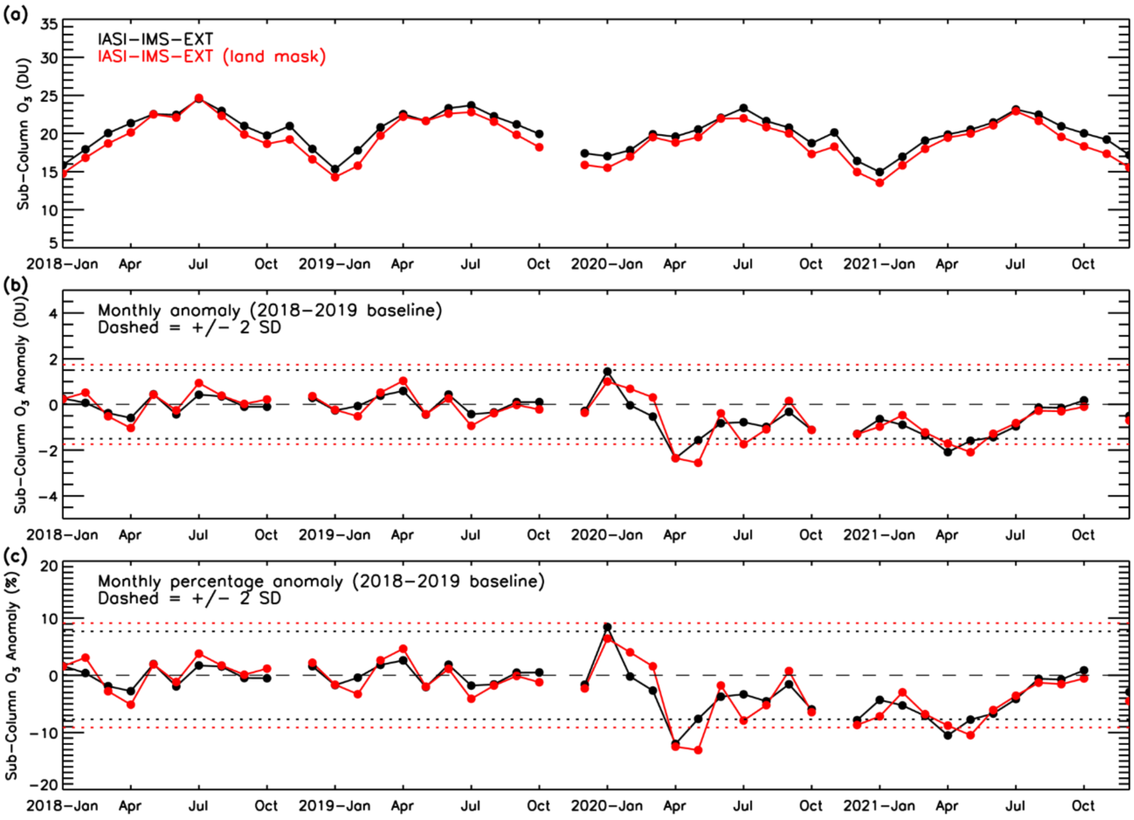

Figure 6.19: (a) European monthly average sub-column (surface – 450 hPa) O_3 record (DU) derived from IASI (IASI-IMS-extended) between 2018 and 2020. (b) Monthly mean absolute anomalies for the records (2018 – 2019 monthly average baseline). (c) Monthly mean percentage anomalies (2018 – 2019 monthly average baseline). The black lines/dots represent an average across the whole domain, the red lines/dots represent an average for the domain with a land mask applied (Figure 6.7). Dotted lines indicate ± 2σ from the average of the record.

Spatially, the IASI-IMS-Extended record shows fairly consistent negative anomalies for April 2020, with larger negative anomalies in northern Europe, and the north Atlantic (Figure 6.20). In May 2020, the negative anomalies are predominately over central continental Europe and Northern Europe, which again could indicate a reduction in anthropogenic surface emissions, with positive anomalies in the southern Atlantic. The distribution is reversed in June 2020, with positive anomalies across central continental Europe and negative anomalies elsewhere. In July 2020, there are positive anomalies in a band from around 30°N to 40°N, and negative anomalies above 40°N, with the largest being in eastern Europe, a pattern which is similar to that seen in GOME-2B. The consistency between the spatial anomalies from GOME-2B and IASI-IMS-Extended, despite the potential differences in sampling pattern and vertical sensitivity between two satellite instruments, suggests confidence in these results.

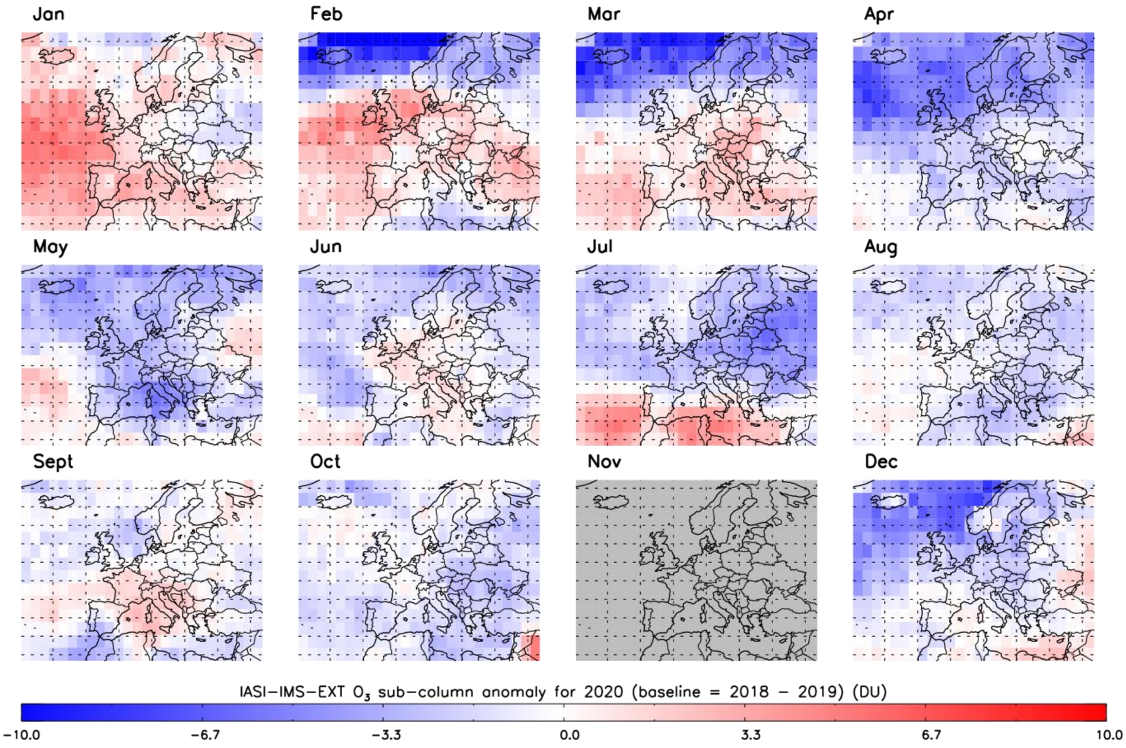

Figure 6.20: IASI-IMS-extended sub-column (surface – 450 hPa) O_3 anomaly for each month of 2020 (DU) relative to a monthly average baseline (2018–2019).

To investigate the significance of the negative anomalies seen in the spring/summer of 2020, these months are compared with a longer timeseries of the IASI-IMS-extended record (2008 – 2021) which will better represent the average baseline state. The Metop-B data (shown in Figure 6.20) and Metop-A IASI-IMS-extended data for 2008 – 2017 (processed for 1-in-10 days) are combined (Figure 6.21). The partially processed 1-in-10 day data shows a good agreement with the record processed for more days, suggesting it is suitable for this comparison. In comparison with a longer record, the negative anomalies of the spring/summer 2020 do stand out, as being around -2σ (2.1 DU/10.4%). April and May 2020 show negative anomalies of -2.4 DU (-12.4%) and -1.9 DU (-9.3%). These negative anomalies are very similar to those compared to a monthly average baseline of only 2018 – 2019. June, July and August, show anomalies of around -5%, which is also similar to anomalies calculated from the shorter baseline. This suggests that the average of 2018 – 2019 is relatively comparable to a baseline from 2008 – 2019. The broadly negative anomalies across the whole of 2020 are also unusual compared to the other years, where we see individual months with large negative anomalies. Events with negative anomalies which are as large (or larger) than the spring/summer 2020, include January 2012 (-18.2%), December 2014 (-13.0%) and Spring 2016 (-11.5%), however, such low values across most months of the year is unusual compared to the long-term record, with most years showing a range of positive and negative anomalies. This suggests that 2020 was influenced over an extended period of time e.g. by reductions in surface emissions and/or a meteorological-based process.

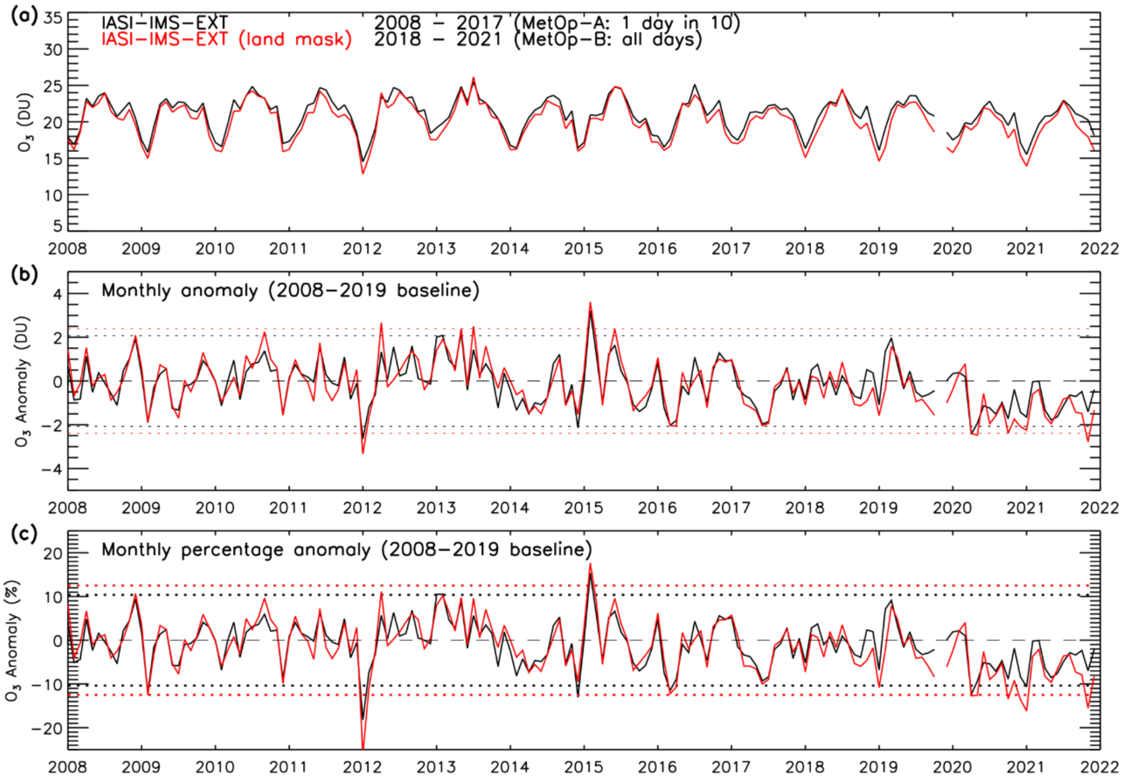

Figure 6.21: (a) European monthly average sub-column (surface – 450 hPa) O_3 record (DU) derived from IASI (IASI-IMS-extended) between 2008 and 2021. For 2008 – 2017, the data is partially processed (1-in-10 days), for 2018 – 2021, the data is fully processed (all days) (see Section 6.3.1). (b) Monthly mean absolute anomalies for the records (2008 – 2019 monthly average baseline). (c) Monthly mean percentage anomalies (2008 – 2019 monthly average baseline). The black lines represent an average across the whole domain, the red lines represent an average for the domain with a land mask applied. Dotted lines indicate ± 2σ from the average of the record.

6.4.1.3 IASI-SOFRID

The longer timeseries IASI-IMS-Extended record (Figure 6.21) is compared to another retrieval scheme of IASI, IASI-SOFRID (2008 – 2020 from MetOp-A). In 2020, the IASI-SOFRID record shows negative anomalies from April – September, with the largest in April at -1.4 DU (-8.1%), which is larger than the -2σ value of 1.0 DU (6.0%) (Figure 6.22). There is a large off-set between the two retrieval schemes, with the IASI-SOFRID record being on average -3.0 DU lower. Despite the offset, the records are well correlated (r = 0.76). The difference between the records, may be in part due to the difference in vertical sensitivity, with IASI-IMS-Extended being more sensitive in the lower troposphere (Figure 6.9). Across the complete time period, the anomalies are generally larger in the IASI-IMS-Extended record compared to IASI-SOFRID. In 2020, the timing of the large negative anomaly is fairly consistent, both showing large negative anomalies in April. IASI-SOFRID shows a smaller reduction in May compared to IASI-IMS-Extended, where May shows comparably low values to April. Towards the end of the year, the IASI-IMS-Extended record shows large negative anomalies which are not present in the IASI-SOFRID record, which shows smaller negative and then positive anomalies from around August onwards. Therefore overall 2020 in the IASI-SOFRID record looks more consistent with the previous years, contrasting to the continuation of low O_3 in IASI-IMS-Extended.

Spatially, April and May show negative anomalies across the European domain for IASI-SOFRID, with fairly consistent negative anomalies everywhere in April, apart from across the Iberian peninsula (Figure 6.23). In May, the negative anomalies are over central Europe e.g. France, and SE Europe e.g. Turkey, with near-zero anomalies across the rest of the domain. In June there are negative anomalies over the Iberian peninsula and Scandinavia, with near-zero anomalies across central Europe and in July there are negative anomalies consistently between 36°N and 52°N. Although the anomalies are smaller than IASI-IMS-Extended, the similar spatial pattern gives confidence to the spring/summer anomaly results.

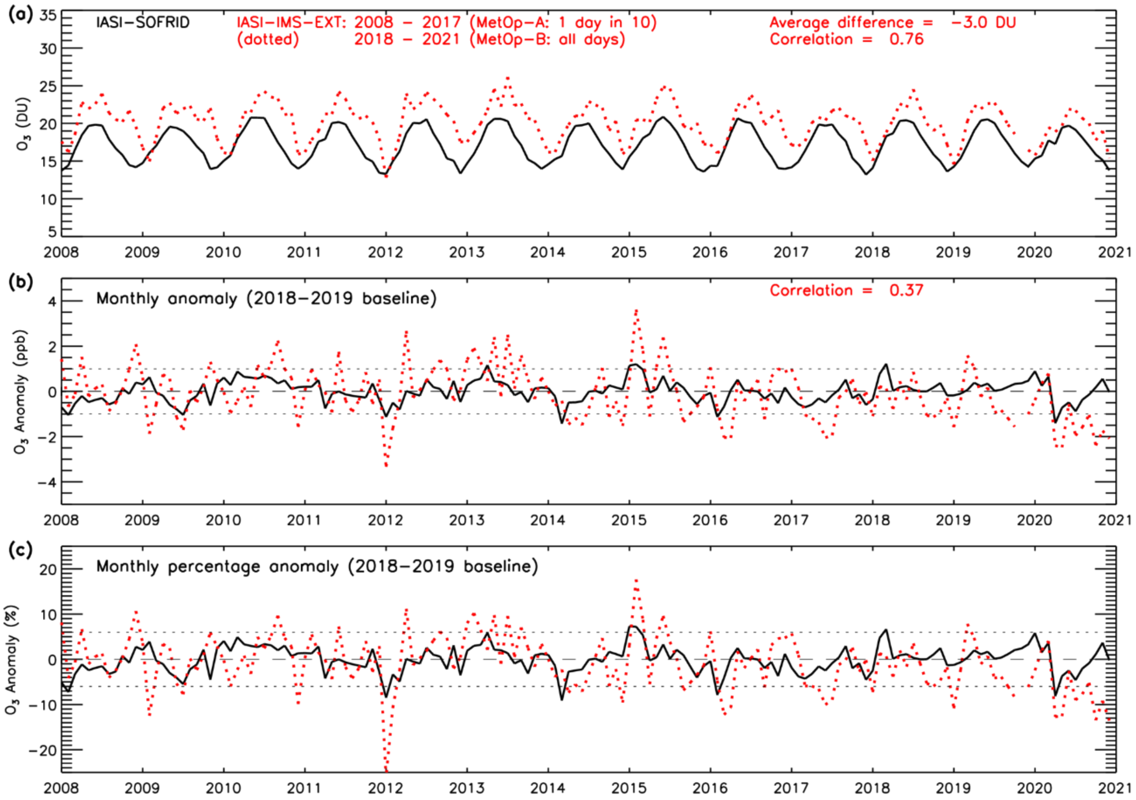

Figure 6.22: As Figure 6.21, with comparison to the IASI-SOFRID record. IASI-SOFRID (black solid line) is shown as tropospheric sub-columns (DU) between 2008 and 2021. The IASI-IMS-Extended record (dotted red line) has had a land mask applied, for consistency with the IASI-SOFRID product used (land-only). Black dotted lines indicate ± 2σ from the average of the record for IASI-SOFRID.

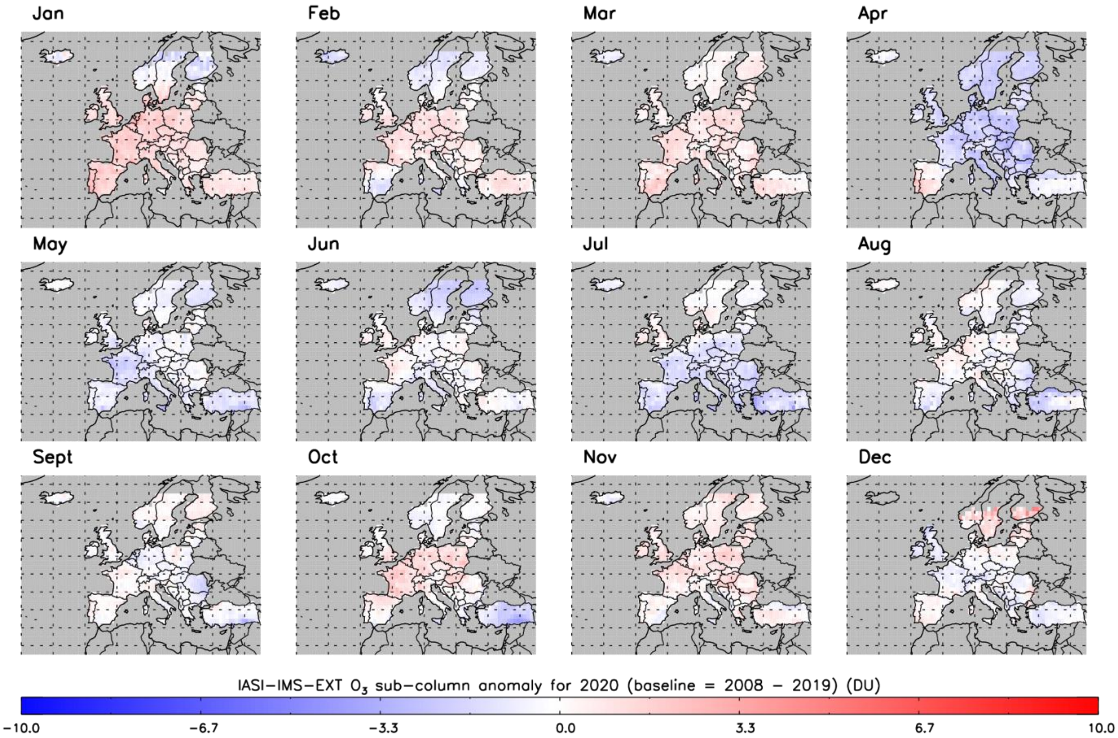

Figure 6.23: IASI-SOFRID sub-column (surface – 450 hPa) O_3 anomaly for each month of 2020 (DU) relative to a monthly average baseline (2008–2019).

6.4.1.4 Satellite data comparison

A comparison of the two RAL satellite datasets (IASI-IMS-Extended and GOME-2B) with both datasets relative to the same monthly average baseline (2018 – 2019) is shown in Figure 6.24. The two records are well correlated, with a Pearson correlation coefficient of 0.82 for the absolute record, and 0.85 for the anomalies. However, the records do show an average difference of 2.9 DU. This offset is not surprising due to instrumental differences, e.g. UV/Vis vs. IR instrument, and the uncertainty involved in the detrending of the GOME-2B record. In 2020, both records have the largest negative anomalies in April and May, with very similar absolute anomaly values in April (-2.2/2.4 DU), corresponding to -14.7% for GOME-2B and -12.0% for IASI-IMS-Extended. Generally the pattern of negative anomalies across 2020 is similar between the records, decreasing in size from April/May towards the end of the year. Overall, the good comparison in the anomaly plot gives more confidence to the results, suggests that we are seeing a signal of a reduction in lower tropospheric O_3 in the satellite record.

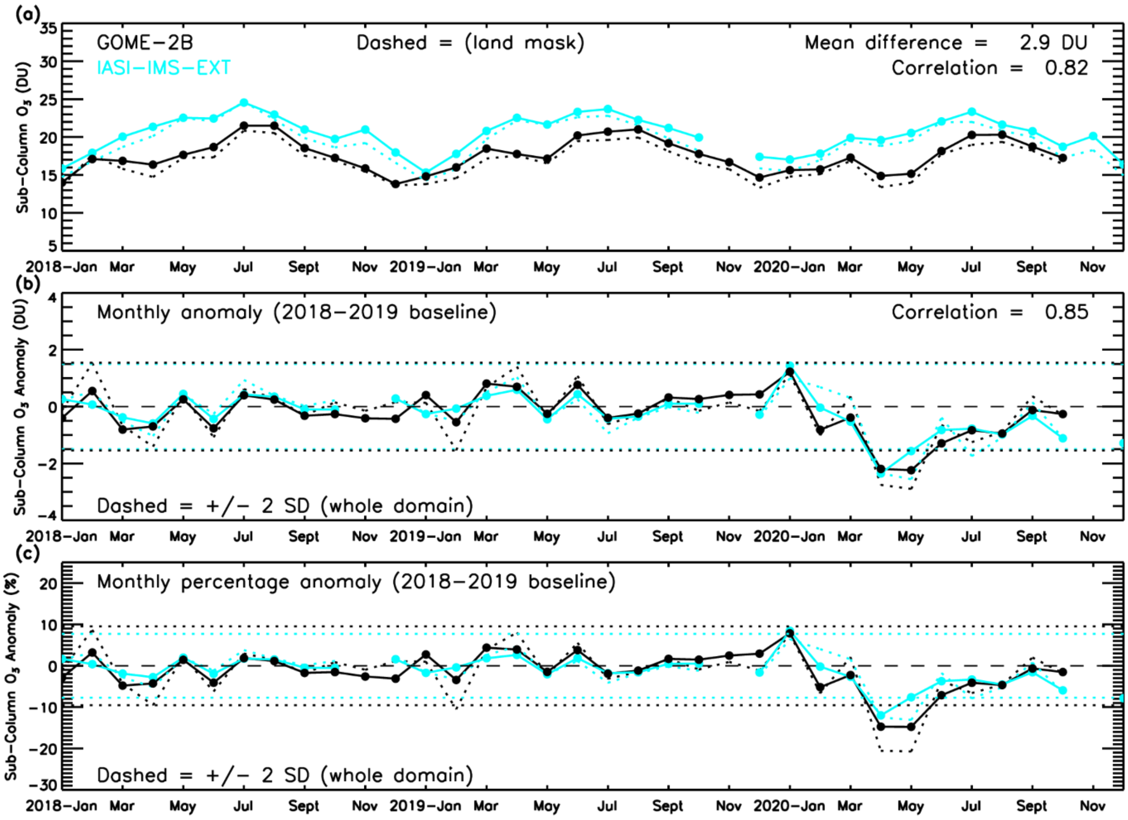

Figure 6.24: (a) European monthly average sub-column (surface – 450 hPa) O_3 record (DU) from IASI (IASI-IMS-extended, light blue line) and GOME-2B (black line) between 2018 and 2021. For the two satellite products, a dashed line represents an average for the domain with a land mask applied. (b) Monthly mean absolute anomalies for the two records (2018 – 2019 monthly average baseline) (DU). (c) Monthly mean percentage anomalies for the two records (2018 – 2019 monthly average baseline). Black dotted lines lines indicate ± 2σ from the average of the record.

6.4.1.5 Satellite observations in 2021

Ziemke et al. (2022) found anomalously low tropospheric O_3 in the spring/summer of 2021, as well as 2020, from their combined NASA satellite product record. The IASI-IMS-Extended record shows a similar story, with large negative anomalies in spring/summer 2021 (Figure 6.19). March, April, May and June all show large negative anomalies, around the value of -2σ, with -1.4 DU (-7.1%), -2.1 DU (-10.5%), -1.6 DU (-7.8%) and -1.4 DU (-6.7%) respectively. The land mask record anomalies show very similar values to the whole domain in 2021, especially from June onwards, which is more consistent with previous years e.g. 2018 – 2019, as opposed to 2020. As with 2020, in the longer-term IASI-IMS-Extended comparison (Figure 6.21), the negative anomalies in spring/summer 2021 are similar to the shorter record, and this year stands out for having broadly negative anomalies for all months of the year. Overall, the repetition of a large negative anomaly in the spring/summer of 2021, is consistent with the NASA satellite products shown by Ziemke et al. (2022). The recurrence of these low O_3 values suggests a potential continuation of the reduced anthropogenic emissions into 2021, or a feature linked to meteorology, which could be deduced using a model simulation.

6.4.2 Ozonesonde record

For the ozonesonde record, 2020 shows lower values of tropospheric O_3 for most months of 2020, compared to previous years (2000 – 2019, Figure 6.25). The values are around or just below -2σ from the average for March, May, June, July and October. In 2020, July shows the largest anomaly, at -3.2 DU (-15.1%). The other months in spring/summer 2020 also show negative anomalies, with -1.5 DU (-7.5%) in March, -1.5 DU (-6.8%) in May and -2.0 DU (-9.3%) in June. These values are all the same or larger than 2σ for the specific month. Due to the long timeseries, the standard deviation has been calculated for each month. July shows the largest variability over the 11 year timeseries, however, in 2020, the negative anomaly was still larger than the larger 2σ value (12.0%). April also shows a negative anomaly of -0.5 DU (-2.2%), however it is smaller than the other months in spring/summer and not large in comparison to the standard deviation for April (2σ = 7.5%). Steinbrecht et al. (2021) also find the largest monthly negative anomaly for 2020 in July (~ -11%), for a NH average at 6 km altitude (~ near the top of the sub-column used in this study). However, they also find a similarly large negative anomaly for April, which we do not find in our ozonesonde European sub-columns. The ozonesonde record for 2021 also shows large negative anomalies in the spring/summer, especially in April (-1.7 DU/-7.7%) and May (-1.9 DU/-8.8%), which are both larger than -2σ from the average (7.5%/7.3%, respectively). The anomalies are positive from September onwards, with very large positive anomalies in September and November. The number of ozonesonde profiles in the monthly average during 2020/2021 is towards the lower end of the range from 2000-2021, which should be considered in the interpretation of these results. However, the number of profiles for 2020/2021 is still within the range of other years for most months. This is suggests that we can trust these results with respect to number of profiles.

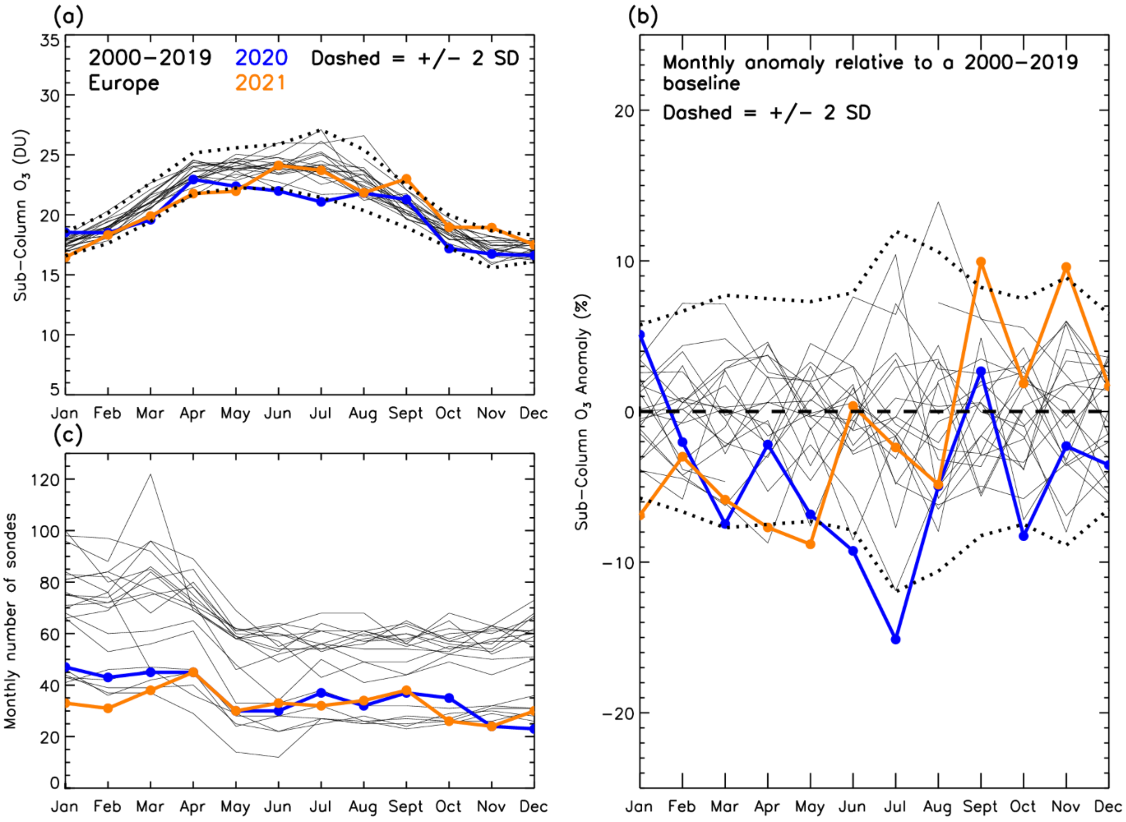

Figure 6.25: (a) Ozonesonde tropospheric sub-column (surface – 450 hPa) O_3 monthly variation (DU) for each year between 2000 – 2021. 2σ range for each month is shown with a dashed line above and below the monthly average. (b) Monthly anomaly of sub-column O_3 relative to a monthly average baseline (2000 – 2019). 2σ displayed as in panel (a). (c) Monthly number of ozonesonde profiles for each year between 2000 – 2021. In each panel, 2020 is displayed in blue and 2021 in orange.

Ozonesondes were launched from only a few sites across Europe from 2000 - 2021 (Figure 6.12), and therefore have a limited spatial coverage and sampling in comparison to the satellite-derived records. Differences in spatial sampling is likely to be a cause of the differences between the records. To account for this difference, for each ozonesonde profile, the sub-column value from the nearest satellite grid-box daily average has been selected to form a co-located satellite record. Co-locating the satellite record to the ozonesondes shows a reduction in the satellite sub-column absolute values, which increases in the difference between the satellite and the ozonesondes, by 2.7 DU for IASI-IMS-Extended and 2.1 DU for GOME-2B (Figure 6.26). The co-located satellite record has an improved correlation (r = 0.82) for IASI, compared to the non-co-located record (r = 0.76). However, for GOME-2B, the correlation is lower for the co-located satellite record (r = 0.19), compared to the non-co-located record (r = 0.63). The ozonesonde record shows the largest negative anomaly in July 2020, which contrasts to the timing of the peak satellite negative anomaly. The co-located IASI record shows a small decrease in July 2020 compared to the non-co-located record, and a larger decrease is seen in the co-located GOME-2B record. These decreases associated with the co-location in July imply that the differences seen in the satellite and ozonesonde records in July may be, in part, due to the difference in spatial sampling. However, this is not the case for all months of 2020, as there are some which show a conflicting story e.g. in April 2020, co-locating the GOME-2B record to the ozonesonde sampling shows a larger negative anomaly, when a smaller negative anomaly would be more in line with the ozonesonde record. This co-location process is likely to have large uncertainties, overall, this partly suggests that some of the differences between the ozonesonde and satellite records (e.g. in July 2020) are due to difference spatial sampling methods.

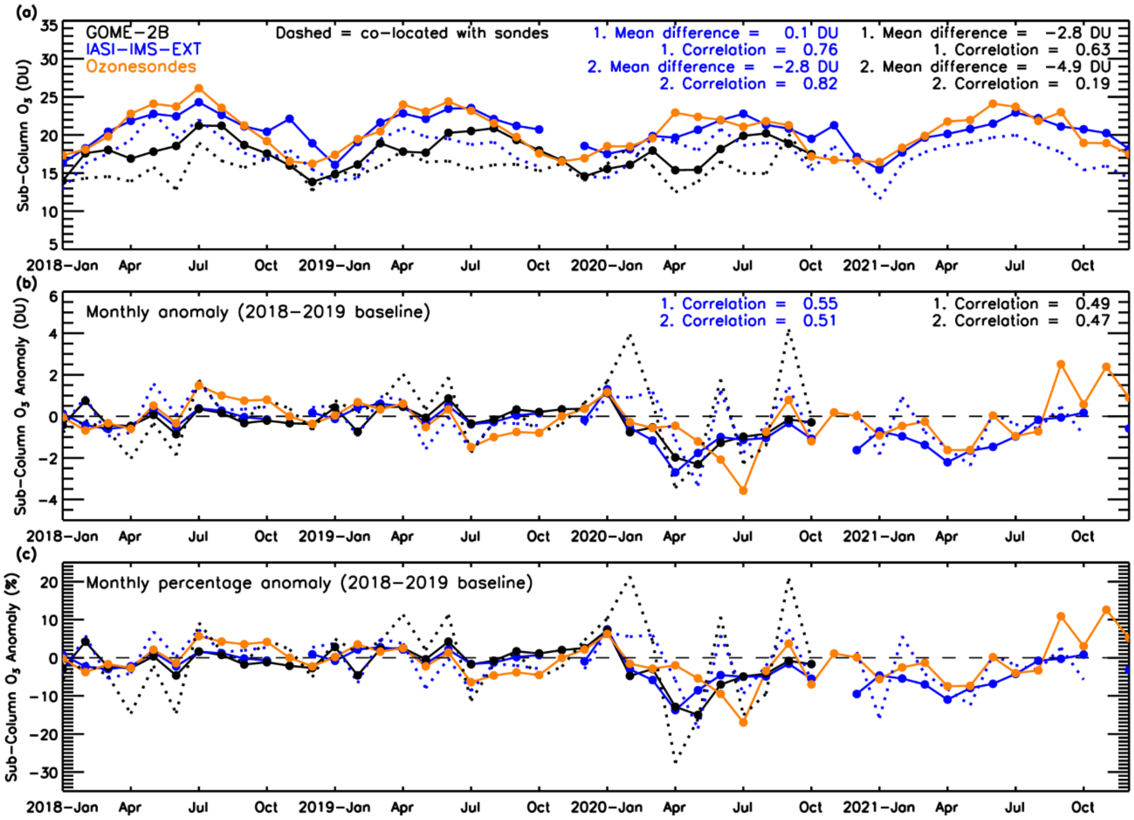

Figure 6.26: (a) European monthly average sub-column (surface – 450 hPa) O_3 record (DU) from IASI (IASI-IMS-extended) (blue solid line), GOME-2B (black solid line) and ozonesondes (orange solid line), between 2018 and 2021. For the two satellite products, a dashed line represents the record co-located to the ozonesondes. The mean difference and correlation are presented for each satellite record with respect to the ozonesonde records. (1) refers to the satellite record before co-location, (2) refers to the satellite record after co-location. (b) Monthly mean absolute anomalies for the records (DU, 2018 – 2019 monthly average baseline). (c) Monthly mean percentage anomalies for the records (2018 – 2019 monthly average baseline).

6.4.3 Surface data

The EMEP surface O_3 record provides an opportunity to compare this study of the free troposphere, using satellite-derived observations and ozonesonde measurements, with the surface. Information on O_3 concentration at the surface is very important as this is where it interacts with people and plants, causing negative health impacts. There are large negative anomalies in the monthly mean across the 115 sites in late spring/summer of 2020, with smaller negative/positive anomalies in early spring (Figure 6.27). There is an anomaly of -0.4% in March, +0.7% in April, -5.0% in May, -7.1% in June, -15.2% in July and -1.7% in August. This pattern follows closely to that seen in the ozonesondes (Section 6.4.2), although March has a comparatively lower negative anomaly than the other months in the surface data, and April has a small positive anomaly. Ozonesondes have a greater sensitivity near the surface and lower troposphere, compared to satellites, which could explain the good agreement between the timings of the 2020 negative anomalies for the surface sites and the ozonesondes. As with the ozonesondes (Figure 6.25), 2σ has been calculated for each month, due to the long timeseries available. The pattern of monthly 2σ is similar to the ozonesondes, with the largest values in summer and lowest in winter. For the surface data, the large negative anomalies in June and July are approximately equal to -2σ from the mean (8.3% in June, 14.9% in July). The negative anomalies in March and May are much smalller than the values of -2σ from the mean (8.2% in March, 9.7% in May). The larger surface negative anomalies in summer, not spring, could indicate that reductions in surface precussor emissions were more influential on FT O_3 in summer, rather than spring, as emissions will be the dominant influence at the surface.

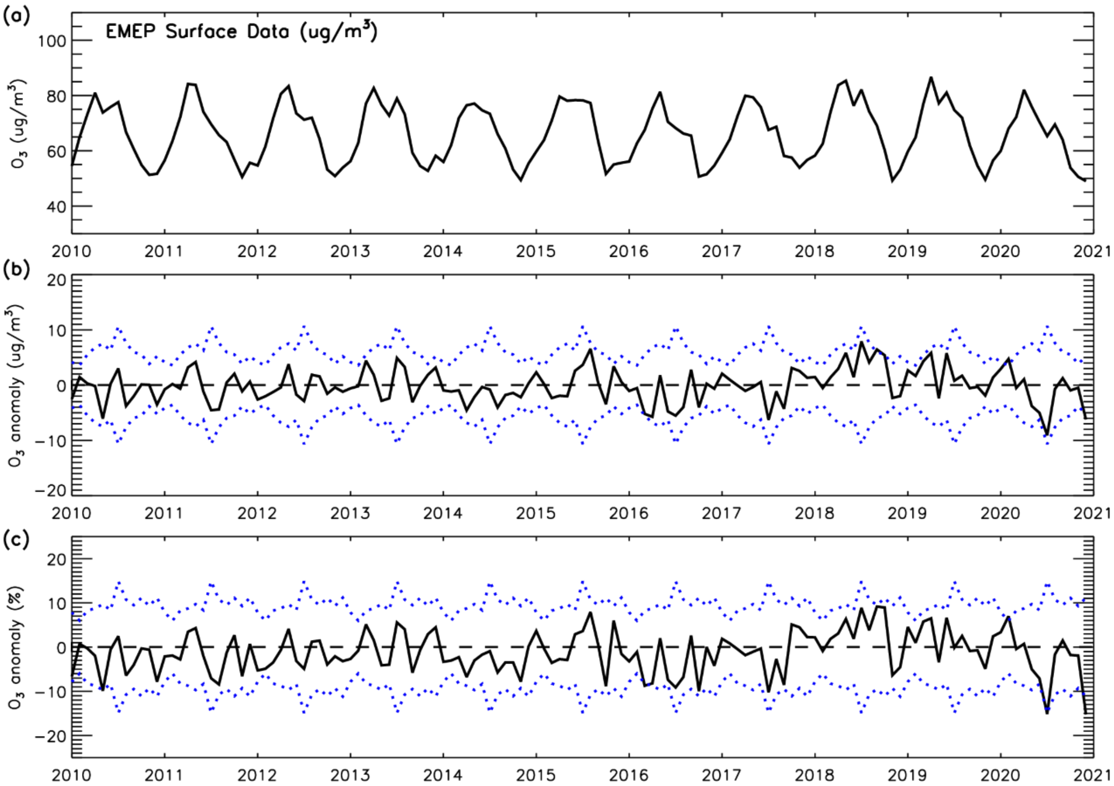

Figure 6.27: (a) EMEP surface tropospheric O_3 record for 2010 to 2020 (µg m^{-3}). (b) Monthly mean absolute anomalies (2010 – 2019 monthly average baseline) (µg m^{-3}). (c) Monthly mean percentage anomalies (2010 – 2019 monthly average baseline). The solid black lines represents the mean value (for the 115 surface sites). The dotted blue lines represents ± 2σ from the average. Note the differing units to other analysis in this chapter.

The values presented here are daily averages, but for a more consistent comparison, the surface data was filtered to between 8am and 11am LST to correspond with the satellite overpass time. The filtered timeseries for the surface data is very similar to the unfiltered timeseries, with very similar negative anomalies, peaking at -15.0% in July.

Spatially, in April 2020 there are large positive O_3 anomalies across central Europe, e.g. France, Germany, Austria, Northern Italy, Belgium and negative anomalies across Northern Europe and the Iberian Peninsula (Figure 6.28). This spatial distribution pattern is consistent with the surface data anomalies presented by Ordóñez et al. (2020) and also by Cuesta et al. (2022) (Figure 6.3), which compares the 1st – 15th April 2020 with the same period in 2019. Therefore, the spatial distribution of anomalies between 2019 and 2020 seems to be consistent between 2020 and a longer baseline, as in this study. A possible explanation of positive O_3 anomalies in April at the surface is that a reduction in NO_x, reduced the suppression of O_3 by NO that happens in very high NO_x environments, which are common across the industrial regions of central Europe. May and June 2020, show mostly negative anomalies across the domain, with a small region of positive anomalies around Belgium, the Netherlands and the UK. In July 2020, the sites are consistently negative across the domain, apart from a few on the Iberian Peninsula, with the largest anomalies found across central Europe. August shows a similar pattern to May and June. The good agreement between the ozonesondes and the surface data may also be due to the location of the ozonesonde launch sites being in Central Europe (Figure 6.12), which has a denser network of surface sites than other regions in the domain, or the higher vertical sensitivity of ozonesondes at the surface, compared to satellite observations.

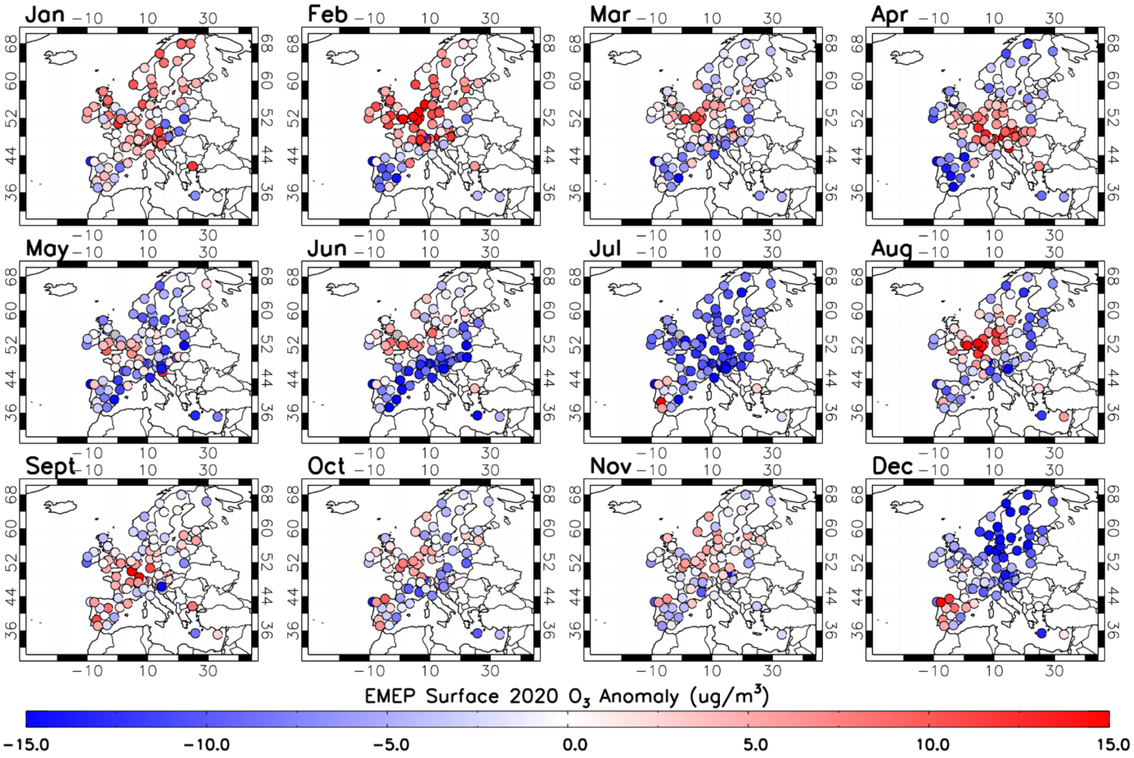

Figure 6.28: EMEP O_3 anomalies for each month of 2020 (µg m^3) relative to a monthly average baseline (2010 – 2019).

6.4.4 Modelling results

6.4.4.1 Scaled emissions in 2020 & 2021

Across Europe, the scaled emissions scenario caused a monthly reduction in tropospheric O_3 from around March to December 2020 (Figure 6.29). The difference between the BAU and scaled emissions scenarios is negligible in January and February, increases through the spring and peaks in May; at -1.9 DU (-8.0%), and then reduces through the year to December (-0.8 DU/ -4.2%). In 2021, the scaled emissions scenario shows consistent large reductions in all months of the year, starting at -0.6 DU (-3.5%) in January, peaking at -1.0 DU (-4.0%) in May, and getting slightly smaller towards the end of the year, ending with -0.6 DU (-3.2%) in December. TOMCAT O_3 across only the land shows lower values than the whole domain, but a similar difference between the scaled and BAU scenarios. The pattern of differences follows the emission scaling reduction closely, although the O_3 difference peaks in May, compared to the emission reduction peaking in April. Although the pattern is similar, the percentage change is much smaller for tropospheric O_3 (~ 8% in May) compared to the surface emissions (~ 25% in May), highlight the magnitude of emission reductions needed to see a signal in the tropospheric O_3. This indicates that to see a large reduction in tropospheric O_3, more stringent restrictions are required on surface emissions leading to large precursor gas reductions.

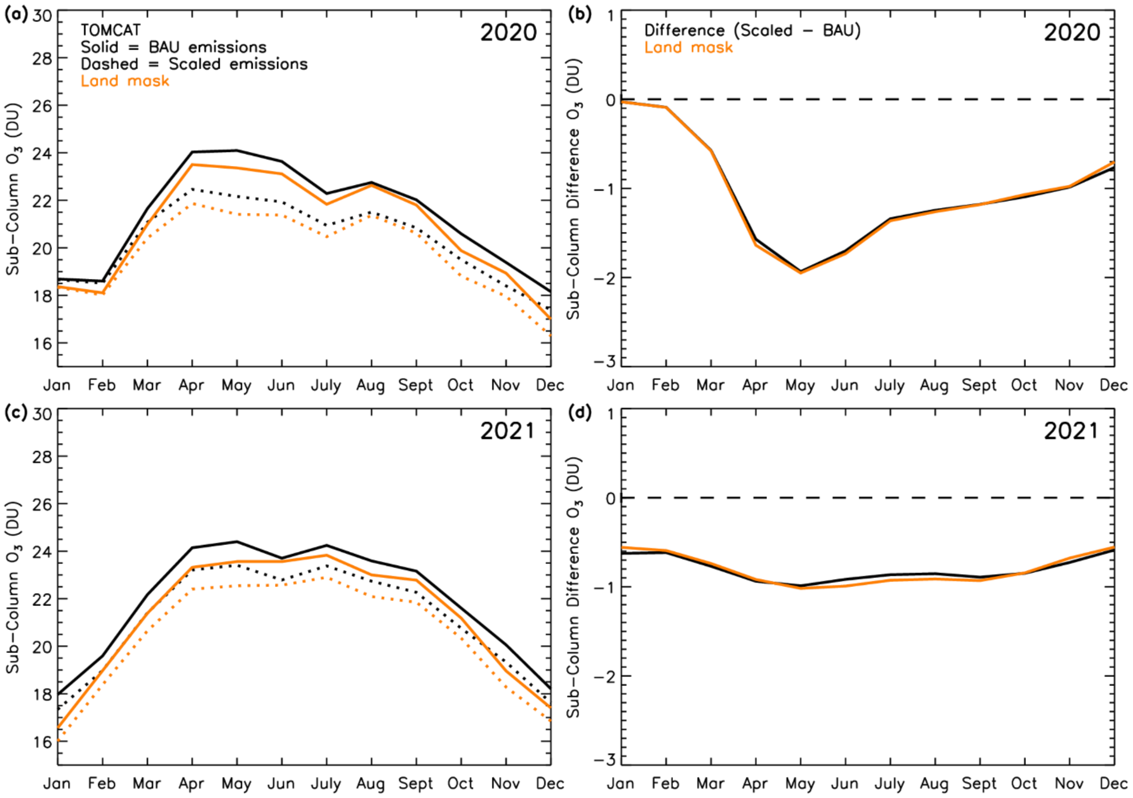

Figure 6.29: (a) TOMCAT European monthly sub-column (surface – 450 hPa) O_3 in 2020 (DU). The solid lines represent the BAU scenario, and the dashed lines represent the scenario with scaled emissions. The black lines represent the whole domain and the orange lines represent the domain with the land mask applied. (b) Difference between BAU scenario and scaled emissions scenario. (c) As panel (a) for 2021. (d) As panel (b) for 2021.

6.4.4.2 Long-term results (2017 – 2020)

The BAU simulation between 2017 – 2020 highlights that tropospheric O_3 in 2020 is lower compared to previous years, especially compared to the high O_3 values in 2019 (Figure 6.30(a)). The BAU simulation has no emission scaling, therefore this shows the large impact of meteorology in 2020. In the BAU scenario, there are negative anomalies of up to -1.3 DU (-5.4%) in the spring and summer of 2020, with April, May and July showing the largest reductions, which are around the value of -2σ from the mean (1.3 DU/ 5.7%) (Figure 6.30(b)/(d)). The variation in the BAU scenario is due to meteorology and variation in the surface emissions used. The BAU emissions only vary slightly interannually, and therefore can be considered to be relatively constant (Figure 6.16). Therefore, the negative anomalies show meteorology had a large impact on the simulated tropospheric O_3 in the spring and summer of 2020.

For a 'realistic' scenario, the BAU scenario for 2017 – 2019 has been combined with the scaled emissions scenario for 2020 and 2021. This combined record shows large negative anomalies in 2020, peaking at -3.2 DU (-14.5%) in May 2020, which is much larger than -2σ from the average (1.8 DU/ 8.3%) (Figure 6.30(b)). In comparison with the BAU scenario, the combined scenario suggests that ~1 DU of the negative anomaly is due to meteorology (and small variations in BAU emissions) and the remaining contribution (~ 1 – 2 DU in spring/summer) of the negative anomaly is due to the scaled emissions for 2020. To further quantify the relative contributions, the difference between the anomalies for the BAU and 'realistic' scenario as a percentage of the 'realistic' scenario for 2020 was calculated. This was performed for months with a negative anomaly in both the BAU and 'realistic' scenarios (February – August 2020 and February – June 2021). This values represent the contribution of the emission reduction to the negative anomalies seen in the 'realistic' scenarios, and the corresponding contribution of meteorology (and annual differences in the BAU emissions). The contribution of emissions to the 'realistic' scenario in spring/summer 2020 is 49% (March), 59% (April), 60% (May), 72% (June), 58% (July) and 93% (August), with an average of 65% across these months (Figure 6.31). Although scaling the emissions dominated across most of the months in 2020 (~ $^{2}/_{3}$), the meteorology impact is considerable (~ $^{1}/_{3}$).

The impact of meteorology on the scaled emissions scenarios is explored in Figure 6.30(c). The blue dashed line represents the average of the scaled emissions scenario using the meteorology of 2017, 2018 and 2019. This further confirms the impact of the 2020 meteorology on tropospheric O_3, as the 2020 scaled emissions scenario timeseries is broadly lower than the 2017/2018/2019 averaged scaled emissions scenario. The greatest differences between these two timeseries is in the spring and summer (February – July), peaking at a 1.1 DU difference in May. The timeseries is much more consistent from August to the end of the year, with differences below 0.5 DU. The ozonesonde and surface data showed the peak negative O_3 anomalies in July 2020. The 'dip' seen in O_3 for July 2020 in the BAU and scaled scenarios, compared to the surrounding months, is not present in the 2017–2019 averaged scaled emission scenario (Figure 6.30(c)). This suggests that in the model data, the meteorology in July 2020 is contributing to the low O_3 values in July, not only the reduction in emissions. Therefore, meteorology could be contributing to the large negative anomalies seen in the ozonesonde and surface records in July 2020. There is no clear European-wide indicator of an extreme meteorological event in July 2020, as western and northern Europe were colder compared to average (1981 – 2010), and southern and eastern Europe were warmer than average (Copernicus Climate Change Service, 2020). Precipitation (an indicator of cloudy conditions) also shows a mixed picture with some of northern Europe and eastern Europe/the Balkans had more rain than normal, but central Europe was drier than normal.

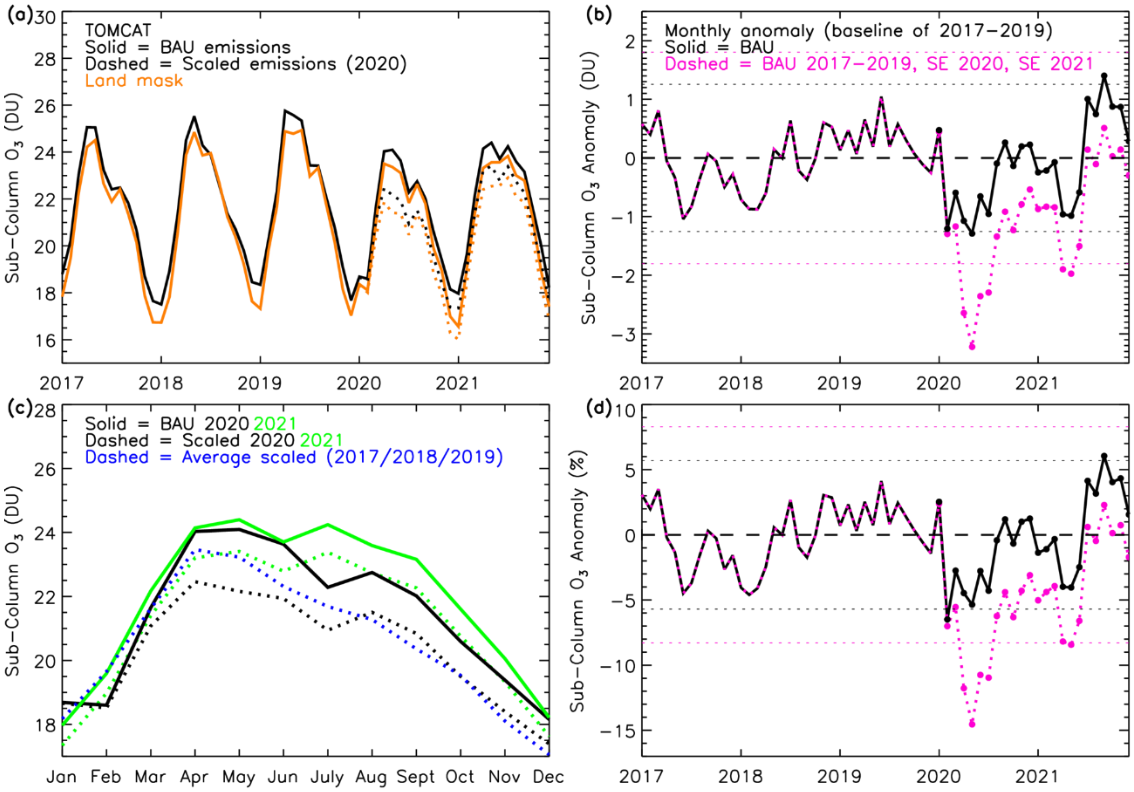

Figure 6.30: (a) TOMCAT European monthly sub-column (surface – 450 hPa) O_3 from 2017 – 2021 (DU). The solid black line represents the BAU scenario, the solid orange line represents the BAU scenario with the land mask applied. For 2020, the dashed line represents the scenario with scaled emissions. (b) TOMCAT O_3 anomalies relative to a monthly average baseline (2017 – 2019). Solid line represents the BAU scenario, the pink dashed line represents the anomaly of the BAU scenario from 2017 – 2019 combined with the scaled emissions scenario in 2020. (c) BAU (solid) and scaled emission scenario (dotted) records for 2020 (black), 2021 (green) and the 2017/2018/2019 averaged scaled emission scenario shown in a dark blue dashed line. (d) As panel (b) with % anomalies. In panels (b) and (d) the horizonal dashed lines indicate ± 2σ from the average of the record.

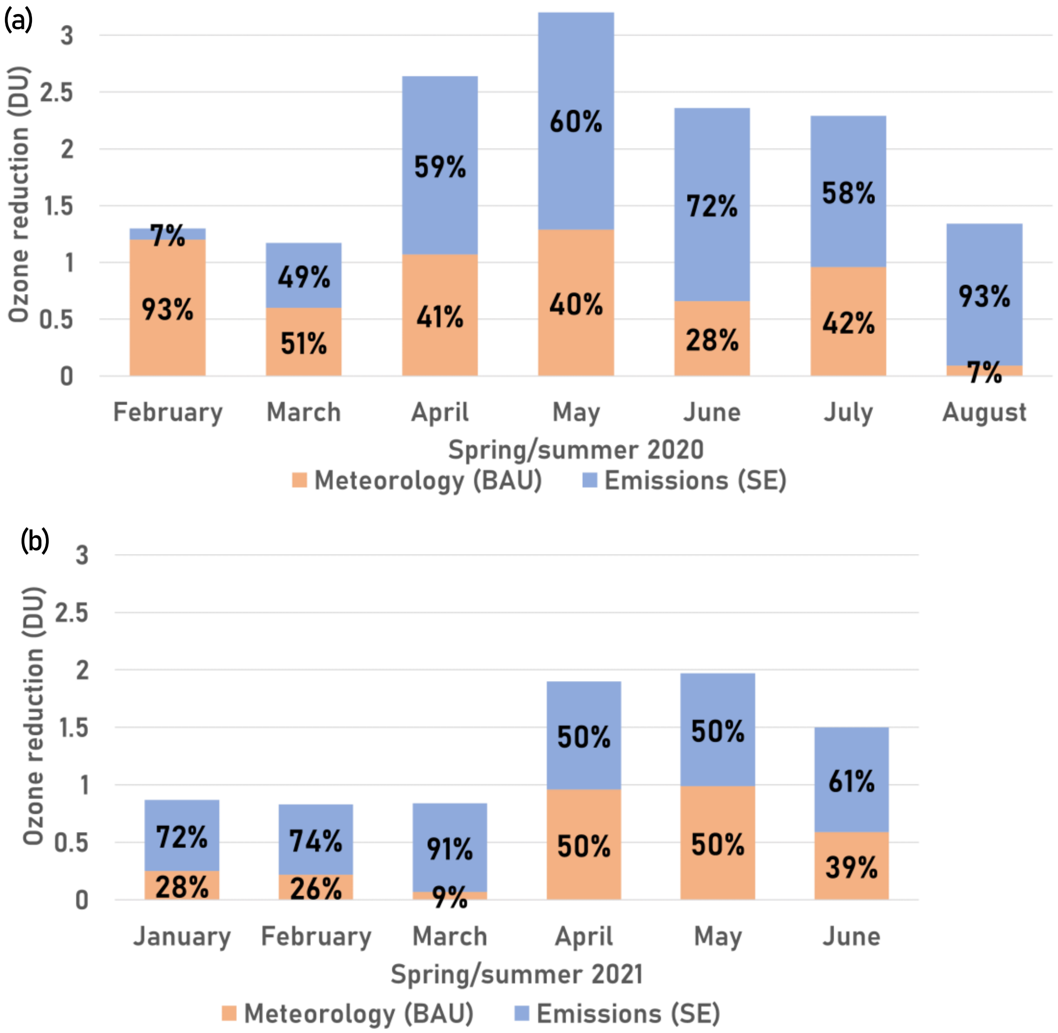

Figure 6.31: (a) TOMCAT O_3 reduction (DU) for February – August 2020. The total reduction is the negative anomaly in the ‘realistic’ scenario, with the relative contribution of meteorology (and BAU emissions) shown in orange (percentage labelled) and the relative contribution of scaling the emissions (difference between BAU and SE simulations) shown in blue. The relative contribution as a percentage is labelled onto each section of the bars. (b) As panel (a) but for the months of January – June 2021.

6.4.4.3 Stratosphere-troposphere exchange

The TOMCAT model provides information about the contribution of STE to tropospheric O_3. The timeseries of the STE contribution of the tropospheric sub-column (STE-sub-column) in relation to the total tropospheric sub-column record for the BAU simulation is shown in Figure 6.32. The STE-sub-column shows a large negative anomaly in the spring/summer of 2020, of -1.4 DU in April and May (-64.4% and -64.0% respectively). The STE-sub-column absolute negative anomaly is larger than the total sub-column anomaly from March - October in 2020, suggesting that during this period, the low STE contribution was a dominant factor in the BAU negative anomaly of the tropospheric sub-column. As the STE-sub-column absolute anomaly is larger than the BAU anomaly, it suggests that some of the other controlling factors in the BAU simulation O_3 are around neutral or even slightly positive.

The stratospheric O_3 used in the model simulation is a climatology, and so has a constant volume mixing ratio for each year. Therefore any variation on the STE contribution is from variation in the STE flux (not related to amount of O_3 in the stratosphere). Therefore the negative anomaly seen here in the STE-sub-column is not due to the large depletion found in stratospheric Arctic O_3 in spring 2020, and the impact of this depletion cannot be diagnosed here. It is possible that the low stratospheric Arctic O_3 could have enhanced the spring tropospheric O_3 negative anomaly and giving greater significance to meteorological (transport) processes, which could be studied using varying stratospheric O_3 in TOMCAT.

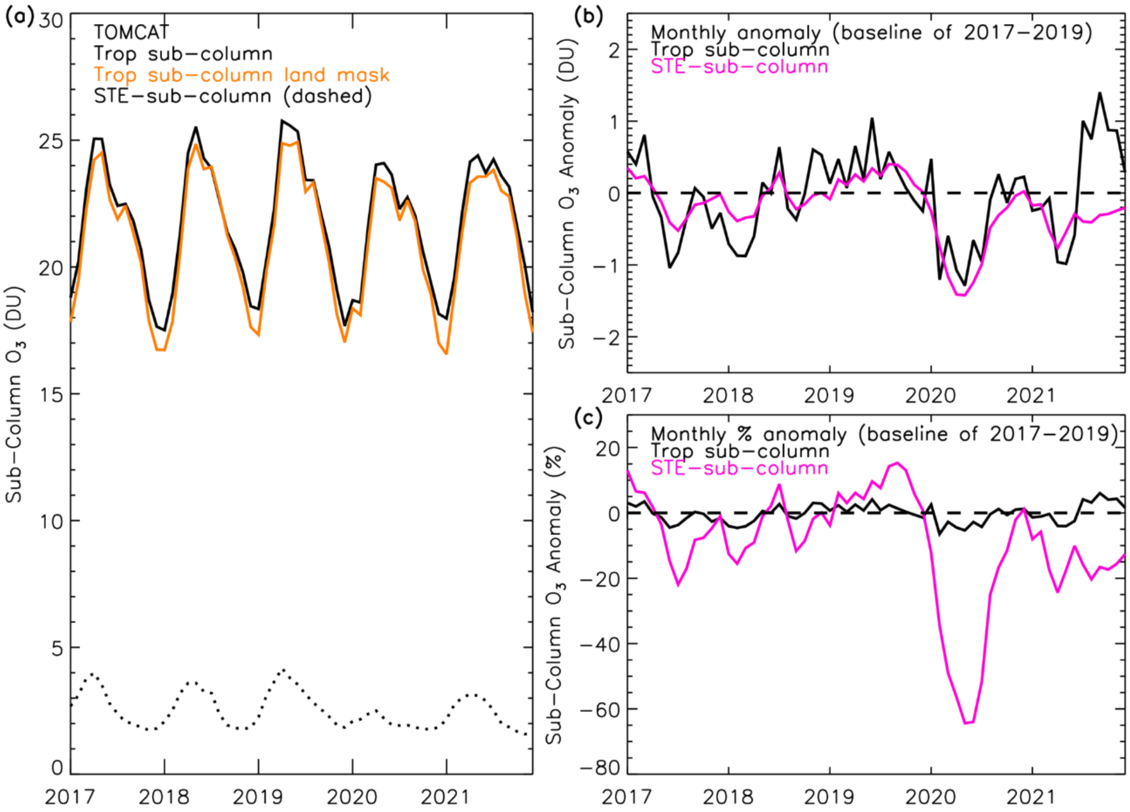

Figure 6.32: (a) As Figure 6.30(a) (no scaled scenario) with the addition of TOMCAT European monthly sub-column O_3 based on the contribution of tropospheric O_3 from STE from 2017 – 2021 (DU), which is shown as a dotted line. (b) As Figure 6.30(b) with the anomaly of the STE sub-column O_3 in addition (pink solid line). (c) As panel (b) with percentage anomalies.

6.4.4.4 O_3 reduction in 2021

The modelling results show that there are also large negative anomalies in the spring/summer of 2021 for the BAU scenario, although across a shorter time period. In 2021, the BAU scenario shows negative anomalies in January – June, peaking at -1.0 DU (-4.0%) in May (Figure 6.30(b)/(d)). The scaled emission scenario has larger negative anomalies, peaking at -2.0 DU (-8.4%) in May. ~ 72%, 74%, 91%, 50%, 50% and 61%, for January – June, respectively, of the scaled negative anomaly is due to scaling the emissions, with the rest due to meteorology (and BAU emissions) (Figure 6.31). This is an average of 66% across the 6 months. The negative anomalies in the first half of 2021 are consistent with the satellite data, and the results in Ziemke et al. (2022). However, the Ziemke et al. (2022) record stops in August 2021, so no further comparison is possible. Both the ‘realistic’ and BAU scenarios show predominantly positive anomalies in the second half of 2021 (from July onwards), with very large positive anomalies of up to +1.4 DU (+6.1%). This is consistent with the ozonesonde record, but diverges from the long-term IASI-IMS-Extended record which still shows negative anomalies in the second half of 2021. This could suggest a stronger positive anomaly signal towards the surface, with a weaker or negative signal higher up in the sub-column (up to 450 hPa).

In 2021, the negative anomaly in STE-sub-column is smaller than for 2020, reaching a peak value of -0.8 DU (-24.3%) in April (Figure 6.32). The negative anomaly for STE-sub-column is not larger than for the total sub-column in 2021, suggesting that the STE reduction has a smaller impact on the negative tropospheric sub-column anomalies seen in 2021, in comparison with 2020. Therefore, this shows that other meteorological processes (e.g. temperature, photolysis rates, tropospheric transport) had a bigger impact on the reduction in 2021.

6.4.4.5 Comparison to satellite data

The GOME-2B record is compared with co-located model simulations with AKs applied for 2017 – 2020 (Figure 6.33). In this case, the effect of co-locating the model with the satellite records is very small (dark and light blue dotted lines), with a much larger difference coming from applying the AKs. There is a large offset between the model and the satellite record of 7.1 DU on average (2017 – 2019), which is reduced to 4.3 DU when the AKs are applied. Despite the large offset, the records are well correlated between 2017 – 2019 (r = 0.80). Applying the AKs also improves the correlation, increasing the Pearson’s correlation coefficient from 0.69 to 0.80. In 2020, the scaled emissions simulation is also shown (co-located and with AKs applied), which shows a much better agreement with the satellite in the anomaly plots (Figure 6.33(b) and (c)). For the BAU simulation, there are negative anomalies from January to May 2020, however, the negative anomaly values in April and May are much smaller than shown in the GOME-2B record. In the scaled emissions scenario, the negative anomaly values are much more similar to the GOME-2B record, and this similarity continues for June – September.

This model analysis is repeated for the IASI-IMS-Extended record (Figure 6.34). As with the GOME-2B record, the impact of co-locating the model with the satellite retrievals has a very small impact. Applying the AKs, reduces a 2.5 DU average overestimate by the model to a 1.1 DU underestimate, improving the comparison. The Pearson’s correlation coefficient is also improved, from 0.91 to 0.98. In 2020, the model simulation with scaled emissions (and AKs applied) produces a very similar peak negative anomaly to the satellite, with -2.6 DU (-13.8%) from the model and -2.7 DU (-13.4%) from the satellite. The anomaly agreement is also very close throughout the other months of 2020. In 2021, both the BAU and scaled emissions model records with AKs applied show much smaller anomalies than the satellite for the first half of the year (February to August). For the scaled emissions simulation especially, the application of the AKs reduces the negative anomaly shown in spring/summer.

Overall, the good agreement between the model with AKs applied and the two satellite records show that the model is potentially capturing the tropospheric O_3 sufficiently, demonstrating that the model is appropriate for use in this analysis. The agreement between the model (with AKs) and satellite anomalies is very close in 2020, but the agreement is less close in 2021, suggesting we can be more confident in the 2020 model results, compared to 2021.

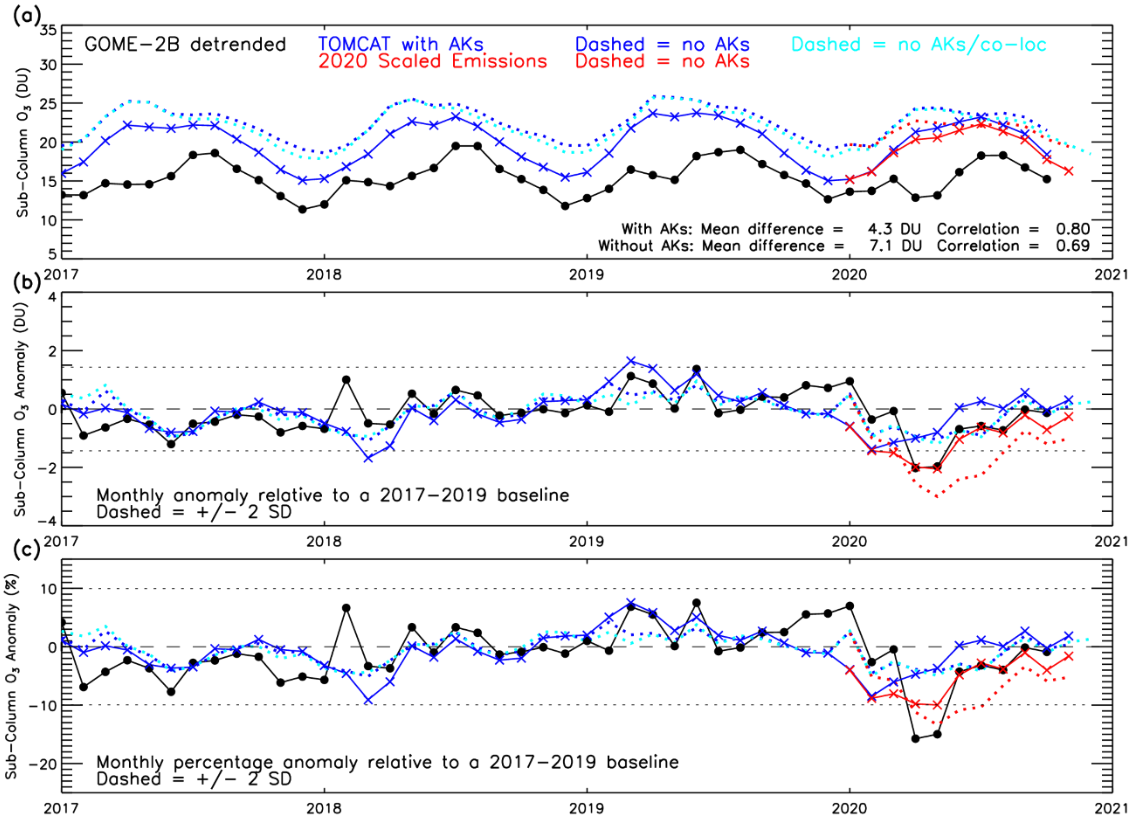

Figure 6.33: (a) European monthly average sub-column (surface – 450 hPa) detrended O_3 record (DU) derived from GOME-2B from 2017 - 2020. TOMCAT BAU O_3 record co-located with the GOME-2B instrument, and with (solid) and without (dashed) GOME-2B AKs applied is also shown. The TOMCAT BAU O_3 record which is not co-located is also shown (light blue dashed). In 2020, the TOMCAT SE O_3 record is also shown. Dots represent the monthly satellite averages, crosses represent the monthly TOMCAT averages. (b) Monthly mean absolute anomalies (2017 – 2019 monthly average baseline) (DU). (c) Monthly mean percentage anomalies (2017 – 2019 monthly average baseline). Dotted lines indicate ± 2σ from the average of the GOME-2B record. Mean difference and correlation values are calculated for 2017 – 2019 (i.e. excludes 2020).

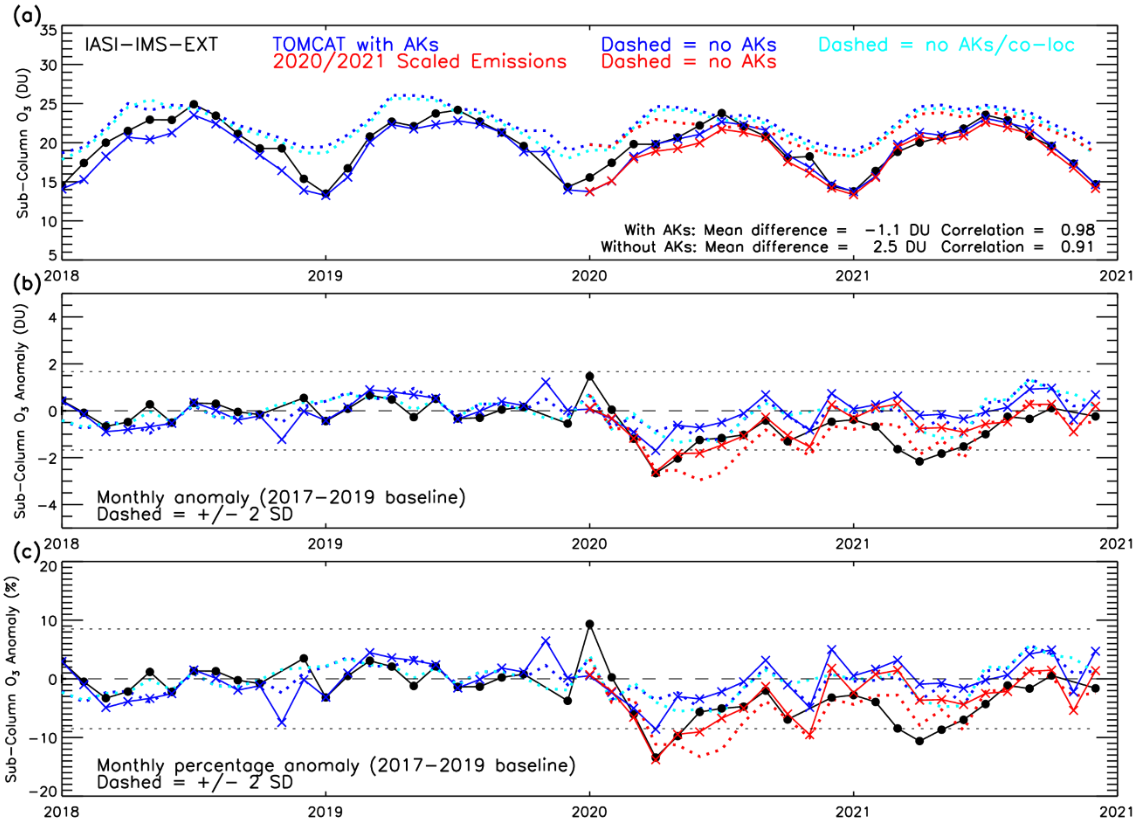

Figure 6.34: Timeseries of European monthly average sub-column (surface – 450 hPa) O_3 record (DU) derived from IASI from 2018 - 2021. TOMCAT BAU O_3 record co-located with the IASI instrument, and with (solid) and without (dashed) IASI AKs applied is also shown. The TOMCAT BAU O_3 record which is not co-located is also shown (light blue dashed). In 2020 and 2021, the TOMCAT SE O_3 record is also shown. Dots represent the monthly satellite averages, crosses represent the monthly TOMCAT averages. Dashed lines indicate ± 2σ from the average of the IASI record. Mean difference and correlation values are calculated for 2018 – 2019 (excludes 2020/2021).

6.4.5 Ozone reduction summary across all records

The negative anomalies of tropospheric O_3 found across all the records in this chapter (satellite, model, surface and ozonesondes) are summarised in Figure 6.35. To make the comparison more consistent, they are all relative to the same baseline years (2018 – 2019). Therefore, the anomaly values differ from those described in the previous sections, but the patterns are broadly the same. Despite using the same baseline years, there are still notable inconsistencies in their comparison which are not resolved here, e.g. spatial sampling, surface vs. free troposphere and vertical sensitivity. All records show large negative anomalies across Europe during the spring-summer of 2020 and 2021, however, the records show different stories in terms of anomaly magnitude and timing of peak anomaly (Figure 6.35), which adds complexity to the story. The satellite datasets show their largest negative anomalies in April and May 2020, with IASI-IMS-Extended showing large negative anomalies in April and May 2021 as well. The model broadly agrees with this, showing similar percentage anomalies. The surface and ozonesonde records show smaller negative anomalies in spring, with much larger values later in July, potentially due to spatial sampling differences or to a different signal towards the surface, not captured in the satellite retrievals. Although the model shows peaks values in April/May, it still shows large negative anomalies in July, of a similar order of magnitude to the surface and ozonesondes. In 2021, the satellite, ozonesondes and model all show fairly consistent negative anomalies in April and May. This could suggest that there was a more similar tropospheric O_3 reduction towards the surface and also higher up in the FT.

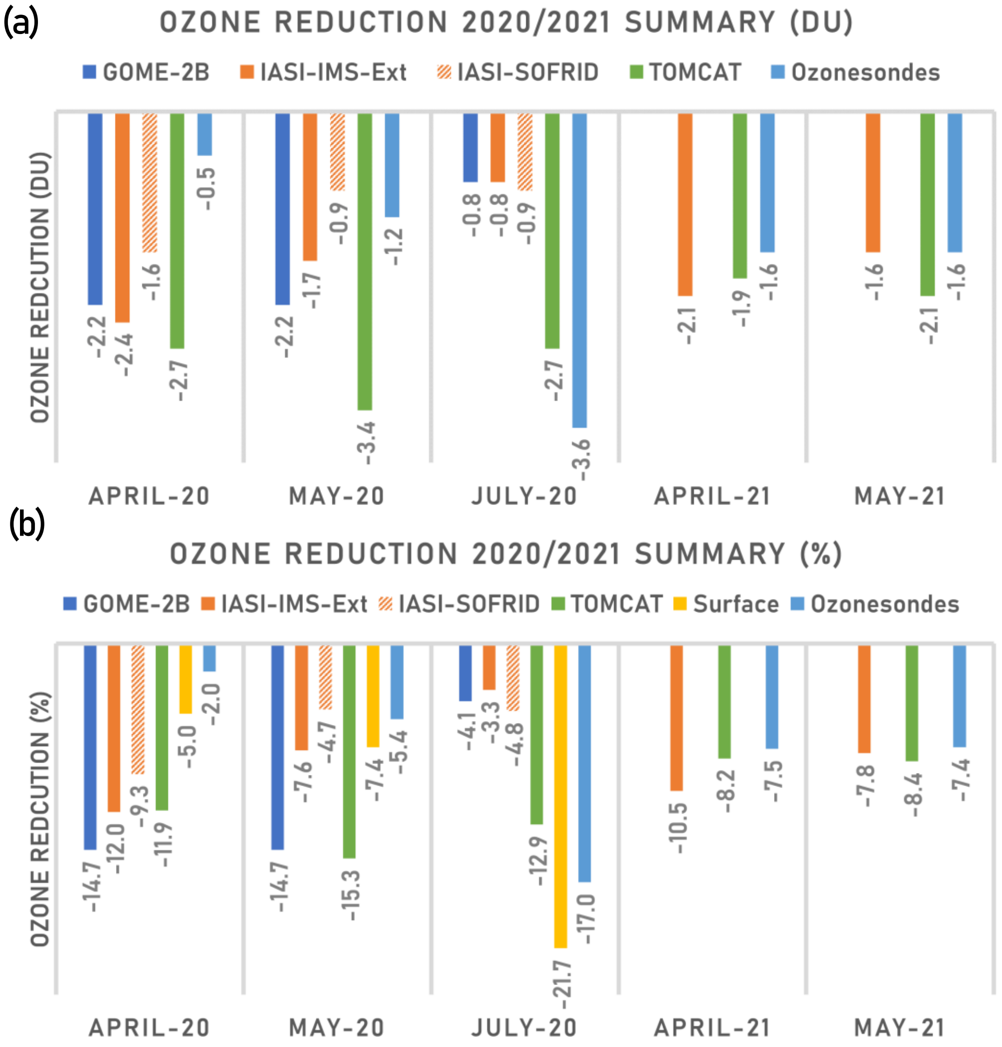

Figure 6.35: Summary of reductions in tropospheric O_3 found in this chapter as (a) an absolute anomaly (DU) and (b) a percentage negative, all relative to the same monthly average baseline (2018 – 2019). Results are presented for April/May/July in 2020 and April/May 2021. The records are GOME-2B, IASI-IMS-Extended, IASI-SOFIRD, TOMCAT, EMEP surface data and the ozonesondes. The surface absolute results are not presented as they are not a sub-column.

6.4.6 Global hydroxyl radical in 2020

To investigate the global OH variation in 2020, the methodology developed in Chapter 4 is extended, using the MetOp-B IASI-IMS-Extended data. The global, hemispheric and tropical OH variation across this time period, averaged for the 400 – 800 hPa pressure region, is shown in Figure 6.36. In 2020, a large negative global anomaly in OH in March, of -0.3 $\times 10^6$ molecule cm^{-3} (-20.1%), which is larger than 2σ (13.2%). Across the hemispheres and tropics, the percentage negative anomaly is similar, with a slightly smaller negative anomaly of -15.0% in the NH. Broadly there are negative anomalies between January and May, with March being the largest. The dominant controls on this satellite-derived OH estimation are the input species of O_3 (source) and CO (sink). In March 2020, globally (averaged across 400 – 800 hPa) there was a negative anomaly in O_3 of -8.0% and a positive anomaly in CO of 4.7% (Figure 6.37). This negative anomaly in the key source species and positive anomaly in the key sink species are likely producing the large negative anomaly seen in the derived OH.

There are currently few observation-constrained estimates of OH anomalies in 2020 with which to compare. Miyazaki et al. (2021) found a smaller peak negative anomaly in the global average tropospheric mean OH of -4.0% in May 2020, which varied up to 20% – 30% locally (compared to a 2010 – 2019 monthly average baseline). However, the satellite-derived OH here is an estimate for the 400 – 800 hPa pressure region, so this is not a direct comparison. Using model emission reduction scenarios (for transport, aircraft and industry), Weber et al. (2020) found a decrease of OH across the troposphere between mid-March to mid-May 2020, compared to a model control simulation (with no emission reductions). The average reduction in mean tropospheric air-mass-weighted OH was between 0.018 $\times 10^6$ – 0.033 $\times 10^6$ molecule cm^{-3} for the model scenarios, which varied up to ~ -10% in the mid-troposphere. Around the NH mid-troposphere, they found that the predominant cause of OH reduction was due to surface transport emission reductions. The absolute reductions found are smaller than those calculated here, although the reduction here is for the 400 – 800 hPa pressure region and studies 2020 relative to the previous 3 years rather than a reduction compared to a control simulation. Many of these estimates of OH are based on information about variation during this time-period in NO_x concentrations or emissions. The satellite-derived OH estimation used here in this thesis does not use information about NO_x in the approximation, which could be a source of the disagreement between the estimates. Other methods of estimating annual OH change during this period include using methane inversions, for example, Peng et al. (2022) found a global average reduction of 1.6 ± 0.2% in 2020 compared to 2019 for tropospheric OH concentrations using in situ data, and Feng et al. (2023) found a global average reduction of 1.4 ± 1.7% in 2020 compared to 2019 for tropospheric OH concentrations using satellite CH_4 data. Again, a direct comparison is due to the satellite-derived OH estimate being for the mid-troposphere at ~9.30 only.

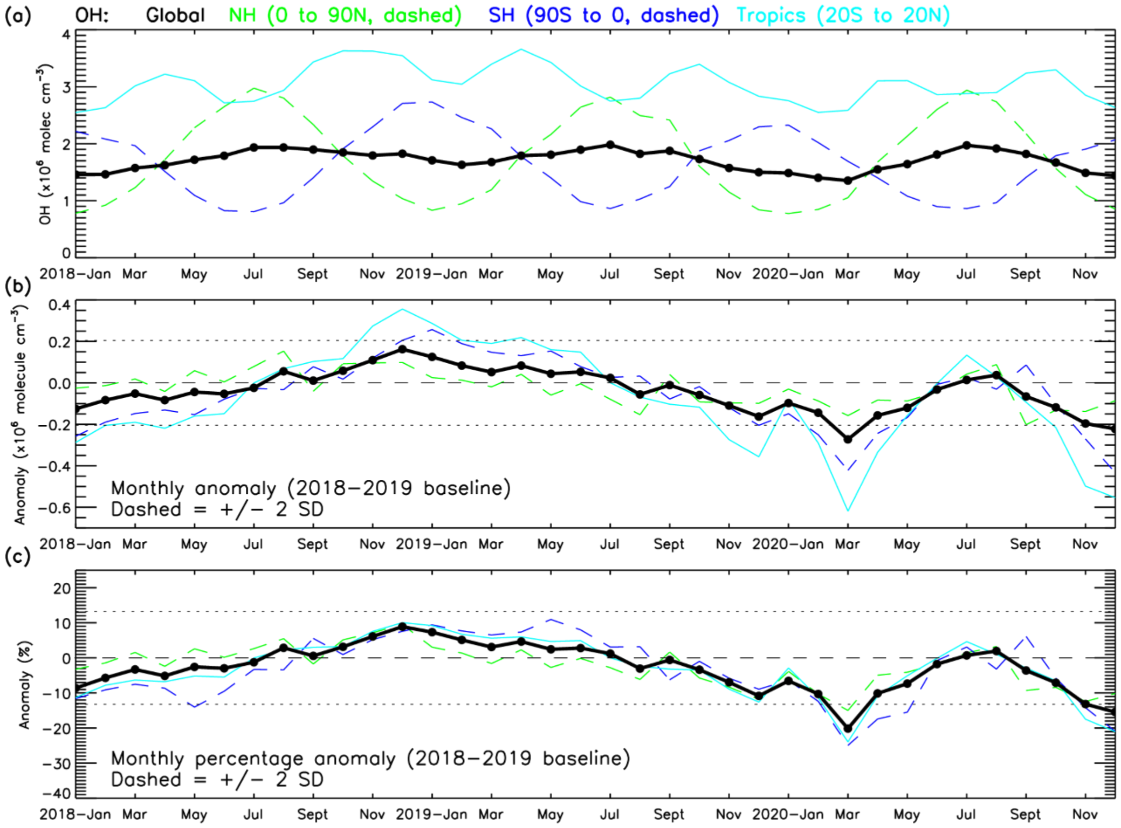

Figure 6.36: (a) Monthly mean satellite-derived OH for 2018 – 2020 (averaged across the pressure layer 400 – 800 hPa). Global, NH (dashed), SH (dashed) and tropical latitude regions are shown. (b) Monthly mean absolute anomalies (2018 – 2019 monthly average baseline) (DU). (c) Monthly mean percentage anomalies (2018 – 2019 monthly average baseline). Dotted lines indicate ± 2σ from the global average of the record.

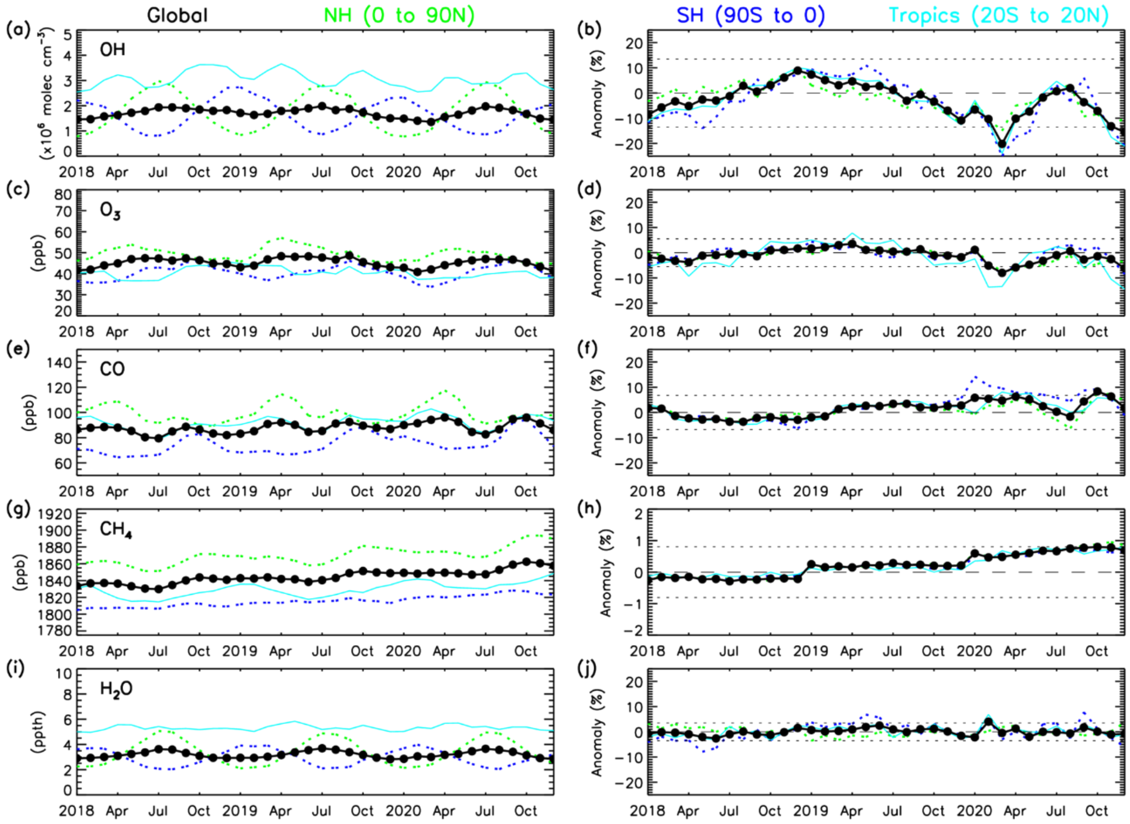

Figure 6.37: 2018 – 2020 monthly mean (a) satellite-derived OH (averaged across the pressure layer 400 – 800 hPa) and (b) percentage anomalies for the satellite-derived OH (2018 – 2019 monthly average baseline). Panels (c) – (j) are the same as (a) and (b) for IASI-IMS-Extended retrievals of O_3 (c & d), CO (e & f), CH_4 (g & h, note difference scale in panel h) and H_2O (i & j). Global (solid with circles), NH (dotted), SH (dotted) and tropical (solid) latitude regions are shown. In the right hand side panels black dotted lines indicate ± 2σ from the global average of the record.

6.5 Summary

In this chapter, multiple records of lower tropospheric and surface O_3 across Europe in 2020 and 2021 are presented, to identify what happened to tropospheric O_3 in these two unusual years. The methodology developed in Chapter 4 is used to provide one of the first observationally-constrained studies of the impact of tropospheric composition variations to global [OH] in 2020.

The European tropospheric satellite record shows consistent negative anomalies in the spring and summer of 2020, indicating that a large tropospheric O_3 reduction did occur during this time period. Two RAL satellite records show large negative anomalies, of -14.7% for both April and May from GOME-2B and -12.0%/-7.6% in April/May from IASI-IMS-Extended (monthly average baseline of 2018 – 2019). Spatially, the satellite records show the most consistent negative anomalies across the European domain in April and May 2020, with large reductions across central continental Europe in May 2020, which corresponds well to surface precursor emission reductions, as this signal would be land-based. A third satellite record, IASI from a different retrieval scheme (IASI-SOFRID), shows similar, but slightly smaller, negative anomalies in the spring and summer 2020 (-9.3%/-4.7% in April/May). An offset of ~ 3.0 – 3.5 DU between the IASI records, highlights the importance in considering the uncertainty in the retrieval process when studying satellite derived O_3. However, the good agreement in negative anomalies (albeit slightly smaller) suggests that these IASI results can be concluded with more confidence.

The ozonesonde record also shows large negative anomalies across Europe in the spring and summer of 2020, however, these peak later in the summer. The largest negative anomaly is in July 2020 of -17.0% (baseline of 2018 – 2019). In comparison to the satellite records, the ozonesondes show a lower negative anomaly for April, of -2.0%, but the record is more consistent with the surface data. Both records show the peak negative anomaly to be in July (-21.7% for the surface data), and a smaller negative anomaly in April/May. Differences compared to the satellite records could be caused by differences in spatial coverage and sampling or differences in vertical resolution. However, it could also suggest a variation in the tropospheric O_3 reduction between the surface and higher up in the FT sub-column (up to 450 hPa), with peak reductions across the sub-column at different times.

The satellite and ozonesonde records also show a reoccurrence of low spring and summer tropospheric O_3 values across Europe in 2021. In 2021, there is a similar pattern to 2020 of negative anomalies in the spring and summer, which corresponds well to the findings of Ziemke et al. (2022) across the NH FT from their combined NASA satellite O_3 product (EPIC, OMI and OMPS) between 2016 and August 2021. Both the IASI-IMS-Extended and ozonesonde records show large negative anomalies, which are more temporally consistent than in 2020, with peak negative anomalies in April/May of -10.5%/-7.8% (IASI) and -7.5%/-7.4% (ozonesondes). The reoccurrence of low tropospheric O_3 in the spring and summer of 2021 indicates a continued impact of reduced precursor emissions from the global pandemic in this year.

Simulations of European tropospheric O_3 highlights that the reduction was more influenced by reduced surface precursor emissions than meteorology. Global anthropogenic emissions were scaled based on activity data changes (Forster et al., 2020), for use in TOMCAT simulations in 2020 and 2021. Using both a BAU and scaled emissions scenario, TOMCAT model simulations from 2017 – 2021 show negative anomalies of up to -5.4% (BAU simulation) and -14.5% (scaled emissions scenario) for the spring and summer 2020. Although scaling the emissions was the dominant influence on the negative anomaly from April – August, a substantial proportion (~ 41%, 40%, 28%, 42% and 7% for April – August respectively) is due the meteorology (and small BAU emission variation) of 2020, highlighting it's importance to inter-annual O_3 variation. Therefore, meteorology can significantly enhance or reduce any potential variation due to emission reductions, which is relevant when considering implementation of measures aiming to reduce anthropogenic emissions in order to reduce tropospheric O_3. 2021 shows a reoccurrence of spring/summer O_3 reductions, however, as with the satellite record, these are slightly smaller (up to -4.0% in the BAU scenario, -8.4% in the scaled emissions scenario). The large negative anomaly in April/May 2021 is similarly influenced by both meteorology and emission reductions.

The TOMCAT tropospheric O_3 simulations indicate a large contribution of the negative anomaly in the BAU scenario is due to a reduction in the STE flux. The BAU scenario shows a large negative anomaly in the O_3 sub-column from STE, of up to -1.4 DU in April and May (~ -64.4%). This indicates a very large proportion of the negative anomaly seen in the BAU scenario is due to this negative anomaly in the flux of STE, however this is not temporally universal as the same is not repeated for 2021. Although there are negative anomalies in the STE tracer in 2021, these are smaller (up to -0.8 DU/-24.3%) and do not explain most of the negative anomaly in the BAU scenario. This indicates that different meteorological processes vary in their contribution to tropospheric O_3 on an annual scale.

Lastly, an application of the method developed in Chapter 4 is demonstrated, to investigate the variation in satellite-derived OH in 2020 (mid-tropospheric pressure region of 400 – 800 hPa). Globally, the satellite-derived OH shows a large negative anomaly of -20.1% in March 2020. This negative anomaly in OH corresponds to anomalies in the key drivers in the approximation, with a negative anomaly in O_3 (controls the source term) and a positive anomaly in the sink term of CO. This observationally-constrained OH record for 2020, has the potential to be used in model experiments to understand the impact of the global pandemic on other important species e.g. CH_4.

Overall, all records show large tropospheric O_3 reductions across Europe during the spring and summer of 2020, as highlighted in the summary bar chart (Figure 6.35), however, there were contrasts in the timing of the peak reduction. Broad consistency between the records suggests that a real tropospheric O_3 reduction occurred during the period. The model experiments indicate that the majority of the tropospheric O_3 reduction was due to reduced surface emissions, which suggests that a large emission reduction (~ 30%) will produce a reduction in free tropospheric O_3 (~ 10%) across Europe. However, meteorology still plays an important part and shows large interannual variability, enhancing or diminishing any potential O_3 reductions from reduced anthropogenic surface emissions.

Chapter 7 Conclusions

In this thesis, interannual to multidecadal changes of two important tropospheric species, OH and O_3, have been explored using satellite datasets and an atmospheric chemistry transport model. A better understanding of the spatio-temporal variation of OH is important due to its control of the lifetime of other notable species e.g. air pollutants, GHGs and stratospheric ODSs, and also of O_3 due to its harmful health impacts to humans and plants and large contribution to global RF. This thesis has addressed 3 main research gaps: enhanced spatio-temporal information about OH; quantification of European O_3 trends from satellite; and characterisation of O_3 and OH changes in the spring/summer of 2020 and 2021 in response to the global COVID-19 pandemic. In addressing these research gaps, the potential and also limitations of using satellite retrievals to better understand long-term changes in tropospheric composition has been highlighted. In the future, satellite instruments with enhanced spatial resolution, enhanced sensitivity at the surface and reduced uncertainties will add further value to studies such as this. Such data could provide identification of long-term variation on smaller scales, e.g. individual cities, which would provide valuable information in the context of air quality. In this chapter, the thesis results are brought together and discussed in the context of the overarching research gaps and corresponding research questions addressed in this thesis. The key results are discussed and suggestions of potential future work based on the results and limitations of this thesis are also presented.

7.1 Overview of thesis results

Research gap 1: Information about OH abundance, distribution and long-term variation.

The work presented in Chapter 4 developed and evaluated a new method, of applying satellite retrievals of O_3, CO, CH_4 and H_2O to a simplified steady-state approximation (S-SSA). The aim was to address the need to better understand OH and it's long-term variation, for which new indirect methods are required. New methods are required due to the limited availability of direct measurements and the decline in viability of the MCF method, and to enhance the spatio-temporal information available for OH. The method developed shows the potential to meet this need, providing monthly global coverage. However, the simplified approximation OH was found to be an underestimate compared to modelled and aircraft observations, in the region of ~ 30%, likely due to not sufficiently capturing more complex OH chemistry in some regions. The method would benefit from further development, focusing on missing source and sink reactions, e.g. by including additional satellite retrievals e.g. NO_2, HCHO and isoprene. However, as these other satellite species are mostly column measurements, the method would require further development to use these retrievals. Further improvement to this method would also come from a reduction in satellite data uncertainties and enhanced spatial and vertical resolution. The method was extended to 2020 in Chapter 6, demonstrating its potential use in approximating OH in specific periods of interest, e.g. in this unusual year for atmospheric composition from a large reduction in surface emissions due to the global COVID-19 pandemic. The work from Chapter 4 was published in the journal *Atmospheric Chemistry and Physics* (Pimlott et al., 2022). Answers to the research questions for this research gap are summarised as follows.

Research Question (RQ) 1.1: In what regions of the atmosphere are different steady-state approximations for [OH] valid?

TOMCAT simulations showed that a simplified approximation is only valid in the mid-troposphere, around 400 – 800 hPa, with a focus on 600 – 700 hPa for this study. More complex approximations are required to sufficiently capture the OH chemistry in other regions of the atmosphere, e.g. the production of OH from HO_2 + NO, and sinks of OH such as isoprene and formaldehyde.

RQ 1.2: Can satellite data be applied to a simplified steady-state approximation and how does it compare to modelled [OH]?

IASI retrievals of O_3, CO, CH_4 and H_2O were applied to the simplified steady-state approximation, creating monthly fields of OH in 2010 and 2017. In comparison with TOMCAT modelled OH, global monthly averages of satellite-derived OH were lower by ~ 20% – 30%.

RQ 1.3: How does the satellite-derived [OH] distribution compare to direct measurements of [OH] in the free troposphere?

Satellite-derived OH was compared with measurements from the aircraft campaign, ATOM (2016 – 2018). The satellite-derived OH underestimated measured OH by ~ 40%. The agreement was poor at the northern mid-latitudes (30°N – 90°N), likely due to the greater importance of other sources in this region which are not included in the approximation e.g. HO_2 + NO. Applying ATom data as the input species to the S-SSA produced an underestimate of ~ 26% compared to ATom measured OH.

RQ 1.4: What is the uncertainty associated with the satellite-derived OH?

A combination of the systematic errors of the satellite products when compared to other observations (e.g. ozonesondes, radiosondes) were used to estimate the uncertainty on the satellite-derived OH. The average uncertainty across the global domain was ~23 – 24%.

RQ 1.5: What can this method tell us about long-term variations in [OH]?

The long-term IASI record (2008 – 2017) was applied to the simplified approximation to derive a 10-year global monthly OH record. The record showed that in this period, annual global OH varied between -3.0% and 4.7%. In the approximation, the variation in O_3 and CO were the key drivers of the OH variation. The method was also used in Chapter 6 to understand the impact on OH of unusual years for atmospheric composition, i.e. the large variations in emissions in 2020.

Research gap 2: More robust quantification of European O_3 trends.

Chapter 5 presents an analysis of 3 satellite records across different time periods within 1996 – 2018, with the aim to better understand long-term trends in European tropospheric O_3. This study builds upon a comparison of satellite trends for different latitude regions shown in Gaudel et al. (2018), which found conflicting trends in different records above Europe. The work investigated the RAL satellite UV-Vis tropospheric O_3 records in greater depth, exploiting the spatial and temporal information that they provide, and exploring the associated uncertainties. The satellite records show small negative trends across the first part of the study period, 1996 – 2010, and a near-zero trend in the OMI record from 2005 – 2017. This work highlights the large uncertainties in using satellite products which should be considered when interpreting the results, which would mask small long-term changes. In the context of conflicting trends, the three instruments show relatively good agreement in the 6-year overlap period (2005 – 2010), however, the model showed that the differences are due to more than just the differences in sampling and vertical sensitivity between the instruments. The satellite and ozonesonde records demonstrate a small or near-zero trend in O_3 since 1996, despite continued reductions in O_3 precursor gas emissions across Europe during this time. This implies that more stringent measures for reducing precursor emissions in Europe and tackling transboundary sources of O_3, would need to be introduced to see reductions in free tropospheric O_3. Answers to the research questions for this research gap are summarised as follows.

RQ 2.1: What are the trends in satellite-observed lower tropospheric O_3 over Europe since 1996?

The three RAL UV-Vis satellite lower tropospheric O_3 records show small negative, or near-zero trends across the period. GOME shows a negative trend of -0.2 DU year^{-1} from 1996 – 2010, SCIAMACHY shows a negative trend of -0.2 DU year^{-1} from 2003 – 2010 and OMI shows a near-zero trend from 2005 – 2017.

RQ 2.2: How do these trends vary spatially and seasonally?

Spatially, the GOME negative trend is consistent across the European domain, SCIAMACHY shows a negative trend across most of the European domain, with some positive trends towards the southern Mediterranean. OMI shows small positive trends in southern Europe (30°N – 45°N) and northern Europe (60°N – 70°N) and small negative trends around 45°N – 60°N. Seasonally, the GOME negative trend is consistent to the average trend in the spring and autumn, with a larger negative trend in summer (-0.4 DU year^{-1}) and a zero trend in winter. The SCIAMACHY negative trend is consistent across winter, spring and autumn (largest trend in spring of -0.5 DU year^{-1}) but positive in summer. The zero-trend in OMI is consistent across all seasons.

RQ 2.3: How do these trends vary between instruments? What could be causing the differences?

In the 6 years of overlap between the 3 satellite records (2005 – 2010), they show similar negative trends in tropospheric O_3, ranging from -0.17 to -0.47 DU year-1. There is also some consistency in their anomalies during the period. In the co-located model records, there is even greater agreement, suggesting that sampling differences (e.g. overpass time, spatial resolution, vertical sensitivity, which are accounted for in the co-location and AK application) are not entirely causing the differences seen between the satellite records. The other factors that could be responsible for these differences are individual caveats with the instruments e.g. the OMI row anomaly, or UV degradation for GOME and SCIAMACHY.

RQ 2.4: Are these trends captured by a model and other observations of the troposphere, (e.g. ozonesondes)?

When co-located with the satellite and AKs applied, the model does not capture the trends, broadly showing near-zero trends co-located with GOME and SCIAMACHY and a negative trend co-located with OMI. Ozonesondes show a near-zero trend across 1996 – 2018, which is the same for the co-located TOMCAT record. TOMCAT (not co-located) shows a near-zero trend across the time period as well.

RQ 2.5: How do variations in O_3 precursor gas emissions and meteorology impact these trends?

Fixed-emission and fixed-meteorology TOMCAT simulations demonstrate that the near-zero trend in the control simulation across the whole domain is not due to conflicting trends in emissions and meteorology. However, the model experiments show that the small trends of some regions are influenced more by either emissions or meteorology, e.g. trends across mainland Europe and the Mediterranean were predominantly influenced by emissions, and trends across the Atlantic were predominantly influenced by meteorology.

Research gap 3: Characterisation and quantification of European O_3 and global OH variation, compared to previous years, in spring/summer 2020 and 2021, in the context of the global COVID-19 pandemic.

Chapter 6 presents an in-depth analysis of the free tropospheric O_3 record above Europe in 2020 and 2021, to study how these years, impacted by a global pandemic, compared to previous years. This work expands on the initial studies for the NH by Steinbrecht et al. (2021), Cuesta et al. (2022) and Ziemke et al. (2022) by studying different satellite records over Europe (GOME-2B and IASI), extending the analysis to the end of 2021 and using a model to quantify the impact of reducing the emissions versus meteorological effects. There was a large reduction of O_3 precursor gases due to activity restrictions in 2020 in response to the global COVID-19 pandemic. This is a unique chance to study how this might impact O_3 at the surface and in the free troposphere, in the context of continual precursor gas emission reductions in the future. Due to the relatively large uncertainties in satellite tropospheric O_3 data, e.g. a random error for each grid-box monthly average of ~ 1.1 – 1.4 DU (~ 6%) across the 3 satellite instruments used in Chapter 5, it is important to study more than one satellite record. Therefore this chapter builds on the work by Ziemke et al. (2022) from the NASA satellite tropospheric O_3 records, examining 3 satellite-derived products with a focus on Europe. Large O_3 reductions were found across Europe in 3 satellite records (GOME-2B, IASI-IMS-Extended, IASI-SOFRID) in spring/summer 2020 which are consistent with the previous studies. In 2021, reductions were found in the first 6 months of the year, but enhanced O_3 levels were found for the last 6 months. The model was used to attribute ~60% of the negative anomaly in April/May 2020 to emissions reductions, with the remaining ~40% to meteorology, specifically to a reduced STE flux. Therefore, suggesting that despite the unprecedented reductions in emissions seen in 2020, meteorology still plays a very important part in controlling O_3 in the free troposphere. Satellite data for several species was combined to derive [OH] in 2020, as currently there are few observationally-constrained studies of OH change in the pandemic period, finding a large negative anomaly peaking in March. This followed the method developed in Chapter 4, which demonstrated the potential of the method to capture global [OH] in the mid-troposphere compared to modelled OH and aircraft measurements. Answers to the research questions for this research gap are summarised as follows.

RQ 3.1: What happened to satellite-observed lower tropospheric O_3 *in the spring/summer of 2020 and 2021? How does this compare to previous years?*

Three satellite records (GOME-2B, IASI-IMS-Extended, IASI-SOFRID) showed reduced O_3 values in a lower tropospheric sub-column (surface – 450 hPa/0 – ~ 6km) in the spring/ summer 2020 and also in the first half of 2021. Relative to a monthly average baseline of 2018 – 2019, these satellite records showed negative anomalies of -9.3% to -14.7% in April 2020, and -4.7 to -14.7% in May 2020. In 2021, negative anomalies are found in the IASI-IMS-Extended record between January and July, peaking at -12% in April.

RQ 3.2: How does the satellite record compare to the ozonesonde and surface data records in the spring/summer of 2020 & 2021?

Ozonesondes and surface sites show a similar story of negative anomalies in spring/summer 2020, peaking at -17.0% and -21.7% in July 2020 (2018 – 2019 monthly average baseline), respectively. The negative anomalies seen in April/May are smaller. Therefore, in comparison with the satellite records, there is a temporal difference in when the largest O_3 reductions are seen. The satellite records are less sensitive at the surface, which could explain the difference between the satellite and the surface. For the difference between the ozonesondes and the satellite, this could be caused by differences in spatial sampling and coverage, due to the limited number of ozonesonde launch sites in Europe, or vertical resolution differences, from the greater vertical sensitivity of ozonesondes to the surface.

RQ 3.3: What information can atmospheric CTM simulations provide about the causes of the spring/summer 2020 reduction of lower tropospheric O_3? Can a quantification of the relative contribution of emissions and meteorology be calculated?

A TOMCAT simulation with reduced emissions, based on activity data, shows negative anomalies in 2020 peaking at -14.5% in May. Compared to a BAU scenario, reducing the emissions contributed more to the total scaled negative anomaly than the meteorology. This was quantified at ~60% due to the emission reduction for April and May 2020. 2021 showed smaller negative anomalies, peaking at 8.4% in the scaled emissions scenario, due equally to the emissions reduction and meteorology. A tracer for STE showed that the 2020 O_3 reduction from meteorology was predominantly due to a large reduction in the STE flux, but STE had less of an influence in 2021.

RQ 3.4: What happened to global satellite-derived OH in 2020?

Using the method developed in Chapter 4, satellite-derived OH showed a large global negative anomaly (across 400 – 800 hPa) of -20.1%. This is likely due to a negative anomaly in O_3 (source term) and a positive anomaly in CO (sink term).

7.2 Discussion of thesis results

This thesis has demonstrated the current potential of several satellite-derived datasets to provide important information about long-term changes in tropospheric composition. Quantification of changes in these two important species (O_3 and OH) is vital to understand exactly how the troposphere is changing. The satellite records used in this thesis have shown success in quantifying changes in tropospheric OH and O_3 over the last few decades. However, there are large uncertainties involved with using satellite retrievals and species such as O_3 show large interannual variability, which both potentially mask any long-term changes. These large uncertainties mean that small changes found e.g. for European O_3 between 1996 – 2017, cannot be concluded confidently. Larger changes which are consistent across several satellite records, e.g. tropospheric O_3 reductions of larger than ~ 2 DU (~ 10%) found in this thesis in 2020, can be concluded with more confidence. Studying multiple satellite species together can provide further insights, e.g. using O_3, CO, CH_4, H_2O to approximate OH can provide information on long-term OH change, and also allows for identification of how these OH sources and sinks varied in importance to approximated OH over time.

An atmospheric chemistry transport model, TOMCAT, was used to provide an insight into what may be causing these changes e.g. variation in surface emissions, meteorological processes, and understanding differences between satellite records. The TOMCAT record showed that surface emissions were the dominant influence on tropospheric O_3 trends over main-land continental Europe since the mid-1990s, suggesting that further restrictions are needed to see larger negative trends over this region. The large emission reductions seen during the global COVID pandemic of 2020-2021 suggest that similar large emission reductions will cause notable negative reductions in tropospheric O_3 over Europe, however, meteorology still has a large impact (~ $^1/_3$ in this case) so can either enhance or reduce O_3 improvements.

7.3 Future work

Despite continual improvement in satellite earth observation techniques e.g. increased resolution, new retrieval techniques, there are still currently limitations associated with using satellite-derived products. The uncertainty associated with the satellite retrievals are large, e.g. in Chapter 5, the average random retrieval error for each grid-box for the 3 instruments was ~ 6 – 7 DU or ~ 31%, which reduces to ~1.0 – 1.5 DU or ~ 6% when considered as a monthly average. These errors are large, especially when compared to small long-term changes, e.g. trends in the region of < 0.5 DU year^{-1}, or monthly anomalies in the region of < 3 DU. There are also other instrument specific caveats to consider, such as the OMI row anomaly and UV degradation of GOME and SCIAMACHY, especially considering the impact of these uncertainties is likely to have changed over time. To confidently quantify long-term changes, improvements in the satellite uncertainties are required. As these instruments and the retrieval techniques advance, with smaller errors and uncertainties, similar analysis could be performed and small trends quantified more accurately.

Another important consideration for this work is the representation of the key processes which impact tropospheric O_3 in the model, TOMCAT. The representation of factors which affect tropospheric O_3 in TOMCAT, e.g. surface deposition, STE, stratospheric O_3 and surface precursor gas emissions, are all important when trying to quantify long-term changes. Studying the impact of the representation of these factors on the O_3 simulations would be the next step to improving the model and proving an estimate of the uncertainty produced by these processes. For example, relevant to Chapter 6, a valuable further development for this work would be the representation of interactive stratospheric O_3 in TOMCAT. In the TOMCAT version used here, there is a fixed climatology for stratospheric O_3. Therefore, these results cannot be used as evidence towards the impact of the low Arctic stratospheric O_3 in the winter/spring of 2019/2020 (Wohltmann et al., 2020; Weber et al., 2021; Feng et al., 2021) on tropospheric O_3. A better representation of stratospheric O_3 could potentially show an enhancement or reduction in the negative anomaly seen in the model presented in this work, and could potentially be used to distinguish the influence of the amount of stratospheric O_3 to the STE flux. Another example, relevant to Chapter 4, is the use of model photolysis rates of O_3 in the simplified steady-state approximation for the long-term variation (2008 – 2017). The accuracy of the modelled j_1 needs to be further investigated, beyond the limited temporal and spatial comparison using aircraft measurements in Appendix D.

There is scope to study further satellite records to investigate long-term changes, to complement those used here. In the method developed in Chapter 4, the simplified selection of sources and sinks did not sufficiently represent the more complex OH chemistry in some regions of the atmosphere e.g. mid-troposphere NH at latitudes 30°N – 60°N had a greater influence from NO_x. If NO could be constrained by satellite data, the addition of this source into the S-SSA would improve the agreement in this region. Satellite retrievals of NO_2 exist for a co-located instrument (GOME-2, also aboard the MetOp satellites) (Munro et al., 2016), which could be used to derive NO. Satellite observations of other species, e.g. isoprene and formaldehyde, could also be implemented into the approximation to improve the agreement. In Chapter 5, differences between instruments were highlighted, showing the different long-term trends the satellite products present. Therefore, it would be beneficial to study any further satellite tropospheric O_3 products which are available, e.g. the IR instruments (IASI), to see if they show a similar story.

As the satellite records cover different time periods, with limited usable lifetimes in some cases, it would be interesting to produce a merged or composite record to study a longer time period of changes. This technique has been used previously, e.g. Ziemke et al. (2019) and can provide trends over a much longer time period. Chapter 5 showed little evidence to suggest there has been a linear change in tropospheric O_3 since 1996. An alternative approach to consider how tropospheric O_3 has changed since 1996 would be to consider how a multi-year (e.g. 5-year) average at the start and end of the record are different. However, due to the limited lifetime of the products, this could be better achieved using a longer merged record. A merged record could also provide further insights into the relative variation of 2020/2021 compared to previous years. Parrish et al. (2022) highlighted the impact of reductions in the baseline surface O_3 in recent years (from ~2014), which had previously stabilised since the late 1990s, to studying 2020 relative to the last two decades. The study of 2020 tropospheric O_3 in relation to long-term O_3 trends was also investigated by Chang et al. (2022). A long-term merged record, from products used in Chapters 5 and 6, could provide a means of studying 2020/2021 in comparison to the long-term satellite trend from a much longer time period than presently, which could be compared with Chang et al. (2022) and Parrish et al. (2022). However, a merged record would require development and testing due to the impact of differences between the instruments, as highlighted in Chapter 5. There is a potential to use artificial intelligence (AI), e.g. machine learning (ML) techniques, to merge and harmonise several satellite records, as performed for the stratosphere by Dhomse et al. (2021).

References

van der A., R.J., Eskes, H.J., Boersma, K.F., van Noije, T.P.C., Van Roozendael, M., De Smedt, I., Peters, D.H.M.U. and Meijer, E.W. 2008. Trends, seasonal variability and dominant NOx source derived from a ten year record of NO2 measured from space. *Journal of Geophysical Research Atmospheres*. **113**(4), pp.1–12.

van der A, R.J., Van Oss, R.F., Piters, A.J.M., Fortuin, J.P.F., Meijer, Y.J. and Kelder, H.M. 2002. Ozone profile retrieval from recalibrated Global Ozone Monitoring Experiment data. *Journal of Geophysical Research Atmospheres*. **107**(15), ACH 2-1-ACH 2-10.

van der A, R.J., Peters, D.H.M.U., Eskes, H., Boersma, K.F., Van Roozendael, M., De Smedt, I. and Kelder, H.M. 2006. Detection of the trend and seasonal variation in tropospheric NO2 over China. *Journal of Geophysical Research Atmospheres*. **111**(12), pp.1–10.

Anderson, D.C., Duncan, B.N., Fiore, A.M., Baublitz, C.B., Follette-Cook, M.B., Nicely, J.M. and Wolfe, G.M. 2021. Spatial and temporal variability in the hydroxyl (OH) radical: Understanding the role of large-scale climate features and their influence on OH through its dynamical and photochemical drivers. *Atmospheric Chemistry and Physics*. **21**(8), pp.6481–6508.

Anderson, D.C., Duncan, B.N., Nicely, J.M., Liu, J., Strode, S.A. and Follette-Cook, M.B. 2023. Technical note: Constraining the hydroxyl (OH) radical in the tropics with satellite observations of its drivers – first steps toward assessing the feasibility of a global observation strategy. *Atmospheric Chemistry and Physics*. **23**(11), pp.6319–6338.

Arnold, S.R., Chipperfield, M.P. and Blitz, M.A. 2005. A three-dimensional model study of the effect of new temperature-dependent quantum yields for acetone photolysis. *Journal of Geophysical Research Atmospheres*. **110**(22), pp.1–14.

Ashmore, M.R. 2005. Assessing the future global impacts of ozone on vegetation. *Plant, Cell \& Environment*. **28**(8), pp.949–964.

Atkinson, R., Baulch, D.L., Cox, R.A., Crowley, J.N., Hampson, R.F., Hynes, R.G., Jenkin, M.E., Rossi, M.J. and Troe, J. 2006. Evaluated kinetic and photochemical data for atmospheric chemistry: Volume II – gas phase reactions of organic species. *Atmospheric Chemistry and Physics*. **6**(11), pp.3625–4055.

Banerjee, A., C. Maycock, A., T. Archibald, A., Luke Abraham, N., Telford, P., Braesicke, P. and A. Pyle, J. 2016. Drivers of changes in stratospheric and tropospheric ozone between year 2000 and 2100. *Atmospheric Chemistry and Physics*. **16**(5), pp.2727–2746.

Barret, B., Emili, E. and Le Flochmoen, E. 2020. A tropopause-related climatological a priori profile for IASI-SOFRID ozone retrievals: Improvements and validation. *Atmospheric Measurement Techniques*. **13**(10), pp.5237–5257.

Barret, B., Le Flochmoen, E., Sauvage, B., Pavelin, E., Matricardi, M. and Cammas, J.P. 2011. The detection of post-monsoon tropospheric ozone variability over south Asia using IASI data. *Atmospheric Chemistry and Physics*. **11**(18), pp.9533–9548.

Bethan, S., Vaughan, G. and Reid, S.J. 1996. A comparison of ozone and thermal tropopause heights and the impact of tropopause definition on quantifying the ozone content of the troposphere. *Quarterly Journal of the Royal Meteorological Society*. **122**(532), pp.929–944.

BIRA-IASB 2023. What is the Dobson Unit (DU)? [Accessed 1 June 2023]. Available from: https://sacs.aeronomie.be/info/dobson.php.

Bloss, W.J., Lee, J.D., Heard, D.E., Salmon, R.A., Bauguitte, S.J.B., Roscoe, H.K. and

Jones, A.E. 2007. Observations of OH and HO2 radicals in coastal Antarctica. *Atmospheric Chemistry and Physics*. **7**(16), pp.4171–4185.

Boleti, E., Hueglin, C., K. Grange, S. and Takahama, S. 2020. Temporal and spatial analysis of ozone concentrations in Europe based on timescale decomposition and a multi-clustering approach. *Atmospheric Chemistry and Physics*. **20**(14), pp.9051–9066.

Boothe, A.C. and Homeyer, C.R. 2017. Global large-scale stratosphere-troposphere exchange in modern reanalyses. *Atmospheric Chemistry and Physics*. **17**(9), pp.5537–5559.

Bouarar, I., Gaubert, B., Brasseur, G.P., Steinbrecht, W., Doumbia, T., Tilmes, S., Liu, Y., Stavrakou, T., Deroubaix, A., Darras, S., Granier, C., Lacey, F., Müller, J.F., Shi, X., Elguindi, N. and Wang, T. 2021. Ozone Anomalies in the Free Troposphere During the COVID-19 Pandemic. *Geophysical Research Letters*. **48**(16), pp.1–11.

Bovensmann, H., Burrows, J.P., Buchwitz, M., Frerick, J., Noël, S., Rozanov, V. V., Chance, K. V. and Goede, A.P.H. 1999. SCIAMACHY: Mission objectives and measurement modes. *Journal of the Atmospheric Sciences*. **56**(2), pp.127–150.

Brewer, A. 1949. Evidence for a world circulation provided by the measurements of helium and water vapour distribution in the stratosphere. *Quarterly Journal of the Royal Meteorological Society*. **75**(326), pp.351–363.

Brune, W.H., Faloona, I.C., Tan, D., Weinheimer, A.J., Campos, T., Ridley, B.A., Vay, S.A., Collins, J.E., Sachse, G.W., Jaeglé, L. and Jacob, D.J. 1998. Airborne in-situ OH and HO2 observations in the cloud-free troposphere and lower stratosphere during SUCCESS. *Geophysical Research Letters*. **25**(10), pp.1701–1704.

Brune, W.H., Miller, D.O., Thames, A.B., Allen, H.M., Apel, E.C., Blake, D.R., Bui, T.P., Commane, R., Crounse, J.D., Daube, B.C., Diskin, G.S., DiGangi, J.P., Elkins, J.W., Hall, S.R., Hanisco, T.F., Hannun, R.A., Hintsa, E.J., Hornbrook, R.S., Kim, M.J., McKain, K., Moore, F.L., Neuman, J.A., Nicely, J.M., Peischl, J., Ryerson, T.B., St. Clair, J.M., Sweeney, C., Teng, A.P., Thompson, C., Ullmann, K., Veres, P.R., Wennberg, P.O. and Wolfe, G.M. 2019. Exploring Oxidation in the Remote Free Troposphere: Insights From Atmospheric Tomography (ATom). *Journal of Geophysical Research: Atmospheres*. **125**(1), pp.1–17.

Brune, W.H., Tan, D., Faloona, I.F., Jaeglé, L., Jacob, D.J., Heikes, B.G., Snow, J., Kondo, Y., Shetter, R., Sachse, G.W., Anderson, B., Gregory, G.L., Vay, S., Singh, H.B., Davis, D.D., Crawford, J.H. and Blake, D.R. 1999. OH and HO2 chemistry in the North Atlantic free troposphere. *Geophysical Research Letters*. **26**(20), pp.3077–3080.

Burkholder, J.B., Sander, S.P., Abbatt, J.P.D., Barker, J.R., Huie, R.E., Kolb, C.E., Kurylo, M.J., Orkin, V.L., Wilmouth, D.M. and Wine, P.H. 2019. Chemical Kinetics and Photochemical Data for Use in Atmospheric Studies, Evaluation No. 19. *JPL Publications 19-5*. (19).

Burrows, J.P., Weber, M., Buchwitz, M., Rozanov, V., Ladstätter-Weißenmayer, A., Richter, A., Debeek, R., Hoogen, R., Bramstedt, K., Eichmann, K.U., Eisinger, M. and Perner, D. 1999. The Global Ozone Monitoring Experiment (GOME): Mission concept and first scientific results. *Journal of the Atmospheric Sciences*. **56**(2), pp.151–175.

Butchart, N. 2014. The Brewer-Dobson circulation. *Rev. Geophys*. **52**, pp.157–184.

Butchart, N., Scaife, A.A., Bourqui, M., Grandpré, J., Hare, S.H.E., Kettleborough, J., Langematz, U., Manzini, E., Sassi, F., Shibata, K., Shindell, D. and Sigmond, M. 2006. Simulations of anthropogenic change in the strength of the Brewer-Dobson circulation. *Climate Dynamics*. **27**(7–8), pp.727–741.

Cai, Z., Liu, Y., Liu, X., Chance, K., Nowlan, C.R., Lang, R., Munro, R. and Suleiman, R. 2012. Characterization and correction of global ozone monitoring experiment 2 ultraviolet measurements and application to ozone profile retrievals. *Journal of Geophysical Research Atmospheres*. **117**(7), pp.1–16.

Callies, J., Corpaccioli, E., Eisinger, M., Hahne, A. and Lefebvre, A. 2000. GOME-2-Metop's second-generation sensor for operational ozone monitoring. *ESA bulletin*. **102**(may), pp.28–36.

Cantrell, C.A., Shetter, R.E., Gilpin, T.M., Calvert, J.G., Eisele, F.L. and Tanner, D.J. 1996. Peroxy radical concentrations measured and calculated from trace gas measurements in the Mauna Loa Observatory Photochemistry Experiment 2. *Journal of Geophysical Research Atmospheres*. **101**(D9), pp.14653–14664.

Chance, K. V., Burrows, J.P., Perner, D. and Schneider, W. 1997. Satellite measurements of atmospheric ozone profiles, including tropospheric ozone, from ultraviolet/visible measurements in the nadir geometry: A potential method to retrieve tropospheric ozone. *Journal of Quantitative Spectroscopy and Radiative Transfer*. **57**(4), pp.467–476.

Chang, K.L., Cooper, O.R., Gaudel, A., Allaart, M., Ancellet, G., Clark, H., Godin-Beekmann, S., Leblanc, T., Van Malderen, R., Nédélec, P., Petropavlovskikh, I., Steinbrecht, W., Stübi, R., Tarasick, D.W. and Torres, C. 2022. Impact of the COVID-19 Economic Downturn on Tropospheric Ozone Trends: An Uncertainty Weighted Data Synthesis for Quantifying Regional Anomalies Above Western North America and Europe. *AGU Advances*. **3**(2).

Chipperfield, M.P. 2006. New version of the TOMCAT/SLIMCAT off-line chemical transport model: Intercomparison of stratospheric tracer experiments. *Quarterly Journal of the Royal Meteorological Society*.

Christiansen, A., Mickley, L.J., Liu, J., Oman, L.D. and Hu, L. 2022. Multidecadal increases in global tropospheric ozone derived from ozonesonde and surface site observations: Can models reproduce ozone trends? *Atmospheric Chemistry and Physics*. **22**(22), pp.14751–14782.

Clark, D.B., Mercado, L.M., Sitch, S., Jones, C.D., Gedney, N., Best, M.J., Pryor, M., Rooney, G.G., Essery, R.L.H., Blyth, E., Boucher, O., Harding, R.J., Huntingford, C. and Cox, P.M. 2011. The Joint UK Land Environment Simulator (JULES), model description – Part 2: Carbon fluxes and vegetation dynamics. *Geoscientific Model Development*. **4**(3), pp.701–722.

Clark, H., Bennouna, Y., Tsivlidou, M., Wolff, P., Sauvage, B., Barret, B., Le Flochmoën, E., Blot, R., Boulanger, D., Cousin, J.M., Nédélec, P., Petzold, A. and Thouret, V. 2021. The effects of the COVID-19 lockdowns on the composition of the troposphere as seen by In-service Aircraft for a Global Observing System (IAGOS) at Frankfurt. *Atmospheric Chemistry and Physics*. **21**(21), pp.16237–16256.

Clerbaux, C., Boynard, A., Clarisse, L., George, M., Hadji-Lazaro, J., Herbin, H., Hurtmans, D., Pommier, M., Razavi, A., Turquety, S., Wespes, C. and Coheur, P.F. 2009. Monitoring of atmospheric composition using the thermal infrared IASI/MetOp sounder. *Atmospheric Chemistry and Physics*. **9**(16), pp.6041–6054.

Clerbaux, C., Turquety, S. and Coheur, P. 2010. Infrared remote sensing of atmospheric composition and air quality: Towards operational applications. *Comptes Rendus - Geoscience*. **342**(4–5), pp.349–356.

Cooper, O.R., Parrish, D.D., Ziemke, J., Balashov, N. V., Cupeiro, M., Galbally, I.E., Gilge, S., Horowitz, L., Jensen, N.R., Lamarque, J.F., Naik, V., Oltmans, S.J., Schwab, J., Shindell, D.T., Thompson, A.M., Thouret, V., Wang, Y. and Zbinden, R.M. 2014. Global distribution and trends of tropospheric ozone: An observation-based review. *Elementa*. **2**, pp.1–28.

Copernicus Climate Change Service 2020. State-of-the-European-climate: July 2020. [Accessed 24 October 2023]. Available from: https://surfobs.climate.copernicus.eu/stateoftheclimate/july2020.php.

Creasey, D.J., Evans, G.E., Heard, D.E. and Lee, J.D. 2003. Measurements of OH and HO2 concentrations in the Southern Ocean marine boundary layer. *Journal of Geophysical Research: Atmospheres*. **108**(15), pp.1–12.

Cuesta, J., Costantino, L., Beekmann, M., Siour, G., Menut, L., Bessagnet, B., Landi, T.C., Dufour, G. and Eremenko, M. 2022. Ozone pollution during the COVID-19 lockdown in the spring of 2020 over Europe, analysed from satellite observations, in situ measurements, and models. *Atmospheric Chemistry and Physics*. **22**(7), pp.4471–4489.

Dalsøren, S.B., Myhre, C.L., Myhre, G., Gomez-Pelaez, A.J., Søvde, O.A., Isaksen, I.S.A., Weiss, R.F. and Harth, C.M. 2016. Atmospheric methane evolution the last 40 years. *Atmospheric Chemistry and Physics*. **16**(5), pp.3099–3126.

Dee, D.P., Uppala, S.M., Simmons, A.J., Berrisford, P., Poli, P., Kobayashi, S., Andrae, U., Balmaseda, M.A., Balsamo, G., Bauer, P., Bechtold, P., Beljaars, A.C.M., van de Berg, L., Bidlot, J., Bormann, N., Delsol, C., Dragani, R., Fuentes, M., Geer, A.J., Haimberger, L., Healy, S.B., Hersbach, H., Hólm, E. V., Isaksen, L., Kållberg, P., Köhler, M., Matricardi, M., Mcnally, A.P., Monge-Sanz, B.M., Morcrette, J.J., Park, B.K., Peubey, C., de Rosnay, P., Tavolato, C., Thépaut, J.N. and Vitart, F. 2011. The ERA-Interim reanalysis: Configuration and performance of the data assimilation system. *Quarterly Journal of the Royal Meteorological Society*. **137**(656), pp.553–597.

Derwent, R.G., Manning, A.J., Simmonds, P.G., Spain, T.G. and O'Doherty, S. 2013. Analysis and interpretation of 25 years of ozone observations at the Mace Head Atmospheric Research Station on the Atlantic Ocean coast of Ireland from 1987 to 2012. *Atmospheric Environment*. **80**, pp.361–368.

Derwent, R.G., Manning, A.J., Simmonds, P.G., Spain, T.G. and O'Doherty, S. 2018. Long-term trends in ozone in baseline and European regionally-polluted air at Mace Head, Ireland over a 30-year period. *Atmospheric Environment*. **179**(February), pp.279–287.

Derwent, R.G. and Parrish, D.D. 2022. Analysis and assessment of the observed long-term changes over three decades in ground-level ozone across north-west Europe from 1989 - 2018. *Atmospheric Environment*. **286**(January), p.119222.

Derwent, R.G., Simmonds, P.G. and Collins, W.J. 1994. Ozone and carbon monoxide measurements at a remote maritime location, mace head, Ireland, from 1990 to 1992. *Atmospheric Environment*. **28**(16), pp.2623–2637.

Dhomse, S.S., Arosio, C., Feng, W., Rozanov, A., Weber, M. and Chipperfield, M.P. 2021. ML-TOMCAT: Machine-learning-based satellite-corrected global stratospheric ozone profile data set from a chemical transport model. *Earth System Science Data*. **13**(12), pp.5711–5729.

Van Dingenen, R., Dentener, F.J., Raes, F., Krol, M.C., Emberson, L. and Cofala, J. 2009. The global impact of ozone on agricultural crop yields under current and future air quality legislation. *Atmospheric Environment*. **43**(3), pp.604–618.

Dlugokencky, E. 2020. NOAA Global Monitoring Laboratory - Trends in Atmospheric Methane. [Accessed 1 May 2020]. Available from: https://gml.noaa.gov/ccgg/trends_ch4/.

Dobson, G.M.B. 1956. Origin and distribution of the polyatomic molecules in the atmosphere. *Proceedings of the Royal Society A*. **236**(1205).

Doumbia, T., Granier, C., Elguindi, N., Bouarar, I., Darras, S., Brasseur, G., Gaubert, B., Liu, Y., Shi, X., Stavrakou, T., Tilmes, S., Lacey, F., Deroubaix, A. and Wang, T. 2021. Changes in global air pollutant emissions during the COVID-19 pandemic: A dataset for atmospheric modeling. *Earth System Science Data*. **13**(8), pp.4191–4206.

Dyson, J.E., Whalley, L.K., Slater, E.J., Woodward-Massey, R., Ye, C., Lee, J.D., Squires, F., Hopkins, J.R., Dunmore, R.E., Shaw, M., Hamilton, J.F., Lewis, A.C., Worrall, S.D., Bacak, A., Mehra, A., Bannan, T.J., Coe, H., Percival, C.J., Ouyang, B., Hewitt, C.N., Jones, R.L., Crilley, L.R., Kramer, L.J., Acton, W.J.F., Bloss, W.J., Saksakulkrai, S., Xu, J., Shi, Z., Harrison, R.M., Kotthaus, S., Grimmond, S., Sun, Y., Xu, W., Yue, S., Wei, L., Fu, P., Wang, X., Arnold, S.R. and Heard, D.E. 2023. Impact of HO2 aerosol uptake on radical levels and O3 production during summertime in Beijing. *Atmospheric Chemistry and Physics*. **23**(10), pp.5679–5697.

EBAS 2022. EBAS. [Accessed 1 December 2022]. Available from: https://ebas.nilu.no/.

Ebojie, F., Burrows, J.P., Gebhardt, C., Ladstätter-Weißenmayer, A., Von Savigny, C., Rozanov, A., Weber, M. and Bovensmann, H. 2016. Global tropospheric ozone variations from 2003 to 2011 as seen by SCIAMACHY. *Atmospheric Chemistry and Physics*. **16**(2), pp.417–436.

Edwards, P.M., Evans, M.J., Furneaux, K.L., Hopkins, J., Ingham, T., Jones, C., Lee, J.D., Lewis, A.C., Moller, S.J., Stone, D., Whalley, L.K. and Heard, D.E. 2013. OH reactivity in a South East Asian tropical rainforest during the oxidant and particle photochemical processes (OP3) project. *Atmospheric Chemistry and Physics*. **13**(18), pp.9497–9514.

Eisele, F.L., Mauldin, L., Cantrell, C., Zondlo, M., Apel, E., Fried, A., Walega, J., Shetter, R., Lefer, B., Flocke, F., Weinheimer, A., Avery, M., Vay, S., Sachse, G., Podolske, J., Diskin, G., Barrick, J.D., Singh, H.B., Brune, W., Harder, H., Martinez, M., Bandy, A., Thornton, D., Heikes, B., Kondo, Y., Riemer, D., Sandholm, S., Tan, D., Talbot, R. and Dibb, J. 1996. Measurements and steady state calculations of OH concentrations at Mauna Loa Observatory. *Journal of Geophysical Research Atmospheres*. **101**(D9), pp.14665–14679.

Eisele, F.L., Mauldin, L., Cantrell, C., Zondlo, M., Apel, E., Fried, A., Walega, J., Shetter, R., Lefer, B., Floke, F., Weinheimer, A., Avery, M., Vay, S., Sachse, G., Podolske, J., Diskin, G., Barrick, J.D., Singh, H.B., Brune, W., Harder, H., Martinez, M., Bandy, A., Thornton, D., Heikes, B., Kondo, Y., Riemer, D., Sandholm, S., Tan, D., Talbot, R. and Dibb, J. 2003. Summary of measurement intercomparisons during TRACE-P. *Journal of Geophysical Research: Atmospheres*. **108**(20), pp.1–20.

Emmons, L.K., Arnold, S.R., Monks, S.A., Huijnen, V., Tilmes, S., Law, K.S., Thomas, J.L., Raut, J.-C., Bouarar, I., Turquety, S., Long, Y., Duncan, B., Steenrod, S., Strode, S., Flemming, J., Mao, J., Langner, J., Thompson, A.M., Tarasick, D., Apel, E.C., Blake, D.R., Cohen, R.C., Dibb, J., Diskin, G.S., Fried, A., Hall, S.R., Huey, L.G., Weinheimer, A.J., Wisthaler, A., Mikoviny, T., Nowak, J., Peischl, J., Roberts, J.M., Ryerson, T., Warneke, C. and Helmig, D. 2015. The POLARCAT Model Intercomparison Project (POLMIP): overview and evaluation with observations. *Atmospheric Chemistry and Physics*. **15**(12), pp.6721–6744.

EUMETSAT n.d. Metop series. [Accessed 19 December 2022]. Available from: https://www.eumetsat.int/our-satellites/metop-series.

European Commission 2023. TIMELINE OF THE EU'S HEALTH ACTIONS DURING THE COVID-19 PANDEMIC: Epidemiological situation.

European Environment Agency 2021. Air quality in Europe 2021. [Accessed 1 March 2023]. Available from: https://www.eea.europa.eu/publications/air-quality-in-europe-2021.

European Environment Agency 2022. *Air quality in Europe 2022* [Online]. Available from: https://www.eea.europa.eu/publications/air-quality-in-europe-2022.

European Environment Agency 2009. *Assessment of ground-level ozone in EEA member countries, with a focus on long-term trends*.

European Space Agency n.d. GOME Overview. [Accessed 20 December 2022]. Available from: https://earth.esa.int/eogateway/instruments/gome/description.

European Space Agency 2023. Types of Orbit. [Accessed 2 June 2023]. Available from: https://www.esa.int/Enabling_Support/Space_Transportation/Types_of_orbits.

Fahey, D.W. and Hegglin, M.I. 2011. *Twenty Questions and Answers About the Ozone Layer: 2010 Update, Scientific Assessment of Ozone Depletion* [Online]. Geneva, Switzerland. Available from: https://csl.noaa.gov/assessments/ozone/2010/twentyquestions/.

Faloona, I.C., Tan, D., Lesher, R.L., Hazen, N.L., Frame, C.L., Simpas, J.B., Harder, H., Martinez, M., Di Carlo, P., Ren, X. and Brune, W.H. 2004. A laser-induced fluorescence instrument for detecting tropospheric OH and HO2: Characteristics and calibration. *Journal of Atmospheric Chemistry*. **47**(2), pp.139–167.

Feng, L., Palmer, P.I., Parker, R.J., Lunt, M.F. and Bösch, H. 2023. Methane emissions are predominantly responsible for record-breaking atmospheric methane growth rates in 2020 and 2021. *Atmospheric Chemistry and Physics*. **23**(8), pp.4863–4880.

Feng, L., Smith, S.J., Braun, C., Crippa, M., Gidden, M.J., Hoesly, R., Klimont, Z., Van Marle, M., Van Den Berg, M. and Van Der Werf, G.R. 2020. The generation of gridded emissions data for CMIP6. *Geoscientific Model Development*. **13**(2), pp.461–482.

Feng, W., Dhomse, S.S., Arosio, C., Weber, M., Burrows, J.P., Santee, M.L. and Chipperfield, M.P. 2021. Arctic Ozone Depletion in 2019/20: Roles of Chemistry, Dynamics and the Montreal Protocol. *Geophysical Research Letters*. **48**(4), pp.1–10.

Ferracci, V., Heimann, I., Luke Abraham, N., Pyle, J.A. and Archibald, A.T. 2018. Global modelling of the total OH reactivity: Investigations on the 'missing' OH sink and its atmospheric implications. *Atmospheric Chemistry and Physics*. **18**(10), pp.7109–7129.

Fiore, A.M., Dentener, F.J., Wild, O., Cuvelier, C., Schultz, M.G., Hess, P., Textor, C., Schulz, M., Doherty, R.M., Horowitz, L.W., MacKenzie, I.A., Sanderson, M.G., Shindell, D.T., Stevenson, D.S., Szopa, S., Van Dingenen, R., Zeng, G., Atherton, C., Bergmann, D., Bey, I., Carmichael, G., Collins, W.J., Duncan, B.N., Faluvegi, G., Folberth, G., Gauss, M., Gong, S., Hauglustaine, D., Holloway, T., Isaksen, I.S.A., Jacob, D.J., Jonson, J.E., Kaminski, J.W., Keating, T.J., Lupu, A., Manner, E., Montanaro, V., Park, R.J., Pitari, G., Pringle, K.J., Pyle, J.A., Schroeder, S., Vivanco, M.G., Wind, P., Wojcik, G., Wu, S. and Zuber, A. 2009. Multimodel estimates of intercontinental source-receptor relationships for ozone pollution. *Journal of Geophysical Research Atmospheres*. **114**(4), pp.1–21.

Fishman, J. and Larsen, J.C. 1987. Distribution of total ozone and stratospheric ozone in the tropics: implications for the distribution of tropospheric ozone. *Journal of Geophysical Research*. **92**(D6), pp.6627–6634.

Fishman, J., Watson, C.E., Larsen, J.C. and Logan, J.A. 1990. Distribution of tropospheric ozone determined from satellite data. *Journal of Geophysical Research*. **95**(D4), pp.3599–3617.

Forster, P.M., Forster, H.I., Evans, M.J., Gidden, M.J., Jones, C.D., Keller, C.A., Lamboll, R.D., Quéré, C. Le, Rogelj, J., Rosen, D., Schleussner, C.F., Richardson, T.B., Smith, C.J. and Turnock, S.T. 2020. Current and future global climate impacts resulting from COVID-19. *Nature Climate Change*. **10**(10), pp.913–919.

Fowler, D., Pilegaard, K., Sutton, M.A., Ambus, P., Raivonen, M., Duyzer, J., Simpson, D., Fagerli, H., Fuzzi, S., Schjoerring, J.K., Granier, C., Neftel, A., Isaksen, I.S.A., Laj, P., Maione, M., Monks, P.S., Burkhardt, J., Daemmgen, U., Neirynck, J., Personne, E., Wichink-Kruit, R., Butterbach-Bahl, K., Flechard, C., Tuovinen, J.P., Coyle, M., Gerosa, G., Loubet, B., Altimir, N., Gruenhage, L., Ammann, C., Cieslik, S., Paoletti, E., Mikkelsen, T.N., Ro-Poulsen, H., Cellier, P., Cape, J.N., Horváth, L., Loreto, F., Niinemets, Ü., Palmer, P.I., Rinne, J., Misztal, P., Nemitz, E., Nilsson, D., Pryor, S., Gallagher, M.W., Vesala, T., Skiba, U., Brüggemann, N., Zechmeister-Boltenstern, S., Williams, J., O'Dowd, C., Facchini, M.C., de Leeuw, G., Flossman, A., Chaumerliac, N. and Erisman, J.W. 2009. Atmospheric composition change: Ecosystems-Atmosphere interactions. *Atmospheric Environment*. **43**(33), pp.5193–5267.

Gaudel, A., Cooper, O.R., Ancellet, G., Barret, B., Boynard, A., Burrows, J.P., Clerbaux, C., Coheur, P.F., Cuesta, J., Cuevas, E., Doniki, S., Dufour, G., Ebojie, F., Foret, G., Garcia, O., Granados-Muñoz, M.J., Hannigan, J.W., Hase, F., Hassler, B., Huang, G., Hurtmans, D., Jaffe, D., Jones, N., Kalabokas, P., Kerridge, B., Kulawik, S., Latter, B., Leblanc, T., Le Flochmoën, E., Lin, W., Liu, J., Liu, X., Mahieu, E., McClure-Begley, A., Neu, J.L., Osman, M., Palm, M., Petetin, H., Petropavlovskikh, I., Querel, R., Rahpoe, N., Rozanov, A., Schultz, M.G., Schwab, J., Siddans, R., Smale, D., Steinbacher, M., Tanimoto, H., Tarasick, D.W., Thouret, V., Thompson, A.M., Trickl, T., Weatherhead, E., Wespes, C., Worden, H.M., Vigouroux, C., Xu, X., Zeng, G. and Ziemke, J. 2018. Tropospheric Ozone Assessment Report: Present-day distribution and trends of tropospheric ozone relevant to climate and global atmospheric chemistry model evaluation. *Elementa*.

Gaudel, A., Cooper, O.R., Chang, K.L., Bourgeois, I., Ziemke, J.R., Strode, S.A., Oman, L.D., Sellitto, P., Nédélec, P., Blot, R., Thouret, V. and Granier, C. 2020. Aircraft observations since the 1990s reveal increases of tropospheric ozone at multiple locations across the Northern Hemisphere. *Science Advances*. **6**(34), pp.1–12.

Giannakopoulos, C., Chipperfield, M.P., Law, K.S. and Pyle, J.A. 1999. Validation and intercomparison of wet and dry deposition schemes using 210-Pb in a global three-dimensional off-line chemical transport model. . **104**(D19), pp.23761–23784.

Gidden, M.J., Riahi, K., Smith, S.J., Fujimori, S., Luderer, G., Kriegler, E., van Vuuren, D.P., van den Berg, M., Feng, L., Klein, D., Calvin, K., Doelman, J.C., Frank, S., Fricko, O., Harmsen, M., Hasegawa, T., Havlik, P., Hilaire, J., Hoesly, R., Horing, J., Popp, A., Stehfest, E. and Takahashi, K. 2019. Global emissions pathways under different socioeconomic scenarios for use in CMIP6: a dataset of harmonized emissions trajectories through the end of the century. *Geoscientific Model Development*. **12**(4), pp.1443–1475.

Gilge, S., Plass-Duelmer, C., Fricke, W., Kaiser, A., Ries, L., Buchmann, B. and Steinbacher, M. 2010. Ozone, carbon monoxide and nitrogen oxides time series at four alpine GAW mountain stations in central Europe. *Atmospheric Chemistry and Physics*. **10**(24), pp.12295–12316.

Gottwald, M., Bovensmann, H., Lichtenberg, G., Noel, S., Bargen, A., von Slijkhuis, S., Piters, A., Hoogeveen, R., von Savigny, C., Buchwitz, M., Kokhanovsky, A., Richter, A., Rozanov, A., Holzer-Popp, T., Bramstedt, K., Lambert, J.-C., Skupin, J., Wittrock, F., Schrijver, H. and Burrows, J.P. 2006. *SCIAMACHY, Monitoring the Changing Earth's Atmosphere*. DLR.

Grange, S.K., Lee, J.D., Drysdale, W.S., Lewis, A.C., Hueglin, C., Emmenegger, L. and Carslaw, D.C. 2021. COVID-19 lockdowns highlight a risk of increasing ozone pollution in European urban areas. *Atmospheric Chemistry and Physics*. **21**(5), pp.4169–4185.

Granier, C., Bessagnet, B., Bond, T., D’Angiola, A., van der Gon, H.D., Frost, G.J., Heil, A., Kaiser, J.W., Kinne, S., Klimont, Z., Kloster, S., Lamarque, J.F., Liousse, C., Masui, T., Meleux, F., Mieville, A., Ohara, T., Raut, J.C., Riahi, K., Schultz, M.G., Smith, S.J., Thompson, A., van Aardenne, J., van der Werf, G.R. and van Vuuren, D.P. 2011. Evolution of anthropogenic and biomass burning emissions of air pollutants at global and regional scales during the 1980-2010 period. *Climatic Change*. **109**(1), pp.163–190.

Granier, C., Darras, S., Gon, H.D. van der, Doubalova, J., Elguindi, N., Galle, B., Gauss, M., Guevara, M., Jalkanen, J.-P., Kuenen, J., Liousse, C., Quack, B., Simpson, D. and Sindelarova, K. 2019. *The Copernicus Atmosphere Monitoring Service global and regional emissions (April 2019 version)*.

Granier, C., Guenther, A., Lamarque, J.F., Mieville, A., Muller, J.F., Olivier, J., Orlando, J., Peters, J., Petron, G., Tyndall, G. and Wallens, S. 2005. POET, a database of surface emissions of ozone precursors.

Grenfell, J.L., Savage, N.H., Harrison, R.M., Penkett, S.A., Forberich, O., Comes, F.J., Clemitshaw, K.C., Burgess, R.A., Cárdenas, L.M., Davison, B. and McFadyen, G.G. 1999. Tropospheric box-modelling and analytical studies of the hydroxyl (OH) radical and related species: Comparison with observations. *Journal of Atmospheric Chemistry*.

Griffiths, P.T., Keeble, J., Shin, Y.M., Abraham, N.L., Archibald, A.T. and Pyle, J.A. 2020. On the Changing Role of the Stratosphere on the Tropospheric Ozone Budget: 1979–2010. *Geophysical Research Letters*. **47**(10), pp.1–9.

Guevara, M., Jorba, O., Soret, A., Petetin, H., Bowdalo, D., Serradell, K., Tena, C., Van Der Gon, H.D., Kuenen, J., Peuch, V.H. and Pérez Garciá-Pando, C. 2021. Time-resolved emission reductions for atmospheric chemistry modelling in Europe during the COVID-19 lockdowns. *Atmospheric Chemistry and Physics*. **21**(2), pp.773–797.

Hard, T.M., O’Brien, R.J., Chan, C.Y. and Mehrabzadeh, A.A. 1984. Tropospheric Free Radical Determination by FAGE. *Environmental Science and Technology*. **18**(10), pp.768–777.

Hayes, F., Sharps, K., Harmens, H., Roberts, I. and Mills, G. 2020. Tropospheric ozone pollution reduces the yield of African crops. *Journal of Agronomy and Crop Science*. **206**(2), pp.214–228.

He, J., Naik, V., Horowitz, L., Dlugokencky, E. and Thoning, K. 2020. Investigation of the global methane budget over 1980–2017 using GFDL-AM4.1. *Atmospheric Chemistry and Physics Discussions*. **20**, pp.805–827.

Hegglin, M.I. and Shepherd, T.G. 2009. Large climate-induced changes in ultraviolet index and stratosphere-to- troposphere ozone flux. *Nature Geoscience*. **2**(10), pp.687–691.

Hersbach, H., Bell, B., Berrisford, P., Hirahara, S., Horányi, A., Muñoz-Sabater, J., Nicolas, J., Peubey, C., Radu, R., Schepers, D., Simmons, A., Soci, C., Abdalla, S., Abellan, X., Balsamo, G., Bechtold, P., Biavati, G., Bidlot, J., Bonavita, M., De Chiara, G., Dahlgren, P., Dee, D., Diamantakis, M., Dragani, R., Flemming, J., Forbes, R., Fuentes, M., Geer, A., Haimberger, L., Healy, S., Hogan, R.J., Hólm, E., Janisková, M., Keeley, S., Laloyaux, P., Lopez, P., Lupu, C., Radnoti, G., de Rosnay, P., Rozum, I., Vamborg, F., Villaume, S. and Thépaut, J.N. 2020. The ERA5 global reanalysis. *Quarterly Journal of the Royal Meteorological Society*. **146**(730), pp.1999–2049.

Hocking, W.K., Carey-Smith, T., Tarasick, D.W., Argall, P.S., Strong, K., Rochon, Y., Zawadzki, I. and Taylor, P.A. 2007. WMO Bulletin. *Nature*. **450**(7167), pp.281–284.

Hogan, R. 2006. How to combine errors. [Accessed 1 December 2021]. Available from: http://cree.reading.ac.uk/~swrhgnrj/combining_errors.pdf.

Hollaway, M.J. 2012. *Modelling interactions between vegetation and tropospheric ozone*. University of Leeds.

Holton, J.R., Haynes, P.H., McIntyre, M.E., Douglass, A.R., Rood, R.B. and Pfister, L. 1995. Stratosphere-troposphere exchange. *Reviews of Geophysics*. **33**(4), pp.403–439.

Holtslag, A.A.M. and Boville, B.A. 1993. Local Versus Nonlocal Boundary-Layer Diffusion in a Global Climate Model. *Journal of Climate*. **6**(10), pp.1825–1842.

Hsu, J., Prather, M.J. and Wild, O. 2005. Diagnosing the stratosphere-to-troposphere flux of ozone in a chemistry transport model. *Journal of Geophysical Research D: Atmospheres*. **110**(19), pp.1–12.

Huang, J. and Prinn, R.G. 2002. Critical evaluation of emissions of potential new gases for OH estimation. *Journal of Geophysical Research Atmospheres*. **107**(24), pp.1–12.

Huijnen, V., Wooster, M.J., Kaiser, J.W., Gaveau, D.L.A., Flemming, J., Parrington, M., Inness, A., Murdiyarso, D., Main, B. and Van Weele, M. 2016. Fire carbon emissions over maritime southeast Asia in 2015 largest since 1997. *Scientific Reports*. **6**(May), pp.1–8.

Iglesias-Suarez, F., Kinnison, D.E., Rap, A., Maycock, A.C., Wild, O. and Young, P.J. 2018. Key drivers of ozone change and its radiative forcing over the 21st century. *Atmospheric Chemistry and Physics*. **18**(9), pp.6121–6139.

IPCC 2021. *Climate Change 2021: The Physical Science Basis: Contribution of Working Group I to the Sixth Assessment Report of the Intergovernmental Panel on Climate Change* (V. Masson-Delmotte, P. Zhai, A. Pirani, S. L. Connors, C. Péan, S. Berger, N. Caud, Y. Chen, L. Goldfarb, M. I. Gomis, M. Huang, K. Leitzell, E. Lonnoy, J. B. R. Matthews, T. K. Maycock, T. Waterfield, O. Yelekçi, R. Yu, & B. Zhou, eds.). Cambridge, United Kingdom: Cambridge University Press.

Jacob, D.J. 1999. *Introduction to Atmospheric Chemistry*. Princeton University Press.

Jaume, T., Anna, R., Lorena, B., Ortiz, A.G. and Joana, S. 2021. ETC/ATNI Report 7/2021: Status report of air quality in Europe for year 2021, using validated and up-to-date data. , p.56.

Jenkin, M.E. 2008. Trends in ozone concentration distributions in the UK since 1990: Local, regional and global influences. *Atmospheric Environment*. **42**(21), pp.5434–5445.

Karion, A., Sweeney, C., Wolter, S., Newberger, T., Chen, H., Andrews, A., Kofler, J., Neff, D. and Tans, P. 2013. Long-term greenhouse gas measurements from aircraft. *Atmospheric Measurement Techniques*. **6**(3), pp.511–526.

Keppens, A., Lambert, J.C., Granville, J., Hubert, D., Verhoelst, T., Compernolle, S., Latter, B., Kerridge, B., Siddans, R., Boynard, A., Hadji-Lazaro, J., Clerbaux, C., Wespes, C., Hurtmans, D.R., Coheur, P.F., Van Peet, J.C.A., Vander, R.J.A., Garane, K., Elissavet Koukouli, M., Balis, D., Delcloo, A., Kivi, R., Stübi, R., Godin-Beekmann, S., Van Roozendael, M. and Zehner, C. 2018. Quality assessment of the Ozone-cci Climate Research Data Package (release 2017) - Part 2: Ground-based validation of nadir ozone profile data products. *Atmospheric Measurement Techniques*. **11**(6), pp.3769–3800.

Kim, H., Park, R.J., Kim, S., Brune, W.H., Diskin, G.S., Fried, A., Hall, S.R., Weinheimer, A.J., Wennberg, P., Wisthaler, A., Blake, D.R. and Ullmann, K. 2022. Observed versus simulated OH reactivity during KORUS-AQ campaign: Implications for emission inventory and chemical environment in East Asia. *Elementa*. **10**(1), pp.1–26.

Kim, J., Jeong, U., Ahn, M.H., Kim, J.H., Park, R.J., Lee, Hanlim, Song, C.H., Choi, Y.S., Lee, K.H., Yoo, J.M., Jeong, M.J., Park, S.K., Lee, K.M., Song, C.K., Kim, Sang Woo, Kim, Y.J., Kim, Si Wan, Kim, M., Go, S., Liu, X., Chance, K., Miller, C.C., Al-Saadi, J., Veihelmann, B., Bhartia, P.K., Torres, O., Abad, G.G., Haffner, D.P., Ko, D.H., Lee, S.H., Woo, J.H., Chong, H., Park, S.S., Nicks, D., Choi, W.J., Moon, K.J., Cho, A., Yoon, J., Kim, S. kyun, Hong, H., Lee, K., Lee, Hana, Lee, S., Choi, M., Veefkind, P., Levelt, P.F., Edwards, D.P., Kang, M., Eo, M., Bak, J., Baek, K., Kwon, H.A., Yang, J., Park, J., Han, K.M., Kim, B.R., Shin, H.W., Choi, H., Lee, E., Chong, J., Cha, Y., Koo, J.H., Irie, H., Hayashida, S., Kasai, Y., Kanaya, Y., Liu, C., Lin, J., Crawford, J.H., Carmichael, G.R., Newchurch, M.J., Lefer, B.L., Herman, J.R., Swap, R.J., Lau, A.K.H., Kurosu, T.P., Jaross, G., Ahlers, B., Dobber, M., McElroy, C.T. and Choi, Y. 2020. New era of air quality monitoring from space: Geostationary environment monitoring spectrometer (GEMS). *Bulletin of the American Meteorological Society*. **101**(1), pp.E1–E22.

Kinnison, D.E., Brasseur, G.P., Walters, S., Garcia, R.R., Marsh, D.R., Sassi, F., Harvey, V.L., Randall, C.E., Emmons, L., Lamarque, J.F., Hess, P., Orlando, J.J., Tie, X.X., Randel, W., Pan, L.L., Gettelman, A., Granier, C., Diehl, T., Niemeier, U. and Simmons, A.J. 2007. Sensitivity of chemical tracers to meteorological parameters in the MOZART-3 chemical transport model. *Journal of Geophysical Research Atmospheres*. **112**(20), pp.1–24.

Knappett, D., Siddans, R., Ventress, L., Kerridge, B. and Latter, B. 2022. STFC RAL methane retrievals from IASI on board MetOp-B, version 2.0. Available from: https://dx.doi.org/10.5285/4bbcb1722f2842c1b0a5ebc19160a863.

Koffi, B., Dentener, F., Janssens-Maenhout, G., Guizzardi, D., Crippa, M., Diehl, T. and Galmarini, S. 2016. *Hemispheric Transport Air Pollution (HTAP): Specification of the HTAP2 experiments* [Online]. Available from: https://ec.europa.eu/jrc.

Koukouli, M.E., Balis, D.S., Loyola, D., Valks, P., Zimmer, W., Hao, N., Lamber, J.C., Van Roozendael, M., Lerot, C. and Spurr, R.J.D. 2012. Geophysical validation and long-term consistency between GOME-2/MetOp-A total ozone column and measurements from the sensors GOME/ERS-2, SCIAMACHY/ENVISAT and OMI/Aura. *Atmospheric Measurement Techniques*. **5**(9), pp.2169–2181.

Koumoutsaris, S., Bey, I., Generoso, S. and Thouret, V. 2008. Influence of El Niño-Southern Oscillation on the interannual variability of tropospheric ozone in the northern midlatitudes. *Journal of Geophysical Research Atmospheres*. **113**(19), pp.1–21.

Kovacs, T.A., Brune, W.H., Harder, H., Martinez, M., Simpas, J.B., Frost, G.J., Williams, E., Jobson, T., Stroud, C., Young, V., Fried, A. and Wert, B. 2003. Direct measurements of urban OH reactivity during Nashville SOS in summer 1999. *Journal of Environmental Monitoring*. **5**(1), pp.68–74.

Krol, M.C., Meirink, J.F., Bergamaschi, P., Mak, J.E., Lowe, D., Jöckel, P., Houweling, S. and Röckmann, T. 2008. What can 14CO measurements tell us about OH? *Atmospheric Chemistry and Physics*. **8**(16), pp.5033–5044.

Lamarque, J.F., Bond, T.C., Eyring, V., Granier, C., Heil, A., Klimont, Z., Lee, D., Liousse, C., Mieville, A., Owen, B., Schultz, M.G., Shindell, D., Smith, S.J., Stehfest, E., Van Aardenne, J., Cooper, O.R., Kainuma, M., Mahowald, N., McConnell, J.R., Naik, V., Riahi, K. and Van Vuuren, D.P. 2010. Historical (1850-2000) gridded anthropogenic and biomass burning emissions of reactive gases and aerosols: Methodology and application. *Atmospheric Chemistry and Physics*. **10**(15), pp.7017–7039.

Lawrence, M.G., Jöckel, P. and Von Kuhlmann, R. 2001. What does the global mean OH concentration tell us? *Atmospheric Chemistry and Physics*. **1**(1), pp.37–49.

Lelieveld, J., Gromov, S., Pozzer, A. and Taraborrelli, D. 2016. Global tropospheric hydroxyl distribution, budget and reactivity. *Atmospheric Chemistry and Physics*. **16**(19), pp.12477–12493.

Levelt, P.F., Joiner, J., Tamminen, J., Veefkind, J.P., Bhartia, P.K., Zweers, D.C.S., Duncan, B.N., Streets, D.G., Eskes, H., Van Der, R.A., McLinden, C., Fioletov, V., Carn, S., De Laat, J., Deland, M., Marchenko, S., McPeters, R., Ziemke, J., Fu, D., Liu, X., Pickering, K., Apituley, A., Abad, G.G., Arola, A., Boersma, F., Miller, C.C., Chance, K., De Graaf, M., Hakkarainen, J., Hassinen, S., Ialongo, I., Kleipool, Q., Krotkov, N., Li, C., Lamsal, L., Newman, P., Nowlan, C., Suleiman, R., Tilstra, L.G., Torres, O., Wang, H. and Wargan, K. 2018. The Ozone Monitoring Instrument: Overview of 14 years in space. *Atmospheric Chemistry and Physics*. **18**(8), pp.5699–5745.

Levelt, P.F., Van Den Oord, G.H.J., Dobber, M.R., Mälkki, A., Visser, H., De Vries, J., Stammes, P., Lundell, J.O.V. and Saari, H. 2006. The ozone monitoring instrument. *IEEE Transactions on Geoscience and Remote Sensing*.

Levy, H. 1971. Normal atmosphere: Large radical and formaldehyde concentrations predicted. *Science*. **173**(3992), pp.141–143.

Lewis, A.C., Evans, M.J., Methven, J., Watson, N., Lee, J.D., Hopkins, J.R., Purvis, R.M., Arnold, S.R., McQuaid, J.B., Whalley, L.K., Pilling, M.J., Heard, D.E., Monks, P.S., Parker, A.E., Reeves, C.E., Oram, D.E., Mills, G., Bandy, B.J., Stewart, D., Coe, H., Williams, P. and Crosier, J. 2007. Chemical composition observed over the mid-Atlantic and the detection of pollution signatures far from source regions. *Journal of Geophysical Research Atmospheres*. **112**(10), pp.1–17.

Liang, Q., Chipperfield, M.P., Fleming, E.L., Abraham, N.L., Braesicke, P., Burkholder, J.B., Daniel, J.S., Dhomse, S., Fraser, P.J., Hardiman, S.C., Jackman, C.H., Kinnison, D.E., Krummel, P.B., Montzka, S.A., Morgenstern, O., McCulloch, A., Mühle, J., Newman, P.A., Orkin, V.L., Pitari, G., Prinn, R.G., Rigby, M., Rozanov, E., Stenke, A., Tummon, F., Velders, G.J.M., Visioni, D. and Weiss, R.F. 2017. Deriving Global OH Abundance and Atmospheric Lifetimes for Long-Lived Gases: A Search for CH3CCl3 Alternatives. *Journal of Geophysical Research: Atmospheres*. **122**(21), 11,914-11,933.

Lin, M., Horowitz, L.W., Oltmans, S.J., Fiore, A.M. and Fan, S. 2014. Tropospheric ozone trends at Mauna Loa Observatory tied to decadal climate variability. *Nature Geoscience*. **7**(2), pp.136–143.

Lippmann, M. 1991. Health effects of tropospheric ozone. *Environmental Science & Technology*. **25**(12), pp.1954–1962.

Liu, C., Liu, X. and Chance, K. 2013. The impact of using different ozone cross sections on ozone profile retrievals from OMI UV measurements. *Journal of Quantitative Spectroscopy and Radiative Transfer*. **130**, pp.365–372.

Liu, X., Bhartia, P.K., Chance, K., Spurr, R.J.D. and Kurosu, T.P. 2010. Ozone profile retrievals from the ozone monitoring instrument. *Atmospheric Chemistry and Physics*. **10**(5), pp.2521–2537.

Liu, X., Chance, K. and Kurosu, T.P. 2007. Improved ozone profile retrievals from GOME data with degradation correction in reflectance. *Atmospheric Chemistry and Physics*. **7**(6), pp.1575–1583.

Logan, J.A., Staehelin, J., Megretskaia, I.A., Cammas, J.P., Thouret, V., Claude, H., De Backer, H., Steinbacher, M., Scheel, H.E., Stbi, R., Frhlich, M. and Derwent, R. 2012. Changes in ozone over Europe: Analysis of ozone measurements from sondes, regular aircraft (MOZAIC) and alpine surface sites. *Journal of Geophysical Research Atmospheres*. **117**(9), pp.1–23.

Lovelock, J.E. 1977. Methyl chloroform in the troposphere as an indicator of OH radical abundance. *Nature*. **267**(32).

Maahn, M., Turner, D.D., Löhnert, U., Posselt, D.J., Ebell, K., Mace, G.G. and Comstock, J.M. 2020. Optimal estimation retrievals and their uncertainties. *Bulletin of the*

American Meteorological Society. **101**(9), pp.E1512–E1523.

Mann, G.W., Carslaw, K.S., Spracklen, D. V., Ridley, D.A., Manktelow, P.T., Chipperfield, M.P., Pickering, S.J. and Johnson, C.E. 2010. Description and evaluation of GLOMAP-mode: A modal global aerosol microphysics model for the UKCA composition-climate model. *Geoscientific Model Development*. **3**(2), pp.519–551.

Martin, R. V. 2008. Satellite remote sensing of surface air quality. *Atmospheric Environment*. **42**(34), pp.7823–7843.

Mauldin, R.L., Eisele, F.L., Canttell, C.A., Kosciuch, E., Ridley, B.A. and Lefer, B. 2001. Measurements of OH aboard the NASA P-3 during PEM-Tropics B. . **106**(D23), pp.32657–32666.

Mcnorton, J., Chipperfield, M.P., Gloor, M., Wilson, C., Feng, W., Hayman, G.D., Rigby, M., Krumme, P.B., O'Doherty, S., Prinn, R.G., Weiss, R.F., Young, D., Dlugokencky, E. and Montzka, S.A. 2016. Role of OH variability in the stalling of the global atmospheric CH4 growth rate from 1999 to 2006. *Atmospheric Chemistry and Physics*. **16**(12), pp.7943–7956.

McPeters, R.D., Labow, G.J. and Logan, J.A. 2007. Ozone climatological profiles for satellite retrieval algorithms. *Journal of Geophysical Research Atmospheres*. **112**(5), pp.1–9.

Met Office 2023. Radiative transfer modelling. [Accessed 26 June 2023]. Available from: https://www.metoffice.gov.uk/research/weather/satellite-and-surface-assimilation/radiative-transfer-modelling.

Miles, G.M., Siddans, R., Kerridge, B.J., Latter, B.G. and Richards, N.A.D. 2015. Tropospheric ozone and ozone profiles retrieved from GOME-2 and their validation. *Atmospheric Measurement Techniques*. **8**(1), pp.385–398.

Mills, G., Hayes, F., Simpson, D., Emberson, L., Norris, D., Harmens, H. and Büker, P. 2011. Evidence of widespread effects of ozone on crops and (semi-)natural vegetation in Europe (1990–2006) in relation to AOT40- and flux-based risk maps. *Global Change Biology*. **17**(1), pp.592–613.

Miyazaki, K., Bowman, K., Sekiya, T., Takigawa, M., Neu, J.L., Sudo, K., Osterman, G. and Eskes, H. 2021. Global tropospheric ozone responses to reduced NOx emissions linked to the COVID-19 worldwide lockdowns. *Science Advances*. **7**(24), pp.1–15.

Monks, P.S. 2000. A review of the observations and origins of the spring ozone maximum. *Atmospheric Environment*. **34**(21), pp.3545–3561.

Monks, P.S., Archibald, A.T., Colette, A., Cooper, O., Coyle, M., Derwent, R., Fowler, D., Granier, C., Law, K.S., Mills, G.E., Stevenson, D.S., Tarasova, O., Thouret, V., Von Schneidemesser, E., Sommariva, R., Wild, O. and Williams, M.L. 2015. Tropospheric ozone and its precursors from the urban to the global scale from air quality to short-lived climate forcer. *Atmospheric Chemistry and Physics*. **15**(15), pp.8889–8973.

Monks, S.A., Arnold, S.R., Hollaway, M.J., Pope, R.J., Wilson, C., Feng, W., Emmerson, K.M., Kerridge, B.J., Latter, B.L., Miles, G.M., Siddans, R. and Chipperfield, M.P. 2017. The TOMCAT global chemical transport model v1.6: Description of chemical mechanism and model evaluation. *Geoscientific Model Development*.

Monteiro, A., Carvalho, A., Ribeiro, I., Scotto, M., Barbosa, S., Alonso, A., Baldasano, J.M., Pay, M.T., Miranda, A.I. and Borrego, C. 2012. Trends in ozone concentrations in the Iberian Peninsula by quantile regression and clustering. *Atmospheric Environment*. **56**, pp.184–193.

Montzka, S.A., Krol, M., Dlugokencky, E., Hall, B. and Jo, P. 2011. Small Interannual

Variability of Global Atmospheric Hydroxyl. *Science*. **331**(January), pp.67–69.

Morgenstern, O., Hegglin, M., Rozanov, E., O'Connor, F., Luke Abraham, N., Akiyoshi, H., Archibald, A., Bekki, S., Butchart, N., Chipperfield, M., Deushi, M., Dhomse, S., Garcia, R., Hardiman, S., Horowitz, L., Jöckel, P., Josse, B., Kinnison, D., Lin, M., Mancini, E., Manyin, M., Marchand, M., Marécal, V., Michou, M., Oman, L., Pitari, G., Plummer, D., Revell, L., Saint-Martin, D., Schofield, R., Stenke, A., Stone, K., Sudo, K., Tanaka, T., Tilmes, S., Yamashita, Y., Yoshida, K. and Zeng, G. 2017. Review of the global models used within phase 1 of the Chemistry-Climate Model Initiative (CCMI). *Geoscientific Model Development*. **10**(2), pp.639–671.

Müller, S., Hoor, P., Bozem, H., Gute, E., Vogel, B., Zahn, A., Bönisch, H., Keber, T., Krämer, M., Rolf, C., Riese, M., Schlager, H. and Engel, A. 2016. Impact of the Asian monsoon on the extratropical lower stratosphere: Trace gas observations during TACTS over Europe 2012. *Atmospheric Chemistry and Physics*. **16**(16), pp.10573–10589.

Munir, S., Chen, H. and Ropkins, K. 2013. Quantifying temporal trends in ground level ozone concentration in the UK. *Science of the Total Environment*. **458–460**, pp.217–227.

Munro, R., Lang, R., Klaes, D., Poli, G., Retscher, C., Lindstrot, R., Huckle, R., Lacan, A., Grzegorski, M., Holdak, A., Kokhanovsky, A., Livschitz, J. and Eisinger, M. 2016. The GOME-2 instrument on the Metop series of satellites: Instrument design, calibration, and level 1 data processing - An overview. *Atmospheric Measurement Techniques*. **9**(3), pp.1279–1301.

Munro, R., Siddans, R., Reburn, W.J. and Kerridge, B.J. 1998. Direct measurement of tropospheric ozone distributions from space. *Nature*. **392**, pp.168–171.

Murguia-Flores, F., Arndt, S., Ganesan, A.L., Murray-Tortarolo, G. and Hornibrook, E.R.C. 2018. Soil Methanotrophy Model (MeMo v1.0): A process-based model to quantify global uptake of atmospheric methane by soil. *Geoscientific Model Development*. **11**(6), pp.2009–2032.

Naik, V., Voulgarakis, A., Fiore, A.M., Horowitz, L.W., Lamarque, J.F., Lin, M., Prather, M.J., Young, P.J., Bergmann, D., Cameron-Smith, P.J., Cionni, I., Collins, W.J., Dalsøren, S.B., Doherty, R., Eyring, V., Faluvegi, G., Folberth, G.A., Josse, B., Lee, Y.H., MacKenzie, I.A., Nagashima, T., Van Noije, T.P.C., Plummer, D.A., Righi, M., Rumbold, S.T., Skeie, R., Shindell, D.T., Stevenson, D.S., Strode, S., Sudo, K., Szopa, S. and Zeng, G. 2013. Preindustrial to present-day changes in tropospheric hydroxyl radical and methane lifetime from the Atmospheric Chemistry and Climate Model Intercomparison Project (ACCMIP). *Atmospheric Chemistry and Physics*. **13**(10), pp.5277–5298.

Naus, S., Montzka, S.A., Pandey, S., Basu, S., Dlugokencky, E.J. and Krol, M. 2019. Constraints and biases in a tropospheric two-box model of OH. *Atmospheric Chemistry and Physics*. **19**(1), pp.407–424.

Neu, J.L., Flury, T., Manney, G.L., Santee, M.L., Livesey, N.J. and Worden, J. 2014. Tropospheric ozone variations governed by changes in stratospheric circulation. *Nature Geoscience*. **7**(5), pp.340–344.

Nicely, J.M., Canty, T.P., Manyin, M., Oman, L.D., Salawitch, R.J., Steenrod, S.D., Strahan, S.E. and Strode, S.A. 2018. Changes in Global Tropospheric OH Expected as a Result of Climate Change Over the Last Several Decades. *Journal of Geophysical Research: Atmospheres*. **123**(18), 10,774-10,795.

Nicely, J.M., Salawitch, R.J., Canty, T., Anderson, D.C., Arnold, S.R., Chipper, M.P., Emmons, L.K., Flemming, J., Huijnen, V., Kinnison, D.E., Lamarque, J. and Mao, J. 2017. Quantifying the causes of differences in tropospheric OH within global models. *Journal of Geophysical Research: Atmospheres*. **122**, pp.1983–2007.

NOAA 2021. Multivariate ENSO Index Version 2 (MEI.v2). [Accessed 11 September 2021]. Available from: https://psl.noaa.gov/enso/mei/.

Nölscher, A.C., Yañez-Serrano, A.M., Wolff, S., De Araujo, A.C., Lavrič, J. V., Kesselmeier, J. and Williams, J. 2016. Unexpected seasonality in quantity and composition of Amazon rainforest air reactivity. *Nature Communications*. **7**.

Nussbaumer, C.M., Pozzer, A., Tadic, I., Roder, L., Obersteiner, F., Harder, H., Lelieveld, J. and Fischer, H. 2022. Tropospheric ozone production and chemical regime analysis during the COVID-19 lockdown over Europe. *Atmospheric Chemistry and Physics*. **22**(9), pp.6151–6165.

Nuvolone, D., Petri, D. and Voller, F. 2018. The effects of ozone on human health. *Environmental Science and Pollution Research*. **25**(9), pp.8074–8088.

Olivier, J., Peters, J., Granier, C., Pétron, G., Müller, J.F. and Wallens, S. 2003. *Present and future surface emissions of atmospheric compounds, POET report #2*.

Olivier, J.G., Peters, J.A. and Janssens-Maenhout, G. 2012. *Trends in Global CO2 Emissions 2012 Report* [Online]. Available from: https://www.pbl.nl/en/publications/trends-in-global-co2-emissions-2012-report.

Olsen, S.C., McLinden, C.A. and Prather, M.J. 2001. Stratospheric N2O-NOy system: Testing uncertainties in a three-dimensional framework. *Journal of Geophysical Research Atmospheres*. **106**(D22), pp.28771–28784.

Oltmans, S.J., Lefohn, A.S., Shadwick, D., Harris, J.M., Scheel, H.E., Galbally, I., Tarasick, D.W., Johnson, B.J., Brunke, E.G., Claude, H., Zeng, G., Nichol, S., Schmidlin, F., Davies, J., Cuevas, E., Redondas, A., Naoe, H., Nakano, T. and Kawasato, T. 2013. Recent tropospheric ozone changes - A pattern dominated by slow or no growth. *Atmospheric Environment*. **67**, pp.331–351.

Ordóñez, C., Brunner, D., Staehelin, J., Hadjinicolaou, P., Pyle, J.A., Jonas, M., Wernli, H. and Prévot, A.S.H. 2007. Strong influence of lowermost stratospheric ozone on lower tropospheric background ozone changes over Europe. *Geophysical Research Letters*. **34**(7), pp.1–5.

Ordóñez, C., Garrido-Perez, J.M. and García-Herrera, R. 2020. Early spring near-surface ozone in Europe during the COVID-19 shutdown: Meteorological effects outweigh emission changes. *Science of the Total Environment*. **747**(December 2019), p.141322.

Parrish, D.D., Derwent, R.G., Faloona, I.C. and Mims, C.A. 2022. Technical note: Northern midlatitude baseline ozone - Long-term changes and the COVID-19 impact. *Atmospheric Chemistry and Physics*. **22**(20), pp.13423–13430.

Parrish, D.D., Derwent, R.G. and Staehelin, J. 2021. Long-term changes in northern mid-latitude tropospheric ozone concentrations: Synthesis of two recent analyses. *Atmospheric Environment*. **248**(January), p.118227.

Parrish, D.D., Lamarque, J.F., Naik, V., Horowitz, L., Shindell, D.T., Staehelin, J., Derwent, R., Cooper, O.R., Tanimoto, H., Volz-Thomas, A., Gilge, S., Scheel, H.E., Steinbacher, M. and Fröhlich, M. 2014. Long-term changes in lower tropospheric baseline ozone concentrations: Comparing chemistry-climate models and observations at northern midlatitudes. *Journal of Geophysical Research*. **119**, pp.5719–5736.

Parrish, D.D., Law, K.S., Staehelin, J., Derwent, R., Cooper, O.R., Tanimoto, H., Volz-Thomas, A., Gilge, S., Scheel, H.E., Steinbacher, M. and Chan, E. 2012. Long-term changes in lower tropospheric baseline ozone concentrations at northern mid-latitudes. *Atmospheric Chemistry and Physics*. **12**(23), pp.11485–11504.

Parrish, D.D., Law, K.S., Staehelin, J., Derwent, R., Cooper, O.R., Tanimoto, H., Volz-Thomas, A., Gilge, S., Scheel, H.E., Steinbacher, M. and Chan, E. 2013. Lower tropospheric ozone at northern midlatitudes: Changing seasonal cycle. *Geophysical Research Letters*. **40**(8), pp.1631–1636.

Patra, P.K., Krol, M.C., Montzka, S.A., Arnold, T., Atlas, E.L., Lintner, B.R., Stephens, B.B., Xiang, B., Elkins, J.W., Fraser, P.J., Ghosh, A., Hintsa, E.J., Hurst, D.F., Ishijima, K., Krummel, P.B., Miller, B.R., Miyazaki, K., Moore, F.L., Mühle, J., O'Doherty, S., Prinn, R.G., Steele, L.P., Takigawa, M., Wang, H.J., Weiss, R.F., Wofsy, S.C. and Young, D. 2014. Observational evidence for interhemispheric hydroxyl-radical parity. *Nature*. **513**(7517), pp.219–223.

Patra, P.K., Krol, M.C., Prinn, R.G., Takigawa, M., Mühle, J., Montzka, S.A., Lal, S., Yamashita, Y., Naus, S., Chandra, N., Weiss, R.F., Krummel, P.B., Fraser, P.J., O'Doherty, S. and Elkins, J.W. 2021. Methyl Chloroform Continues to Constrain the Hydroxyl (OH) Variability in the Troposphere. *Journal of Geophysical Research: Atmospheres*. **126**(4).

Peng, S., Lin, X., Thompson, R.L., Xi, Y., Liu, G., Hauglustaine, D., Lan, X., Poulter, B., Ramonet, M., Saunois, M., Yin, Y., Zhang, Z., Zheng, B. and Ciais, P. 2022. Wetland emission and atmospheric sink changes explain methane growth in 2020. *Nature*. **612**(7940), pp.477–482.

Petetin, H., Thouret, V., Athier, G., Blot, R., Boulanger, D., Cousin, J.M., Gaudel, A., Nédélec, P. and Cooper, O. 2016. Diurnal cycle of ozone throughout the troposphere over Frankfurt as measured by MOZAIC-IAGOS commercial aircraft. *Elementa*. **4**, pp.1–11.

Pey, J. and Cerro, J.C. 2022. Reasons for the observed tropospheric ozone weakening over south-western Europe during COVID-19: Strict lockdown versus the new normal. *Science of the Total Environment*. **833**(March).

Pimlott, M.A., Pope, R.J., Kerridge, B.J., Latter, B.G., Knappett, D.S., Heard, D.E., Ventress, L.J., Siddans, R., Feng, W. and Chipperfield, M.P. 2022. Investigating the global OH radical distribution using steady-state approximations and satellite data. *Atmospheric Chemistry and Physics*. **22**(16), pp.10467–10488.

Podolske, J.R., Sachse, G.W. and Diskin, G.S. 2003. Calibration and data retrieval algorithms for the NASA Langley/Ames Diode Laser Hygrometer for the NASA Transport and Chemical Evolution over the Pacific (TRACE-P) mission. *Journal of Geophysical Research: Atmospheres*. **108**(20), pp.1–9.

Pope, R.J., Arnold, S.R., Chipperfield, M.P., Latter, B.G., Siddans, R. and Kerridge, B.J. 2018. Widespread changes in UK air quality observed from space. *Atmospheric Science Letters*. **19**(5), pp.1–8.

Pope, R.J., Chipperfield, M.P., Savage, N.H., Ordóñez, C., Neal, L.S., Lee, L.A., Dhomse, S.S., Richards, N.A.D. and Keslake, T.D. 2015. Evaluation of a regional air quality model using satellite column NO2: Treatment of observation errors and model boundary conditions and emissions. *Atmospheric Chemistry and Physics*. **15**(10), pp.5611–5626.

Pope, R.J., Kerridge, B.J., Siddans, R., Latter, B.G., Chipperfield, M.P., Arnold, S.R., Ventress, L.J., Pimlott, M.A., Graham, A.M., Knappett, D.S. and Rigby, R. 2021. Large enhancements in southern hemisphere satellite-observed trace gases due to the 2019/2020 Australian wildfires. *Journal of Geophysical Research: Atmospheres*., pp.1–13.

Pöschl, U., von Kuhlmann, R., Poisson, N. and Crutzen, P.J. 2000. Development and Intercomparison of Condensed Isoprene Oxidation Mechanisms for Global Atmospheric Modeling. *Journal of Atmospheric Chemistry*. **37**, pp.29–52.

Prather, M.J. 1986. Numerical advection by conservation of second-order moments. *Journal of Geophysical Research*. **91**(D6), p.6671.

Prinn, R.G., Huang, J., Weiss, R.F., Cunnold, D.M., Fraser, P.J., Simmonds, P.G., McCulloch, A., Harth, C., Reimann, S., Salameh, P., O'Doherty, S., Wang, R.H.J., Porter, L.W., Miller, B.R. and Krummel, P.B. 2005. Evidence for variability of atmospheric hydroxyl radicals over the past quarter century. *Geophysical Research Letters*. **32**(7), pp.1–4.

Prinn, R.G., Huang, J., Weiss, R.F., Cunnold, D.M., Fraser, P.J., Simmonds, P.G., McCulloch, A., Harth, C., Salameh, P., O'Doherty, S., Wang, R.H.J., Porter, L. and Miller, B.R. 2001. Evidence for substantial variations of atmospheric hydroxyl radicals in the past two decades. *Science*. **292**(5523), pp.1882–1888.

Pyle, J.A., Keeble, J., Abraham, N.L., Chipperfield, M.P. and Griffiths, P.T. 2022. Integrated ozone depletion as a metric for ozone recovery. *Nature*. **608**(7924), pp.719–723.

Reed, R.J. and Danielsen, E.F. 1958. Fronts in the vicinity of the tropopause. *Archiv für Meteorologie, Geophysik und Bioklimatologie,Ser. A, Meteorologie und Geophysik*. **11**(1), pp.1–17.

Reimann, S., Manning, A.J., Simmonds, P.G., Cunnold, D.M., Wang, R.H.J., Li, J., McCulloch, A., Prinn, R.G., Huang, J., Weiss, R.F., Fraser, P.J., O'Doherty, S., Greally, B.R., Stemmler, K., Hill, M. and Follni, D. 2005. Low European methyl chloroform emissions inferred from long-term atmospheric measurements. *Nature*. **433**(7025), pp.506–508.

Ren, X., Olson, J.R., Crawford, J.H., Brune, W.H., Mao, J., Long, R.B., Chen, Z., Chen, G., Avery, M.A., Sachse, G.W., Barrick, J.D., Diskin, G.S., Huey, L.G., Fried, A., Cohen, R.C., Heikes, B., Wennberg, P.O., Singh, H.B., Blake, D.R. and Shetter, R.E. 2008. HOx chemistry during INTEX-A 2004: Observation, model calculation, and comparison with previous studies. *Journal of Geophysical Research Atmospheres*. **113**(5), pp.1–13.

Reutter, P., Škerlak, B., Sprenger, M. and Wernli, H. 2015. Stratosphere-troposphere exchange (STE) in the vicinity of North Atlantic cyclones. *Atmospheric Chemistry and Physics*. **15**(19), pp.10939–10953.

Riahi, K., van Vuuren, D.P., Kriegler, E., Edmonds, J., O'Neill, B.C., Fujimori, S., Bauer, N., Calvin, K., Dellink, R., Fricko, O., Lutz, W., Popp, A., Cuaresma, J.C., KC, S., Leimbach, M., Jiang, L., Kram, T., Rao, S., Emmerling, J., Ebi, K., Hasegawa, T., Havlik, P., Humpenöder, F., Da Silva, L.A., Smith, S., Stehfest, E., Bosetti, V., Eom, J., Gernaat, D., Masui, T., Rogelj, J., Strefler, J., Drouet, L., Krey, V., Luderer, G., Harmsen, M., Takahashi, K., Baumstark, L., Doelman, J.C., Kainuma, M., Klimont, Z., Marangoni, G., Lotze-Campen, H., Obersteiner, M., Tabeau, A. and Tavoni, M. 2017. The Shared Socioeconomic Pathways and their energy, land use, and greenhouse gas emissions implications: An overview. *Global Environmental Change*. **42**, pp.153–168.

Rigby, M., Montzka, S.A., Prinn, R.G., White, J.W.C., Young, D., O'Doherty, S., Lunt, M.F., Ganesan, A.L., Manning, A.J., Simmonds, P.G., Salameh, P.K., Harth, C.M., Mühle, J., Weiss, R.F., Fraser, P.J., Steele, L.P., Krummel, P.B., McCulloch, A. and Park, S. 2017. Role of atmospheric oxidation in recent methane growth. *Proceedings of the National Academy of Sciences of the United States of America*. **114**(21), pp.5373–5377.

Rodgers, C.D. 2000. Inverse methods for atmospheric sounding: Theory and Practice *In*: *Series on Atmospheric, Oceanic and Planetary Physics: Volume 2*. World Scientific.

Rodgers, C.D. 1976. Retrieval of Atmospheric Temperature and Composition From Remote Measurements of Thermal Radiation. *REVIEWS OF GEOPHYSICS AND SPACE PHYSICS*. **14**(4), pp.609–624.

Van Roozendael, M., Spurr, R., Loyola, D., Lerot, C., Balis, D., Lambert, J.C., Zimmer, W., Van Gent, J., Van Geffen, J., Koukouli, M., Granville, J., Doicu, A., Fayt, C. and Zehner, C. 2012. Sixteen years of GOME/ERS-2 total ozone data: The new direct-fitting GOME Data Processor (GDP) version 5Algorithm description. *Journal of Geophysical Research Atmospheres*. **117**(3), pp.1–18.

Rossow, W.B. and Schiffer, R.A. 1999. Advances in Understanding Clouds from ISCCP. *Bulletin of the American Meteorological Society*. **80**(11), pp.2261–2287.

Rowlinson, M.J., Rap, A., Arnold, S.R., Pope, R.J., Chipperfield, M.P., McNorton, J., Forster, P., Gordon, H., Pringle, K.J., Feng, W., Kerridge, B.J., Latter, B.L. and Siddans, R. 2019. Impact of El Niño Southern Oscillation on the interannual variability of methane and tropospheric ozone. *Atmospheric Chemistry and Physics Discussions*. **2**, pp.1–20.

Rozanov, V. V., Diebel, D., Spurt, R.J.D. and Burrow, J.P. 1997. GOMETRAN: A radiative transfer model for the satellite project GOME, the plane-parallel version. . **102**, pp.16683–16695.

Safieddine, S.A., Heald, C.L. and Henderson, B.H. 2017. The global nonmethane reactive organic carbon budget: A modeling perspective. *Geophysical Research Letters*. **44**(8), pp.3897–3906.

Saunders, R., Hocking, J., Rundle, D., Rayer, P., Havemann, S., Matricardi, M., Geer, A., Lupu, C., Brunel, P. and Vidot, J. 2017. *RTTOV-12 Science and Validation Report* [Online]. Available from: https://nwp-saf.eumetsat.int/site/software/rttov/documentation/.

Saunders, R., Matricardi, M. and Brunel, P. 1999. An improved fast radiative transfer model for assimilation of satellite radiance observations. *Quarterly Journal of the Royal Meteorological Society*. **125**(556), pp.1407–1425.

Saunois, M., Stavert, A.R., Poulter, B., Bousquet, P., Canadell, J.G., Jackson, R.B., Raymond, P.A., Dlugokencky, E.J., Houweling, S., Patra, P.K., Ciais, P., Arora, V.K., Bastviken, D., Bergamaschi, P., Blake, D.R., Brailsford, G., Bruhwiler, L., Carlson, K.M., Carrol, M., Castaldi, S., Chandra, N., Crevoisier, C., Crill, P.M., Covey, K., Curry, C.L., Etiope, G., Frankenberg, C., Gedney, N., Hegglin, M.I., Höglund-Isaksson, L., Hugelius, G., Ishizawa, M., Ito, A., Janssens-Maenhout, G., Jensen, K.M., Joos, F., Kleinen, T., Krummel, P.B., Langenfelds, R.L., Laruelle, G.G., Liu, L., Machida, T., Maksyutov, S., McDonald, K.C., McNorton, J., Miller, P.A., Melton, J.R., Morino, I., Müller, J., Murguia-Flores, F., Naik, V., Niwa, Y., Noce, S., O'Doherty, S., Parker, R.J., Peng, C., Peng, S., Peters, G.P., Prigent, C., Prinn, R., Ramonet, M., Regnier, P., Riley, W.J., Rosentreter, J.A., Segers, A., Simpson, I.J., Shi, H., Smith, S.J., Steele, L.P., Thornton, B.F., Tian, H., Tohjima, Y., Tubiello, F.N., Tsuruta, A., Viovy, N., Voulgarakis, A., Weber, T.S., van Weele, M., van der Werf, G.R., Weiss, R.F., Worthy, D., Wunch, D., Yin, Y., Yoshida, Y., Zhang, W., Zhang, Z., Zhao, Y., Zheng, B., Zhu, Q., Zhu, Q. and Zhuang, Q. 2020. The Global Methane Budget 2000-2017. *Earth System Science Data*. **12**(3), pp.1561–1623.

Savage, N.H., Harrison, R.M., Monks, P.S. and Salisbury, G. 2001. Steady-state modelling of hydroxyl radical concentrations at Mace Head during the EASE '97 campaign, May 1997. *Atmospheric Environment*.

Schenkeveld, V.M.E., Jaross, G., Marchenko, S., Haffner, D., Kleipool, Q.L., Rozemeijer, N.C., Pepijn Veefkind, J. and Levelt, P.F. 2017. In-flight performance of the Ozone Monitoring Instrument. *Atmospheric Measurement Techniques*. **10**(5), pp.1957–1986.

von Schneidemesser, E., Monks, P.S. and Plass-Duelmer, C. 2010. Global comparison of VOC and CO observations in urban areas. *Atmospheric Environment*. **44**(39), pp.5053–5064.

Sellar, A.A., Jones, C.G., Mulcahy, J.P., Tang, Y., Yool, A., Wiltshire, A., O'Connor, F.M., Stringer, M., Hill, R., Palmieri, J., Woodward, S., de Mora, L., Kuhlbrodt, T., Rumbold, S.T., Kelley, D.I., Ellis, R., Johnson, C.E., Walton, J., Abraham, N.L., Andrews, M.B., Andrews, T., Archibald, A.T., Berthou, S., Burke, E., Blockley, E., Carslaw, K., Dalvi, M., Edwards, J., Folberth, G.A., Gedney, N., Griffiths, P.T., Harper, A.B., Hendry, M.A., Hewitt, A.J., Johnson, B., Jones, A., Jones, C.D., Keeble, J., Liddicoat, S., Morgenstern, O., Parker, R.J., Predoi, V., Robertson, E., Siahaan, A., Smith, R.S., Swaminathan, R., Woodhouse, M.T., Zeng, G. and Zerroukat, M. 2019. UKESM1: Description and Evaluation of the U.K. Earth System Model. *Journal of Advances in Modeling Earth Systems*. **11**(12), pp.4513–4558.

Shetter, R.E. and Müller, M. 1999. Photolysis frequency measurements using actinic flux spectroradiometry during the PEM-Tropics mission: Instrumentation description and some results. *Journal of Geophysical Research Atmospheres*. **104**(D5), pp.5647–5661.

Siddans, R. 2019. *Water Vapour Climate Change Initiative (WV_cci) - Phase One* [Online]. Available from: https://climate.esa.int/media/documents/Water_Vapour_CCI_D2.2_ATBD_Part2-IMS_L2_product_v1.0.pdf.

Siddans, R., Knappett, D., Kerridge, B., Latter, B. and Waterfall, A. 2020. STFC RAL methane retrievals from IASI on board MetOp-A, version 2.0.

Siddans, R., Knappett, D., Kerridge, B., Waterfall, A., Hurley, J., Latter, B., Boesch, H. and Parker, R. 2017. Global height-resolved methane retrievals from the Infrared Atmospheric Sounding Interferometer (IASI) on MetOp. *Atmospheric Measurement Techniques*. **10**(11), pp.4135–4164.

Simmonds, P.G., Derwent, R.G., Manning, A.L. and Spain, G. 2004. Significant growth in surface ozone at Mace Head, Ireland, 1987-2003. *Atmospheric Environment*. **38**(28), pp.4769–4778.

Sindelarova, K., Granier, C., Bouarar, I., Guenther, A., Tilmes, S., Stavrakou, T., Müller, J.-F., Kuhn, U., Stefani, P. and Knorr, W. 2014. Global data set of biogenic VOC emissions calculated by the MEGAN model over the last 30 years. *Atmospheric Chemistry and Physics*. **14**(17), pp.9317–9341.

Singh, H.B. 1977. Preliminary estimation of average tropospheric HO concentrations in the northern and southern hemispheres. *Geophysical Research Letters*.

Skeie, R.B., Myhre, G., Hodnebrog, Ø., Cameron-Smith, P.J., Deushi, M., Hegglin, M.I., Horowitz, L.W., Kramer, R.J., Michou, M., Mills, M.J., Olivié, D.J.L., Connor, F.M.O., Paynter, D., Samset, B.H., Sellar, A., Shindell, D., Takemura, T., Tilmes, S. and Wu, T. 2020. Historical total ozone radiative forcing derived from CMIP6 simulations. *npj Climate and Atmospheric Science*. **3**(1).

Slater, E.J., Whalley, L.K., Woodward-Massey, R., Ye, C., Lee, J.D., Squires, F., Hopkins, J.R., Dunmore, R.E., Shaw, M., Hamilton, J.F., Lewis, A.R., Crilley, L.R., Kramer, L., Bloss, W., Vu, T., Sun, Y., Xu, W., Yue, S., Ren, L., Joe, W., Nicholas Hewitt, C., Wang, X., Fu, P. and Heard, D.E. 2020. Elevated levels of OH observed in haze events during wintertime in central Beijing. *Atmospheric Chemistry and Physics*. **20**(23), pp.14847–14871.

Smith, S.C., Lee, J.D., Bloss, W.J., Johnson, G.P., Ingham, T. and Heard, D.E. 2006. Concentrations of OH and HO2 radicals during NAMBLEX: Measurements and steady state analysis. *Atmospheric Chemistry and Physics*. **6**(5), pp.1435–1453.

Sommariva, R., Haggerstone, A.-L., Carpenter, L.J., Carslaw, N., Creasey, D.J., Heard, D.E., Lee, J.D., Lewis, A.C., Pilling, M.J. and Zádor, J. 2004. OH and HO2 chemistry in clean marine air during SOAPEX-2. *Atmospheric Chemistry and Physics*. **4**(3), pp.839–856.

Souri, A.H., Chance, K., Bak, J., Nowlan, C.R., González Abad, G., Jung, Y., Wong, D.C., Mao, J. and Liu, X. 2021. Unraveling pathways of elevated ozone induced by the 2020 lockdown in Europe by an observationally constrained regional model using TROPOMI. *Atmospheric Chemistry and Physics*. **21**(24), pp.18227–18245.

Spivakovsky, C.M., Logan, J.A., Montzka, S.A., Balkanski, Y.J., Foreman-Fowler, M., Jones, D.B.A., Horowitz, L.W., Fusco, A.C., Brenninkmeijer, C.A.M., Prather, M.J., Wofsy, S.C. and McElroy, M.B. 2000. Three-dimensional climatological distribution of tropospheric OH: Update and evaluation. *Journal of Geophysical Research Atmospheres*. **105**(D7), pp.8931–8980.

Spracklen, D. V., Pringle, K.J., Carslaw, K.S., Chipperfield, M.P. and Mann, G.W. 2005. A global off-line model of size-resolved aerosol microphysics: I. Model development and prediction of aerosol properties. *Atmospheric Chemistry and Physics*. **5**(8), pp.2227–2252.

Steinbrecht, W., Kubistin, D., Plass-Dülmer, C., Davies, J., Tarasick, D.W., Von Der Gathen, P., Deckelmann, H., Jepsen, N., Kivi, R., Lyall, N., Palm, M., Notholt, J., Kois, B., Oelsner, P., Allaart, M., Piters, A., Gill, M., Van Malderen, R., Delcloo, A.W., Sussmann, R., Mahieu, E., Servais, C., Romanens, G., Stübi, R., Ancellet, G., Godin-Beekmann, S., Yamanouchi, S., Strong, K., Johnson, B., Cullis, P., Petropavlovskikh, I., Hannigan, J.W., Hernandez, J.L., Diaz Rodriguez, A., Nakano, T., Chouza, F., Leblanc, T., Torres, C., Garcia, O., Röhling, A.N., Schneider, M., Blumenstock, T., Tully, M., Paton-Walsh, C., Jones, N., Querel, R., Strahan, S., Stauffer, R.M., Thompson, A.M., Inness, A., Engelen, R., Chang, K.L. and Cooper, O.R. 2021. COVID-19 Crisis Reduces Free Tropospheric Ozone Across the Northern Hemisphere. *Geophysical Research Letters*. **48**(5), pp.1–11.

Stevens, P.S., Mather, J.H. and Brune, W.H. 1994. Measurement of tropospheric OH and HO2 by laser-induced fluorescence at low pressure. *Journal of Geophysical Research*. **99**(D2), pp.3543–3557.

Stevenson, D.S., Dentener, F.J., Schultz, M.G., Ellingsen, K., van Noije, T.P.C., Wild, O., Zeng, G., Amann, M., Atherton, C.S., Bell, N., Bergmann, D.J., Bey, I., Butler, T., Cofala, J., Collins, W.J., Derwent, R.G., Doherty, R.M., Drevet, J., Eskes, H.J., Fiore, A.M., Gauss, M., Hauglustaine, D.A., Horowitz, L.W., Isaksen, I.S.A., Krol, M.C., Lamarque, J.F., Lawrence, M.G., Montanaro, V., Müller, J.F., Pitari, G., Prather, M.J., Pyle, J.A., Rast, S., Rodriquez, J.M., Sanderson, M.G., Savage, N.H., Shindell, D.T., Strahan, S.E., Sudo, K. and Szopa, S. 2006. Multimodel ensemble simulations of present-day and near-future tropospheric ozone. *Journal of Geophysical Research Atmospheres*. **111**(8).

Stevenson, D.S., Zhao, A., Naik, V., O'Connor, F.M., Tilmes, S., Zeng, G., Murray, L.T., Collins, W.J., Griffiths, P.T., Shim, S., Horowitz, L.W., Sentman, L.T. and Emmons, L. 2020. Trends in global tropospheric hydroxyl radical and methane lifetime since 1850 from AerChemMIP. *Atmospheric Chemistry and Physics*. **20**(21), pp.12905–12920.

Stockwell, D.Z., Giannakopoulos, C., Plantevin, P.H., Carver, G.D., Chipperfield, M.P., Law, K.S., Pyle, J.A., Shallcross, D.E. and Wang, K.Y. 1999. Modelling NOx from lightning and its impact on global chemical fields. *Atmospheric Environment*. **33**(27), pp.4477–4493.

Stohl, A., Bonasoni, P., Cristofanelli, P., Collins, W., Feichter, J., Frank, A., Forster, C., Gerasopoulos, E., Gäggeler, H., James, P., Kentarchos, T., Kromp-Kolb, H., Krüger, B., Land, C., Meloen, J., Papayannis, A., Priller, A., Seibert, P., Sprenger, M., Roelofs, G.J., Scheel, H.E., Schnabel, C., Siegmund, P., Tobler, L., Trickl, T., Wernli, H., Wirth, V., Zanis, P. and Zerefos, C. 2003. Stratosphere-troposphere exchange: A review, and what we have learned from STACCATO. *Journal of Geophysical Research Atmospheres*. **108**(12).

Stone, D., Whalley, L.K. and Heard, D.E. 2012. Tropospheric OH and HO2 radicals: Field measurements and model comparisons. *Chemical Society Reviews*. **41**(19), pp.6348–6404.

Streets, D.G., Canty, T., Carmichael, G.R., De Foy, B., Dickerson, R.R., Duncan, B.N., Edwards, D.P., Haynes, J.A., Henze, D.K., Houyoux, M.R., Jacob, D.J., Krotkov, N.A., Lamsal, L.N., Liu, Y., Lu, Z., Martin, R. V., Pfister, G.G., Pinder, R.W., Salawitch, R.J. and Wecht, K.J. 2013. Emissions estimation from satellite retrievals: A review of current capability. *Atmospheric Environment*. **77**(2013), pp.1011–1042.

Stübi, R., Levrat, G., Hoegger, B., Viatte, P., Staehelin, J. and Schmidlin, F.J. 2008. In-flight comparison of Brewer-Mast and electrochemical concentration cell ozonesondes. *Journal of Geophysical Research Atmospheres*. **113**(13), pp.1–11.

Tarasick, D.W., Carey-Smith, T.K., Hocking, W.K., Moeini, O., He, H., Liu, J., Osman, M.K., Thompson, A.M., Johnson, B.J., Oltmans, S.J. and Merrill, J.T. 2019. Quantifying stratosphere-troposphere transport of ozone using balloon-borne ozonesondes, radar windprofilers and trajectory models. *Atmospheric Environment*. **198**(October 2018), pp.496–509.

Tarasick, D.W., Fioletov, V.E., Wardle, D.I., Kerr, J.B. and Davies, J. 2005. Changes in the vertical distribution of ozone over Canada from ozonesondes: 1980-2001. *Journal of Geophysical Research D: Atmospheres*. **110**(2), pp.1–19.

Tarasick, D.W., Galbally, I.E., Cooper, O.R., Schultz, M.G., Ancellet, G., Leblanc, T., Wallington, T.J., Ziemke, J., Liu, X., Steinbacher, M., Staehelin, J., Vigouroux, C., Hannigan, J.W., García, O., Foret, G., Zanis, P., Weatherhead, E., Petropavlovskikh, I., Worden, H., Osman, M., Liu, J., Chang, K.-L., Gaudel, A., Lin, M., Granados-Muñoz, M., Thompson, A.M., Oltmans, S.J., Cuesta, J., Dufour, G., Thouret, V., Hassler, B., Trickl, T. and Neu, J.L. 2019. *Tropospheric Ozone Assessment Report: Tropospheric ozone from 1877 to 2016, observed levels, trends and uncertainties*.

Thames, A.B., Brune, W.H., Miller, D.O., Allen, H.M., Apel, E.C., Blake, D.R., Paul Bui, T., Commane, R., Crounse, J.D., Daube, B.C., Diskin, G.S., Digangi, J.P., Elkins, J.W., Hall, S.R., Hanisco, T.F., Hannun, R.A., Hintsa, E., Hornbrook, R.S., Kim, M.J., McKain, K., Moore, F.L., Nicely, J.M., Peischl, J., Ryerson, T.B., St. Clair, J.M., Sweeney, C., Teng, A., Thompson, C.R., Ullmann, K., Wennberg, P.O. and Wolfe, G.M. 2020. Missing OH reactivity in the global marine boundary layer. *Atmospheric Chemistry and Physics*. **20**(6), pp.4013–4029.

Tiedtke, M. 1989. A Comprehensive Mass Flux Scheme for Cumulus Parameterization in Large-Scale Models. *Monthly Weather Review*. **117**(8), pp.1779–1800.

Tørseth, K., Aas, W., Breivik, K., Fjeraa, A.M., Fiebig, M., Hjellbrekke, A.G., Lund Myhre, C., Solberg, S. and Yttri, K.E. 2012. Introduction to the European Monitoring and Evaluation Programme (EMEP) and observed atmospheric composition change during 1972-2009. *Atmospheric Chemistry and Physics*. **12**(12), pp.5447–5481.

Travis, K., Heald, C., Allen, H., Apel, E., Arnold, S., Blake, D., Brune, W., Chen, X., Commane, R., Crounse, J., Daube, B., Diskin, G., Elkins, J., Evans, M., Hall, S., Hintsa, E., Hornbrook, R., Kasibhatla, P., Kim, M., Luo, G., McKain, K., Millet, D., Moore, F., Peischl, J., Ryerson, T., Sherwen, T., Thames, A., Ullmann, K., Wang, X., Wennberg, P., Wolfe, G. and Yu, F. 2020. Constraining remote oxidation capacity with ATom observations. *Atmospheric Chemistry and Physics Discussions*. (January), pp.1–41.

Trent, T., Siddens, R., Kerridge, B., Schroeder, M., Scott, N.A. and Remedios, J. 2023. Evaluation of tropospheric water vapour and temperature profiles retrieved from Metop-A by the Infrared and Microwave Sounding scheme. *Atmospheric Meas.*, pp.1–32.

Turner, A.J., Frankenberg, C. and Kort, E.A. 2019. Interpreting contemporary trends in atmospheric methane. *Proceedings of the National Academy of Sciences of the United States of America*. **116**(8), pp.2805–2813.

Turner, A.J., Frankenberg, C., Wennberg, P.O. and Jacob, D.J. 2017. Ambiguity in the causes for decadal trends in atmospheric methane and hydroxyl. *Proceedings of the National Academy of Sciences of the United States of America*. **114**(21), pp.5367–5372.

Veefkind, J.P., Aben, I., McMullan, K., Förster, H., de Vries, J., Otter, G., Claas, J., Eskes, H.J., de Haan, J.F., Kleipool, Q., van Weele, M., Hasekamp, O., Hoogeveen, R., Landgraf, J., Snel, R., Tol, P., Ingmann, P., Voors, R., Kruizinga, B., Vink, R., Visser, H. and Levelt, P.F. 2012. TROPOMI on the ESA Sentinel-5 Precursor: A GMES mission for global observations of the atmospheric composition for climate, air quality and ozone layer applications. *Remote Sensing of Environment*.

Voulgarakis, A., Marlier, M.E., Faluvegi, G., Shindell, D.T., Tsigaridis, K. and Mangeon, S. 2015. Interannual variability of tropospheric trace gases and aerosols: The role of biomass burning emissions. *Journal of Geophysical Research: Atmospheres*. **120**, pp.7157–7173.

Wayne, R.P. 1991. *Chemistry of Atmospheres* Second Edi. Oxford: Oxford University Press, Inc.

Weatherhead, E.C., Reinsel, G.C., Tiao, G.C., Meng, X.L., Choi, D., Cheang, W.K., Keller, T., DeLuisi, J., Wuebbles, D.J., Kerr, J.B., Miller, A.J., Oltmans, S.J. and Frederick, J.E. 1998. Factors affecting the detection of trends: Statistical considerations and applications to environmental data. *Journal of Geophysical Research Atmospheres*. **103**(D14), pp.17149–17161.

Weber, J., Shin, Y.M., Staunton Sykes, J., Archer-Nicholls, S., Abraham, N.L. and Archibald, A.T. 2020. Minimal Climate Impacts From Short-Lived Climate Forcers Following Emission Reductions Related to the COVID-19 Pandemic. *Geophysical Research Letters*. **47**(20).

Weber, M., Arosio, C., Feng, W., Dhomse, S.S., Chipperfield, M.P., Meier, A., Burrows, J.P., Eichmann, K.U., Richter, A. and Rozanov, A. 2021. The Unusual Stratospheric Arctic Winter 2019/20: Chemical Ozone Loss From Satellite Observations and TOMCAT Chemical Transport Model. *Journal of Geophysical Research: Atmospheres*. **126**(6), pp.1–14.

van der Werf, G.R., Randerson, J.T., Giglio, L., Van Leeuwen, T.T., Chen, Y., Rogers, B.M., Mu, M., Van Marle, M.J.E., Morton, D.C., Collatz, G.J., Yokelson, R.J. and Kasibhatla, P.S. 2017. Global fire emissions estimates during 1997-2016. *Earth System Science Data*. **9**(2), pp.697–720.

WHO 2020. Naming the coronavirus disease (COVID-19) and the virus that causes it. [Accessed 14 April 2023]. Available from: https://www.who.int/emergencies/diseases/novel-coronavirus-2019/technical-guidance/naming-the-coronavirus-disease-(covid-2019)-and-the-virus-that-causes-it.

Wild, O. 2007. Modelling the global tropospheric ozone budget: Exploring the variability in current models. *Atmospheric Chemistry and Physics*. **7**(10), pp.2643–2660.

Wild, O., Voulgarakis, A., O’Connor, F., Lamarque, J.F., Ryan, E.M. and Lee, L. 2020. Global sensitivity analysis of chemistry-climate model budgets of tropospheric ozone and OH: Exploring model diversity. *Atmospheric Chemistry and Physics*. **20**(7), pp.4047–4058.

Wilkinson, S., Mills, G., Illidge, R. and Davies, W.J. 2012. How is ozone pollution reducing our food supply? *Journal of Experimental Botany*. **63**(2), pp.527–536.

Wilson, R.C., Fleming, Z.L., Monks, P.S., Clain, G., Henne, S., Konovalov, I.B., Szopa, S. and Menut, L. 2012. Have primary emission reduction measures reduced ozone across Europe? An analysis of European rural background ozone trends 1996-2005. *Atmospheric Chemistry and Physics*. **12**(1), pp.437–454.

Wofsy, S.C., Afshar, S., Allen, H.M., Apel, E., Asher, E.C., Bar letta, B., Bent, J., Bian, H., Biggs, B.C., Blake, D.R., Blake, N., Bourgeois, I., Brock, C.A., Brune, W.H., Budney, J.W., Bui, T.P., Butler, A., Campuzano-Jost, P., Chang, C.S., Chin, M., Commane, R., Correa, G., Crounse, J.D., Cullis, P.D., Daube, B.C., Day, D.A., Dean-Day, J.M., Dibb, J.E., Di Gangi, J.P., Diskin, G.S., Dollner, M., Elkins, J.W., Erdesz, F., Fiore, A.M., Flynn, C.M., Froyd, K., Gesler, D.W., Hall, S.R., Hanisco, T.F., Hannun, R.A., Hills, A.J., Hintsa, E.J., Hoffman, A., Hornbrook, R.S., Huey, L.G., Hughes, S., Jimenez, J.L., Johnson, B.J., Katich, J.M., Keeling, R.F., Kim, M.J., Kupc, A., Lait, L.R., Lamarque, J.-F., Liu, J., McKain, K., Mclaughlin, R.J., Meinardi, S., Miller, D.O., Montzka, S.A., Moore, F.L., Morgan, E.J., Murphy, D.M., Murray, L.T., Nault, B.A., Neuman, J.A., Newman, P.A., Nicely, J.M., Pan, X., Paplawsky, W., Peischl, J., Prather, M.J., Price, D.J., Ray, E., Reeves, J.M., Richardson, M., Rollins, A.W., Rosenlof, K.H., Ryerson, T.B., Scheuer, E., Schill, G.P., Schroder, J.C., Schwarz, J.P., St. Clair, J.M., Steenrod, S.D., Stephens, B.B., Strode, S.A., Sweeney, C., Tanner, D., Teng, A.P., Thames, A.B., Thompson, C.R., Ullmann, K., Veres, P.R., Vieznor, N., Wagner, N.L., Watt, A., Weber, R., Weinzierl, B., Wennberg, P., Williamson, C.J., Wilson, J.C., Wolfe, G.M., Woods, C.T. and Zeng, L.H. 2018. ATom: Merged Atmospheric Chemistry, Trace Gases, and Aerosols. *ORNL Distributed Active Archive Center*.

Wohltmann, I., von der Gathen, P., Lehmann, R., Maturilli, M., Deckelmann, H., Manney, G.L., Davies, J., Tarasick, D., Jepsen, N., Kivi, R., Lyall, N. and Rex, M. 2020. Near-Complete Local Reduction of Arctic Stratospheric Ozone by Severe Chemical Loss in Spring 2020. *Geophysical Research Letters*. **47**(20).

Wolfe, G.M., Nicely, J.M., Clair, J.M.S., Hanisco, T.F., Liao, J., Oman, L.D., Brune, W.B., Miller, D., Thames, A., Abad, G.G., Ryerson, T.B., Thompson, C.R., Peischl, J., McKain, K., Sweeney, C., Wennberg, P.O., Kim, M., Crounse, J.D., Hall, S.R., Ullmann, K., Diskin, G., Bui, P., Chang, C. and Dean-Day, J. 2019. Mapping hydroxyl variability throughout the global remote troposphere via synthesis of airborne and satellite formaldehyde observations (Proceedings of the National Academy of Sciences of the United States of America (2019) 116 (11171–11180) DOI: 10.1073/. *Proceedings of the National Academy of Sciences of the United States of America*. **116**(26), p.13144.

World Health Organisation 2018. Ambient (outdoor) air pollution factsheet. [Accessed 4 February 2019]. Available from: https://www.who.int/en/news-room/fact-sheets/detail/ambient-(outdoor)-air-quality-and-health.

World Health Organization 2022. Ambient (outdoor) air pollution. [Accessed 18 June 2023]. Available from: https://www.who.int/news-room/fact-sheets/detail/ambient-(outdoor)-air-quality-and-health.

World Meterological Organization 1957. WMO Bulletin. *WMO Bulletin*. **5**(4).

WOUDC 2021. OzoneSonde. [Accessed 1 January 2021]. Available from: http://dx.doi.org/10.14287/10000008.

Xing, J., Mathur, R., Pleim, J., Hogrefe, C., Gan, C.M., Wong, D.C., Wei, C., Gilliam, R. and Pouliot, G. 2015. Observations and modeling of air quality trends over 1990-2010 across the Northern Hemisphere: China, the United States and Europe. *Atmospheric Chemistry and Physics*. **15**(5), pp.2723–2747.

Yan, Y., Lin, J., Pozzer, A., Kong, S. and Lelieveld, J. 2019. Trend reversal from high-to-low and from rural-to-urban ozone concentrations over Europe. *Atmospheric Environment*. **213**(January), pp.25–36.

Yang, Y., Shao, M., Wang, X., Nölscher, A.C., Kessel, S., Guenther, A. and Williams, J. 2016. Towards a quantitative understanding of total OH reactivity: A review. *Atmospheric Environment*. **134**(2), pp.147–161.

Young, P.J., Archibald, A.T., Bowman, K.W., Lamarque, J.-F., Naik, V., Stevenson, D.S., Tilmes, S., Voulgarakis, A., Wild, O., Bergmann, D., Cameron-Smith, P., Cionni, I., Collins, W.J., Dalsøren, S.B., Doherty, R.M., Eyring, V., Faluvegi, G., Horowitz, L.W., Josse, B., Lee, Y.H., MacKenzie, I.A., Nagashima, T., Plummer, D.A., Righi, M., Rumbold, S.T., Skeie, R.B., Shindell, D.T., Strode, S.A., Sudo, K., Szopa, S. and Zeng, G. 2013. Pre-industrial to end 21st century projections of tropospheric ozone from the Atmospheric Chemistry and Climate Model Intercomparison Project (ACCMIP). *Atmospheric Chemistry and Physics*. **13**(4), pp.2063–2090.

Young, P.J., Naik, V., Fiore, A.M., Gaudel, A., Guo, J., Lin, M.Y., Neu, J.L., Parrish, D.D., Rieder, H.E., Schnell, J.L., Tilmes, S., Wild, O., Zhang, L., Ziemke, J., Brandt, J., Delcloo, A., Doherty, R.M., Geels, C., Hegglin, M.I., Hu, L., Im, U., Kumar, R., Luhar, A., Murray, L., Plummer, D., Rodriguez, J., Saiz-Lopez, A., Schultz, M.G., Woodhouse, M.T. and Zeng, G. 2018. Tropospheric ozone assessment report: Assessment of global-scale model performance for global and regional ozone distributions, variability, and trends. *Elementa*. **6**.

Zhang, H., Wu, S., Huang, Y. and Wang, Y. 2014. Effects of stratospheric ozone recovery on photochemistry and ozone air quality in the troposphere. *Atmospheric Chemistry and Physics*. **14**(8), pp.4079–4086.

Zhang, J. (Jim), Wei, Y. and Fang, Z. 2019. Ozone Pollution: A Major Health Hazard Worldwide. *Frontiers in Immunology*. **10**.

Zhao, Y., Saunois, M., Bousquet, P., Lin, X., Berchet, A., Hegglin, M., Canadell, J., Jackson, R., Deushi, M., Jöckel, P., Kinnison, D., Kirner, O., Strode, S., Tilmes, S., Dlugokencky, E. and Zheng, B. 2020. On the role of trend and variability of hydroxyl radical (OH) in the global methane budget. *Atmospheric Chemistry and Physics Discussions*. **2011**, pp.1–28.

Zheng, B., Chevallier, F., Yin, Y., Ciais, P., Fortems-Cheiney, A., Deeter, M.N., Parker, R.J., Wang, Y., Worden, H.M. and Zhao, Y. 2019. Global atmospheric carbon monoxide budget 2000-2017 inferred from multi-species atmospheric inversions. *Earth System Science Data*. **11**(3), pp.1411–1436.

Zhou, P., Yang, X. Lou, Wang, X.G., Hu, B., Zhang, L., Zhang, W., Si, H.R., Zhu, Y., Li, B., Huang, C.L., Chen, H.D., Chen, J., Luo, Y., Guo, H., Jiang, R. Di, Liu, M.Q., Chen, Y., Shen, X.R., Wang, X., Zheng, X.S., Zhao, K., Chen, Q.J., Deng, F., Liu, L.L., Yan, B., Zhan, F.X., Wang, Y.Y., Xiao, G.F. and Shi, Z.L. 2020. A pneumonia outbreak associated with a new coronavirus of probable bat origin. *Nature*. **579**(7798), pp.270–273.

Ziemke, J.R., Chandra, S., Duncan, B.N., Froidevaux, L., Bhartia, P.K., Levelt, P.F. and Waters, J.W. 2006. Tropospheric ozone determined from Aura OMI and MLS: Evaluation of measurements and comparison with the Global Modeling Initiative's Chemical Transport Model. *Journal of Geophysical Research Atmospheres*. **111**(19), pp.1–18.

Ziemke, J.R., Kramarova, N.A., Frith, S.M., Huang, L.K., Haffner, D.P., Wargan, K., Lamsal, L.N., Labow, G.J., McPeters, R.D. and Bhartia, P.K. 2022. NASA Satellite Measurements Show Global-Scale Reductions in Free Tropospheric Ozone in 2020 and Again in 2021 During COVID-19. *Geophysical Research Letters*. **49**(15).

Ziemke, J.R., Oman, L.D., Strode, S.A., Douglass, A.R., Olsen, M.A., McPeters, R.D., Bhartia, P.K., Froidevaux, L., Labow, G.J., Witte, J.C., Thompson, A.M., Haffner, D.P., Kramarova, N.A., Frith, S.M., Huang, L.-K., Jaross, G.R., Seftor, C.J., Deland, M.T. and Taylor, S.L. 2019. Trends in Global Tropospheric Ozone Inferred from a Composite Record of TOMS/OMI/MLS/OMPS Satellite Measurements and the

MERRA-2 GMI Simulation. *Atmospheric Chemistry and Physics Discussions*., pp.1–29.

Appendix A

Approximation	Source Reactions	Sink Reactions
Simplified (S-SSA)	$O_3 + hv\ (\lambda < 330\ \mathrm{nm}) \rightarrow O(^1D) + O_2$ $O(^1D) + H_2O \rightarrow 2OH$	$CO + OH\ (+ O_2) \rightarrow CO_2 + HO_2$ $CH_4 + OH\ (+ O_2) \rightarrow H_2O + CH_3OO$ $O_3 + OH \rightarrow HO_2 + O_2$
Savage et al. (2001) (Sav-SSA)	$O_3 + hv\ (\lambda < 330\ \mathrm{nm}) \rightarrow O(^1D) + O_2$ $O(^1D) + H_2O \rightarrow 2OH$ $H_2O_2 + \underline{hv} \rightarrow 2OH$ $CH_3OOH + \underline{hv} \rightarrow HO_2 + HCHO + OH$ $HO_2 + NO \rightarrow OH + NO_2$ $HO_2 + O_3 \rightarrow OH + 2O_2$	$CO + OH\ (+ O_2) \rightarrow CO_2 + HO_2$ $CH_4 + OH\ (+ O_2) \rightarrow H_2O + CH_3OO$ $O_3 + OH \rightarrow HO_2 + O_2$ $HCHO + OH\ (+ O_2) \rightarrow H_2O + HO_2 + CO$ $SO_2 + OH\ (+ O_2) \rightarrow SO_3 + HO_2$ $NO_2 + OH + M \rightarrow HONO_2 + M$ $NO + OH + M \rightarrow HONO + M$ DMS + OH → products $H_2O_2 + OH \rightarrow H_2O + HO_2$ $CH_3OOH + OH \rightarrow H_2O + CH_3OO$ $H_2 + OH\ (+ O_2) \rightarrow H_2O + HO_2$ $C_2H_4 + OH + M \rightarrow C_3H_7OOO + M$ $C_2H_6 + OH \rightarrow H_2O + EtOO$ $C_3H_6 + OH + M \rightarrow C_3H_7OOO + M$ $C_3H_8 + OH \rightarrow n\text{-}PrOO + H_2O$ $C_3H_8 + OH \rightarrow i\text{-}PrOO + H_2O$ $C_4H_{10} + OH \rightarrow C_4H_{10}OO + H_2O$ $C_5H_8 + OH \rightarrow ISO_2$ $C_{10}H_{16} + OH \rightarrow TERPO_2$

Full Chemistry (FC-SSA) **(Monks et al., 2017)**	$O_3 + hv\ (\lambda < 330\ nm) \rightarrow O(^1D) + O_2$ $O(^1D) + H_2O \rightarrow 2OH$ $HO_2 + NO \rightarrow OH + NO_2$ $HO_2 + NO_3 \rightarrow OH + NO_2$ $HO_2 + O_3 \rightarrow OH + O_2$ $HO_2 + CH_3CO_3 \rightarrow OH + CH_3OO$ $O(^1D) + CH_4 \rightarrow OH + CH_3OO$ $O_3 + MACR \rightarrow CH_3C(O)CHO + HCOOH + HO_2 + CO + OH + CH_3CO_3$ $O_3 + C_{10}H_{16} \rightarrow OH + CH_3COCH_2CH_3 + HO_2$ $C_2H_4 + O_3 \rightarrow HCHO + HO_2 + OH + CO + H_2 + CO_2 + HCOOH$ $C_3H_6 + O_3 \rightarrow HCHO + CH_3CHO + OH + HO_2 + C_2H_5OO + CH_3C(O)CHO + CH4 + CO + CH_3OH + CH_3OO + HCOOH$ $C_2H_5OOH + hv \rightarrow CH_3CHO + HO_2 + OH$ $H_2O_2 + hv \rightarrow OH + OH$ $HONO_2 + hv \rightarrow OH + NO_2$ $CH_3OOH + hv \rightarrow HO_2 + HCHO + OH$ $HONO + hv \rightarrow OH + NO$ $C_3H_7OOH + hv \rightarrow C_2H_5CHO + HO_2 + OH$ $C_3H_7OOH + hv \rightarrow (CH_3)_2CO + HO_2 + OH$ $CH_3COCH_2OOH + hv \rightarrow CH_3CO_3 + HCHO + OH$	$CH_4 + OH\ (+ O_2) \rightarrow H_2O + CH_3OO$ $C_2H_6 + OH\ (+ O_2) \rightarrow H_2O + C2H_5OO$ $C_3H_8 + OH\ (+ O_2) \rightarrow n\text{-}PrOO + H_2O$ $C_3H_8 + OH\ (+ O_2) \rightarrow i\text{-}PrOO + H_2O$ $CO + OH\ (+ O_2) \rightarrow CO_2 + HO_2$ $C_2H_5CHO + OH \rightarrow H_2O + C_2H_5CO_3$ $C_2H_5OOH + OH \rightarrow H_2O + C_2H_5OO$ $H_2 + OH\ (+ O_2) \rightarrow H_2O + HO_2$ $H_2O_2 + OH \rightarrow H_2O + HO_2$ $HCHO + OH\ (+ O_2) \rightarrow H_2O + HO_2 + CO$ $HO_2 + OH \rightarrow H_2O\ (+ O_2)$ $HO_2NO_2 + OH \rightarrow H_2O + NO_2$ $HO_2NO_2 + OH \rightarrow H_2O + NO_3$ $HONO + OH \rightarrow H_2O + NO_2$ $CH_3OOH + OH \rightarrow H_2O + CH_3OO$ $CH_3ONO_2 + OH \rightarrow HCHO + NO_2 + H_2O$ $(CH_3)_2CO + OH \rightarrow H_2O + CH_3COCH_2OO$ $CH_3COCH_2OOH + OH \rightarrow H_2O + CH_3COCH_2OO$ $CH_3CHO + OH \rightarrow H_2O + CH_3CO_3$ $NO_3 + OH \rightarrow HO_2 + NO_2$ $O_3 + OH \rightarrow HO_2 + O_2$ $PAN + OH \rightarrow HCHO + NO_2 + H_2O$

	$\mathrm{TERPOOH} + h\nu \rightarrow \mathrm{OH + HO_2 + MACR + MACR + TERPOOH + (CH_3)_2CO}$ $\mathrm{ISOOH} + h\nu \rightarrow \mathrm{OH + MACR + HCHO + HO_2}$ $\mathrm{MACROOH} + h\nu \rightarrow \mathrm{OH + HO_2 + OH + HO_2 + HAC + CO + CH_3C(O)CHO + HCHO}$ $\mathrm{CH_3CO_3H} + h\nu \rightarrow \mathrm{CH_3OO + OH}$ $\mathrm{C_4H_{10}OOH} + h\nu \rightarrow \mathrm{CH_3COCH_2CH_3 + CH_3COCH_2CH_3 + C_2H_5OO + CH_3CHO + HO_2 + HO_2 + OH + OH + OH}$ $\mathrm{CH_3COCH_2CH_3OOH} + h\nu \rightarrow \mathrm{CH_3CO_3 + CH_3CHO + OH}$ $\mathrm{AROMOOH} + h\nu \rightarrow \mathrm{OH + (CH_3)_2CO + HO_2 + CO + CH_3CO_3 + AROMOOH}$	$\mathrm{PPAN + OH \rightarrow CH_3CHO + NO_2 + H_2O}$ $\mathrm{n\text{-}C_3H_7OOH + OH \rightarrow n\text{-}C_3H_7OO + H_2O}$ $\mathrm{i\text{-}C_3H_7OOH + OH \rightarrow i\text{-}C_3H_7OO + H_2O}$ $\mathrm{C_5H_8 + OH \rightarrow ISO_2}$ $\mathrm{ISON + OH \rightarrow CH_3C(O)CH_2OH + NALD}$ $\mathrm{MACR + OH \rightarrow MACRO_2}$ $\mathrm{MPAN + OH \rightarrow CH_3C(O)CH_2OH + NO_2}$ $\mathrm{MACROOH + OH \rightarrow MACRO_2}$ $\mathrm{CH_3C(O)CH_2OH + OH \rightarrow CH_3C(O)CHO + HO_2}$ $\mathrm{CH_3C(O)CHO + OH \rightarrow CH_3CO_3 + CO}$ $\mathrm{NALD + OH \rightarrow HCHO + CO + NO_2}$ $\mathrm{CH_3CO_3H + OH \rightarrow CH_3CO_3}$ $\mathrm{CH_3CO_2H + OH \rightarrow CH_3OO}$ $\mathrm{HCOOH + OH \rightarrow HO_2}$ $\mathrm{CH_3OH + OH \rightarrow HCHO + HO_2}$ $\mathrm{C_{10}H_{16} + OH \rightarrow TERPO_2}$ $\mathrm{TERPOOH + OH \rightarrow TERPO_2}$ $\mathrm{C_4H_{10} + OH \rightarrow C_4H_{10}OO + H_2O}$ $\mathrm{CH_3C(O)CH_2CH_3 + OH \rightarrow CH_3C(O)CH_2CH_3OO}$ $\mathrm{ONIT + OH \rightarrow CH_3C(O)CH_2CH_3 + NO_2 + H_2O}$ $\mathrm{C_3H_7OOOH + OH \rightarrow C_3H_7OOO + H_2O}$ $\mathrm{AROM + OH \rightarrow AROMO_2 + HO_2}$ $\mathrm{AROMOOH + OH \rightarrow AROMO_2}$

		$NO + OH + M \rightarrow HONO + M$ $NO_2 + OH \rightarrow HONO_2 + M$ $C_2H_4 + OH + M \rightarrow C_3H_7OOO + M$ $C_3H_6 + OH + M \rightarrow C_3H_7OOO + M$

Table A.1: Source and sink reactions of OH for the 3 proposed steady-state approximations (Section 4.3.1). MACR represents a lumped species (methacrolein, methyl vinyl ketone and other C4 carbonyls), ISO_2 represents peroxy radicals from the reaction of isoprene and OH (Pöschl et al., 2000), TERP represents generic terpene compound, NALD represents nitroxy acetaldehyde, ONIT represents organic nitrate and AROM represents a generic aromatic compound (Monks et al., 2017).

Appendix B

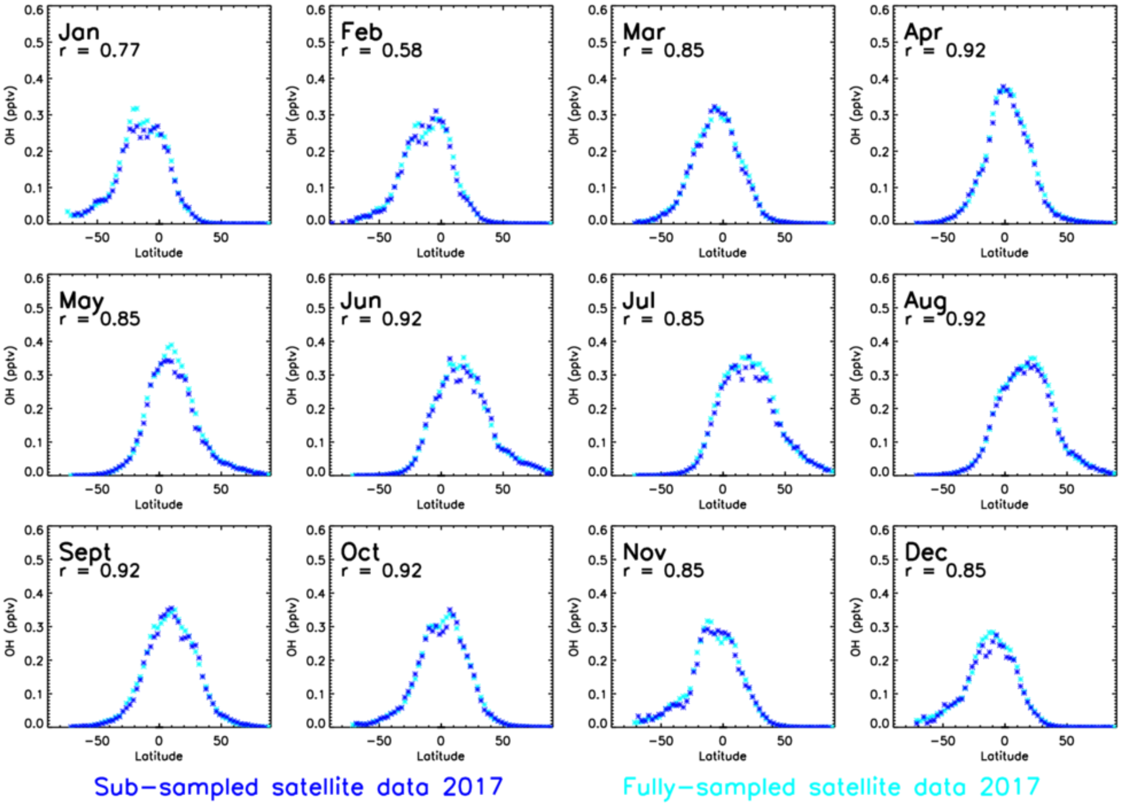

Figure B.1: Zonal mean comparison of S-SSA OH (latitude-averaged) between sub-sampled and fully sampled satellite data for all months in 2017. The Pearson correlation coefficient (r) is displayed for each month.

Appendix C

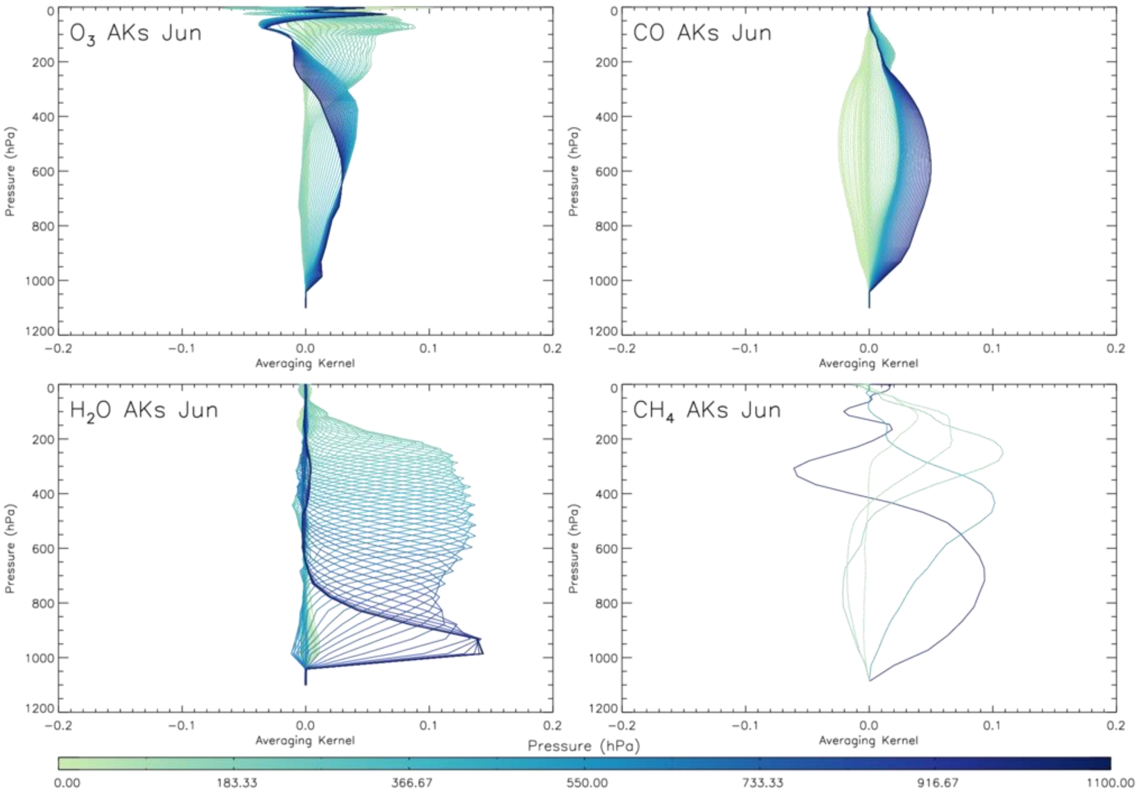

Figure C.1: Globally averaged vertical AKs for June 2010 for O_3, CO and H_2O retrievals from the IASI IMS-Extended scheme and CH_4 retrievals from the IASI scheme.

Appendix D

An uncertainty estimate for the satellite S-SSA OH is derived using relative systematic errors for each of the four retrieved quantities: ~10 % for CO (Pope et al., 2021), ~10 % for H_2O (Trent et al., 2023), ~20 % for O_3 (Pimlott et al. (2022) – supplementary material) and an average of 0.55 % for CH_4 (Siddans et al., 2017). For the random errors, large-scale averaging in the analysis in Chapter 4 will reduces random errors to values which are much smaller by comparison. Here, the errors on the retrieved species are assumed to be uncorrelated.

The simplified steady-state approximation used in Section 4.3.1 (Equation 4.2) is repeated here as Equation D.1:

$$[\mathrm{OH}]_{\mathrm{steady-state}} = \frac{\left(\frac{2 j_1 k_1 [\mathrm{O_3}][\mathrm{H_2O}]}{k_2[\mathrm{N_2}] + k_3[\mathrm{O_2}] + k_1[\mathrm{H_2O}]}\right)}{(k_4[\mathrm{CH_4}] + k_5[\mathrm{CO}] + k_6[\mathrm{O_3}])} \qquad \textbf{Equation D.1}$$

To estimate the error on the satellite-derived S-SSA OH, the systematic errors of the satellite retrieved species were combined. The combination of the uncertainties is based on Equation D.2 and Equation D.3 from Hogan (2006):

$$For\ a = b + c\ \ then\ (\Delta a)^2 = (\Delta b)^2 + (\Delta c)^2 \qquad \textbf{Equation D.2}$$

$$For\ a = bc\ or\ a = b/c\ \ then\ \left(\frac{\Delta a}{a}\right)^2 = \left(\frac{\Delta b}{b}\right)^2 + \left(\frac{\Delta c}{c}\right)^2 \qquad \textbf{Equation D.3}$$

where b and c are variables and Δa indicates the uncertainty of a etc.

For an equation with numerator (γ) and denominator (δ), the uncertainty ($\Delta[OH]$) is shown in Equation D.4 (based on Equation D.2 and Equation D.3):

$$\Delta[OH] = \sqrt{\left(\frac{\Delta\gamma}{\gamma}\right)^2 + \left(\frac{\Delta\delta}{\delta}\right)^2} \times [OH] \qquad \textbf{Equation D.4}$$

The numerator of Equation D.1 (γ) is defined here in Equation D.5:

$$\gamma = \frac{2\, j_1\, k_1\, [H_2O]\, [O_3]}{k_2\, [N_2] + k_3\, [O_2] + k_1\, [H_2O]} = \frac{\alpha}{\beta} \qquad \textbf{Equation D.5}$$

Uncertainty in γ is calculated in Equation D.6 - Equation D.9:

$$\left(\frac{\Delta\gamma}{\gamma}\right)^2 = \left(\frac{\Delta\alpha}{\alpha}\right)^2 + \left(\frac{\Delta\beta}{\beta}\right)^2 \qquad \textbf{Equation D.6}$$

$$\left(\frac{\Delta\alpha}{\alpha}\right)^2 = \left(\frac{\Delta[H_2O]}{[H_2O]}\right)^2 + \left(\frac{\Delta[O_3]}{[O_3]}\right)^2 \qquad \textbf{Equation D.7}$$

$$(\Delta\beta)^2 = (k_1 \Delta[H_2O])^2 \qquad \textbf{Equation D.8}$$

$$\left(\frac{\Delta\beta}{\beta}\right)^2 = \frac{(k_1 \Delta[H_2O])^2}{(k_2\, [N_2] + k_3\, [O_2] + k_1\, [H_2O])^2}. \qquad \textbf{Equation D.9}$$

The denominator of Equation D.1 (δ) is defined here in Equation D.10:

$$\delta = k_4\,[CH_4] + k_5\,[CO] + k_6\,[O_3] \qquad \textbf{Equation D.10}$$

Uncertainty in δ is calculated in Equation D.11 and Equation D.12:

$$(\Delta\delta)^2 = (k_4\Delta[CH_4])^2 + (k_5\Delta[CO])^2 + (k_6\Delta[O_3])^2 \qquad \textbf{Equation D.11}$$

$$\left(\frac{\Delta\delta}{\delta}\right)^2 = \frac{(k_4\Delta[CH_4])^2 + (k_5\Delta[CO])^2 + (k_6\Delta[O_3])^2}{(k_4\,[CH_4] + k_5\,[CO] + k_6\,[O_3])^2} \qquad \textbf{Equation D.12}$$

Uncertainty in [OH] is then calculated in Equation D.13:

$$\Delta[OH] = \sqrt{\left(\frac{\Delta\alpha}{\alpha}\right)^2 + \left(\frac{\Delta\beta}{\beta}\right)^2 + \left(\frac{\Delta\delta}{\delta}\right)^2} \times [OH] \qquad \textbf{Equation D.13}$$

Figure D.1 shows the spatial distribution of OH for all months of 2010, which corresponds to an average of 0.5 ×10^6 – 0.7 ×10^6 molecule cm^{-3} (23 – 24%).

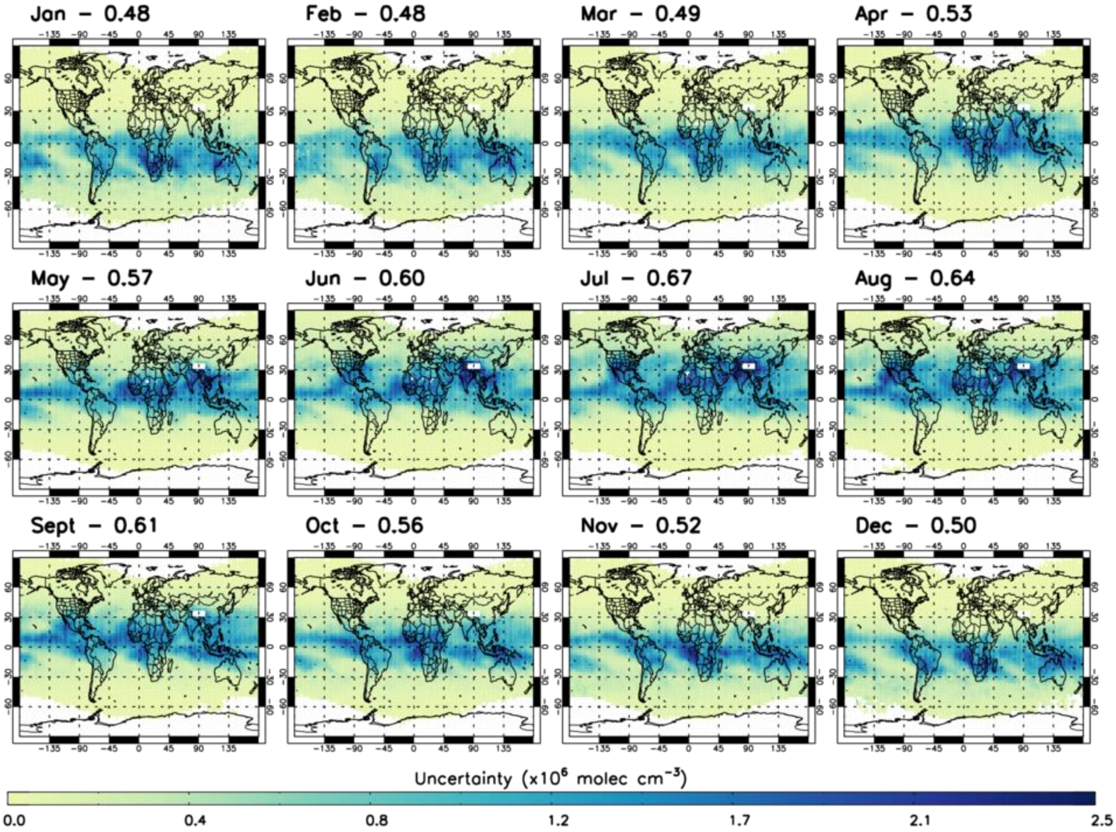

Figure D.1: Estimated uncertainty for satellite S-SSA OH for all months of 2010 in units of ×10^6 molecule cm^{-3}. Global mass-weighted mean estimated uncertainty in OH (×10^6 molecule cm^{-3}) are labelled for each month.

This method assumes there is no uncertainty in the rate constants. To assess the validity of this assumption, TOMCAT and ATom measurements of j_1 have been compared (Figure D.2). The TOMCAT model values of j_1 are low compared to the ATom measurements. The MB ranges between -0.09 ×10^{-5} and -1.29 ×10^{-5} s^{-1} across the 4 campaigns. Notably, there are several areas of disagreement, such as near the equator in ATom-2, between 60°S and 20°S in ATom-3, between the equator to 20°N in ATom-

4 and between 40°N to 60°N in ATom-4. However, the datasets have very different spatial resolutions and therefore the comparison is difficult.

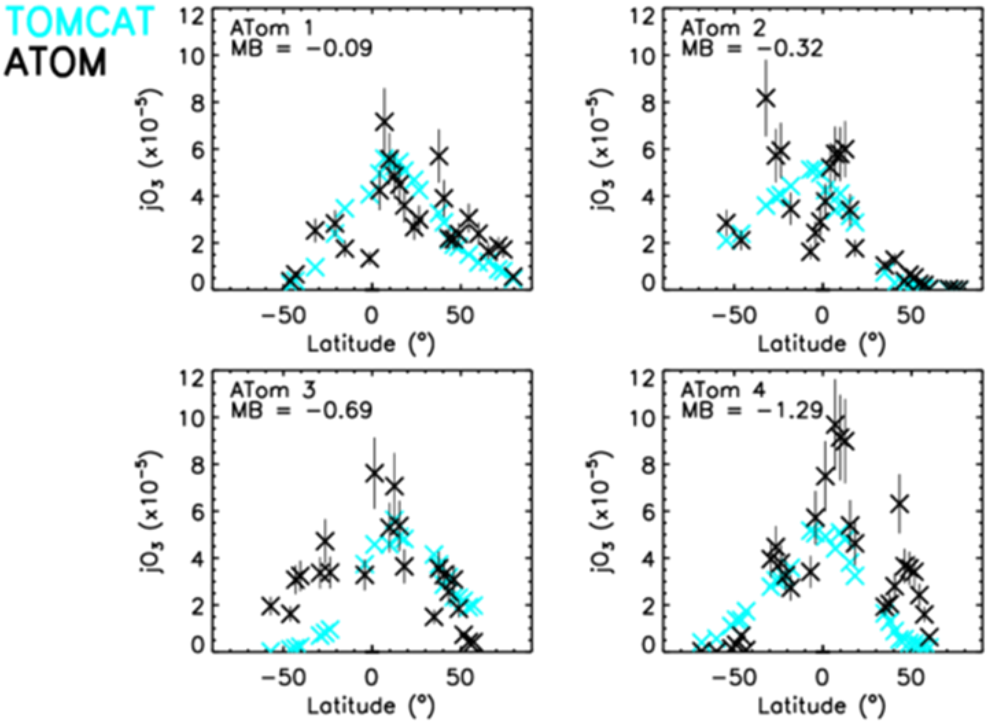

Figure D.2: Comparison between TOMCAT simulated j_1 and ATom j_1 measurements (from the CAFS instrument). Both datasets are averaged for each model latitude bin (2.8°). The four panels show the data split into the individual campaigns. ATom observations are filtered for 600–700 hPa and 08:00–11:00 LT. The MB (TOMCAT subtract ATom) are displayed in each panel. Error bars of ± 20 % (representing CAFS uncertainty (Shetter and Müller, 1999)) are displayed. All data is in units of ×10^{-5} s^{-1}.

Appendix E

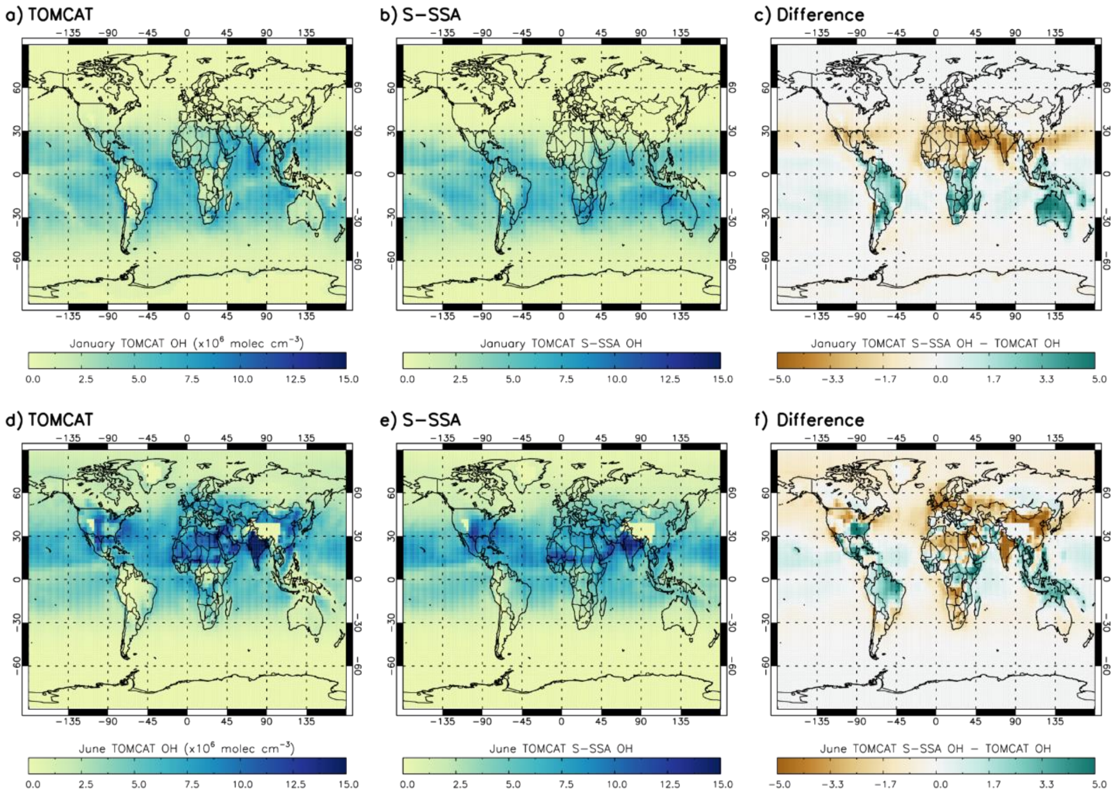

Figure E.1: [OH] averaged over the 800-1000 hPa range for (a) TOMCAT (full model), (b) TOMCAT S-SSA and (c) the difference (TOMCAT S-SSA subtract TOMCAT) for January 2010. Panels (d)-(f) represent comparisons for June 2010. All values are in in units of ×10^6 molecule cm^{-3}.

Appendix F

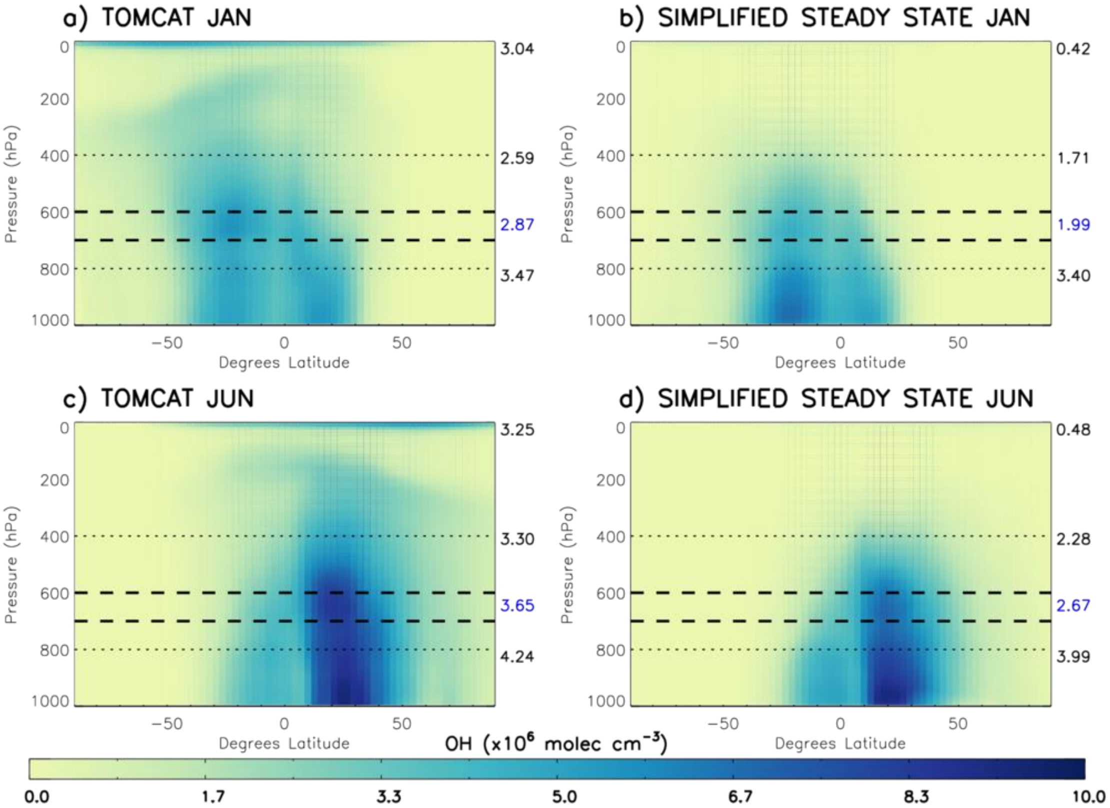

Figure F.1: (a) TOMCAT OH in January 2017, (b) TOMCAT S-SSA OH in January 2017, (c) TOMCAT OH in June 2017, (d) TOMCAT S-SSA OH in June 2017. The dashed lines represent the proposed area of best agreement (600–700 hPa). The numbers on the right edge of each plot represent the mass-weighted mean OH of the pressure region shown by the dotted lines (from top to bottom): < 400 hPa, 400 – 800 hPa, 600 – 700 hPa (blue) and 800 hPa – surface. All units are in ×10^6 molecule cm^{-3}.

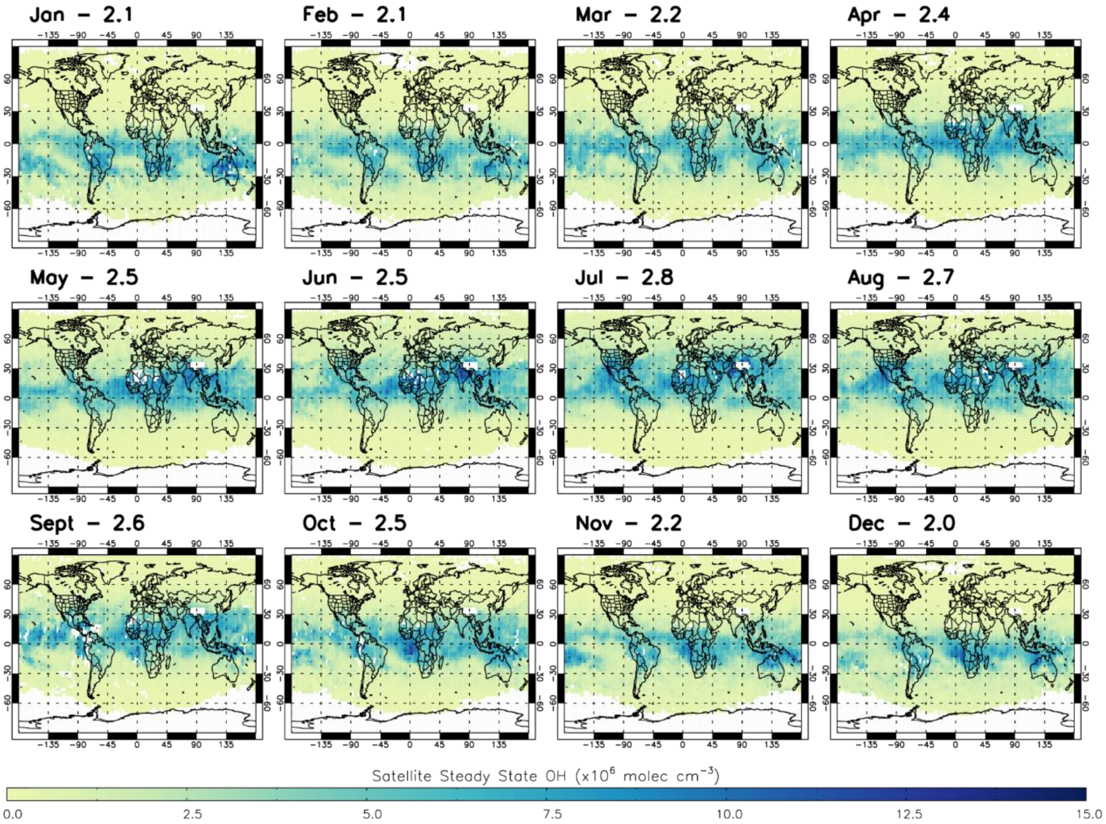

Figure F.2: Global satellite-derived OH (S-SSA) in units of ×10^6 molecule cm^{-3} for 2017. Mass-weighted global monthly means are presented above each panel.

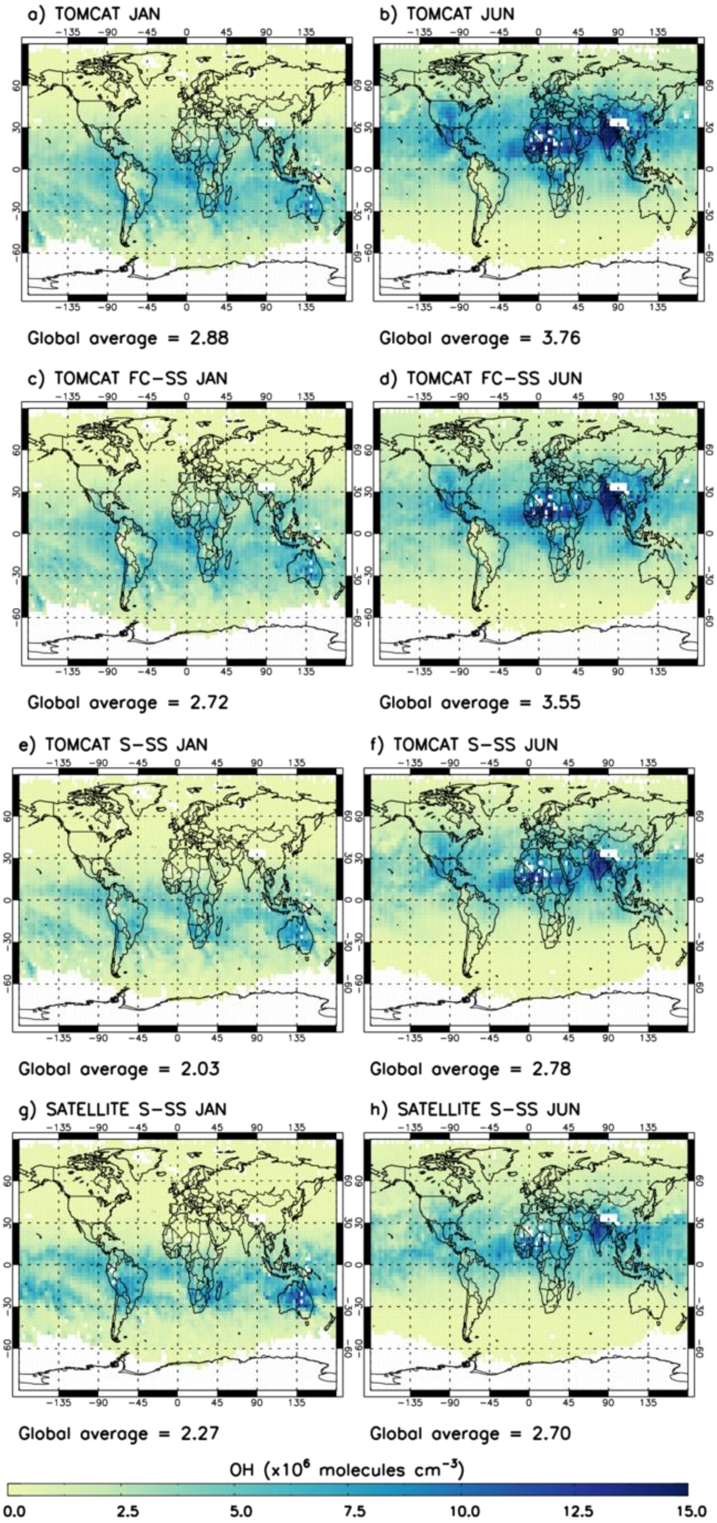

Figure F.3: (a) TOMCAT OH in January 2017, (b) repeated for June 2017, (c) TOMCAT FC-SSA OH in January 2017, (d) repeated for June 2017, (e) TOMCAT S-SSA OH in January 2017, (f) repeated for June 2017, (g) satellite S-SSA in January 2017, (h) repeated for June 2017. All averaged across the 600 – 700 hPa pressure layer. Global average OH values for the selected pressure layer are given below each panel in units of ×10^6 molecule cm^{-3}.

Appendix G

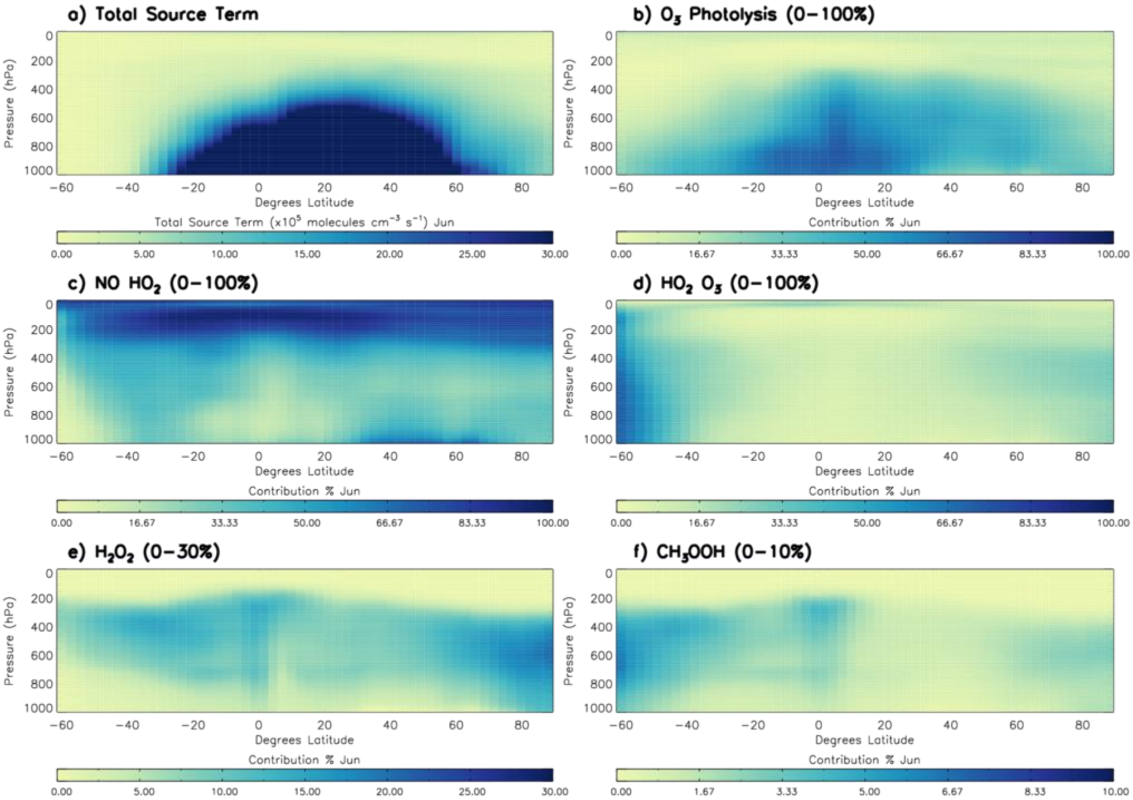

Figure G.1: June 2010 latitude averaged (a) total Sav-SSA source term and (b) – (f) the different source terms as a % of the total source term. The individual source terms are: (b) photolysis of O_3 to form $O(^1D)$ which reacts with H_2O for form OH, (c) reaction of NO + HO_2, (d) reaction of HO_2 + O_3, (e) photolysis of H_2O_2 and (f) photolysis of CH_3OOH. The data is presented from 60°S–90°N due to polar night at latitudes >60°S during June. Note the differing scales on the panels.

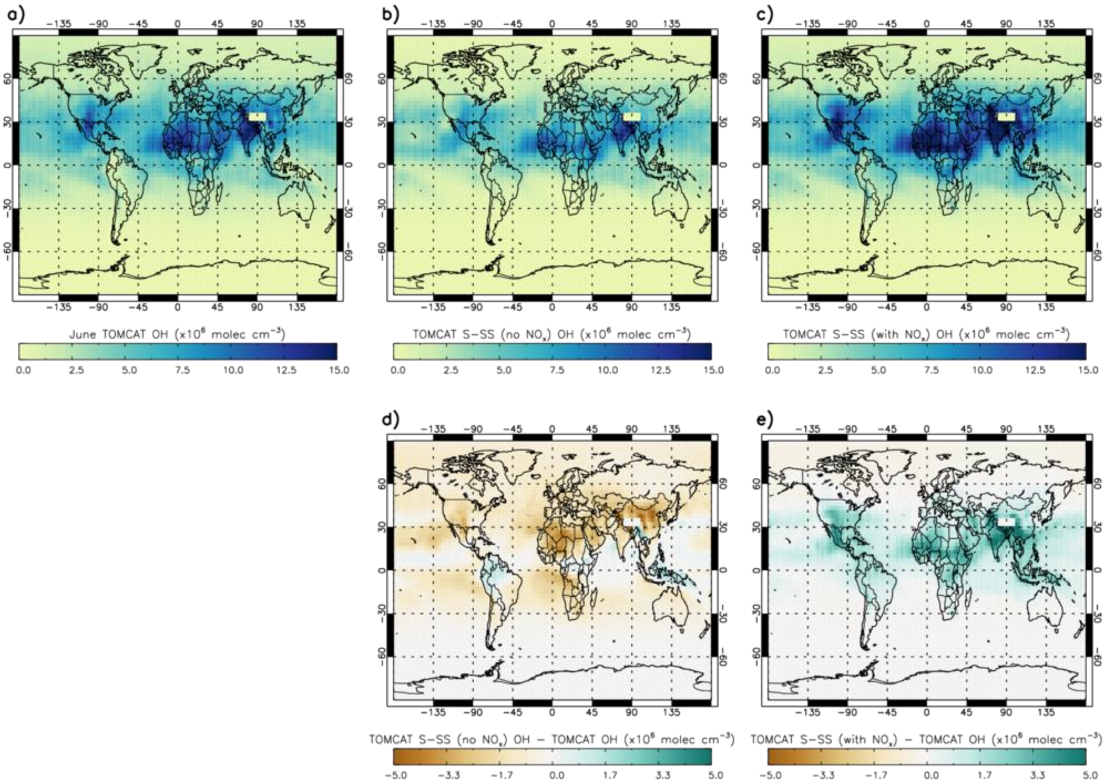

Figure G.2: Comparison of [OH] for June 2010. (a) TOMCAT [OH], (b) S-SSA [OH], (c) S-SSA with NO_x sources/sinks ($NO + HO_2$, $NO + OH + M$, $NO_2 + OH + M$), (d) difference between S-SSA [OH] and TOMCAT [OH] and (e) difference between S-SSA [OH] with NO_x sources/sinks and TOMCAT [OH]. All values are averaged for the 600-700 hPa pressure region.

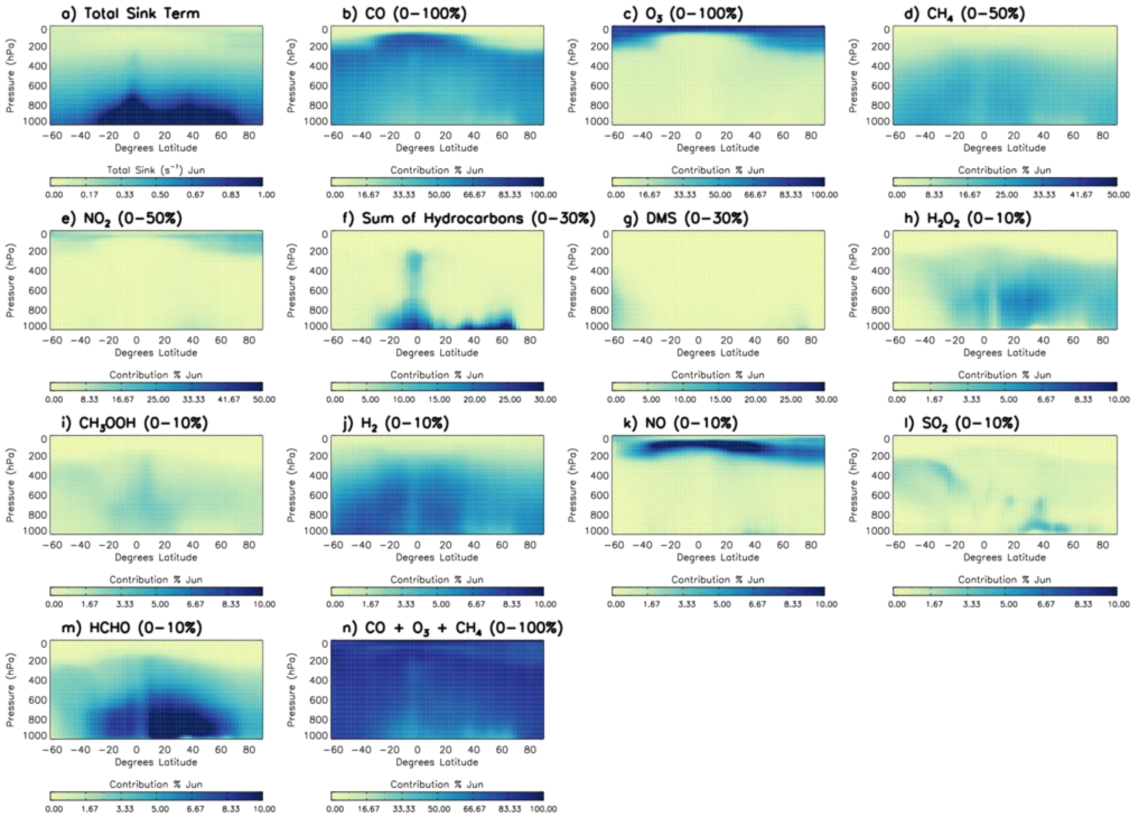

Figure G.3: June 2010 latitude averaged (a) total Sav-SSA sink term and (b) – (n) the different sink terms as a % of the total sink term. The individual sink terms are: b) CO, (c) O_3, (d) CH_4, (e) NO_2, (f) sum of hydrocarbons (C_2H_4, C_2H_6, C_3H_6, C_3H_8, C_5H_8, C_4H_{10}), (g) dimethyl sulfide (DMS), (h) H_2O_2, (i) CH_3OOH, (j) H_2, (k) NO, (l) SO_2, (m) HCHO and (n) sum of CO, O_3 and CH_4 (total sink term for S-SSA/Equation 4.2). The data is presented from 60°S–90°N due to polar night at latitudes >60°S during June. Note the differing scales on the panels.

Appendix H

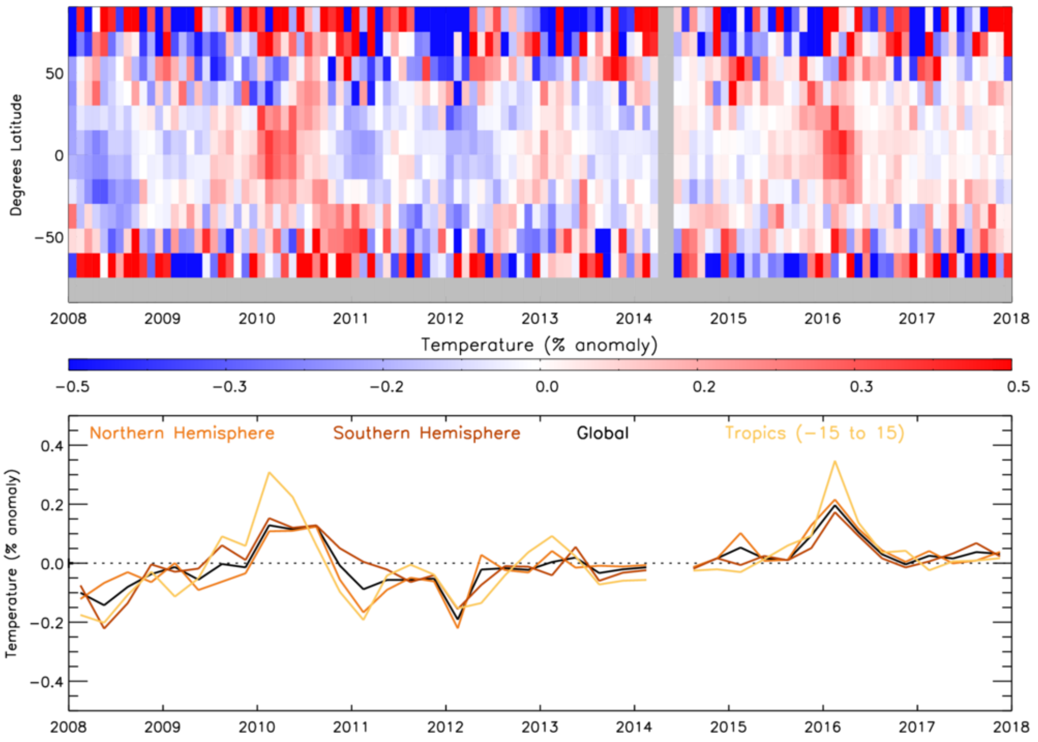

Figure H.1: Monthly mean temperature anomaly for 2008–2017 (pressure layer 600 – 700 hPa): (a) 15° latitude bins and (b) 3-month average for global (all latitudes), NH (equator – 90°N), SH (90°S – equator) and tropics (15°S – 15°N). Anomaly is relative to a 2008–2017 baseline.

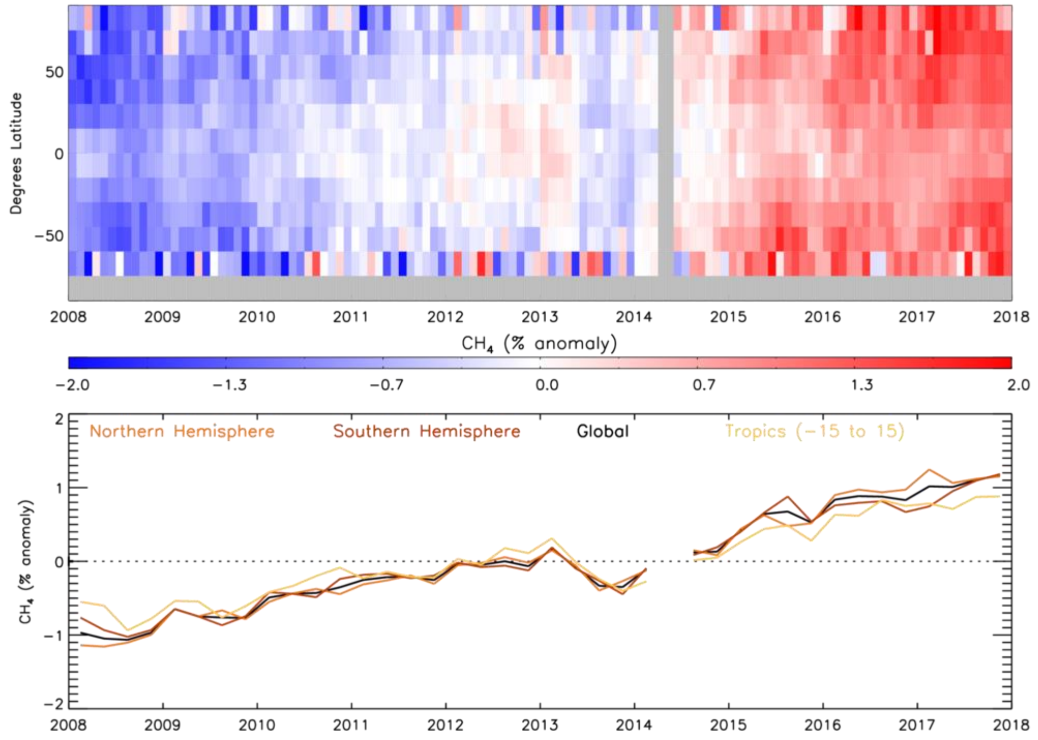

Figure H.2: As Figure H.1 for CH_4.

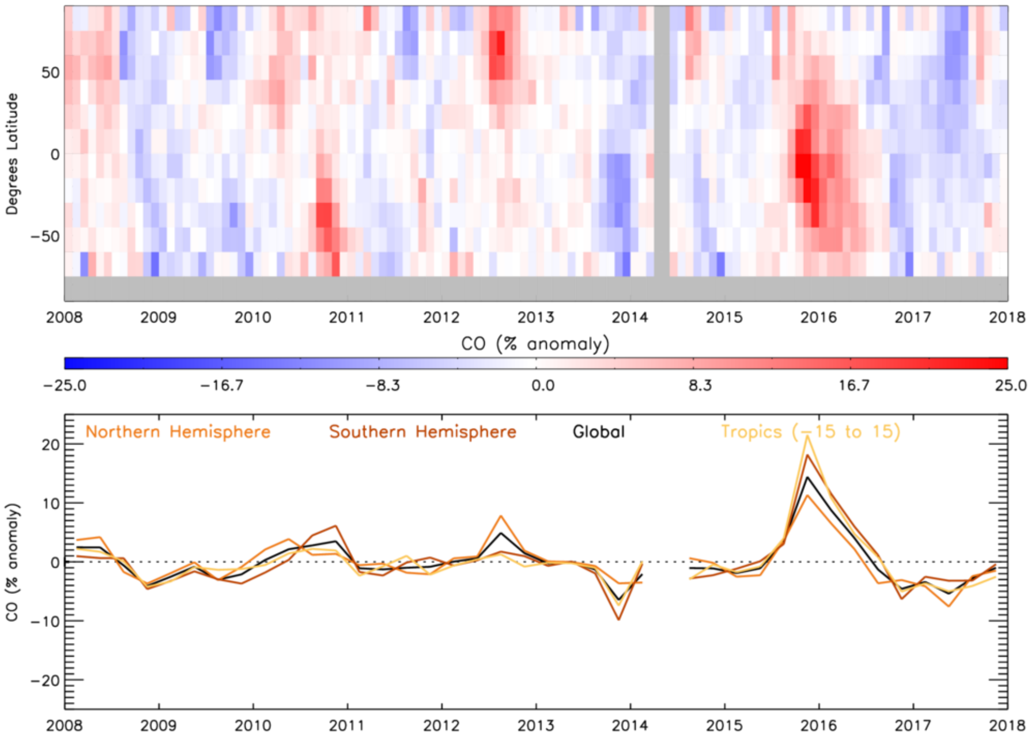

Figure H.3: As Figure H.1 for CO.

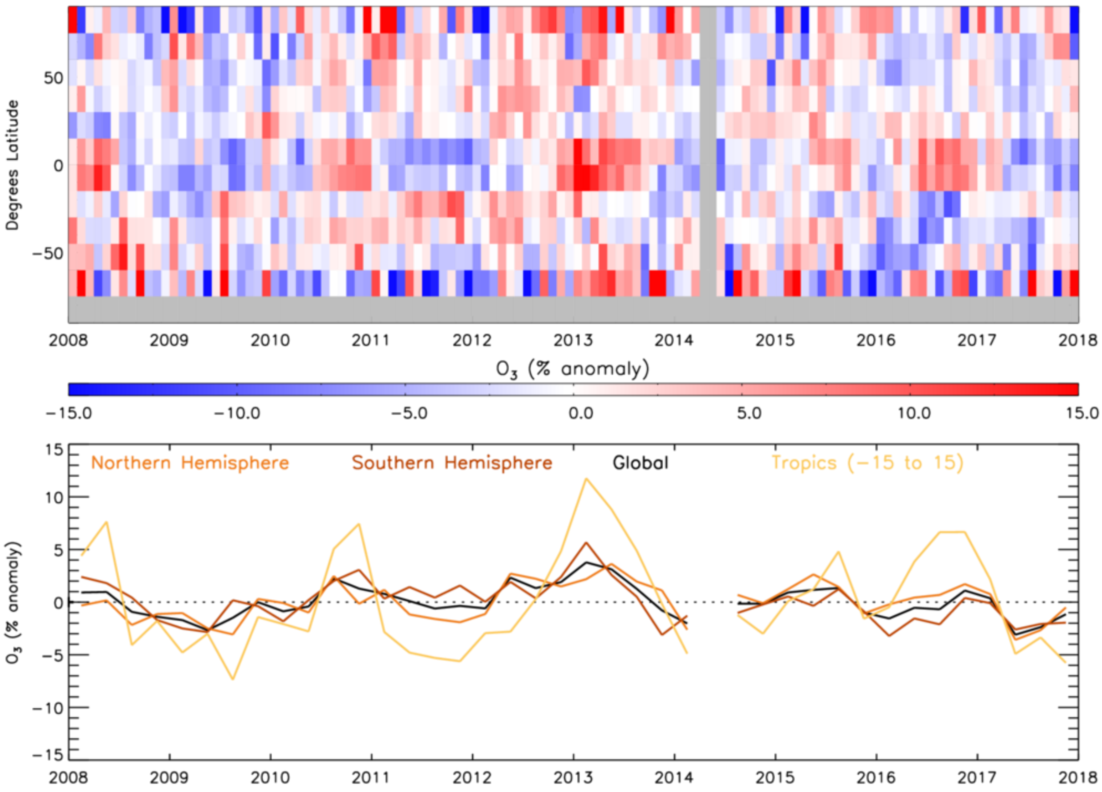

Figure H.4: As Figure H.1 for O_3.

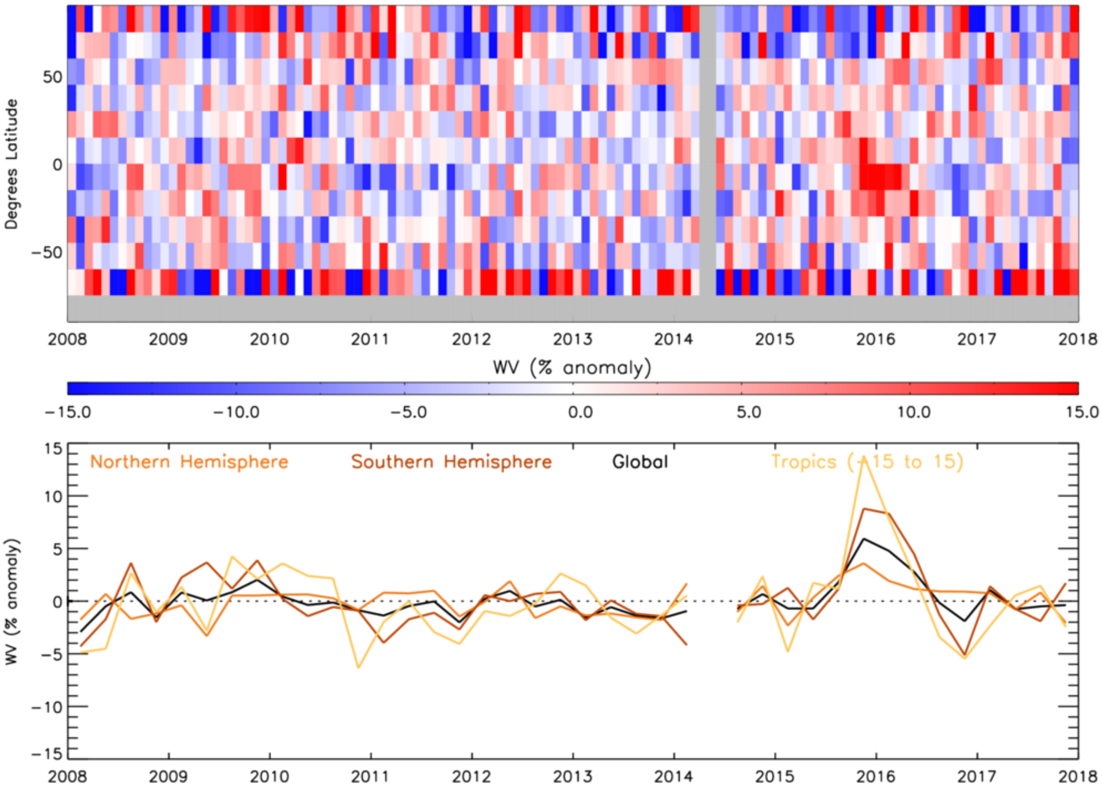

Figure H.5: As Figure H.1 for H_2O.

Appendix I

1

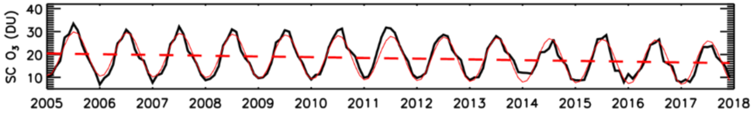

INCLUDED – whole record
*Trend= −0.33 DU/year

3

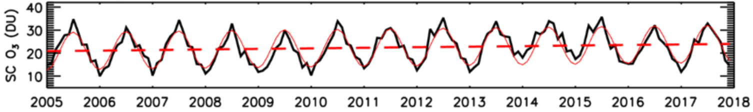

INCLUDED – whole record
*Trend= 0.24 DU/year

5

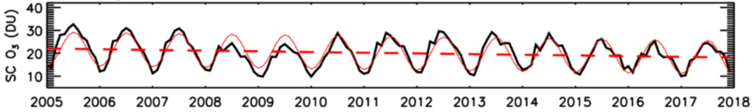

INCLUDED – whole record
*Trend= −0.30 DU/year

7

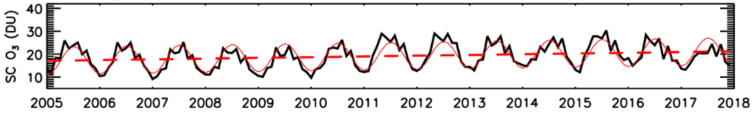

INCLUDED – whole record
*Trend= 0.32 DU/year

9

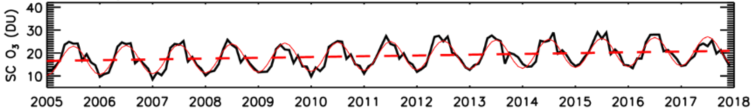

INCLUDED – whole record
*Trend= 0.34 DU/year

11

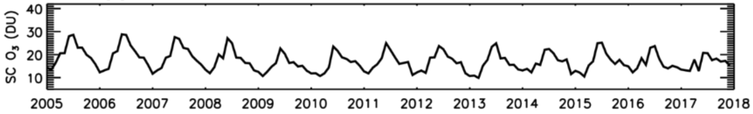

EXCLUDED

13

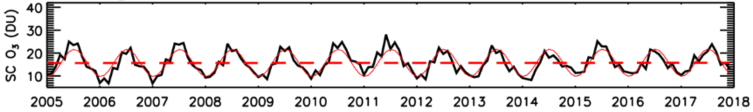

INCLUDED – whole record
Trend= 0.01 DU/year

15

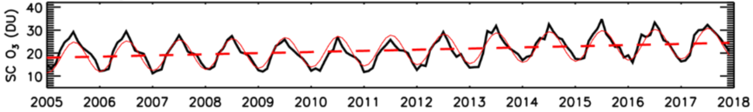

INCLUDED – whole record
*Trend= 0.50 DU/year

17

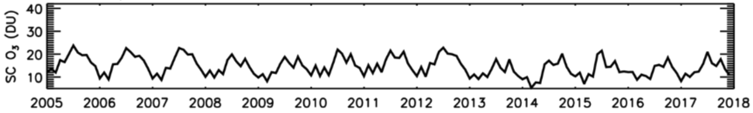

EXCLUDED

19

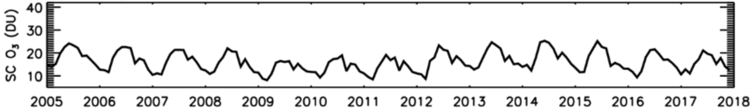

EXCLUDED

21

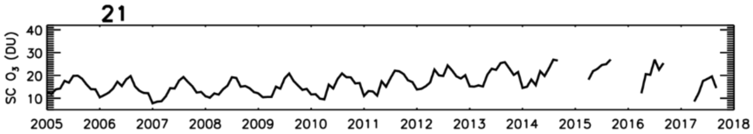

INCLUDED – partial record

23

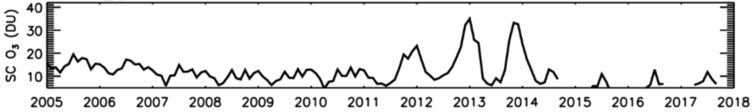

EXCLUDED

25

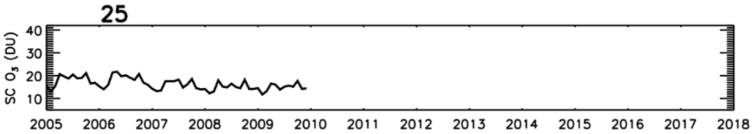

EXCLUDED

27

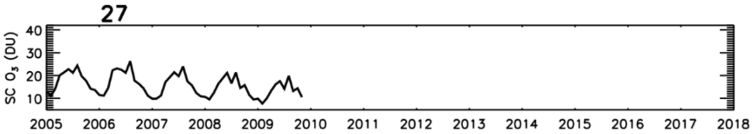

INCLUDED – partial record

29

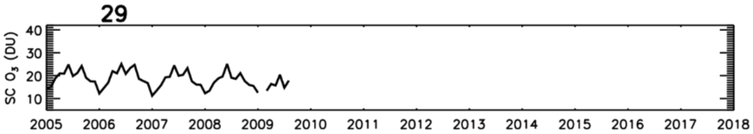

INCLUDED – partial record

31

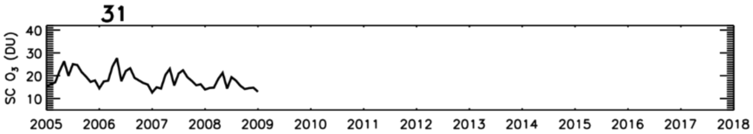

EXCLUDED

33

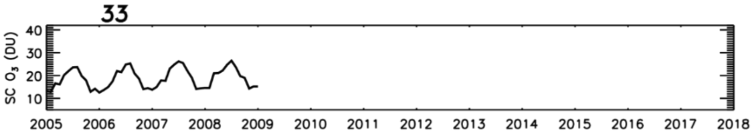

INCLUDED – partial record

35

EXCLUDED

37

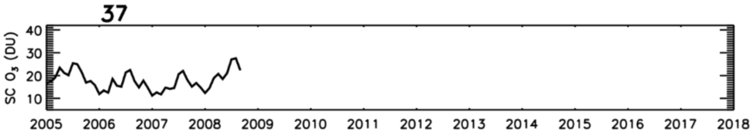

EXCLUDED

39

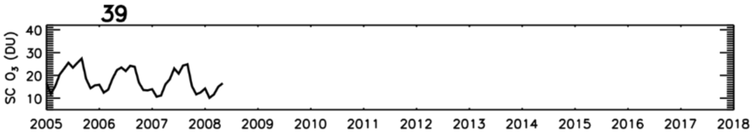

INCLUDED – partial record

41

INCLUDED – partial record

43

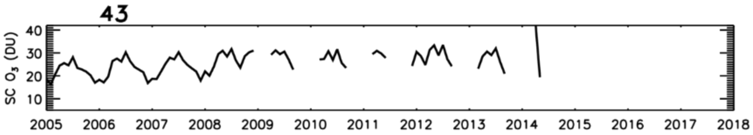

INCLUDED – partial record

45

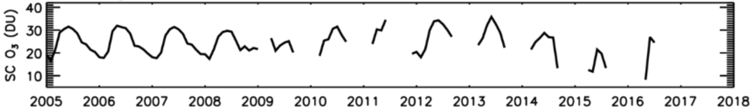

INCLUDED – partial record

47

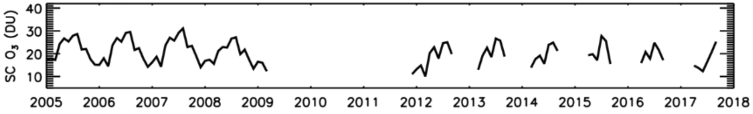

INCLUDED – partial record

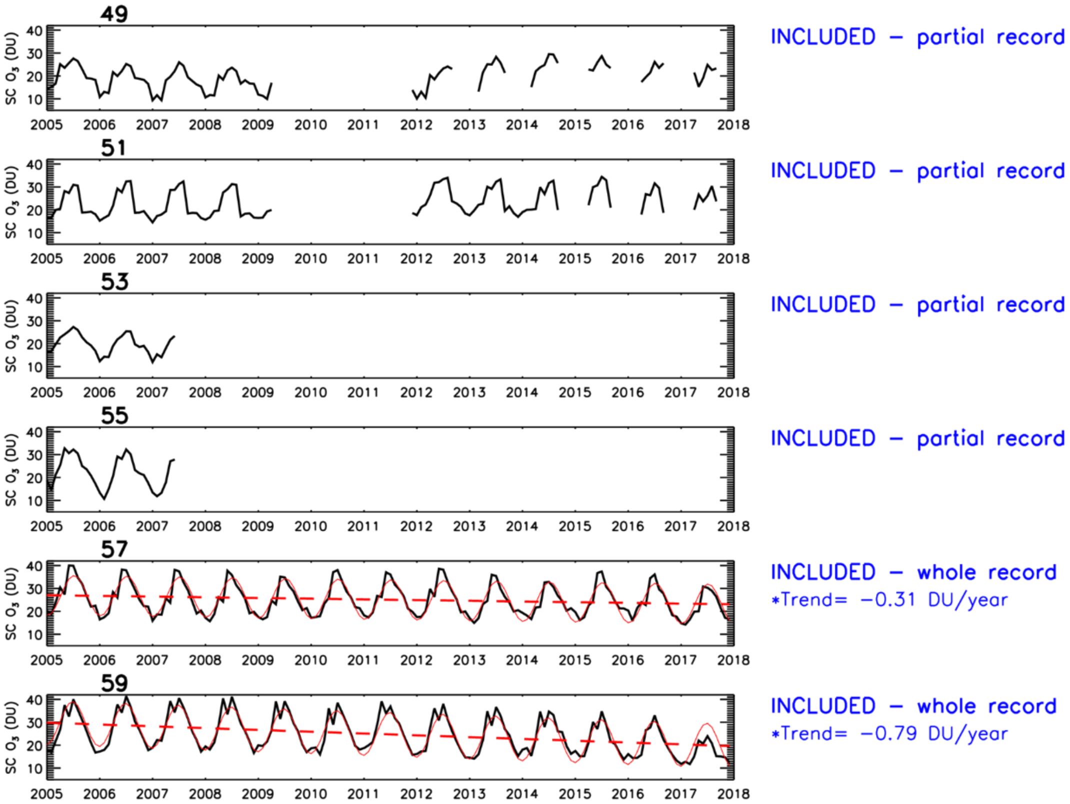

Figure I.1: Timeseries of European sub-column O_3 (surface – 450 hPa, DU) across all 30 OMI viewing angles/rows (labelled as odd numbers between 1 and 60). The rows are labelled as included, either for the whole record or part of the record, or excluded from the BE scenario described in 5.3.1.1. For the records that have been included for the whole record, a seasonal model and linear trend (DU year^{-1}) based on the row record are shown. An * before the word "Trend" indicates that the trend is significant at the 95% confidence level.

Appendix J

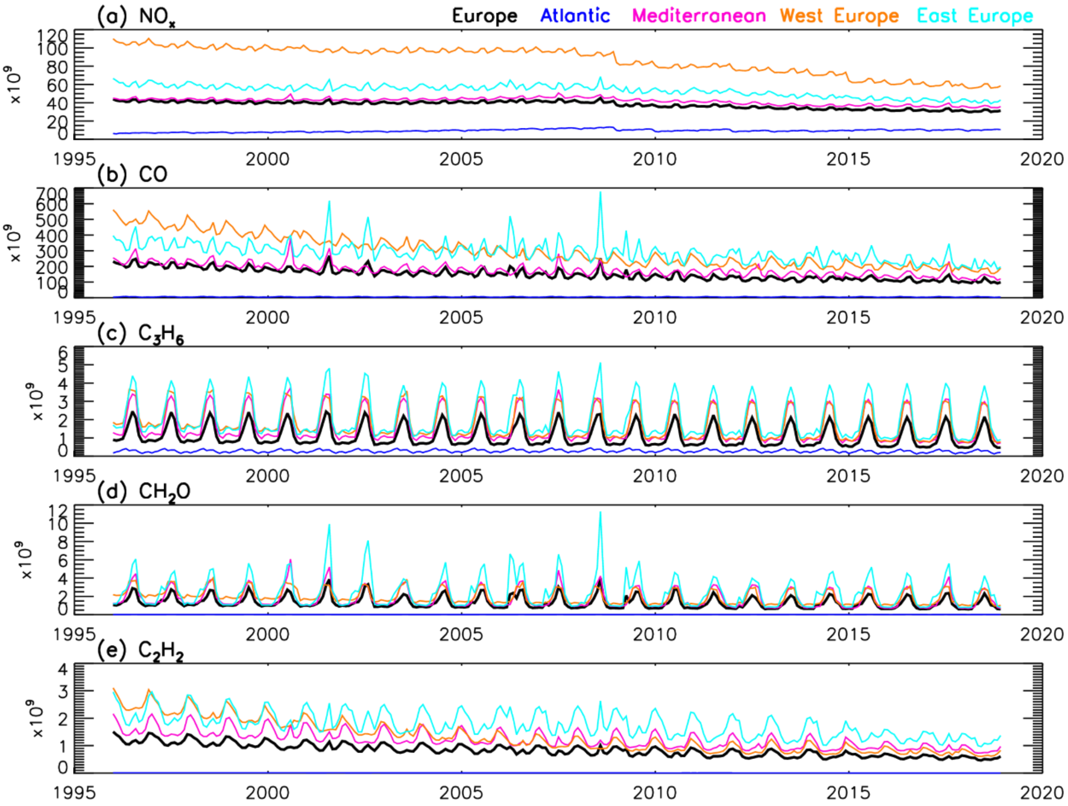

Figure J.1: Averaged surface emissions across the European domain for 1996 – 2018 of (a) NO$_x$, (b) CO, (c) C$_3$H$_6$, (d) HCHO and (e) C$_2$H$_2$. All in units of ×10^9 molecules cm^{-2} s^{-1}. Four sub-regions of Europe (Atlantic, Mediterranean, West and East Europe) are shown.

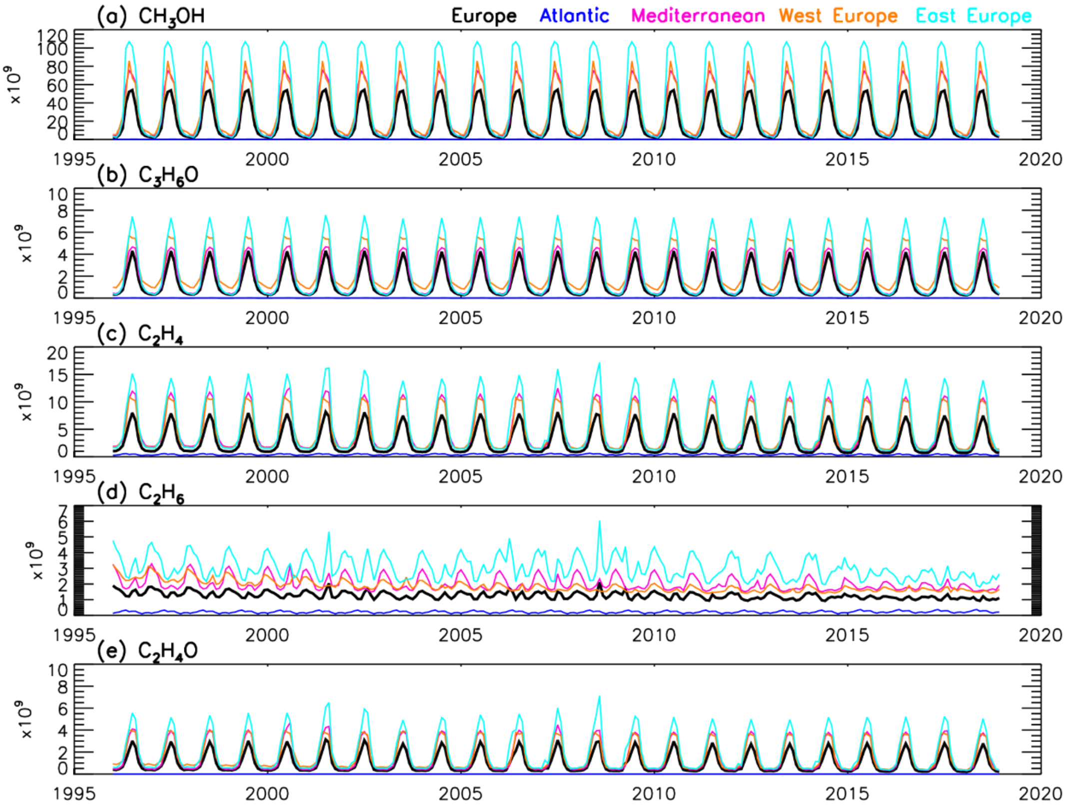

Figure J.2: As Figure J.1 for (a) CH_3OH, (b) C_3H_6O, (c) C_2H_4, (d) C_2H_6 and (e) C_2H_4O.

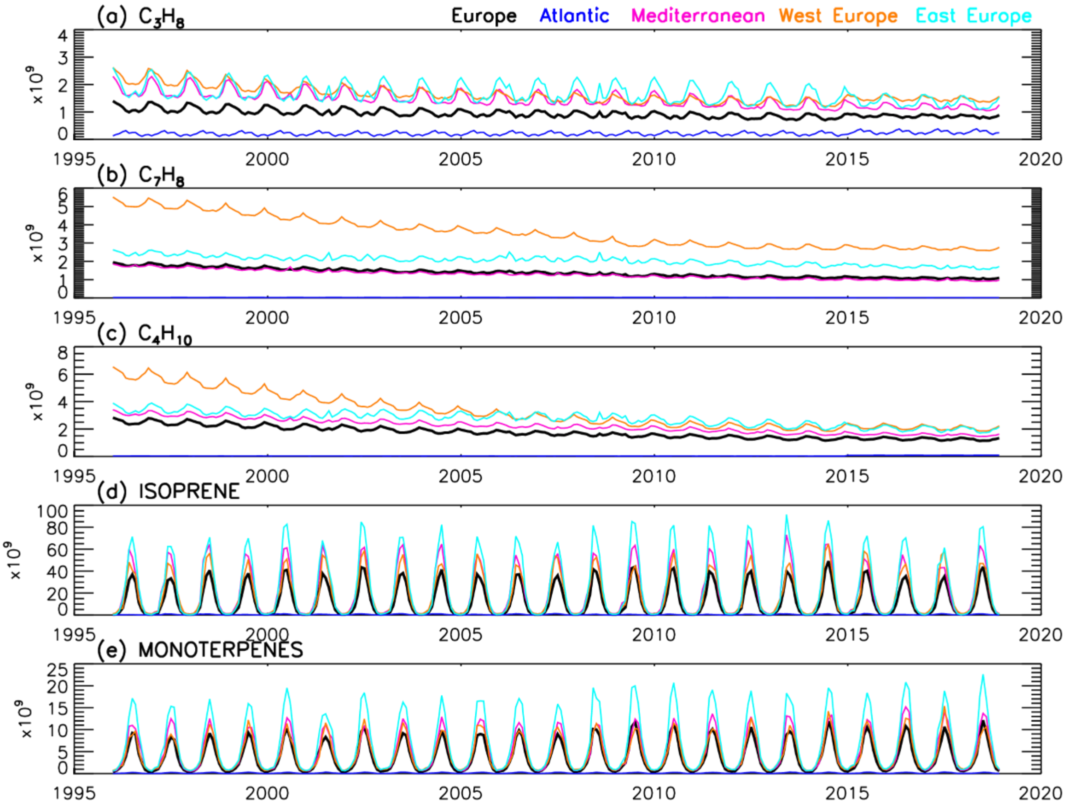

Figure J.3: As Figure J.1 for (a) C_3H_8, (b) C_7H_8, (c) C_4H_{10}, (d) isoprene and (e) monoterpenes.

Appendix K

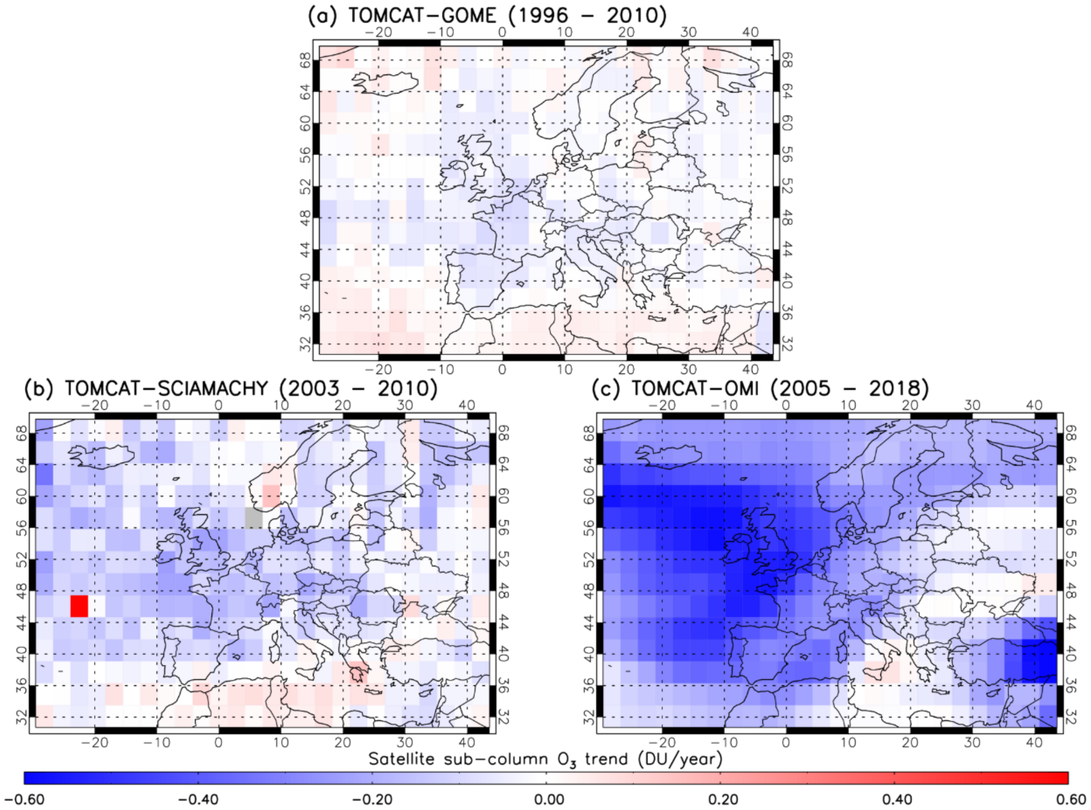

Figure K.1: Linear component of the linear-seasonal trend model applied to a timeseries of co-located model record (with AKs applied) sub-column O_3 (surface – 450 hPa) for each grid-box across the European domain (DU year^{-1}) for (a) TOMCAT-GOME, (b) TOMCAT-SCIAMACHY and (c) TOMCAT-OMI. The respective time periods are labelled.